Quantitative electrical imaging of slope moisture dynamics

Rosalind Mary Hen-Jones

BSc (Hons), MSc

A thesis submitted for the degree of Doctor of Philosophy

at Newcastle University

School of Civil Engineering and Geosciences

Newcastle University

Newcastle-upon-Tyne

NE1 7RU

February 2018

Abstract

Future climate change is likely to affect the factors which determine the stability of engineered slopes, which constitute a third of UK transport infrastructure. The cost of remediation works being approximately ten times that of preventative action, accurate methods of stability assessment are of increasing importance to stakeholders. Electrical resistivity tomography allows high resolution volumetric time-lapse imaging of subsurface resistivity distribution, which, combined with proxy relationships, offers the potential to quantitatively investigate slope moisture dynamics. Therefore, it is essential that the relationships between resistivity and the geotechnical parameters which impact slope stability (water content, suction and shear strength) are fully resolved, particularly where soils undergo significant cycles of drying and wetting, which progressively weaken fill material. This PhD thesis presents a study to establish these relationships for a remoulded clay taken from a purpose-built test embankment in Northumberland, United Kingdom. A rigorous, multi-scalar laboratory testing programme was combined with a three year geoelectrical field monitoring experiment, supported by a network of point sensors. To verify the resolution of the geoelectric method, the test site was subjected to series of hydrodynamic perturbations.

To simulate seasonal effects, drying and wetting cycles were imposed on laboratory specimens. Results indicated an inverse power relationship between soil resistivity and water content, and showed the more conventional, two point method to over-estimate values due to the inclusion of contact resistances. Linear hysteretic relationships were established between undrained shear strength and water content, demonstrating suction loss between drying and wetting paths due to hysteretic soil water retention. Laboratory relationships were observed to evolve with ongoing seasonal cycling, due to soil fabric deterioration associated with drying beyond the continuity of the pore water phase. Trends observed in the laboratory were supported by images obtained from scanning electron microscopy. Waxman-Smits and Van Genuchten modelling parameters were applied to resistivity – water content and soil water retention curves respectively, defining proxy relationships which were then used to translate field resistivity data into estimates of both water content and suction.

These images captured general seasonal trends in subsurface moisture processes, in response to sustained environmental conditions, allowing a structured hydrological model of the test embankment to be resolved. Localised damping of the geotechnical response was observed, as a function of depth, aspect and compaction. On a weekly scale, the development of near-surface cracks was captured during the summer months. Rainwater ingress following rapid rainfall events was investigated via daily time-lapse imaging, and highlighted seasonal differences in infiltration processes. Proxy-derived water content estimates compared very well with those measured using the point sensor network, both qualitatively and quantitatively, providing invaluable information on the dynamic moisture processes which precede slope failure, with particular reference to soil fabric deterioration.

Ultimately, this thesis describes a methodology for translating ERT-derived resistivity data into information directly relevant to slope stability. It highlights the importance of considering soil water retention when estimating in situ soil suctions, employing a localised saturation history-based approach to account for spatial variation. The issue of ambiguity inherent to the nature of inverse theory is discussed, with suggestions for its minimisation, including the use of three- rather than two-dimensional resistivity data, temperature correction and correlation with point sensors. This methodology has been incorporated into a set of computer programmes which read in raw ERT data and automatically convert to geotechnical data, furthering the development of a fully-automated slope stability monitoring system.

Acknowledgements

First of all, I would like to thank my wonderful supervisory team, who guided me every step of the way through writing this thesis. This includes Paul Hughes, Stephanie Glendinning and Colin Davie at Newcastle University, and Jon Chambers and David Gunn at the British Geological Survey; without these people, this project would not have been possible. Although not officially part of my supervisory team, I cannot thank enough, also, Seb Uhlemann and Paul Wilkinson at the British Geological Survey, who both gave me so much of their time and help throughout this project, and for being so patient with me.

I want to thank my close friends Ross Stirling and Pete Helm for making the last four years a lot of fun, but also for all of their help and advice.

The technical component of this project would not have been possible without Stuart Patterson, Fred Beadle and Billy Cragie, who were always so generous with their time and their expertise.

I would also like to recognise the efforts of all of the students who contributed to this project, by the collection of field and laboratory data.

I am grateful to my best friends and housemates: Pickles, Boat, Panda and Mak Tak, for the indoor barbecues, the cups of jim, the cocktails and cheeseboards, and the energising gym sessions.

Finally, I want to thank my Uncle Neil, my boyfriend Malcolm, and my mum, for their unending love and support over the last four years.

Table of Contents

List of Figures

List of Tables

List of Symbols

Van Genuchten Parameters

Θ – volumetric water content

Θ_r – residual water content

Θ_s – saturated water content

Ψ – soil matric suction

α – curve-fitting parameter

η – curve-fitting parameter; measure of pore size distribution

$m\eta$ – curve-fitting parameter; $1 – (1/\eta)$

Geomechanical parameters

σ – total normal stress

σ' – effective normal stress

τ_f – shear strength

u – pore water pressure

c – cohesion

c' – effective cohesion

c_u – undrained cohesion

Φ – friction angle

Φ' – effective friction angle

φ – porosity

S – degree of saturation

P – density

P_{bulk} – bulk density

P_d – dry density

$P_{d(max)}$ – maximum dry density

P_w – density of water

P_s – density of soil solids

G_s – specific gravity

GWC – gravimetric water content, percentage

gwc – gravimetric water content, fractional

Electrical parameters

V – voltage

I – current

R – resistance

K – geometric factor

A – cross-sectional area of resistive medium

L – length of resistive medium

ρ – resistivity

ρ_a – apparent resistivity

ρ_s – soil resistivity

ρ_w – water resistivity

ε_a – dielectric permittivity

C1, C2 – current electrodes

P1, P2 – potential electrodes

a – dipole separation

n – ratio between dipole separation, a, and distance between current and potential electrodes

X – separation between potential electrodes

Waxman-Smits parameters

ρ_{WS} – Waxman-Smits soil resistivity

q – tortuosity factor

m – cementation exponent

p – saturation exponent

B – average ionic mobility of cations in the double diffuse layer

Q_v – cation concentration per unit volume

C – cation exchange capacity

f – area of intersection between ERT and porosity cells

Temperature correction and thermal parameters

T – temperature

T(z, t) – soil temperature as a function of depth and time

T_{lab} – *laboratory temperature*

T_{cor} – reference temperature

T_m – annual mean air temperature

z – soil depth

d – characteristic soil depth

$ç$ – temperature correction factor

δ – phase offset

t – time

ρ_{Tcor} – soil resistivity corrected to reference temperature, T_{cor}

λ – thermal conductivity

Additional parameters

F – Fréchet derivative i.e. sensitivity of ERT array at a given location

M – mass

D or d – depth

W – width

V – volume

d – depth to water table

h – height

R_u – Plaxis scaling factor

This PhD thesis is dedicated to the loving memory of my Papa, Patrick Hen, who never got to see it completed.

Chapter 1. Introduction

1.1 Project rationale

In recent years, extreme weather events have become increasingly commonplace in the UK, with record numbers of landslides occurring following exceptionally heavy rainfall in 2012, 2014 and 2016. Projections that flood risk will increase considerably across the UK have damaging implications for transport infrastructure, up to a third of which is composed of engineered slopes. As yet, there is no generally accepted method of assessing slope stability on a large scale.

Geoelectrical imaging methods such as Electrical Resistivity Tomography (ERT) are well-established as a means of subsurface imaging for a wide range of applications: increasingly, time-lapse tomography is being deployed to investigate hydrodynamic processes within landslides, due to a direct dependence of soil resistivity upon water content. Most such studies have focussed on active natural slopes, which have different associated failure mechanisms than the engineered slopes typical of earthworks. Therefore, there is a need for further investigation of engineered slope moisture dynamics, which, combined with proxy relationships, may allow resistivity imaging to quantitatively inform on the geotechnical parameters directly relevant to slope stability.

In this study, a 3D electrical resistivity tomography array is installed at the purpose-built BIONICS test embankment representative of UK earthworks embankments, facilitating a three year field monitoring programme supported by a network of point sensors. Field experiments are combined with a rigorous, multi-scalar laboratory testing programme targeted at resolving resistivity proxy relationships. Ultimately, this thesis describes a methodology for translating ERT-derived resistivity data into information more directly relevant to slope stability (water content and soil suction), furthering the development of a fully-automated slope stability monitoring system. The resultant geotechnical images are then used to inform on the hydrodynamic processes, providing invaluable insight as to the antecedent moisture conditions relevant to engineered slope failure.

1.2 Aim and Objectives

This project aims to use 3D time-lapse resistivity data to make quantitative assessments of the stability of engineered slopes. Ultimately, it seeks to use these data as a geophysical proxy for the spatial and temporal geotechnical property changes associated with relevant slope moisture dynamics. To this end, the following objectives have been identified:

1. Development of a thorough understanding of the factors affecting engineered slope failure in clay slopes in the UK, and of current practice in slope stability assessment methods.
2. Establishment of geophysical proxies for the geotechnical properties of engineered clay fill.
3. Acquisition of observational, geotechnical and time-lapse volumetric geophysical data from the BIONICS embankment, as it is subjected to environmental forcings.
4. Application of the geophysical proxies to the geophysical data to yield geotechnical property data.
5. Spatial and temporal cross-correlation of datasets in order to validate the geoelectrical imaging method, and to identify hydrodynamic processes relevant to slope stability.

1.3 Thesis structure

This PhD thesis is structured as follows: a brief introduction to the research project is given in Chapter 1. Chapter 2 provides a detailed background and literature review which starts by developing the motivation for this study, within the context of a changing climate. This then leads into a discussion of the factors affecting engineered slope stability within the United Kingdom, and the means of assessing slope stability, focussing on geoelectric imaging methods. The chapter concludes by summarising the literature review and background, resolving the summary into the identification of the research gap to be investigated within this PhD project. Chapter 3 presents the site for the field study, describing the criteria for site selection, the fill materials and construction methods. The methodologies for the principal components of the thesis are presented in Chapter 4, describing the laboratory testing programme into geophysical-geotechnical relationships, field experiments at the test embankment, and the processing and translation of electrical resistivity data into

quantitative geotechnical property information. All results are presented in Chapter 5, and discussed in Chapter 6, describing three distinct experimental components, pertaining to the laboratory testing programme, the long-term ERT study and the point sensor network. In Chapter 7 the project conclusions are presented, including recommendations for further work. Finally, the reference studies used in this thesis are given in Chapter 8. Additional supporting information is provided in the Appendices.

1.4 Scope

This study focusses on moisture dynamics and failure mechanisms associated with engineered slopes, which are directly investigated at the purpose-built BIONICS test embankment, representative of high specification modern earthworks. As such, natural slopes and those built using Victorian-era construction methods will not be directly considered within this thesis. Although earthworks may be composed from a range of engineering soils, clay is particularly susceptible to shear failure and of special relevance to UK transport infrastructure, therefore, only clay soils are investigated. Several geoelectrical methods exist, however, this study concerns electrical resistivity tomography methods only.

Chapter 2. Background and literature review

2.1 Climate change projections

The concept of climate change is now widely accepted by the scientific community: in 1988, the Intergovernmental Panel for Climate Change (IPCC) was established; a scientific body within the framework of the United Nations, for assessment of climate change, with thousands of contributing authors from 195 member countries. In its Fifth Assessment report, it states:

"In recent decades, changes in climate have caused impacts on natural and human systems on all continents and across the oceans. Impacts are due to observed climate change, irrespective of its cause, indicating the sensitivity of natural and human systems to changing climate".

The report explains that under all assessed emission scenarios, surface temperature is projected to rise over the 21st century, due to past and future anthropogenic emissions, and natural climate variability (IPCC, 2014). There is a wealth of ongoing research into how global climate change will affect the UK, with recent government-funded projects including the UK Climate Change Risk Assessment (CCRA) in 2012, the UK Climate Projections (UKCP) in 2009 and the UK Climate Impacts Programme (UKCIP) in 1998. These suggest that the UK will experience warmer, drier summers and milder, wetter winters, with more days of heavy rainfall and rising sea levels (CCRA, 2012a). These projections are supported by evidence that the Central England Temperature (the longest continuous temperature record in existence) has increased by approximately 1 ˚C since 1980 (Figure 2.1) and that all regions of the UK have experienced an increase in the contribution to winter rainfall from heavy precipitation events (UKCP, 2009).

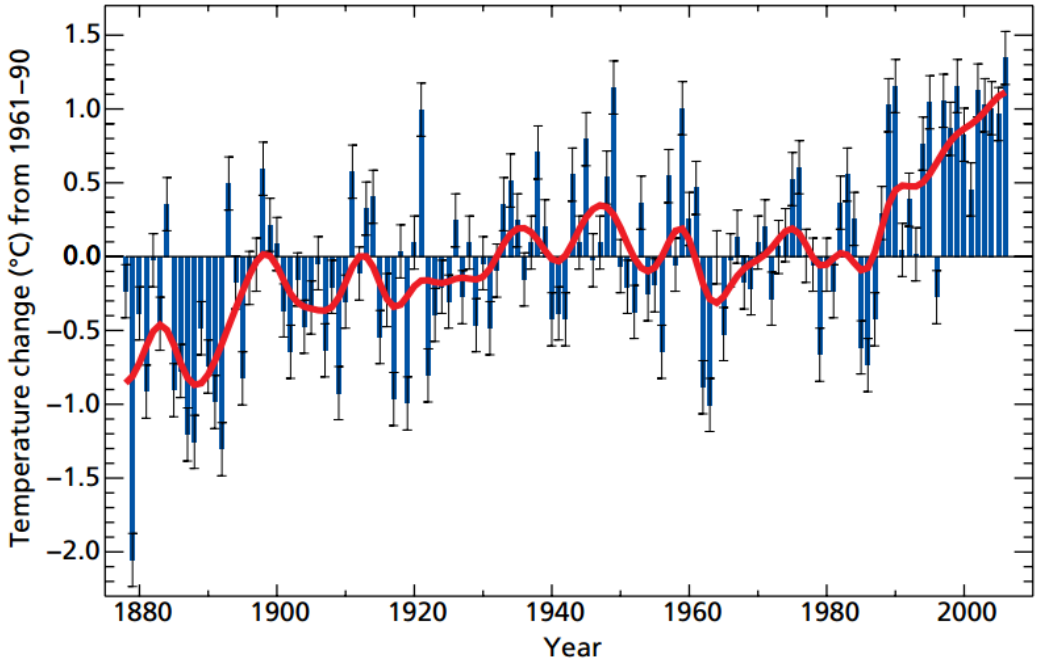

Figure 2.1 Increase in Central English Temperature (image from UKCP, 2009)

In addition to the general acknowledgement of the existence of climate change, it is widely accepted that *"Climate change will amplify existing risks and create new risks for natural and human systems"* (IPCC, 2014), with the CCRA describing a need for continued action to manage risks associated with a country already vulnerable to extreme weather including flooding and heat waves, even if the additional pressures of climate change are not considered (CCRA, 2012a).

There is a great deal of uncertainty in how these projected changes in climate will affect the occurrence of landslides, as they involve multiple feedback processes: precipitation and temperature extremes may contribute to slope destabilisation, and could potentially also affect boundary conditions such as topography (Huggel et al., 2012). Precipitation, in particular, acts on very short timescales, and therefore has high associated uncertainties (Meehl et al., 2007). Figure 2.2 shows a comparison of studies into critical threshold rainfall intensities for slope failures from several studies, and shows that the thresholds can differ by an order of magnitude depending on climate, hydrology, topography, geology, land cover, land use, and other factors (as described in Huggel et al., 2012).

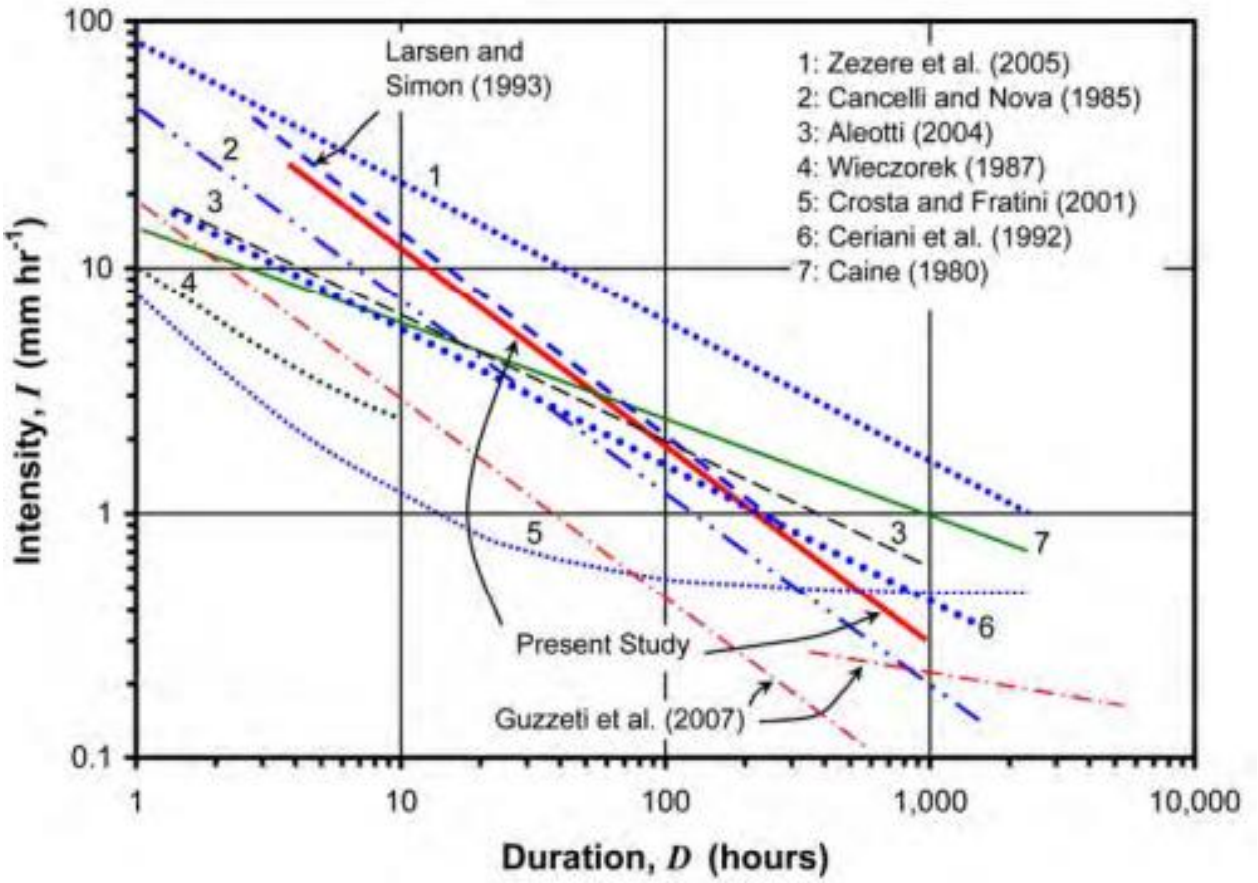

Figure 2.2 Comparison of landslide rainfall intensity-duration thresholds from several studies (image from Dahal and Hasegawa, 2008)

Despite the uncertainty in quantifying the long-term effects of climate change on slope stability, however, it is still reasonable to anticipate that there may be adverse effects. Given that a direct correlation can be made between heavy precipitation and the incidence of landslides (Figure 2.3 and Figure 2.4) and that flood risk is projected to increase considerably across the UK (CCRA, 2012a), it is necessary to consider the particularly damaging implications for transport infrastructure: widespread flooding in 2007 caused disruption estimated to have cost £100 million. In 2009, 500 billion motor vehicle kilometres were made, with 1.3 billion rail journeys completed in 2009/10: the UK transport sector plays an increasingly important role in linking an increasing population of 65.6 million, and is valued at approximately £100 billion per year. If no action is taken, the CCRA suggest that costs similar to those of 2007 may be incurred almost annually (CCRA, 2012b).

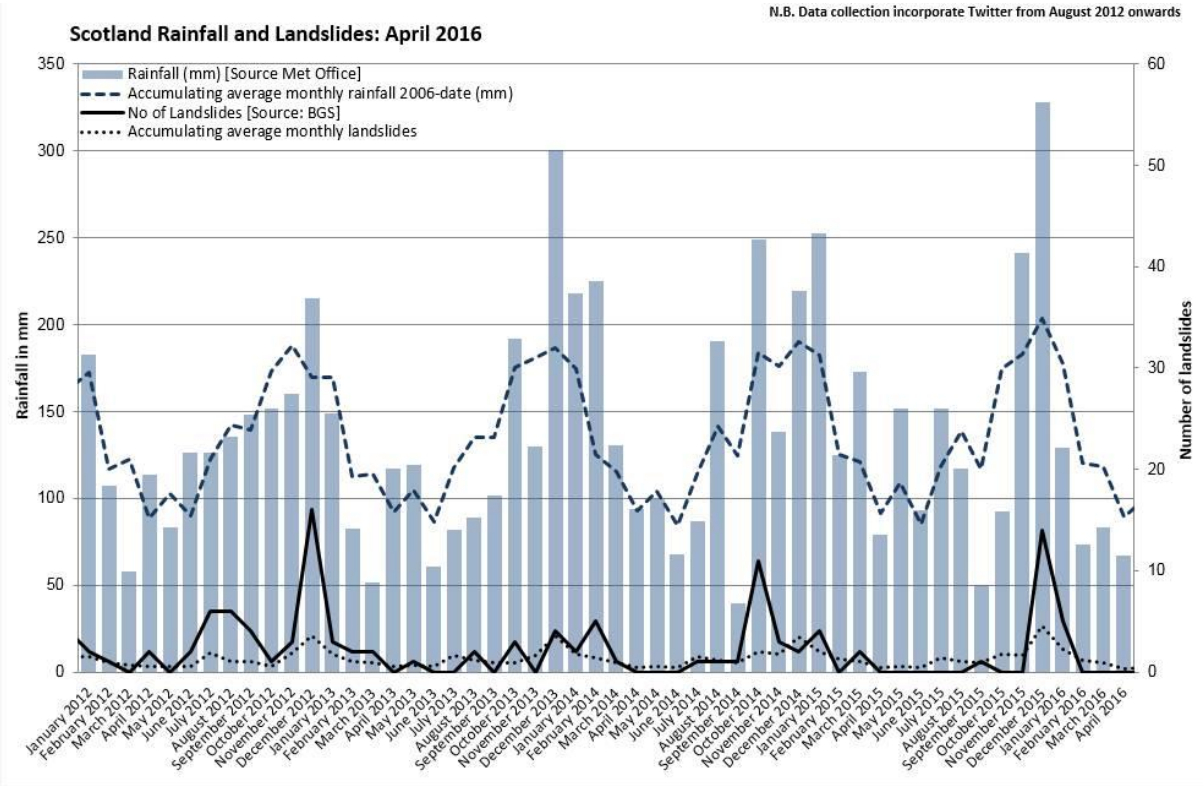

Figure 2.3 Graph showing UK average rainfall and number of landslides from January 2012 to April 2016 (image from BGS, 2016a)

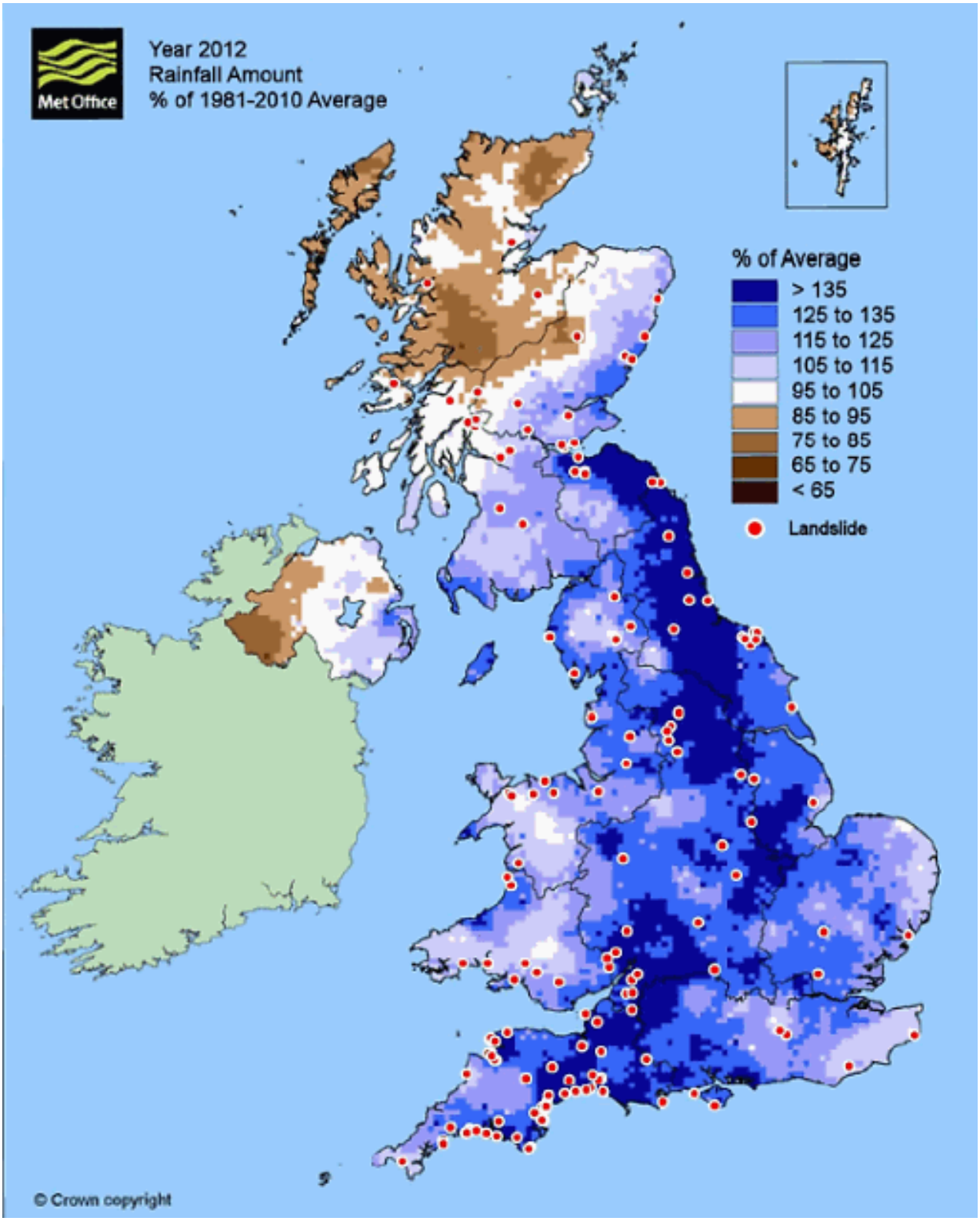

Figure 2.4 Map showing distribution of UK landslides during 2012 (image from Met Office, 2012)

2.2 Slope stability

2.2.1 *UK transport infrastructure*

Engineered and natural slopes constitute an important part of UK transport infrastructure; it is estimated that as much as one third of its total asset value is derived from engineered slopes alone (Perry et al., 2001). Presently, the length of British road network considered to be at risk from landslides is well in excess of 1000 km (CCRA, 2012b), not considering that of the UK rail network, with the cost of remediation works being approximately ten times that of preventative actions (Glendinning et al., 2009). In addition to the considerable financial cost of failures on infrastructure slopes, they can be devastatingly disruptive and dangerous: the Hatfield Colliery landslip in February 2013 saw the five month closure of a segment of track through which approximately 20 % of UK rail freight is conducted, as well as numerous passenger trains (Bickerdike, 2013); in July 2012, two people were killed when their car became trapped in a landslide by a tunnel in Beaminster, Dorset (BBC, 2014).

The engineered slopes which constitute much of the UK road and rail infrastructure comprise both embankments and cuttings, however, these differ greatly with respect to their stress histories; embankments are formed by the excavation of selected fill material i.e. unloading – and subsequent compaction into an elevated embankment slope i.e. loading, during which excess pore pressures build up, and dissipate following construction. Cuttings, formed by the removal of material to expose a slope made of pre-existing material, therefore have only been subjected to unloading (Smith, 2014). Additionally, given that embankments are formed from carefully selected fill material, there is much more control over the engineering properties of the material, and over the construction process itself. Owing to this difference in stress history, embankments and cuttings are subject to different modes of failure, with cuttings usually failing along pre-existing planes of weakness, such as bedding planes (Bell, 1981), whilst failure of embankments is more often associated with moisture-driven variations in pore pressure (Jardine et al., 2004). Therefore, embankment slopes are of prime importance in the consideration of the increased precipitation associated with climate change.

UK infrastructure may be broadly split into two categories: those built to modern specifications and those built using Victorian construction methods (Loveridge et al., 2010). The 19th century saw significant expansion of UK railways, with nine main lines of railway built in England between 1834 and 1841, totalling 660 miles in length; some 70 million cubic

metres of material was excavated for cuttings, the bulk of which was used for embankment construction. During this time, efforts were made to balance 'cut' and 'fill', with excavated material being carried in horse-drawn earth wagons, or over greater distances, by locomotives, thereby achieving an integrated system of cutting and embanking, capable of handling vast volumes within a relatively short time (Skempton, 1996). Over the course of the railways expansion, a range of construction approaches were employed, some involving various degrees of compaction within layers (Vaughan et al., 2003), however, these were largely considered too slow (and therefore costly); the most commonly used method by the mid 1830s was to construct embankments at full height, by end-tipping excavated material. This method was correlated with increased settlements in railway embankments, but could be remediated by packing more ballast under the railway sleepers and even sometimes by imposing speed restrictions until the bank became consolidated (Skempton, 1996).

Significant expansion in the road network followed in the mid 20th century, after the passing of the Special roads Act in 1949 which saw construction start on the first motorways. By this time, both the understanding of soil mechanics and construction methods had vastly improved with respect to the period of rail expansion, with dedicated government research into construction and engineering practice beginning with the establishment of the Road Research Laboratory in 1933 (TRL, 2016). This move ultimately led to the establishment of the first standards and codes for engineering practice, which are continuously evolving, with current standards described in the Design Manual for Roads and Bridges (Highways Agency, 2016).

For both modern and Victorian embankments, the construction material is key to its engineering properties, and is a function of the local geologies from which it is won. Analysis of the spatial distribution of unstable slopes indicate that some 10 % of Great Britain can be classed as having "moderate to significant landslide hazard potential" (Dixon et al., 2007) (Figure 2.5), the main source materials including the London Clay Formation, Lias Group and Gault Formation. Of the main transport network, it is estimated that over 7 % is located in these high risk areas (Dijkstra and Dixon, 2010). Despite being composed of largely similar materials, however, older Victorian-era embankments are inherently less stable, resulting from poor compaction and construction on unprepared foundations, leading to a heterogeneous fill of increased permeability subject to excessive settlement (Loveridge et

al., 2010). Additional destabilising factors include poor drainage, poorly maintained slope vegetation, and the presence of a thick ballast capping layer, as can be seen from Figure 2.6.

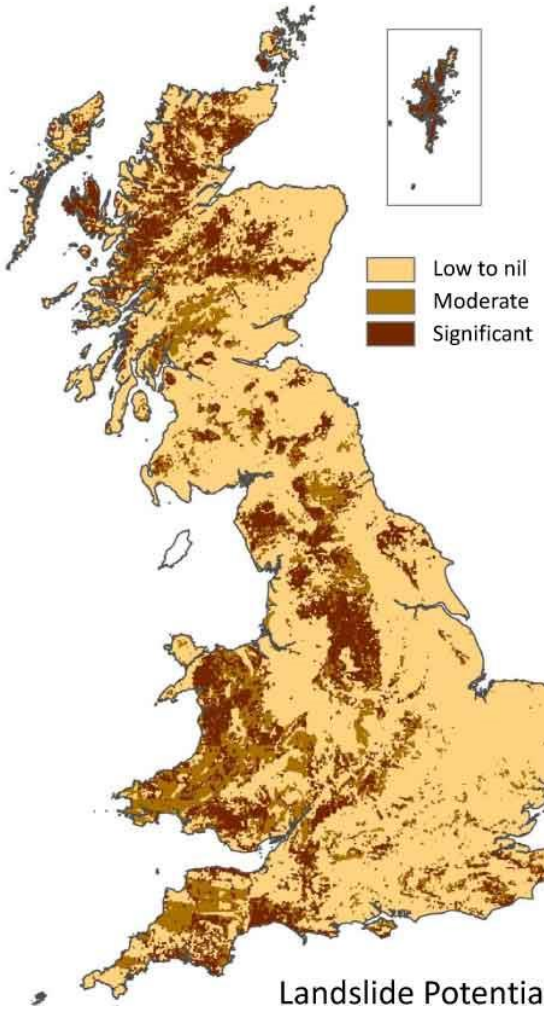

Figure 2.5 Map of Great Britain landslide hazard potential (image from BGS, 2016b)

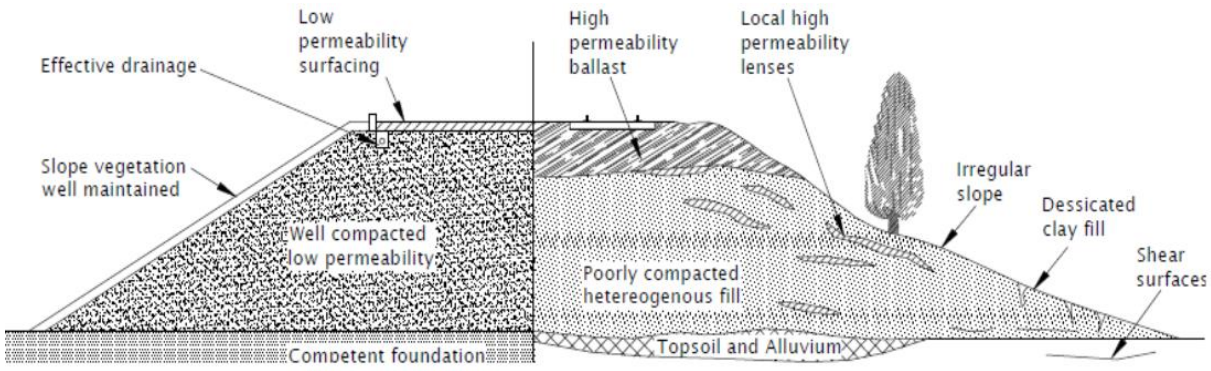

Figure 2.6 Cross – section of modern highway embankments versus Victorian railway embankments (image after O'Brien, 2007)

2.2.2 *Landslides*

A landslide is defined as a "movement of a mass of rock, earth or debris down a slope" by Cruden (1991) for the Working Party on World Landslide Inventory. A broad distinction can be made between deep slides, and near-surface, superficial slides, and precedes the study of modern Geotechnics, described by Collin as early as 1846. Several classification schemes for landslides exist (Hutchinson, 1988; Cruden and Varnes, 1996; Hungr et al., 2014), however, these make no distinction between natural and engineered slopes. The US Federal Highway Administration defines four principal failure mechanisms of relevance to earthworks failures, as shown in Figure 2.7 (FHWA, 2001), including shallow translational failure, rotational failure, sliding block failure and foundation settlement. Landslides which occur on embankments are generally superficial (Rail Technology Magazine, 2012), and associated with the development of positive pore pressures due to rapid infiltration of water from heavy rainfall. Occasionally, however, water infiltration may occur from other sources, e.g. leaking underground pipes (Highland and Bobrowsky, 2008) or embankment dams (Cenderelli, 2000). There is often, however another pre-existing cause of instability, which is then exacerbated by water infiltration. Veder (1981) lists the following morphological causes: excessive steepening of slope inclinations; weakening of slope toe; excessive-pressure load on slope head. Considering modern earthworks, the first two factors are unlikely to result directly from poor geotechnical design, due to strict current highway design specifications, but may occur due to gradual erosion over time (Loveridge et al., 2010). During periods of extreme rainfall, suctions usually present in the ground may be drastically reduced (Lim et al., 1996), meaning that the fill material's resistance to shear is also reduced. This is often evident in the reduction of rail traffic across vulnerable embankments following heavy precipitation, in order to reduce pressure on the slope head, which can normally be supported without cause for concern.

In addition to morphological sources of slope instability, many authors discuss those rooted in the regional geology (Veder, 1981; Fell et al., 2012; Korup, 2012), citing tectonic activity, bedrock type, structure, stratigraphy and weathering as potentially destabilising factors. These factors are certainly relevant to the failure of natural slopes and to deep-seated landslides, but within the context of engineered fill slopes, considerations on this scale are not of great significance. Of most relevance is the composite fill material, and its degree of homogeneity; with perching of the water table possible where high permeability soils are

underlain by low permeability layers. This is more likely to occur in more heterogeneous, Victorian-era engineered slopes, with high permeability lenses, as shown in Figure 2.6. In addition to the arrangement of the composite material, certain types of fill are inherently more susceptible to failure than others, such as clays which are volume sensitive (Reeves et al., 2006).

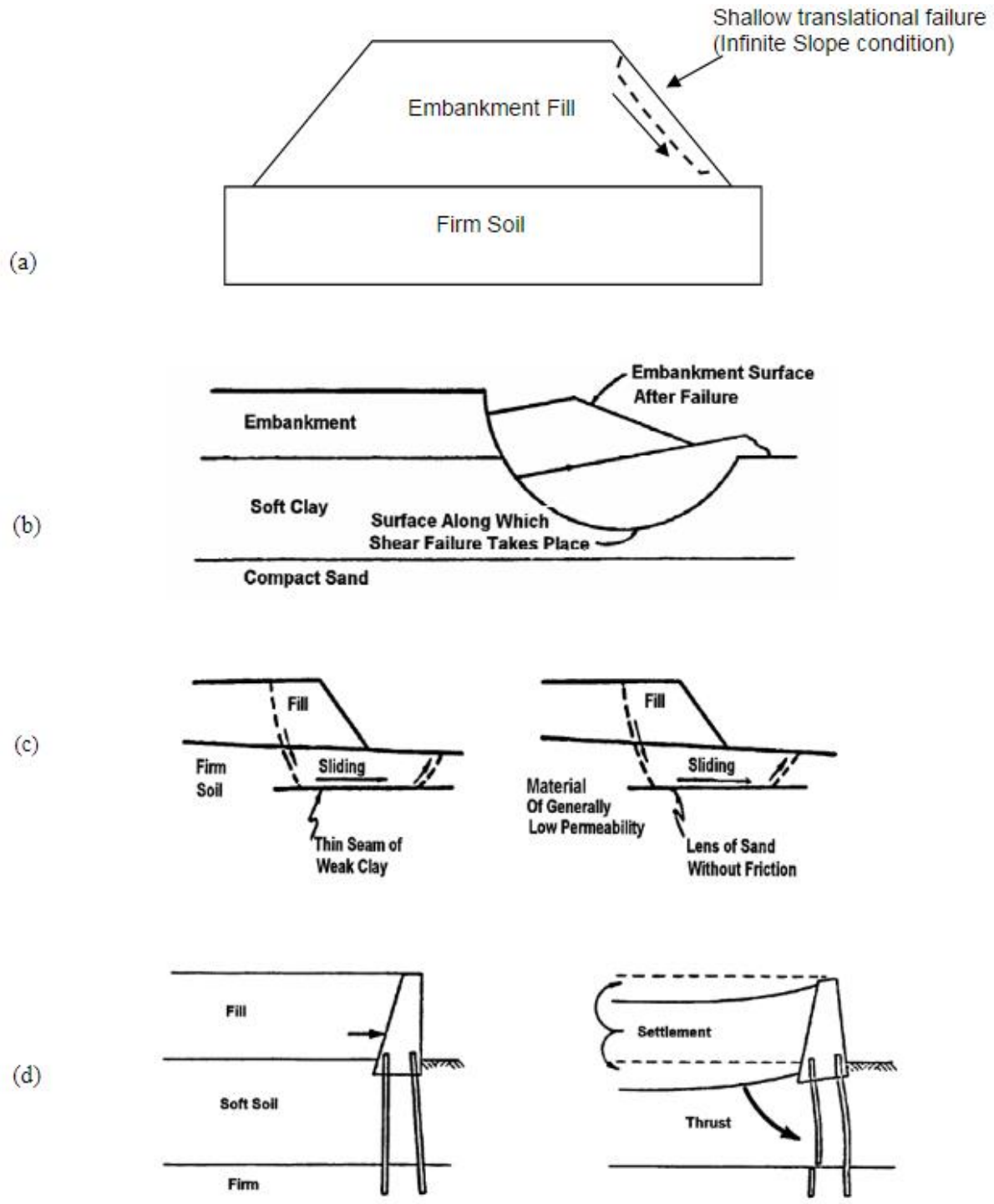

Figure 2.7 Earthworks failure mechanisms: (a) Shallow translational slope failure in embankment fill; (b) rotational failure in embankment fill and foundation soil; (c) sliding block failure; (d) settlement of foundation soil (image from FHWA, 2001)

2.2.3 *Clays and glacial tills*

Much of the UK's superficial geology is dominated by the presence of tills, derived from glaciers present during the Devensian era, believed to have covered some 60 % of UK total land area (Trenter, 1999). The properties of these tills are a function of their composition, mode of deposition, loading history, and weathering processes (Reeves et al., 2006). Due to the roles of these parameters, they are regarded as highly variable, and may range from extremely dense non-plastic tills to weak plastic clay tills (Bell, 2002). Till may be defined as a poorly sorted mixture of clay, silt, sand, gravel, cobble and boulder-sized material (Hambrey, 1994). Mudstones and shales are easily eroded, and therefore, produce fine-grained tills which are rich in clay minerals (Reeves et al., 2006): for this reason, clay dominates UK glacial tills, with the term Boulder Clay often used to describe highly variable clay deposits containing irregular-sized boulders of varying lithologies, ranging from pebbles to rock fragments which may weigh several tons.

Within the UK, the principal source materials generating unstable slopes include the London Clay Formation, the Gault Clay Formation, and the Lias Group (Dijkstra and Dixon, 2010), which all constitute examples of Boulder Clay. Owing to the large amount of construction that has taken place on the London Clay outcrop, it is of particular interest to engineers, and its properties are therefore relatively well-documented (e.g. Cripps and Taylor, 1986; Atkinson, 2000; Chandler, 2000).

The London Clay Formation is a thick, relatively homogenous clay sequence, underlying much of Greater London, with outcrops in Essex, Kent, Hampshire, Sussex and the Isle of Wight. It is a firm to stiff, over-consolidated, fissured, silty clay, and predominantly illite/smectite, which is derived from montmorillonite. Typical values for its bulk density are between 1.70 and 2.04 Mg/m^3, with shear strength values in the range of 50 to 150 kPa in the near-surface. London Clay is generally of high to very high plasticity, which is a reflection of the presence of the swelling mineral montmorillonite and other clay minerals, as can be seen from Figure 2.8 (Reeves et al., 2006).

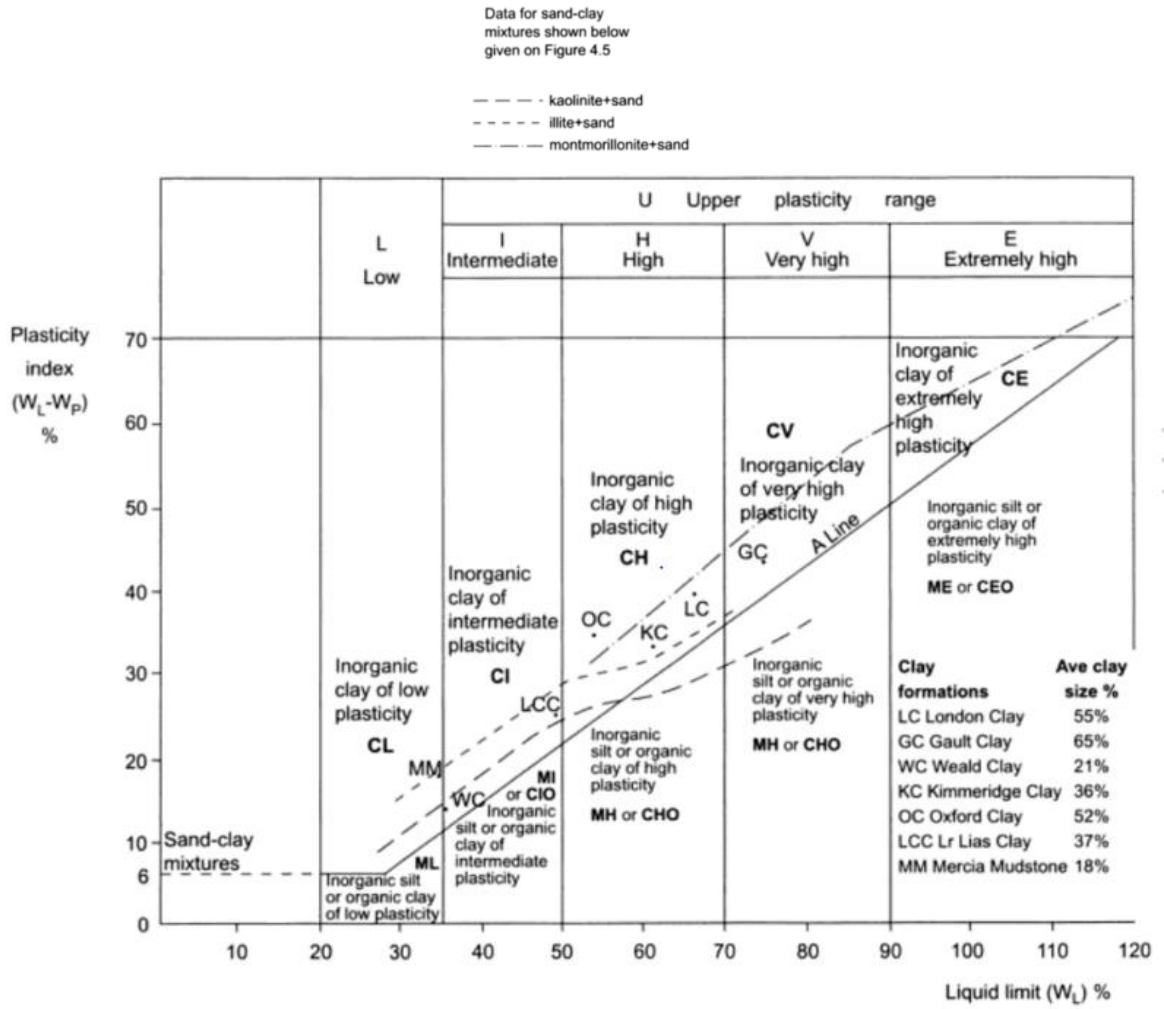

Figure 2.8 Plasticity chart for selected British clays, showing London Clay (LC) (image from Reeves et al., 2006)

2.2.4 *Seasonal moisture cycles*

Due to the presence of minerals such as montmorillonite, all clays are subject to shrink-swell behaviour (Reeves et al., 2006). Grim (1962) described volume change occurring by two processes: inter-crystalline swelling where volume increase happens as a result of an increase in the amount of pore water between grains; and intra-crystalline swelling where water enters the clay crystal itself, causing expansion (see Figure 2.9), as is the case for montmorillonite and other swelling clay minerals. As a result of this shrink-swell behaviour, fissuring and displacements of the subsurface may occur, which have the potential to cause damage to many earthworks types. Figure 2.10 shows a map of the distribution of volume-sensitive soils across the UK, highlighting their proximity to the main railway lines.

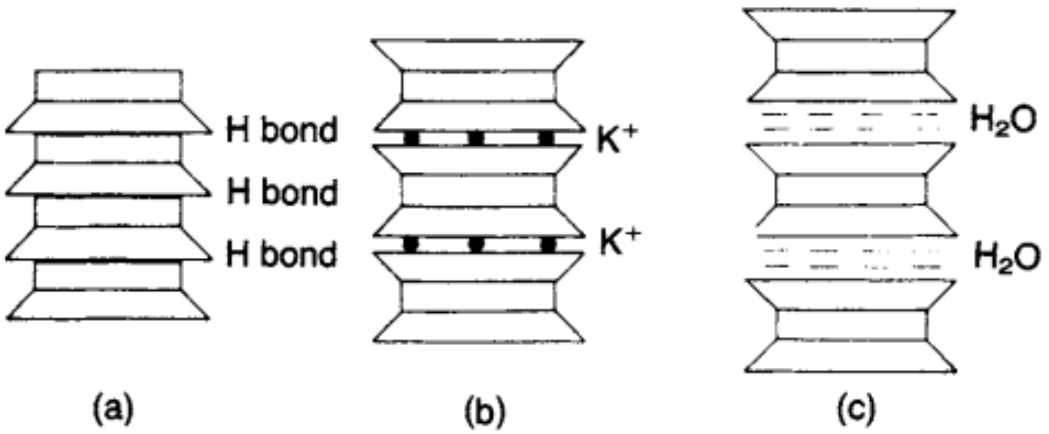

Figure 2.9 Clay minerals , showing (a) kaolinite; (b) illite; (c) montmorillonite (image from Craig, 2006)

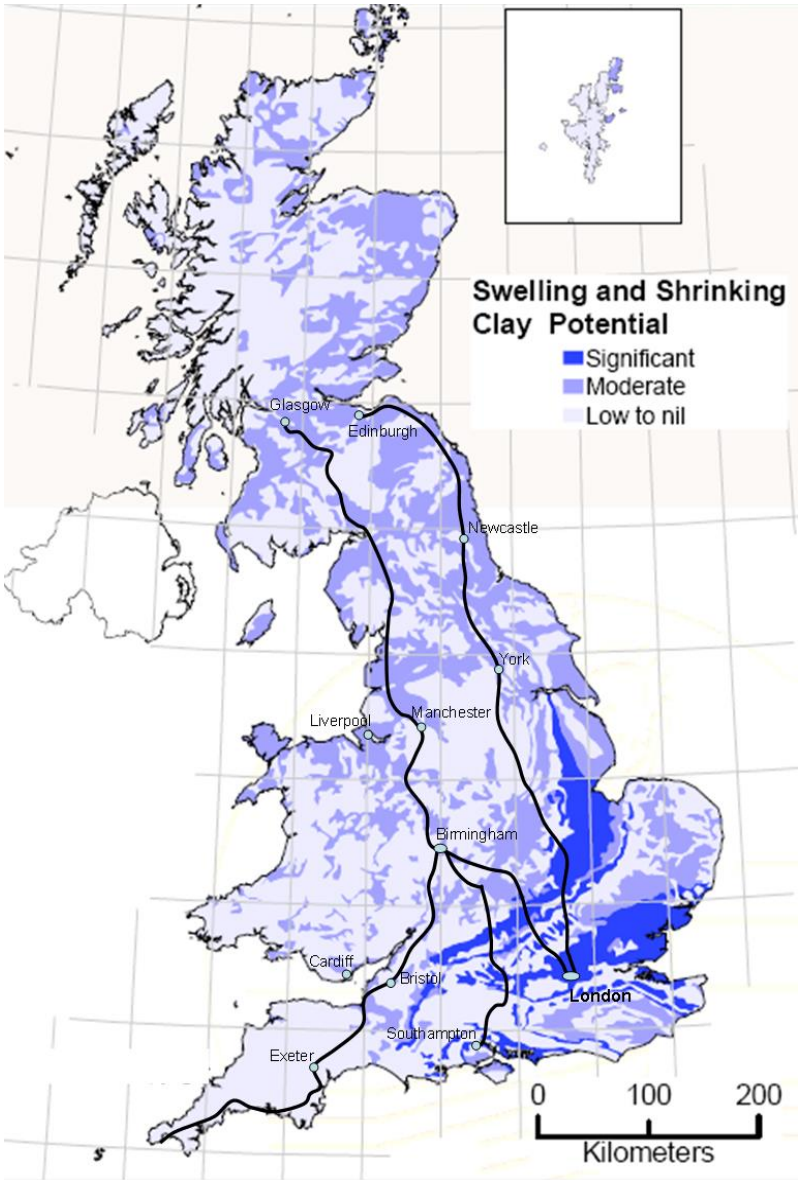

Figure 2.10 Map of UK shrink-swell potential (image from BGS, 2013)

In clays, cyclic changes in water content resulting from seasonal variations will result in corresponding cyclic changes in pore water pressure, and hence effective stress (Smethurst et al., 2006). Over time, soil experiencing shrink-swell behaviour may be subjected to a reduction in the mean effective stresses: for slopes, this phenomenon, known as strain softening, starts from the slope toe, penetrating deeper over time, and reducing soil strength from a peak to a residual state. The strength loss is progressive, as the rupture surface propagates through the slope over time; over a period of several years, this strain softening can lead to progressive failure (Potts et al., 1997; Smethurst et al., 2006). This process may be exacerbated by seasonal shrink-swell moisture cycles, as fissures developed lead to the additional ingress of water, further reducing effective stresses. This is supported by statistics which indicate particularly high numbers of landslides occurring following the exceptionally warm summer of 2003 (MottMacdonald, 2011), which would have been accompanied by desiccation cracking.

In addition to seasonal shrink-swell behaviour, stresses in the soil are affected by the saturation history of the soil itself. This is incorporated within the Soil Water Retention Curve (SWRC), which describes the relationship between soil water content and potential, effectively describing the ability of a soil to store water. The water retention behaviour of a soil is related to the volume and distribution of pore spaces, and hence strongly affected by soil texture and structure (Tuller and Or, 2005). Figure 2.11 shows an example SWRC for a silty soil, demonstrating both a drying and a wetting path. It can be observed that as the soil is dried out from an initial state of saturation, the suction increases rapidly. As the suction approaches the Air Entry Value (AEV), the rate of increase declines. As the soil then reaches the residual water content, there is an associated increase in the rate of suction. The wetting branch of the SWRC demonstrates similar behaviour (in reverse), but with considerably lower suctions for a given water content. This relates to an inherent difference between the mechanics of desorption and adsorption, such that as a soil dries, the water tension increases rapidly due to large pores emptying first; during wetting, small pores fill first, resulting in lower suctions (Ward and Trimble, 2004). The saturation values of the drying and wetting curves may also differ, as is a result of entrapped air, replacing volume previously occupied by water (Fredlund and Xing, 1994).

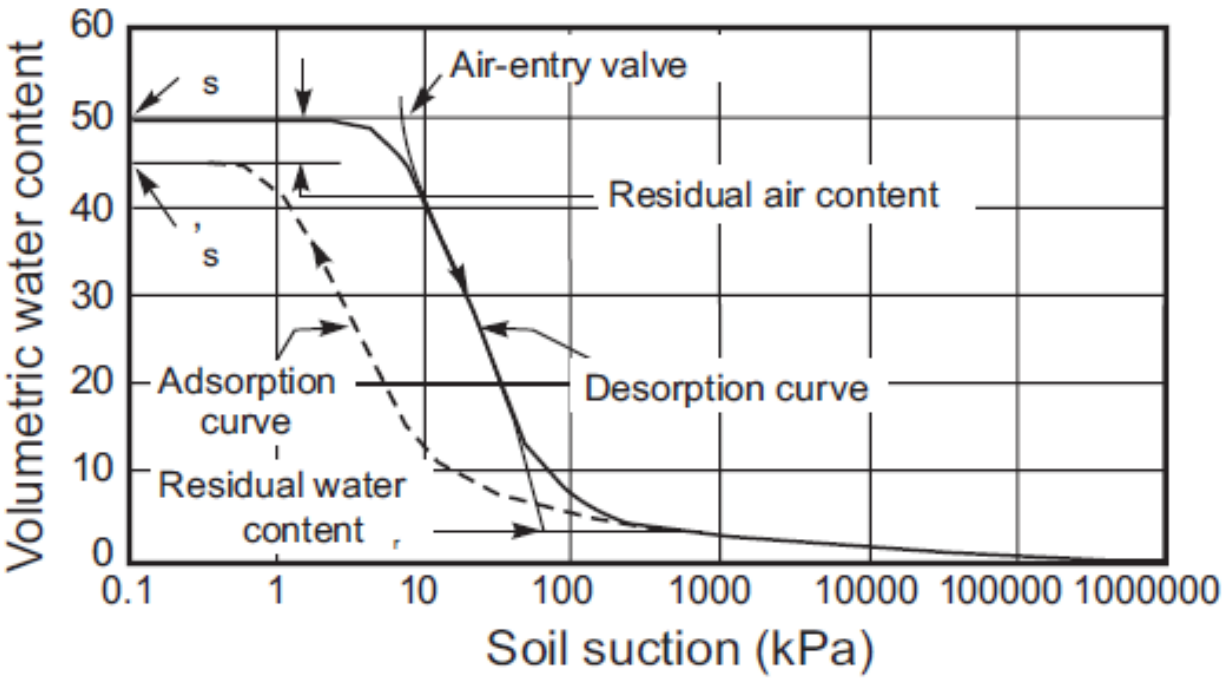

Figure 2.11 Typical soil water retention curve, showing both drying (desorption) and wetting (adsorption) paths, for a silty soil (image from Fredlund and Xing, 1994)

Much research has been undertaken into the development of a model which describes the soil water retention behaviour of soils (e.g. Williams et al., 1983; McKee and Bumb, 1984); the work by Van Genuchten (1980) is largely considered to be the defining study on this subject. The Van Genuchten model describes volumetric water, Θ, content as a function of soil potential, Ψ, as follows:

$$\theta(\Psi) = \theta_r + \left[\frac{(\theta_s - \theta)}{(1 + (\alpha|\Psi|)^{\eta})^{m}}\right] \qquad \text{Eqn. 2.1}$$

where Θ_r is the residual water content, Θ_s is the saturated water content, α is a curve-fitting parameter relating to the air entry value, η, relates to the pore size distribution, and $m = 1 - (1/\eta)$. Using Eqn. 2.1, separate drying and wetting branches may be defined by fitting model parameters to field or laboratory data, accounting for seasonal moisture variations.

2.2.5 *Principles of slope stability*

Engineered slope stability can be described, in broad terms, as a function of the composite material and the environmental conditions to which it is subjected. The resistance of a soil to shear is key to its stability, as landslides occur due to shear failure of the soil mass, along a plane (Figure 2.12). Shear strength can then be defined as the "internal resistance per unit

area that the soil mass can offer to resist failure and sliding along any plane inside it" (Das and Sobhan, 2014). If the stress at a point on a plane within a soil mass becomes equal to its shear strength, then failure will occur at that point. The effective stress acting on a soil is governed by Terzhagi's principle (Terzhagi, 1925):

$$\sigma' = \sigma - u \qquad \text{Eqn. 2.2}$$

where σ' is effective normal stress, σ is total normal stress (derived from interparticle forces, considering a single-phase material) and u is pore water pressure, which may be either positive or negative (suction). Prior to the development of Eqn. 2.2, the shear strength τ_f of a soil was resolved by Coulomb (1773) into a linear function of the normal stress at failure (σ_f) at that same point, a generalised form of which was later developed by Mohr (1900), termed the Mohr-Coulomb Failure Criterion:

$$\tau_f = c + \sigma_f tan\Phi \qquad \text{Eqn. 2.3}$$

where c is the cohesion intercept, and Φ is the angle of shearing resistance (also described as the angle of internal friction), together termed the *shear strength parameters*. Given the acceptance of Eqn. 2.2, however, shear strength should be expressed instead as a function of effective normal stress, σ'_f, modifying Eqn. 2.3 to read:

$$\tau_f = c' + \sigma'_f \, tan\Phi' \qquad \text{Eqn. 2.4}$$

where c' and Φ' are the *effective stress parameters*. Eqn. 2.4 then describes a scenario where a critical combination of shear and effective normal stress will result in failure at that point (Craig, 2006). For cohesionless soils (e.g. sands), the cohesion intercept c' is 0, meaning that if there is no effective normal stress acting along a plane, there is no resistance to shear. It should be understood that these stress parameters are simply mathematical constants defining the linear relationship between shear strength and effective normal stress (Craig, 2006), which is usually a fair approximation, but not necessarily always representative of a soil's stress state.

The linear relationship described Eqn. 2.4 can be observed in Figure 2.13, which also shows the representation of the stress state using a Mohr circle defined by the effective principal stresses σ'_1 and σ'_3, to which the Mohr-Coulomb failure envelope is tangential.

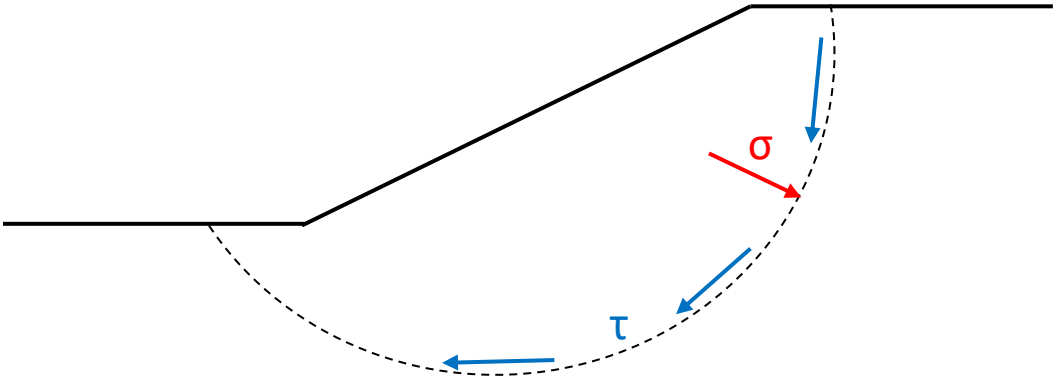

Figure 2.12 Schematic of a rotational failure on an embankment slope. At failure, stress, τ, along the failure surface reaches the shear strength τ_f

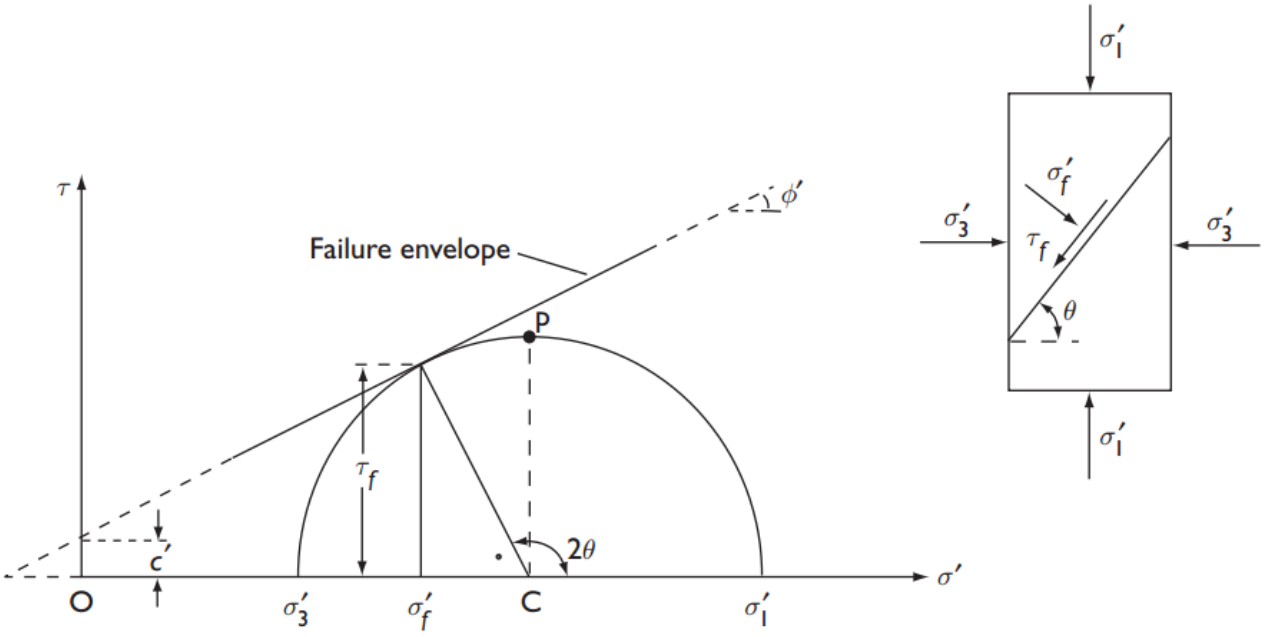

Figure 2.13 Mohr-Coulomb failure criterion (image from Craig, 2006)

2.2.6 *Laboratory testing of shear strength*

Several laboratory methods exist for determining the shear strength of soils, using a variety of approaches, as described in BS 1377-7: 1990 and BS 1377-8: 1990 (BSI, 1990d and 1990e).

Direct shear test

The direct shear test is considered to be the simplest method of measurement of soil shear strength, and may be performed on both cohesionless and cohesive soils (although it is mainly used to test dry, granular soils, for speed and simplicity). A soil specimen is compacted into a metal shear box, which may be square or circular, formed of two halves which are stacked (Figure 2.14) and free to move horizontally with respect to one another. A normal load is applied to the shear box, and a shear force imparted by applying a constant rate of shear displacement to the bottom half of the box relative to the top until failure, using a motor. If clays are to be tested, the applied strain rate must be low enough that excess pore pressures are able to dissipate, due to their very low hydraulic conductivity. The resulting resistance to shear of the soil is measured directly using a load cell, and any volume change in the specimen using a vertical displacement gauge. Following this process, a measure of the shear strength may be easily derived. The limitations of the test must be considered (in addition to the issue of representability of the soil mass as a whole, inherent to all soil laboratory tests), the main disadvantage being that drainage cannot be controlled; the test does not allow pore pressures to be measured, and as such, only the total normal stress may be determined. Other issues include that the specimen is made to fail along a predetermined failure plane over which shear stress is not uniform, and that the area of contact between the plates does not remain constant throughout the test (Craig, 2006).

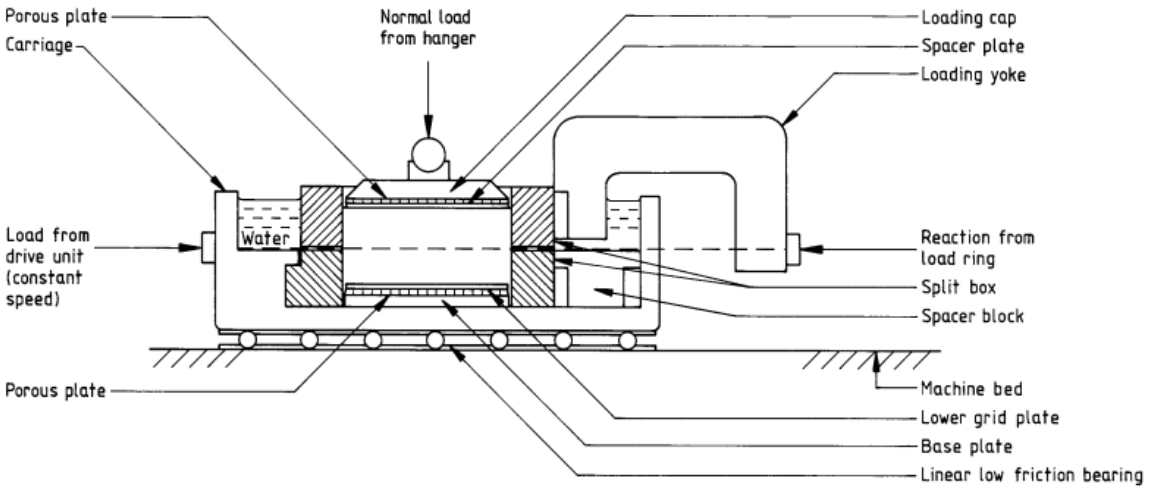

Figure 2.14 Shear box test apparatus (image from BS: 1377-7 1990, BSI, 1990d)

Triaxial test

Shear strength can be determined indirectly from the triaxial test, which is the most widely used shear test and is suitable for all types of soil. A cylindrical soil specimen (usually 76 mm length by 36 mm diameter) encased in a rubber membrane, is placed in a fluid-filled triaxial test chamber, as described in BS 1377-8: 1990, BSI, 1990e (Figure 2.15). The fluid is then pressurised in order to apply a confining pressure σ_3 to the specimen, and the deviator stress ($\sigma_1 - \sigma_3$) applied axially by a loading ram. One advantage of the test is that it allows drained testing, and pore pressures to be measured. Three types of triaxial test exist.

1. Consolidated-drained (CD), whereby the specimen is allowed to drain while subjected to the confining pressure, until consolidation is complete. The deviator stress is then applied, still under drained conditions, at a rate sufficiently slow that excess pore pressures are not developed.
2. Consolidated-undrained (CU), which follows the same process until consolidation is complete, but applies the deviator stress without permitting drainage, during which pore pressures may be measured.
3. Unconsolidated-undrained (UU) – also known as the Quick Undrained test, during which the specimen is sheared to failure by application of the deviator stress, with drainage not permitted at any point. For this reason, the test can be performed in a matter of minutes, even on clay specimens. For fully-saturated clays, a special condition applies, whereby the additional axial stress at failure ($\sigma_1 - \sigma_3$) is the same, regardless of the applied confining pressure (σ_3), such that $\Phi = 0$, and Eq. 2 becomes $\tau_f = c = c_u$, where c_u is the undrained shear strength. If no confining pressure is applied ($\sigma_3 = 0$), the recorded strength parameter is the “unconfined compressive strength” (UCS).

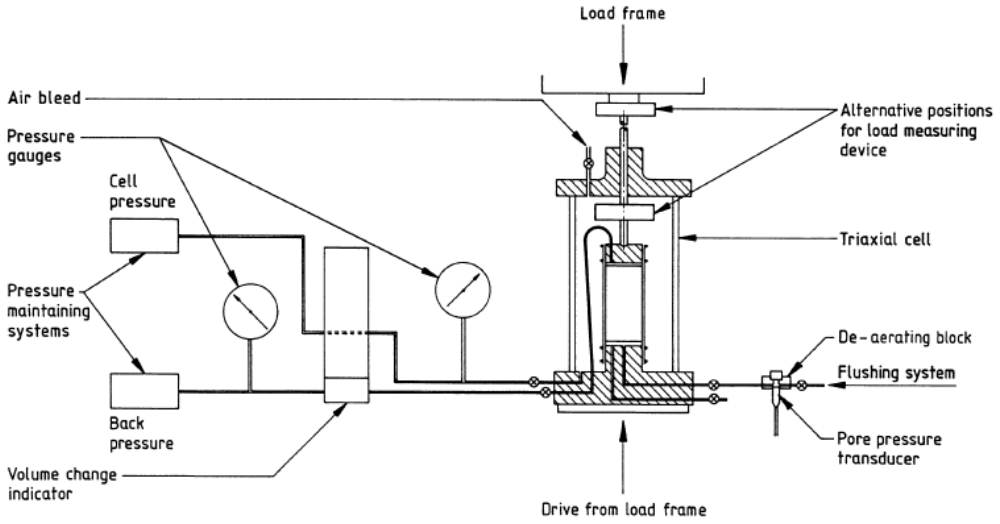

Figure 2.15 Triaxial test apparatus (image from BS 1377-7: 1990, BSI, 1990d)

Limitations of shear testing of clays

Despite the availability of these tests, there are many difficulties associated with obtaining a value for the shear strength of clay structures. One inherent limitation of laboratory testing is that of representability, such that any test results are ultimately only truly representative of the soil specimen which has actually been tested. Although efforts are made to use samples representative of the soil mass as a whole, this can be difficult to achieve. So-called "undisturbed" samples can be extruded from field test sites, but upon extraction these are subject to a stress relief from the confining pressure of the surrounding ground, potentially altering the stress-deformation characteristics of the material (Terzhagi et al., 1996). Hence, this term is misleading. Extraction of undisturbed samples may involve the extraction of bulk soil, from which a sample is extruded in the laboratory; samples may then be disturbed during both stages, an effect which may be exacerbated for highly overconsolidated clays (Murthy, 2003). These "undisturbed" samples may also contain boulders or other fragments which could cause local deformation during testing, yielding a shear strength lower than that in the field. Much testing is undertaken on remoulded clays, which can be prepared to emulate in situ field conditions, whilst removing larger particles, which again, raises the issue of representability. Following remoulding, the maximum shear stress which a sample can resist at a given water content generally decreases, the ratio between these strengths being termed the *sensitivity* (Craig, 2006). Therefore, it is necessary to consider the implications of the specimen preparation when interpreting laboratory results to make inferences about the strength of a soil mass.

In addition to issues pertaining to the representability of the specimen, it is necessary to consider the saturation state during testing, including the drainage conditions. Using both the experimental methods described above, both saturated and unsaturated testing are possible. Shear box testing does not allow drainage to be controlled, whereas triaxial testing does. The fact that cohesionless soils such as sands derive their strength from interparticle friction, combined with a very high hydraulic conductivity means that pore pressures developed during shearing dissipate quickly. Therefore, dry shear strength is comparable to saturated shear strength for sands, and may be easily investigated using the direct shear method as drainage conditions are not significant. Clays, however, are cohesive, with very low hydraulic conductivities, and therefore their dry and saturated behaviours are completely different. The direct shear method is therefore rarely used to test clays, due to the inability to control drainage conditions. The unconsolidated undrained triaxial test allows rapid measurement of clay shear strength to be obtained, under undrained conditions. Although the long-term stability of clay slopes is determined by its drained behaviour, undrained conditions are representative of short-term stability (Wood, 1990), which is relevant to sudden failures associated with rapid changes in subsurface moisture conditions (e.g. rainfall-induced landslides). The unconsolidated undrained test is usually performed on saturated samples, yielding the undrained shear strength (c_u). If an unsaturated sample is sheared, the shear strength at failure is not a "true" undrained shear strength, but does still describe the maximum shear resistance encountered during shearing under undrained conditions.

Ultimately, the choice of test method is heavily dependent on the applicability of the results to a given engineering situation. Given the many considerations involved with laboratory testing of clays, standard practice is to perform laboratory tests in conjunction with field tests, to provide as full as possible an assessment of the soil strength for a given engineering scenario.

2.2.7 *Methods of slope stability assessment and monitoring*

Current methods and limitations

The above methods relate to the investigation of soil strength, however, in order to provide an assessment of the slope stability of a specific engineering scenario, many other factors must be considered. Methods of assessing the stability of engineered and natural slopes rely

largely on making geotechnical measurements, using different types of point sensor. Most of these are focussed on making measurements which relate to the amount of moisture in the ground, and to its internal stresses. Rainfall gauges provide useful inform ation on precipitation levels, but do not account for surface runoff and therefore cannot be used to provide quantitative information regarding ground moisture dynamics. Different types of sensor exist which measure the volumetric water content of soils, generally deriving water content from the dielectric properties of the soil (e.g. Decagon Devices EC-TM (Decagon Devices, Inc., 2008), Delta-T SM150 (Delta T Devices Ltd., 2014)). Tensiometers make point measurements of soil pore pressure, and have increased in sophistication over the years (Dunnicliffe, 1988; Cui et al., 2008; Toll et al., 2011). These use a sensor to record the induced pressure as moisture is drawn from a water-filled tube into the surrounding soil (Abramson et al., 2001). Piezometers are used to measure both water levels and water pressure, using a filter tip connected to a riser pipe (DGSI, 2016). Although both tensiometers and piezometers are relatively easy to install and use, their operation can be slow and they are highly sensitive to soil particles plugging the porous filter components (Abrahamson et al., 2001). All of the above methods provide point measurements, therefore, a high density of measuring instruments is required in order to provide enough information to resolve a spatially-integrated cross-sectional model. This approach requires a great deal of interpretative effort.

In addition to methods which record soil moisture properties, another approach is to consider changes in slope morphology. Walk-over surveys may be undertaken to provide surface observations, particularly following periods of intense rainfall. Inclinometers are frequently used in slope stability assessments to record ground displacements in two perpendicular planes, allowing displacement magnitudes and directions to be calculated (Machan and Bennett, 2008). As above, multiple instruments are required to provide quantitative information regarding ground movement. Investigation of ground movement over larger areas can be accomplished using aerial reconnaissance and LIDAR, and is done regularly by asset owners such as Network Rail (Birch and Anderson, 2010). These methods, however, provide topographical information only, and therefore are not currently capable of capturing potentially rapid changes in subsurface hydrogeological conditions prior to slope failure, for example, in the case of rainfall-induced landslides.

All of the above methods certainly provide useful information in slope stability assessments. However, a considerable volume of instrumentation is required in order to gather enough information to make any quantitative inferences regarding the susceptibility of engineered slopes to failure. Therefore, direct monitoring in this way is expensive, both from equipment and human resource perspectives, and is unable to satisfy the large-scale slope assessment requirements of UK transport infrastructure, particularly faced with additional pressures from a changing climate. For this reason, there is a wealth of ongoing research into geophysical imaging methods which may be able to provide a cost-effective monitoring solution to this problem.

Geophysical methods

Gravimetric methods allow changes in subsurface density to be mapped by the detection of gravimetric anomalies. However, due to difficult associated data processing, non-uniqueness of interpretation of results, and a low temporal resolution (Jongmans and Garambois, 2007), the use of gravimetric methods in landslide investigations is uncommon (Del Gaudio et al., 2000).

Seismic methods are well-established as a means of characterising unstable slopes (Bichler et al., 2004; Heincke et al., 2006; Samyn et al., 2012) and are based on measuring the propagation of elastic waves through the subsurface. These waves are then reflected or refracted on boundaries characterised by different densities and/or deformation properties, allowing the internal structure of materials in a slope to be determined (Hack, 2000). Due to the nature of the method, to identify discontinuities where the material properties change, it is particularly suited to characterising deep-seated landslides which may form, in part, due to the underlying bedrock geology. For engineered slopes, however, the composite material is unlikely to vary greatly in its material properties, therefore, seismic methods may be useful in mapping the subsurface, but are not ideally-suited to stability assessments.

Ground penetrating radar (GPR) presents a high resolution means of subsurface investigation, with a wide range of investigation depths in the field. It operates by emitting an electromagnetic pulse and detecting reflected signals from subsurface structures. However, its use in the investigation of landslides is severely limited by the fact that GPR signals are significantly attenuated in highly conductive formations, thereby inhibiting its use

in clay slopes and high moisture environments. Despite this, GPR has been successful in aiding the identification of potential slip surfaces when combined with other geophysical methods (Bichler et al., 2004). Other electromagnetic (EM) survey methods investigate changes in the subsurface conductivity by the application of a known current to establish a subsurface magnetic field (Hack, 2000). Several studies have used EM surveying for landslide investigation, including Caris and Van Asch, 1991, Schmutz et al., 2000 and Bruno and Marillier, 2000. EM methods are able to capture changes in subsurface conductivity of as little as 3 % (Sub Surface Surveys, 2016), and therefore are capable of identifying hydrogeological property changes associated with engineered slope instability. Given that the method of data collection, however, involves a walk-over survey with EM equipment, EM surveying has a low temporal resolution, and high associated costs. Other geoelectrical imaging methods such as electrical resistivity tomography (ERT), involve in situ sensors, and therefore have the potential to provide a high resolution, cost-effective monitoring solution.

2.3 Electrical resistivity tomography (ERT)

2.3.1 *Principles of resistivity imaging methods*

Basic principles

Electrical resistivity tomography is a geoelectrical method which allows minute changes in the ground resistivity distribution to be imaged. It relies upon Ohm's Law (Eqn. 2.5) which defines current as a function of input voltage and circuit resistance:

$$V = IR \qquad \text{Eqn. 2.5}$$

where *V* is voltage, *I* is current and *R* is resistance. Therefore, if the input voltage of a system is known, and the current measured, then the circuit resistance may be obtained. Resistance, however, depends upon the geometry of the resistive medium, and therefore cannot be considered an inherent material property. This geometry is accounted for in the Geometric Factor, *K*, which describes how current diffuses within the medium:

$$K = \frac{A}{L} \qquad \text{Eqn. 2.6}$$

where *A* is the cross-sectional area of the resistive medium, and *L* is its length, as shown in Figure 2.16. The geometric factor can then be used to effectively normalise the resistance

for geometry, allowing resistivity to be defined as an inherent material property:

$$\rho = RK \qquad \text{Eqn. 2.7}$$

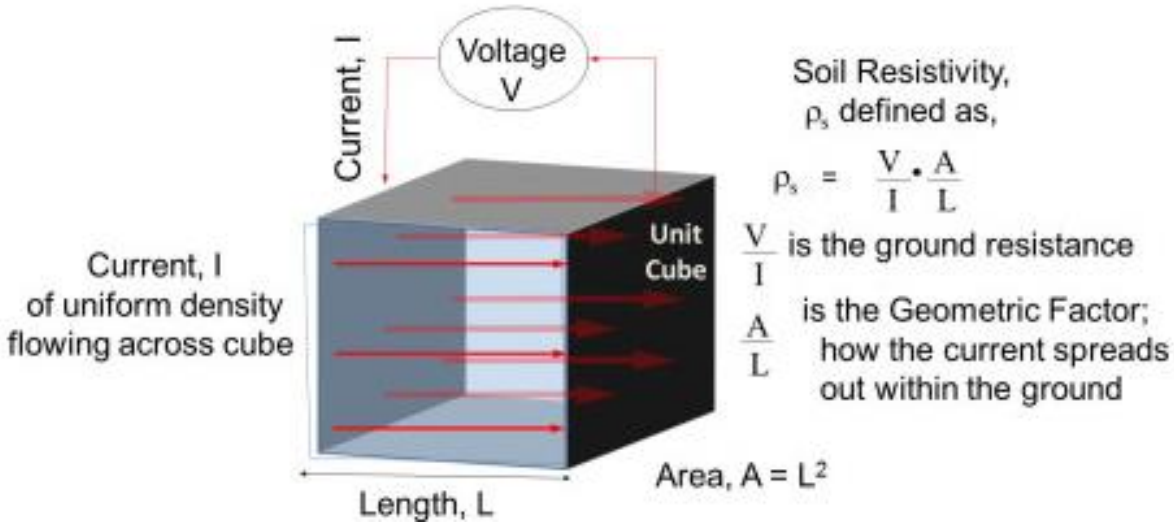

Figure 2.16 Definition of electrical resistivity (image taken from Gunn et al., 2015)

Measurement of resistivity

Following the approach outlined above, material resistivity measurements may be obtained using either of two methods: the two point method involves setting up a potential difference between two electrodes, and then using the same two electrodes to measure the induced current; the four point method also uses a pair of electrodes to set up a potential difference, thereby inducing a current, but uses a separate pair to measure a potential difference (voltage). The two point method is described in BS 1377-3: 1990 and ASTM G187 (BSI, 1990c and ASTM, 2012), and is recognised as the current industry standard within the field of Geotechnics, which is a function of its simplicity. In any electrical circuit, current flow may be impeded as a result of contact resistances at interfaces between electrical conductors within the circuit, defined by a voltage drop, as described in ASTM B539-02, "Standard Test Method for Measuring Resistance of Electrical Connections" (ASTM, 2013). In general, these resistances are relatively small, however, for materials which are poor electrical conductors, weak coupling may result in significant contact resistances. Within the two point method, the fact that the same pair of electrodes is used for both current and potential measurements dictates that the recorded voltage describes the potential drop at the meter terminals, rather than across the material tested (Cropico, 2017). Therefore, the effects of contact resistances at the specimen-electrode interface are included, as are all resistances within the rest of the circuit, which may cause resistivity to be over-estimated (Heaney,

2003). The advantage of the four point method, however, is that because the current and potential electrode pairs are distinct, their measurements are electrically isolated from one another. As such, the recorded voltage describes the potential drop across the tested material, excluding contact resistances within the rest of the circuit. Therefore, the only source of contact resistance is that between the potential electrodes and the specimen, which can be minimised (although there will be some current flow in the potential leads, this is negligible in comparison (Cropico, 2017)). The result is that contact resistances present within four point measurements are considerably lower than those present within two point measurements. There is relatively little published work which compares these two methods for the purposes of testing earth materials, however, several works discuss them within the context of other applications (Janesch, 2013; Miccoli et al., 2015). These authors note the significance of the inclusion of additional contact resistances inherently associated with two point testing.

Resistivity relationships

These basic principles which describe the flow of current may be applied to soils, due to the fact that many of their material properties affect their ability to conduct electrical current.

The relationship between resistivity and temperature is well-established for a range of materials, and describes a linear decrease in material resistivity associated with an increase in temperature. Within the field of soil science, this relationship is broadly characterised by a 2 % decrease in resistivity per 1 °C increase in temperature; standard practice for reporting resistivity values is to correct to a standard reference temperature (Tanji, 1990). Specific research studies into the temperature-dependence of clay resistivity have reported comparable values, of between 1.8 % and 2.2 % bulk resistivity change per °C (Hayley et al., 2007).

Subsurface resistivity is largely determined by ground water content: since the amount of moisture stored within the composite soil or rock is controlled by the volume of pore space (i.e. the porosity), and the composite material density, these factors also contribute towards determining subsurface resistivity (Gunn et al., 2015). At the micro-scale, the explanation for the dependence of ground resistivity on water content pertains to additional ionic conduction through pore water, and therefore, the ionic content of the pore water (and of

the composite soil or rock) must also be considered. Typical resistivity values of earth materials are shown in Figure 2.17, and describe a range of values for any one material, resulting from the parameters described above varying naturally in the field.

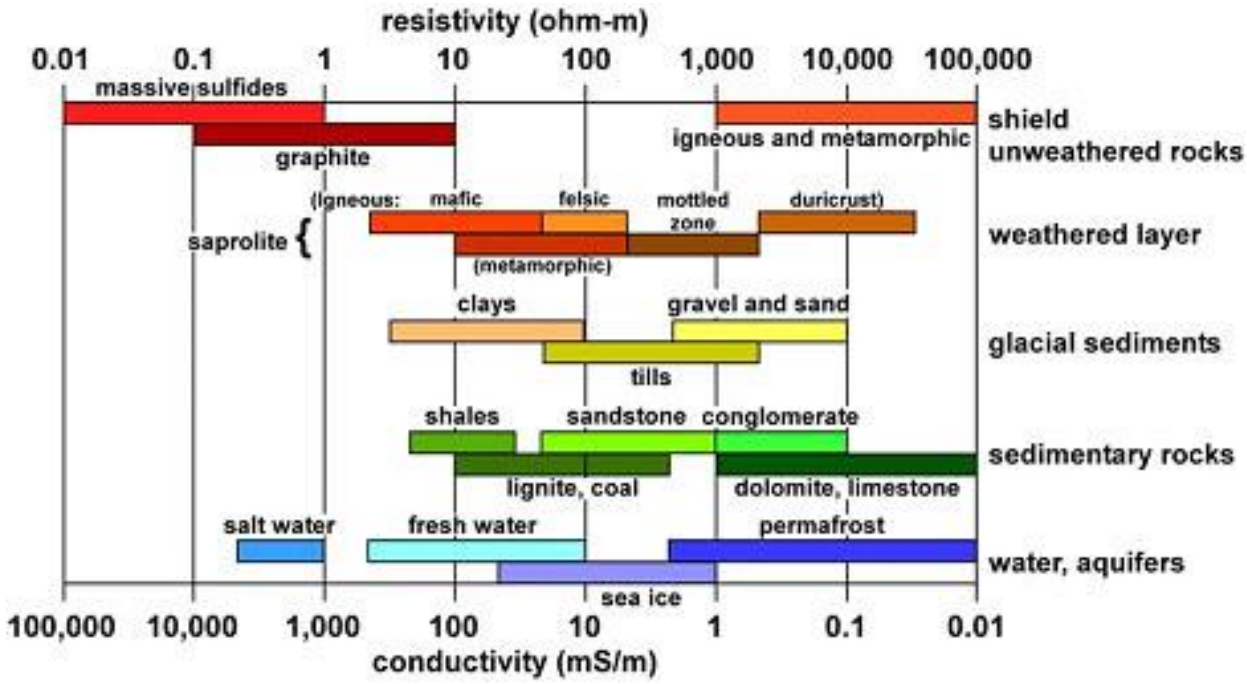

Figure 2.17 Typical resistivity values for selected earth materials (image from Palacky, 1988)

A distinction can be made between the processes which determine electrical conduction between different soil materials, as can be observed from Figure 2.18: in sands and gravels, current flow is via ionic migration, within the saturation fluid (Figure 2.18a); within clays, however, there is additional matrix current flow generated by the movement of ions distributed across the surfaces of the clay particles, which can be explained as follows: most clay particles have a negative surface charge, attracting cations to the particle surfaces, which are deposited under dry conditions. In the presence of water, these cations diffuse away from the clay surface, creating another layer of charge, as shown in Figure 2.18b and d. The charge distribution at the clay surface is controlled by the equilibrium between the tendency to diffuse and the electrical attraction. The application of a potential gradient across clays promotes migration of these additional charges, contributing additional matrix conduction to the fluid current flow, as explained in Gunn et al., 2015. For mixed soils which contain both spherical grains and clay particles, the clay particles may cause the development of a conducting film across otherwise non-conducting grains (as shown in Figure 2.18c).

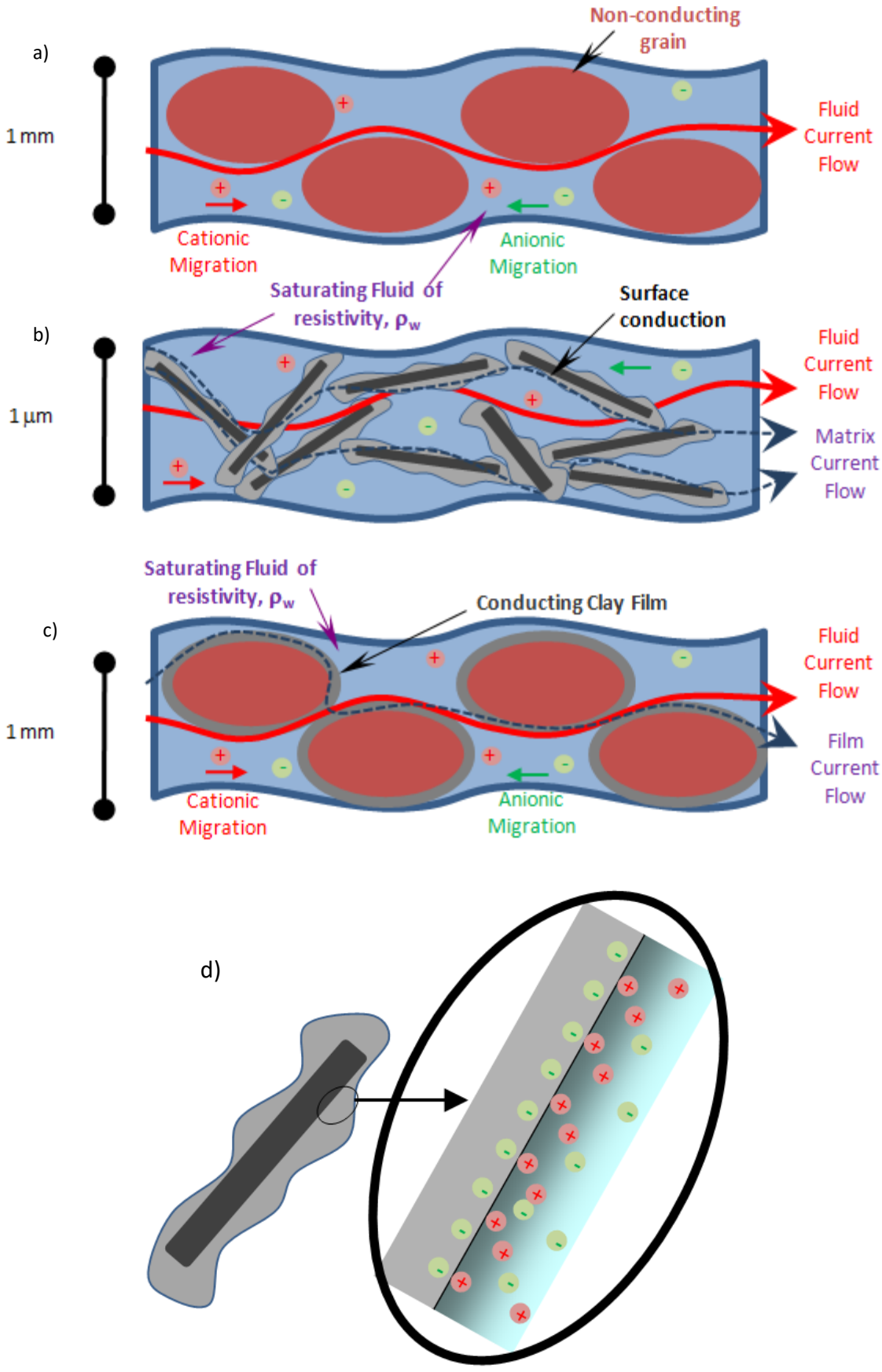

Figure 2.18 Current flow and resistivity of different soil types, showing (a) granular; (b) clay; (c) mixed material (image adapted from BGS, 2010)

2.3.2 *Petrophysical relationships*

The correlation between resistivity and moisture has been resolved into a number of different petrophysical relationships, which account for the different parameters described in the previous section. The Archie equation (Archie, 1942) describes a single conducting phase through pore water (Eqn. 2.8), where the soil resistivity ρ_s is related to the pore water resistivity ρ_w by the degree of saturation, S, and the saturation exponent, p. The compaction characteristics of the soil are incorporated within the tortuosity factor, q, and the porosity, φ. The cementation exponent, m, is related to the conductivity of the conductive phase.

$$\rho_s = q\ \rho_w\ \varphi^{-m}\ S^{-p} \qquad \text{Eqn. 2.8}$$

As the Archie equation describes only a single conducting phase, it can be applied to granular soils such as sands and gravels, as in Figure 2.18, but does not describe the water content-resistivity relationship for clays or mixed soils.

The Waxman-Smits equation (Waxman and Smits, 1968) describes the relationship for clays, which are in general, much less resistive than granular materials because of additional matrix conduction. The equation employs the same parameters as the Archie equation, but with the addition of two terms to account for matrix conduction: B, the average ionic mobility of cations in the double diffuse layer, and Q_v, the cation concentration per unit volume (proportional to the cation exchange capacity, C).

$$\rho_s = \frac{q\ \rho_w\ \varphi^{-m}\ S^{(1-p)}}{(S + \rho_w\ BQ_v)} \qquad \text{Eqn. 2.9}$$

High resistivity clays, including Kaolinite, have a low cation exchange capacity, compared to low resistivity clays such as Smectite, which have a high cation exchange capacity. Due to the fact that the plasticity index generally increases with cation exchange capacity, resistivity imaging could potentially be used to provide a proxy for shear strength as well as water content, and therefore to aid in the quantitative assessment of slope stability (after Gunn et al., 2015). It should be noted that the Waxman-Smits and Archie expressions are equivalent if the cation concentration, Q_v, is 0, i.e. if there is no additional matrix current flow.

2.3.3 *ERT data collection*

In subchapter 2.3.1, the principles of resistivity testing were discussed, describing two types of measurement (two and four point, respectively). In the field, which can be considered a

half-space, the dissipation of electrical current in three dimensions prohibits a two point measurement from being obtained, as it requires a closed circuit. Therefore, field electrical resistivity tomography is based on four point measurements of a half-space, using a network of electrodes to gather resistivity data at a range of locations. Lines of electrodes are installed in the near-surface, and alternating pairs used to impart current (by setting up a potential difference) and measure voltage (Figure 2.19), where *C1*, *2* and *P1*, *2* refer to the current and potential electrodes, respectively. Parameters *a* and *n* then describe the electrode separation. A number of different electrode configurations exist, with correspondingly different geometric factors, as shown in Figure 2.20. In Eqns. 2.6 and 2.7, the method for determination of the geometric factor, *K*, was presented, showing its application in the calculation of resistivity. These equations refer to testing of discrete samples of material, and must be modified for field testing in order to reflect a half-space, as shown in Figure 2.20.

ERT sensitivity and electrode configurations

The selection of the most-appropriate configuration for a field survey depends on the specific environmental setting (after Loke, 1999), as is highlighted by the sensitivity contour diagram shown in Figure 2.21. The figure illustrates the degree to which a change in the resistivity of a particular portion of the subsurface will influence the potential measured by a given array (Loke, 2015b), as determined by the sensitivity function. This sensitivity is described mathematically by the Fréchet derivative for a half-space (McGillivray and Oldenburg, 1990, as reported in Loke, 2015b), and given in Eqns. 2.10a and b, describing the sensitivity function in two and three dimensions, respectively. The coordinate system is defined by *x* (in plane distance), *y* (out of plane, lateral distance) and *z* (depth):

$$F_{2D}(x,z) = \frac{1}{4\pi}\int_{-\infty}^{+\infty} \frac{x(x-a)+y^2+z^2}{\left[x^2+y^2+z^2\right]^{1.5}\left[(x-a)+y^2+z^2\right]^{1.5}}\,dy \qquad \text{Eqn. 2.10a}$$

$$F_{3D}(x,y,z) = \frac{1}{4\pi^2}\frac{x(x-a)+y^2+z^2}{\left[x^2+y^2+z^2\right]^{1.5}\left[(x-a)+y^2+z^2\right]^{1.5}} \qquad \text{Eqn. 2.10b}$$

where $F_{2D}(x,z)$ is the sensitivity of the ERT array at position (x,z), with potential electrode separation, a, and lateral contributions to the measured resistivity from $y = \pm \infty$, and $F_{3D}(x,y,z)$ is the sensitivity of the ERT array at position (x,y,z). Regions with higher relative sensitivity values have greater influence on the measured resistivity than do those with lower values. In Figure 2.21, general 2D qualitative distribution patterns are shown for different electrode configurations (actual numerical values are not shown as these are dependent on the dimensions of the array in question, as is evident from Eqn. 2.10a), aiding in the explanation of the response of the different configurations to different subsurface structures: the Wenner configuration, for example, has near-horizontal contours in the sensitivity plot shown in Figure 2.21g, and is therefore relatively sensitive to vertical changes in subsurface resistivity below the centre of the array (i.e. horizontal structures), however, its horizontal resolution is poorer. Due to the fact that the geometric factor is inversely proportional to the signal strength, the low geometric factor of the Wenner array (compared to other configurations) results in it having the strongest signal strength, which may be important in high background noise survey areas. The Wenner-Schlumberger array differs slightly from the Schlumberger array resulting in different sensitivity contours (Figure 2.21i), such that the array is moderately sensitive to both horizontal and vertical resistivity changes, which is useful in survey settings where the presence of both horizontal and vertical structures are anticipated. Additionally, the median depth of investigation (detailed further in the following section) is approximately 10 % greater than that of the Wenner array. The dipole-dipole array (Figure 2.21b) involves distinct current and potential pairs which do not overlap, resulting in low electromagnetic coupling between them, and is widely used as a result. The dipole separation, a, is common to both pairs, and n describes the ratio of the distance between the inner electrodes and the dipole separation. During surveying, a is initially kept fixed, and n increased incrementally, in order to increase the depth of investigation. The sensitivity plot demonstrates that the highest sensitivity values occur between the dipole pairs. By varying the location of the dipole pairs, it is then possible to vary the depth of investigation, and the high-sensitivity zones. From Figure 2.21b, near-vertical sensitivity contours are observed, resulting in the configuration being highly sensitive to horizontal resistivity changes (e.g. dykes), but relatively insensitive to vertical ones such as sedimentary layers. In general, the dipole-dipole configuration has a shallower depth of investigation compared to the Wenner configuration, but better horizontal data coverage. For greater values of n, there is a considerable decrease in the signal strength,

constituting a potential disadvantage of the method, but this may be overcome by increasing the dipole separation, *a*.

The above demonstrates how sensitivity plots are used as an aid in selecting configuration parameters for field surveys. Figure 2.21 describes the sensitivity distribution patterns arising from one set of current and potential electrodes only, capable of making a single resistivity measurement: in order to produce a bespoke sensitivity plot for an entire array, the sensitivity function must be applied at all measurement points within that array. In Figure 5.34a and b, a comparison of planar 2D and 3D dipole-dipole sensitivity plots was generated along a central profile of the ERT array employed in this study. These figures were used to highlight the higher relative sensitivity of 3D electrical resistivity tomography, which, as a result, became the focus of the analysis undertaken in Chapter 5, demonstrating the use of sensitivity plots in interpreting ERT data, in addition to aiding in survey design.

Apparent resistivity pseudosections

For each of the configurations, recorded currents and voltages are inverted using Ohm's law (Eqn. 2.5), and converted to resistivity using the appropriate geometric factor (following the method described in subchapter 2.3.1). Along an ERT profile, the variation of current and electrode pairs allows resistivity data points to be gathered for a range of grid points, as shown in Figure 2.22 for the Wenner configuration. Generally, the horizontal location of the resistivity measurement is set at the midpoint of the set of electrodes employed in the measurement (Loke, 2015b). In order to increase the depth of investigation, the distance between the electrode pairs is increased, however, there is some disagreement as to how this depth should be derived. One method involves placing the measurement point at the intersection of two lines at 45˚ to the horizontal, originating from the midpoints of the current and electrode pairs. This method, demonstrated in Figure 2.19, is commonly used for dipole-dipole surveys, but is merely a convention, which simplifies the processing of ERT data but has no specific physical basis. A second method involves placing the vertical component of the measurement point at the median depth of investigation (Edwards, 1977). This "pseudodepth" is obtained from the sensitivity section (e.g. Figure 5.34) as follows: between one set of current and potential electrodes, the sensitivity plot demonstrates the range of depths which may affect a resistivity measurement; the median value is then taken as the pseudodepth. Due to the fact that this method uses the sensitivity contours which are

described by the Fréchet derivative, this second method has a more established mathematical basis (Loke, 2015b).

Following each resistivity measurement, the current and electrode pairs may be switched and a reciprocal measurement obtained, as a means of verifying the initial value, as recommended by Binley et al., 1996 and Slater et al., 1997. It is crucial to understand that the recorded values represent an apparent resistivity of the subsurface, which differs from the true resistivity for heterogeneous materials. This suite of apparent resistivity values, as shown in Figure 2.19 and Figure 2.22, is then compiled in order to form an "apparent resistivity pseudosection", an example of which is given in Figure 4.51a. Inverse modelling is required to translate gathered apparent resistivity information into true resistivity values, which account for inhomogeneity within the subsurface resistivity distribution. This type of modelling is the primary function of resistivity inversion software, which is available for both 2D and 3D ERT arrays (e.g. Res2DInv, Res3DInv, see Loke, 2015 and Loke, 2016).

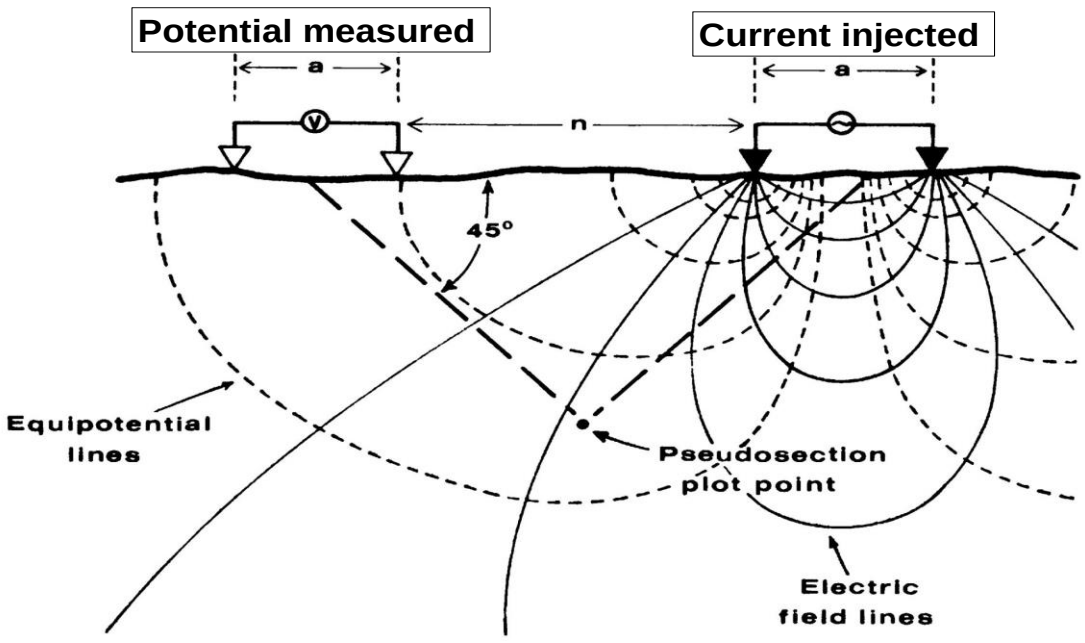

Figure 2.19 Current and potential electrode pairs (example uses the dipole-dipole configuration) (image from Zonge International, 2013)

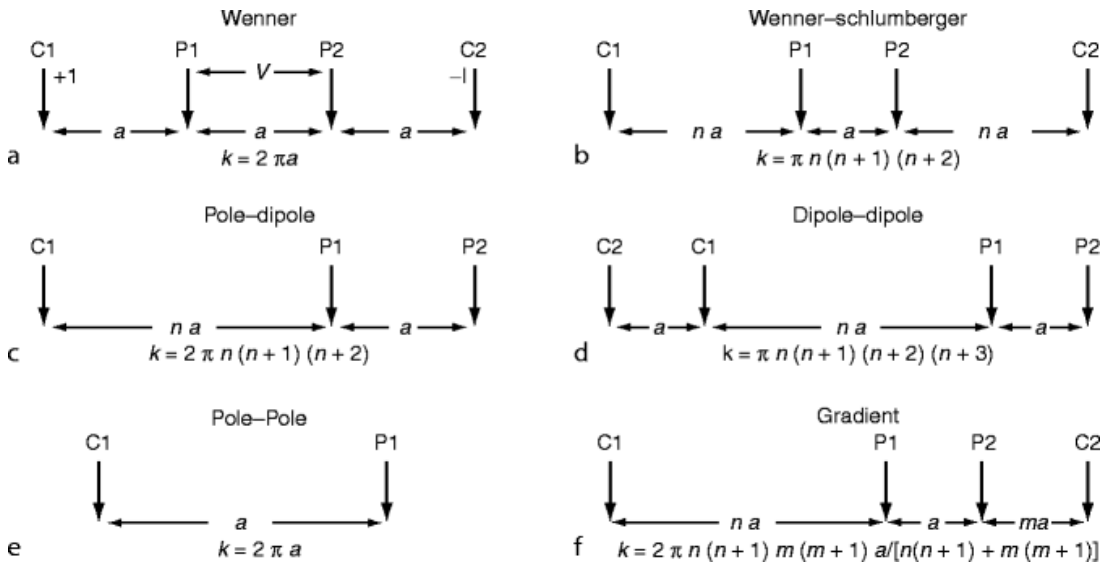

Figure 2.20 Principal ERT array configurations (image from Loke et al., 2011)

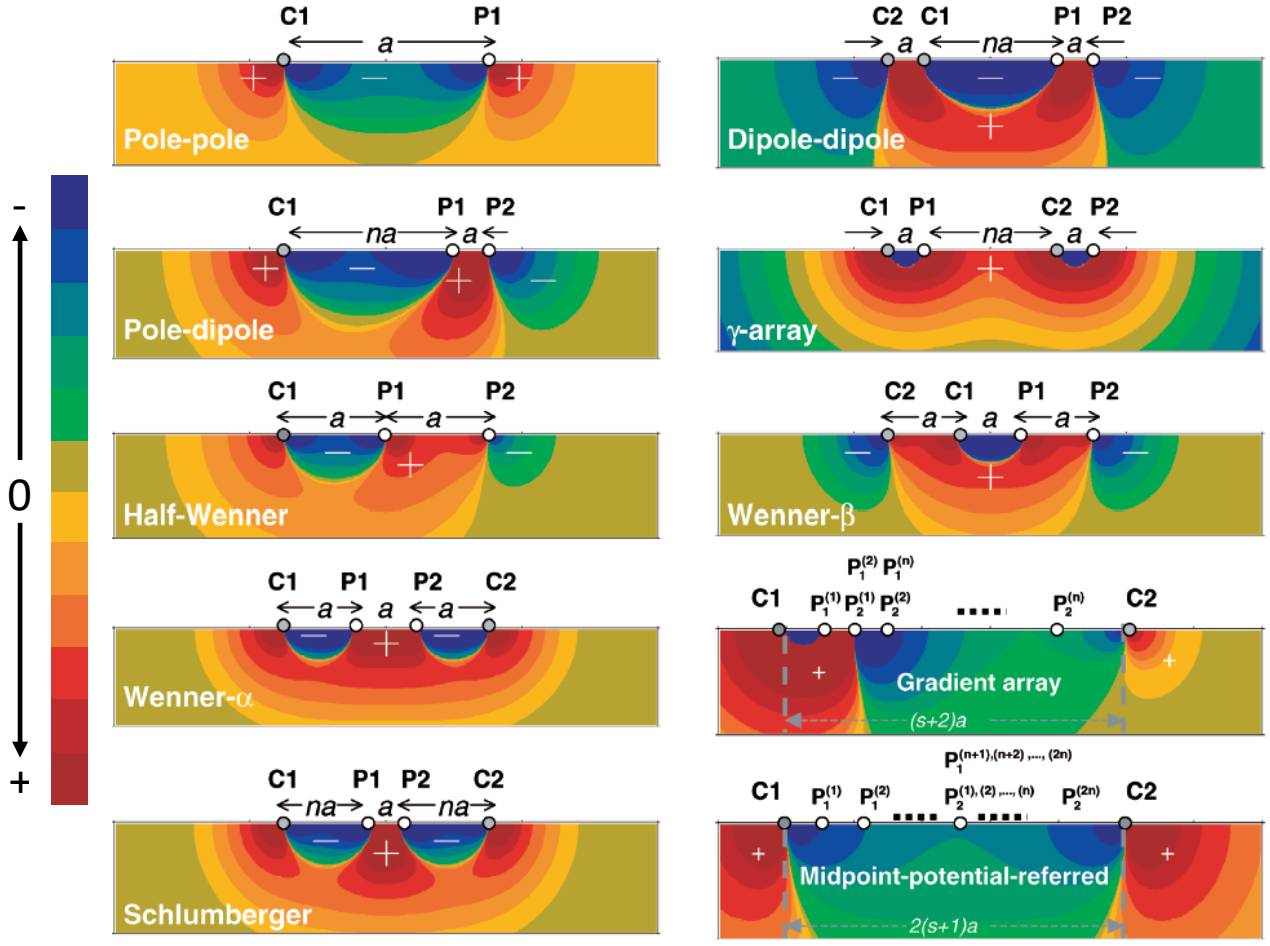

Figure 2.21 2D sensitivity sections for different electrode configurations (image modified from Dahlin and Zhou, 2004)

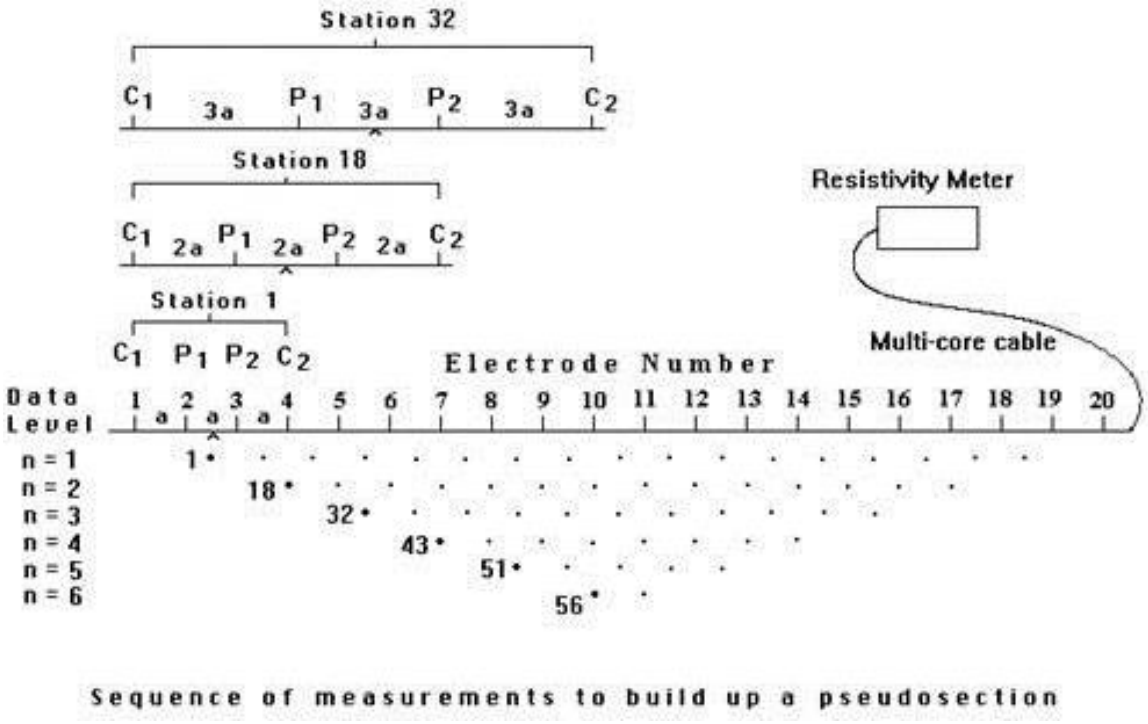

Figure 2.22 Construction of a resistivity pseudosection. The example shown uses the Wenner configuration (image from Loke et al., 2011)

Accuracy of ERT

There are several different facets which influence the accuracy of an ERT-derived ground resistivity measurement. In the first instance, the reciprocal error gives an indication as to the quality of recorded data, whereby a high value indicates non-robustness; these may then be excluded from analysis. In the previous subchapter, the inversion process was described, whereby the apparent resistivity pseudosection is translated into a resistivity model (see Figure 4.51c). This model is then used to produce a calculated apparent resistivity pseudosection, which may be compared to the original, measured pseudosection (see Figure 4.51a and b). An absolute error may then be calculated, relating the two; a high error indicates discrepancy between the model and the survey site, and often arises from poor-quality data. By increasing the distance between measurement electrodes, the investigation depth is increased, however, there is an associated loss in model resolution at depth due to the longer electrical flow path, leading to greater dissipation of current, and hence a lower signal to noise ratio.

The previous subchapters have discussed the factors affecting soil resistivity and the physical relationships which relate it to the material environment. In order to account for the effects

of these parameters (including temperature and porosity), it is necessary to have physical models which describe them, which are then used in the processing of ERT data to construct a final resistivity model. As such, the final resistivity model may only be as good as the physical models which are used to derive it. Efforts must therefore be made to ensure that these physical models are as robust as possible, and where possible, verified with the results of in situ point sensors.

2.3.4 *Applications*

Electrical resistivity tomography is widely used across several disciplines, due to the fact that material changes with associated resistivity contrasts are relevant to a wide range of applications. The use of ERT is well-established within permafrost monitoring (Hauck et al., 2003; Hilbich et al., 2011) and archaeology (Hesse et al., 1986; Collier and Hobbs, 2003; Negri et al., 2008) to locate revetments and artefacts. It is used as standard method of geological characterisation (Sass, 2007; Hirsh et al., 2008; Hsu et al., 2010) due to its ability to identify differing geologies, and more recently, for monitoring CO_2 storage using cross-hole and down-hole ERT (Kiessling et al., 2010). ERT also has applications within cavities prospecting including for caves (Antonio-Carpio et al., 2004; Santos and Afonso, 2005) and sinkholes (Dobecki and Upchurch, 2006). It has applications within contaminant tracing, having been used to characterise contaminated fills (Boudreault et al., 2010) and to trace leachates (Depountis et al., 2005). A significant proportion of current research is concerned with groundwater; due to low resistivities associated with saltwater (a function of its high ionic content), ERT has been successful in imaging salinisation (Nassir et al., 2000; Bauer et al., 2006), contaminant tracing (Aaltonen, 2001), and in investigating aquifer hydraulics (Monego et al., 2010). Some of these applications are illustrated in Figure 2.23.

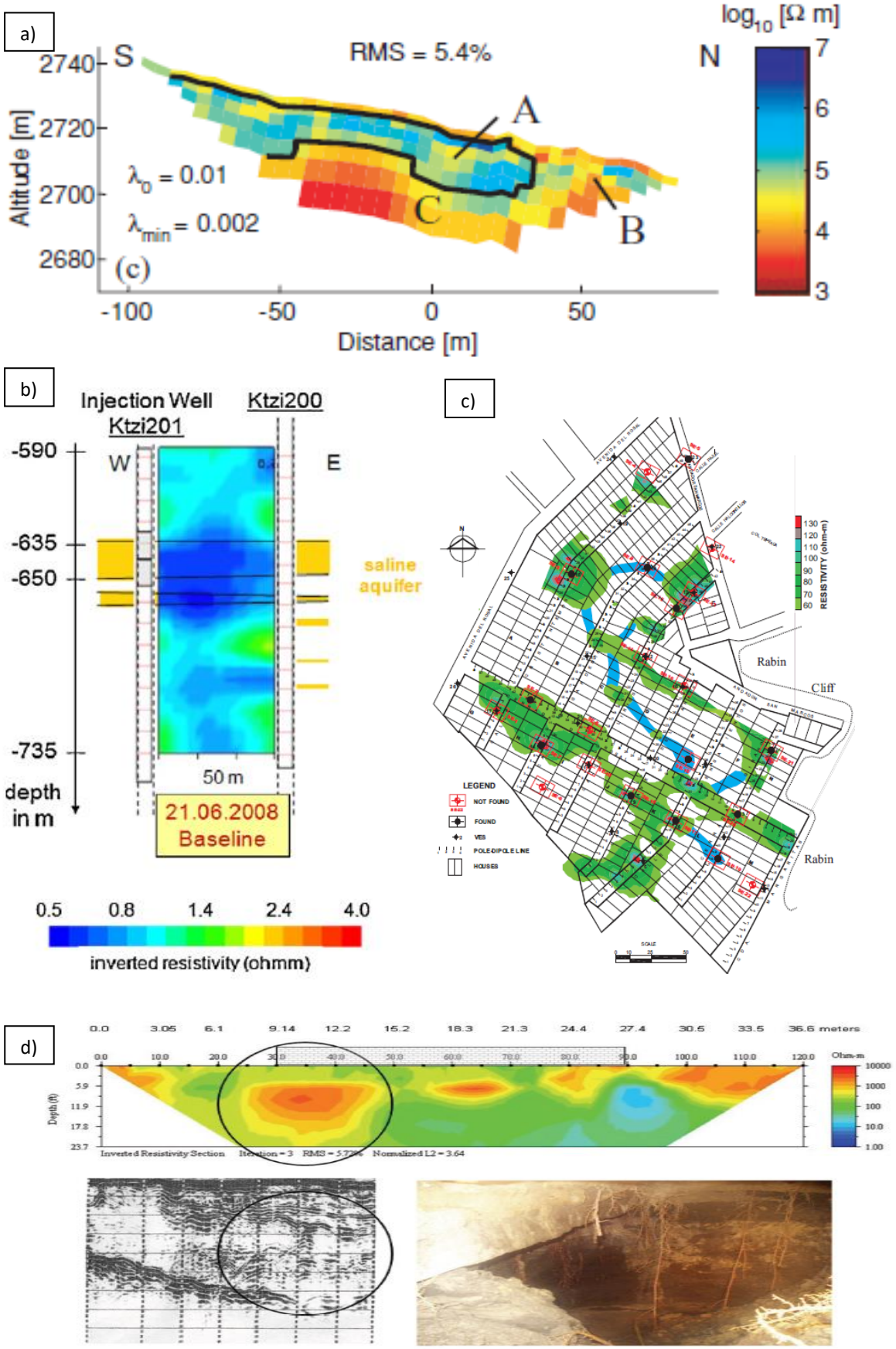

Figure 2.23 Examples of different applications of ERT investigation (a) permafrost monitoring (Hauck et al., 2003); (b) monitoring CO_2 storage (Kiessling et al., 2010); (c) urban cave detection (Antonio-Carpio et al., 2004); (d) sinkhole detection (also showing GPR and observational data) (Dobecki et al., 2006)

2.3.5 *ERT monitoring of slope stability*

In addition to the above, ERT is often used to investigate deep-seated natural landslides, and has been successfully used to map potential slip surfaces by identifying lithological discontinuities (Jomard et al., 2010). Figure 2.24 shows a resistivity cross-section from Lapenna et al., 2005 for the highly complex roto-translational Giarossa landslide. ERT results (obtained using the dipole-dipole configuration) were combined with data gathered at two bore holes within the survey area, allowing a potential slip surface to be identified. A similar study, undertaken by Perrone et al. (2008) on another clay slope in Italy, was able to infer a geotechnical model of the slope, again using a combination of bore holes and ERT investigation (see Figure 2.25). For both of these studies, several ERT surveys were undertaken, sampling different portions of the slopes, and ultimately providing subsurface information in three dimensions.

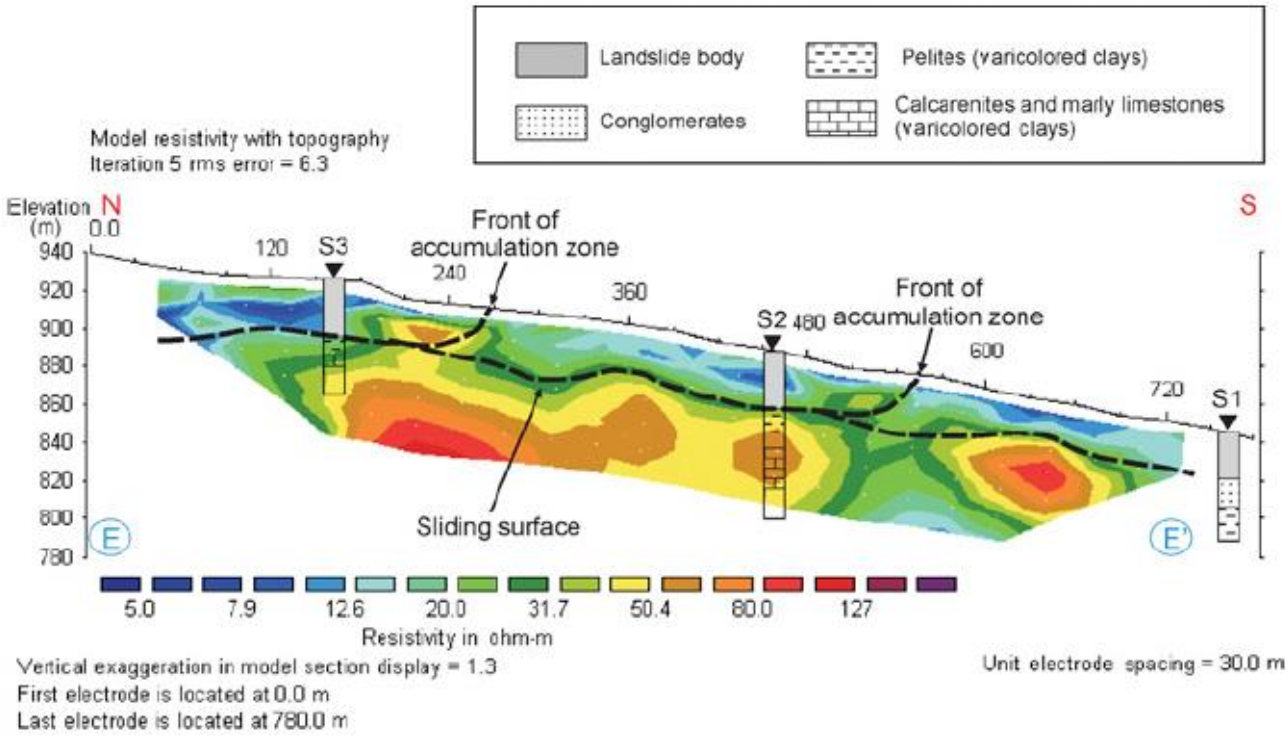

Figure 2.24 Use of ERT to identify lithological discontinutities within a deep-seated landslide system - the complex Giarossa landslide in the Lucanian Apennine chain of Southern Italy (image from Lapenna et al., 2005)

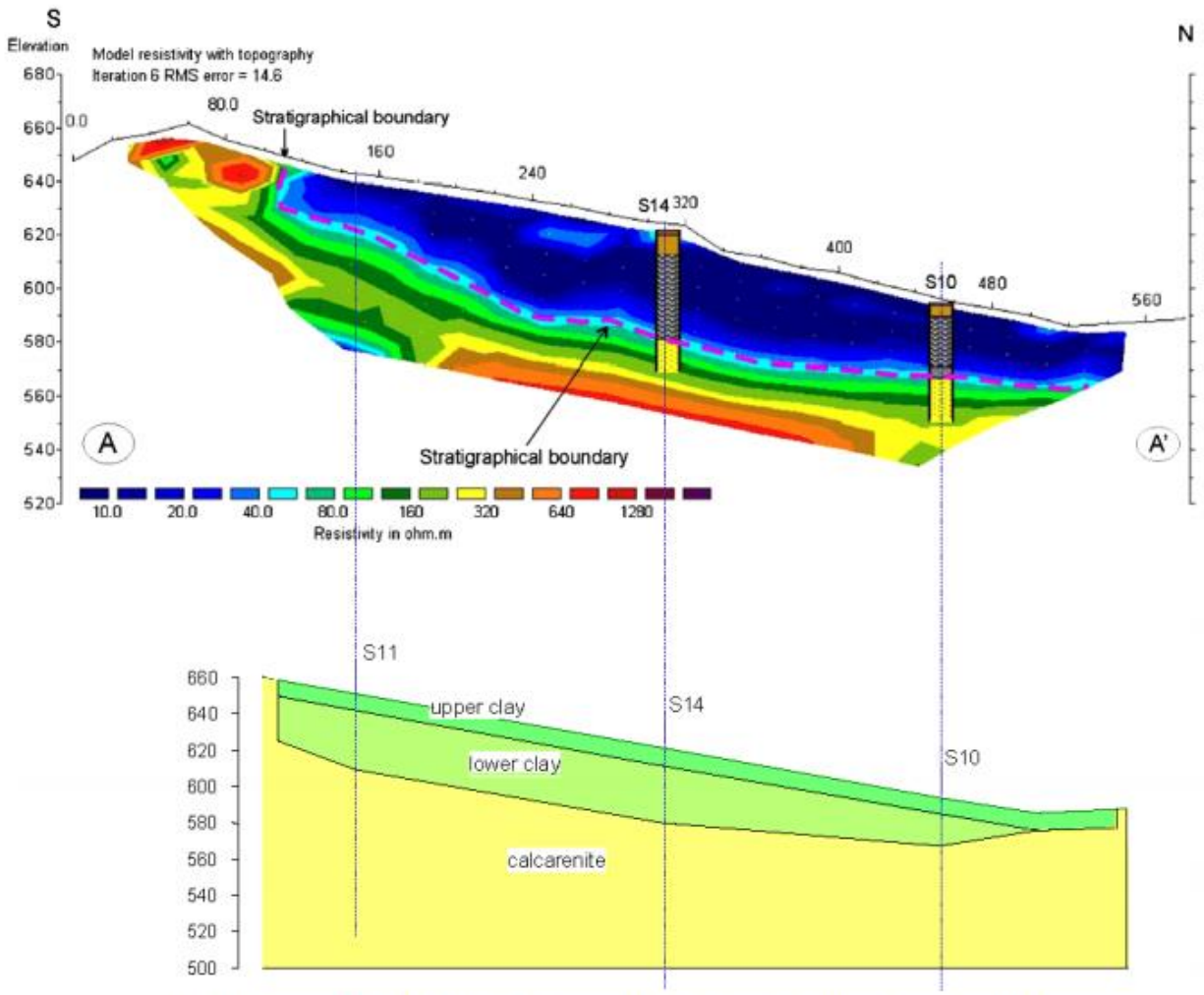

Figure 14. Geotechnical model resulting from the combined use of geotechnical investigations and ERTs.

Figure 2.25 ERT and bore hole investigation of a clay slopein the Southern Apennines of Italy, and an inferred geotechnical model (image from Perrone et al., 2008)

In the study by Bichler et al., 2004, on the Quesnel Forks landslide in British Columbia, Canada, a total of ten ERT profiles were gathered, in directions both perpendicular and parallel to the head scarp, covering a total of 4100 m (see Figure 2.26). Using this grid-based approach, the authors were able to identify the slip surface by the presence of low resistivities beneath the landslide, in three dimensions. The ERT investigation formed part of a multi-geophysical approach, employing both ground penetrating radar and seismic reflection and refraction surveys; ERT data were supported by those gathered from the other survey types.

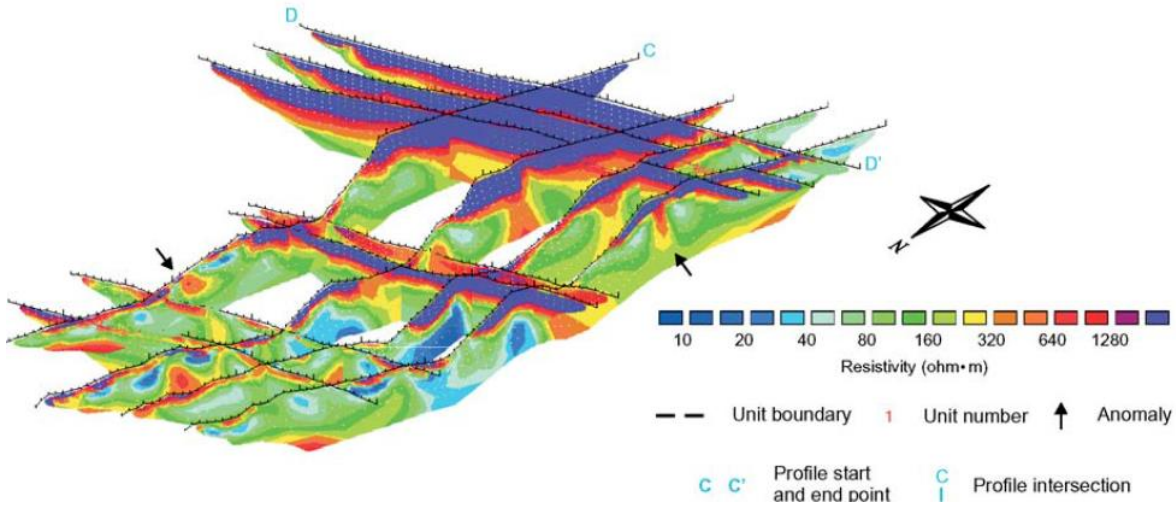

Figure 2.26 Grid-based ERT profiling for landslide investigation (image from Bichler et al., 2004)

Within the context of infrastructure slopes, the dynamics of the near-surface are the determining factors for slope instability. As explained previously, near-surface landslides are broadly associated with hydrodynamically-generated instability, and therefore, ERT investigation of near-surface landslides employs the same basic principle involved in that for groundwater investigation: essentially, that groundwater is highly conductive due to its high ionic content. Using this principle, ERT has been deployed to broadly investigate the hydrogeological environment of landslide-prone areas (e.g. Lee et al., 2008; Cassiani et al., 2009) and also to locate high moisture zones (e.g. Amidu and Dunbar, 2007 (see Figure 2.30); Schmutz et al., 2009). The role of fissures in slope failure (particularly for volume-sensitive clay soils) was discussed in subchapter 2.2.4, therefore, the ability of ERT imaging to capture soil cracking is essential. LaBrecque et al. (2004) conducted laboratory experiments to show that fractures in rocks had associated high resistivity anomalies (air-filled fractures) and low resistivity anomalies (water-filled fractures); using this principal, Bièvre et al. (2012) were successful in identifying the presence of fissures within a clay landslide, from temporal changes in resistivity investigated using time-lapse ERT. Ultimately, if ERT imaging is to be used to monitor the stability of engineered slopes, both a high spatial and temporal resolution are required.

In recent years, developments in time-lapse ERT methods have facilitated research into the triggering factors of slope instability. Friedel et al. (2006) employed both 2D and 3D time-lapse methods to investigate a slope endangered by rainfall-induced landslides, leading to an improved understanding of the hydrogeological conditions leading to failure; the images

were then combined with geotechnical data and used to optimise the design of a forthcoming monitoring experiment. The study by Perrone et al. (2008) employed a multi-disciplinary approach, whereby inclinometers and piezometers were used to measure slope displacements and pore pressures respectively, and correlated against ERT images. In this way, the authors were able to derive a geotechnical model which served as the basis for studying the pore water pressure distribution and for analysing the influence of hydraulic conditions on slope stability. In a similar study, Lebourg et al. (2010) used time-lapse ERT imaging of a recurrent natural landslide to identify correlations between rainfall, infiltration and resistivity variation in a sliding mass. Subsequently, the authors were able to identify a critical resistivity level, corresponding to a piezometric elevation which they interpreted as a precursor to the reactivation of the landslide.

These studies ultimately describe a methodology for the use of electrical resistivity tomography as a qualitative tool for monitoring slope stability. The logical next step involves the development of methodologies for using ERT imaging in a more quantitative capacity, which may then be used to monitor slope stability in real-time.

2.3.6 *Quantitative resistivity studies*

Several studies have investigated the nature of resistivity-moisture relationships both independently, and in conjunction with field electrical resistivity tomography studies for a range of earth materials. Roberts and Lin (1997) performed a suite of two point resistivity tests on partially-saturated tuff, resolving an inverse power relationship, where dry resistivity differed from saturated resistivity by up to four orders of magnitude. A study by Knight (1991) on sandstone resolved a similar relationship. Laboratory tests on clays by McCarter (1984), Fukue et al. (1999) and Michot (2003) employed two point resistivity methods on clay soils, each resolving an inverse power relationship. The results of these three studies are illustrated in Figure 2.27, showing results which are in close agreement with each other. Generally, at high water contents, large changes in soil moisture are accompanied by small changes in resistivity; at low water contents, however, small changes in moisture correspond to large changes in resistivity. For all three datasets, a steep increase in the resistivity curve is seen at water contents below approximately 20 %, which may coincide with the break in continuity of the water phase, as described in Fukue et al., 1999.

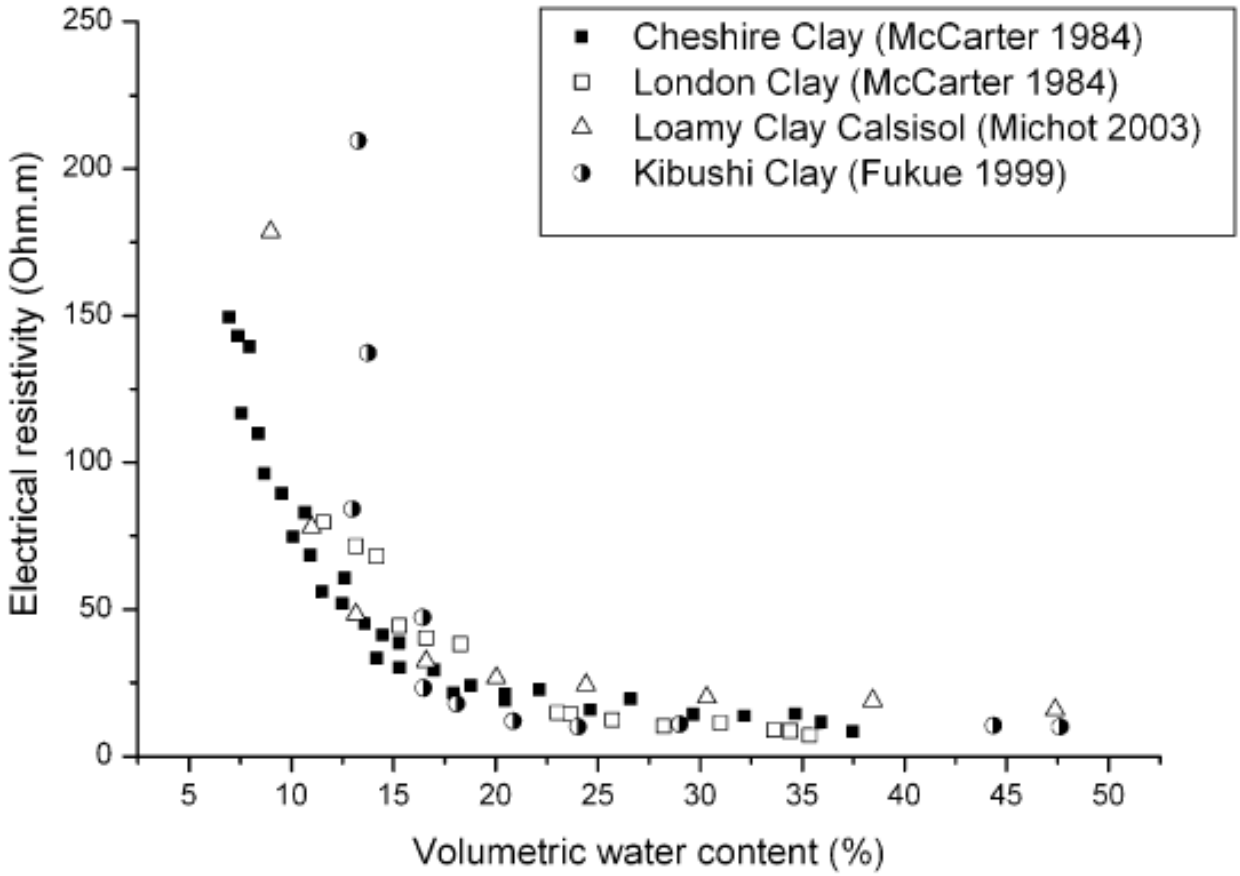

Figure 2.27 Published relationship between two point electrical resistivity and volumetric water content for selected clays, as determined by three independent studies (image from Samouelian et al., 2005)

Due to the inclusion of higher contact resistances within two point resistivity measurements, recent studies have focussed on four point resistivity testing (e.g. Amidu and Dunbar, 2007; Brunet et al., 2010; Hassan, 2014; Merritt, 2014). All of these works, performed on clay-rich materials, also resolved inverse power relationships between resistivity and water content (see Figure 2.28 and Figure 2.29). However, none of the above studies employed both two and four point methods, so although it is likely that lower resistivity values would have been recorded using the four point method, this is impossible to state with certainty.

In general, an inverse power relationship is resolved between resistivity and moisture content of earth materials (soil and rock), regardless of whether a two point or a four point measurement is made, which is in keeping with the petrophysical relationships presented in subchapter 2.3.2 (Archie and Waxman-Smits relationships). Due to the effects of desiccation at very low water contents, all of the studies discussed exhibit a minimum water content at which resistivity data may be recorded (as described by Amidu and Dunbar, 2007), as current flow is interrupted.

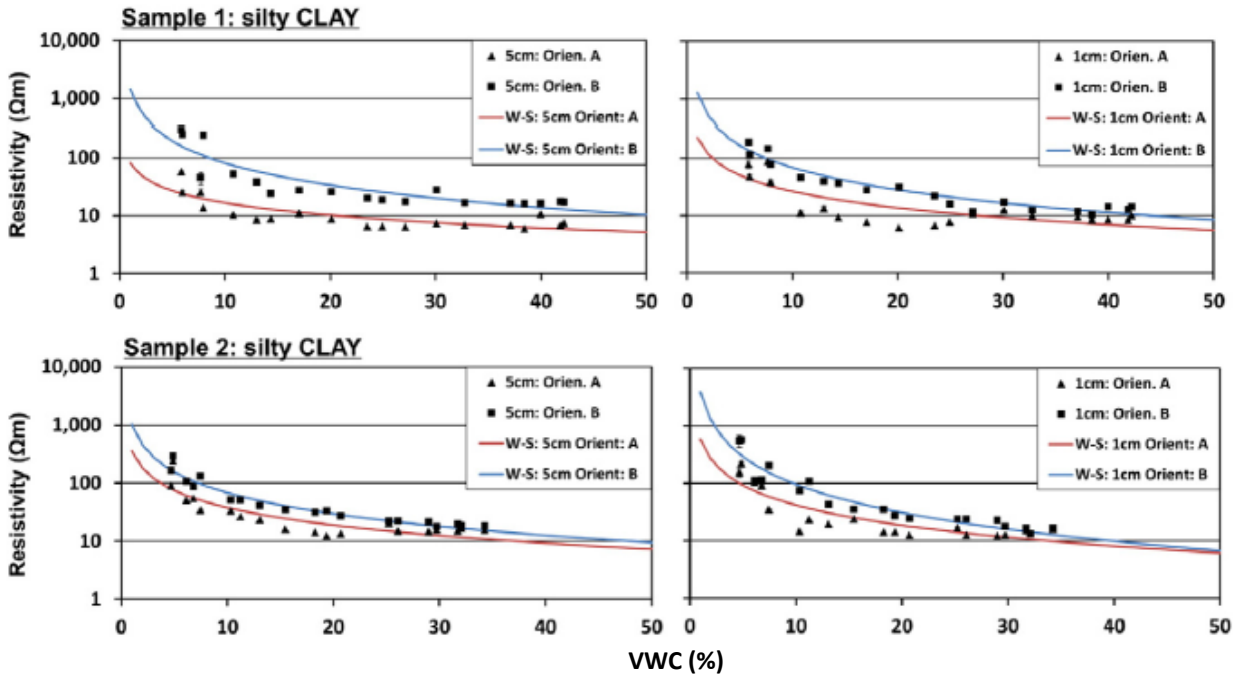

Figure 2.28 Published relationship between four point electrical resistivity and volumetric water content for a silty clay (image from Merritt et al., 2016)

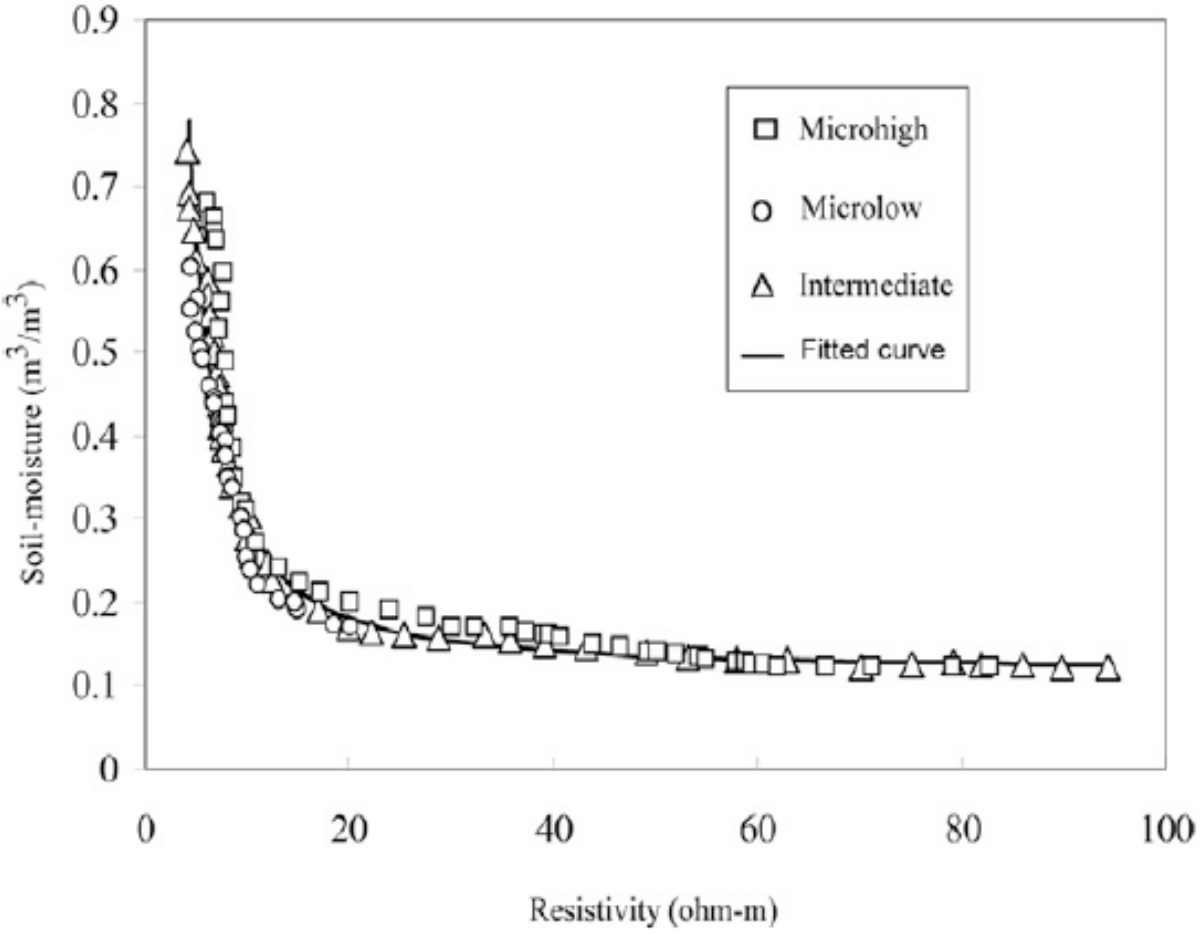

Figure 2.29 Published relationship between four point electrical resistivity and volumetric water content for a Vertisol (clay). Note, axes are reversed compared to Figure 2.27 and Figure 2.28 (image from Amidu and Dunbar, 2007)

The success of these recent studies to resolve robust relationships between resistivity and water content for earth materials forms the basis for the concept of ERT as a quantitative imaging tool. In Figure 2.29, Archie model parameters have been fitted to experimental data for a clay-rich Texas Vertisol (Amidu and Dunbar, 2007). The fitted parameters were then used to translate time-lapse ERT data into water content distribution images, as shown in Figure 2.30, for a duration of approximately six weeks, during a period of drying. In order to improve the resolution of the ERT, the images were temperature-corrected to 25° (as described in subchapter 2.3.1). This study, to the author's knowledge, constitutes the first instance of the use of ERT to directly infer subsurface geotechnical property distribution, and track their evolution over time.

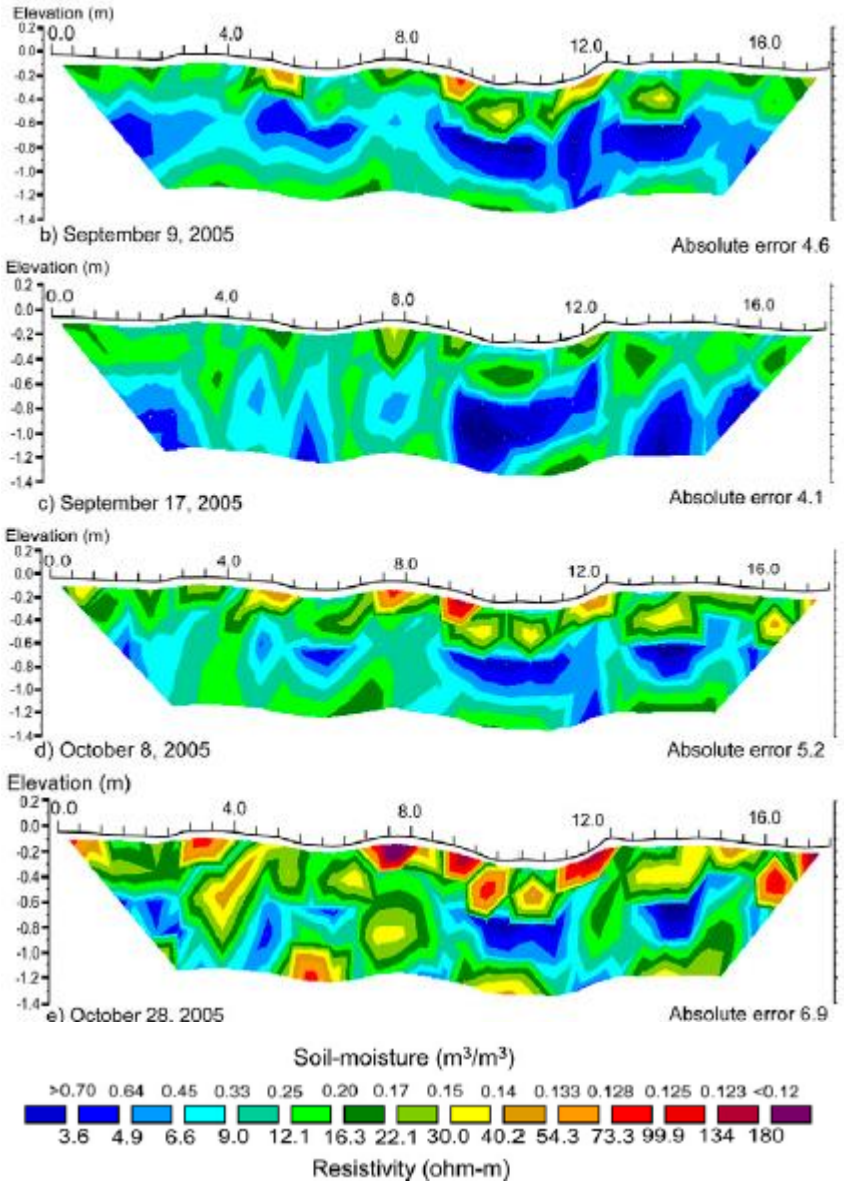

Figure 2.30 Inferred water content distribution from ERT imaging of Vertisol (image from Amidu and Dunbar, 2007)

In subchapter 2.2.4, the role of seasonal moisture cycles in the progressive weakening of clay fills over time was discussed. If laboratory relationships such as those described above are to be used to derive geotechnical information from field ERT data, then it is necessary to understand how they are affected by these seasonal cycles. This process is likely to be exacerbated by the increasingly frequent and extreme weather events suggested by climate change projections. Of the studies presented above, that by Roberts and Lin (1997) on partially-saturated tuff observed hysteresis in the electrical response to varying degrees of saturation between imbibition (wetting) and drainage. Similar studies, performed on sand (Kavian et al., 2011) and on sandstone (Knight, 1991) also observed such hysteresis, however, Munoz-Castelblanco et al. (2012) found resistivity to be independent of whether a drying or wetting path was followed, for a loess soil. There is, however, little research into the effects of repeated seasonal cycles on the resistivity response of volume-sensitive clay soils.

2.3.7 *Quantitative slope stability monitoring systems*

Given the success of both time-lapse ERT studies as described in subchapter 2.3.5, and in resolving resistivity-moisture relationships for different earth materials, some recent studies have begun work into the development of a quantitative landslide monitoring system. The British Geological Survey, and in particular the geophysical tomography team (GTom), have been highly instrumental in this, managing a series of different ERT field sites, in conjunction with other research institutes. The first of these sites is an embankment at East Leake, comprising a 140 m long section of the former Great Central Railway. The Victorian-era embankment was built using the end-tipping method described in subchapter 2.2.1, using local material, resulting in a highly heterogeneous fill composed of glaciofluvial sand and gravel, occasionally bound within layers of fine, white, powdery non-carbonate cement believed to be gypsum leached from other fill materials. Installations at the East Leake site include nine bore holes as well as permanent in situ 2D and 3D ERT arrays. These arrays were fitted with an ALERT system (automated time-lapse electrical resistivity tomography), a remote monitoring platform which combines the resistivity imaging with wireless telecommunications, allowing the gathered data to be remotely communicated to the geophysical tomography team (Wilkinson et al., 2011). These arrays have been used to aid in the interpretation of embankment structure and condition, and to monitor ground water

movement. Ongoing research regarding the East Leake site is focussed on developing quantitative relationships between resistivity and water content, which account for the effects of repeated seasonal moisture cycles for the fill materials, allowing temporal resistivity variations to be used as a proxy for geotechnical property changes. In Gunn et al., 2015, the authors discuss how ALERT technology may be combined with such proxies in order to provide a quantitative system for earthworks management, describing "On-Demand" asset inspection scheduling. The authors describe a programmable field imaging schedule, whereby resistivity images are processed using the aforementioned proxies, to yield 2D, 3D and 4D (time-lapse) images of geotechnical property distributions. They describe how threshold moisture levels could be set, following the concept described in Lebourg et al., 2010 of a critical piezometric level acting as a precursor to slope reactivation. If such a threshold value were reached, automated alarms would be triggered, recommending certain actions. More detail on the East Leake test site may be found in Gunn et al., 2015.

The second of these research sites is the active natural landslide at Hollin Hill, near Malton, North Yorkshire, on a hill slope on farm pasture land. The slope, which dips at approximately 12 °, is composed of four geological formations: the Dogger, Whitby Mudstone, Straithes Sandstone and Redcar Mudstone formations – the landslide system itself occurring mainly in the Whitby Mudstone formation. 4D ERT was deployed at the site over the course of four and half years, in the dipole-dipole configuration, covering an area of 38 m x 147 m, providing a resolution of down to 1 m. As before, an ALERT system was fitted to the ERT array. Full details of the ERT study are given in Merritt, 2014. The field study was combined with a laboratory testing schedule, which investigated the inter-relationships between electrical resistivity, water content and matric suction of the various Hollin Hill fill materials. The study was able to correlate resistivity changes with hydrogeological processes, and found that the system responds well to rises and falls in piezometric levels, and to soil desiccation and healing during seasonal cycles. It found no evidence for the existence of threshold water contents for landslide activation, however, but suggested this to be a function of the complexity of the landslide system.

The third site, the BIONICS embankment in Northumberland (jointly managed by Newcastle University), forms the field site for this PhD thesis, and is described in detail in the following chapter. The BIONICS embankment is conceptually very different to both the East Leake and

Hollin Hill sites: it is a purpose-built research embankment, constructed from locally-sourced clay using modern methods, and ultimately constitutes a relatively homogenous site, in contrast to the two other sites described. Over the course of 2008-2011, 2D electrical resistivity imaging was performed along two toe-to-toe transects, across well and poorly-compacted sections of the embankment (see Figure 3.7). These studies are described in Glendinning et al., 2014 and Gunn et al., 2015. The former of these focusses on weather-induced pore water pressures and their implications for embankment stability, whereas the latter concentrates more on the quantitative imaging of hydrogeological processes.

All three of these sites are invaluable in the development of an ERT-based slope monitoring system. That at East Leake provides the opportunity to investigate a genuine relic of the Victorian-era railway expansion as described in subchapter 2.2.1. Due to its granular fill, however, it does not offer insight to the failure modes relating to volume-sensitive clay soils. Hollin Hill constitutes an ERT investigation rooted in clay soils, and has been the subject of extensive laboratory characterisation, providing insight to the nature of slope hydrodynamics at a very high resolution. Due to the complexity of the site, however, resulting from the fact that it is a natural slope, it cannot be considered representative of the engineered earthworks slopes typical of UK transport infrastructure.

2.3.8 *Limitations of ERT-based slope monitoring systems*

Over the course of this chapter, the evidence has been presented for the merit of an ERT-based slope stability monitoring system. There are, however, limitations to considered, as with any new technology.

In general, ERT survey methods involve four point measurements of electrical resistivity, which have significantly lower associated contact resistances than do two point measurements. However, the four point method still requires good contact between the electrodes and the soil in order to resolve a good quality resistivity measurement. Under dry climatic conditions or on rocky ground, this contact may be affected, resulting in poor contact between the electrodes and the surrounding soil. In general, systematic errors such as this can be avoided by performing repeated and reciprocal measurements (Samouelian et al., 2005).

Most of the studies discussed in the previous subchapters describe investigations of a qualitative nature, whereby subsurface resistivity variations were used to infer changes in the lithology, water content or structure of the ground. Because electrical resistivity tomography is an inverse method, it requires inversion to resolve a model of the subsurface resistivity distribution, which fits measured apparent resistivity values. It is necessary to understand, however, that an infinite number of such models exist, and that inversion software such as Res2DInv will only yield what it determines to be the most probabilistic model. Therefore, the non-uniqueness of inverse theory results in an inherent ambiguity of inverted ERT data. This point is noted by several authors (Garambois et al., 2002; Samouelian et al., 2005; Perrone et al., 2008). In general, the suggested approach to mitigate this ambiguity involves combining ERT with other investigation methods, such as seismic tomography (e.g. Grandjean et al., 2011; Hilbert et al., 2012), in order to constrain the number of potential resistivity models. Given that seismic tomography is also an inverse problem, it too has associated ambiguity resulting from the inversion process; therefore many authors have sought to verify ERT findings using direct geotechnical measurements, from bore holes or point sensors (e.g. Perrone et al., 2008; Schmutz et al., 2009), as can be seen in Figure 2.24 and Figure 2.25. Additional constraints arise from assumptions made within the ERT inversion process, as detailed further in subchapter 4.3.5.

The previous subchapter presented some recent studies which have sought to derive robust relationships describing the resistivity response to a varying water content. This type of calibration, however, cannot be generalised to other soil types (Gupta and Hanks, 1972), and therefore any quantitative resistivity relationships (e.g. Waxman-Smits, 1968) which are derived within a study are valid for the test soil only. As such, any ERT-based slope monitoring system would require laboratory calibration prior to deployment. In subchapter 2.2.6, the inherent issue of the representability of laboratory testing of the shear strength of soils was discussed; this issue must also be considered for resistivity testing of soils.

2.4 Summary

The background and literature review may be summarised as follows:

- There is a wide consensus that climate change will manifest itself in warmer, drier summers and milder, wetter winters for the United Kingdom

- Such a change in atmospheric conditions will have an effect on the factors which determine slope stability; given the correlation between flooding events and the incidence of landslides, it is likely that the frequency of slope failures will increase as a result of projected climate change

- Engineered slopes constitute a third of the total asset value of UK transport infrastructure, and their stability is a function of both their construction methods and the local geologies from which they are won: it is estimated that 7 % of the main UK transport network is constructed is located within high landslide risk zones

- Many factors may be involved in the failure of a slope, but ultimately, rainfall-induced pore pressures are likely to be the catalyst for failure. These are especially relevant for impermeable, volume-sensitive clay soils, which cover much of the UK, and which demonstrate shrink-swell behaviour due to their mineralogy

- Seasonal moisture cycles result in corresponding cyclic changes in pore pressure and hence effective stress, which may, over time, cause strain softening, which can lead to progressive slope failure

- Hysteretic soil water retention may cause considerable changes in soil suctions depending on whether soils are undergoing a drying or a wetting path, affecting their strength

- If the stress at a point on a plane within a soil mass becomes equal to its shear strength, then failure will occur: this is the basis for the Mohr-Coulomb failure criterion

- Laboratory testing of clay shear strength has many associated difficulties, including drainage conditions and representability. For this reason, laboratory assessments of soil strength are performed in conjunction with field assessments of slope stability

- Due to the limitations of conventional methods of slope stability assessment, much research is focussed on geoelectric imaging methods. Electrical resistivity tomography could provide a high resolution, cost-effective monitoring solution, but requires laboratory calibration if it is to be used as a tool for quantitative monitoring

- Electrical resistivity of clays is principally dependent on water content. The mechanism for current conduction in clays is different to that of granular soils, with additional conduction provided by matrix resulting from a double diffuse layer of charge. This mechanism is described by the Waxman-Smits model, relating resistivity and water content, which may be investigated in the laboratory using the industry-standard two point method, or the four point method, which has significantly lower associated contact resistances

- Recent studies have begun developing an ERT-based slope-monitoring system, by combining laboratory test programmes with 4D ERT field investigations, but further work is needed

2.5 Identification of research gap

From completion of the literature review, a clear research gap may be identified. There is a wealth of research into the factors affecting slope stability, particularly for volume-sensitive clay soils which present a challenge for engineers. However, it is not well-understood how these factors will be affected by future climate change, which promotes the need for improved methods of slope stability assessment. Electrical resistivity tomography is well-established as a means of subsurface investigation, but not within the context of near-surface hydrodynamics, which dictate the stability of earthworks slopes. If ERT is to be used to make inferences about the stability of such slopes, then any such systems must be of adequate spatial and temporal resolution to capture the precursors to slope failure.

The ongoing experiments at East Leake are invaluable in the investigation of ERT as a tool for monitoring hydrogeological processes, but due to the presence of granular fill material, do not provide a basis for investigating the failure modes associated with volume-sensitive clay soils. The recent studies at Hollin Hill (where landslide activity occurs mainly within clay) were successful in combining 4D ERT with laboratory-derived geophysical-geotechnical relationships; field resistivity values were then used as a proxy for geotechnical property information. The site, however, is highly complex, and, given that it is a natural slope, not representative of UK transport earthworks. Therefore, in order to further the development of a quantitative, real-time slope stability monitoring system for infrastructure slopes, a high resolution, 4D (time-lapse) electrical resistivity tomography investigation is warranted on a purpose-built field test site. This investigation would be combined with a comprehensive laboratory testing programme, to derive geophysical-geotechnical relationships such that resistivity proxies would be developed for translation of ERT data into information more directly relevant to slope stability.

Chapter 3. Field site description

3.1 Selection criteria

In the selection of a suitable site for the construction of a full-scale test embankment, intended for the deployment of an ERT research study, several selection criteria were considered in keeping with the project objectives:

1. Suitable subsurface conditions for placement of a full-scale test embankment;
2. Proximity to suitable fill material, such that material could be transported to the site at reasonable price;
3. Proximity to Newcastle University;
4. Affordable rental cost of the site;
5. Ease of access to the site, particularly for the range of construction machinery which would be required.

Nafferton Farm in Northumberland was considered to satisfy all these criteria, and was therefore selected for the construction of the BIONICS test embankment, where all field experiments would be conducted, in conjunction with laboratory experimentation. In addition to the principal test site, clay material from the Hollin Hill site (discussed briefly in subchapter 2.3.7) was used as a basis for comparison. Therefore, a broad description is given of the Hollin Hill research site and its materials is given at the end of this Chapter (following on from the description in subchapter 2.3.7), in subchapter 3.3.

3.2 BIONICS test embankment

The following description of the BIONICS test embankment site has been developed from the results of geotechnical laboratory tests and from an internal report on the embankment construction (Hughes et al., 2006), results and details of which are published in Hughes et al., 2009 and Glendinning et al., 2014.

The BIONICS embankment is situated at Nafferton Farm in Northumberland, at Ordnance Survey grid reference NZ 064 657. The site is immediately North of the A69, and near the towns of Ovington and Stocksfield, approximately 15 miles from Newcastle University (Figure 3.1).

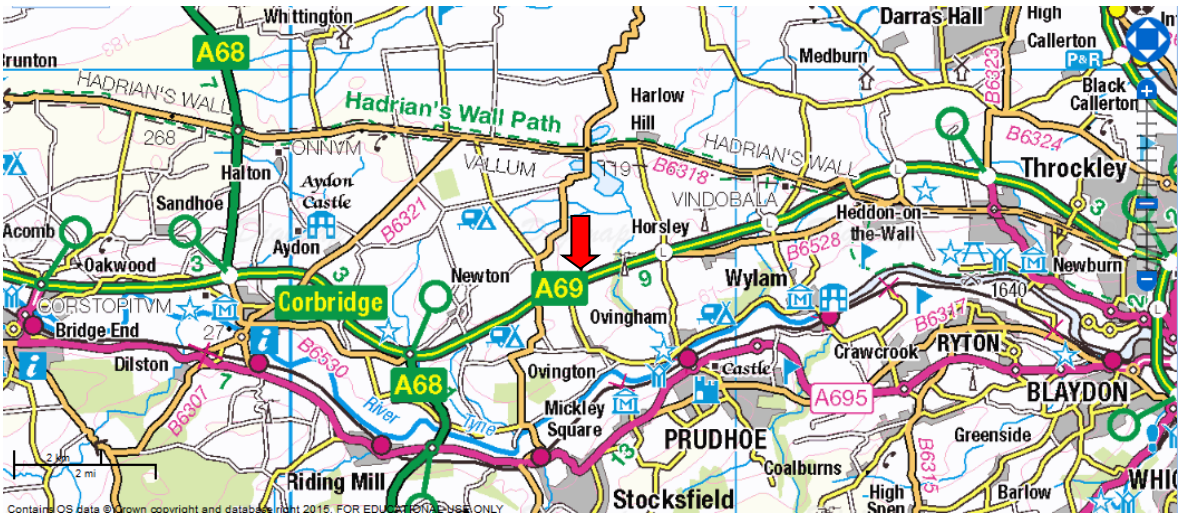

Figure 3.1. Map showing location of Nafferton Farm near Stocksfield, Northumberland

Site investigation prior to the construction of the embankment (shown in Figure 3.2) demonstrated that the underlying conditions at the test site were stiff to hard glacial till, to depths of over 16 m underlain by carboniferous limestone. Historical records showed that there had not been any structures present on the site for the period since records began (1870-present), an important consideration in a region with a strong history of mining. The phreatic surface was recorded as being 2.0 m below ground surface. During site investigation, undisturbed and bulk samples were recovered, and their geotechnical properties tested in accordance with BS 1377. These tests yielded that the material was of low to intermediate plasticity, with an average gravimetric water content of 12 %. Consolidated drained triaxial tests yielded an effective cohesion (c') of 10 kPa, and an angle of shearing resistance of 28°.

Following selection of the site itself, work began towards finding a fill material from which to construct the embankment. As described in the Project Rationale (subchapter 1.1), the principal design specifications pertained to the representativeness of the test embankment with respect to UK infrastructure slopes. London clay was identified by stakeholders as being of particular relevance, with well-researched material properties, and so it was decided that efforts would be focussed on recreating a London clay-type slope, of moderate to high plasticity, in order to be able to study the failure modes described in subchapter 2.2.2. As well as respecting the design considerations, the choice of fill material would also be required to respect the budget constraints. Due to the prohibitive cost of transporting London Clay from the South East of England to Nafferton farm, Durham Lower Boulder Clay

(a locally-sourced glacial till) was instead sourced from an industrial estate to the East of Durham city, considered to reasonably approximate the properties of London Clay.

Figure 3.2 Image of the BIONICS site prior to embankment construction

3.2.1 *Description and characterisation of fill material*

The Durham Lower Boulder Clay fill can be characterised as a slightly silty sandy clay (see Figure 3.3). Laboratory testing of the material showed it to be of intermediate plasticity (Atterberg limits tested in accordance with BS 1377-2: 1990 (BSI, 1990b) yielding a plastic limit of 23 %, liquid limit 45 %, and plasticity index 22 % (averages taken from twelve individual tests, see Figure 3.4), of moderately high shear strength, with peak effective stress parameters, c' equal to 4 kPa, and Φ' equal to 27.5° (effective cohesion and friction angle, respectively). These material properties differ somewhat from the material properties of London Clay (typical peak values of Φ' equal to 20° and c' equal to 12 kPa), however, boulder clay is representative of over 60 % of UK transport infrastructure and hence the compromise was deemed acceptable within the time and budget constraints (Hughes et al., 2009). For the purposes of this study, the Durham Lower Boulder Clay used as fill for the BIONICS test embankment will be referred to as "BIONICS" clay/fill/material, to distinguish it from other similar soils which may be discussed in this thesis.

Laboratory assessment of the compaction characteristics of BIONICS clay were performed according to BS 1377-4: 1990 (BSI, 1990d). From normal Proctor (light) compaction, the maximum dry density, $P_{d(max)}$, of the embankment fill was recorded as 1.82 Mg/m^3 at an optimum (gravimetric) water content (GWC_{opt}) of 15.5 %. From modified (heavy) Proctor compaction, maximum dry density, $P_{d(max)}$, was measured to be 2.03 Mg/m^3 at a GWC_{opt} of 10.5 % (Glendinning et al., 2014) (Figure 3.5). The above geotechnical laboratory test data are shown graphically in the following images, and summarised in Table 3.1.

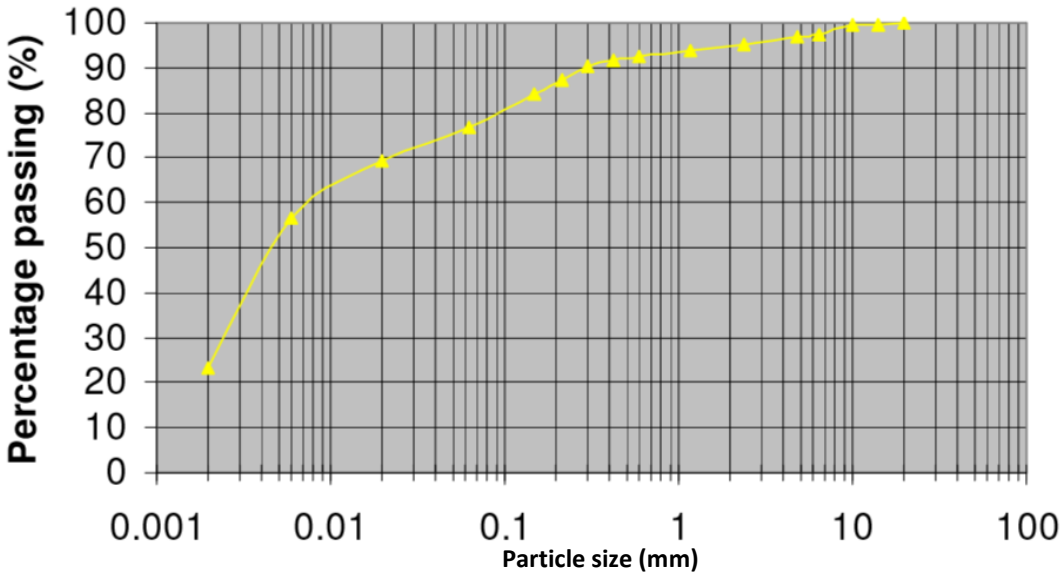

Figure 3.3 Particle size distribution for BIONICS clay , showing it to be a slightly silty sandy clay

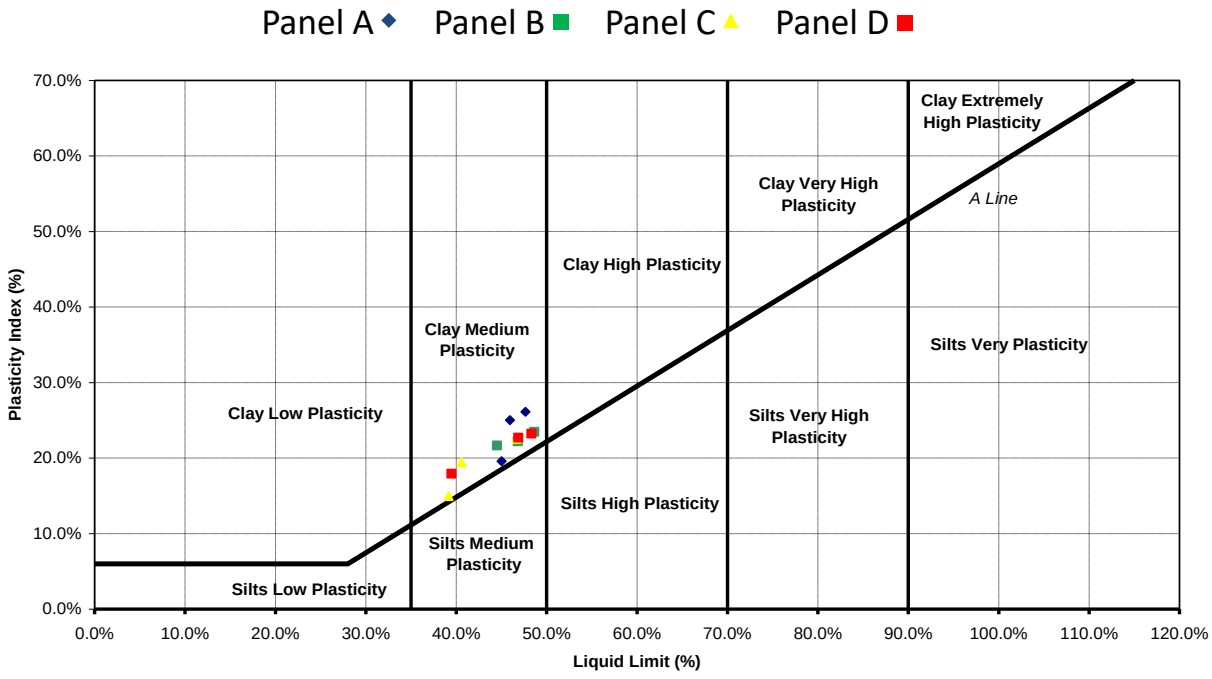

Figure 3.4 Results of Atterberg limit tests on BIONICS fill material, following BS 1377-2, shown on a Casagrande Chart. Samples were taken from embankment Panels A, B, C and D, as shown in Figure 3.7

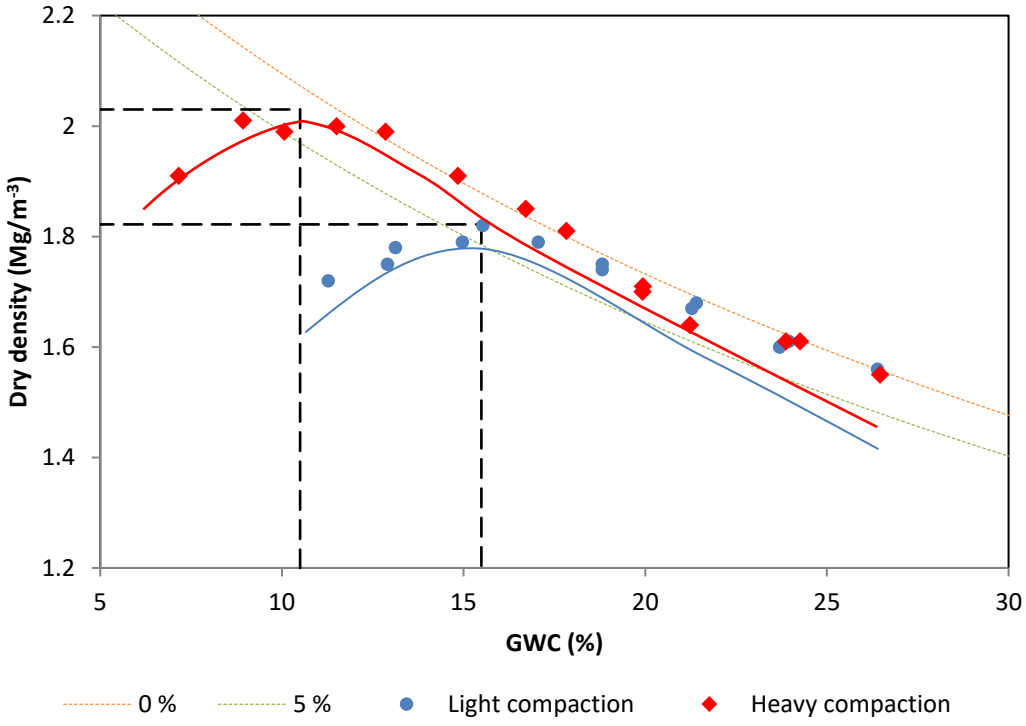

Figure 3.5 Compaction curves for BIONICS fill material, showing 0 % and 5 % Air Voids lines

Table 3.1 Summary of geotechnical testing results for BIONICS clay

Parameter	Units	Value
Plastic limit	% GWC	23
Liquid limit	% GWC	45
Plasticity index (% GWC)	% GWC	22
Peak effective cohesion	kPa	4
Peak effective friction angle	°	27.5
Max. dry density – Proctor (light) (Mg/m^3)	Mg/m^3	1.82
Optimum water content – Proctor (light) (% GWC)	% GWC	15.5
Max. dry density – Proctor (heavy)	Mg/m^3	2.03
Optimum water content – Proctor (heavy)	% GWC	10.5

Mineralogy

Quantitative XRD analyses on the sub 2 μm fraction of the BIONICS fill material (performed on samples taken following construction) suggest generally similar clay mineral assemblages, composed of variable amounts of illite/smectite (ranging from 42-54 %, with a mean of 49 %), chlorite/smectite (3-7 % range, mean 5 %), illite (16-26 % range, mean 19 %) and kaolinite (23-31 % range, mean 26 %). Small quantities of quartz and lepidocrocite (γ-FeOOH) were found in all cases of the separated sub-2 μm fractions. Table 3.2 shows the results of the XRD tests, for samples taken from both the Northern and Southern flanks of the BIONICS test embankment.

Table 3.2 BIONICS quantitative XRD results. Table taken from Kemp and Wagner, 2016

Original sample name		**Depth (m)**	**MPL code**	**% clay mineral**				**Non-clay minerals**
				illite/ smectite (I/S)	**chlorite/ smectite (C/S)**	**illite**	**kaolinite**	
South facing slope	M1	0.95-1.00	MPLP251	42	6	26	27	quartz, calcite, lepidocrocite
	M2	0.95-1.00	MPLP252	46	7	16	31	quartz, lepidocrocite
	M3	0.95-1.00	MPLP253	45	7	20	29	quartz, lepidocrocite
	M4	0.95-1.00	MPLP254	54	6	16	25	quartz, lepidocrocite
	M5	0.75-0.85	MPLP255	50	5	17	27	quartz, lepidocrocite
North facing slope	M6	0.95-1.00	MPLP256	49	5	21	26	quartz, lepidocrocite
	M7	0.95-1.00	MPLP257	51	4	21	24	quartz, lepidocrocite
	M8	0.95-1.00	MPLP258	51	3	19	26	quartz, lepidocrocite
	M9	0.95-1.00	MPLP259	53	4	21	23	quartz, lepidocrocite

3.2.2 *Embankment construction*

Construction of the BIONICS embankment began in September 2005 from the locally sourced glacial till, and was completed by the end of that year. It was constructed to be 90 m long (orientated East-North-East to West-South-West, see Figure 3.6), 6 m high, with a slope of 2:1, corresponding to a toe to toe distance of 29 m and a crest of 5 m width (see Figure 3.7). This particular geometry was chosen so as to be representative of typical UK infrastructure embankments based on the report published by Perry et al., (2001).

Figure 3.6 Aerial view of Nafferton farm, with embankment circled in yellow, showing ENE – WNW orientation. Image from Google Maps – satellite view

The embankment itself was divided into four sections, two of which were designed to be representative of poorly-compacted Victorian railway embankments (outer panels, A and D), and the other two representative of modern embankments, constructed to Method 3 of the Specification for Highway Works (Highways Agency, 1998) (inner panels, B and C). The compaction difference was achieved as follows: the well-compacted sections were achieved in 0.3 m lifts, each receiving 9 passes of a 7300 kg drum vibrating roller (Figure 3.8a); the poorly-compacted sections were constructed in 1 m lifts with minimum tracking by a tracked excavator rather than by compaction plant (Figure 3.8b), which has a weight of 22172 kg with a ground bearing pressure of 36 kg/m, which will have had a compacting effect on the fill. The different compaction efforts resulted in the poorly-compacted panels A and D having nine compacted layers of fill (average bulk density, P_{bulk}, 1.95 Mg/m^3), and the well-compacted panels B and C having sixteen (average bulk density, P_{bulk}, 2.01 Mg/m^3). Throughout the construction of the embankment, cores were taken from each of the layers of the four panels, and their densities recorded in the laboratory. These results are shown in

Table 3.3, and show a small but significant difference in density between the two compaction zones. The four panels are hydrologically isolated from each other by an impermeable geo-membrane (vertical double layers of Visqueen sealed with waterproof adhesive tape, Figure 3.11).

At the ends of the embankment, there are two 6 m wide panels, initially intended for use in testing vegetation growth, and are referred to in previous papers relating to the BIONICS experiment (Hughes et al., 2009; Glendinning et al., 2014) as the "biological test plots". Both of these panels were compacted to the "well-compacted" specification, and therefore also comprise sixteen layers. The Easternmost of these two end panels constitutes the location of the electrical resistivity tomography array used in this research project, and will be referred to in this study as "the ERT test plot". The ends of the embankment were angled at 45°, and the earth reinforced: primary reinforcements (Tensar 55RE) penetrating 4.25 m, and secondary reinforcement (Tensar SS20) penetrating 1.0 m (see Figure 3.9).

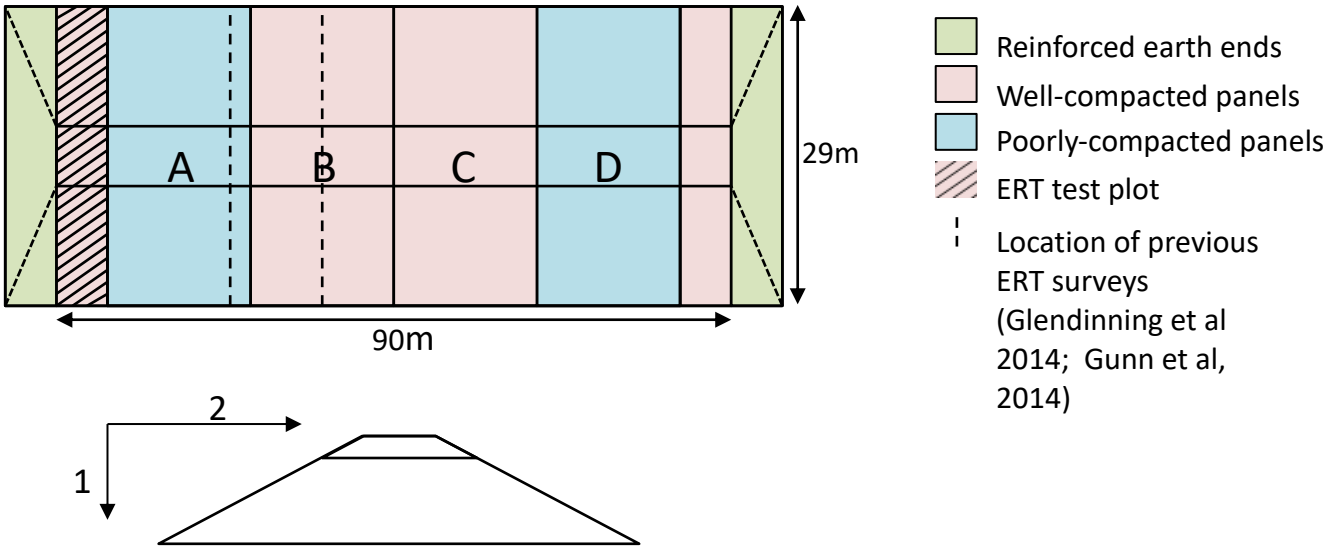

Figure 3.7. Geometry of the BIONICS embankment (image adapted from Hughes et al., 2006)

Figure 3.8 Embankment compaction methods (a) self-propelled roller used on well-compacted panels; (b) plant used on poorly-compacted panels (image taken from Hughes et al., 2009)

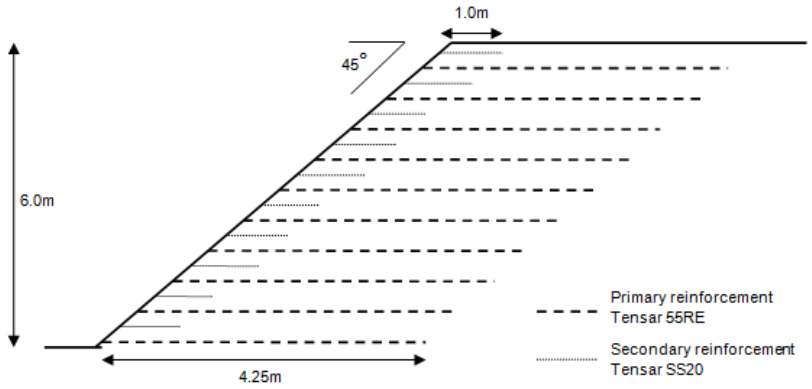

Figure 3.9 Reinforced earth slope design (image taken from Hughes et al., 2006)

Table 3.3 Summary of core cutter density results for BIONICS embankment panels

Layer	Height above g.l.	Layer thickness	Bulk density	Dry density	Grav. water content	Air voids	Degree of saturation	Porosity
	m	m	Mg/m^3	Mg/m^3	%	-	-	-
Panel A (poorly compacted)								
1	0.3	0.3	2.05	1.71	1.95	0.021	0.941	0.356
2	0.6	0.3	1.93	1.64	18.3	0.084	0.781	0.384
2	0.9	0.3	2.00	1.67	19.9	0.040	0.893	0.374
4	1.2	0.3	1.99	1.63	22.2	0.022	0.942	0.379
5	1.5	0.3	2.00	1.65	21.0	0.031	0.919	0.383
6	1.8	0.3	1.99	1.66	20.5	0.036	0.904	0.375
7	3	1.2	1.93	1.61	20.1	0.069	0.824	0.392
8	4	1	1.68	1.36	23.4	0.167	0.655	0.484
9A	5	1	1.98	1.61	23.0	0.022	0.943	0.386
9B	5	1	1.96	1.60	22.6	0.035	0.911	0.393
Average			**1.95**	**1.61**	**21.1**	**0.053**	**0.871**	**0.391**
Panel D (poorly compacted)								
1	0.3	0.3	2.01	1.67	20.3	0.033	0.912	0.375
2	0.6	0.3	2.01	1.66	21.2	0.021	0.943	0.368
3	0.9	0.3	1.93	1.62	19.3	0.077	0.801	0.387
4	2	1	2.01	1.64	22.0	0.018	0.953	0.383
5	3	1	2.03	1.71	18.9	0.033	0.907	0.355
6								
7								
8A	4	1	1.89	1.59	18.8	0.102	0.746	0.402
8B	4	1	1.87					
9	5	1	1.86	1.54	20.4	0.104	0.752	0.419
Average			**1.95**	**1.63**	**20.1**	**0.055**	**0.859**	**0.384**

Blank spaces indicate missing data.

Panel B (well-compacted)								
Layer	Height above g.l.	Layer thickness	Bulk density	Dry density	Grav. water content	Air voids	Degree of saturation	Porosity
	m	m	Mg/m³	Mg/m³	%	-	-	-
1	0.3	0.3	2.01	1.68	19.7	0.037	0.899	0.366
2	0.6	0.3	1.99	1.61	23.2	0.018	0.954	0.391
2	0.9	0.3	1.94	1.61	20.4	0.065	0.835	0.394
4	1.2	0.3	2.02	1.70	18.8	0.038	0.894	0.358
5	1.5	0.3	2.12	1.81	17.1	0.007	0.977	0.304
6	1.8	0.3	2.03	1.68	20.7	0.016	0.955	0.356
7	2.1	0.3	1.99	1.64	21.4	0.029	0.924	0.382
8	2.4	0.3	2.03	1.72	18.2	0.037	0.894	0.349
9	2.7	0.3	2.02	1.71	18.4	0.041	0.884	0.353
10	3.0	0.3	2.02	1.68	20.4	0.024	0.935	0.369
11	3.3	0.3	2.08	1.73	20.4	0.005	1.000	0.357
12	3.6	0.3	2.04	1.69	20.6	0.011	0.970	0.367
13	3.9	0.3	2.02	1.68	20.0	0.028	0.923	0.364
14	4.2	0.3	1.95	1.62	20.6	0.057	0.854	0.390
15	4.5	0.3	2.0	1.67	19.7	0.04	0.891	0.367
16	4.8	0.3	2.0	1.65	21.4	0.026	0.932	0.382
Average			**2.02**	**1.68**	**20.1**	**0.03**	**0.921**	**0.366**
Panel C (well compacted)								
1	0.3	0.3	1.98	1.62	22.4	0.028	0.928	0.389
2	0.6	0.3	2.02	1.68	20.0	0.030	0.919	0.370
3	0.9	0.3	2.03	1.70	19.1	0.031	0.913	0.356
4	1.2	0.3	2.02	1.67	18.9	0.038	0.895	0.362
5	31.5	0.3	2.02	1.67	21.0	0.019	0.947	0.358
6	1.8	0.3	2.01	1.69	19.0	0.043	0.882	0.364
7	2.1	0.3	2.00	1.67	19.7	0.040	0.891	0.367
8	2.4	0.3	2.00	1.67	20.2	0.035	0.905	0.368
9	42.72.7	0.3	1.98	1.63	21.5	0.035	0.908	0.380
10	53.0	0.3	1.95	1.62	20.6	0.055	0.858	0.387
11	3.3	0.3	2.04	1.76	16.2	0.053	0.842	0.335
12	3.6	0.3	2.03	1.69	20.2	0.021	0.946	0.389
13	3.9	0.3	1.98	1.62	22.5	0.027	0.932	0.397
14	4.2	0.3	2.03	1.68	20.8	0.018	0.952	0.375
15	4.5	0.3	2.00	1.67	20.0	0.037	0.901	0.374
16	4.8	0.3	2.00	1.65	21.4	0.026	0.932	0.382
Average			**2.01**	**1.67**	**20.1**	**0.034**	**0.908**	**0.372**

Prior to the construction of the embankment, a 200 mm thick layer of topsoil was stripped from the surface of the site. This layer was then placed on the flanks of the embankment after completion of the compaction layers (Figure 3.10). On the crest, a 0.5 m capping layer of ballast was added (see Figure 3.11), which acts to allow drainage, and is representative of UK rail infrastructure (Perry et al., 2001). The material selected for ballast was 6F5 Northumberland Basalt won from Barrasford Quarry, chosen due to its mineral inertness.

After the completion of the embankment, a seed mixture of grasses and wildflowers, selected to represent both typical Highways Agency infrastructure and UK grassland, was sown across the flanks (Hughes et al., 2009). A considerable amount of wheat was also present, as this was pre-existing in the topsoil strip (removed from the embankment site prior to its construction).

A drainage system was installed on both the North and South flanks of the embankment, running parallel to its length, such that surface runoff flows into a 200 mm x 300 mm collection drain, lined with impermeable membrane and filled with coarse gravel. The runoff then flows to a 1 m x 1 m soakaway drain, lined with Terram and filled with coarse gravel (Figure 3.12).

Figure 3.10 Placement of topsoil layer on embankment flanks

Figure 3.11 Granular capping layer on the BIONICS embankment crest . The hydrologically-isolating Visqueen layers can be observed

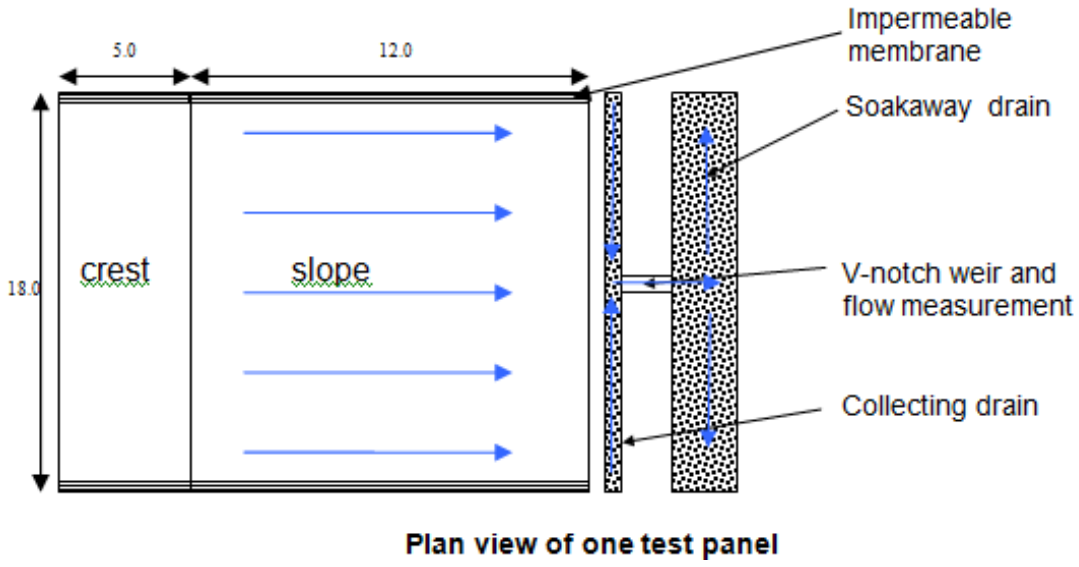

Figure 3.12 Drainage system installed at the BIONICS test embankment (image from Hughes et al., 2006)

The completed embankment is shown in Figure 3.13, and shows the four different panels hydrologically separated from one another, ballast capping layer and drainage system. Figure 3.14 (taken in November 2005) shows the presence of tension cracks in Panel A, two months after the end of construction, and is the earliest observation of tension cracking at

the test site. Figure 3.15 shows the embankment one year after its completion, showing the presence of grassy vegetation across its entirety.

Figure 3.13 Completed embankment, view taken from a point Southwest of Panel A

Figure 3.14 Tension cracks in Panel A South flank (November 2005)

Figure 3.15 Embankment one year after construction (September 2006), showing grass coverage

3.3 Hollin Hill test site

In subchapter 2.3.7, the Hollin Hill research site was introduced, describing an active natural landslide, where movement occurs primarily within the clay-rich Whitby Mudstone formation. Site observations describe the near-surface material as distinctly weathered or destructured (Gunn et al., 2013). Tests performed on samples of the material classify it as a silty clay, of high to very high plasticity (Merritt, 2014). Average in situ bulk and dry densities were found to be 2.00 and 1.61 Mg/m^3 respectively, with an average in situ gravimetric water content of 24 %, and degree of saturation 0.989.

Chapter 4. Methodology

Having satisfied Objective 1 by completion of a literature review (Chapter 2), and presented the test site and materials (Chapter 3), this chapter describes the procedures and techniques which were used to achieve the stated aim. It is split broadly into three parts:

4.1 Laboratory investigation of geophysical-geotechnical relationships: subchapter describing the laboratory component of this study, which seeks to characterise the evolution of resistivity relationships when subjected to seasonal cycles of drying and wetting. Resistivity relationships established in the laboratory then form the basis for the geophysical-geotechnical proxies, as described in subchapter 1.2, thus satisfying Objective 2.

4.2 Field experiments at the BIONICS embankment: subchapter describing the programme of field experimentation at the test site, including the installation of a network of point sensors and of the four dimensional electrical resistivity tomography array. This subchapter relates directly to Objective 3.

4.3 ERT data processing and translation into geotechnical information: subchapter describing the collection, pre-processing and post-processing of raw ERT data from the BIONICS field experiments, and their resolution into geotechnical property information, satisfying Objective 4.

The interactions between the three experimental components of this study are presented in Figure 4.1, which also demonstrates how they lead into the subsequent chapters.

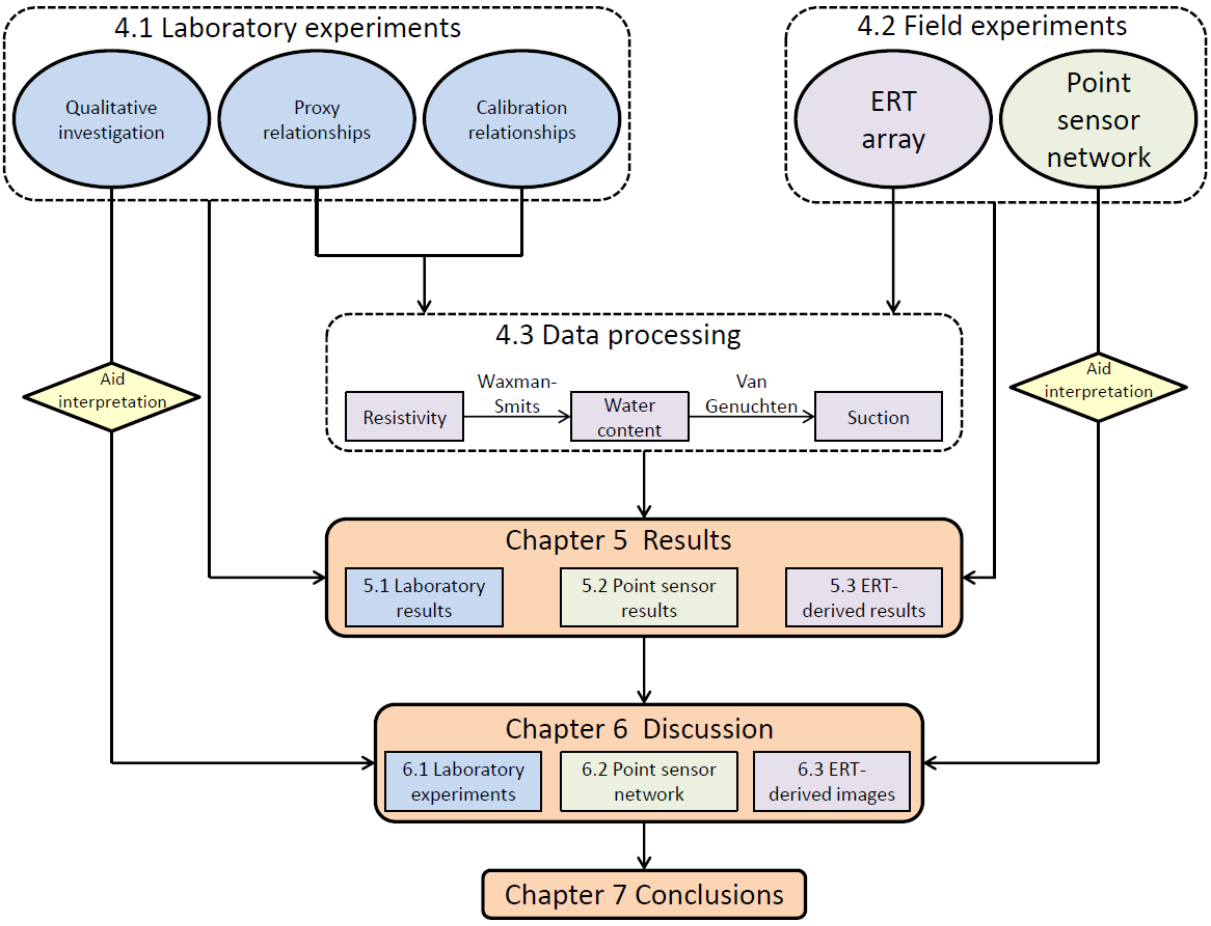

Figure 4.1 Flowchart showing interactions between experimental components and subsequent chapters

4.1 Laboratory investigation of geophysical-geotechnical inter-relationships

The purposes of the laboratory tests are threefold:

1. To provide qualitative information regarding the behaviour of engineered clay fill subject to seasonal dry-wet moisture cycles;
2. To establish a set of proxy relationships for translating ERT data into quantitative estimates of water content and suction;
3. To derive calibration relationships for calibrating these proxies for use in the field.

In the following subchapters (4.1.2, 4.1.3), the soil processing methods for the test material are described. Subsequently, the individual experiments (six in total) are presented. Where indicated, a reduced number of tests have also been performed on material recovered from Hollin Hill (see subchapter 2.3.7), to allow comparison with another clay soil (Hollin Hill material description in Merritt, 2014).

4.1.2 *Soil preparation*

The following section describes the soil preparation procedures for materials recovered from both the BIONICS embankment and Hollin Hill.

Bulk clay soil was passed through a 20 mm sieve and allowed to air dry for 24 hours on top of an oven (Figure 4.2) to accelerate drying (the option of drying inside the oven was disregarded due to mineralogical changes associated with such high temperatures (Velde and Meunier, 2008). The dried soil was then crushed using a mechanical crusher with a 3 mm plate separation (Figure 4.3), and passed through a 2 mm sieve. De-ionised water was added to the processed soil, while mixing (Figure 4.4), in order to bring it to the target water content (i.e. corresponding to the initial conditions for the laboratory tests), and sealed inside clear plastic bags. The reason for the use of de-ionised water was that the water resistivity was consistent for every batch of soil prepared; whereas tap water resistivity would vary. Densities and water contents measured in situ at the test site were replicated for these initial conditions, in order to allow for direct comparison with field results. These parameters are summarised in Table 4.1.

Table 4.1 Starting conditions for BIONICS and Hollin Hill laboratory tests

Site	**Average in situ bulk density (Mg/m^3)**	**Average in situ dry density (Mg/m^3)**	**Average in situ GWC (VWC) (%)**	**Average in situ degree of saturation**
BIONICS	2.01	1.65	22 (36.3)	0.962
Hollin Hill	2.00	1.61	24 (38.7)	0.989

Average values obtained from laboratory testing of extruded core samples.

After a homogenisation period of 24 hours, the soil was removed from the sealed plastic bags and compacted into test specimens, the dimensions of which varied according to the test to be conducted.

Figure 4.2 Drying of BIONICS material in tray on top of oven

Figure 4.3 Soil crusher with 3 mm plate separation

Figure 4.4 Soil mixing in a Hobart industrial mixer

4.1.3 *Moisture cycling*

Specimens were then subjected to moisture cycling, in order to investigate the geophysical-geotechnical response to seasonal dry-wet cycles, for the reasons detailed in subchapter 2.2.4. Specific details of the specimen preparation procedure for each experiment are discussed individually in the following sections, although a summary of the saturation history of the individual experiments is given in Table 4.2. Up to two full moisture cycles were applied to laboratory specimens (primary and secondary cycles), each comprising drying (a) and wetting (b) portions.

Table 4.2 Saturation history of laboratory experiments on BIONICS material

Seasonal cycle/Path	**Dataset**	**Method of moisture cycling**
1 (Primary)		
a) Drying	Experiment 1 (SWRC)	Air-drying
	Experiment 2 (GWC - 2pt resistivity - c_u - UCS)*	Air-drying
	Experiment 3 (GWC - 2pt/4pt resistivity comparison)	Air-drying
	Experiment 4 (GWC - 4pt resistivity)	Air-drying
	Experiment 5 (4pt resistivity - T - λ)	Air-drying
	Experiment 6 (soil fabric imaging)*	Evacuation during imaging
b) Wetting	Experiment 1 (SWRC)	Hand-powered water mister
	Experiment 2 (GWC - 2pt resistivity - c_u - UCS)*	Humidifying chamber
	Experiment 4 (GWC - 4pt resistivity)	Humidifying chamber
	Experiment 6 (soil fabric imaging)	Addition of droplet
2 (Secondary)		
a) Re-drying	Experiment 2 (GWC – 2pt resistivity - c_u - UCS)	Air-drying
	Experiment 4 (GWC - 4pt resistivity)	Air-drying
b) Re-wetting	Experiment 2 (GWC – 2pt resistivity - c_u)	Humidifying chamber
	Experiment 4 (GWC - 4pt resistivity)	

*Indicates where Hollin Hill material has also been tested. c_u: undrained cohesion, UCS: unconfined compressive strength, T: temperature, λ: thermal conductivity.

4.1.4 *Laboratory experiments*

Experiment 1. Development of a soil water retention curve (SWRC)

Introduction

In subchapter 2.2.5, the relationship between soil stability and pore water pressure is discussed. Soil water retention behaviour of clays is well-understood in literature (e.g. Fredlund and Xing, 1994; Meskini-Vishkaee et al., 2014); it was necessary to develop a curve specifically for the BIONICS material, for two reasons:

1. To fully characterise the BIONICS material, including air and water entry values;
2. To allow a proxy relationship to be developed at a later stage between resistivity and soil suction, by combining with a resistivity – water content proxy relationship.

This test forms part of the technical report by Stirling and Hen-Jones (2014) and was completed during a short-term scientific mission to École des Ponts ParisTech in February 2014, funded by the COST Action TU1202 funding initiative.

Specimen preparation

Thirteen 38 mm diameter x 8 mm length discs were formed by placing 18.5 g of moistened BIONICS clay into a compaction cell at a strain rate of 0.33 mm/min until a height of 8 mm was achieved, corresponding to the initial conditions summarised in Table 4.1. Specimens were then left in the compaction cell for a period of 30 minutes, in order to prevent them from expanding immediately following compaction. Following the preparation of these specimens, they were placed in plastic cases, which were wrapped in film and sealed in plastic bags and allowed to homogenise for 24 hours. The specimens were then subjected to moisture cycling in the following ways: drying was achieved by allowing the specimens (in the cases) to air-dry on a bench in a temperature-controlled environment (20 °C), until their masses corresponded to target water contents at regular intervals between 22 % and the residual (Figure 4.5); wetting was achieved by spraying specimens using a hand-powered water mister. Eight specimens were used for the primary drying path, whilst five specimens were reserved for the primary wetting path. Following moisture cycling, the specimens were wrapped in plastic film and allowed to homogenise for a further 24 hours.

Method

The specimens were then treated as follows; each specimen was divided into two halves and each half weighed. One portion was placed in the WP4C dewpoint potentiameter (Decagon Devices Inc., 2014) for rapid measurement of pore pressures (a measurement taking approximately ten minutes). Upon removal from the WP4C, the portion was then weighed again and oven-dried in accordance with BS 1377-1: 1990 (BSI, 1990a), to calculate the gravimetric water content of the sample prior to suction testing. The remaining half of each specimen was then was used for the calculation of bulk density (P_{bulk}) as follows: it was first weighed in air (M_{air}), then weighed within a beaker filled with petrol (i.e. a non-wetting fluid, yielding M_{petrol}) of known density (P_{petrol}), which was suspended from a balance, as shown in Figure 4.6. The volume of petrol displaced then corresponds to the volume of the soil tested (V_{soil}) (Eqn. 4.1), allowing bulk density (Eqn. 4.2) to be calculated. Using the moisture content figure derived from the oven-baked portion, volumetric water content and degree of saturation of the sample could then be calculated.

$$V_{soil} = \frac{M_{air} - M_{petrol}}{P_{petrol}} \qquad \text{Eqn. 4.1}$$

$$P_{bulk} = \frac{M_{air}}{V_{soil}} \qquad \text{Eqn. 4.2}$$

Errors

The WP4C potentiameter is accurate to within 0.05 MPa from 0 to -5 MPa and to within 1 % thereafter (Decagon Devices Inc., 2007).

Figure 4.5 Air-drying and weighing of specimens on a balance

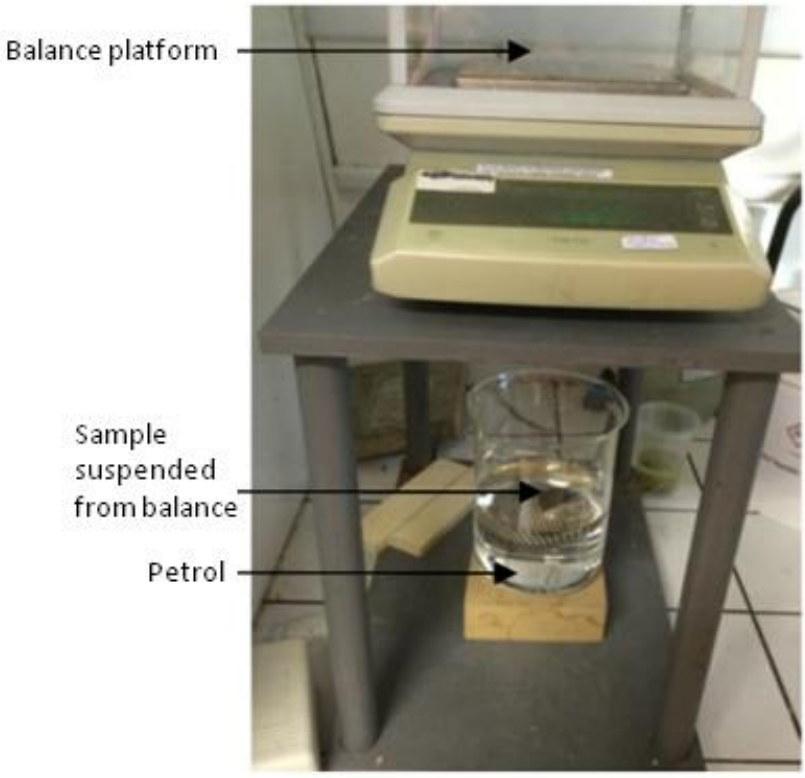

Figure 4.6 Weighing of sample in air and in petrol to derive sample volume

Following testing, the Van Genuchten (1980) expression was fitted to the water content - suction data to create a soil water retention curve (SWRC) for the initial drying and wetting phases of the clay, as shown in Figure 5.1.

Experiment 2. Resistivity (two point) - water content – strength relationships (seasonal cycles)

Introduction

This experiment describes the laboratory investigation of the inter-relationships between the resistivity, water content and strength of BIONICS clay. Where indicated, Hollin Hill material has also been tested. The two point resistivity method is used, as described in BS 1377-3: 1990 (BSI, 1990c), which is currently considered to be the standard, most commonly-used method. Two quantifications of soil strength have been investigated (see subchapter 2.2.6 for further information):

1. Undrained shear strength (c_u)
2. Unconfined compressive strength (UCS)

Emphasis has been put on investigating the first parameter (using the quick undrained triaxial test) as it pertains directly to shear failure (as described in subchapter 2.2.6), therefore a greater number of data points were gathered, for two full dry-wet moisture cycles (Paths 1a, 1b, 2a, 2b from Table 4.2). The second parameter, unconfined compressive strength, was also investigated in order to form a more complete impression of the strength response to varying water content, although only Paths 1a, 1b and 2a were investigated for the BIONICS material (see Table 4.2).

It should be noted that, strictly speaking, c_u describes the undrained shear strength of *fully-saturated* samples. In this experiment, however, water content has been the variable and therefore, c_u does not describe a true value of undrained shear strength, but rather, the maximum shear stress withstood by a partially-saturated clay sample under triaxial loading. Although an important limitation of the quick undrained triaxial test is that it does not allow for measurement of pore water pressures, it is recognised as representative of short-term behaviour (Wood, 1990), which is relevant when considering the rapid changes in subsurface moisture conditions which may trigger slope failure (see subchapter 2.2.6). Undrained triaxial testing of partially-saturated soils is described in Fredlund and Rahardjo, 1993.

Specimen preparation

38 mm diameter by 76 mm length cylindrical specimens were prepared from moistened BIONICS material (prepared following the procedures outlined in subchapter 4.1.2) using a steel mould with removable ends (Figure 4.7) filled by tamping after the addition of each of four approximately equal layers, creating a deliberately rough interface between the layers. 173.5 g of soil (plus 0.5 g to allow for wastage, approximately 3 % of the total soil mass) was weighed out per specimen, corresponding to initial conditions summarised in Table 4.1. Specimens were extruded from the mould via a lever-operated shaft press, before being wrapped in plastic film and allowed to homogenise for 24 hours. In addition, a number of specimens were prepared from moistened Hollin Hill material: 172.4 g (plus 0.5 g) was weighed out per specimen.

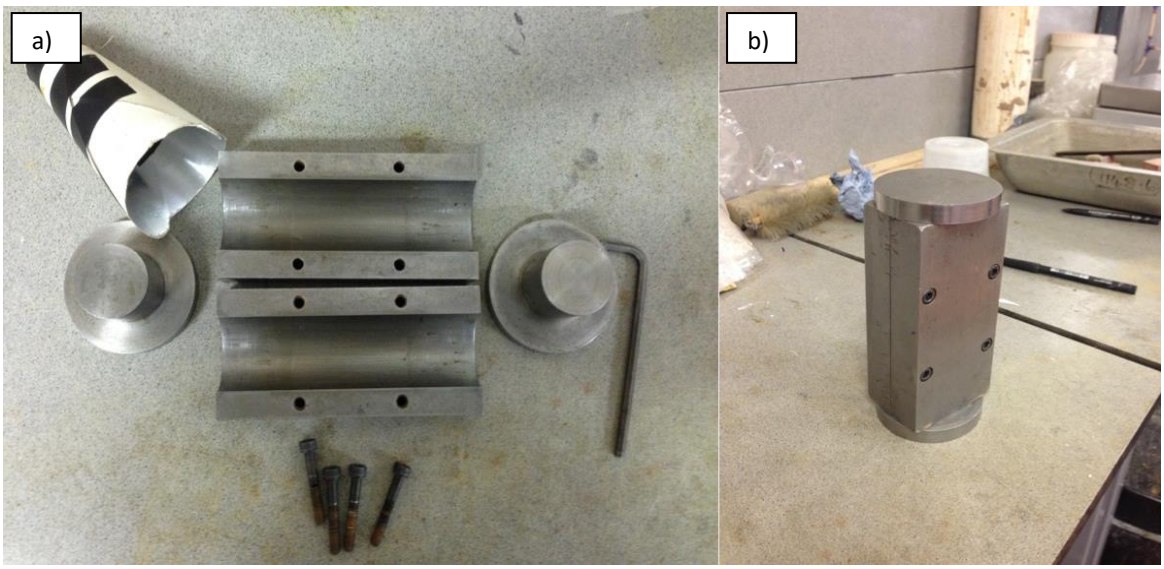

Figure 4.7 Steel mould with removable ends: (a) dissembled; (b) fully assembled.

Following preparation, specimens were moisture cycled, as follows: drying was achieved by allowing specimens to air-dry in a temperature-controlled environment (20 °C), until their masses corresponded to target water contents, at regular intervals between 22 % (24 % for Hollin Hill specimens) and the residual (Figure 4.8); wetting was achieved by allowing specimens to reach their residual water content, and then wetted up by placing specimens in a “humidity chamber“ (an insulated box with two 90 ml/hour mist generators submerged in deionised water, with a grate above to hold the specimens (Figure 4.9, Figure 4.10); concave plastic covers were used to protect the specimens from large droplets of water which tended to gather on the chamber lid and drop down, causing them to disintegrate.

Figure 4.11a and b show the time taken to achieve a given water content during air-drying and rewetting. The reason for the difference in wetting procedure with respect to Experiment 1 (SWRC) specimens is the larger volume of these specimens such that they required a more intense and prolonged wetting environment to achieve a given water content. Following moisture cycling, specimens were wrapped in plastic film and sealed in plastic bags, and allowed to homogenise for a further 24 hours. Table 4.3 shows the total number of specimens which were prepared for each branch of the experiment.

Table 4.3 Total number of specimens prepared for strength tests

Strength parameter	**Seasonal cycle (Path)**			
	1a	**1b**	**2a**	**2b**
c_u	25 (24)	18 (15)	16	16
UCS	19	13	9	-

Brackets indicate number of Hollin Hill specimens prepared.

Figure 4.8 Air drying of specimens

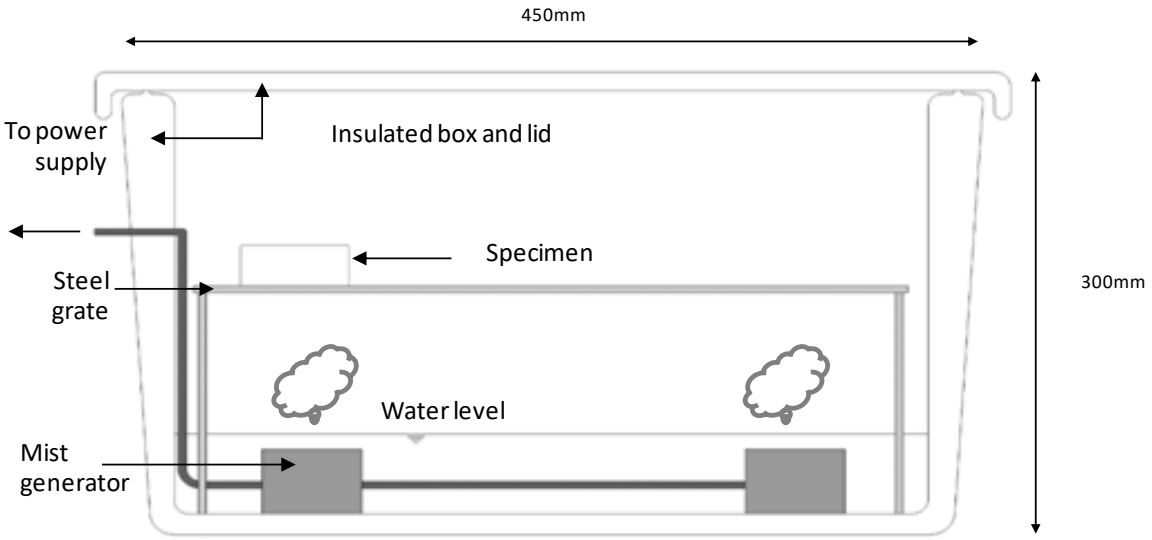

Figure 4.9 Schematic of humidity chamber

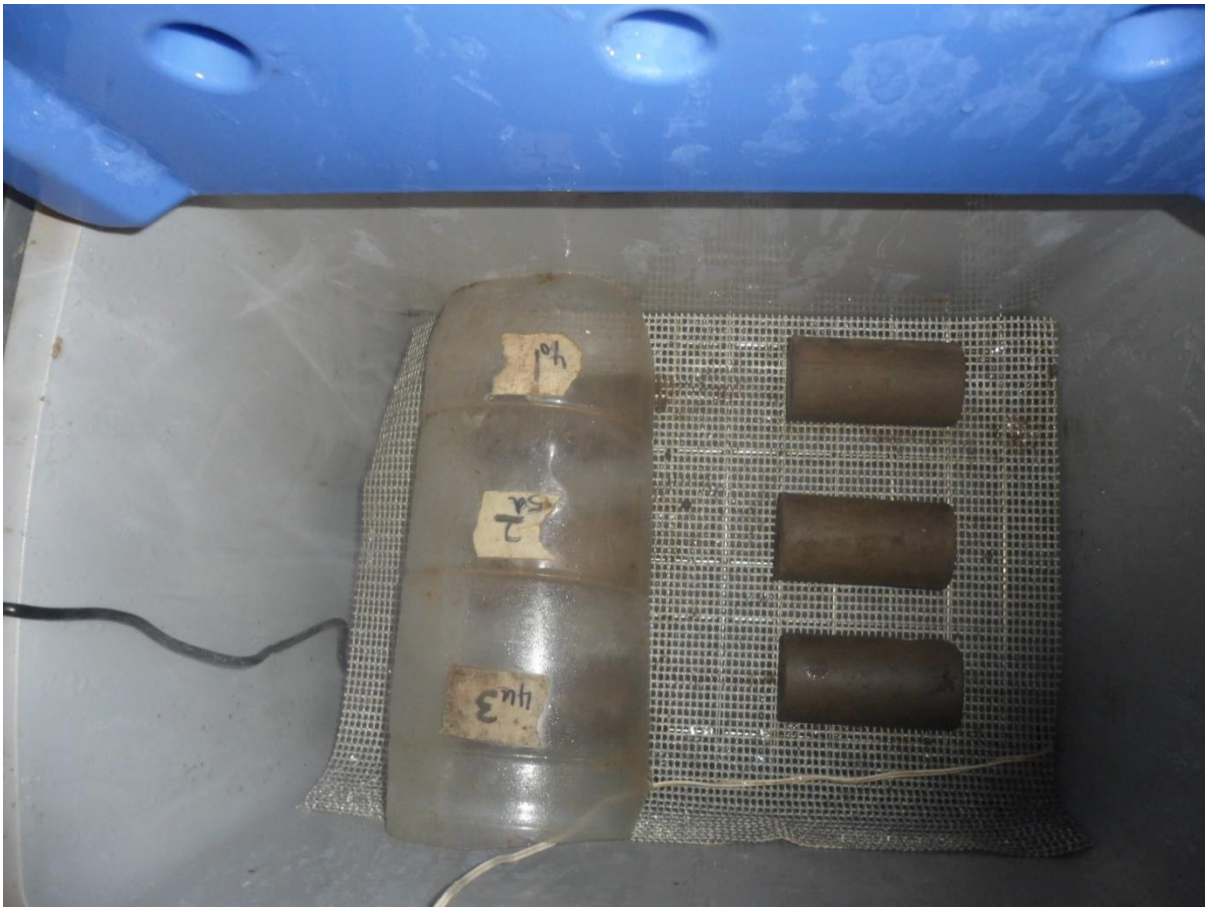

Figure 4.10 Photograph of humidity chamber

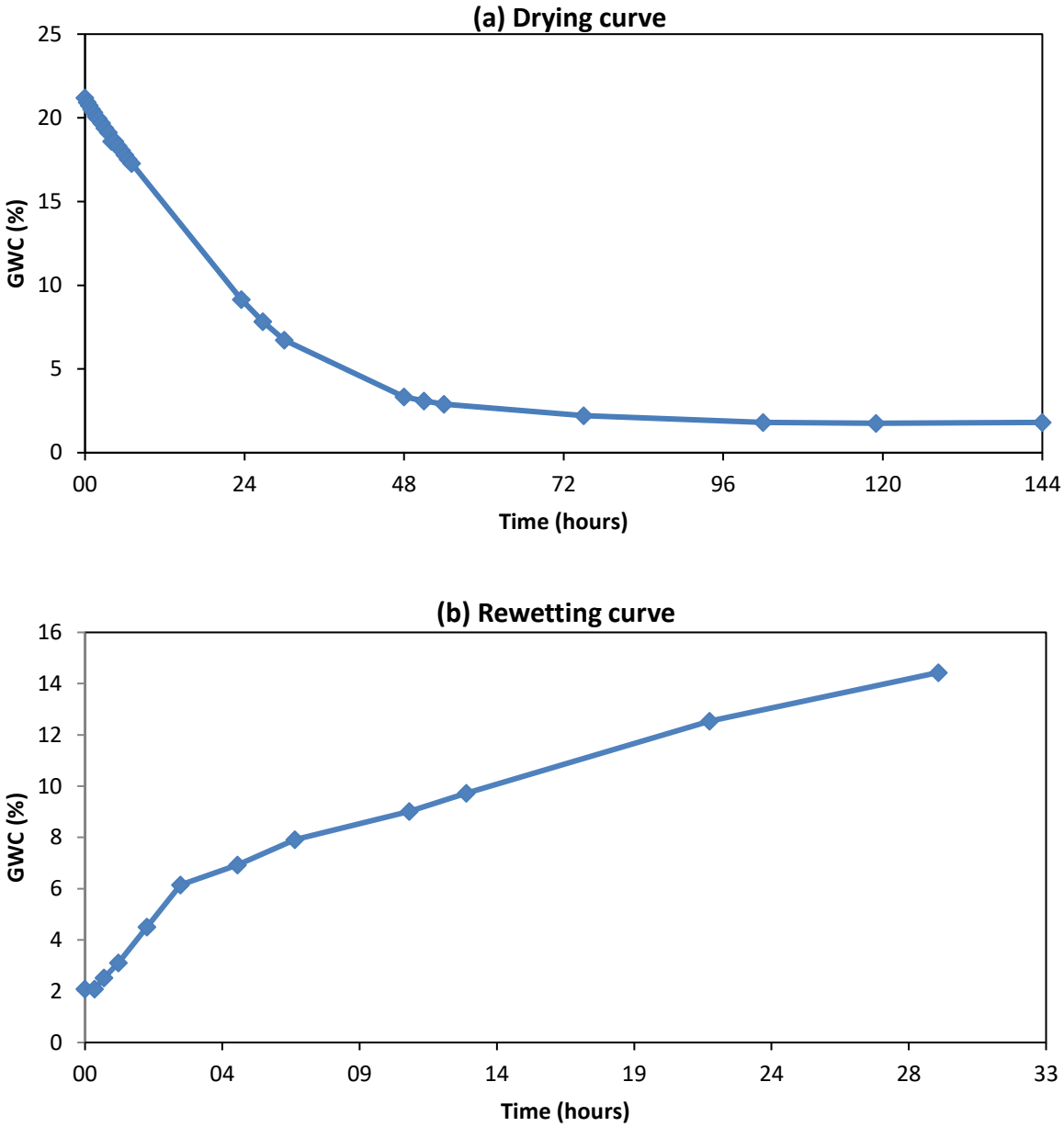

Figure 4.11 Time taken for (a) drying, and (b) rewetting of BIONICS cylindrical specimens. Residual water content for the BIONICS material is approximately 2 %.Both curves show average water contents from six specimens. Drying curve is smoother than wetting curve because specimens air-dry evenly, whereas those nearest the mister in the humidifying chamber wet up faster than others and need to be rotated

Method

Following moisture cycling and homogenisation, specimens were tested for resistivity using the two point method, in accordance with BS 1377-3: 1990 (BSI, 1990c). A DC power source (Thandar TS3022S) was used to set up a potential difference (voltage) across a specimen via the use of two 38 mm diameter copper plate electrodes: one electrode was fixed to a platform to allow a specimen to be stood on top of it, and the other placed on top of the cylindrical specimen, held down by a 50 g mass (test apparatus shown in Figure 4.12). To improve contact resistance at the soil-electrode interface (particularly necessary for drier specimens), both the disc electrodes were coated with a 0.2 mm thick layer of Nyogel 758G electrically-conductive gel (conductivity 3.33 S/m – Newgate Online, 2016). For each two point resistivity measurement, eight different potentials were applied, and the resulting current measured. Table 4.4 shows the values of the potentials which were applied across the specimens, which increase incrementally;

Table 4.4 Potentials applied across BIONICS and Hollin Hill cylindrical specimens

Measurement	**Test voltage (V)**
1	0
2	3.07
3	7.41
4	12.15
5	17.21
6	21.1
7	28.9
8	30.7

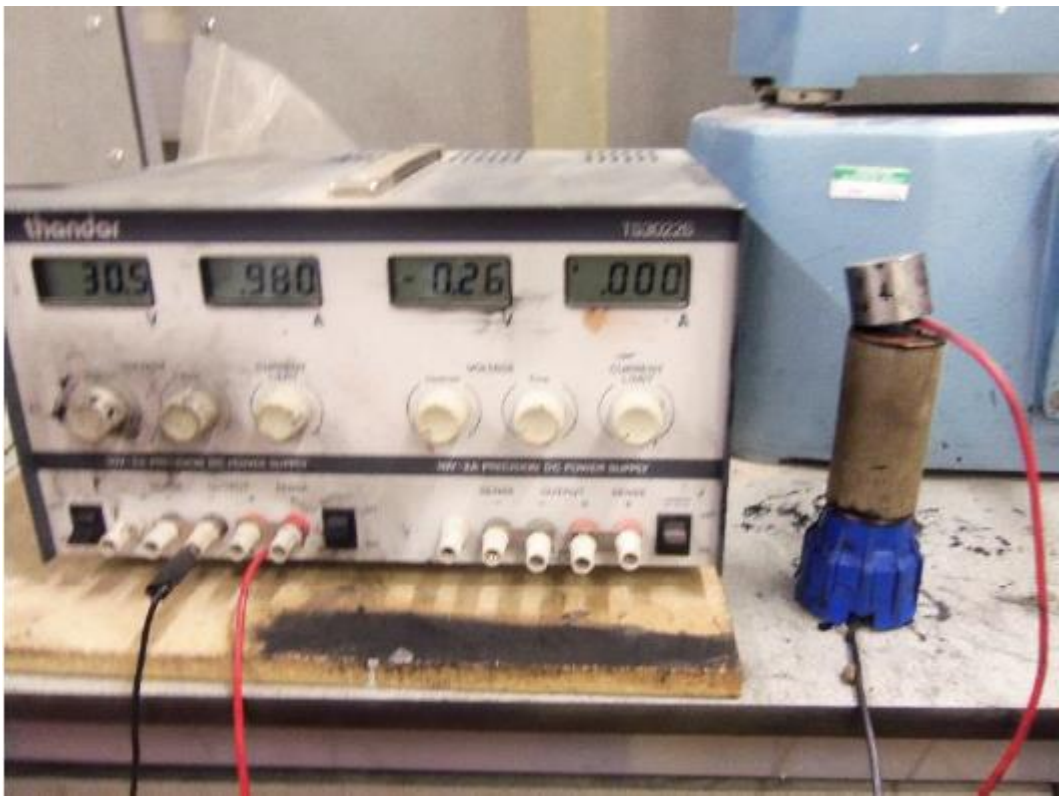

Figure 4.12 Two point resistivity test apparatus

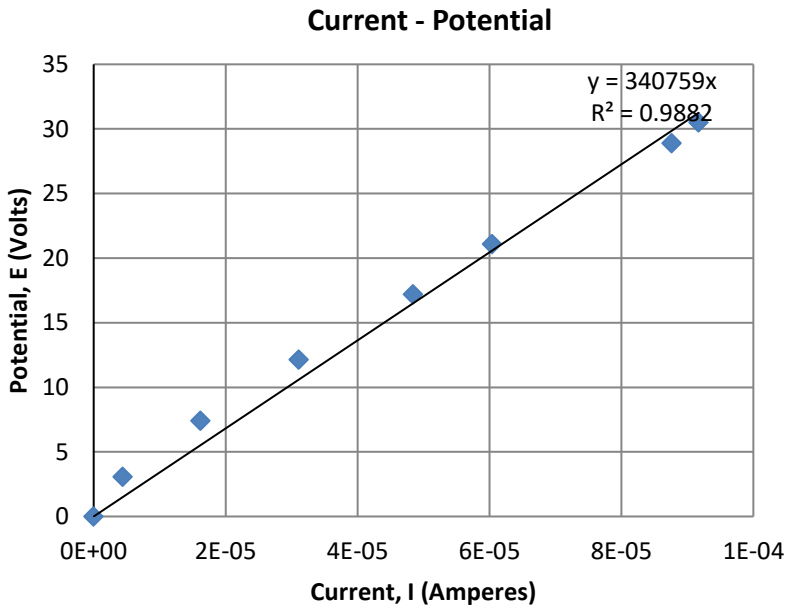

Figure 4.13 Example current-potential graph for BIONICS two point resistivity test . Specimen at 2.6 % GWC. Resistance given by gradient of best-fit line

Following completion of the test, the voltages in Table 4.4 were plotted against the measured resulting currents, as shown in Figure 4.13. A line of best-fit was drawn, the gradient of which gave the resistance, R, of the clay specimen. This figure was then

converted to resistivity, using Eqn. 4.3, adapted from Eqn. 2.6:

$$\rho = R\ x\ \frac{L}{A} \qquad \text{Eqn. 4.3}$$

where *L* is the specimen length (in metres) and *A* is its area (in metres squared).

All specimens were then tested for strength (see Table 4.3 for the numbers of specimens subjected to each test), as follows:

Quick Undrained Triaxial (QUT) Test:
Specimens were tested in accordance with BS 1377-7: 1990 (BSI, 1990d). They were subjected to a confining pressure of 100 kPa at a displacement rate of 1.27 mm/minute, corresponding to a strain rate of 1.67 %/minute. The test apparatus is shown in Figure 4.14.

Unconfined Compressive Strength (UCS) Test:
Specimens were tested in accordance with BS 1377-7: 1990 (BSI, 1990d), at a displacement rate of 1.52 mm/minute, corresponding to a strain rate of 2 %/minute. Figure 4.15a and b show a specimen of BIONICS material before and after compressive failure; Figure 4.16 shows an example stress-strain curve obtained.

The reason for the different displacement rates between the two tests pertains to the limited choice of prescribed displacement rates within the strength testing apparatus. Following failure, the middle third of each clay specimen was oven-dried to determine exact water content, in accordance with BS 1377-2: 1990 (BSI, 1990b).

Figure 4.14 Quick undrained triaxial test

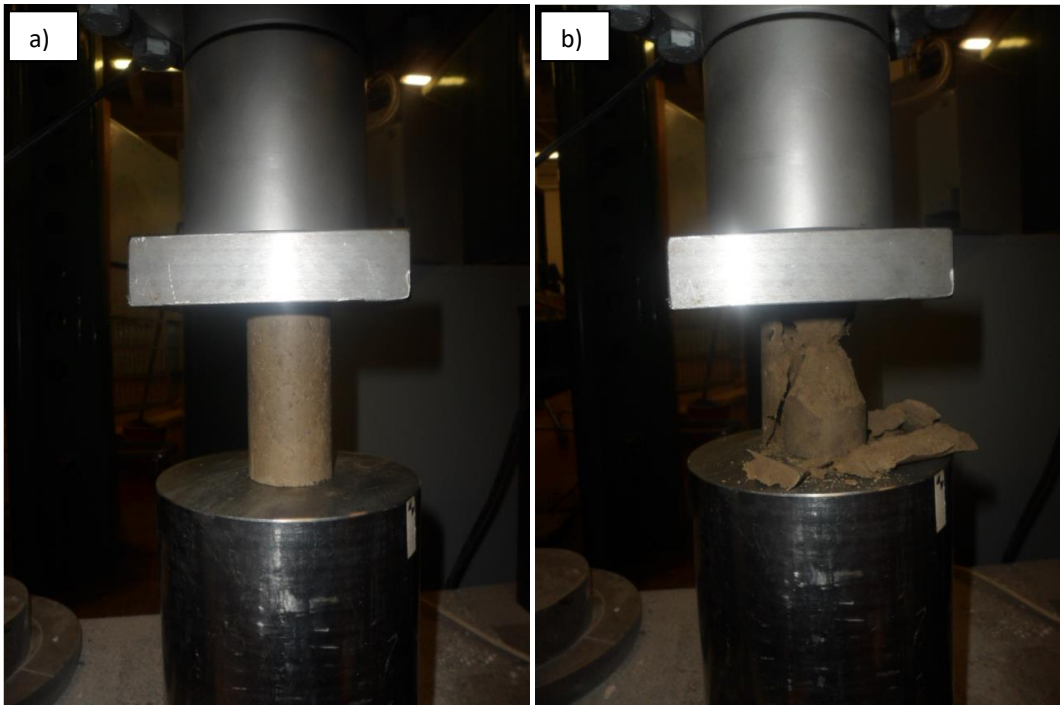

Figure 4.15 Unconfined Compressive Strength test of BIONICS clay specimen (a) specimen in place prior to testing; (b) after compressive failure

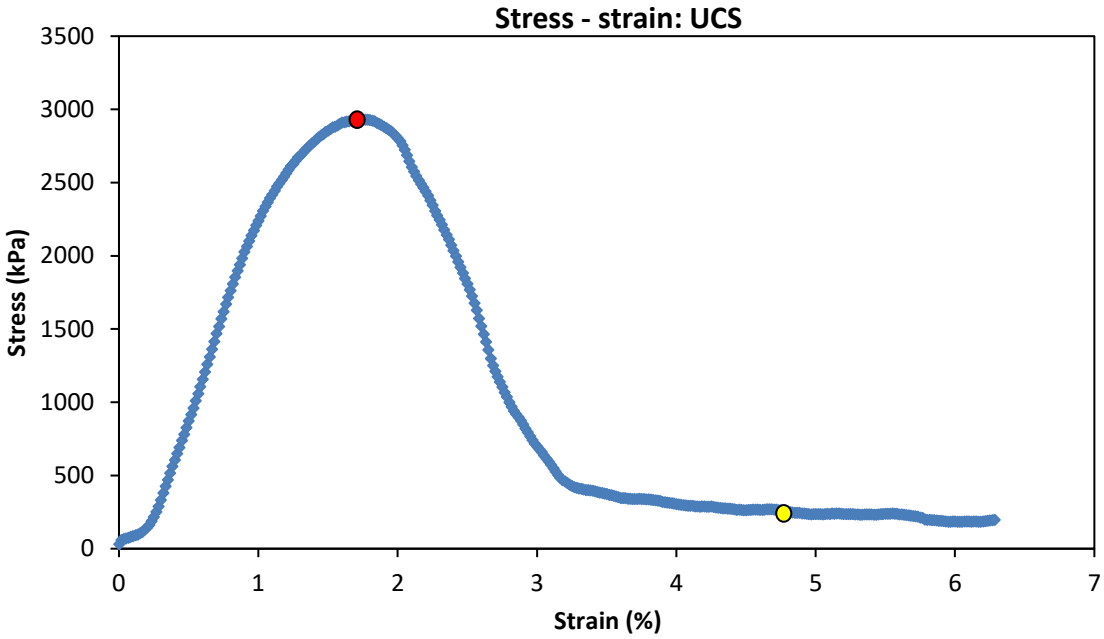

Figure 4.16 Example stress-strain curve for BIONICS clay specimen (UCS). Specimen at 2.6 % GWC, red dot highlights point of failure, at 2930.88 kPa, 1.77 % strain. Yellow dot highlights residual UCS, 240 kPa

Effects of desiccation cracking

Separately to the above tests, it was decided to investigate the effects of desiccation cracking on soil resistivity. In order to stimulate desiccation cracks, fourteen specimens were prepared with in-built planes of weakness which would be more vulnerable to cracking as shrinkage occurred during drying. This was achieved by tamping after the addition of each of the four layers, creating a deliberately smooth surface, orthogonal to the direction of current flow. For this series of tests, only a primary drying path (Path 1a from Table 4.2) was sampled.

Errors

For all of the two point resistivity tests described above, a resistivity measurement error of +/- 12.5 % was calculated, with full calculations provided in Appendix C. These errors pertain solely to the repeatability of the data, and do not account for contact resistances between the specimen and the electrodes, which are incorporated within the two-point resistivity measurement. Large contact resistances can cause soil resistivity to be over-estimated (Heaney, 2003; Hassan, 2014); the four point resistivity test, however, does not include these contact resistances. For this reason, the following experiment was undertaken, comparing the results of two and four point resistivity measurements.

Experiment 3. Comparison of two and four point resistivity methods

Introduction

Over the course of the undertaking of Experiment 2, high contact resistances between the specimen and the plate electrodes were observed at low water contents, despite the application of a conductive gel at this interface. The four point method has considerably lower associated contact resistances, as explained in subchapter 2.3.1.

Apparatus

In order to allow for direct comparison between two and four point tests, it was decided to perform both tests on the same specimens of BIONICS clay material. Therefore a bespoke resistivity test chamber was used, developed at the British Geological Survey laboratories in Keyworth, Nottingham. It comprised a plastic, rectangular prism (constructed using a 3D printer), with internal length 75 mm, depth 25 mm and width 25 mm (Figure 4.17). In preliminary tests, it was observed that, due to the matrix printing method by which the test chamber was constructed, it was liable to absorb water. This was mitigated by spraying the chamber with a waterproof spray paint. The frame is penetrated by a matrix of holes in order to allow for drying of the soil specimen within (Figure 4.17a), and also for the installation of point electrodes for measuring potential difference across the specimen; these point electrodes were installed a distance of 25 mm apart, and penetrated a depth of 5 mm into the specimen (Figure 4.17b, c). Square plate electrodes were installed at either end of the chamber, free to move lengthwise along in order to maintain contact with a specimen which shrinks during drying; steel T-bars were attached to the plate electrodes, in order to allow elastic bands to be placed across them, imparting a compression between the electrodes and the specimen in order to maintain good contact despite shrinkage incurred during drying (Figure 4.17b). With a specimen inside the test chamber, it was possible to first perform a two point resistivity measurement using only the plate electrodes, then to insert the point electrodes through the holes in the frame and perform a four point measurement; the effects of having these two holes present in the soil specimen during the two point test found were to be negligible.*

*A preliminary two point resistivity measurement was made on a “fresh” sample, and performed again with the addition of two 5mm deep, 0.5 mm diameter holes, yielding a difference of 0.05 %.

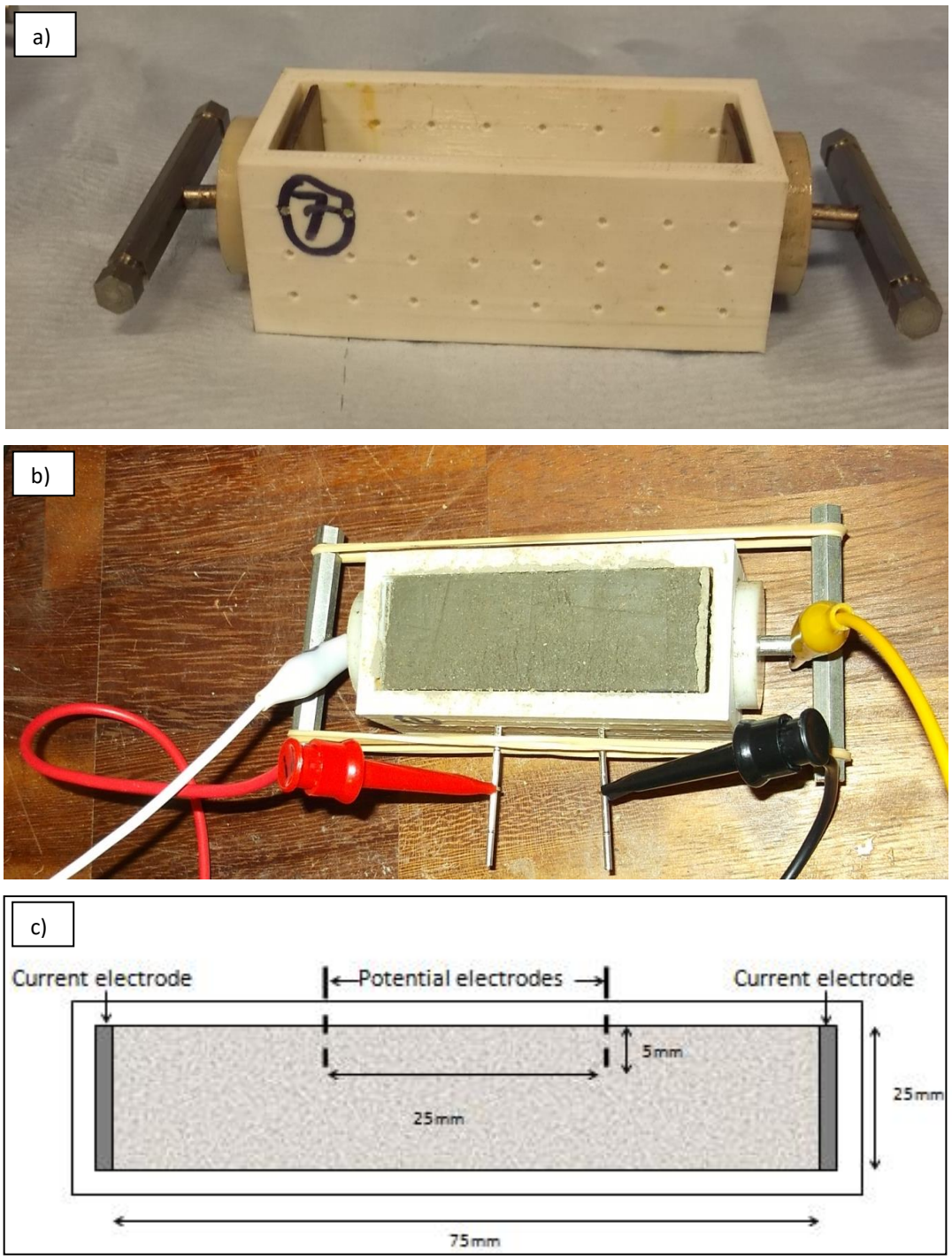

Figure 4.17 Bespoke resistivity test chamber, showing (a) empty chamber; (b) containing BIONICS material, and with the addition of elastic bands across the T-bars; (c) Plan view of open-topped resistivity test chamber with plate current and point potential electrodes

Specimen preparation

To prepare the specimen, 90.45 g of BIONICS clay (plus 0.30 g, approximately 0.3 %) to allow for wastage) at 22 % gravimetric water content (corresponding to target densities summarised in Table 4.1) was compacted into the bespoke resistivity test chamber by

tamping after the addition of each of four layers. Following compaction, the specimen was wrapped in plastic film and sealed in a plastic bag, allowing the specimen to homogenise for 24 hours. The specimen was then subjected to seasonal cycling: for the purpose of comparing two and four point resistivity testing methods, only a primary drying curve (Path 1a from Table 4.2) was sampled. The specimen was unwrapped, and allowed to air-dry in a temperature-controlled environment (20 °C), until its mass corresponded to target water contents, at regular intervals between 22 % and the residual. Upon arriving at the target water content, the specimen was again wrapped in plastic film, and allowed to homogenise for 24 hours, prior to being tested. The specimen was then unwrapped, weighed, and subjected to the following two resistivity tests.

Method

a. Two point resistivity measurement

The two point test was undertaken in accordance with BS 1377-3: 1990 (BSI, 1990c), using the power supply and procedure described in Experiment 2. The resistivity test chamber was placed in the electrical circuit (replacing the copper disc electrodes), and the steel T-bars connected to the circuit using crocodile clips. Due to the fact that the specimen was already compacted into the test chamber, the high conductivity gel could not be applied to the plate electrodes, however, given that the four point method includes only the effects of contact resistances in the potential measurement (i.e. a separate circuit), this was not considered problematic.

b. Four point resistivity measurement

For a four-point resistivity measurement, the test chamber (containing the BIONICS clay specimen) was connected to a generator injecting a square wave alternating current of 1700 µA with a frequency of 60 Hz (see Figure 4.18, Figure 4.19) (a function generator was created by connecting both terminals of the Thandar TS3022S power supply to a bespoke oscillator circuit – see Appendix B for circuit diagram). In order to monitor this current (to verify that it was constant for all tests), the voltage across a known resistance (a 20 Ω resistor) was measured using a Tenma 72-7750 digital multimeter, allowing an accurate measure of current to be obtained for the circuit ($I_{circuit}$), which was inverted using Ohm's Law:

$$I_{circuit} = \frac{V_{20\Omega}}{R_{20\Omega}}$$ Eqn. 4.4

The voltage across the specimen itself (V_{spec}) was determined by use of a PicoScope 3206B oscilloscope (see Figure 4.20), and converted to the specimen resistance, R_{spec}, in the same way, using $I_{circuit}$.

$$R_{spec} = \frac{V_{spec}}{I_{circuit}}$$ Eqn. 4.5

The geometric factor, K_1, for the specimen was obtained, as follows:

$$K_1 = \frac{D\,x\,W}{X}$$ Eqn. 4.6

where *D* and *W* are the width and depth of the specimen respectively, and *X* is the separation between the potential electrodes, all in metres. An alternative method was also used to measure *K*; the test chamber was water-proofed by wrapping in duct tape (Figure 4.21), and filled with a liquid of known resistivity (NaCl solution of 10000 Ω). The four point method was used to obtain a value of resistance for the solution, and the geometric factor, K_2, derived as follows:

$$K_2 = \frac{\rho_{NaCl}}{R_{NaCl}}$$ Eqn. 4.7

where ρ_{NaCl} is the known resistivity of the solution, and R_{NaCl} is the measured resistance. There was close agreement between the two figures, K_1 and K_2, (0.7 % difference for the first test, at a gravimetric water content of 22 % GWC), however, the decision was made to use the geometry-based method (K_1) throughout the experiment due to the fact that K_1 could be easily modified to account for changing volume during shrinkage, whereas it would be impractical to carry out the solution-based test with changing dimensions.

Following completion of the two and four point tests, the specimen was weighed again, and its depth, width and length measured using Vernier callipers. The specimen was then allowed to air-dry until its mass corresponded to the next target water content, before being rewrapped in plastic film and sealed in a plastic bag. A total of ten resistivity – water content

data points were gathered using the two methods, at water content intervals between 22 % and the residual, of approximately 2 %. The BIONICS clay specimen was then extracted from the test chamber, weighed and oven baked in accordance with BS1377-2: 1990 (BSI, 1990b), allowing the water contents of the data points to be verified.

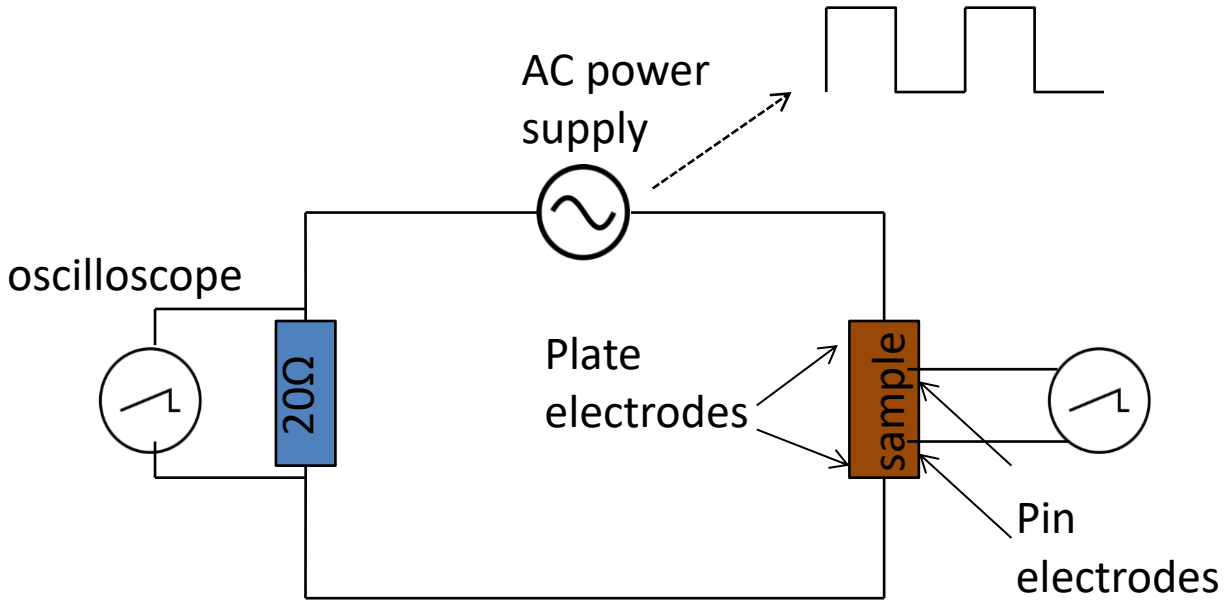

Figure 4.18 Circuit diagram of four point resistivity test apparatus

Figure 4.19 Four point resistivity test apparatus

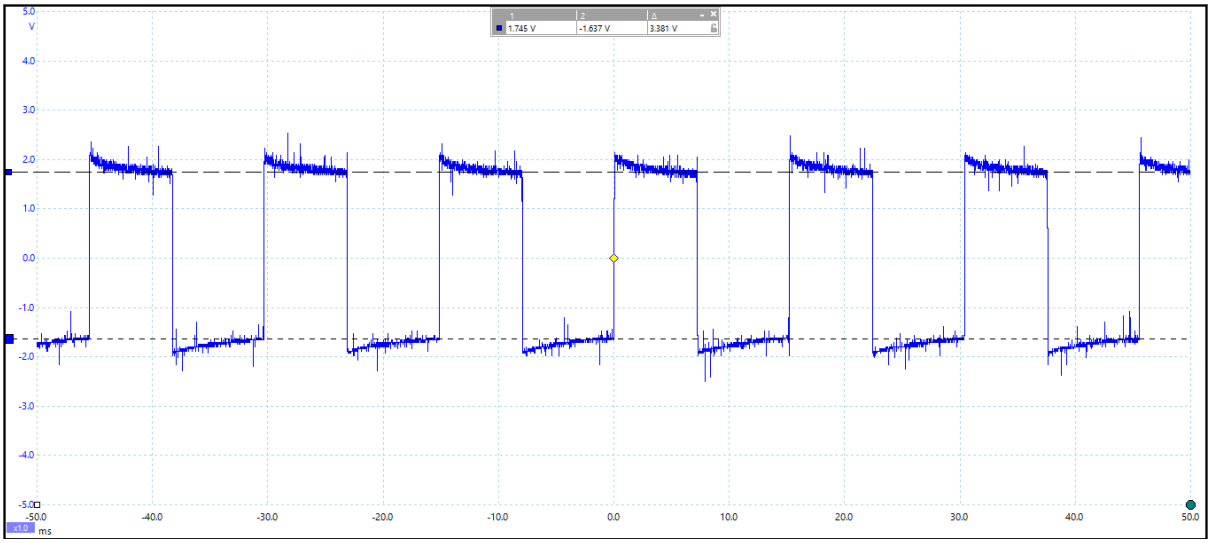

Figure 4.20 Measurement of voltage across specimen using an oscilloscope. Peak-to-trough voltage was divided by two to calculate voltage

Figure 4.21 Waterproofing of resistivity test chamber for derivation of geometric factor

Errors

As for Experiment 2, a two point resistivity measurement error of +/- 12.5 % was calculated. For all four-point measurements, a total error of +/- 16 % was calculated. Full error calculations are provided in Appendix C.

Experiment 4. Resistivity (four point) – water content relationship (seasonal cycles)

Introduction

The results of Experiment 2 (Figure 5.7) indicated a hysteretic path for the resistivity-water content relationship, between primary and secondary seasonal moisture cycles. From the results of Experiment 3, a clear deviation between two point and four point resistivity testing methods was observed, deviating further with decreasing water content (Figure 5.9). This was attributed to an overestimation of recorded two point resistivity values, due to the inclusion of high contact resistances within the electrical circuit (see subchapter 6.1.2). As such, it was decided to use the four point method (using the bespoke resistivity test chambers) to repeat the investigation of the evolution of the resistivity-water content path between primary and secondary moisture cycles, undertaken as part of Experiment 2. To investigate whether or not the specimen compaction method affected the recorded soil resistivity (see subchapter 6.1.2), a different compaction method was used, as described below.

Specimen preparation

A total of four specimens were prepared, by compacting BIONICS material into a standard proctor mould and then extracting a cylindrical core which was trimmed to the internal dimensions of the resistivity chambers. Drying of the specimens was achieved by air-drying in a temperature-controlled environment (20 °C), until the residual water content was reached. Subsequently, they were wet up to 22 % GWC, by placing in the humidifying chamber, following the procedure described in Experiment 2. They were then allowed to homogenise for 24 hours.

Method

The four point resistivity method for testing the prepared specimens was identical to that described in Experiment 3b.

Errors

Four point resistivity measurement errors were calculated to be +/- 16 %, as for Experiment 3 (error calculations for Experiment 3 provided in Appendix C).

Experiment 5. Thermal properties of BIONICS clay

Introduction

In subchapter 2.3.1, the various factors affecting soil resistivity were discussed. Within the context of resistivity surveying of earthworks, the two most relevant factors are soil water content, which varies significantly in the field depending on rainfall, and temperature, which fluctuates both diurnally and seasonally, depending on the depth of penetration within the soil. In this experiment, the thermal properties of BIONICS clay are investigated, for a range of saturation states.

5a. Resistivity (four point) – temperature – water content

In order to be able to more fully interpret electrical resistivity data obtained via tomographic methods, it was deemed necessary to assess the influence of a fluctuating temperature on ground resistivity. To evaluate this influence for different saturation states, this effect was investigated at a range of water contents, using the four point resistivity method.

Specimen preparation

A total of seven cylindrical specimens were prepared, following the procedures outlined Experiment 2. Cylindrical specimens were used rather than the resistivity test chambers for three reasons:

1. To allow for direct comparison with the results of Experiment 2;
2. To avoid any potential boundary effects arising from differing thermal properties of the plastic used in the resistivity test box with respect to the BIONICS material;
3. So that radial distance from the centre of the specimen would be consistent around its circumference.

Six of the cylindrical specimens were intended to be used for testing, with one "control" specimen fitted with a Decagon ECT temperature sensor for estimating the temperature of the six test specimens. This was achieved by slicing the control specimen in half lengthwise, inserting the temperature sensor, and sealing with a BIONICS clay slurry. Following a 24 hour homogenisation period, the specimens were allowed to air-dry until their masses corresponded to gravimetric water contents of 22 %, 16 %, 10 % (two specimens at each water content), and then re-wrapped and allowed to homogenise again.
The water content of the control specimen was 10 %, due to the fact that a lower water content corresponds to a lower thermal conductivity (investigated further in Experiment 5b), such that clay at a lower water content would heat more slowly, ensuring that if the core of the control specimen had achieved a certain temperature, it could be assumed that all of the test specimens had achieved the same temperature.

Once prepared, the specimens (wrapped in plastic film) were each fitted with four copper pin electrodes, in a Wenner Alpha configuration: current electrodes *C1* and *C2* inserted a depth of 5 mm through the centre of the circular ends of the specimens, and potential-measuring electrodes *P1* and *P2* each inserted 22 mm from the ends of the specimen, penetrating a depth of 5 mm. The reason for which point rather than plate electrodes were used at the specimen ends was that these could penetrate the plastic film covering with minimal disturbance, preventing the loss of moisture over the course of the experiment. Due to the use of point electrodes, however, the electrical current could not be approximated as planar along the circular area of the specimen (as with the plate electrodes), but as

spherical, therefore Eqn 4.6 could not be used to approximate the geometric factor, K. For this reason, the specimen geometry including the electrode positions were entered into Comsol modelling software, which calculates a value for K using spherical current originating at a point (Figure 4.22).

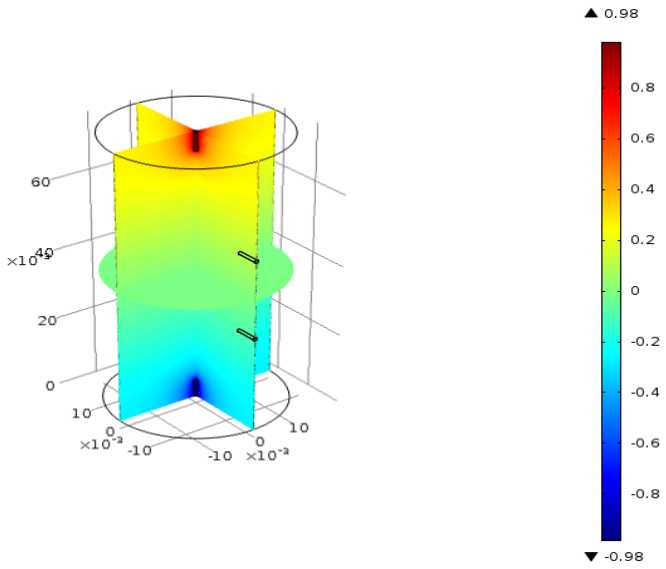

Figure 4.22 Derivation of geometric factor, using Comsol modelling software

Method

All six of the test specimens and the control specimen (all still wrapped in plastic film to avoid drying out during testing), were placed on a grate inside an insulated heating chamber (Figure 4.23), where they would remain undisturbed throughout the experiment. A Polystat heat generator was connected to the heating chamber (Figure 4.24). To avoid disturbing the specimens, all of the electrodes for all of specimens were wired to one central set of cables, extending from inside the heating chamber, outside to the four point testing equipment. In this way, it was possible to connect alternating groups of electrodes to the electrical resistivity testing circuit, without having to remove the individual specimens from the heating chamber (see Figure 4.23, Figure 4.24, Figure 4.25).

The range of temperatures investigated during the experiment was 4 to 26 °C, the maximum and minimum temperatures recorded between depths of 0.1 m and 1.0 m at the BIONICS test embankment over the period June 2013 to June 2014 (Figure 4.26). Using the temperature control, specimens were brought to the starting temperature of 4°, and a four point resistivity test performed, following the procedure described for Experiment 3b. The

resistivity test was performed in 2 °C increments; upon arriving at the target temperature as indicated by the control specimen, all six of the specimens were tested, and the temperature of the heating chamber then increased. After the final measurement at 26 °C, all of the specimens were weighed and oven-dried in accordance with BS 1377-2: 1990 (BSI, 1990b), in order to verify that no moisture had been lost during testing, and to calibrate water contents estimated throughout the tests.

Errors

The EC-TM probe used to measure temperature has an associated error of +/- 1 °C (Decagon Devices, Inc., 2008). A resistivity measurement error of +/- 10.4 % was calculated, with full error calculations provided in Appendix C.

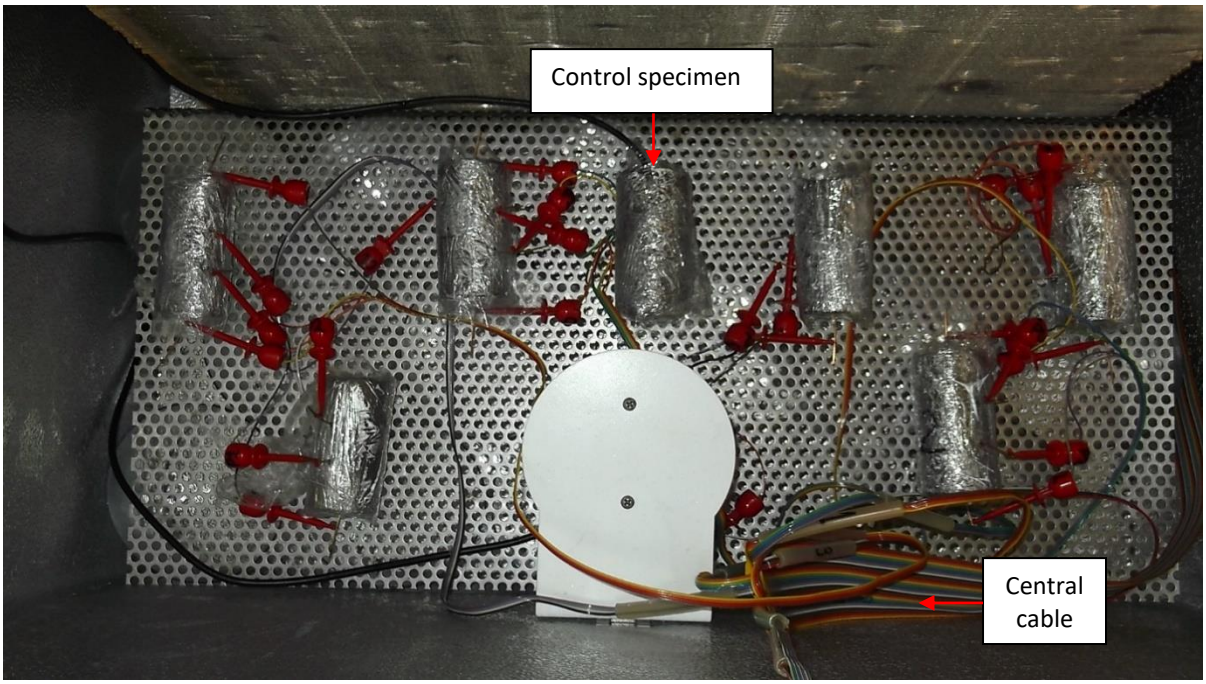

Figure 4.23 BIONICS clay specimens inside insulated heating chamber

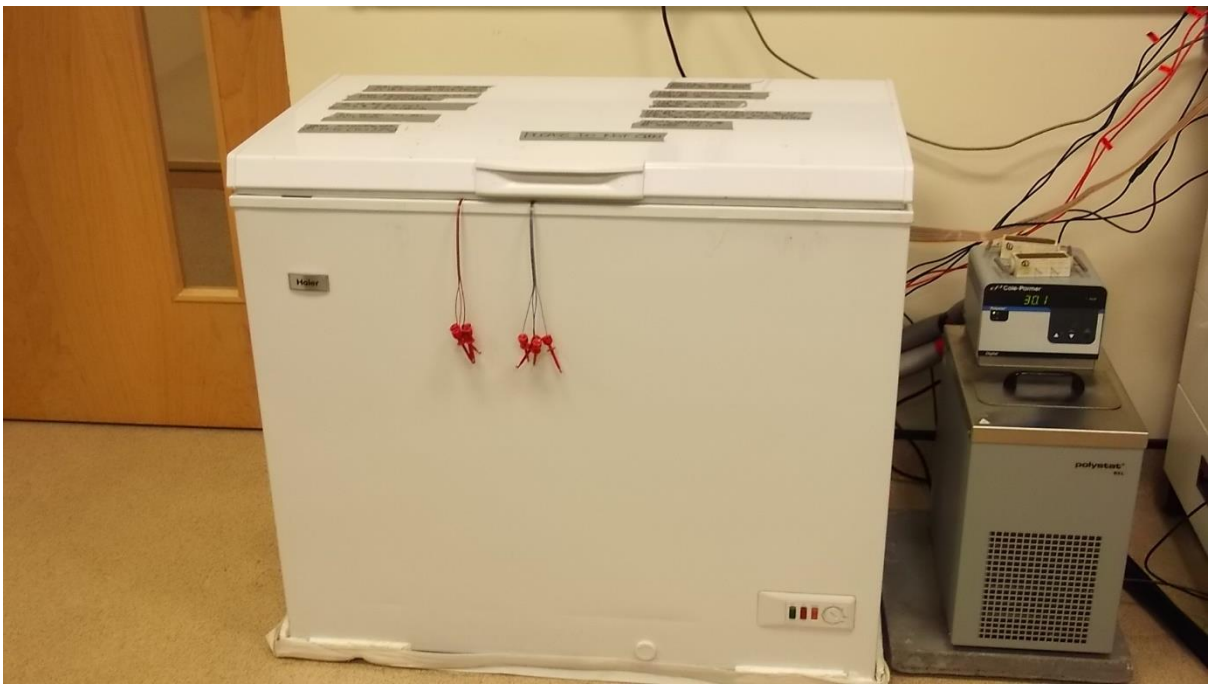

Figure 4.24 Insulated heating chamber and Polystat heat generator

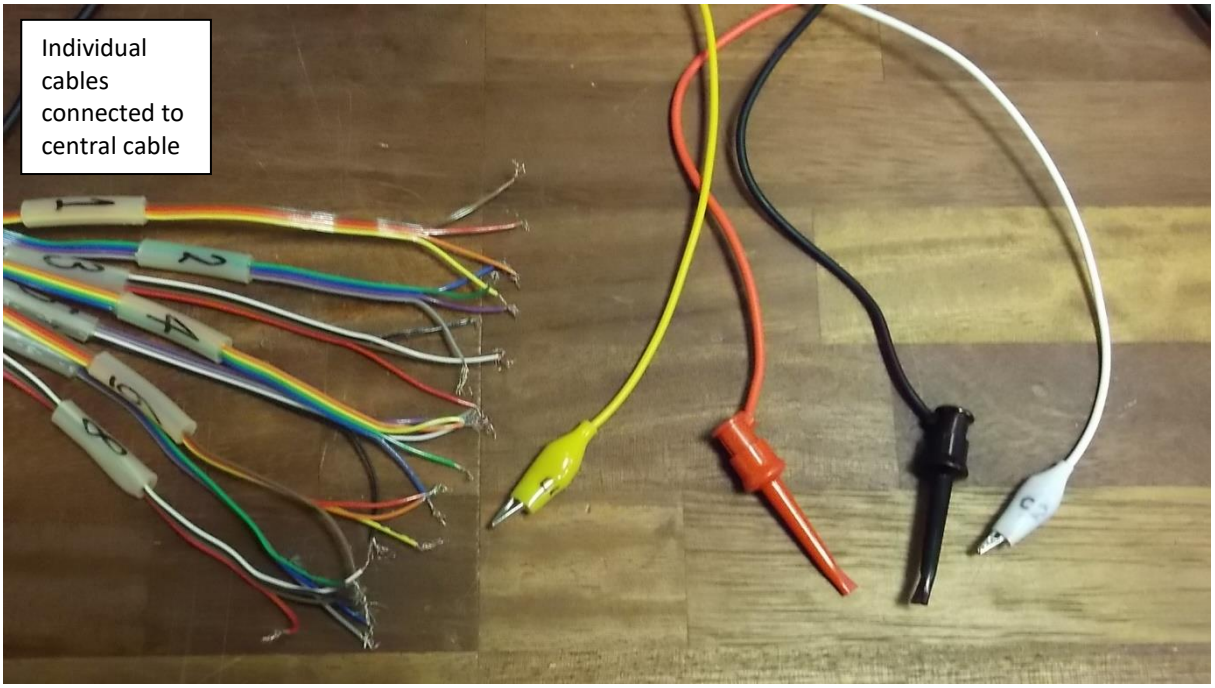

Figure 4.25 Resistivity testing cables from inside the heating chamber

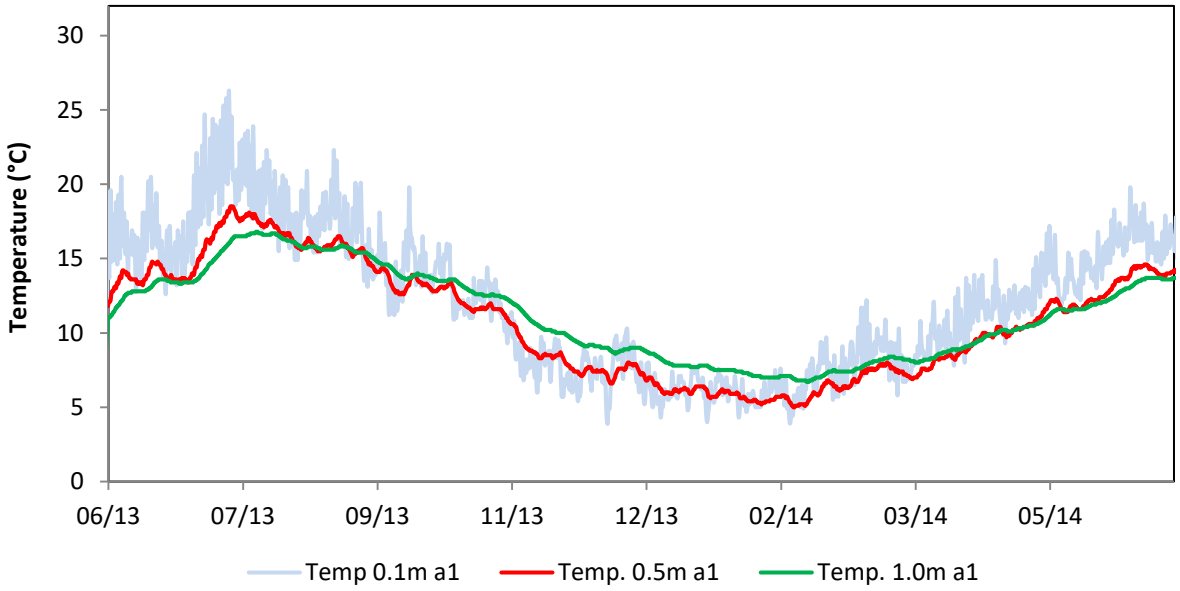

Figure 4.26 Ground temperatures measured at the BIONICS embankment - June 2013 to 2014, at position a1 on the sensor distribution map shown in Figure 4.39

Experiment 5b. Thermal conductivity – water content

As stated previously (subchapter 2.3.1) material resistivity is affected by its temperature, which is the motivation for the previous experiment (5a). The ability of soil to conduct heat, quantified by its thermal conductivity, λ, is largely determined by the same parameters which determine its ability to conduct electrical current, including chiefly, water content. Therefore, the investigation of thermal conductivity for a varying water content is pertinent for two reasons: firstly, to assess whether any comparisons may be made between the water content dependencies of resistivity and thermal conductivity; secondly, in order to aid in the interpretation of Experiment 5a. In this Experiment, the thermal conductivity of BIONICS clay at a range of water contents is investigated using the transient line heat source technique, during a drying path.

Specimen preparation

The dimensions of the test specimens were determined by the use of the Decagon Devices KD2 Pro thermal conductivity probe of length 100 mm: considering the manufacturer's recommendation that there be a minimum 20 mm radius about the probe to avoid boundary effects (Decagon Devices Inc., 2016), two identical cylindrical specimens were prepared from moistened BIONICS clay, of height 120 mm and diameter 50 mm. Static compaction was

used to compact 473.6 g to the desired height, in keeping with the target parameters summarised in Table 4.1. Once compacted, the load on each of the samples was maintained for 30 minutes, in order to prevent them from springing back and expanding in volume. The specimens were then wrapped in plastic film and allowed to homogenise for 24 hours. To accommodate the probe, both the specimens were then drilled with a 2.5 mm bit through their centres, to the probe length of 100 mm (see Figure 4.27).

Method

In order to perform the thermal conductivity test, the probe was first coated in a layer of thermally conductive grease (to ensure good thermal coupling between the soil and the probe), inserted into the specimen, and the thermal conductivity recorded. At each stage in the drying process, the test was performed three times, at 15 minute intervals, due to the nature of the test to raise the internal sample temperature. To prevent moisture loss during this time, the specimens remained wrapped in plastic film throughout. At the start and end of every test, the mass of the specimens was recorded, in order to quantify any loss of moisture.

The specimens were then permitted to air-dry in a temperature-controlled environment (20 ° C), until their masses corresponded to target water contents, at regular intervals (2 % GWC) between the starting water content (22 %) and the residual. Upon arriving at the target, the probe was again coated in a layer of thermally conductive grease, and the above process repeated. Throughout the experiment, specimen dimensions were recorded using Vernier Callipers.

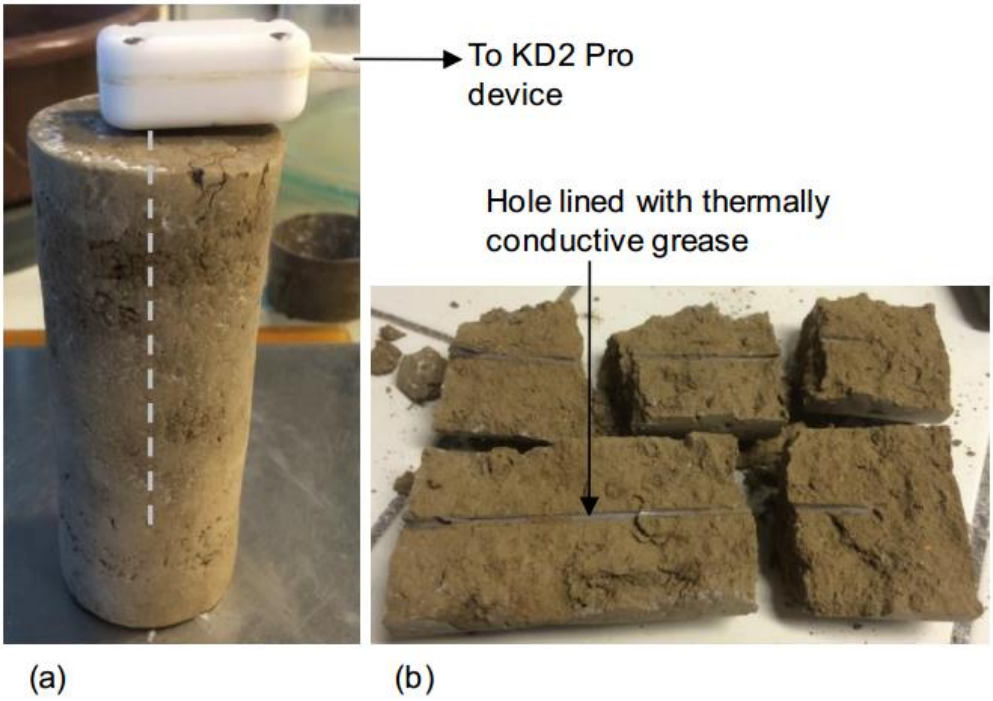

Figure 4.27 Thermal conductivity test apparatus, showing (a) BIONICS clay specimen with probe fully inserted; (b) specimen after completion of drying curve, cut in half lengthwise to demonstrate probe entry hole lined with thermally conductive grease (prior to oven drying in accordance with BS 1377-2: 1990)

Errors

The KD2 Pro thermal conductivity probe has an associated error of +/- 10 % (Decagon Devices Inc., 2016).

Experiment 6. Imaging of soil fabric changes

Introduction

Over the course of the above laboratory experiments performed on BIONICS (and Hollin Hill) clay, several instances of hysteresis were observed in relationships where water content was the variable (Figure 5.7, Figure 5.11, Figure 5.16, Figure 5.17, Figure 5.18, Figure 5.19). This observation was interpreted as an indication of some type of change in the very fabric of the test material resulting from exposure to seasonal moisture cycles, and therefore prompted its direct investigation. In this experiment, BIONICS material is subjected to seasonal dry-wet moisture cycles, and imaged at the microscale, using an environmental-scanning electron microscope (E-SEM), capable of imaging with fields of view down to 10 µm. Using this technology, it is possible to prescribe the temperature and pressure of the immediate atmosphere around a specimen, allowing the humidity and ultimately, the drying rate, to be controlled.

Specimen preparation

Due to the nature of the E-SEM test, there were several constraints to specimen preparation procedure. Specimens were required to be small enough that they could fit on the loading stage within the microscope, and also that they had a low thermal mass, allowing the temperature and evaporation rate inside the chamber to be accurately controlled. They were also required to be sufficiently large that their behaviour was representative of the soil mass as a whole. During testing, the specimens would be subjected to extreme drying, which would cause shrinkage. Given the small specimen size, this could allow a specimen to shrink freely, affecting the representability of the test. Therefore, 10 mm diameter steel nuts were selected to hold the specimens, on the basis of being a low mass, thermally conductive medium between the cooling stage of the microscope and the soil. Due to their internally ribbed texture, they acted to aid interface adhesion and inhibit the test material from shrinking freely. 16 steel nuts were welded on to a sheet of steel, and then cut to separate the individual sample holders (Figure 4.28).

During Experiments 1-5, starting conditions for the test material were made to replicate in situ field conditions at the BIONICS test site. The rapid drying which results from the E-SEM imaging process, however, meant that if specimens at the average in situ water content were imaged, they had dried considerably by the time any images had been gathered. For this reason, all specimens were instead prepared to the liquid limit of the test material, filling the steel nuts to a depth of 5 mm (Figure 4.29); specimens were then wrapped in plastic film and left to homogenise overnight.

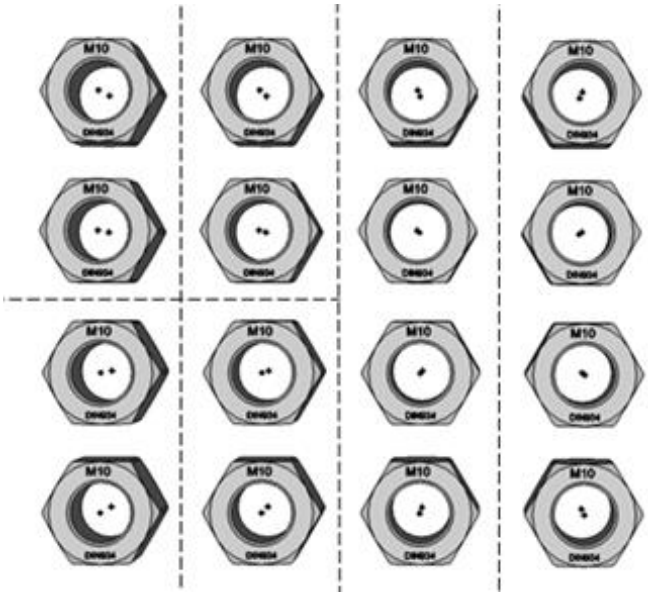

Figure 4.28 Schematic showing 10 mm diameter steel nuts

Figure 4.29 Steel nut filled to a depth of 5 mm

Method

A prepared specimen was placed onto the stage within the E-SEM imaging chamber, and sealed in the chamber (Figure 4.30, Figure 4.31). A drying environment was then promoted by a reduction in relative humidity within the imaging chamber following initial reference imaging. Specimens were then re-wet by the addition of a droplet of water, and allowed to homogenise for 24 hours prior to further imaging. The reason for this method of addition of water is the relatively small sample volume compared to the other laboratory tests (Experiments 1-5), such that the other procedures would be ineffective.

Figure 4.30 E-SEM microscope

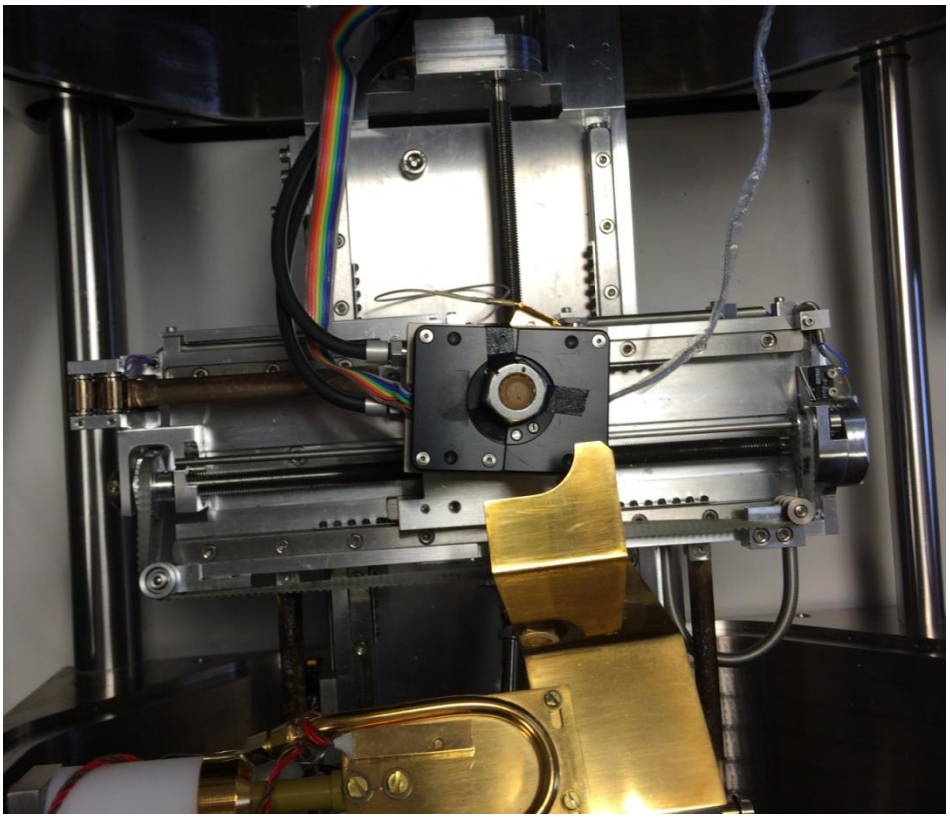

Figure 4.31 E-SEM imaging platform with BIONICS clay specimen in place

4.2 Field experiments at the BIONICS embankment

4.2.1 *Introduction*

The field component of this research project was based around high resolution electrical resistivity imaging of the BIONICS embankment, during which efforts were made to monitor every change in ground and environmental condition. Given that the BIONICS embankment was purpose-built to prescribed specifications, many of its structural properties were known prior to the execution of the field experiments (see Chapter 3).

A series of intervention procedures were performed, to perturb the hydrodynamic stability of the embankment, and to examine whether or not these perturbations could be observed from the high resolution, 4D ERT imaging, in addition to natural environmental forcings. Monitoring of ground and environmental conditions was accomplished by the use of a network of geotechnical point sensors. An explanation of the intervention procedures is given, followed by full details of the experimental installations.

4.2.2 *Experiment design and stability intervention procedures*

For this study, the Southern flank of the BIONICS embankment was selected to be the main focus, due to the fact that it is more exposed than the Northern flank. It therefore exhibits more dynamic hydrological behaviour, with more pronounced seasonally cyclic behaviour than the Northern flank, as is described in Glendinning et al., 2014.

Prior to the installation of the field instrumentation detailed below, simple stability modelling of the BIONICS embankment was undertaken in Plaxis, to provide qualitative information relevant to the development of slope intervention procedures. This modelling is described in detail in Helm, 2012; a brief summary of this information is provided below.

Material and model parameters

Within Plaxis, the simplistic Mohr-Coulomb model was utilised. The geometry of the embankment was set up as shown in Figure 3.7. Material parameters described three components of the embankment: the glacial till foundation material, the embankment fill, and the gravel ballast capping material. Parameters describing the embankment fill material were derived from those published in Hughes et al., 2009, describing the poorly-compacted

section of the BIONICS embankment (also described in subchapter 3.2.2). For the foundation and ballast capping materials, input data were estimated from Tomlinson, 2001, Itasca, 2001 and Brinkgreve et al., 2012. These properties are summarised in Table 4.5, extracted from Helm, 2012.

Table 4.5 Material properties used for the simple embankment model

Parameter (units)	**Glacial Till**	**Embankment Fill Material**	**Gravel Capping Layer**
Dry Density (kN/m^3)	17.00[A]	16.00[B]	16.00[C]
Bulk Density (kN/m^3)	20.00[A]	19.30[B]	18.00[C]
Young's modulus (MPa)	12.00[E]	9.76[F]	15.00[E]
Poisson's ratio (-)	0.35[E]	0.35[E]	0.30[E]
Effective cohesion (kPa)	10.00[A]	4.00[B]	0.01[D]
Effective friction angle (°)	28.00[A]	27.50[B]	30.00[C]

[A]Hughes et al., 2006; [B]Hughes et al., 2009; [C]Tomlinson, 2001; [D]Brinkgreve et al., 2012; [E]Itasca, 2011; [F]derived from drained triaxial testing. Note, the gravel has a small non-zero drained cohesion as this is recommended in PLAXIS for all cohesionless materials. Table modified from Helm, 2012.

A simplistic representation of the water table was implemented, as follows: at point A (see Figure 4.32) the water table depth, d_1, below the surface of the crest was calculated as a ratio of the total embankment height, h_e, where $d_1 = (1 - R_u) \times h_e$ and R_u is a scaling factor. A similar expression was derived for the water table depth below the embankment toe, d_2, relating it to the original depth, h_w, of the phreatic surface, prior to embankment construction: $d_2 = (1 - R_u) \times h_w$. A very simple phreatic geometry was assumed, whereby the water table is linear between a point under the break of the crest and a point beneath the toe (i.e. points A and B on Figure 4.32). This water table was increased incrementally by increasing R_u, and the effect of this on the factor of safety (FoS) analysed.

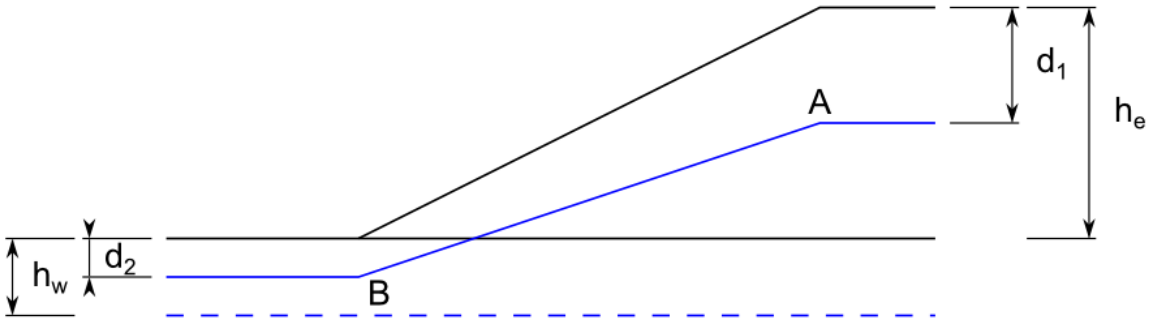

Figure 4.32 Simplified assumption of a linear phreatic surface (image from Helm, 2012). Dashed blue line is the phreatic surface prior to embankment construction; solid blue line is the phreatic surface following embankment construction

From this simple modelling exercise, it was found that the FoS of the embankment drops below 1 when the phreatic surface is at a depth of 0.9 m beneath the crest, and 0.3 m beneath the slope toe, corresponding to R_u = 0.85. The modelled failure is shown in Figure 4.33a and b, which shows the strain and displacement contours respectively. From Figure 4.33a, the highest strains demonstrate a circular strain plane extending from the embankment crest to the toe, intercepting the boundary between the base of the embankment fill and the underlying glacial till. Displacement contours in Figure 4.33b highlight an associated movement of mass, constituting a shear failure of the Southern-facing portion of the BIONICS embankment.

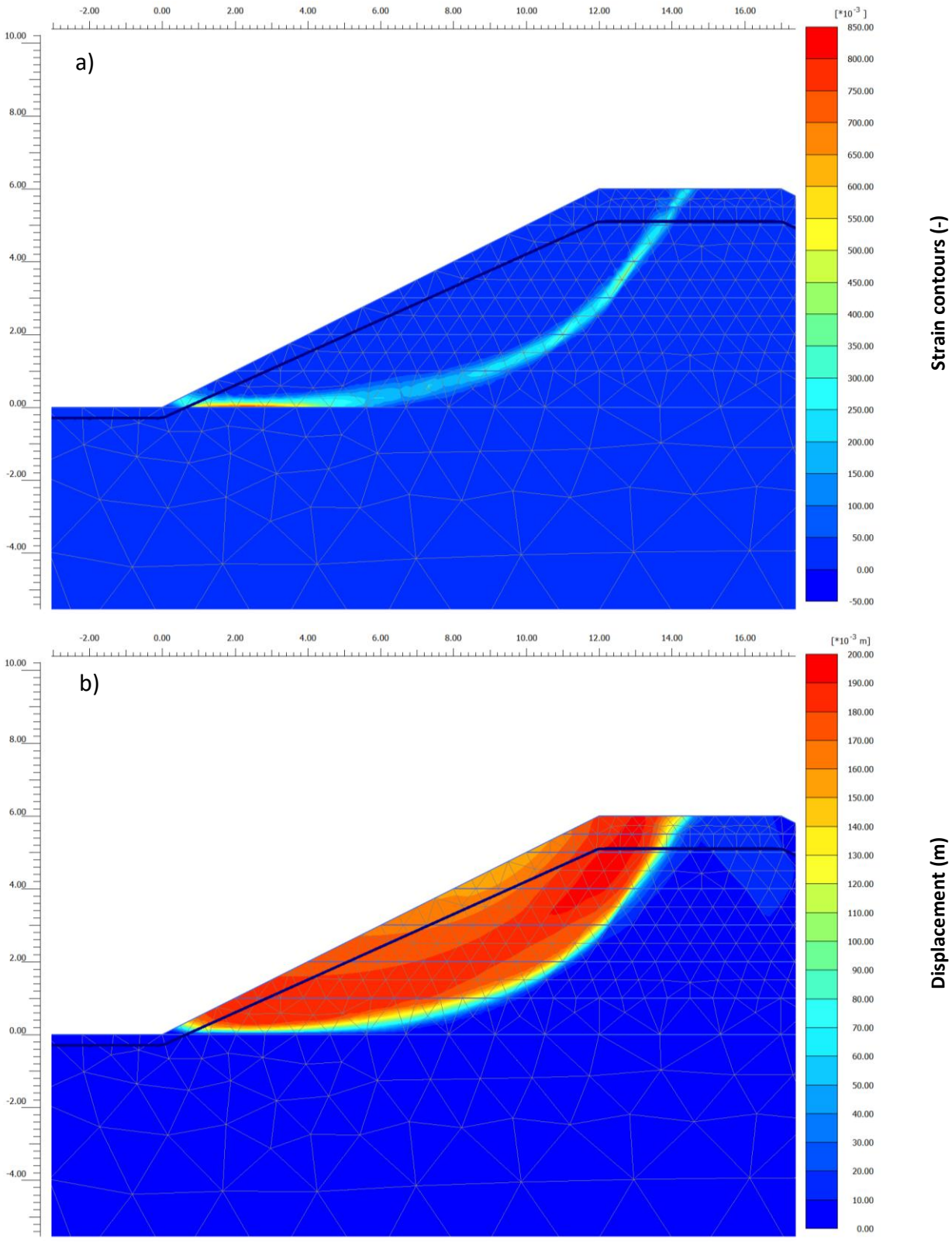

Figure 4.33 Modelled rotational failure, created in Plaxis (image from Helm, 2012), showing (a) strain contours at failure; (b) displacement contours at failure

At the project inception stage of this study, the concept of artificially causing a slope failure of Southern flank of the ERT test plot was considered, which would be recorded using high

resolution 4D ERT imaging. Site investigation of the BIONICS site, prior to construction of the embankment, reported a phreatic surface 2.0 m below ground surface (h_w). It was recognised that it would likely be practically impossible to go from such scenario to slope failure, i.e. that the embankment was effectively too stable to fail. A series of stability intervention procedures were instead designed to perturb its hydrodynamic equilibrium, providing a resolution verification test for the ERT array. The intervention procedures applied to the ERT research plot are as follows:

a. Slope regrading: To lower the FoS of the embankment, and therefore lower its stability, the decision was made to regrade and steepen the slope of the ERT test plot section of the embankment, from 27°, to 30°, on both the Northern and Southern flanks. This was undertaken in November 2012, days before the installation of the ERT array, using a JCB, and is shown in Figure 4.34a to c. Following regrading, a 150 mm thick layer of topsoil was replaced on both the Northern and Southern flanks, to encourage vegetation growth.

b. Simulated cracking: In May 2014, four tension cracks (OS1, OS2, OS3, OS4 - approximately 100 mm depth, 1200 mm length, 70 mm aperture), were observed in the Southern flank of the ERT test plot (these are historic, see Figure 3.14, Figure 4.35). In order to encourage drying during the summer months, and water infiltration during rainfall events, the decision was made to extend these manually, in all directions. Using a spade, all four tension cracks were widened to approximately 300 mm depth, 5000 mm length and 200 mm aperture (see Figure 4.36).

c. Installation of a sprinkler system: A computer-controlled sprinkler system was installed across the ERT test plot in January 2015, comprising eight sprinklers (three on each flank; two on the crest) placed at a height of 1.5 m above the surface, in a central line extending across both flanks and the crest of the embankment, imparting an approximate 33 mm of water per day (Figure 4.37, Figure 4.38). A programme of sprinkling was defined, such that every day, the sprinklers were activated for four one hour periods, each followed by a three hour recharge period to allow the water tanks to refill. The sprinkler system remained activated from 12th January 2015 until 1st June 2015.

Figure 4.34 Slope steepening of the ERT test plot section of the BIONICS embankment, showing (a) regrading using a JCB; (b) angle measuring of regraded slope; (c) after the replacement of topsoil to encourage vegetation growth

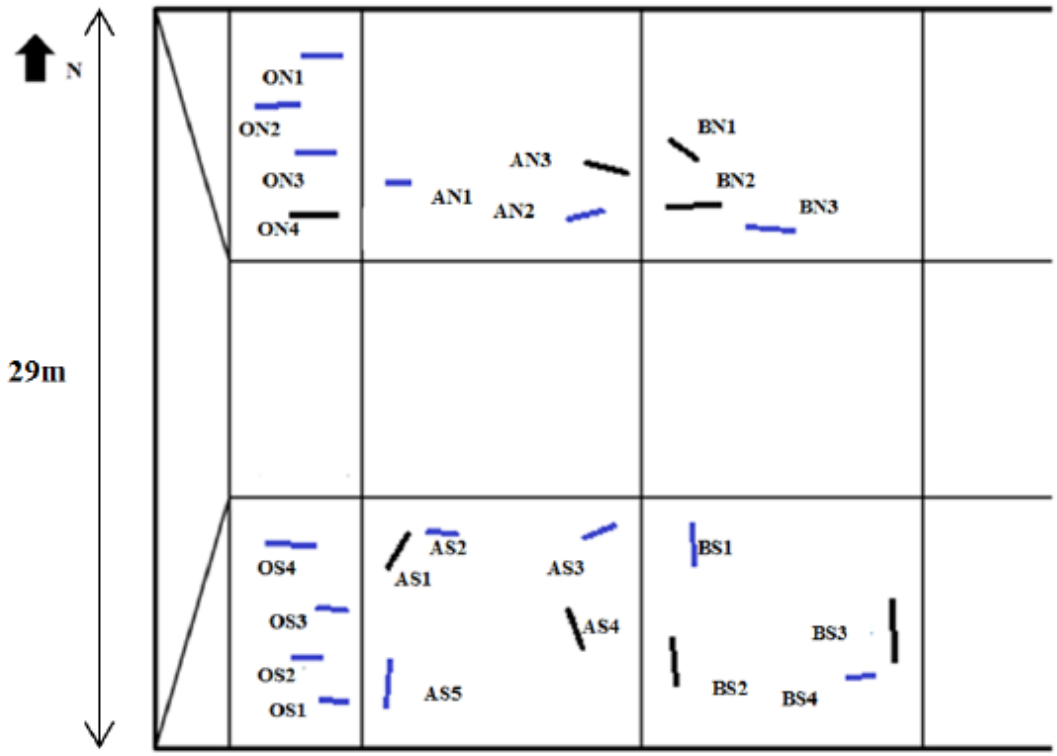

Figure 4.35 Schematic showing crack survey undertaken during Summer 2013. Cracks in blue are historic cracks present in surveys since 2008; cracks in black were newly discovered over the course of Summer 2013. Image from Michelaki, 2013

Figure 4.36 Crack simulation at the ERT test plot section of the BIONICS embankment, showing (a) cracks immediately after extension in May 2014; (b) full of infiltrated rainwater in Winter 2014

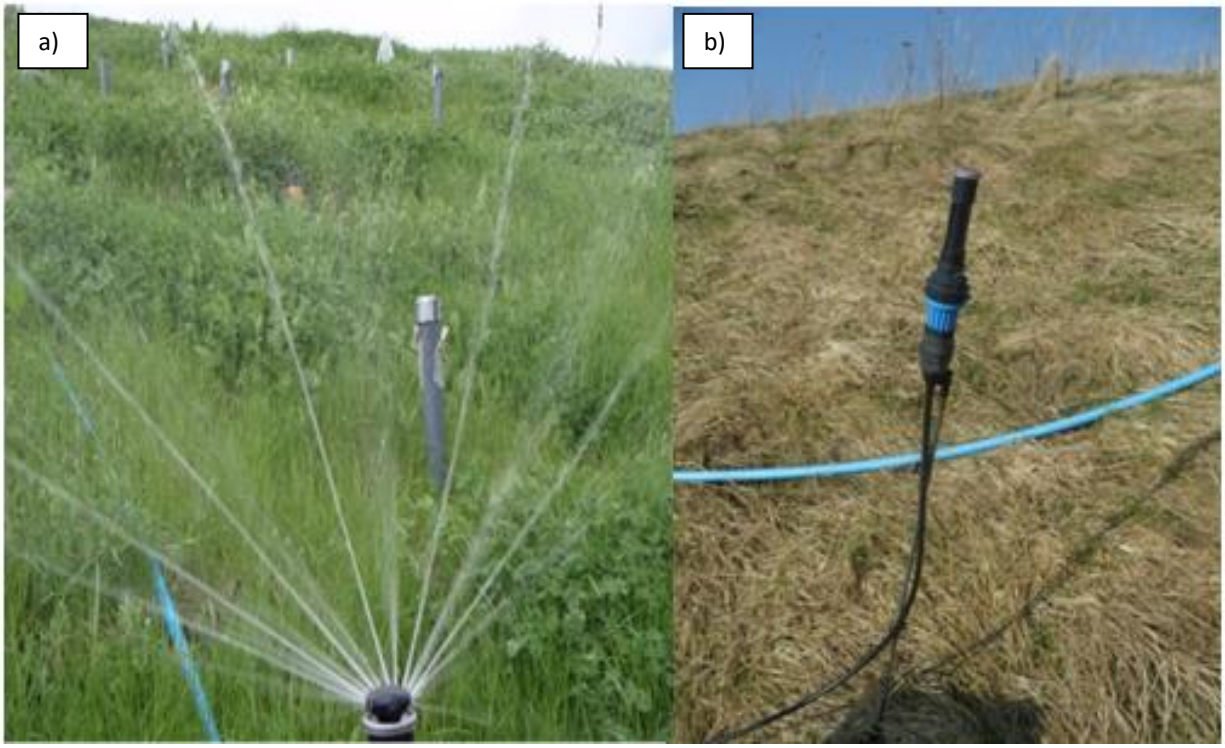

Figure 4.37 Sprinkler system, showing (a) sprinkler system activated; (b) whilst deactivated

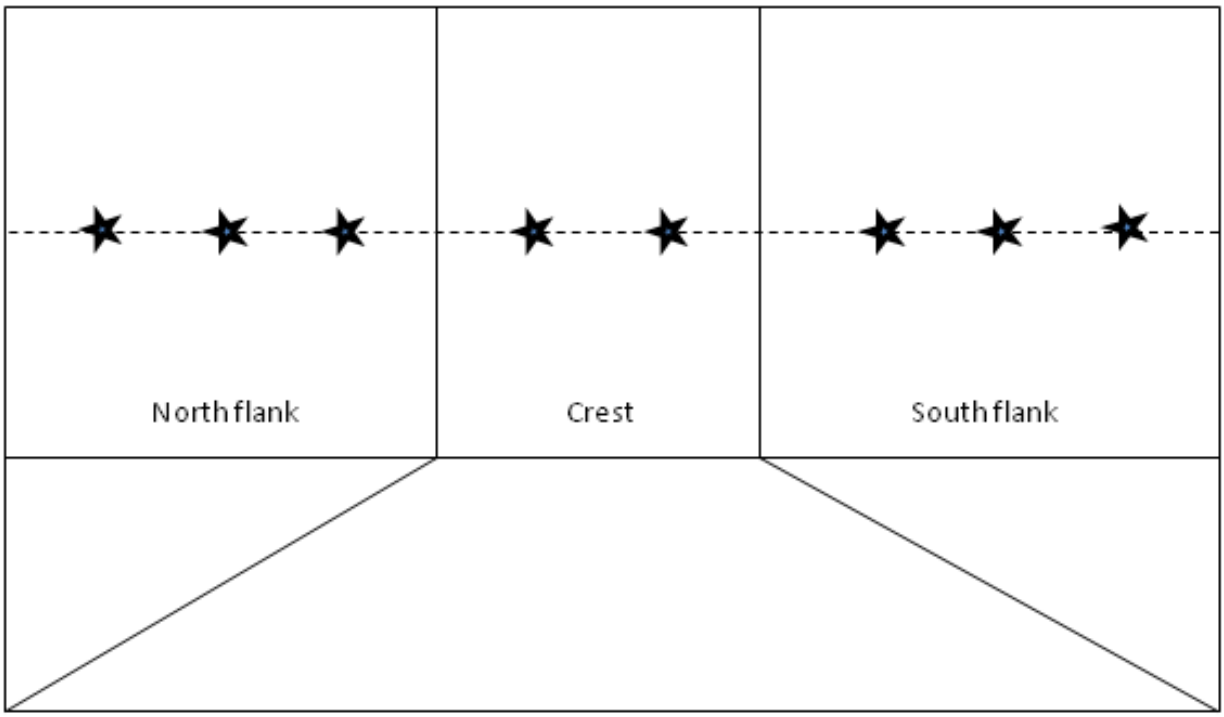

Figure 4.38 Location of sprinklers on the ERT test plot. Black star indicates sprinkler

4.2.3 *Point sensor network*

Following completion of the construction of the BIONICS test embankment in 2005, a number of geotechnical point sensors were installed, recording ground temperature, water content and suction. In the years that have followed, and particularly since the commencement of this research project, this network has grown, to include other sensor types, and to cover the bulk of the western half of the embankment.

Introduction

In subchapter 2.2.7, the limitations of geotechnical point sensors for assessing slope stability were discussed; as part of this field study, a series of geotechnical and geophysical point sensors have been installed at the BIONICS test embankment. The aim of these sensors is not, however, to make any assessment of slope stability, but to:

1. Aid in the monitoring of environmental conditions at the BIONICS test embankment;
2. Allow geophysical-geotechnical inter-relationships to be investigated in the field, and to monitor how these differ as a function of location (depth, aspect) and other variables;
3. Provide a basis against which the laboratory experiments can be compared;
4. Provide a basis against which data obtained using the ERT array can be compared, evaluated and correlated.

Method

At the start of this PhD project in 2012, several additions were made to the point sensor network, focussing on point data collection at the ERT test plot. Over the course of the project, more sensors have been added, sampling not just the ERT research plot, but the whole of panels A and B, in order to provide a comprehensive network of sensors sampling the BIONICS embankment. The majority of the sensors provide information on the near-surface, at depths of less than 1 m, although some deeper sensors have been installed. In the images below (Figure 4.39a and b), maps of the point sensor distribution at the embankment are shown. A full list of the different type of sensor and their measurement parameters is given below (Table 4.6, Table 4.7).

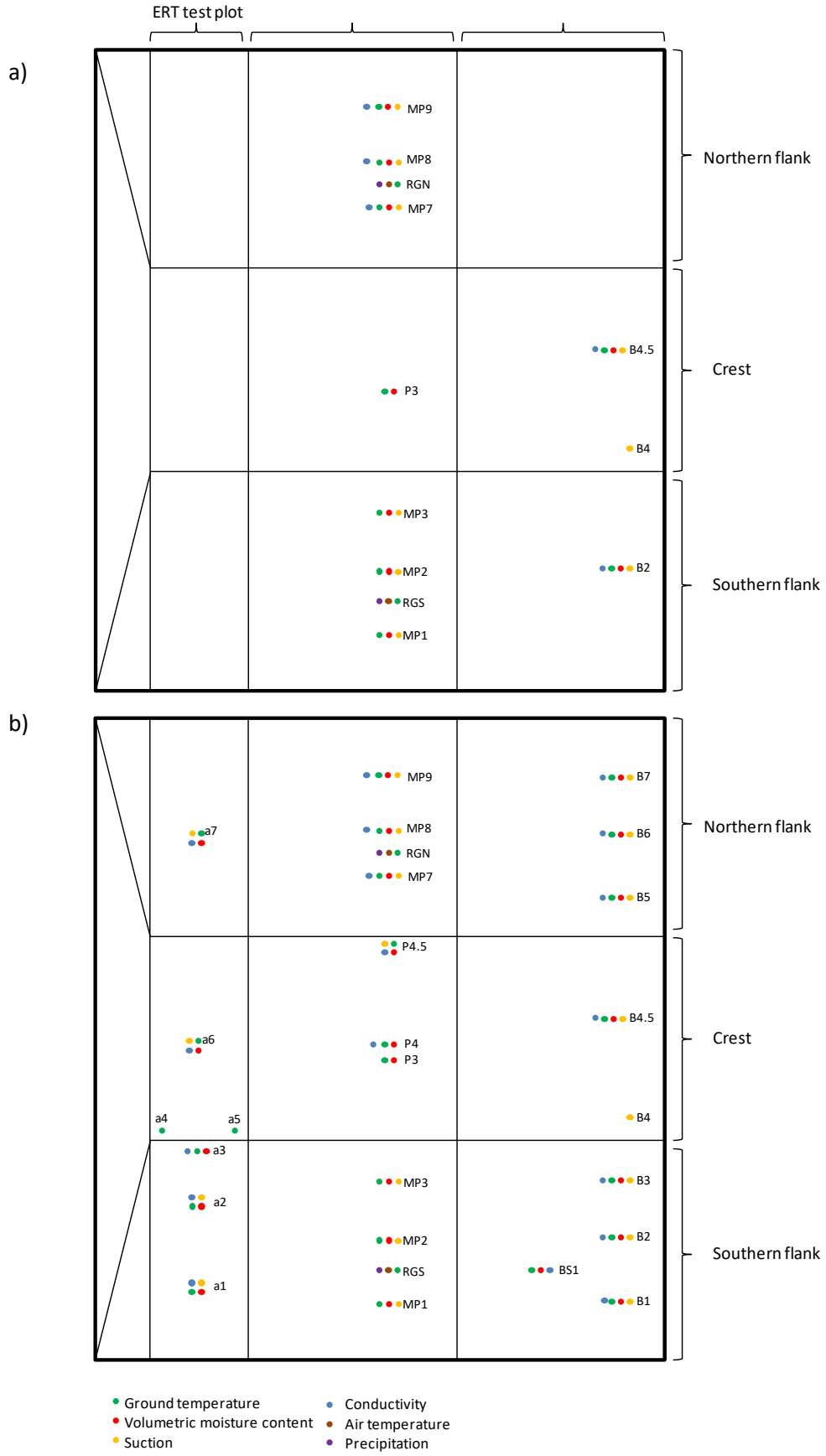

Figure 4.39 BIONICS point sensor distribution maps, showing sensor locations (a) in September 2012, at the start of this research study, and (b) as of March 2016. For sensor depths, see Table 4.6

Table 4.6 BIONICS point sensor locations

Sensor location	Depth (m)	Sensor type
a1, a2	0.1, 0.5, 1.0 0.5, 1.0	5TE MPS-1
a3	0.5	5TE
a4	0.5, 1.0, 2.5, 5.0	ECT
a5	0.5, 1.0, 2.0, 3.0	ECT
a6*, a7	0.5, 1.0	5TE, MPS-1
MP1, MP3	0.5, 1.0	EC-TM, MPS-1
MP2	1.0	EC-TM, MPS-1
RGS, RGN	0.1, 1.0 (above ground) -	ECT ECRN 100
P3*	3.0	EC-TM
P4*	1.0	EC-TM
P4.5*	1.0	5TE
MP7, MP9	0.5, 1.0	5TE, MPS-1
MP8	1.0	5TE
B1	0.5, 1.0 1.5	5TE, MPS-2 MPS-2
BS1	0.5, 1.0	5TE
B2	0.5, 1.5 1.0	MPS-1 5TE
B3	0.5, 1.0 1.5	5TE, MPS-2 MPS-2
B4*	0.5, 1.5 1.0	MPS-1 EC-TM
B4.5*	1.0, 1.5 0.5, 1.0, 1.5	5TE MPS-1
B5, B6, B7	0.5, 1.0 0.5, 1.0, 1.5	5TE MPS-2

*Crest sensors: depths given pertain to depth from top of fill, not ballast.

Table 4.7 BIONICS point sensor technical specifications

Sensor type	**Measurement parameters**	**Range/resolution/accuracy**	**Notes**
EC-TM	Volumetric water content, temperature	0 to 100 °C/0.1 °C/± 1 to 2 % -40 to 50 °C /0.1 °C /± 1 °C	
5TE	Volumetric water content*, electrical conductivity, temperature	ε_a = 1 (air) to 80 (water)/0.08 %/± 1 to 2 % 0 to 23 dSm^{-1}/0.01 dSm^{-1}/± 10 % -40 to 60 °C /0.1 °C /± 1 °C	Two point electrical conductivity measurement
ECT	Air temperature	-40 to 50 °C /0.1 °C/± 1 °C	
MPS-1	Suction	-10 to -500 kPa/4 kPa/± 20 %	Reads zero for positive pressures
MPS-2	Suction, temperature	-10 to -500 kPa/0.1 kPaC -40 to 60 °C /0.1 °C/± 1 °C	Reads zero for positive pressures
ECRN 100	Precipitation	-/0.2 mm/-	Replaced weather station on Panel D

*Derived from dielectric permittivity, ε_a.

Installation

For the Decagon sensors to make measurements at the depths listed in Table 4.6, they first required holes to be augered for their installation. This was achieved using a 5 mm diameter steel hand auger, penetrating vertically down into the embankment. Although this was relatively manageable on the embankment flanks, due to the thick ballast layer on the crest, the ballast first had to be dug out with a spade before the auger could be used. Below the crest, the clay appeared much stiffer than on the flanks, and as such, progress with the auger was challenging, particularly for the deeper holes. Throughout the augering process, the extruded material was retained, to be mixed with water into a slurry and used as backfill for sealing the augered holes after installation of the point sensors.

For the MPS-1 and MPS-2 sensors (soil suction), good hydraulic contact with the surrounding soil is essential, and as such, the recommended installation method involves packing the sensors in a bulb of native soil (Figure 4.40b) (Decagon Devices Inc., 2008). In this way, one sensor could be placed into an augered hole, to the desired depth (e.g. 1.0 m), the augered hole backfilled until the next target depth (e.g. 0.5 m), and the next, shallower sensor placed, requiring only one hole to be augered for MPS suction sensors at multiple depths, for the same location. A plastic “insertion rod” was used to insert the sensors (encased in

BIONICS clay), by pulling the sensor cables through the rod and holding taught while placing in the augered hole (Figure 4.40a, c).

The 5TE, EC-TM and ECT sensors all have a three prong geometry, requiring direct insertion into the ground. As such, individual holes were required to be augered for every sensor. As before, an insertion rod was used (Figure 4.40d).

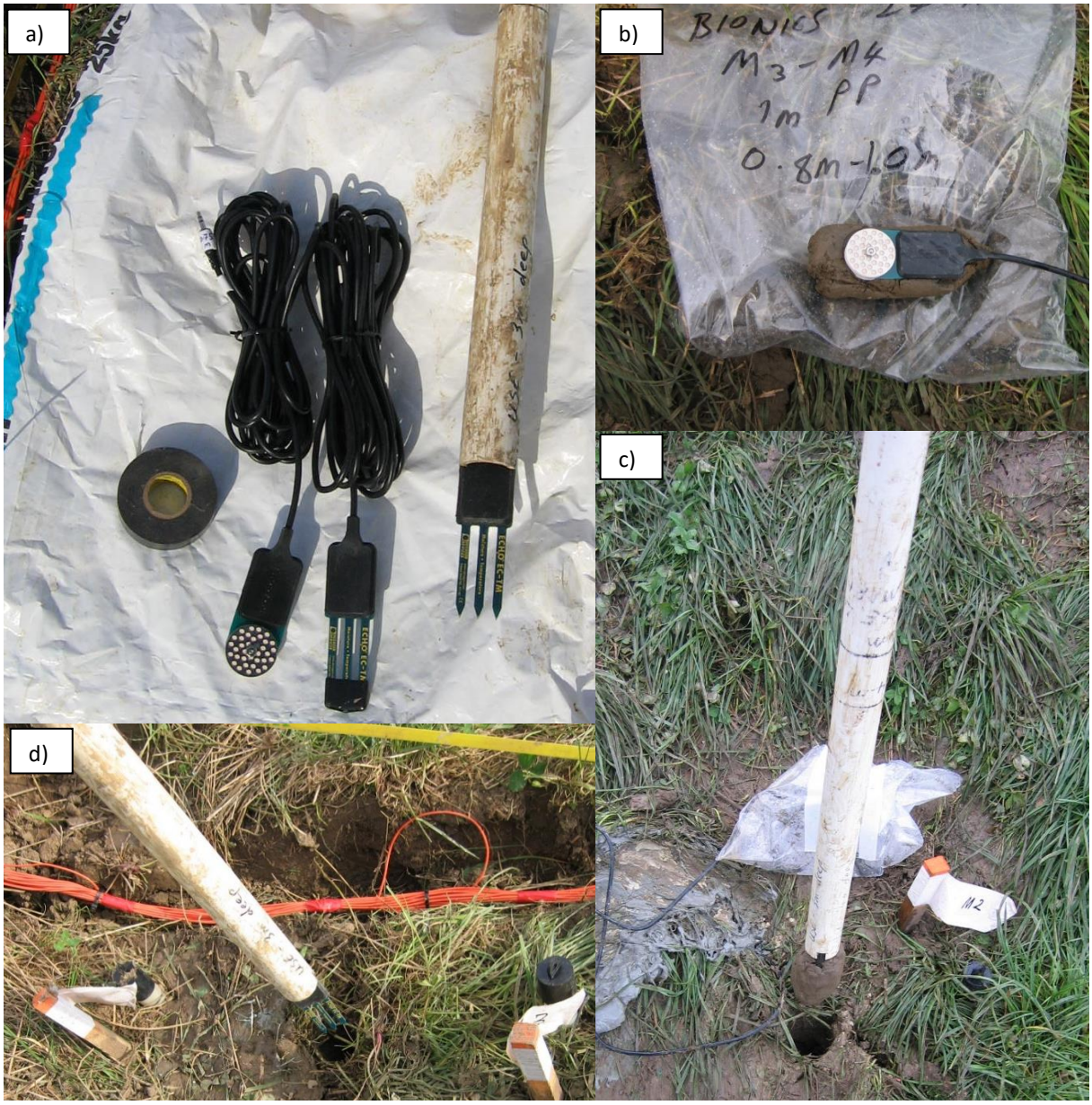

Figure 4.40 Decagon sensor installation, showing (a) MPS and EC-TM sensors; EC-TM sensor mounted on insertion rod; (b) MPS sensor encased in bulb of BIONICS material; (c) installation of MPS sensor; (d). Installation of EC-TM

All of the above Decagon Devices sensors were connected to Em50 digital data loggers with five data collection ports (Figure 4.41) (Decagon Devices Inc., 2016), with an initial

continuous data sample frequency of 30 minutes; this was later adapted to 1 hour in order to reduce the volume of data collected.

Figure 4.41 Em50 digital data logger

For all of the point sensors described, approximately monthly data collection trips were taken to BIONICS, in order to verify sensor functionality, and to manually download all of the data.

Maintenance issues

Throughout the research study period, there were several issues encountered with the point sensor network. Firstly, it was observed that water infiltration was occurring within the Em50 data loggers: this was successfully mitigated by mounting the loggers on wooden stakes, 700 mm above ground, which also help to protect them from overgrowing vegetation. Unfortunately, it proved very difficult to fully protect the sensor cables from rodent damage.

On all monthly data download trips, logger battery life was checked, however, a marked decay in battery life was observed in most of the loggers over the course of this study, and occasionally, loggers would stop recording, resulting in the loss of data.

In addition to issues pertaining to the loggers, there were relatively regular occurrences of sensors which had to be replaced either because of physical damage (e.g. rodents) or other,

more generic malfunctions. The latter issue was particularly problematic because it was often not immediately obvious whether the logger or sensor was faulty. During the data collection visits, all sensors were digitally scanned, to verify that they were recording properly, but these scans only proved functionality at that particular moment, potentially concealing a sensor which had, for example, previously not been recording properly. For these reasons, sensor malfunctions were sometimes not noticed immediately, resulting in few of the sensors shown in Table 4.6 having undisturbed, complete datasets.

4.2.4 *Electrical Resistivity Tomography array*

Array installation

Following regrading of the Southern portion of the ERT test plot, the electrical resistivity tomography array was installed, over two days in mid-November 2012. Eight lines were installed, seven extending from the toe of the Southern flank (Figure 4.42), and over the crest (Figure 4.43), with one long central line extending approximately 5 m beyond the Northern toe of the embankment (Figure 4.44). In total, 281 electrodes were installed (32 for the seven shorter lines and 57 for the long one), spaced at 0.7 m grid points, with a programmed sampling frequency of one measurement per day.

Prior to installing the ERT array, the planned electrode locations were marked out. Eight measuring tapes were extended from the toe of the Southern flank, to the Northern flank, at 0.7 m separations to each other, with 0.7 m markers painted along the length of each of the tapes. Wooden stakes were hammered into the ground along the planned ERT lines, to which the electrode cables would be fixed upon completion of the installation (Figure 4.42a to c).

Each of the eight electrode lines (housed within 100 mm diameter corrugated black piping) were stretched out placed alongside their planned locations. The electrodes were installed, one line at a time, by manually inserting the electrodes (approximately 0.1 m length) fully into the ground at the marked locations, starting from the toe of the Southern slope (Figure 4.42b). On the crest, ballast prohibited the electrodes from being directly inserted, therefore a 0.1 m depth hole was dug using a trowel at each of the crest electrode points and the electrode inserted. These holes were subsequently filled with bentonite which also served to

increase contact around the electrodes (Figure 4.43). Once all the electrodes had been installed, each of the lines was secured to the wooden stakes using cable ties.

The fully-installed ERT array is shown in Figure 4.45a and b, and shows that by the start of Summer 2013, there had been considerable vegetation growth on the slope.

Following installation of the ERT array, GPS locations of all 281 electrodes were collected using a pole-mounted GPS and logger unit. An ALERT system (see subchapter 2.3.7) was installed, which allows the recorded ERT data to be automatically communicated to the GTom team at the British Geological Survey, via GPRS. All eight electrode lines were then connected to the ALERT power supply: a combination of solar panels and methanol fuel cell charging banks of 12 V batteries (Figure 4.46).

Figure 4.42 Installation of 3D ERT array. (a) wooden stakes and measuring tapes for marking electrode positions; (b) installation of electrodes; (c) view of installation from crest

Figure 4.43 ERT electrode installation on crest

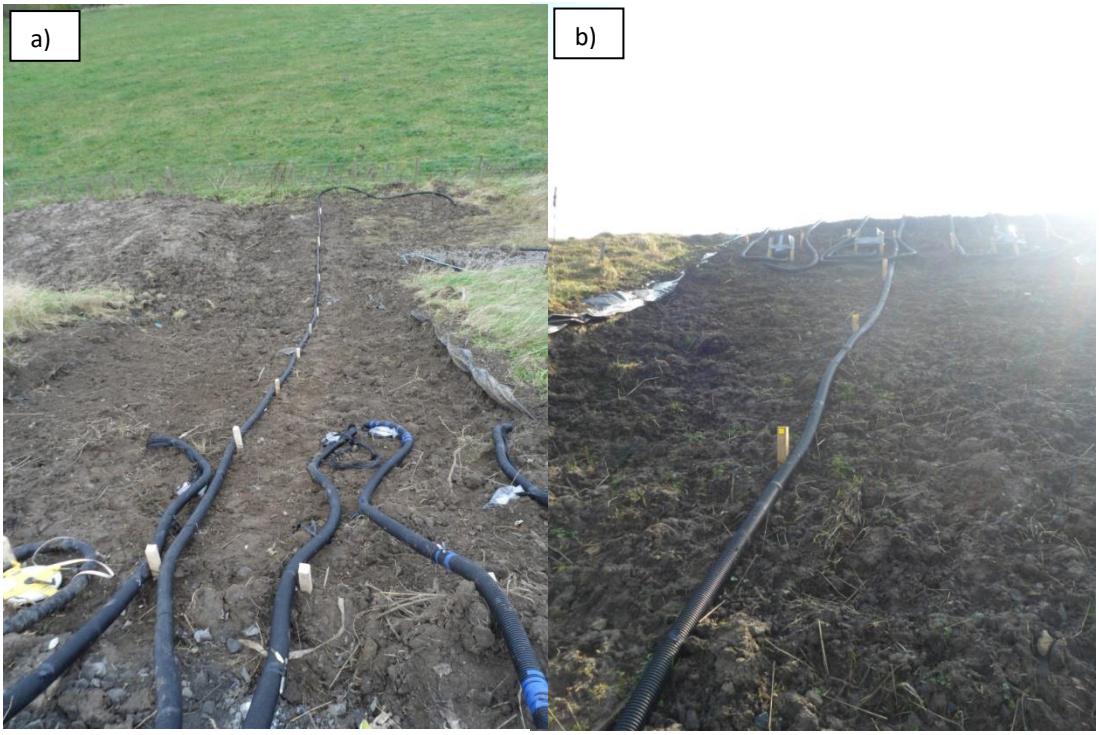

Figure 4.44 North flank of ERT test plot, showing long central line. View from (a) crest, and (b) North toe

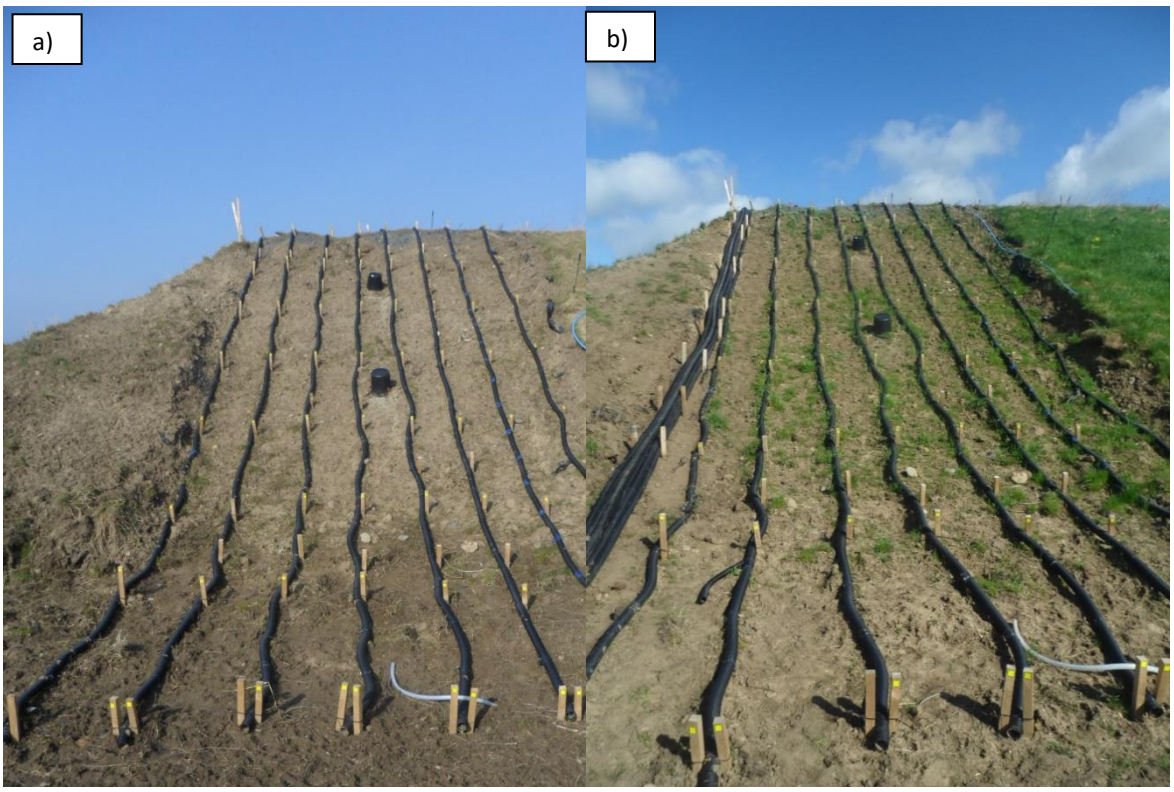

Figure 4.45 View of ERT array from Southern toe, showing considerable vegetation growth between images taken in (a) March 2013, and (b) May 2013

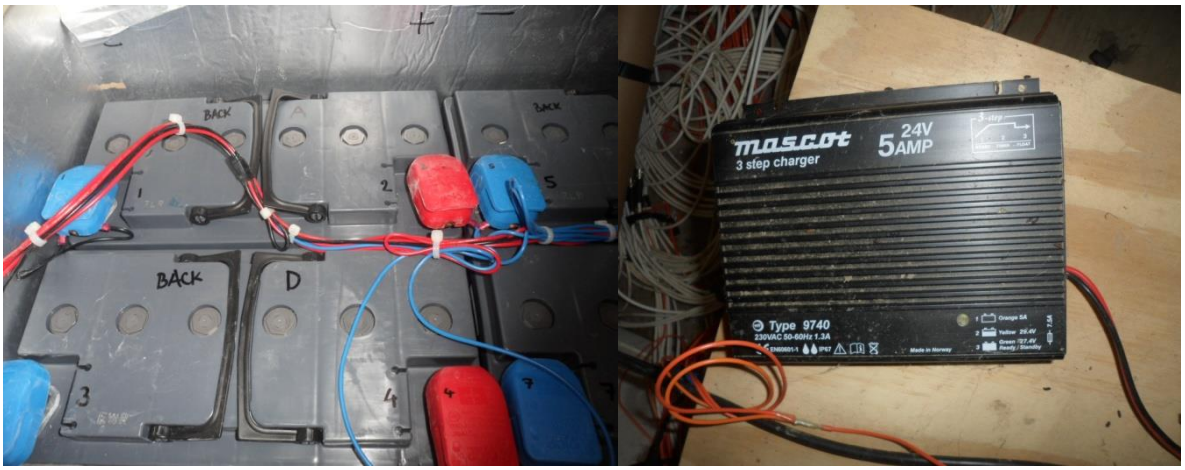

Figure 4.46 ALERT batteries and charger

4.3 ERT data processing and translation into geotechnical information

4.3.1 *Introduction*

Following the installation of the ERT array and ALERT system, the framework had to be established for the collection and management of the raw data, before it could be resolved into other data types. This subchapter describes the methodologies for data collection from the array, and the various steps and processes required to be able to analyse the resistivity data itself, and to image geotechnical properties.

4.3.2 *Reference system*

In order to manage the ALERT data, a three-dimensional reference system was implemented on the BIONICS embankment, such that a point (X, Y, Z) describes the horizontal displacement (in metres) in both directions (see Figure 4.47) and the total elevation above a reference ground level. It should be noted that X is not a true horizontal distance, but the distance along the ground surface itself (i.e. along the 0.7 m grid points). Each of the 281 electrodes installed in the embankment was allocated an ID number, also shown in Figure 4.47.

4.3.3 *Resistivity measurement*

Due to the layered compaction methods applied during the construction of the BIONICS embankment, it was considered that it would be relatively homogeneous in terms of horizontal compositional variability. Therefore, the dipole-dipole ERT configuration was selected for this field study, due to its high sensitivity to horizontal resistivity changes (e.g. dykes) but relatively insensitive to vertical resistivity changes (such as compaction layers). Resistance measurements (later converted to resistivity within the inversion process) were made using an AGI Super Sting R8 resistivity instrument, collected using the dipole-dipole configuration (see Figure 2.19) for all eight ERT lines, with dipole sizes *of a = 0.7, 1.4, 2.1* and *2.8 m*, and dipole separations of *na*, where *n = 1* to *10*. Figure 4.48 illustrates the sequence of measurements used to construct a 2D resistivity profile, using line 1 as an example. The first set of measurements (first point on the vertical axis) uses current electrodes *C1* and *C2* to allow current to flow between electrode positions 1 and 2 (horizontal axis): potential electrode pairs are then used to measure ground voltage between electrode positions 3 and

4, then between 4 and 5, and so on. The second set (second point on the vertical axis) shifts *C1* and *C2* to electrode positions 2 and 3, and performs the same iterations, whilst the third set increases the size of the current electrode separation, and again, performs the same iterations. This was repeated for all available electrodes along the ERT line, describing a full suite of current/potential measurements, which were automatically converted to resistance values using the method described in subchapter 2.3.3. The same sequence of measurements was performed along lines 2 to 8, allowing 2D apparent resistivity pseudosections to be constructed along each of the eight ERT lines (example pseudosection in Figure 4.51a, see Figure 2.22 for schematic showing principle of pseudosection construction). It should be understood that these apparent resistivity pesudosections simply represent the apparent resistivity data points at measured at a specific location, prior to inversion, as described in subchapter 2.3.3.

In addition to the standard dipole-dipole measurements made along lines 1-8, cross-line dipole measurements were made, using current/potential electrode pairs across all eight lines, providing a 3D measurement. The same approach was used as shown in Figure 4.48, but with electrode pairs running along the Y direction rather than the X direction.

For each data point, both forward and reciprocal measurements were made, whereby the current and potential electrode pairs (*C1* and *C2*, *P1* and *P2*, respectively) are alternated. In this way, a reciprocal error may be estimated (see subchapter 2.3.3) for the recorded resistance value, thereby providing a robust means of assessing data quality. For each of the short ERT lines, a total of 1150 measurements were made (including both forward and reciprocal measurements) and a total of 2533 for the long ERT line. The cross-line dipole measurements involved considerably higher numbers of measurements, due to the inclusion of all eight ERT lines. A sampling frequency of one measurement per day was set within the ALERT system, although this was, on occasion, increased to allow multiple measurements per day.

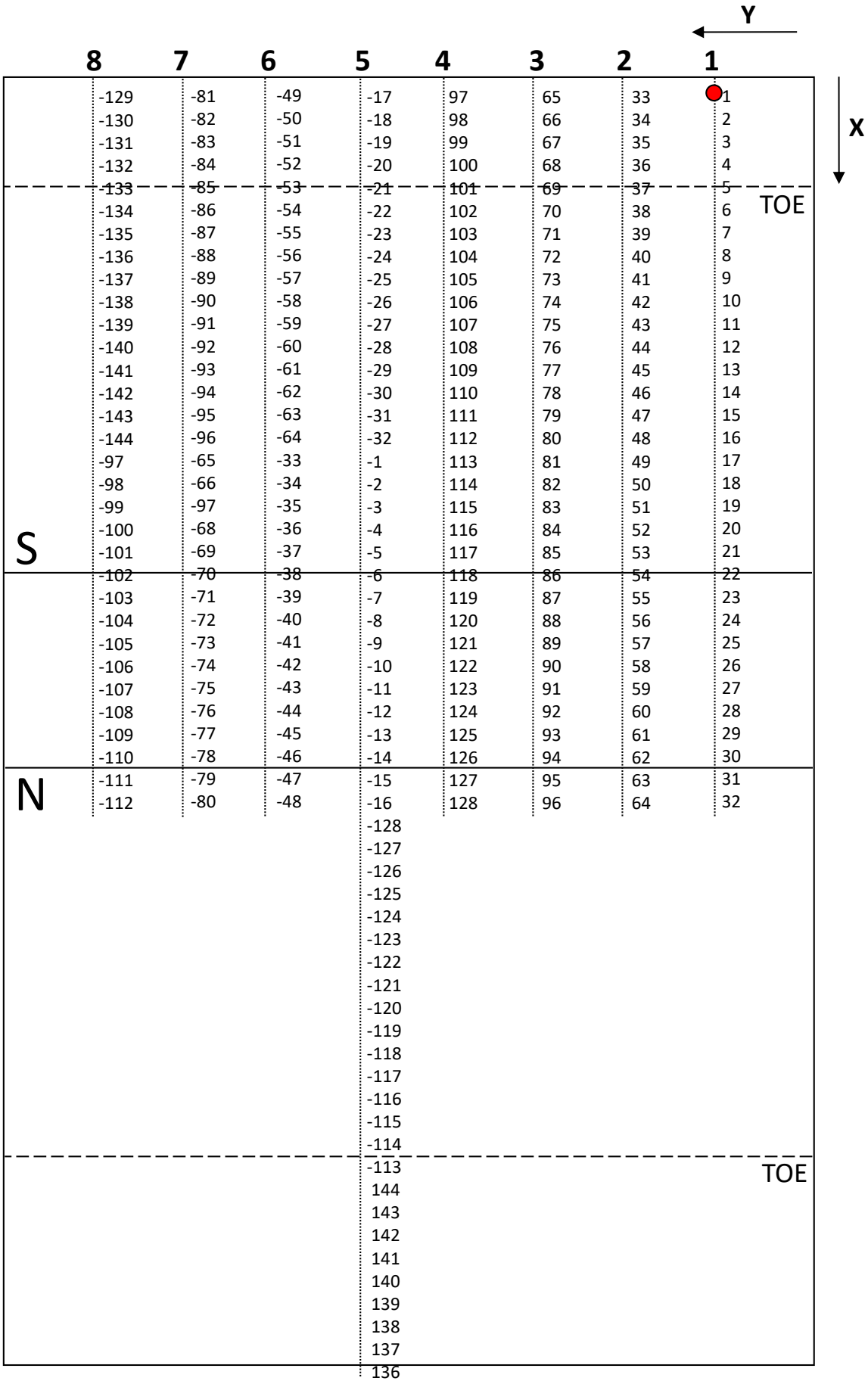

Figure 4.47 Schematic showing all eight ERT lines on the BIONICS embankment, and ID numbers of the electrodes within each line. Also shown are X and Y, vectors representing horizontal distance from the point (0.0, 0.0, 113.2) illustrated by a red dot. The elevation vector, Z, is vertically out of the page

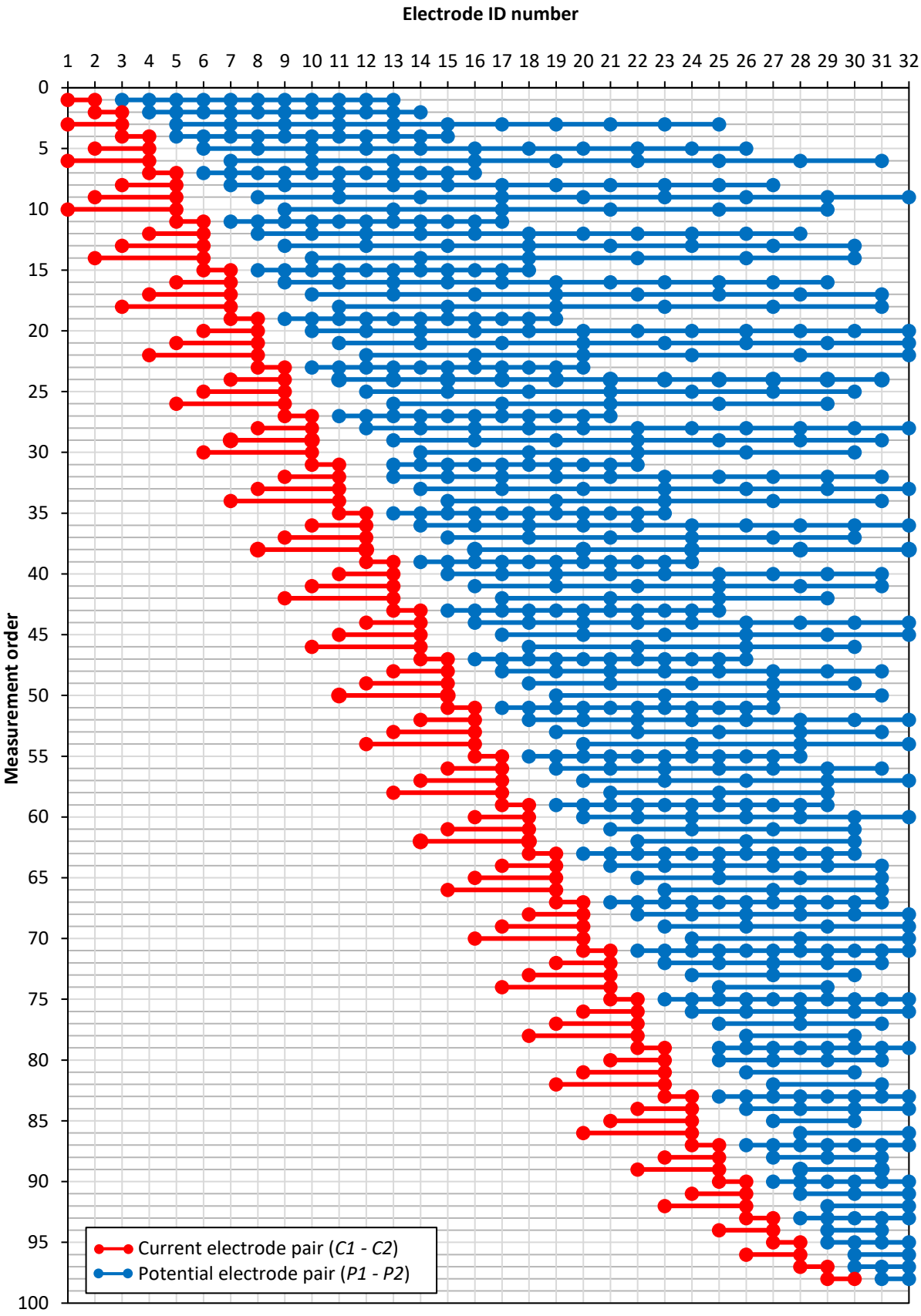

Figure 4.48 Sequence of dipole-dipole forward measurements to construct a resistivity profile. Electrode ID numbers relate to those shown in Figure 4.47, along line 1

4.3.4 *Data processing*

For each suite of dipole-dipole and cross-line dipole measurements, an ID code was attributed as shown in Table 4.8. For each of these, a TAB file was automatically generated by ALERT (title containing the ID code and the time and date of the recording), and sent remotely to the GTom team at BGS Keyworth via GPRS.

The pre-processing of these files (all executed using Matlab) prior to inversion, is described as follows, and summarised in the flowchart (shaded blue area) in Figure 4.50. The pre-processing code is provided in Appendix E.1. Within the TAB files, several different types of information were contained, including the ALERT input settings, measured resistance values and various other electrical parameters. Prior to data processing, any incomplete files were manually filtered out i.e. any files not containing a full set of resistance values recorded during a survey (due to some ALERT malfunction) were removed.

At this stage, it is necessary to make a distinction between 2D and 3D resistivity imaging techniques: 2D inversions were performed on data gathered from the standard dipole-dipole survey lines (ID codes 5001-5005, 5015); for 3D inversion, any number of the 2D lines could be combined, as well as data gathered along the cross-line dipole (ID code 5009).

Due to the volume of information contained within the TAB files, they were reduced into xls files containing only information on electrode position, measured resistances, and measurement quality assessment parameters. For 2D inversions, the xls file contained information from the individual ERT lines only; for 3D volumetric images, a merged xls file was created, containing all the selected data intended for inclusion in the 3D inversion. All of the xls files described standalone ERT surveys only, i.e. for individual dates.

Using the xls spreadsheets, DAT input files for the resistivity inversion programmes were created, filtered to ensure a high data quality, and with the addition of an error estimate for the measured resistances calculated using the reciprocal resistance measurement. Table 4.9 describes the filter criteria which were applied.

Figure 4.49 shows an example of the data considered in the filtering processes, prior to its removal. At this stage, pre-processing was complete and all remaining data were put forward for resistivity inversion. For standalone 2D and 3D inversion, the DAT files could, at this stage, be directly input to the resistivity inversion programs. For time-lapse ERT however, data from all selected dates of interest were combined into one time-lapse DAT

file. These DAT files were then inverted using Res2DInv and Res3DInv (Loke, 2015a; Loke, 2016). A sample DAT input file is provided in Appendix D.3.

Table 4.8 ALERT data processing details

ID Code	Line	Total number of electrodes	Y (m)	Measurement type
5001	1	32	0	Dipole-dipole
5002	2	32	0.7	Dipole-dipole
5003	3	32	1.4	Dipole-dipole
5004	4	32	2.1	Dipole-dipole
5005	5	32	2.8	Dipole-dipole
5015	5	57	2.8	Dipole-dipole (extended central line)
5006	6	32	3.5	Dipole-dipole
5007	7	32	4.2	Dipole-dipole
5008	8	32	4.9	Dipole-dipole
5009	All	281	All	Cross-line dipole-dipole, X = 0.7, 1.4, 2.1 … 4.9 m

Table 4.9 Filtering parameters for BIONICS ALERT data

Filter Values	Explanation
Reciprocal errors greater than 5 %	Measured ground resistances for reciprocal pairs are compared and an error between the two values calculated; low errors imply good data quality
Contact resistances greater than 3000 Ω	Very high contact resistances prevent coupling at the electrode/ground interface
Measured ground resistances greater than 100 Ω	Outside of range considered realistic
Waveform ratios deviating from 1 by more than 15 %	During a resistance measurement, one full DC switched waveform is injected; injection of positive current followed by negative current. This ratio is a measure of the similarity of these, where deviation from 1 suggests a poor-quality measurement

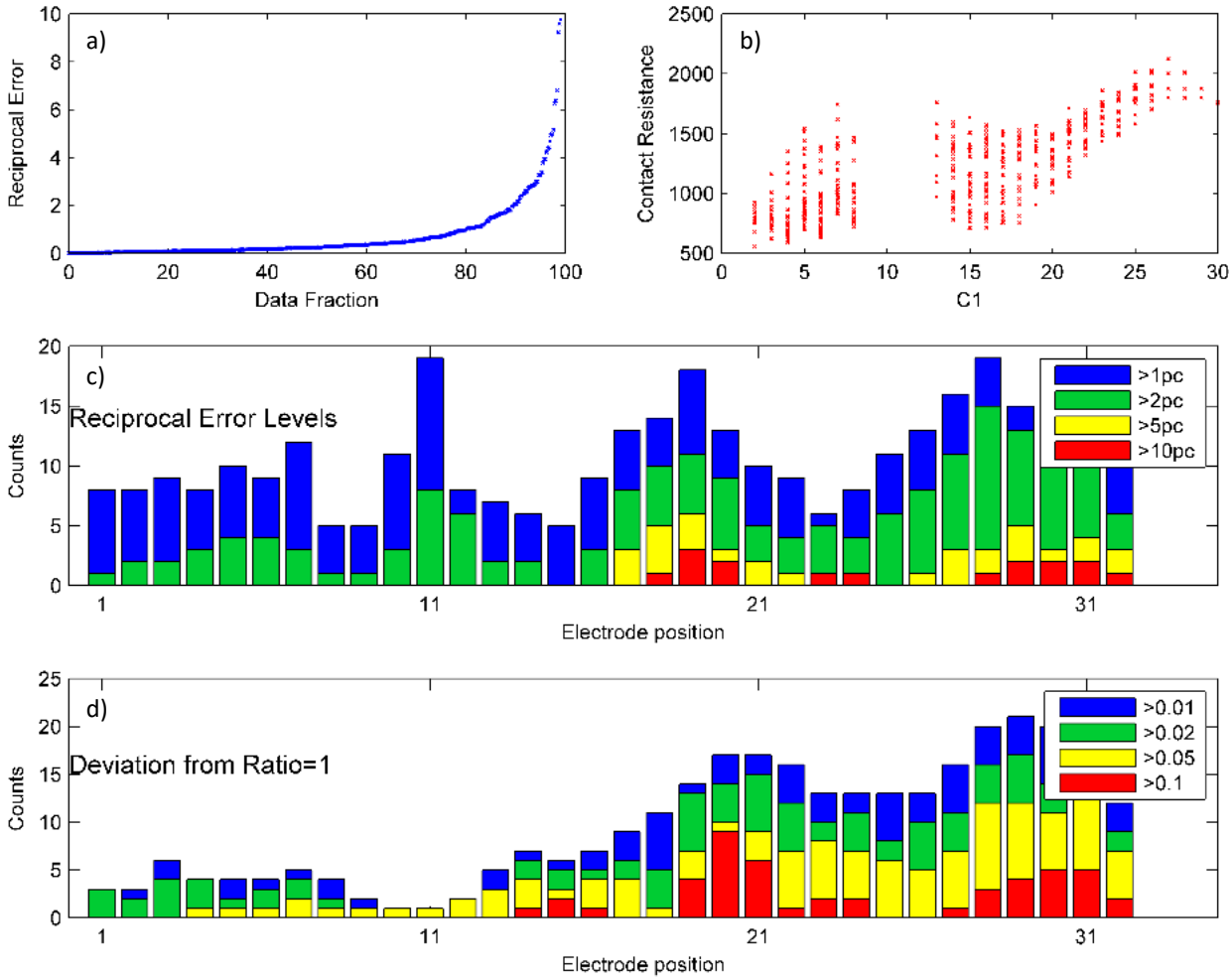

Figure 4.49 Graphed examples of typical pre-filtering statistics for 2D ERT (from 5001 - line 1, 24/06/2014). (a) Reciprocal error against data fraction, showing 99 % of the recorded resistances to have reciprocal errors less than 10 %; (b) contact resistance against electrode number, for a varying position of current injection electrode, *C1*; (c) reciprocal error levels for the individual electrodes, where "counts" refers to the number of resistance measurements involving a given electrode, identified by its position (horizontal axis); (d) waveform ratio deviation for the individual electrodes

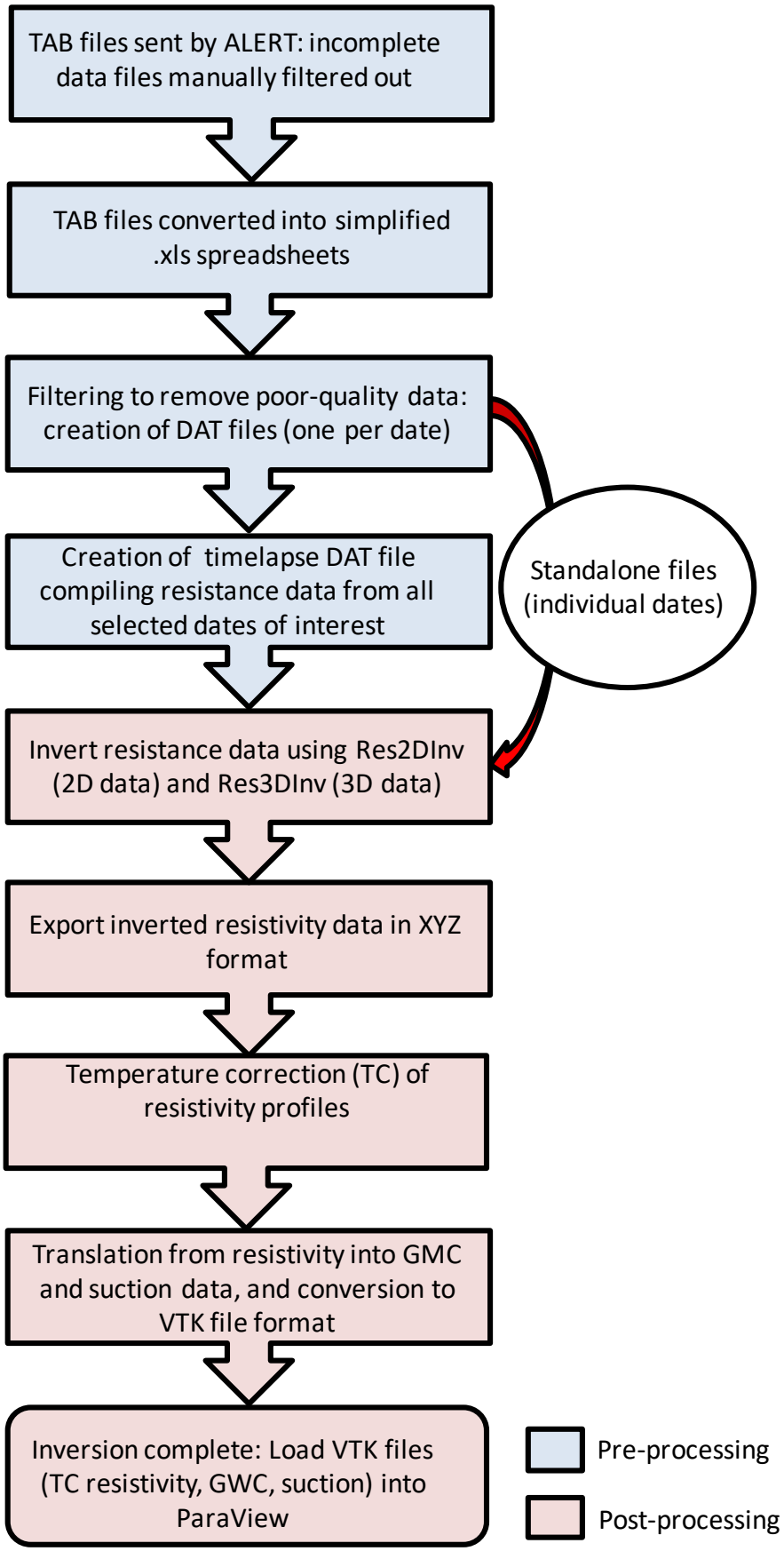

Figure 4.50 ERT data processing flowchart

4.3.5 *Resistivity Inversion – 2D and 3D*

The Res2DInv and Res3DInv software designed by Geotomosoft are Windows-based programs which respectively determine two and three-dimensional resistivity models of the subsurface, by inversion of raw data obtained from electrical resistivity profile surveys (Loke, 2015a; Loke, 2016). As described in the previous subchapter, measured apparent resistances were compiled into DAT files also containing electrode position information. These DAT files are then input to the program, which uses both datasets to create a measured apparent resistivity pseudosection for each suite of data, as shown in Figure 4.51a. In subchapter 2.3, the methodology for undertaking ERT surveys was explained, in general terms applicable to all ERT survey configurations, detailing the injection of a known current, *I*, via two current electrodes, *C1* and *C2*, and measuring the resultant potential field by recording the potential drop, *V*, between two potential electrodes, *P1* and *P2*. Within the Res2DInv and Res3DInv programs, the current and potential values are combined to yield a resistance value, *R*, using Ohm's law (Eqn. 2.5). This resistance is then converted into a value of apparent resistivity, ρ_a, via the geometric factor (Eqn. 2.7). For the dipole-dipole survey, as used at the BIONICS embankment, the following geometric factor defines the diffusion of current in the subsurface:

$$K = \pi n(n+1)(n+2)a \qquad \text{Eqn. 4.8}$$

where *a* is the electrode separation, common to both electrode pairs, and *n* describes the ratio of the distance between the inner electrodes and the dipole separation. For each set of four electrodes (*C1, C2, P1, P2*), an apparent resistivity value was calculated following the methodology above. The calculated apparent resistivity was then assumed to pertain to the midpoint between the potential electrodes, at the pseudodepth as described by the sensitivity function (see subchapter 2.3.3).

The data are then inverted within the program to resolve a true resistivity model, as shown in Figure 4.51c (2D example), essentially attempting to produce a model whose response agrees with the measured data (Loke, 2015a). Figure 4.51b demonstrates the calculated apparent resistivity from that model, which allows a RMS error to be derived between the calculated and measured values (2.1 % for this example). The iterative inversion method implemented within the resistivity inversion programs is based on the smoothness-constrained method, described by DeGroot-Hedlin and Constable, 1990, detailed further in Appendix D.1. Effectively, an initial resistivity model is constructed, which the inversion

programs use as the basis for further refinement, attempting to produce an improved model which has lower data misfit (Loke, 2015a).

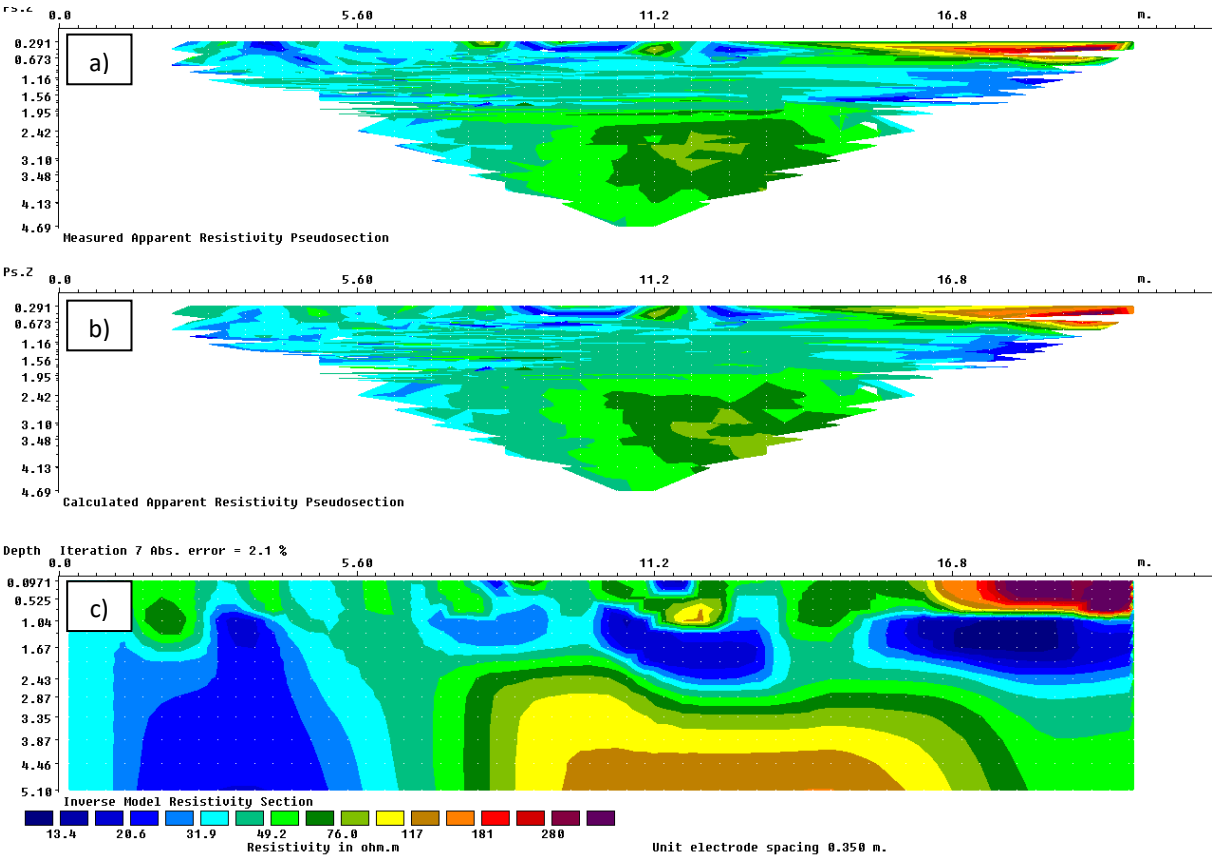

Figure 4.51 Components of the inversion process, showing: (a) measured apparent resistivity pseudosection; (b) model-calculated apparent resistivity pseudosection; (c) true resistivity model

Given the ability of the program to support an extensive variety of different survey types (e.g. boreholes, underwater resistivity survey), for a range of different environments, the selection of the most appropriate inversion parameters for the BIONICS test site and configuration is essential to resolving a representative resistivity model. It should be noted that a trade-off exists between the optimum inversion parameters and the processing power required to implement them, so, where reasonable, reduced accuracy parameters were chosen. The selected inversion parameters were based directly on guidelines given within the Res2DInv and Res3DInv Users' Guide (Loke, 2015a; Loke 2016) and on previous ERT studies of the BIONICS embankment (Glendinning et al., 2014; Gunn et al., 2015). In Appendix D.2, the full list of input parameters is provided; in the following section, a summary of the main inversion parameters is given. The L1 "robust" inversion, which anticipates severe spatial changes in resistivity, was selected due to the sharp interface between the ballast capping layer and the embankment fill. For resistivity surveys which

include topography (unlike for example, a borehole survey), a finite-element subroutine must be used. In this way, a distorted finite-element grid is applied to the apparent resistivity, thereby matching the grid surface to the topography. The finite-element option was combined with the following options, to account for the topography along the survey line:

1. Distorted finite-element grid with uniform distortion;

2. Removal of the average topographical elevation.

By selection of the above options, the slopes and relief of the embankment were accounted for, and an initial mesh described, with strictly vertical edges. The necessity of vertical cell edges was dictated by the need to assign a cell-based porosity model to the inverted data at a later stage, therefore, a deliberately-simplistic grid arrangement was selected. An extended model was used, which extends the model cells to the edge of the survey line. Although the ERT array spacing between electrodes was 0.7 m, the cell width was selected to be half the unit spacing, yielding an improved horizontal resolution of 0.35 m with a better fit between the measured apparent resistivity data and the model calculated data. A total of 18 layers horizontal layers was described, with 112 vertical cells stretching from the Southern toe to the Northern. This grid is shown in Figure 4.52, in two dimensions, describing the ERT cells.

For time-lapse inversions, a cross time model damping factor must be input within the resistivity inversion program. This factor describes the influence of the reference resistivity model (i.e. the calculated true resistivity model for the first date within the time-lapse set) on subsequent entries within the time-lapse set. A value of 0 describes an inversion in which all the input files are inverted independently, whereas a value of 10 ensures that later entries are highly constrained by the reference model. Effectively, increases in this damping factor minimise changes across the individual models, reducing the effects of noise between them. A trade-off exists, however, such that higher temporal damping factors promote data misfit between the measured and calculated apparent resistivity pseudsections. By default, a value of 3 is used within the resistivity inversion program. The optimum value for this factor as applied to this study was derived by trial and error: a reference time-lapse comprising six dates was inverted, using increasing damping factors (starting from 0), with increments of 0.25. At a value of 1.25, the data misfit was observed to increase significantly, therefore, a

value of 1.0 was selected, which gives equal weight to reducing the difference between models at different times, and to the individual model roughness (Loke, 2015a). A time-lapse inversion constraint was added, describing “smooth” changes, due to the relatively impermeable nature of clay embankment fill, such that severe resistivity contrasts were not anticipated.

Following selection of the parameters, the raw apparent resistivity data were inverted (e.g. Appendix D.3). Once the resistivity inversion was completed, the inverted data were extracted in XYZ format, describing discrete inverted resistivity values across the individual cells (one per time-lapse date), in either two or three dimensions.

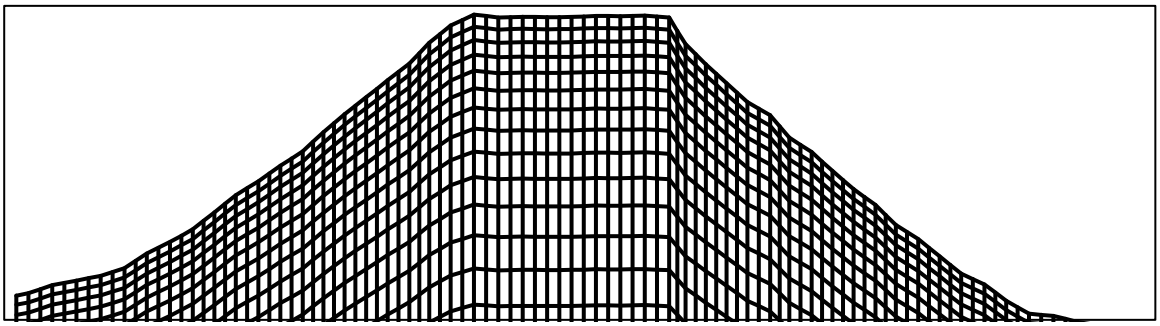

Figure 4.52 Schematic of ERT cells. These have been cut off at the ground surface

4.3.6 *Temperature correction of ERT data*

Following inversion, the inverted resistivity data were corrected for temperature, for two reasons: 1. To account for the temporal (seasonal) and spatial (depth-dependent) variation of field temperatures, and; 2. To allow proxy relationships established in the laboratory (at different temperatures to those of the field) to be applied.

Temperature model for the BIONICS embankment

In order to account for this first factor, a temperature model was designed for the BIONICS test embankment, using field temperature data gathered at depths of 0.1, 0.5, 1.0, 3.5, and 4.0 m in the Southern-facing slope flank, over a three year period (see Figure 4.53). Within Mathematica (mathematical computation software), model parameters were fitted to the

recorded data, as shown in Figure 4.53, yielding the following equation for describing subsurface temperature as a function of depth:

$$T(z,t) = T_m + \frac{\Delta T}{2} e^{-z/d} sin(\frac{2\pi}{365} t + \delta - \frac{z}{d}) \qquad \text{Eqn. 4.8}$$

where *T(z)* is the temperature of the embankment at a depth *z*, T_m is the mean yearly air temperature, ΔT is the peak-to-trough amplitude of the yearly temperature variation, *d* is a characteristic depth and δ is a phase offset to ensure that the maximum temperature occurs in the summer. The fitted model parameters are given in Table 4.10.

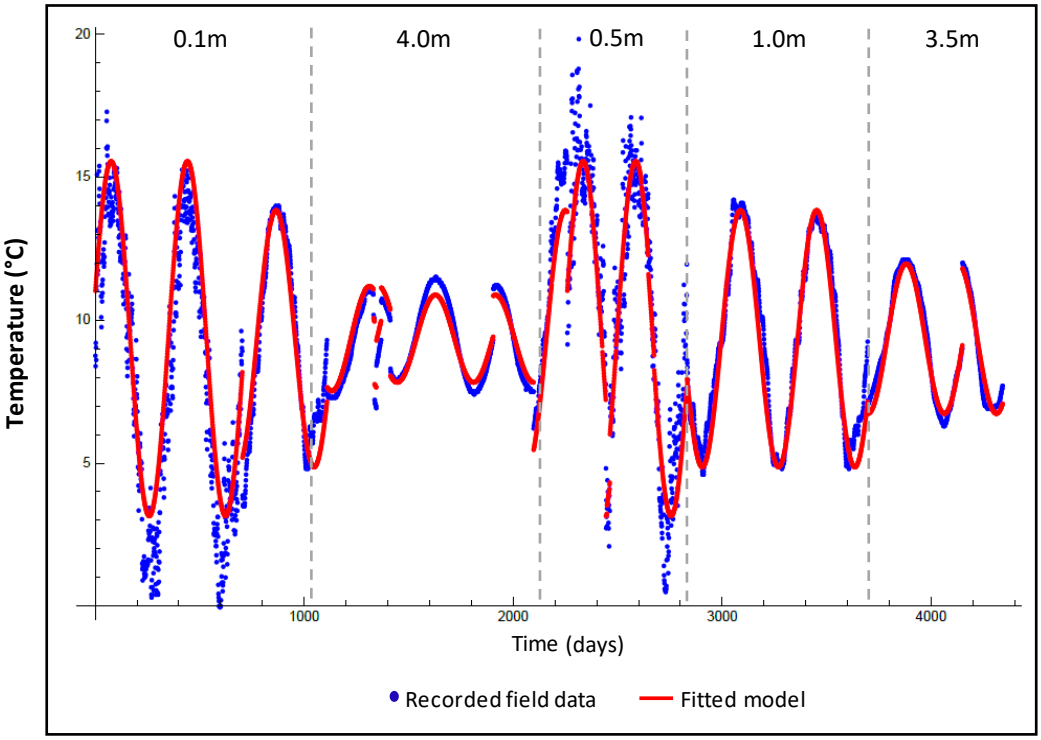

Figure 4.53 Recorded field temperatures and fitted model parameters

Temperature correction

In Experiment 5a, resistivity was found to decrease by 2 % for a 1 °C increase in temperature (Figure 5.15), therefore, a temperature correction factor, *ç = -2 %/*°C, was implemented, allowing field ERT data to be corrected to a selected reference temperature, T_{cor}, effectively describing what the resistivity would be if the soil mass were at a different temperature, i.e. T_{cor}.

The temperature-corrected resistivity, ρ_{Tcor}, can be expressed thus:

$$\rho_{T_{cor}} = \rho + \Delta\rho \qquad \text{Eqn. 4.9}$$

where ρ is the pre-correction resistivity and $\Delta\rho$ is the resistivity increment which would result from a change in the soil temperature from T, as described by $T(z,t)$ from Eqn. 4.8, to the reference temperature, T_{cor}. $\Delta\rho$ is described by Eqn. 4.10:

$$\Delta\rho = \rho\left[\frac{\varsigma}{100}(T_{cor} - T)\right] \qquad \text{Eqn. 4.10}$$

Combining Eqns. 4.9 and 4.10, the following temperature correction expression was derived:

$$\rho_{T_{cor}} = \rho\left\{1 + \left[\frac{\varsigma}{100}(T_{cor} - T)\right]\right\} \qquad \text{Eqn. 4.11}$$

Inverted field resistivity data as presented in subchapter 5.3 are corrected to the mean annual air temperature (i.e. $T_{cor} = T_m$), in keeping with previous ERT studies of the BIONICS test embankment (Glendinning et al., 2014; Gunn et al., 2015). In order to allow laboratory proxy relationships to be applied to field resistivity data, however, inverted field resistivity data were first corrected to the laboratory temperature (i.e. $T_{cor} = T_{lab} = 20$ °C), and the proxy relationships then applied.

Table 4.10 Temperature model parameters

Parameter	***T_m (°C)***	***ΔT (°C)***	***d (m)***	***δ (radians)***	***T_{cor} (°C)***	***ς (%/°C)***
	9.35	12.85	2.78	-1.88	9.35/20	-2

4.3.7 *Development of a porosity model for the BIONICS test embankment*

A porosity model was developed, for two reasons:

1. To aid in the interpretation and analysis of resistivity images of BIONICS;
2. To allow a Waxman-Smits relationship to be applied to ERT data, enabling conversion of resistivity data to gravimetric water content.

The model was developed in two dimensions (and extrapolated to 3D), describing an estimated spatial distribution of the porosity of the embankment, within the ERT test plot ("well-compacted" specification). Several elements were considered in the development of the model, including a characteristic resistivity distribution, knowledge of the construction methods of the BIONICS embankment, point sensor data, and that collected from core samples on the well-compacted Panel B gathered shortly after its completion in 2005 (Table 3.3: such data was not available for the ERT test plot itself). Owing to the construction methods, a layered-based approach was employed.

Beneath the crest of the embankment, the interface between the layers was described by the crest topography; beneath the flanks, the layers still followed the topography, but were tapered linearly to the embankment toes.

Discrete estimates of porosity were estimated from point sensors measuring volumetric water content, in the following way: the assumption was made that the maximum recorded volumetric water content described a saturated state, and therefore that this value corresponded to the porosity (these estimates are shown in Table 5.3). Where available, these point estimates were used to guide the development of the model, in the near-surface. At depth, an average porosity was derived from the results of the core cutter density samples presented in Table 3.3. For the half-space beneath the bottommost layer, the ground was prescribed a porosity of 0.3. The ballast capping layer was not included in the porosity model, as only the geotechnical properties of the clay fill material would be derived from the proxy relationships.

The derived porosity model is shown in Figure 4.54, and compared against ERT images dating from September 2014 in Figure 4.55, confirming its plausibility.

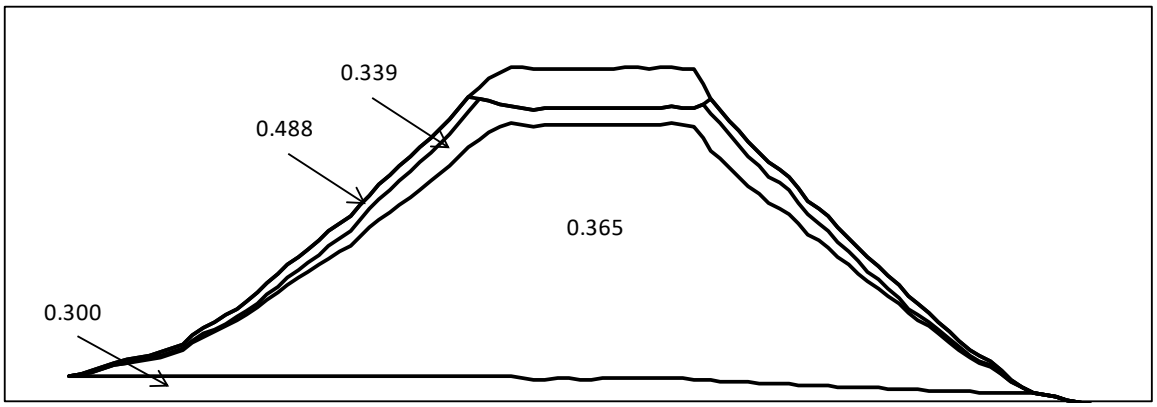

Figure 4.54 Schematic of porosity model

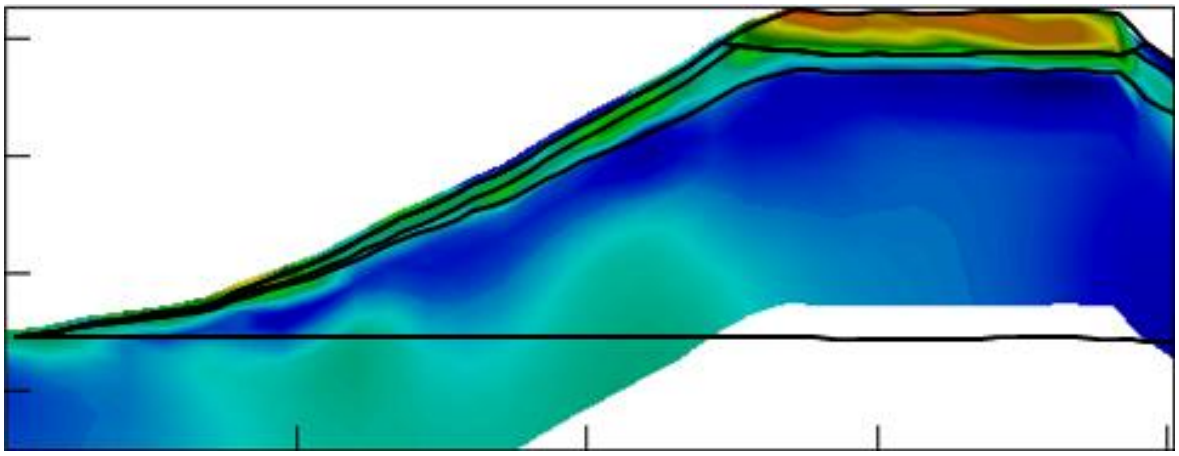

Figure 4.55 Comparison of porosity model with characteristic true resistivity image (September 2014)

Vertical gridlines were then applied to the porosity model, in order to resolve it into a series of porosity cells. The vertical edges of these Waxman-Smits cells were chosen to align with those of the corresponding resistivity model.

4.3.8 *Derivation of water content data from resistivity*

In Experiment 4, a (four point) resistivity-water content relationship content was derived. Using Mathematica, Waxman-Smits (Waxman and Smits, 1968) parameters were fitted to the data (relationship presented in subchapter 2.3.2), allowing resistivity to be expressed as a function of water content. The fitted parameters are as follows: tortuosity factor, *q*; cementation factor, *m*; and saturation exponent, *p*, as shown in Table 5.2, thereby describing a Waxman-Smits relationship between four point resistivity and water content.

The laboratory testing was performed on specimens prepared to emulate average field conditions, with a starting porosity of φ = 0.377, and hence the curve shown in Figure 5.13 is only representative of the resistivity-water content relationship of BIONICS fill material at that starting porosity. The application of Waxman-Smits parameters to this data, however, allows the relationship between resistivity and water content to be adapted for a varying porosity, so that it may be applied to material at a range of porosities, allowing resistivity values to be translated to water content values. In order to account for the decrease in porosity with shrinkage during drying, a variable porosity term was included in the modelling, derived empirically from fitting linear parameters to water content and porosity data of specimens used in Experiment 4 (see Figure 5.12):

$$\varphi \; = \; 0.4664 * gwc \; + \; 0.273 \qquad \text{Eqn. 4.12}$$

where *gwc* is the fractional gravimetric water content.

As described in subchapter 4.3.5, ERT inversion data which were exported from Res2DInv and Res3DInv described a series of vertically-aligned cells in two (or three dimensions), with a discrete resistivity allotted to each ERT cell. The vertical edges of the porosity and resistivity models were then aligned, and a Sutherland-Hodgman polygon-clipping algorithm applied (see Figure 4.56) to derive the area of intersection between the ERT cells and the porosity cells. The resistivity of each ERT cell, *i*, was then expressed as the geometric mean of the resistivity values of the contributing porosity cells, *j* (as described in Glendinning et al., 2014):

$$\rho_i \; = \; exp \; \Sigma f_{ij} \; ln \; \rho_j \; (GWC) \qquad \text{Eqn. 4.13}$$

where ρ_i is the resistivity of ERT cell *i*, f_{ij} is the area of intersection between ERT cell *i* and porosity cell *j*, normalised by the area of *i*, and the gravimetric water content, *GWC*, is assumed to be the same for each of the contributing porosity cells.

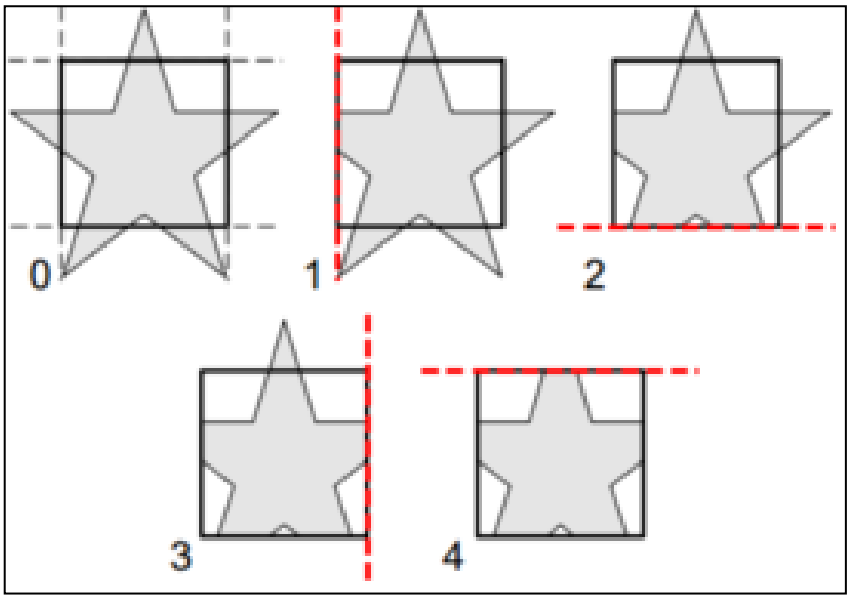

Figure 4.56 Sutherland-Hodgman polygon-clipping algorithm (image from Statnice, 2016)

In subchapter 2.3.2, the Waxman-Smits relationship relating soil porosity to water content was presented (Eqn. 2.9), which can also be expressed:

$$\rho_{WS} = \frac{q}{\varphi^m S^p}\left(\frac{1}{\rho_W} + \frac{BQ_v}{S}\right)^{-1} \quad \text{Eqn. 4.14}$$

The gravimetric water content, GWC, can be expressed in terms of the component parts' densities and the soil porosity:

$$GWC = \frac{\varphi P_w}{(1-\varphi)P_s} S \quad \text{Eqn. 4.15}$$

Where P_w and P_s are the densities of water and solids, respectively. The cation concentration per unit volume, Q_v, can be expressed in terms of the cation exchange capacity, C:

$$Q_v = \frac{(1-\varphi)P_s}{\varphi} * \frac{C}{100} \quad \text{Eqn. 4.16}$$

Combining Eqns. 4.13 and 4.16 and rewriting Eqn. 4.14, then yields Eqn. 4.17 which relates resistivity to gravimetric water content:

$$\rho_{WS} = \left(\frac{\varphi P_w}{(1-\varphi)P_s}\right)^p \frac{q}{\varphi^m GWC^p}\left(\frac{1}{\rho_W} + \frac{BCP_w}{100GWC}\right)^{-1} \quad \text{Eqn. 4.17}$$

Eqn. 4.17 was then solved numerically to derive a gravimetric water content for each cell, effectively "translating" inverted field resistivity values measured using ERT, into water contents. For the numerical values used in Eqn. 4.17, see Table 5.2.

4.3.9 *Conversion of ERT-derived water contents to soil suction estimates*

In Experiment 1, a soil water retention curve was derived for BIONICS fill material, and Van Genuchten (1980) parameters fitted, as shown in Figure 5.1. Following the application of Eqn. 4.17, gravimetric water contents were calculated for each of the ERT cells shown in Figure 4.52. In order to ascribe a soil suction estimate to each of the cells, the derived gravimetric water contents were first converted to volumetric water contents:

$$\theta = GWC * G_s * (1 - \varphi) \qquad \text{Eqn. 4.18}$$

where Θ is volumetric water content, GWC is gravimetric water content, G_s is the specific gravity and φ is porosity, taken from the porosity model. The fitted Van Genuchten curve (parameters shown in Table 5.1) were then applied to each of the ERT cells, as a function of volumetric water content, using the following rearrangement of the Van Genuchten (1980) expression:

$$\Psi(\theta) = 1/\alpha * \left[\left(\frac{\theta_s - \theta_r}{\theta - \theta_r}\right)^{\frac{1}{\eta}} - 1\right]^{1/\eta} \qquad \text{Eqn. 4.19}$$

Where Ψ is the soil matric suction, Θ is the ERT-derived (Waxman-Smits derived) water content, Θ_r is the residual water content, Θ_s is the saturated water content, α relates to the inverse of the air entry value, η is a measure of the pore size distribution, and η is $1-(1/\eta)$. Substituting the Van Genuchten parameters given in Table 5.1 into Eqn. 4.19, an expression for calculating soil matric suction from volumetric water content was derived, accounting for a different response between periods of drying and wetting. This was implemented within the data-processing code by ascribing the appropriate branch of the Van Genuchten soil water retention curve, depending on the sign of the change in water content between one time-lapse date and the previous date; drying behaviour was assumed for the first date within a time-lapse set, where there was no previous date to consider.

4.3.10 *Data visualisation in ParaView*

The steps described in the previous sections were all implemented within Matlab code: to correct recorded ERT data for temperature; to translate the corrected data into water content data; and to convert the water content data into suction. This code then exported all of the data from these steps into a series of time-lapse VTK files, which could be read directly into ParaView scientific imaging software, allowing the resulting resistivity, water content and suction images to be analysed. All of this post-processing Matlab code is provided in Appendix E.2.

Chapter 5. Results

In Chapter 4, three experimental phases were presented, describing a laboratory testing programme to investigate geophysical-geotechnical inter-relationships, a field monitoring programme using the network of point sensors and a 3D ERT array, and a data processing component applying the laboratory proxy relationships to the ERT data. The output of these experimental phases has three components, as shown in the flowchart in Figure 4.1, and detailed below.

5.1 Laboratory results: subchapter presenting the results of the laboratory experiments, describing the proxy relationships relating resistivity to both water content and suction, relevant calibration relationships, and qualitative information on the effect of seasonal moisture cycles on clay soils.

5.2 Field point sensor results: subchapter presenting the results of the field point sensors, aiding in the monitoring the environmental conditions at the BIONICS test embankment, and in assessing the geotechnical response to environmental forcings at different portions of the embankment.

5.3 ERT-derived results: 2D and 3D electrical resistivity tomography images, which, using the laboratory proxy relationships, are converted into subsurface water content and suction distribution images.

5.1 Laboratory results

5.1.1 *Soil water retention curve*

These results pertain to Experiment 1 as described in the Chapter 4.

From Figure 5.1, it can be seen that the drying curve rapidly desaturates from Θ_s = 0.36, at an approximate air entry value (AEV) of 500 kPa. The drying data points are in close agreement with the fitted Van Genuchten (1980) parameters; the wetting path suffers from a reduced number of data points. However, within the measured suction range, the fitted curve is shown to pass through the majority of wetting points. Traditionally, for the wetting path, re-saturated water content is observed to be reduced from the initial content due to the entrapment of air. The presented curve displays an inferred, elevated re-saturated water content on the wetting path considered as a product of increased porosity as a direct result of the formation of micro-cracks. This trend is predicted due to the extreme drying (desiccation) that the specimens had undergone during the latter stages of drying prior to re-wetting. However, limitations in the dewpoint potentiameter technique do not allow behaviour at very low suctions to be accurately investigated and therefore this suggestion cannot currently be confirmed.

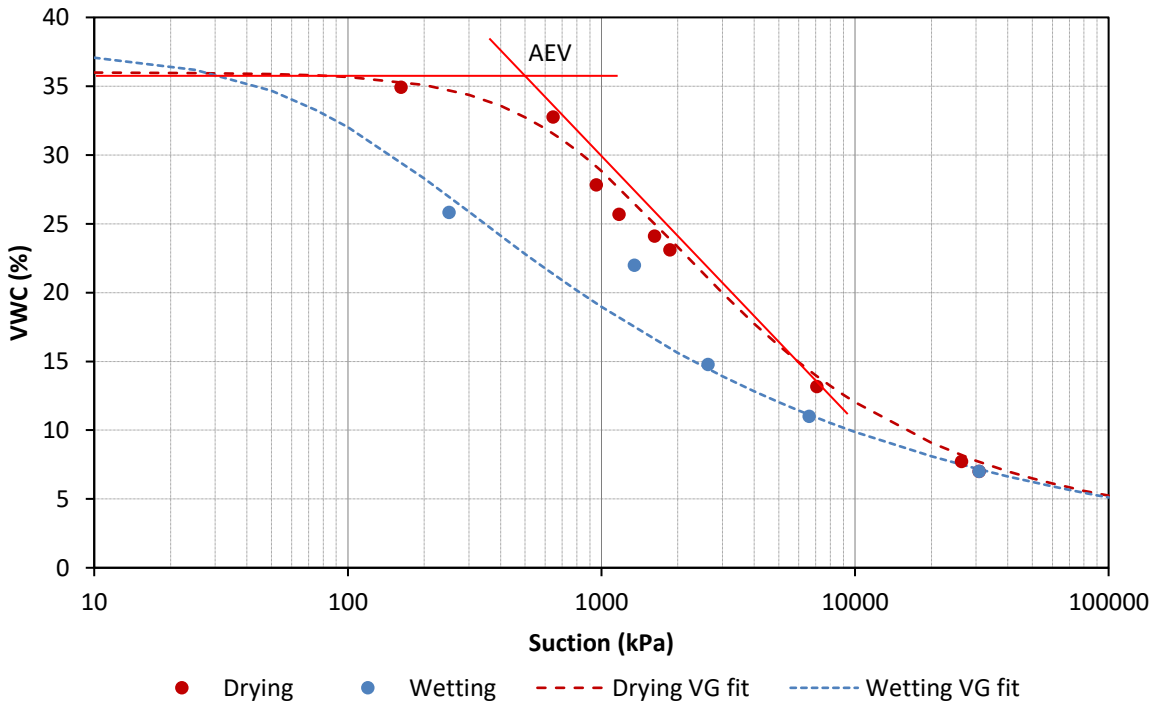

Figure 5.1 BIONICS Soil Water Retention Curve. Plot includes both drying and wetting branches, as measured using the WP4C Dewpoint potentiameter. Van Genuchten parameters have been fitted to the measured data and are summarised in Table 5.1. Air entry value (AEV) shown at the intersection of two linear fitted lines. This graph describes the water content – suction proxy relationship

Table 5.1 Fitted Van Genuchten (1980) parameters

	α	η	ɱ	θ_s	θ_w
Drying	0.0097	1.5448	0.3527	0.3600	0.0250
Wetting	0.1001	1.2900	0.2248	0.3750	0.0010

Figure 5.2 shows the recorded drying data points, compared against drying paths (gathered using the filter paper method) for BIONICS clay material, as published in Mendes and Toll (2013). It can be seen that there is close agreement between the recorded data and the primary drying curve produced by Noguchi et al. (2011), where saturated specimens were dried out from a gravimetric water content of approximately 25 %.

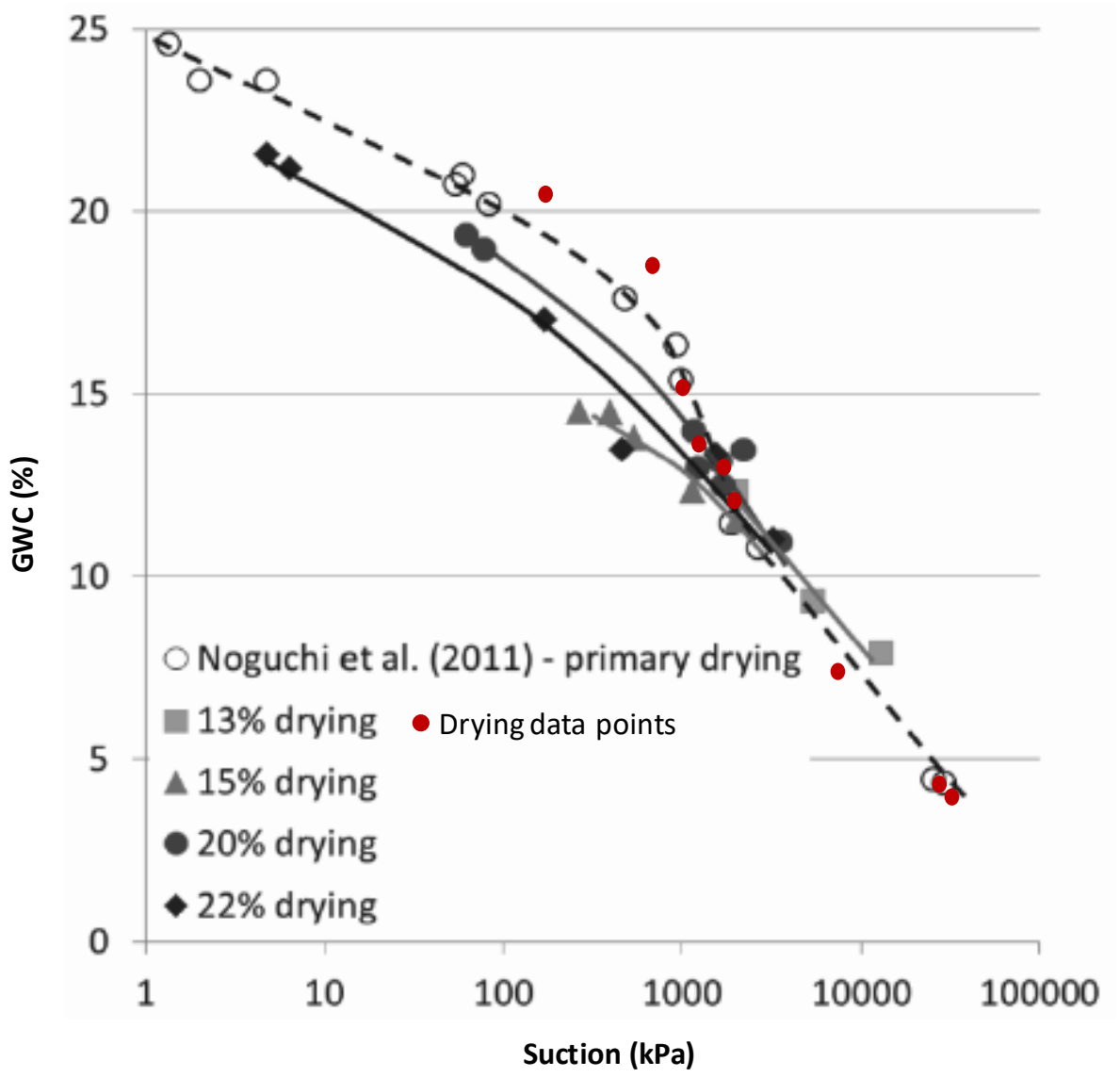

Figure 5.2 BIONICS Soil Water Retention Curve – drying. Drying data points overlaid on existing BIONICS SWRC (also drying). Original graph is from Mendes and Toll, 2013. Note, water content shown is gravimetric

In Figure 5.3, the recorded wetting data points are compared against wetting data (gathered using the filter paper method), also published in Mendes and Toll, 2013; this study did not produce a primary wetting curve. No clear pattern is discernible from the published wetting curves, but it does broadly appear as though the recorded wetting data compares well, however, as mentioned previously, this comparison suffers from a lack of wetting data points.

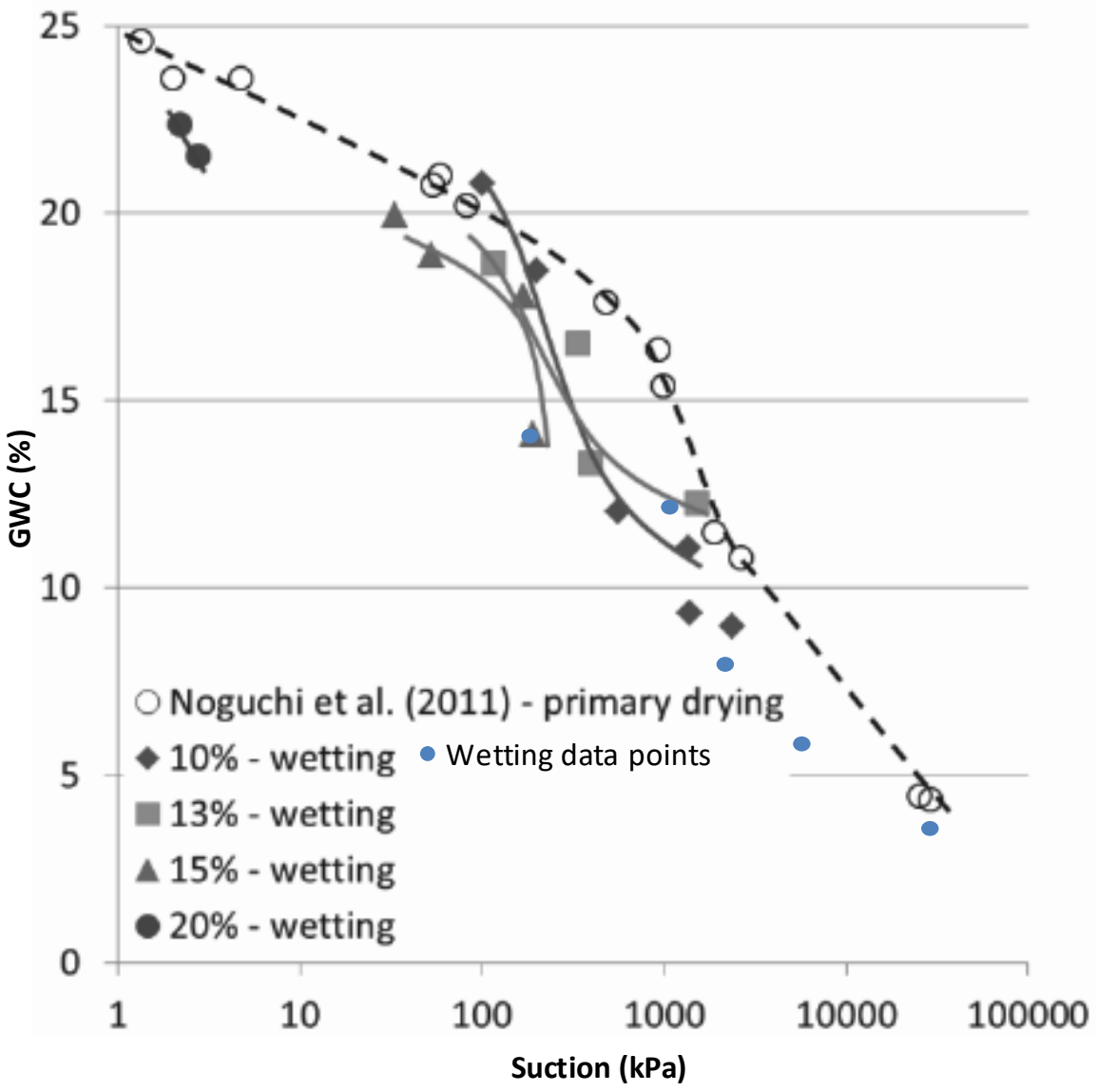

Figure 5.3 BIONICS Soil Water Retention Curve – wetting. Wetting data points overlaid on existing BIONICS SWRC (also drying). Original graph is from Mendes and Toll, 2013. Note, water content is gravimetric

5.1.2 *Resistivity – water content relationships*

Two point resistivity

These results pertain to Experiments 2, 3 and 4 as described in the Chapter 4. All results relate to testing of BIONICS material, except where indicated otherwise.

Figure 5.4 shows the results of two-point resistivity measurements on cylindrical specimens subjected to drying. The addition of the Nyogel conductive gel has improved contact between the specimens and the disc electrodes, yielding lower values of resistivity. For this reason, subsequent resistivity testing on the cylindrical specimens was performed using the conductive gel.

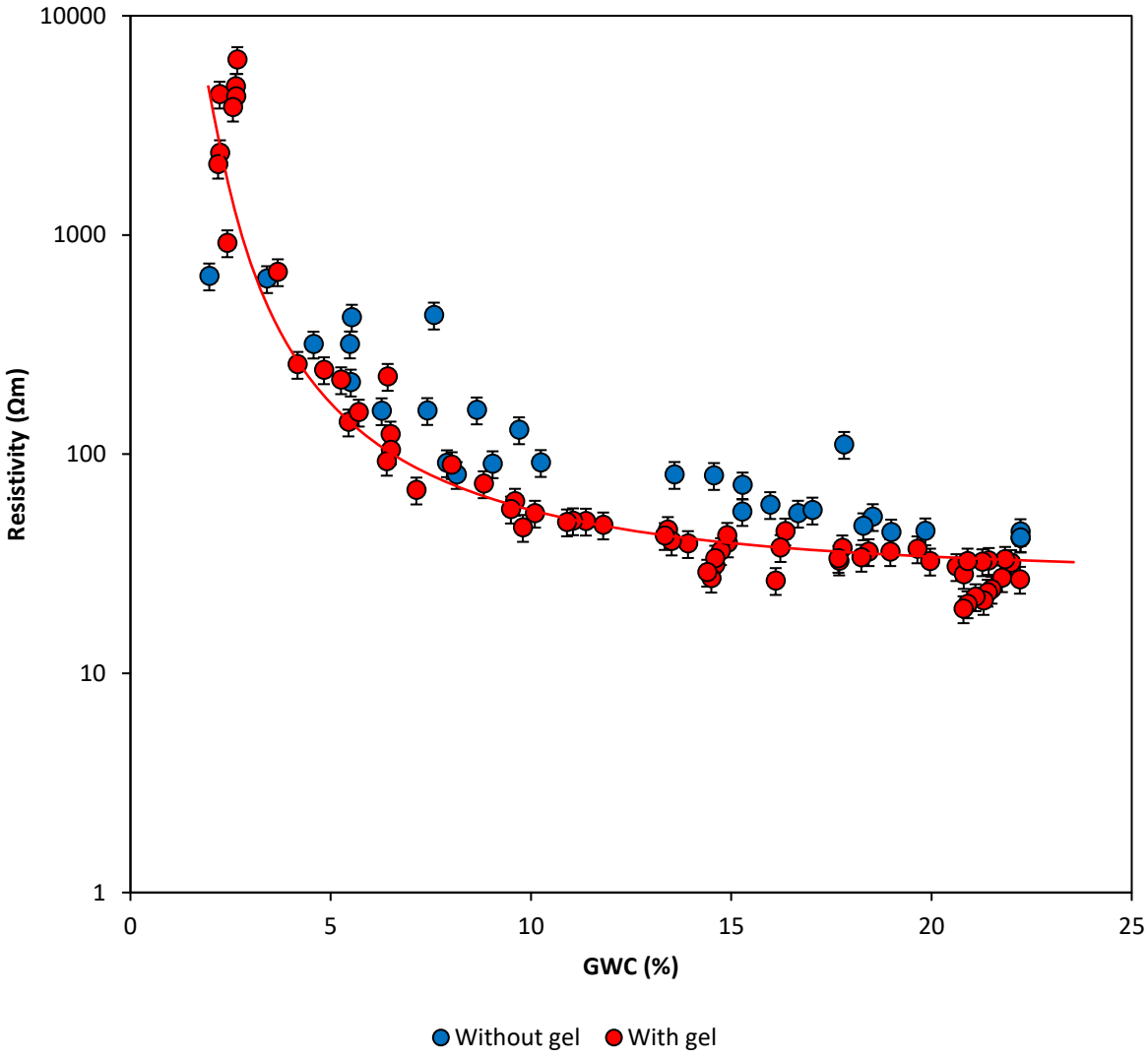

Figure 5.4 Effect of conductive gel on two point resistivity measurements: comparison of resistivity – water content relationships. Inverse power trend line has been fitted to "with gel" dataset only

The two point resistivity – water content drying curve is shown in Figure 5.5, compared against published data for clays, obtained using a similar method to the disc electrode method employed in this study. The BIONICS data compares very well with literature values, demonstrating an inverse power relationship. Below approximately 20 % VWC (corresponding to a GWC of 12 %), the BIONICS material demonstrates a sharp increase in resistivity; similar behaviour is observed from the published data.

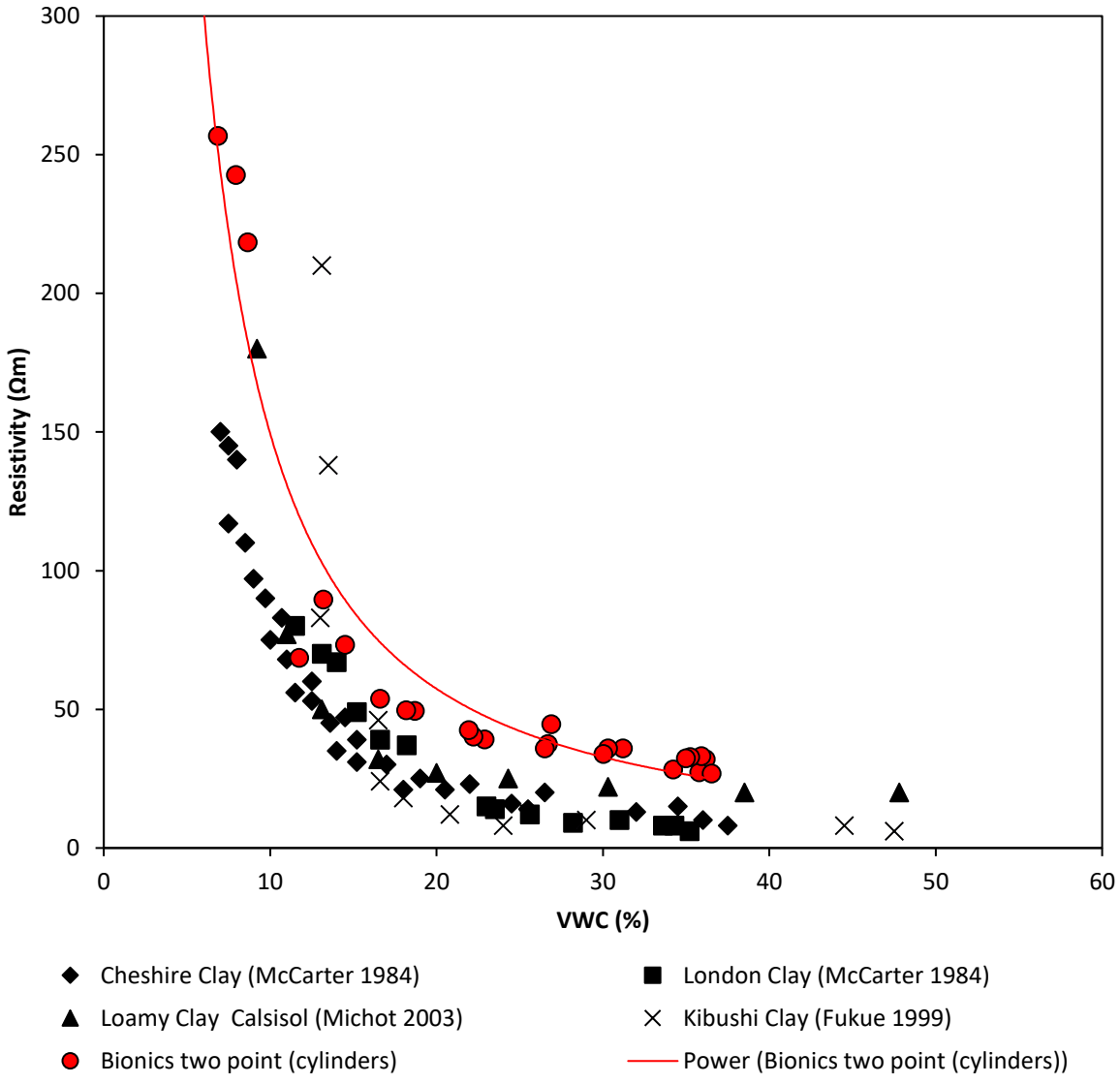

Figure 5.5 Comparison of BIONICS two point resistivity – water content relationship with published data for clay soils (published data extracted from Samouelian et al., 2005, as shown in Figure 2.27). Note that volumetric water content is presented in order to allow correlation with published data.

Figure 5.6 shows the two point resistivity – water content relationship for deliberately-fractured specimens versus those which are intact. It is evident that the presence of these fractures (orthogonal to the current flow) has acted to impede the current, resulting in higher values of resistivity for a given water content.

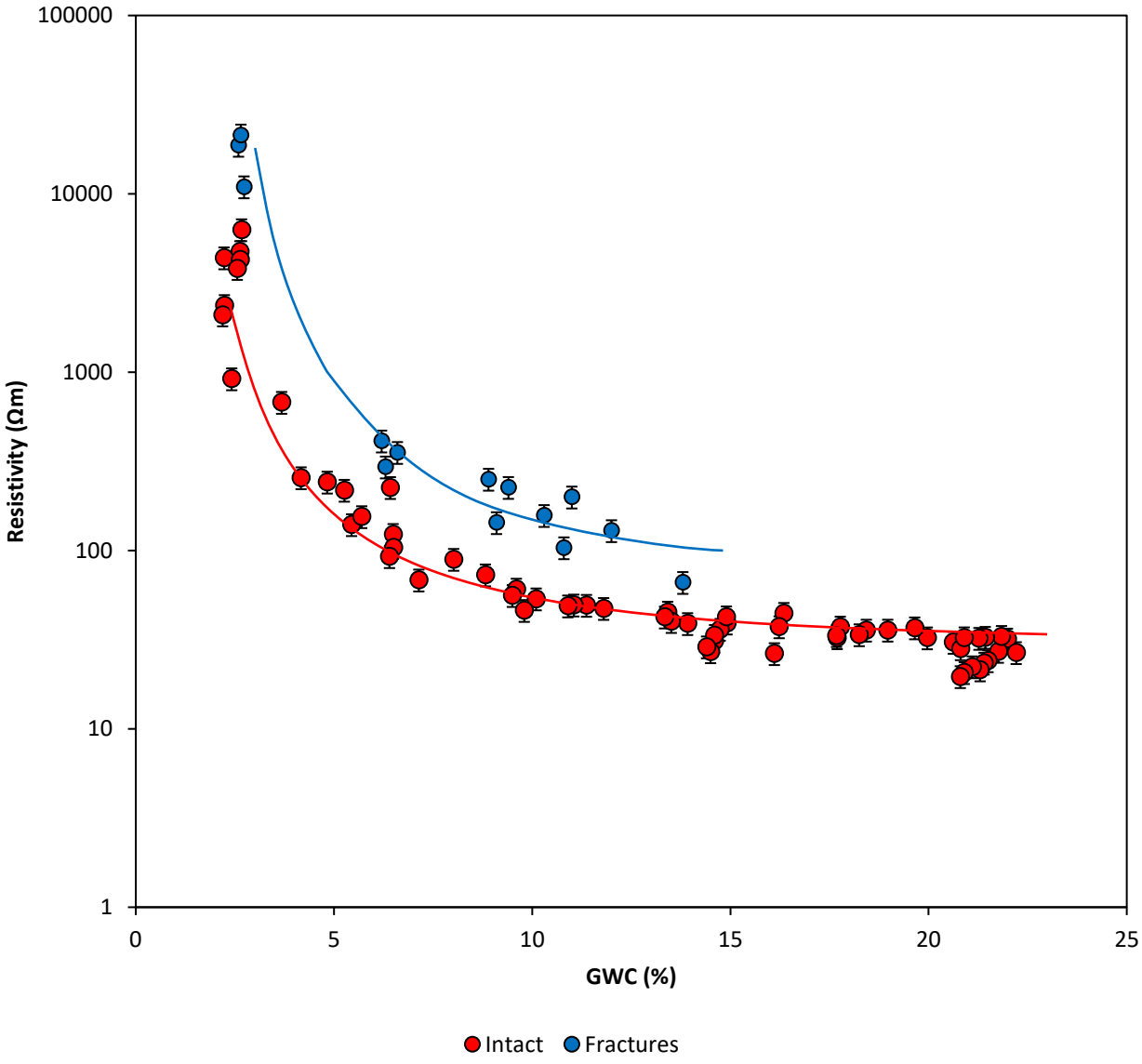

Figure 5.6 Comparison of two point resistivity – water content relationship for fractured and intact cylindrical specimens

In Figure 5.7, the two point resistivity – water content relationship has been divided into four individual paths (see legend, and Table 4.2). Little hysteresis can be observed between drying and wetting paths (half-cycles), suggesting that resistivity is independent of soil suction. If, however, the data are split into primary and secondary moisture cycles, each comprising a full dry-wet cycle, then a hysteretic inverse power relationship is evident: there is a shift of the resistivity - water content path centred at approximately 12 % GWC, such that below this point, specimens on the secondary curve have elevated values of resistivity with respect to the primary, with the opposite being true beyond this point, as is illustrated by two grey arrows. Resistivity error bars of +/- 12.5 % show that this shift is significant.

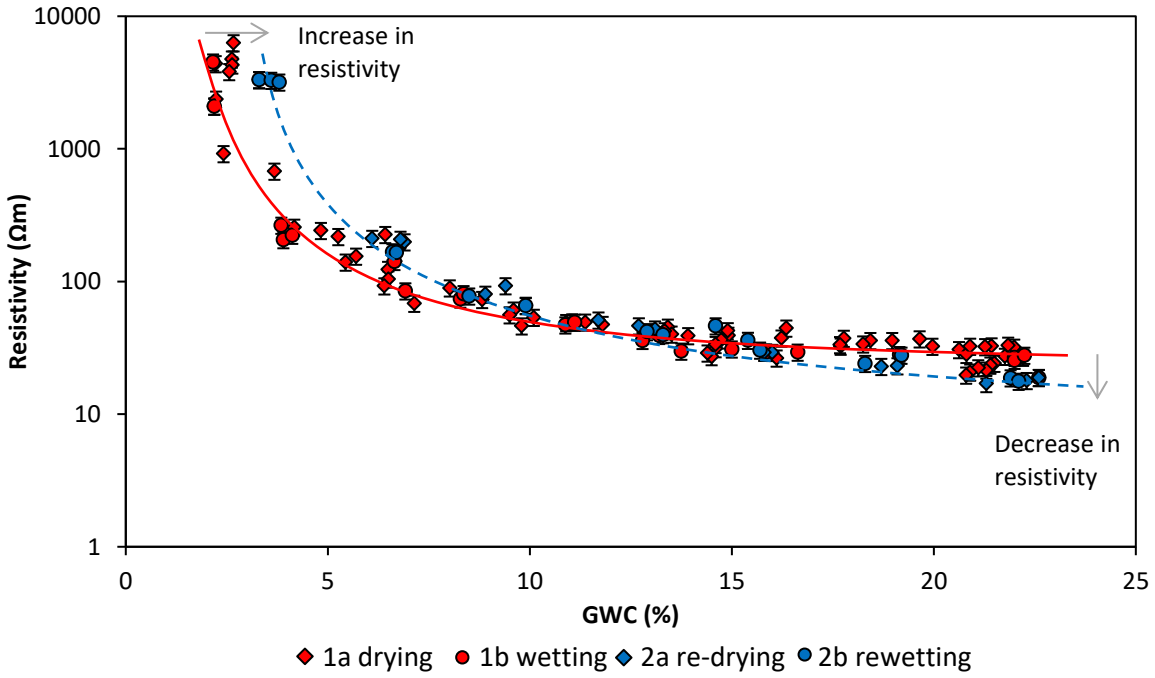

Figure 5.7 Hysteretic two point resistivity – water content relationship for cylindrical specimens for two full moisture cycles (figure published in Hen-Jones et al., 2016)

In Figure 5.8, the two point resistivity – water content relationship for Hollin Hill clay material is presented, showing one full dry-wet cycle. The data are separated into individual drying and wetting curves, showing little to no hysteresis between the two paths, in keeping with the findings of Figure 5.7 describing BIONICS clay material. Comparison of the Hollin Hill primary drying curve with the BIONICS primary drying curve shows Hollin Hill material to be more conductive at higher water contents.

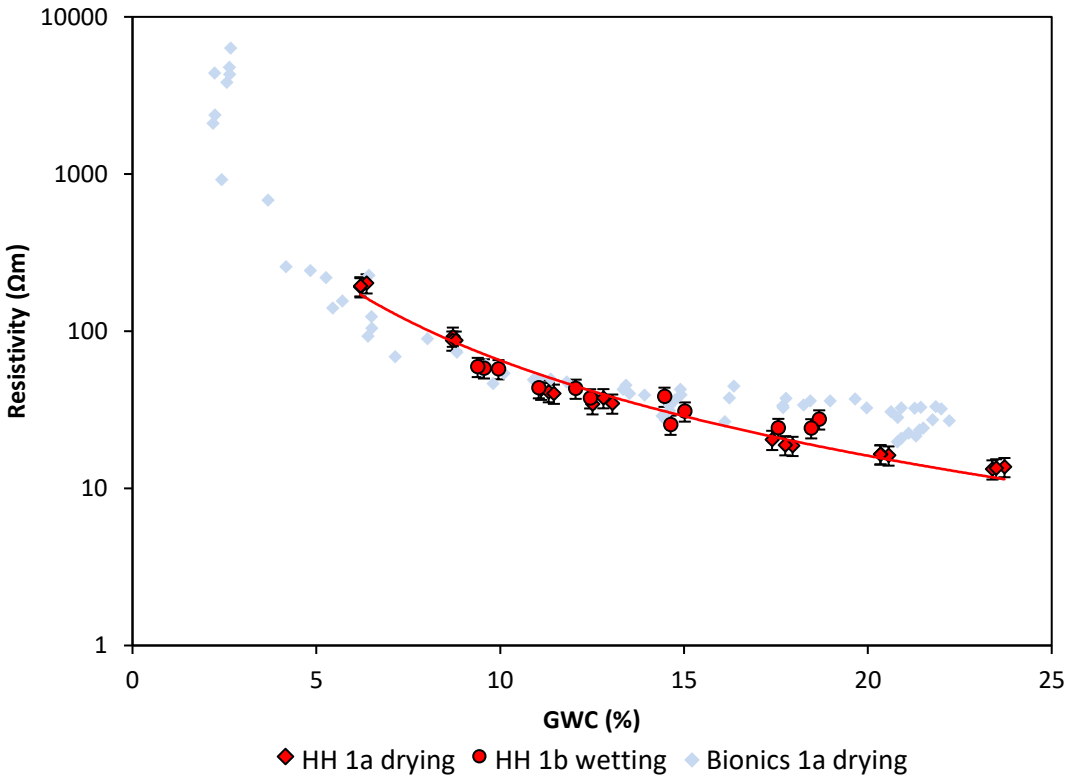

Figure 5.8 Two point resistivity – water content relationship for Hollin Hill material for one full moisture cycle, with an inverse power trend line fitted to both datasets. The BIONICS two point resistivity drying curve is shown for comparison

Four point resistivity

Figure 5.9 shows the results of Experiment 3, comparing two and four point resistivity methods on the same BIONICS clay specimens, using the bespoke resistivity chambers. Trend lines have been fitted to both datasets, and show an inverse power relationship between resistivity and water content, using both methods. The four point resistivity dataset demonstrates considerably lower values of resistivity than the two point dataset, deviating further as the specimens dry. Approaching saturation, the two methods converge. Due to the fact that both methods were used to obtain resistivity values on the same specimens, the difference between the two datasets is a direct result of the methods used: as discussed in subchapter 2.3.1, the two point resistivity method includes higher contact resistances than does the four point method.

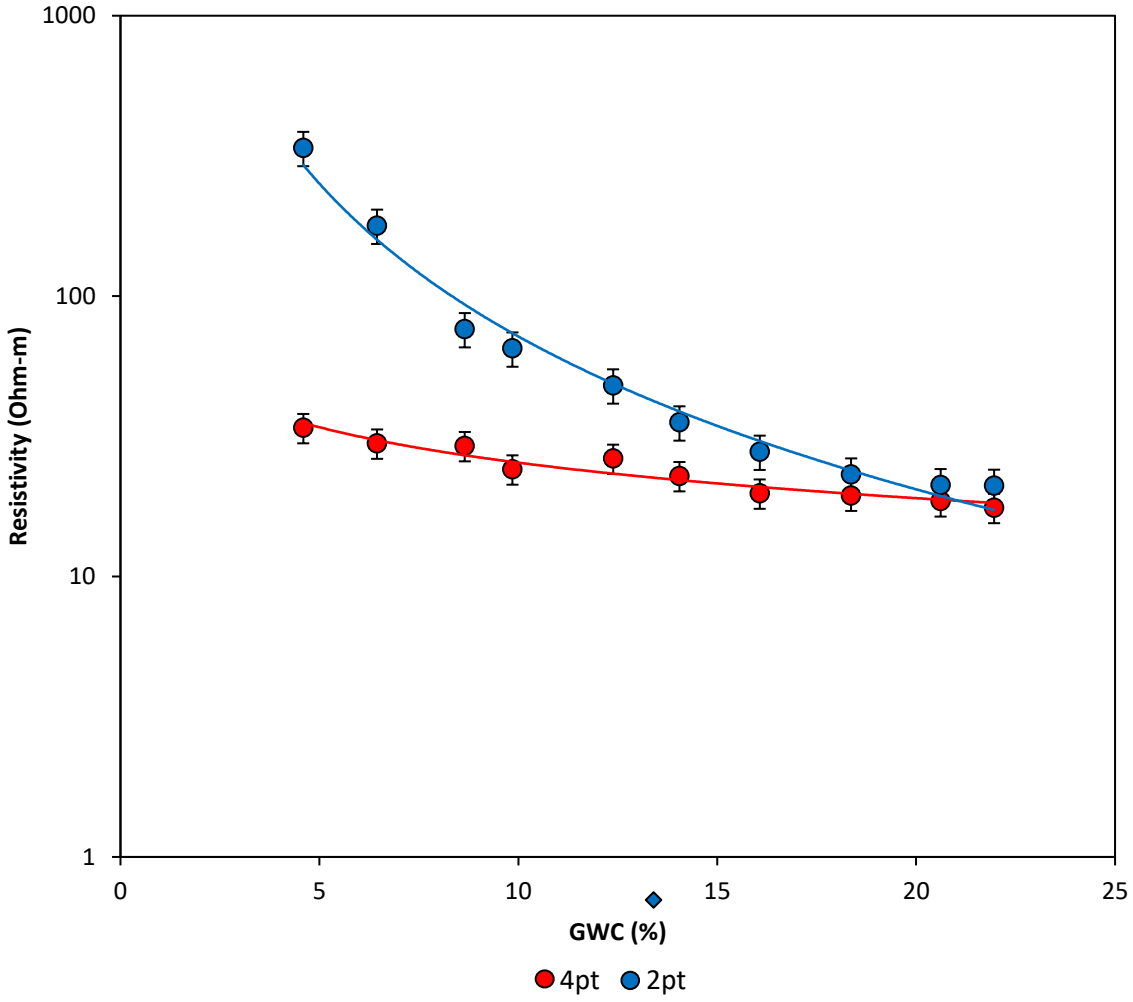

Figure 5.9 Comparison of two point and four point resistivity methods. The data pertain to specimens undergoing a primary drying path. Note, these specimens were compacted in four layers, parallel to the current flow, within the bespoke resistivity test chambers

In Figure 5.10, the four point resistivity – water content relationship for BIONICS material is presented, for specimens compacted into the bespoke resistivity test chambers in two ways: 1. By trimming of a sample from a proctor mould, and; 2. By compacting into the chamber in four layers, as described in Experiment 3. In each case, an initial drying path is shown. Both datasets exhibit similar behaviour at water contents beyond approximately 12 %; below this point the datasets deviate, such that the layered specimens have considerably lower values of resistivity. This is suggested to be due to the layers (created parallel to the direction of current flow) creating preferential current flow paths, increasing the sample conductivity. For this reason, subsequent resistivity tests were performed on proctor-compacted specimens.

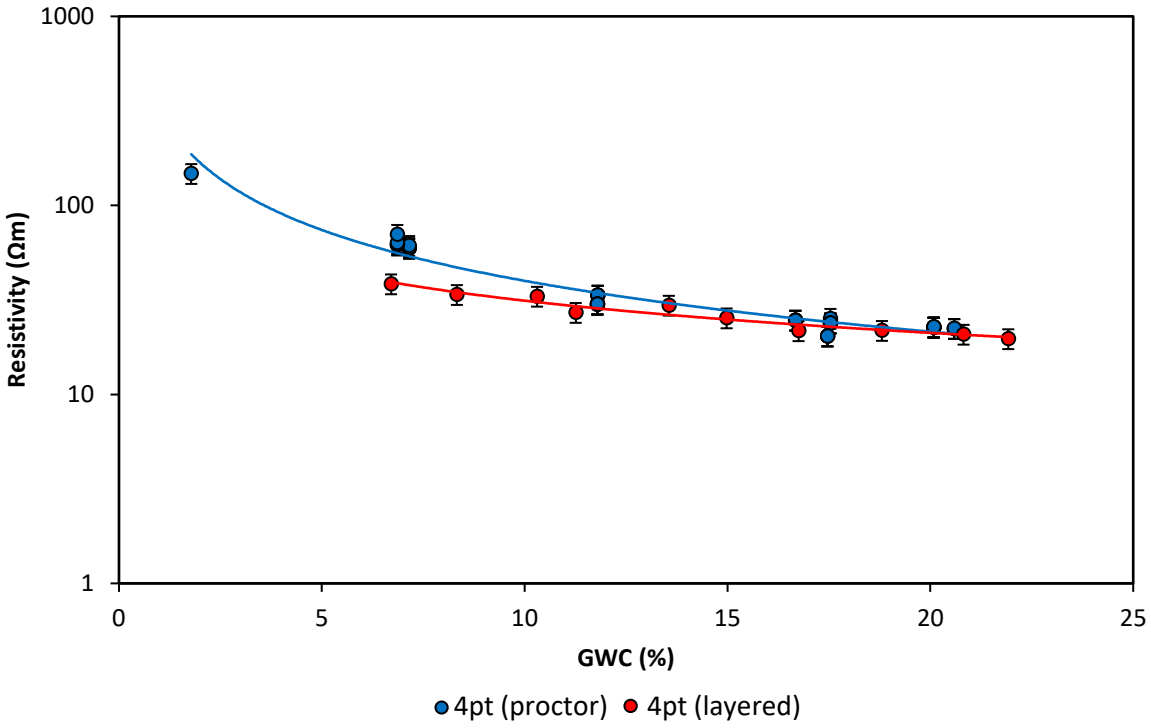

Figure 5.10 Effect of compaction method on four point resistivity – water content relationship of BIONICS material

In Figure 5.11, the four point resistivity – water content relationship for BIONICS material is presented, for two cycles of drying and wetting. If the data points are considered on a standalone basis, then there is no foundation for the suggestion of hysteresis between the primary and secondary moisture cycles. In Figure 5.7, the two point resistivity - water content relationship was shown to be hysteretic between primary and secondary moisture cycles, however, the two point dataset comprised significantly more data points, providing a

far higher resolution, and as such, a strong basis for inferring a hysteretic relationship. It is reasonable to consider that if a hysteretic path is followed on the two point resistivity water content curve (between primary and secondary moisture cycles), that a hysteretic relationship would also exist between four point resistivity and water content. In order to investigate this concept, trend lines have been fitted to suggest a similar relationship for the four point curve shown in Figure 5.11, centred at 12 % GWC. Due to the lack of data points, and to the fact that the resistivity range sampled is relatively small, these trend lines are certainly speculative. They do, however, appear reasonable, illustrating a slight increase in resistivity values at low water contents, and a slight decrease at high water contents, in keeping with the trends observed in Figure 5.7. The addition of these trendlines is purely for the purposes of verifying these trends, as ultimately, there is not enough data for this separation into primary and secondary moisture cycles.

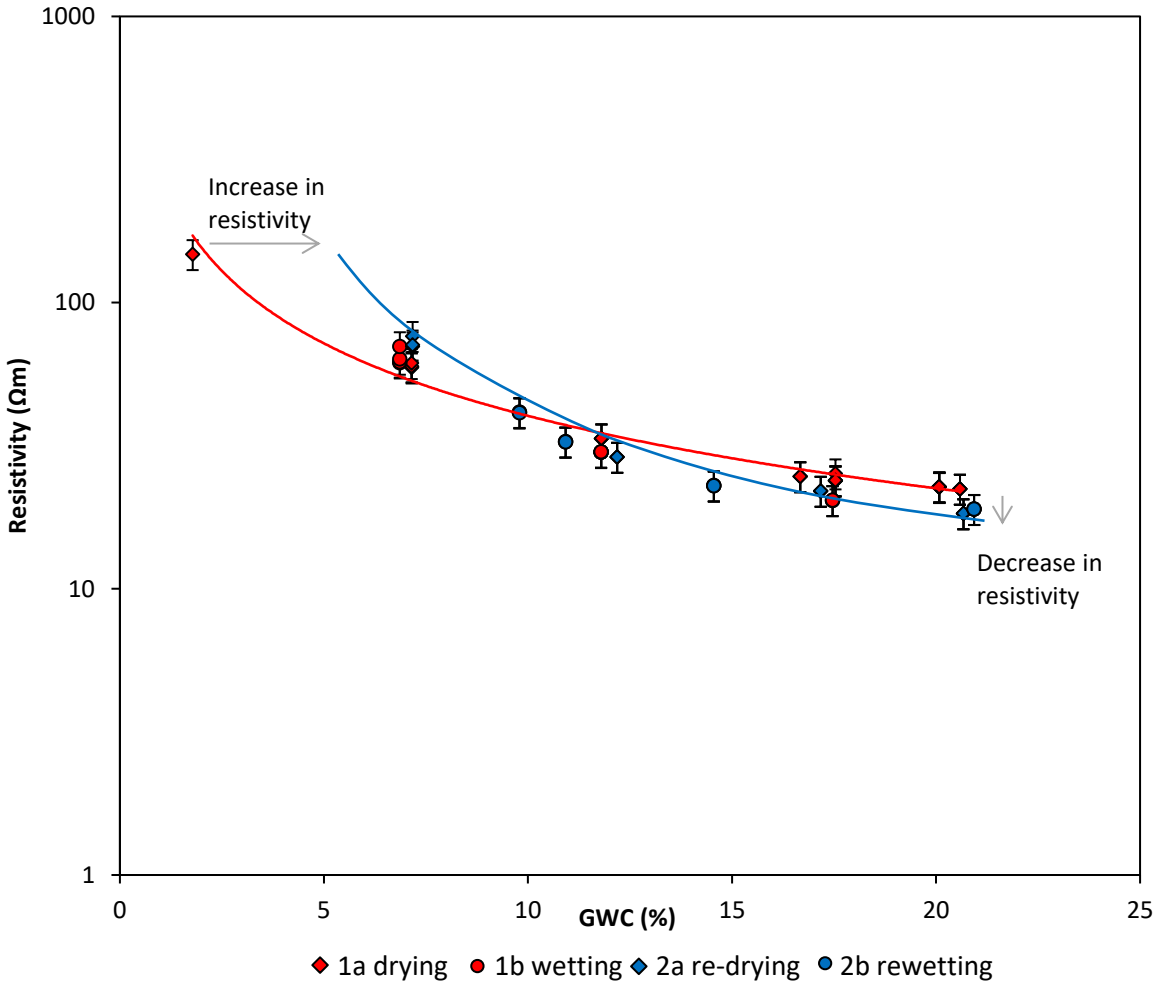

Figure 5.11 Hysteretic four point resistivity – water content relationship for BIONICS material for two full moisture cycles. Note, these specimens were extracted from proctor moulds

Development of the Resistivity – water content proxy relationship

As a result of the observed over-estimation of resistivity using the two point method, as shown in Figure 5.9, the decision was made to use a four point measure of resistivity to develop a resistivity proxy for water content, which would be used to translate field resistivity values into estimated field water contents. In Figure 5.10 it was shown that the layered compaction method resulted in specimens with preferential current pathways, under-estimating bulk soil resistivity, therefore, the decision was made to use the proctor-compacted dataset (Figure 5.11), as it was considered to be more representative of in situ conditions. Given the objective of using resistivity as a proxy for water content in the field, it is pertinent to consider whether or not there is any merit to having distinct primary and secondary cycle relationships. From Figure 5.11, there is simply not enough evidence to confirm a hysteretic relationship, although one has been inferred. The inferred hysteretic relationship itself is only slight, with a maximum recorded resistivity increase of 14 % between moisture cycles, at the dry end. Considering an error of 16 % in the resistivity data points (see Appendix C), it is concluded that this hysteresis is not significant with respect to the development of a resistivity water content proxy relationship. Therefore, it was decided to resolve all of the data from the two full moisture cycles shown in Figure 5.11 into one Waxman-Smits expression.

In order to fit Waxman-Smits parameters, a trend line was fitted to porosity – water content data corresponding to the gathered four point resistivity data, shown in Figure 5.12:

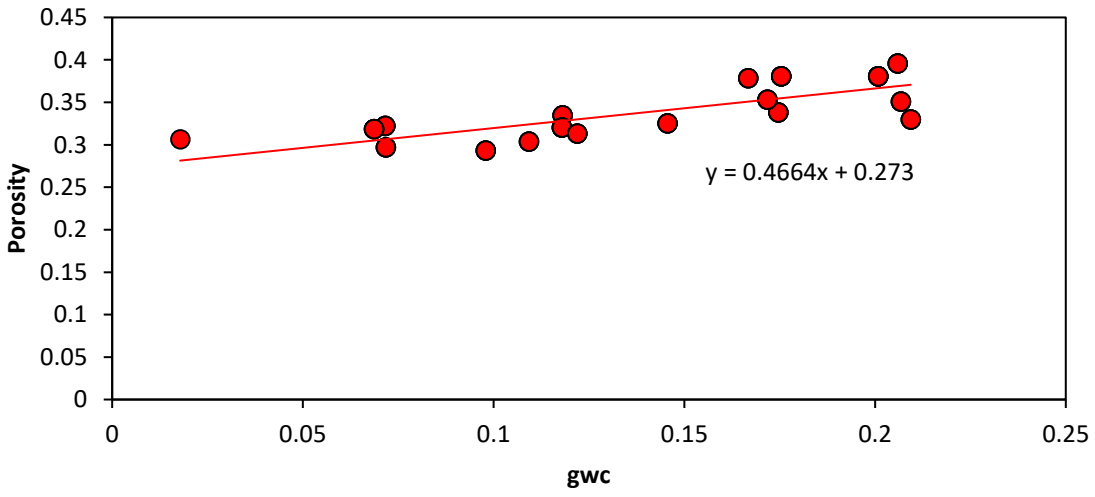

Figure 5.12 Porosity – water content relationship corresponding to the four point resistivity – water content data shown in Figure 5.11. Note, horizontal axis is fractional gravimetric water content

The linear porosity – water content expression was then incorporated into the Waxman-Smits equation, and Waxman-Smits parameters (a, m, n) fitted to the four point resistivity data, as shown in Figure 5.13. The curve-fitting parameters are given in Table 5.2.

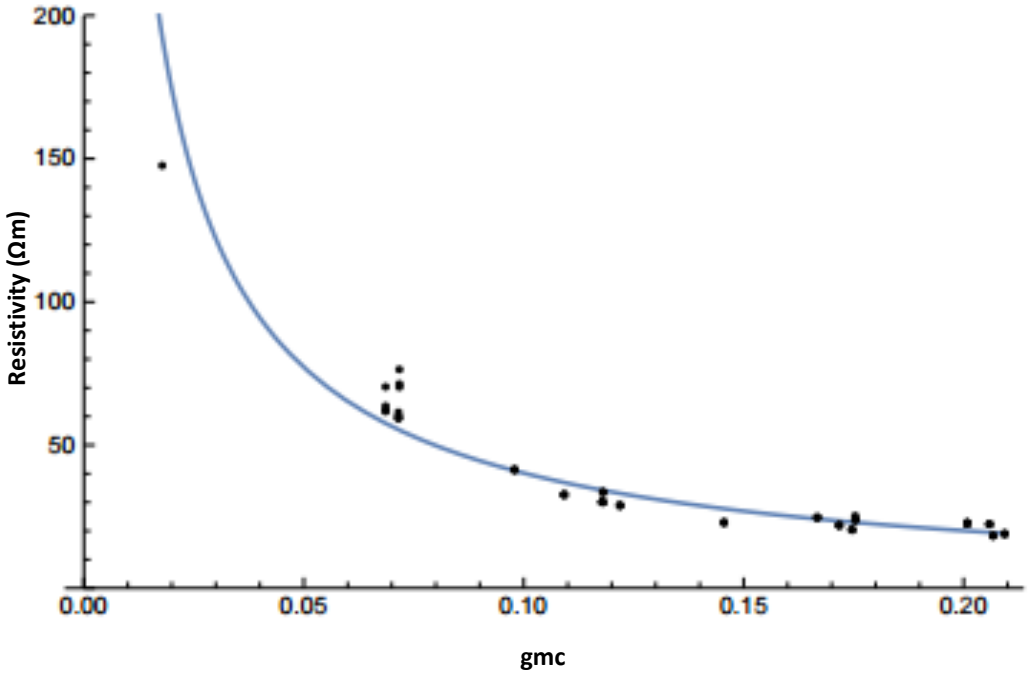

Figure 5.13 Four point resistivity – water content relationship with fitted Waxman-Smits curve. This curve forms the basis for the use of resistivity as a proxy for water content, to convert ERT data to moisture data

Table 5.2 Fitted Waxman-Smits (1968) parameters

Parameter	**Value**	**Notes**	**Units**
Tortuosity actor, a	0.82	Fitted	-
Cementation exponent, m	3.48	Fitted	-
Saturation exponent, p	1.83	Fitted	-
Pore water resistivity, ρ_w	15.0	Estimated	Ωm
Pore water density, P_w	1.0	Estimated	Mg/m^3
Solid density, P_s	2.65	Measured	Mg/m^3
Average ionic mobility, B	1.98	Estimated	(Sm_{-1})
Cation exchange capacity, C	15.2	Measured	meq/100 g

5.1.3 *Thermal properties*

The following figures relate to the characterisation of the thermal properties of BIONICS clay, in order to more fully interpret field ERT data. These results pertain to Experiment 5.

The thermal conductivity of BIONICS material as a function of water content is shown in Figure 5.14. Thermal conductivity was found not to change from the initial water content (22 % GWC), until approximately 12 %. This point is thought to coincide with the continuity of the pore water menisci, and the beginning of rapid desaturation, below which thermal conductivity was found to decrease considerably.

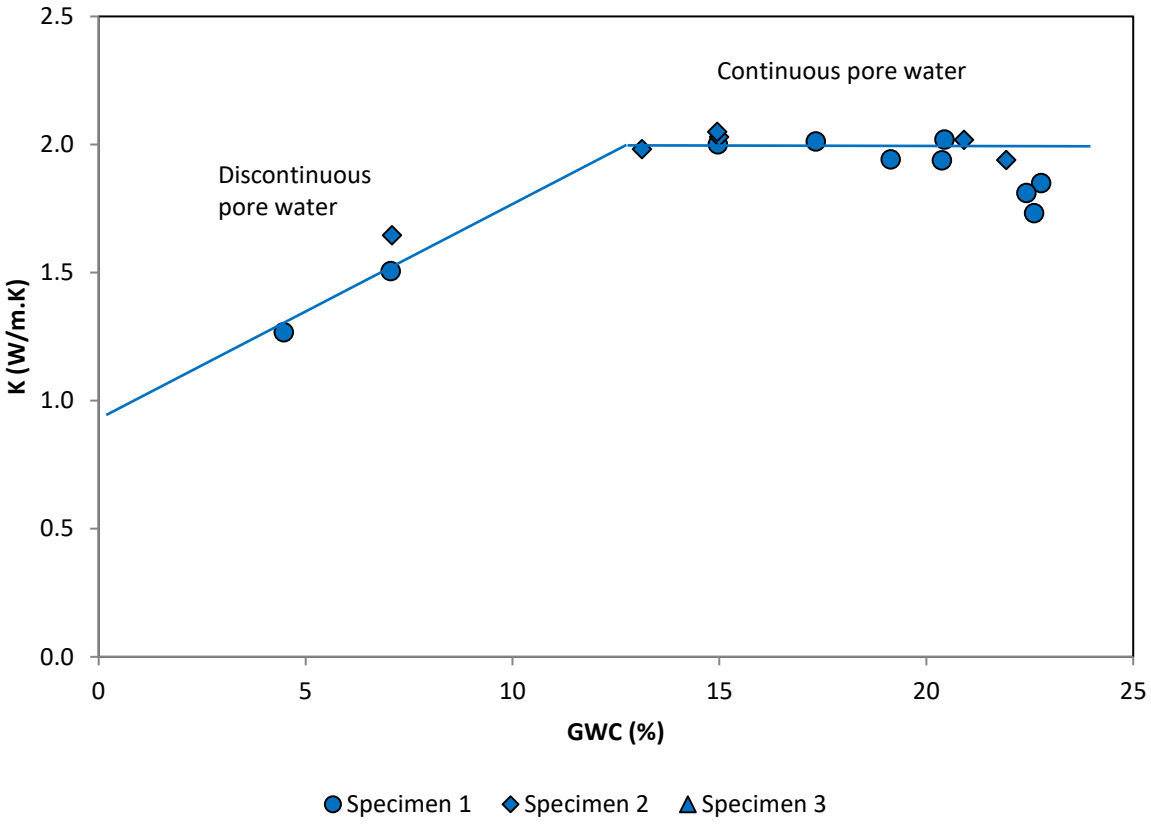

Figure 5.14 Thermal conductivity – water content relationship

In Figure 5.15, the four point resistivity of BIONICS material at a range of water contents (22 %, 16 %, 10 %) is shown, subjected to increasing temperatures. In keeping with previous results, drier specimens are more resistive than wetter ones. It can be seen that specimens at 10 % GWC (red markers) have more scattered data points, thought to be due to their being at a water content less than that required for the continuity of the pore water phase. For all specimens, resistivity is observed to decrease with increasing temperature. A trend line has been fitted to all of the data: this trend line describes a relationship whereby resistivity decreases by 1 % per 2 °C increase in temperature. This trend then served as the basis for temperature correction for ERT data, as described in subchapter 4.3.6.

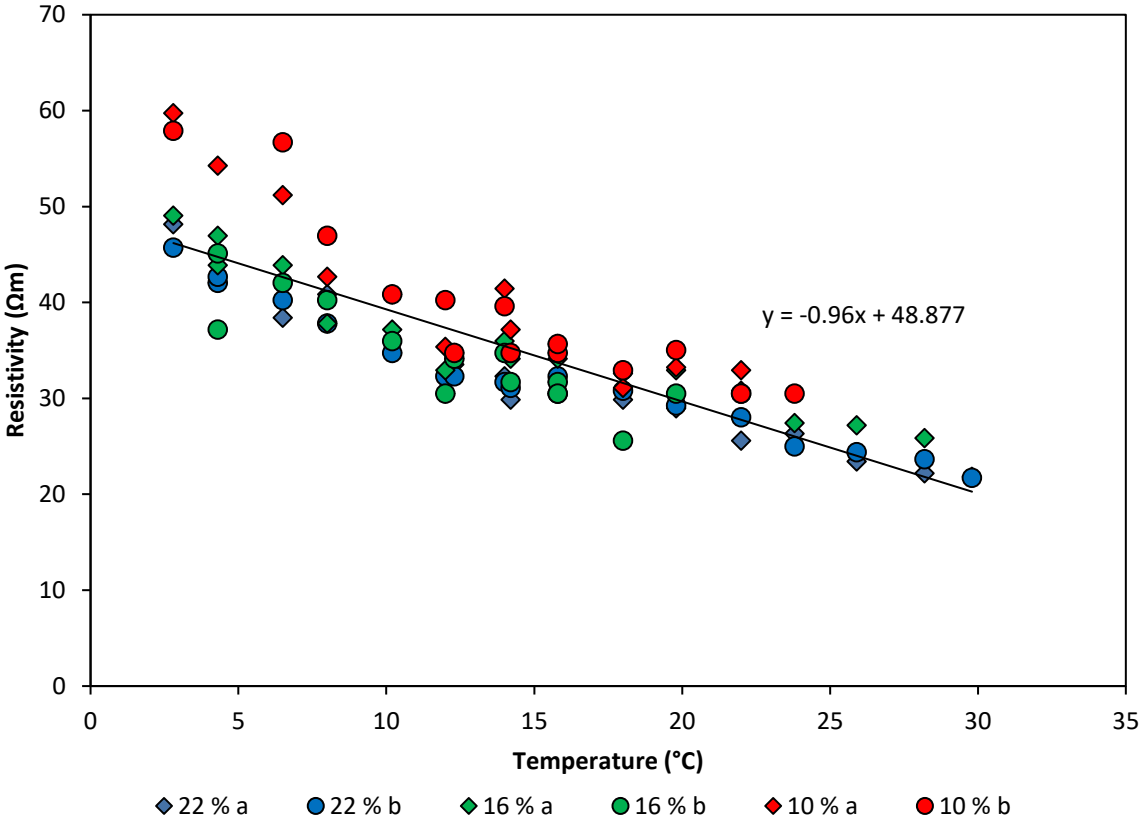

Figure 5.15 Temperature – resistivity relationship

5.1.4 *Soil strength relationships*

The following figures pertain to Experiment 2, and describe the effect of seasonal moisture cycles on the strength of BIONICS and Hollin Hill clay materials. These effects are then interpreted in terms of the resultant effect on the measured soil resistivity.

In Figure 5.16, the unconfined compressive strength (UCS) of BIONICS material is shown, as a function of water content. It can be seen that a linear relationship exists, whereby UCS increases as specimens are dried out from the initial water content. During rewetting, the specimens exhibit lower UCS values than during drying, although these converge approaching saturation. No such hysteresis can be observed between primary and secondary drying paths (1a and 2a), implying that the unconfined compressive strength is relatively unaffected by the development of micro-fractures. However, specimens which developed larger, macro-scale fractures (circled), are observed to have vastly reduced UCS values.

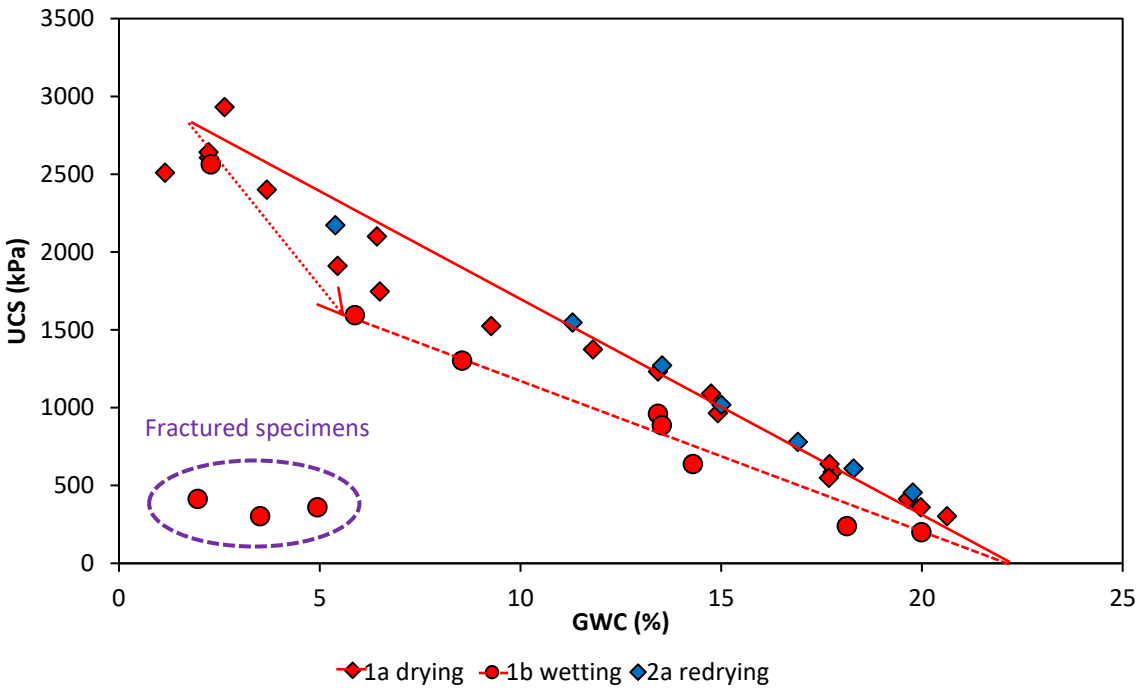

Figure 5.16 Water content – unconfined compressive strength relationship

In Figure 5.17, a hysteretic relationship is shown between water content and shear strength, for repeated dry-wet cycles. For all four dry-wet paths, shear strength is shown to decrease linearly with increasing water content. Both primary and secondary moisture cycles exhibit a drop in shear strength at the transition from a drying to wetting path, illustrated by an arrow. Shear strength values within a secondary moisture cycle are reduced with respect to the primary cycle, but exhibit scanning-type behaviour: at approximately 12 % water content, Path 2a converges with 1a and 2b converges with 1b, such that beyond this water content, there exists only one drying path and one wetting path, which converge approaching saturation.

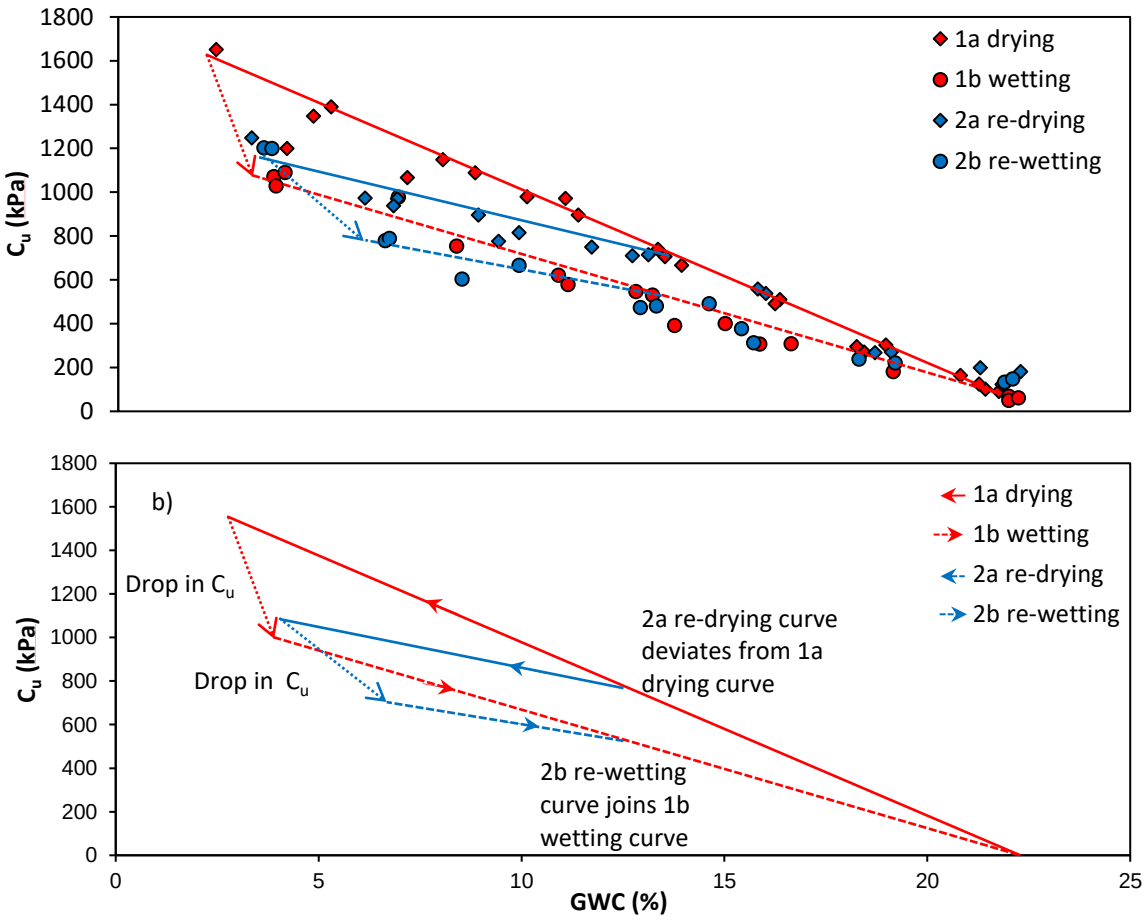

Figure 5.17 Water content – shear strength relationship for two full moisture cycles. (a) Data points with fitted linear trend lines; (b) Data points removed to highlight trend. (Figure published in Hen-Jones et al., 2016)

Figure 5.18 presents a similar relationship, for Hollin Hill material, but for only one full dry-wet moisture cycle. As before, shear strength is observed to decrease linearly with increasing water content, with a clear drop in shear strength between drying and wetting paths.

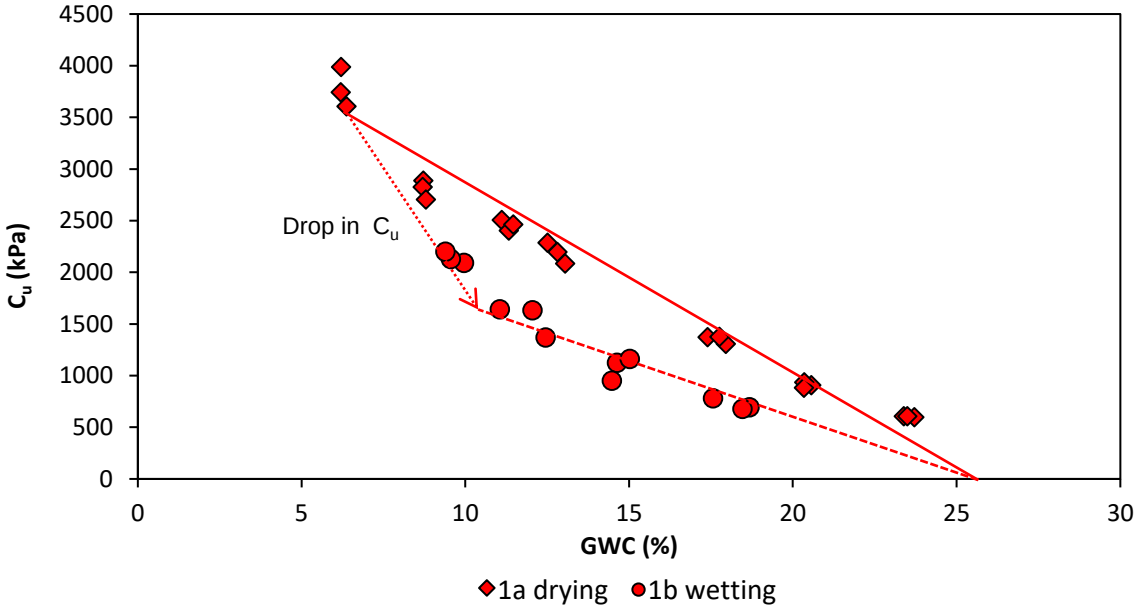

Figure 5.18 Water content – shear strength relationship for Hollin Hill clay for one full moisture cycle

Figure 5.19 shows a hysteretic shear strength - resistivity relationship, for ongoing seasonal cycling. As specimens are dried, there is an associated increase in both soil resistivity and shear strength. At the transition from a drying to a wetting path, there is a drop in C_u, illustrated by an arrow, after which specimens following a wetting path exhibit higher values of resistivity for a given shear strength than those following a drying path. As in Figure 5.17, the secondary drying and wetting paths (2a, 2b) demonstrate scanning-type behaviour and converge with their primary curve counterparts at shear strengths of 700 kPa and 500 kPa respectively.

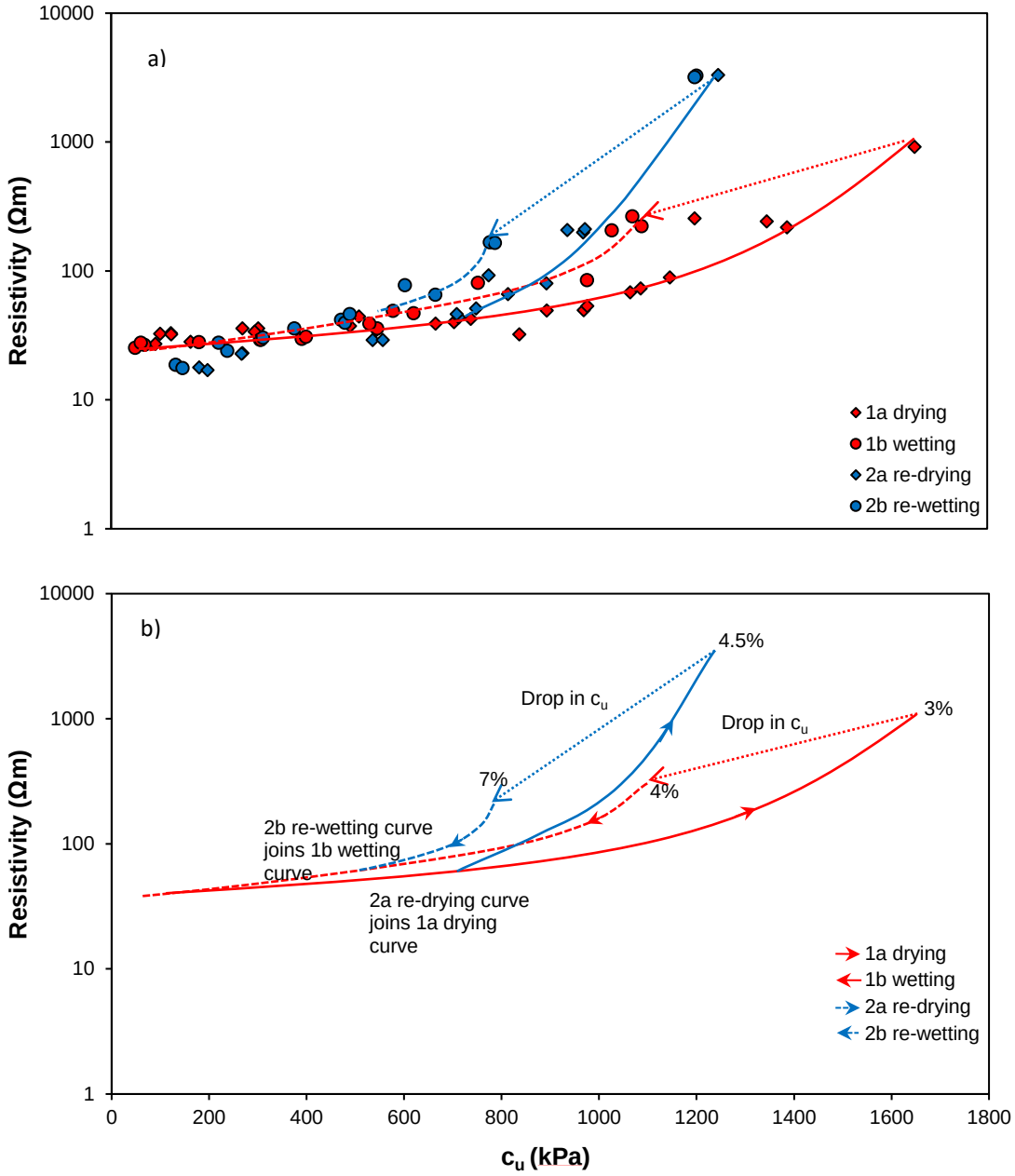

Figure 5.19 Resistivity - shear strength relationship (two-point resistivity method) for four moisture cycles. (a) Data points with fitted trend lines; (b) Data points removed to highlight trend. Volumetric water contents are indicated across the transition boundaries in Figure 7b. (Figure published in Hen-Jones et al., 2016)

Figure 5.20 displays an SEM image of a specimen that has undergone drying in the E-SEM chamber (Experiment 6). A clearly visible crack produced as a result of desiccation can be seen, approximately 800 µm long and 50 µm wide. Upon closer inspection of this feature (Figure 5.20b), particles lining the crack wall are shown to have aligned during drying-induced shrinkage and have created a distinct 'coating' to the crack surface. After the specimen was removed from the E-SEM and rehydrated by the application of a distilled

water droplet and left to homogenise overnight, the specimen surface was again scanned. Figure 5.20c shows a sample that exhibits a much more hydrated clay texture that is centred about a relic crack feature. This location is further magnified in Figure 5.20d and demonstrates both the partial closure and apparent infilling of the previously wider crack aperture. However, such a feature has remained identifiable and is likely to be a product of the permanent realignment of particles at the crack wall. It is therefore anticipated that this discontinuity would be exploited upon re-drying.

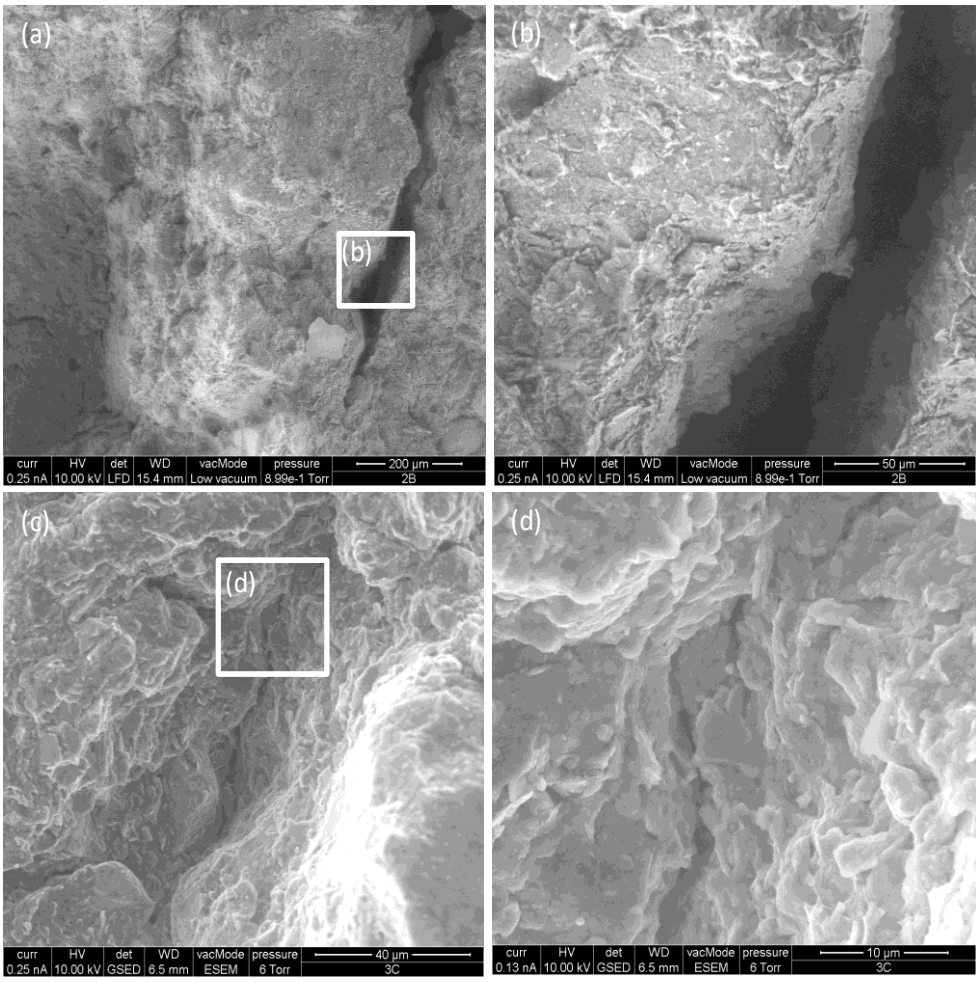

Figure 5.20 E-SEM images of BIONICS clay material, taken at two sites, illustrating (a) Site 1 after 90 min at 10 % RH, and showing the position of (b) Desiccated clay particles and fracture wall under higher magnification; (c) Site 2, showing of reduced crack aperture following re-wetting and the position of (d) Hydrated particles under higher magnification (figure published in Hen-Jones et al., 2016)

5.2 Field point sensor results

The following subchapter presents the data collected using the point sensor network installed at the BIONICS embankment. A map of the point sensor distribution is shown in Figure 4.39. In the first instance, these data are presented as time series information; later, inter-relationships between the datasets are shown. Where possible, presented data are compared against laboratory measurements.

5.2.1 *Time series data*

Initially, time series geotechnical data recorded at the ERT test plot only are presented, in order to provide quantitative information pertaining to the ERT survey area. Subsequently, data from other parts of the embankment are used in order to provide a basis for assessing the response to environmental forcings at different locations.

ERT test plot

Figure 5.21 shows data gathered at two locations on the Southern flank, whilst Figure 5.22 shows that obtained from sensors located on the crest and the Northern flank. The data span from November 2012 to November 2015. Note, the precipitation data presented in Figure 5.21a were gathered at the Nafferton Farm weather station, approximately 50 m from the BIONICS test embankment. The reason for the use of this weather station for precipitation estimates is that the rain gauges installed on the embankment had a tendency to significantly underestimate precipitation, due to a shielding effect caused by the embankment flanks.

From Figure 5.21a, there is little evidence to suggest seasonally drier summer weather over the three year test period, with the opposite in fact appearing to be more accurate: all rainfall maxima (in excess of 20 mm/per day) occur during the summer months. From Figure 5.21b, it can be seen that all of the sensors show degrees of seasonal variability, demonstrating water contents which are higher during the winter months and lower during the summer months, with pore water pressures responding accordingly (Figure 5.21c). Given these observations, it may be said that in a general sense, there is little correlation between the recorded precipitation and the volumetric water contents (Figure 5.21b) gathered on the Southern flank, with periods of high precipitation (summer) correlating with periods of lowest water content, with the opposite true during the winter periods. From Figure 5.21d, it can be seen that the seasonal variability in water content and pore pressure follows the same period of oscillation as the corresponding temperature values (Figure

5.21d). Combining these observations leads to the suggestion that this general lack of correlation between precipitation and field water content at the BIONICS embankment is the result of evapotranspiration. Over shorter periods (days), good correlation is observed at the near-surface (0.1 m), such that rainfall extremes are followed by spikes in recorded volumetric water content values. This response is less noticeable at greater depths (0.5, 1.0 m) which may be the result of a combination of lower suctions at depth (therefore less of a capacity to draw in moisture), evapotranspiration, and surface runoff.

From Figure 5.21b, it can be seen that the water content recorded at the lower position on the Southern flank at a depth of 0.1 m is highly variable, demonstrating seasonal minima and maxima of 12 and 40 % VWC respectively (with considerable diurnal variation), prior to the activation of the sprinkler system in mid-January 2015. At the same location, the range at 0.5 m depth is between 29 and 37 %, the curve demonstrating clear cycles of seasonal drying and wetting, but with no obvious diurnal variability. At an increased depth of 1.0 m, a range of 31 to 33 % is recorded, showing seasonal behaviour to become increasingly damped with depth. During the winter months, water contents at 0.5 m are higher than those at 1.0 m, however, during summer drying events, the opposite becomes true, as the near-surface dries out.

Sensors in place at the upper position on the Southern flank demonstrate more clearly defined seasonal dry-wet behaviour, particularly at 1.0 m depth, suggesting more hydrodynamic variability at depth in the upper portion of the Southern flank than in the lower. Water contents range between 22 and 28 % at 0.5 m, and between 28 and 34 % at 1.0 m (prior to sprinkling), showing water content at greater depth to be consistently higher than that nearer the surface.

Following sprinkler activation, there is an immediate increase in volumetric water content at 0.1 m (lower position), to a maximum of 50 % in April 2015. At 0.5 m depth, however, there is little increase at either upper or lower positions, suggesting water contents near saturation. At 1.0 m, recorded water contents increase by 2 to 3 % with respect to normal seasonal maxima.

As explained in subchapter 4.3.7, a crude approximation of the porosity values at the point sensor locations was obtained by assuming the maximum recorded volumetric water content to be equivalent to the porosity. Therefore, it is estimated from Figure 5.21b that

the porosity values at the point sensor locations run as follows, from most porous to least porous: 0.5 m lower, 1.0 m upper, 1.0 m lower, 0.5 m upper. This estimation then aids in the interpretation of Figure 5.21c, showing the change in recorded pore water pressure over time (note, positive pore pressures cannot be resolved with the installed instrumentation). During summer drying events, the greatest suction values are recorded at 0.5 m at the lower position (600 kPa), which is the least porous. Despite having similar recorded summer volumetric water contents, recorded suction values at 1.0 m depth (both upper and lower positions) are considerably lower (100 to 200 kPa). At both sensor locations, pore water pressure is observed to fluctuate more near the surface, with the response increasingly damped at depth. This damped effect is also evident from a time lag between the initial development of suctions during the summer months, first at 0.5 m, and then at 1.0 m approximately one month later. At the end of the drying season, both demonstrate simultaneous suction losses, suggesting direct water infiltration to both depths.

Further evidence of a damped environmental response at depth is given in Figure 5.21d, which shows the associated temperature values. The greatest maxima and minima are observed at 0.1 m, which demonstrates very high diurnal variability. As depth increases, the amplitude of variation (both diurnal and seasonal) decreases. It can also be observed that during and after the sprinkler activation period, recorded temperature values are significantly lower than in the previous years.

In addition to this depth-related damping, it can be seen from Figure 5.22 that the crest and Northern flank both demonstrate little to no seasonal variation in terms of soil water content or suction, remaining approximately constant over the course of one year. However, two factors must be considered: firstly, these sensors were installed much later than those on the Southern flank (November 2014); secondly, shortly after installation, the sprinkler system was activated. Therefore, it is possible that the crest and Northern flanks do demonstrate seasonal moisture behaviour under normal conditions, but the time series data do not span long enough to capture it; both could then have remained saturated following increased water infiltration from the sprinkling experiments.

On the Northern flank, the water contents at both depths are approximately identical (33 %); at the crest, the embankment fill is wetter directly under the ballast (22 %) than it is at greater depth (19 %). From Figure 5.22b, it can be seen that the recorded suction values at both positions are significantly lower than on the Southern flank, between approximately 10

and 30 kPa, suggesting the fill is near saturation, which explains why little change in either water content or suction can be seen following activation of the sprinkler system.

The temperature fluctuation at the crest and Northern flank is shown in Figure 5.22c, again showing a damped environmental response with depth. Recorded maxima during Summer 2015 are lower at all depths than those recorded on the Southern flank. On the crest, at 1.0 m, the maximum Summer temperature is reached two weeks later than at the other sensors positions, suggesting a mechanism for aspect-related damping.

In Figure 5.21e and Figure 5.22d, the corresponding time series resistivity data are provided. These data support the trends inferred above regarding the structure and hydrology of the embankment. Winter increases in volumetric water content are accompanied by decreases in resistivity at all depths on the Southern flank (as shown on a logarithmic scale), with the greatest variations observed in the near-surface, again, an effect which is progressively damped with depth. At 1.0 m, increases in recorded values have a range of up to three orders of magnitude, which is likely indicative of poor contact between the electrode and the surrounding soil, as a result of low water contents, and a porous topsoil. In general, the resistivity data correlate very well with the water content data, such that datasets ranked in terms of increasing water content correspond to an inverse (decreasing) ranking of resistivity values, which is encouraging for the development of proxy relationships. On the crest and Northern flank, near-constant water content values are accompanied by very little variation in subsurface resistivity, such that linear (rather than conventional logarithmic) axes are used. At greater depths within the embankment crest (1.0 m), resistivity remains entirely constant, indicating that the sensor is not functioning properly.

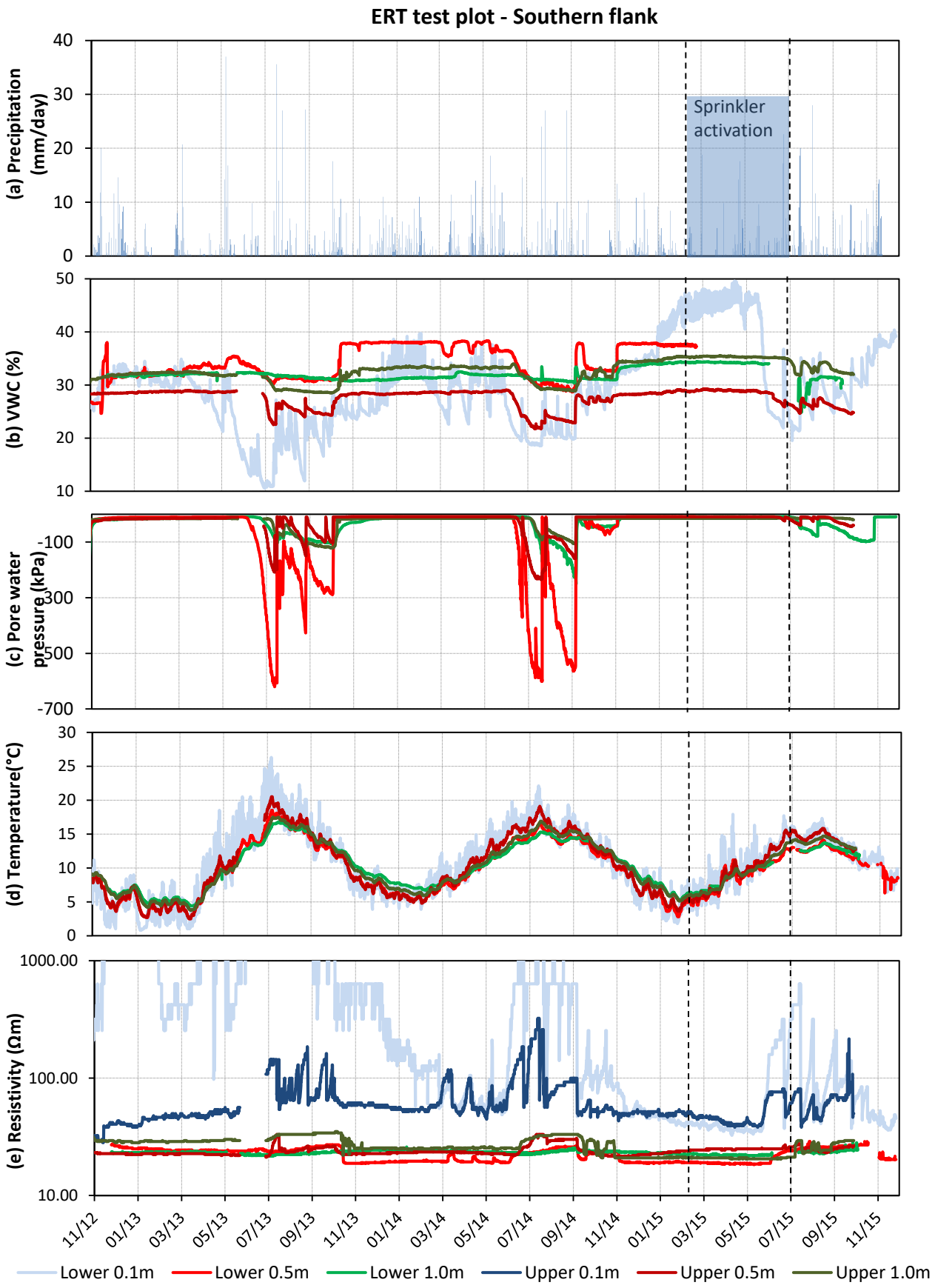

Figure 5.21 Time series geotechnical data – ERT test plot – Southern flank, showing (a) precipitation; (b) volumetric water content; (c) pore water pressure; (d) temperature; (e) resistivity. Note, the Lower and Upper positions relate to positions a1 and a2 respectively, on the sensor distribution map in Figure 4.39. Shaded area on (a) represents 33 mm per day artificial rainfall imparted using the sprinkler system

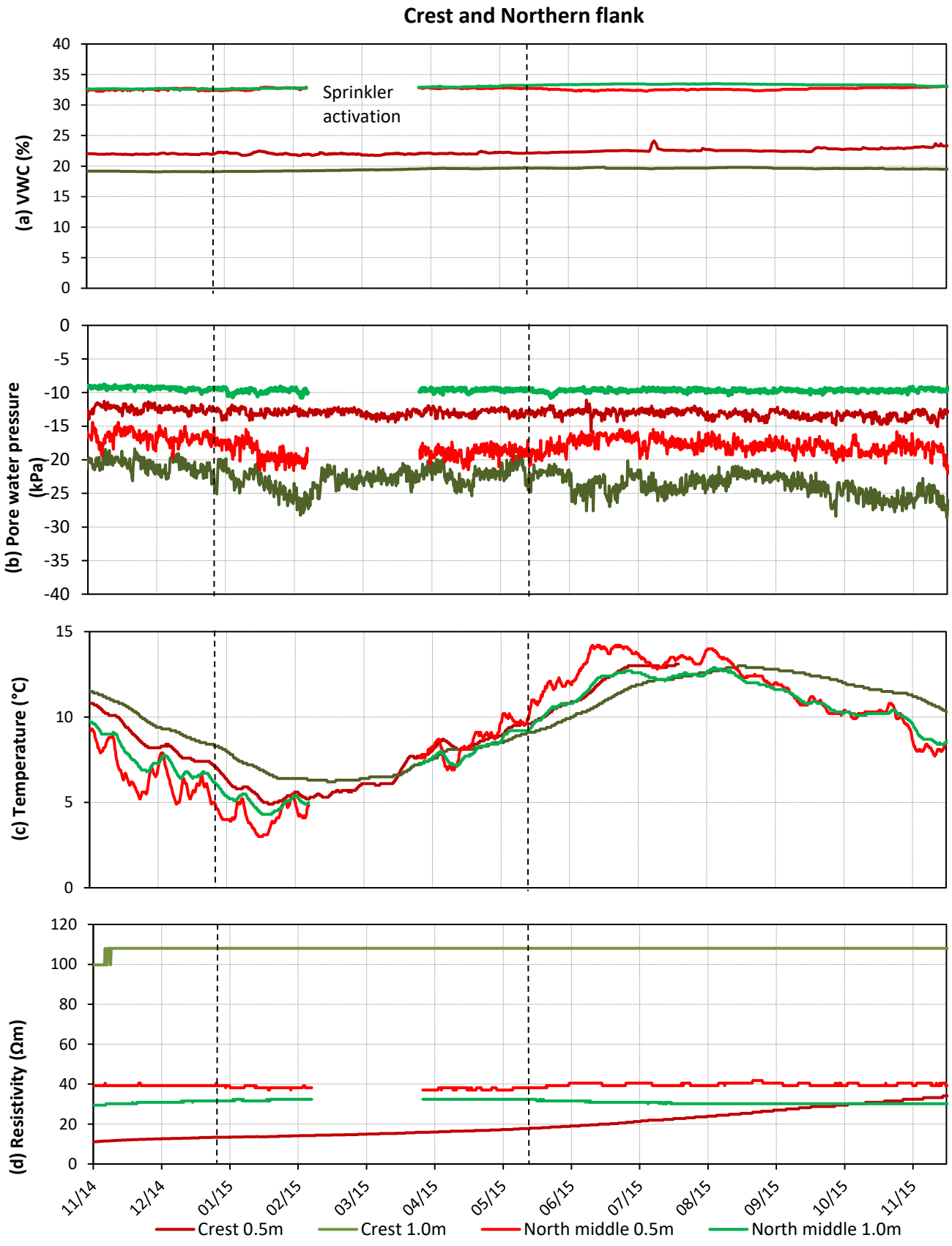

Figure 5.22 Time series geotechnical data – ERT test plot – Crest and Northern flank, showing (a) volumetric water content; (b) pore water pressure; (c) temperature; (d) resistivity. Note, the Crest and North middle positions relate to positions a6 and a7 respectively, on the sensor distribution map in Figure 4.39. Crest depths are taken from the bottom of the ballast. Note, data missing from February to April 2015 due to logger malfunction at North middle position

All of the above observations pertain only to the ERT survey portion of the test embankment, and clearly demonstrate a response to environmental forcings which is progressively damped with depth. There is some evidence for an environmental response which varies with both aspect and degree of compaction (observed from higher suctions at lower porosities). These are investigated further using data gathered at other parts of the test embankment.

Aspect comparison

In the following graphs, time series geotechnical data are used to investigate the role of aspect on the hydrodynamic response to environmental forcings. To this end, each graph presents data collected at mirrored positions on the North and South-facing slope flanks.

Figure 5.23 presents time series geotechnical data gathered at the upper position on the Northern and Southern embankment flanks, at depths of 0.5 and 1.0 m. From Figure 5.23a, it can be seen that the greatest variations in water content occur at 0.5 m depth on the Southern flank, showing seasonal maxima and minima of 44 and 12 %, respectively, with considerable diurnal fluctuation. At the same depth on the Northern flank, seasonal maxima and minima are 41 and 17 %, exhibiting very little diurnal fluctuation. A similar observation can also be made at 1.0 m depth, suggesting that the geotechnical response to environmental forcings is more pronounced on the Southern flank. At 0.5 m depths at both the upper and lower positions (Figure 5.24a), the Southern flank appears wetter than the Northern in the winter months, but then dries out more during the summer months, describing the near-surface Southern flank as more hydrodynamically active than the Northern. At greater depth, the Northern flank is generally wetter than the Southern, at all times of the year.

Figure 5.23b and Figure 5.24b show the corresponding pore water pressures, clearly demonstrating the development of considerable suctions in the Southern flank as the embankment fill rapidly becomes drier than that of the Northern flank. A time lag is observed between the development of these suctions, first registering at the Southern flank and then at the Northern flank up to two weeks later – this offset is more pronounced in the near-surface (0.5 m depth).

The corresponding temperature data are presented in Figure 5.23c and Figure 5.24c, both showing similar amplitudes of fluctuation between the two flanks, but offset such that maximum temperatures occur on the Southern flank – this offset is greatest at 0.5 m, at the upper position.

In summary, the above observations point towards the Southern flank being more hydrodynamically variable than the Northern, both in the near-surface and at greater depth. Within the Southern flank, data gathered at the upper slope position shows the greatest seasonal and diurnal variability.

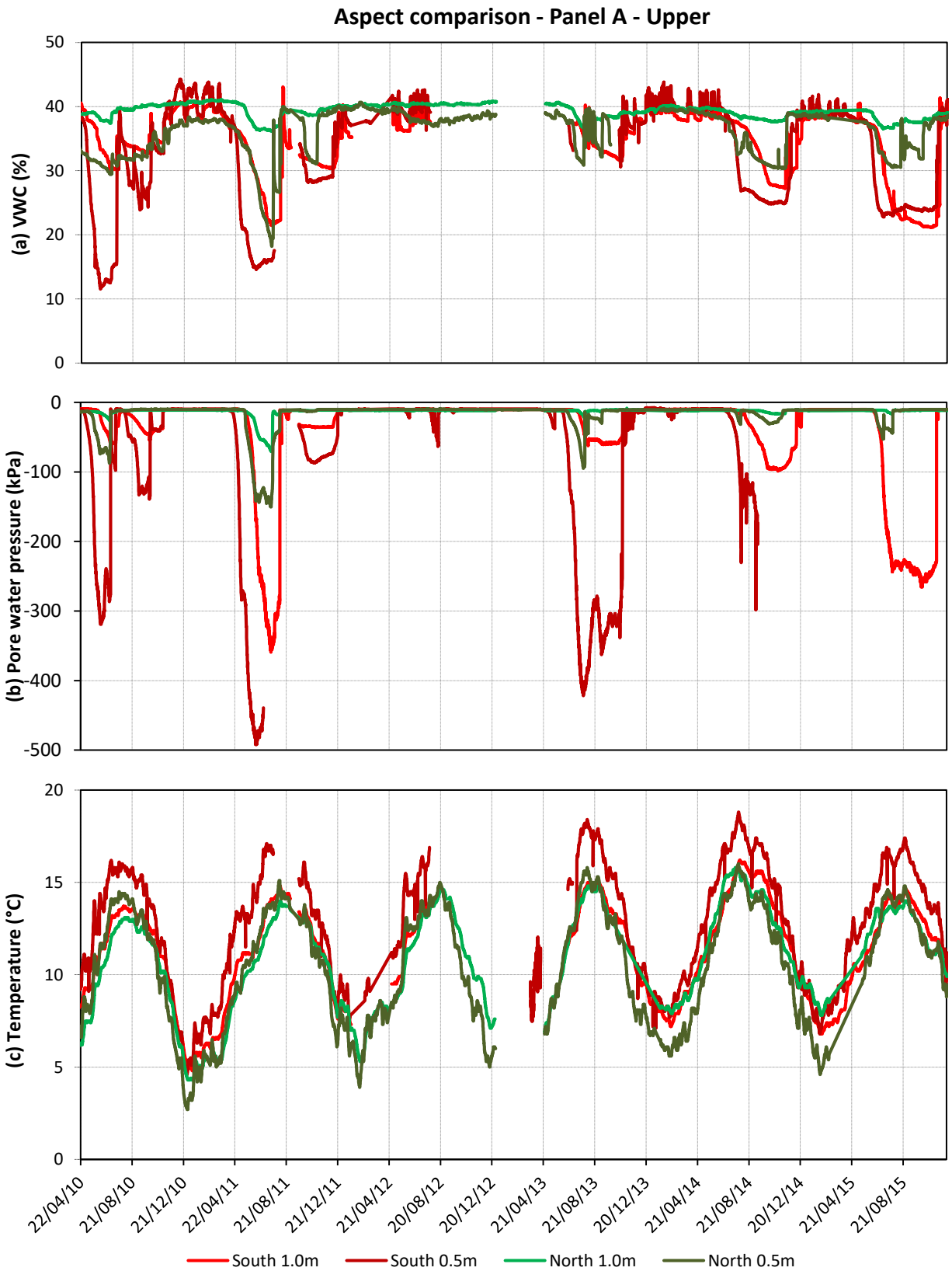

Figure 5.23 Time series geotechnical data – Aspect comparison - Panel A Upper positions, showing (a) volumetric water content; (b) pore water pressure; (c) temperature. Note, the North and South Upper positions relate to positions MP3 and MP7 respectively, on the sensor distribution map in Figure 4.39. Note, data missing from December 2012 to April 2013 due to logger malfunction

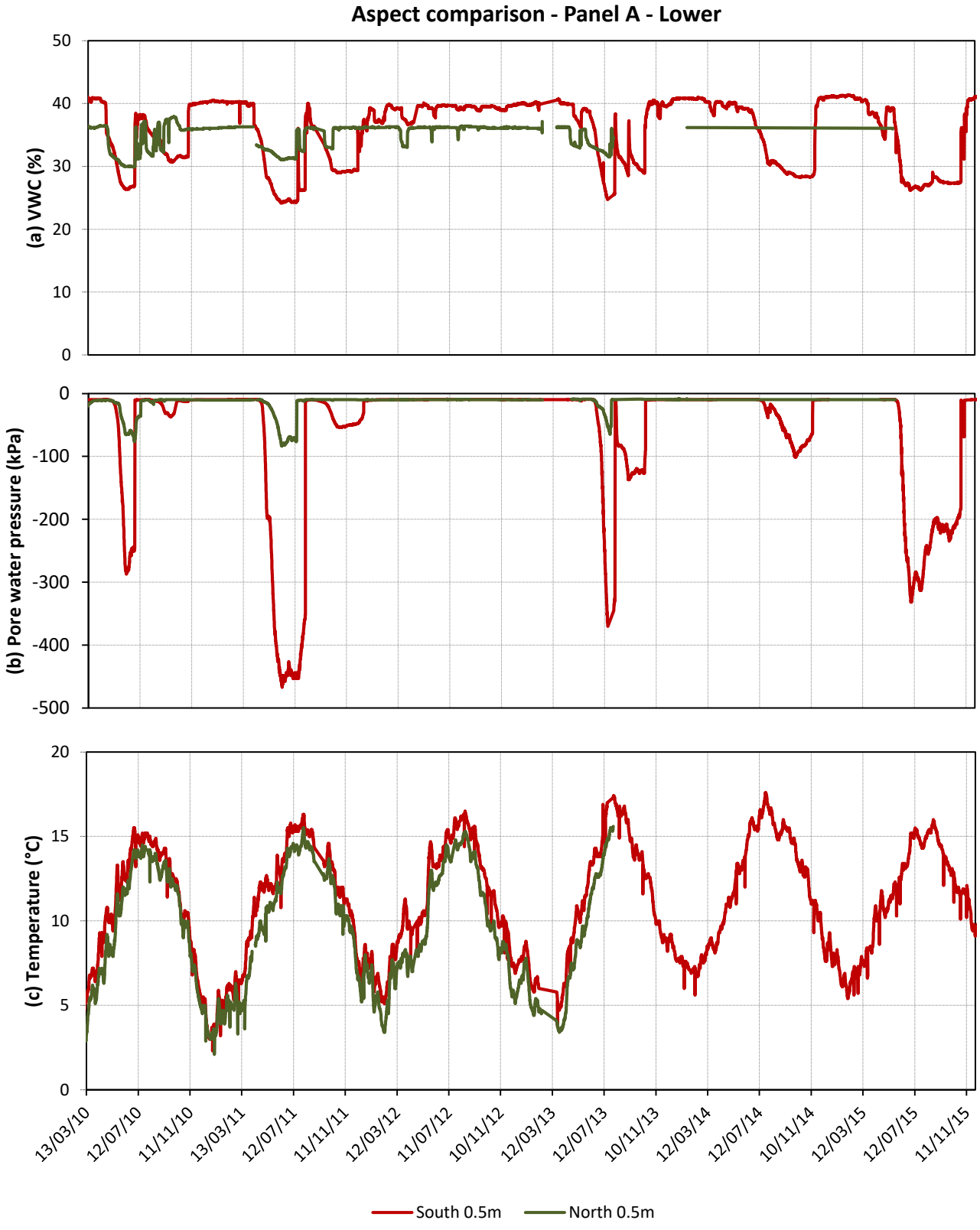

Figure 5.24 Time series geotechnical data – Aspect comparison - Panel A Lower positions, showing (a) volumetric water content; (b) Pore water pressure; (c) Temperature. Note, the North and South Lower positions relate to positions MP1 and MP9 respectively, on the sensor distribution map in Figure 4.39

Degree of compaction comparison

In addition to investigating the effects of depth and aspect on geotechnical parameters, the effects of compaction were considered. This was achieved by comparing moisture data gathered at Panel A (built to "uncompacted" specifications), Panel B ("compacted") and the ERT test plot. Note, Panel B and the ERT test plot were built to the same specifications, and therefore should, in theory, have similar degrees of compaction. Due to the fact that most Panel B point sensors were installed over the course of Summer 2014, the Panel B datasets presented span much shorter time periods.

Figure 5.25 presents time series moisture data gathered at the upper and lower positions on Panels A and B, and the ERT test plot. Figure 5.25a and c (showing water content at the upper positions at depths of 0.5 and 1.0 m respectively) demonstrate higher winter water contents on Panel A with respect to the ERT test plot. This is in keeping with Panel A having a higher porosity, due to a lesser compactive effort, and is therefore able to retain more moisture. It can also be seen from both figures that Panel A demonstrates more diurnal fluctuation of water content than the ERT test plot, which, as before, is in keeping with it having a higher porosity. When considering Panel B, however, mean winter water content values are unexpectedly higher (approximately 41 % at both 0.5 and 1.0 m depths) than those of Panel A and the ERT test plot. Additionally, at 0.5 m depth, Panel B exhibits extreme diurnal fluctuation. These observations suggest that the degree of compaction at Panel B may be lower than previously thought.

Corresponding pore water pressures (Figure 5.25 b and d) show that the greatest recorded suctions (at both depths) occur in Panel A, and the lowest in Panel B. These suctions appear to develop more rapidly at the ERT test plot than at Panel A, where they persist for longer.

In summary, the above observations of Panel A ("uncompacted") and the ERT test plot demonstrate increased porosity resulting from a lower degree of compaction, allowing the fill to retain more moisture. This increased porosity then results in higher suctions, due to a higher matric suction as pore water is under a greater stress due to greater separation between soil particles. However, observations at Panel B, which was thought to be more compacted than Panel A, suggest that it may have a comparable porosity.

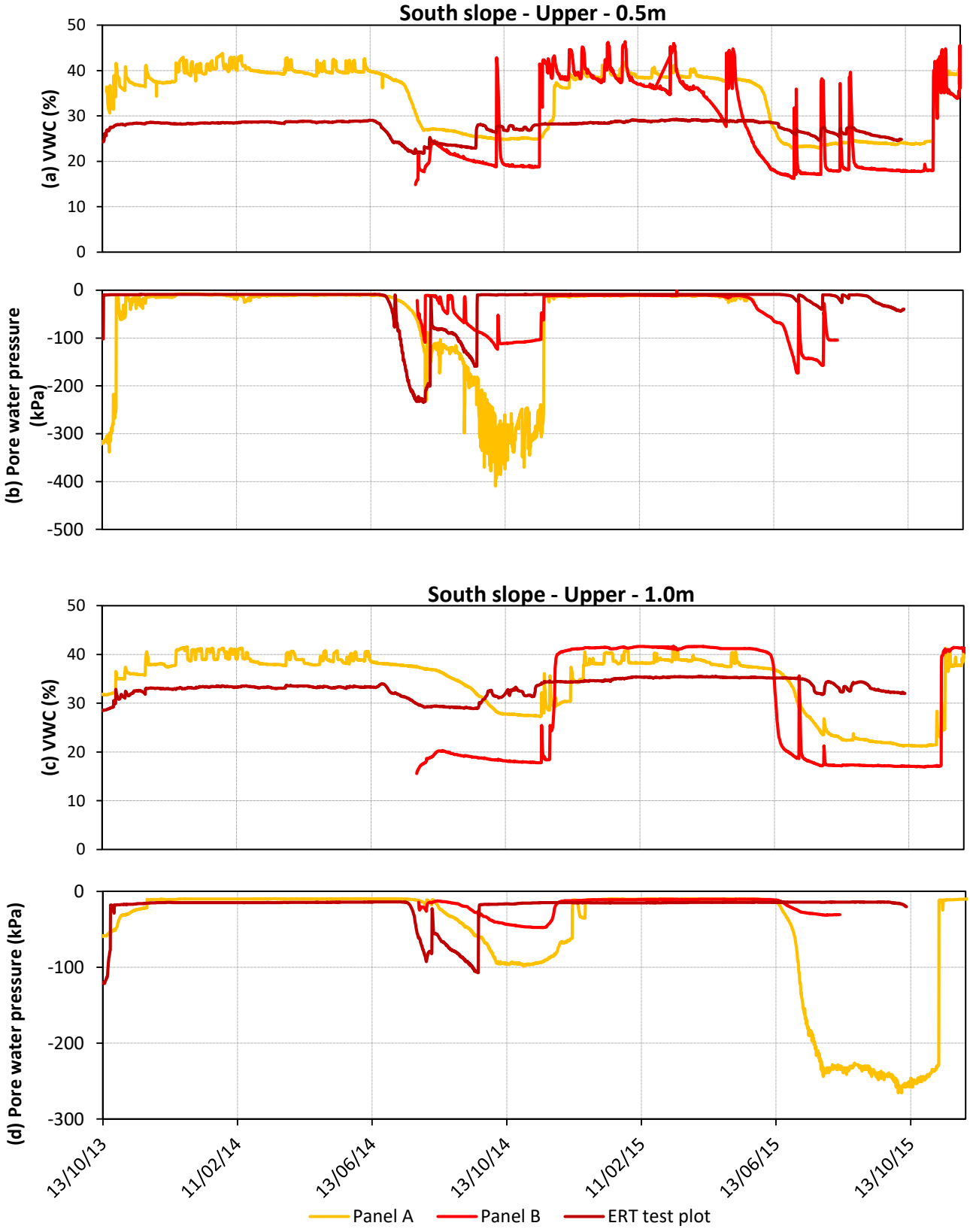

Figure 5.25 Time series geotechnical data – Degree of compaction comparison, showing (a) volumetric water content at 0.5 m; (b) pore water pressure at 0.5 m; (c) volumetric water content at 1.0 m; (d) pore water pressure at 1.0 m. Note, the South Upper positions on Panels A, B and the ERT test plot relate to positions MP3, B3 and a2 respectively, on the sensor distribution map in Figure 4.39

5.2.2 *Soil water retention curves*

In the previous subchapter, time series pore water pressure and water content data were presented. In the following, these data are presented as a soil water retention curves, extracted from periods during which the embankment was undergoing drying. These periods are illustrated in Figure 5.26, showing time series moisture data gathered at the lower position at Panel A, where considerable reductions in water content (resulting in the development of suctions) describe a total of nine drying cycles. Drying curves only are presented, due to the fact that drying occurs very gradually (over the course of the summer months), allowing many data points to be obtained, whereas as wetting occurs very rapidly (days).

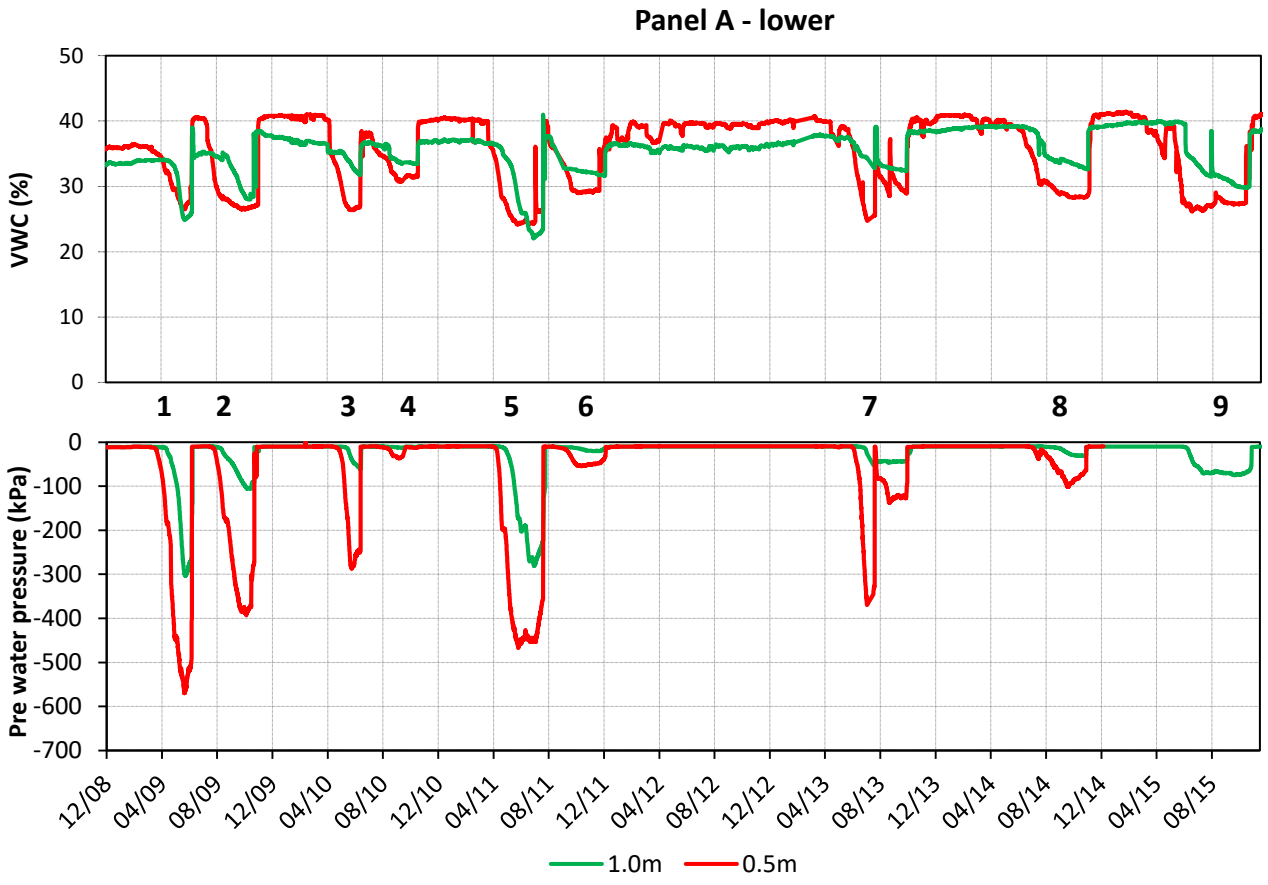

Figure 5.26 Times series moisture data from Panel A – lower position (position MP1 on the sensor distribution map in Figure 4.39)

Point sensors installed at the upper and lower positions on the Southern flank of panel A were used to construct the SWRCs, as they have been in place the longest, and therefore provide the longest-running soil water retention datasets. The fitted laboratory-derived Van Genuchten curves (as shown in Figure 5.1) are shown for the basis of comparison.

From all four curves (Figure 5.27 and Figure 5.28, a and b), it can be seen that the initial drying curve (Cycle 1) follows a path in reasonable agreement with the laboratory-derived Van Genuchten drying curve. This fit is best at 1.0 m depth in the upper position (Figure 5.27b), suggesting that the laboratory specimens were most representative of this portion of the test embankment. All subsequent drying curves, however, plot beneath the Cycle 1 drying curve, nearer the laboratory-derived Van Genuchten wetting curve. This observation describes a progressive loss of suction for ongoing seasonal drying cycles, similar to that characteristic of the drying and wetting portions of the SWRC as described in subchapter 2.2.4. This effect is more gradual in the upper position (Figure 5.27) which demonstrates a progressive suction loss between Cycles 1, 2 and 3. Hereafter, the drying curves follow an approximately consistent residual path (clearest from Figure 5.27b which illustrates a greater number of Cycles). At 0.5 m depth at the lower position, all secondary drying curves follow the residual drying path. At 1.0 m, the difference between the initial and secondary drying curves is less pronounced, all demonstrating soil water retention behaviour in close agreement with the laboratory-derived Van Genuchten wetting curve.

The above observations describe a progressive loss of suction for ongoing seasonal moisture cycling in the field, which may suggest some type of soil fabric degradation.

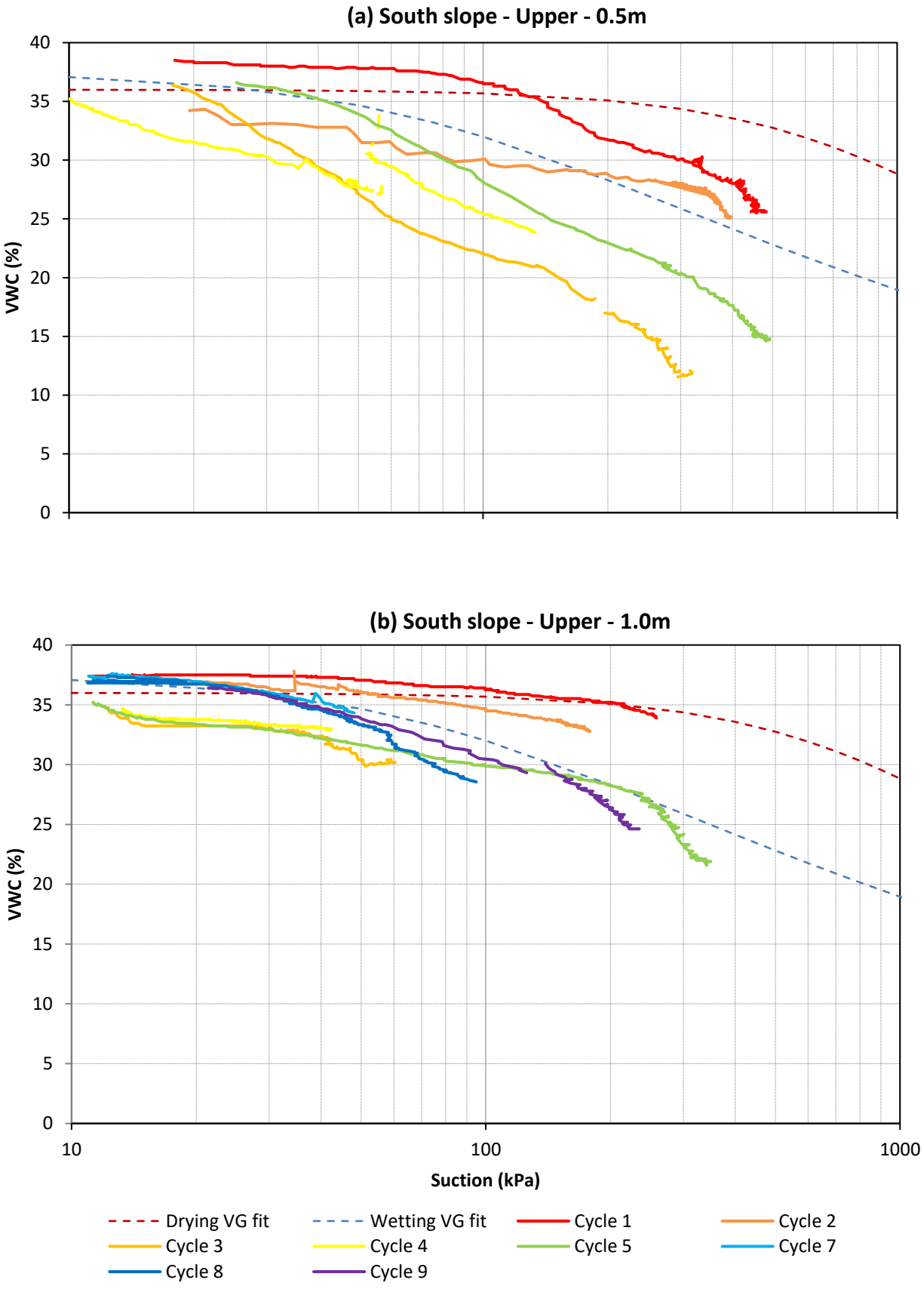

Figure 5.27 Soil water retention curve for Panel A South slope – upper position, at (a) 0.5 m, and (b) 1.0 m. Note, Panel A South Upper position relates to position MP3 on the sensor distribution map shown in Figure 4.39

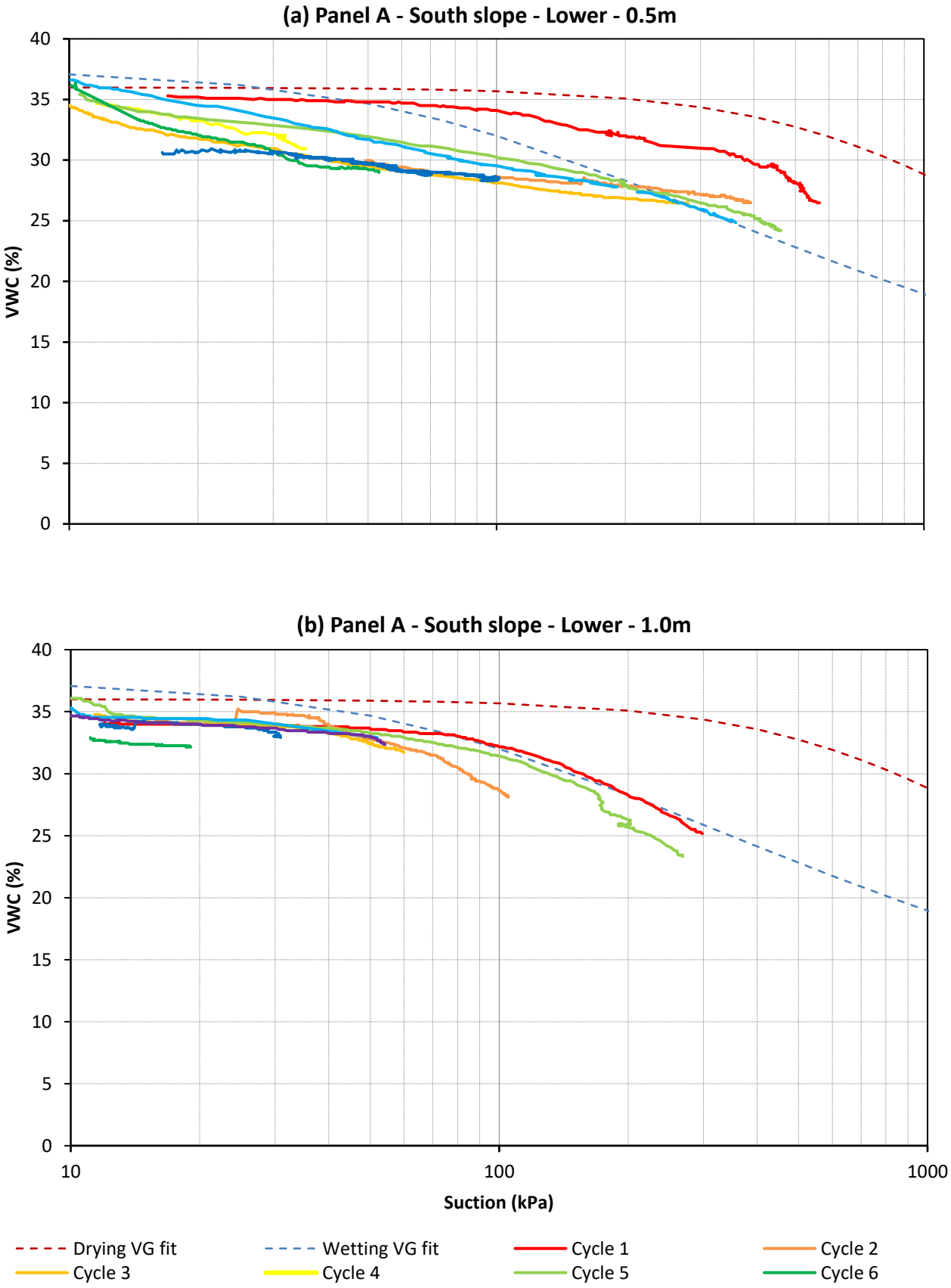

Figure 5.28 Soil water retention curve for Panel A South slope – lower position, at (a) 0.5 m, and (b) 1.0 m. Note, Panel A South Lower position relates to position MP1 on the sensor distribution map shown in Figure 4.39

5.2.3 *Resistivity – water content relationships*

In the following figures, the relationship between resistivity and water content is presented, gathered from the point sensor network at the BIONICS embankment using Decagon 5TE sensors, which make two point resistivity measurements. Laboratory-derived resistivity-water content relationships are presented as a basis for comparison, including both two and four point resistivity – water content curves (pertaining to Figure 5.5 and Figure 5.11 respectively). Note, crest depths are taken from the top of the fill material, beneath the ballast.

Figure 5.29a and b present data collected on the Southern flank of the ERT test plot and Panel B, respectively, at the crest, upper and lower slope positions. From Figure 5.29b, it can be seen that at 0.1 m at the upper position, the resistivity – water content curve demonstrates resistivity values considerably higher than at other depths, likely the result of near-surface cracking impeding current flow. In general, most of the curves are of an inverse power nature, in closer agreement with the four point laboratory-derived curve than the two point curve. This observation may be a function of improved contact at the soil-electrode interface at depth in the field, than in the laboratory. At certain positions, however (0.5 m depth within the crest), the field resistivity – water content path deviates from the laboratory curve at 25 % (at the ERT test plot) and 22 % VWC (Panel B), which may indicate a break in the continuity of the pore water phase. At two locations within Panel B (0.5 m within the upper position, 1.0 m depth within the crest), the resistivity – water content curves follow steeper paths.

In summary, the resistivity – water content behaviour observed in the field from the point sensor network largely follow the four point laboratory-derived curve, despite being a two point measurement.

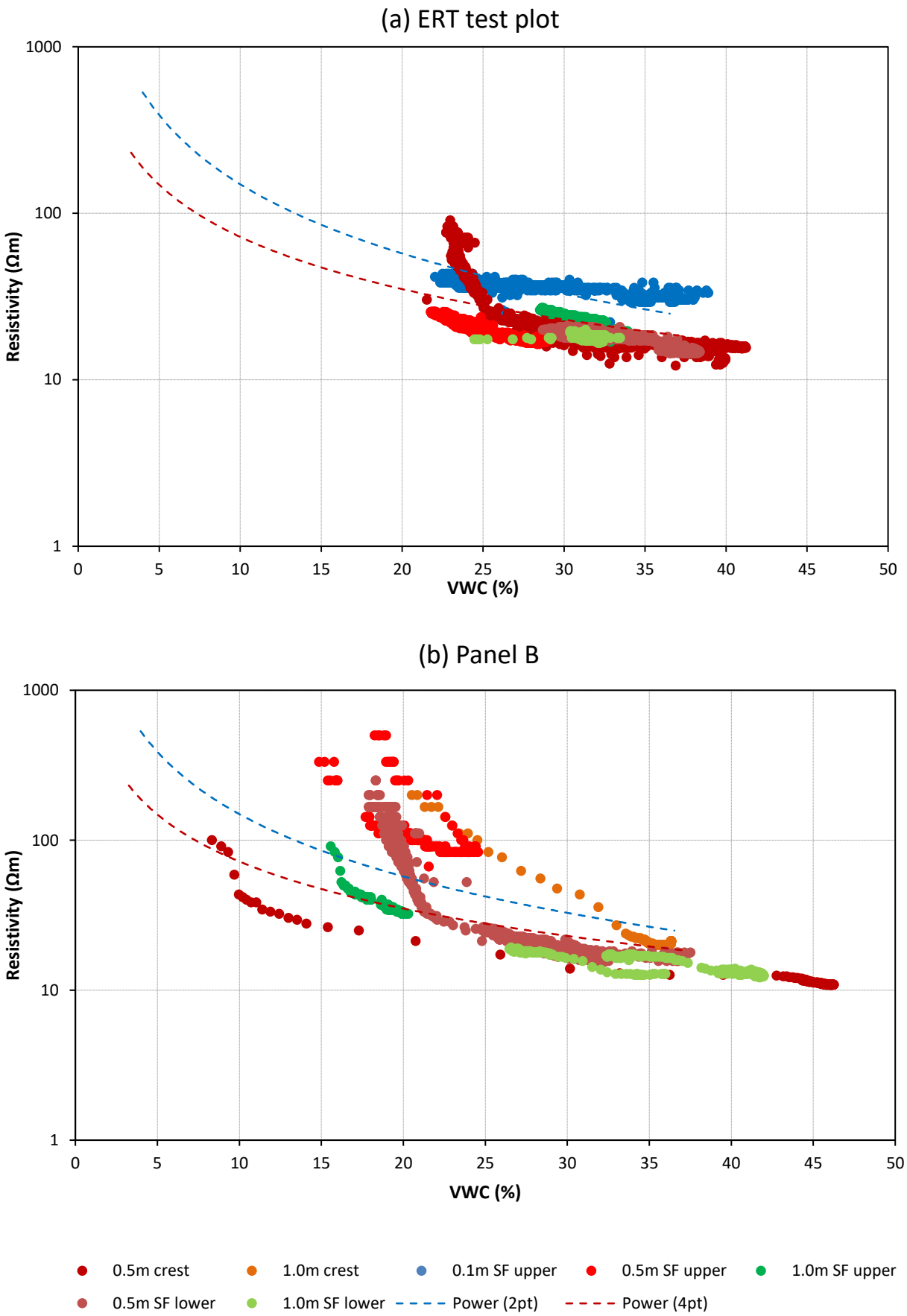

Figure 5.29 Field resistivity – water content relationship (point sensors), showing data collected at (a) the ERT test plot and (b) Panel B. Refer to sensor distribution map shown in Figure 4.39

5.3 ERT-derived results

The following subchapter contains the results of the electrical resistivity tomography monitoring programme at the BIONICS embankment, over the course of three years, starting from June 2013 when data collection began. The availability of data was largely constrained by problems relating to data collection (as detailed later in subchapter 6.3.4), and therefore, for certain periods, reduced amounts of data are presented. All ERT data presented have been temperature-corrected following the procedure outlined in subchapter 4.3.6. Three types of property distribution image are described: resistivity (pure ERT), water content (derived from the Waxman-Smits relationship) and soil suction (derived from the Van Genuchten relationship).

5.3.1 *2D imaging at three monthly intervals*

In order to establish general trends in the resistivity response of the Southern flank of the embankment to environmental factors, Figure 5.30 shows 2D ERT results made along line 5 (Y = 2.8 m, see Figure 4.47), at three-monthly intervals. These intervals relate to the start and end of summer drying (June and September respectively), and the intermediate stages of winter wetting (December and March), as established from the point sensor network. All images clearly show the high resistivity ballast capping layer (200 to 1000 Ωm), implying low water content, which is as expected due to its very high permeability. Directly beneath the ballast, all of the images show a low resistivity zone, approximately 2 m deep, caused by the infiltration of water through the ballast above. Beneath this low resistivity zone, the embankment core demonstrates higher resistivity values, between approximately 100 and 200 Ωm, implying lower water contents at depth. The most dynamic part of the embankment is the flank near-surface, within which the resistivity response to changing environmental factors is clearest; Figure 5.30a from mid-June 2013 (following heavy rainfall over the preceding 6 weeks) shows several low resistivity features, which may be explained by water infiltration into pre-existing cracks, which were observed from crack surveys undertaken in Summer 2013 and earlier (see subchapter 4.2.2). From Figure 5.30b (September 2013), it can be seen that these same features are now characterised by high resistivity values, implying that the cracks have dried out. By December 2013 (Figure 5.30c), approximately two months after the start of the winter wetting season, the cracks are no longer discernible, suggesting that they have healed, and much of the top 1 m of the

Southern flank demonstrates very low resistivity values, implying water contents near saturation. Three months later (Figure 5.30d, March 2014), this low resistivity zone is still present. Over the course of the following two years (Figure 5.30e to l), the same trends are broadly repeated, with the greatest change in resistivity distribution observed between September and December. Of the three September images (Figure 5.30b, f, j; 2013, 2014 and 2015, respectively), the latter shows the least evidence for the presence of cracks, likely resulting from the sprinkling experiments in the first half of that year, rendering the near-surface unseasonably wet, and inhibiting crack development.

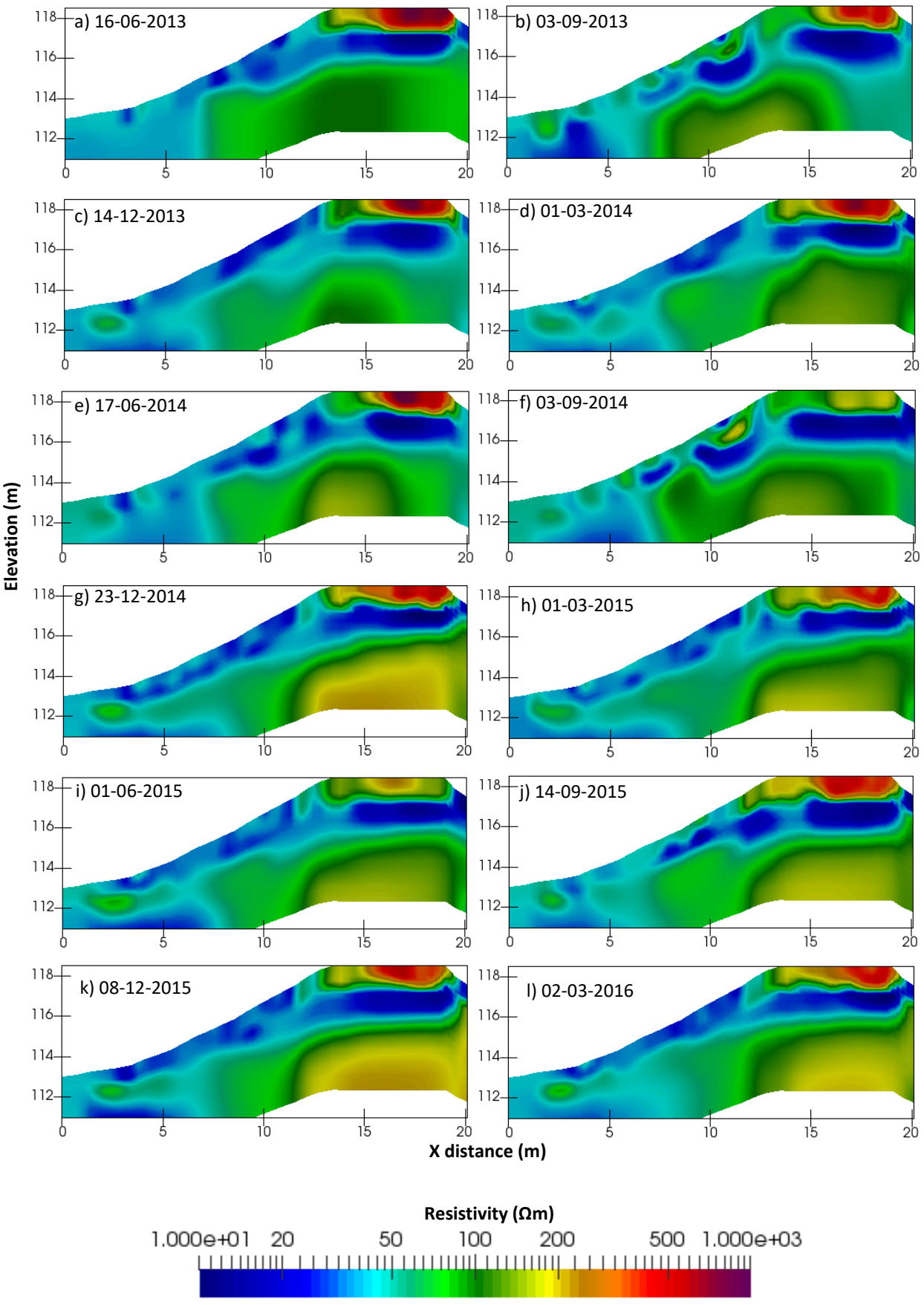

Figure 5.30 2D ERT images, at three monthly intervals (from line 5)

In order to illustrate which parts of the embankment demonstrate the greatest changes in resistivity over time, Figure 5.31 shows the resistivity standard deviation, derived from the twelve images shown in Figure 5.30. The highest standard deviations pertain to the ballast capping layer, resulting from its high permeability, such that its saturation state changes rapidly depending on atmospheric conditions. In the flank near-surface, a number of high deviation anomalies are illustrated by dashed black lines. These are suggested to correspond to the locations of cracks, which appear during the summer and heal during the winter. The upper four lines show where the cracks were manually extended in May 2014 (OS1-4, see subchapter 4.2.2); the uppermost shows the greatest standard deviations, suggesting increased drying and wetting compared to the other cracks. The lowermost, OS0, was not observed from crack surveys undertaken prior to 2013. Beneath the cracks, the embankment fill demonstrates considerably less variability. The least variability occurs beneath the ballast capping layer, particularly towards the Northern flank. The core of the embankment is characterised by high standard deviations, however, little change in resistivity is expected at such depths, and therefore, these values are likely a result of the loss of model resolution at depth (investigated further in subchapter 5.3.3).

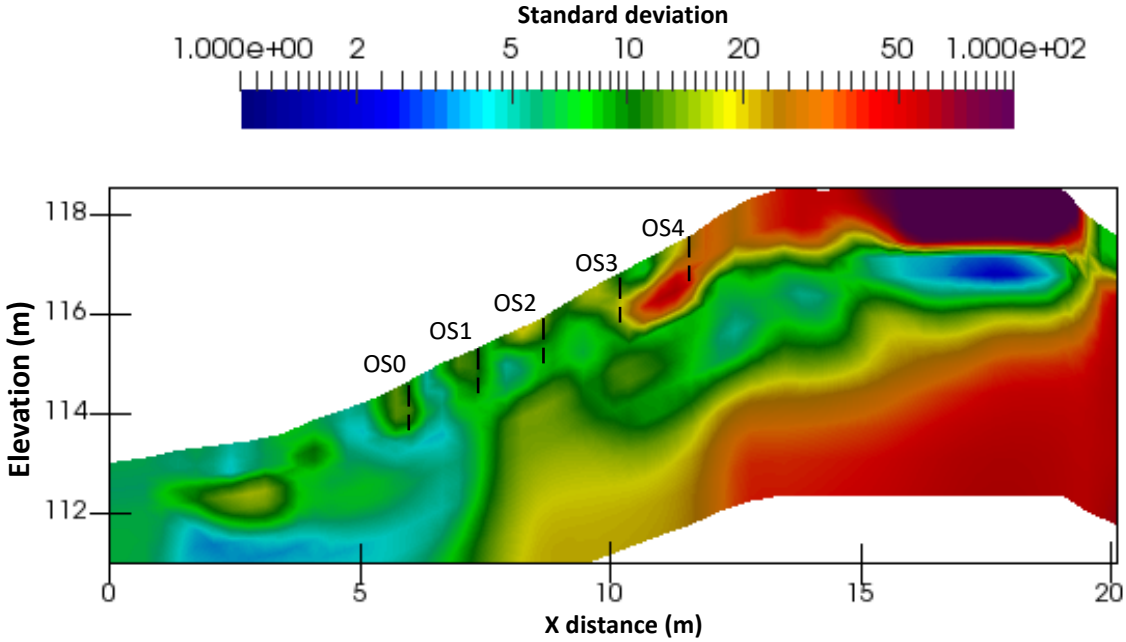

Figure 5.31 2D ERT Resistivity standard deviation over three year period (from line 5)

5.3.2 *3D Imaging at three monthly intervals*

2D ERT measurements (made along a single line) effectively work on the principal that the medium is invariant in the direction perpendicular to the profile (Gance et al., 2016). Therefore, in order to test how representative the 2D-cross sections are (Figure 5.30) 3D ERT images were made for same three month intervals (using data captured on dates as close as possible to those used in Figure 5.30), and cross-sections extracted for the same slice (Y = 2.8 m). These images are shown in Figure 5.32.

From all the images (Figure 5.32a to l), it is evident that the 3D cross-sections demonstrate far lower spatial and temporal change than the corresponding 2D images. They do, however, broadly show the same trends, including the presence of the high resistivity ballast capping layer, a low resistivity zone beneath the crest, and a dynamic near-surface flank. As before, the greatest change occurs between September and December, except in 2015 following the sprinkling experiments. These cracks are clearest in Summer 2014 (Figure 5.32e and f), although evidence for such cracks is, in general, a lot less clear in from the 3D cross-sections, which show them extending to a depth of approximately 0.5 m (with exception of Figure 5.32a, which may show cracking as deep as 1 m). Beneath these, the low resistivity, near-saturation zone extends to a depth of between 1 and 1.5 m. In addition to these differences in the near-surface resistivity distribution between 2D and 3D ERT slices (Figure 5.30 and Figure 5.32, respectively), there are considerable differences at depth: the boundary between the conductive zone beneath the crest and the embankment core is less defined, with the core demonstrating values of resistivity which are considerably lower than from the 2D (in the range of 25 to 35 Ωm, rather than 100 to 200 Ωm in Figure 5.30).

In Figure 5.33, the standard deviations for the slice and for the entire embankment are shown (a solid black line indicates the location of the slice extracted in Figure 5.32). On Figure 5.33a, contours highlight three main zones, characterised by low (L), medium (M) and high (H) standard deviations. As before, the highest standard deviations are observed across the ballast crest. Near the surface of the flank, the top 0.75 m show high deviations, suggesting dynamic temporal behaviour, relating to rapid seasonal drying and wetting. Beneath this, much of the embankment fill demonstrates medium standard deviations, describing a resistivity response to environmental factors which is damped with depth. Two low deviation zones exist, including the embankment core, where little resistivity change over time is expected, as well as a zone on the flank. The presence of medium standard

deviations between these two zones may be evidence of water infiltration between them. From Figure 5.33b, it can be seen that the entire ground surface of the Southern flank is characterised by high standard deviations, which do, approximately, correspond to the locations of the cracks described previously, delineated by dashed lines.

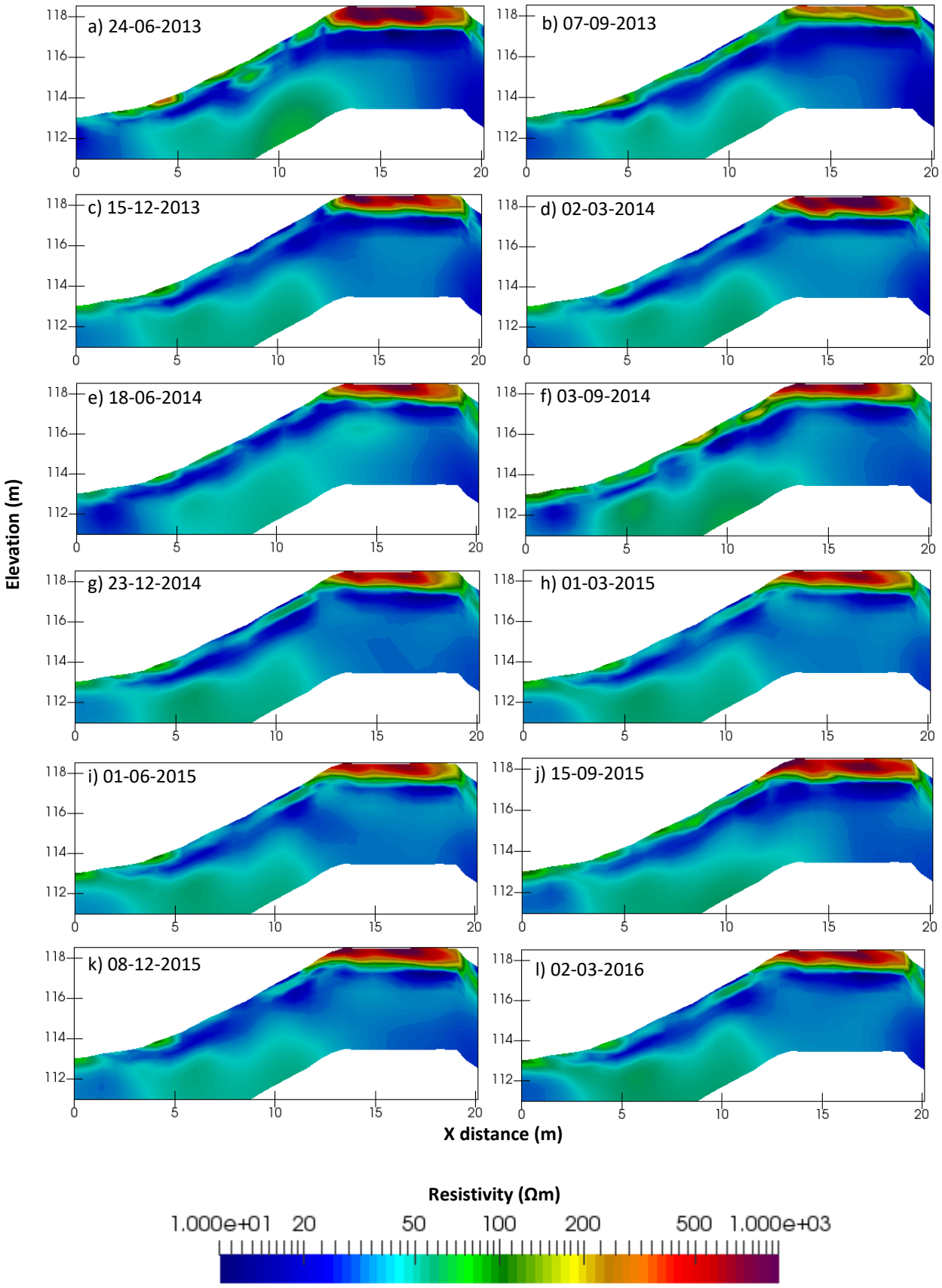

Figure 5.32 3D ERT images, at three-monthly intervals (extracted along line 5)

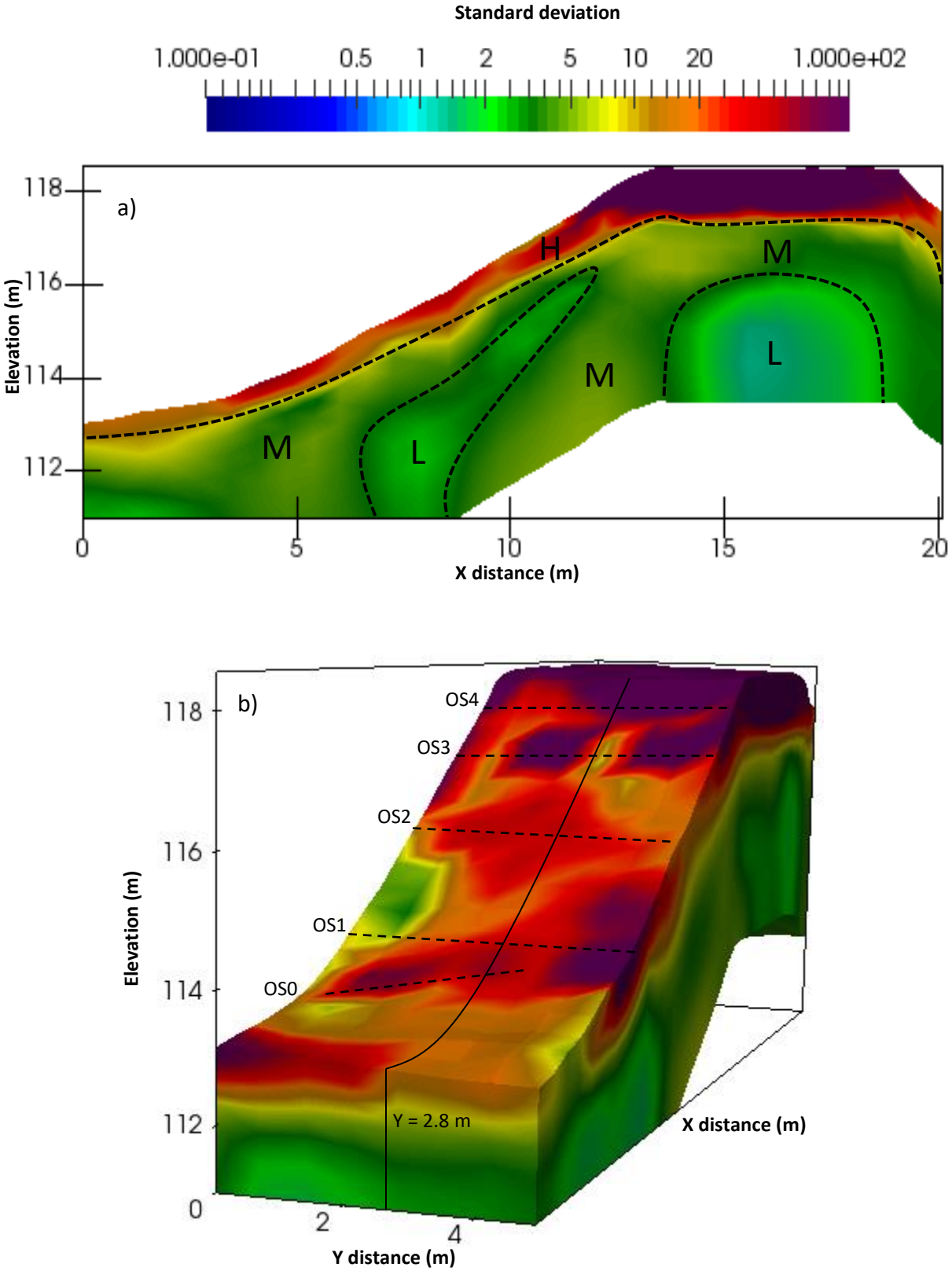

Figure 5.33 3D ERT Resistivity standard deviation over three year period, showing (a) slice extracted along line 5, and (b) volumetric image of ERT test plot

5.3.3 *Comparison of 2D and 3D sensitivity distributions*

Figure 5.34a and b show the model sensitivity distribution of the embankment beneath line 5 corresponding to the data presented in Figure 5.30 and Figure 5.32, respectively. It is evident that the 3D model shows better sensitivity at all depths than does the 2D model. For this reason, ERT monitoring at the embankment became focussed on 3D ERT imaging rather than 2D profiling. For the most part, subsequent ERT data are presented following the same approach as in Figure 5.32, to extract a slice along the line Y = 2.8 m (line 5), for two reasons: firstly, because nearer the middle of the embankment, the ERT data points will be least affected by 3D resistivity anomalies outside of the ERT array; and secondly, because cross-sectional slices rather than volumetric images allow resistivity variations in the embankment fill to be more clearly illustrated.

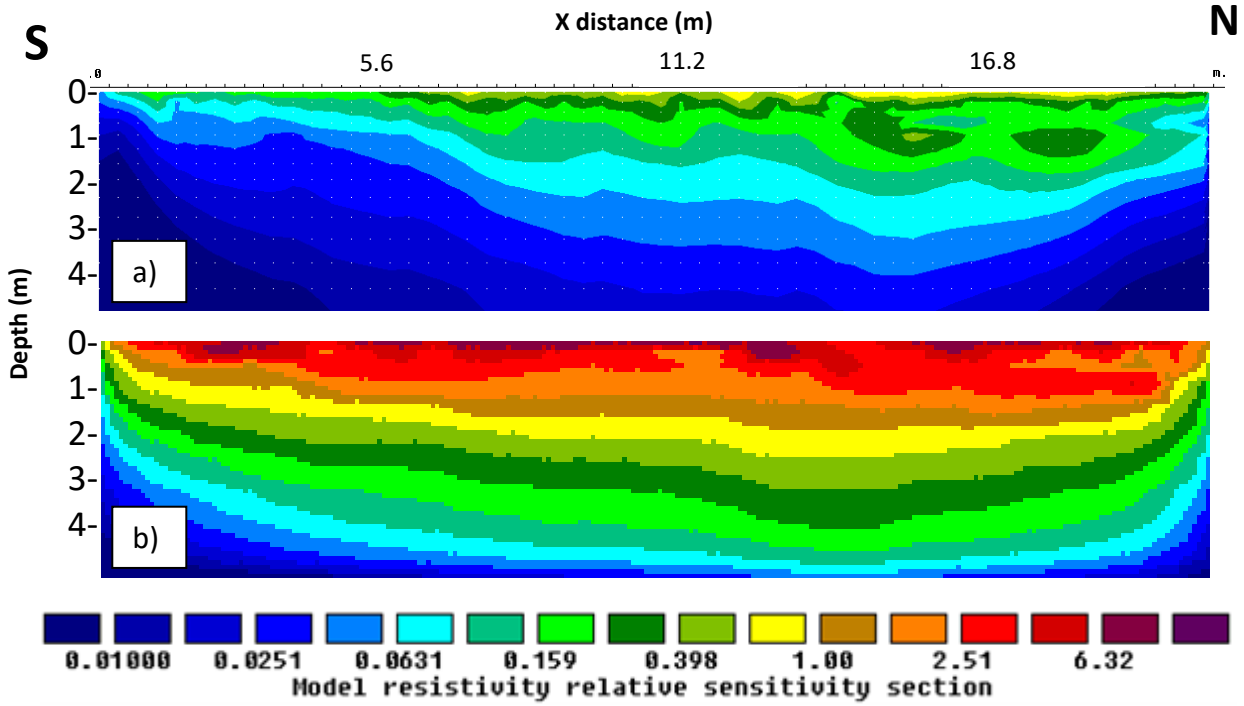

Figure 5.34 2D and 3D ERT model sensitivity distributions showing (a) 2D model sensitivity along line 5, and (b) 3D ERT model sensitivity distribution extracted along line 5

5.3.4 *Conversion of ERT data to water content and suction*

Using the methodology described in subchapter 4.3.8, the 3D ERT data shown in Figure 5.32 were converted to water content using the porosity model shown in Figure 4.54, and the Waxman-Smits curve shown in Figure 5.13. In Figure 5.35, these data are presented in terms of gravimetric water content. These images were then converted to suctions (Figure 5.36)

following the methodology described in subchapter 4.3.9, employing the Van Genuchten parameters described in Table 5.1.

Using these images, it is possible to begin to describe the hydrodynamic behaviour of the BIONICS embankment subjected to environmental forcings, in a quantitative, rather than qualitative manner as with the resistivity images shown in Figure 5.32. From Figure 5.35, the general trends described in subchapters 5.3.1 and 5.3.2 may be observed. Note, that the granular ballast capping layer is excluded from calculation of water contents, as it is composed of different material to that used in the laboratory tests, and therefore the established Waxman-Smits relationship does not apply.

From all the dates shown, it is clear that the most saturated part of the embankment is beneath the permeable ballast layer, showing gravimetric water contents in excess of 30 %, suggesting saturated fill. Figure 5.35a, (June 2013) following a particularly wet spring, shows this zone extending the full width of the crest. Following drying over the course of Summer 2013, the depth and horizontal extent of this saturated zone is reduced, with a high moisture concentration towards the Northern portion. This predisposition towards the North is repeated over the course of the following years, and suggests either preferential inflow of water across the Northern portion of the crest ballast, poorer drainage, or less evapo-transpiration. Surprisingly, despite the sprinkling experiments which took place from January to June 2014, Figure 5.35h and i show this near-saturation zone to occupy the least volume; this is investigated further in subchapter 5.3.6 which includes a description of the results of the sprinkling experiments specifically.

All of the images show a highly dynamic flank near-surface, with water contents of approximately 10 % in September 2014 (Figure 5.35f). This zone extends from the flank surface to a depth of approximately 0.2 m, corresponding to the topsoil layer. It can be seen that there is a tendency for moisture to gather in particular at two locations on the flank surface, which is shown most clearly in Figure 5.35g (December 2014), demonstrating water contents of up to 30 %. This observation suggests water infiltration into pre-existing cracks, and is clearest in September 2014 likely due to the manual extension of these cracks in May 2014 (as described in subchapter 4.2.2). Although there are up to five known cracks on the South flank, these two may extend deeper than the others.

Beneath the flank near-surface layer, a relatively high-moisture zone exists, with a predisposition for moisture to collect in two principal locations, again, most clearly observed from Figure 5.35g, but generally evident throughout both the drying and wetting seasons. This observation suggests preferential infiltration to these locations, and/or poor drainage from them. Within these two locations, water contents vary seasonally between approximately 25 % in June 2014 and 30 % in December 2014 (Figure 5.35e and g, respectively). The embankment core demonstrates very little change in water content over time, as is expected due its depth and assumed lower porosity, exhibiting water contents of between 15 and 18 %. At flank depths greater than 2 m, very low water contents are observed, of between 10 % and 14 %, with little seasonal variation. It appears that in the middle of this zone (X = 7.5 m), water contents are slightly higher (up to 15 %), suggesting preferential water infiltration.

In subchapter 5.4, the estimated water contents using this proxy-based method are compared to those measured using the point sensor network at the BIONICS embankment.

In Figure 5.36, the inferred subsurface suction distribution is shown (note, suctions in the crest are not representative as they are not described by the laboratory-derived Waxman-Smits relationship). Solid logarithmic contours characterise the range of inferred soil suctions by order of magnitude. These values are derived from the Van Genuchten curve presented in Figure 5.1, which describes negative pore water pressures only. Therefore, positive pore pressures cannot be quantitatively estimated using these figures, however, regions coloured dark blue may be assumed to be saturated as they demonstrate suctions approaching 0 kPa.

The trends described above are further reinforced from Figure 5.36, showing very low suctions beneath the ballast crest, with a predisposition for these to be concentrated towards the North. High suctions are observed in the flank topsoil (of the order of 10^4 kPa), which may delineate cracking features, especially visible in September 2014 (Figure 5.36f). Beneath the topsoil, suctions are generally of the order of 10^2 kPa, but with localised lenses demonstrating very low suctions, corresponding to the two high moisture zones described above. At depth, the Southern flank and embankment core demonstrate suctions of the order of 10^2 to 10^3 kPa.

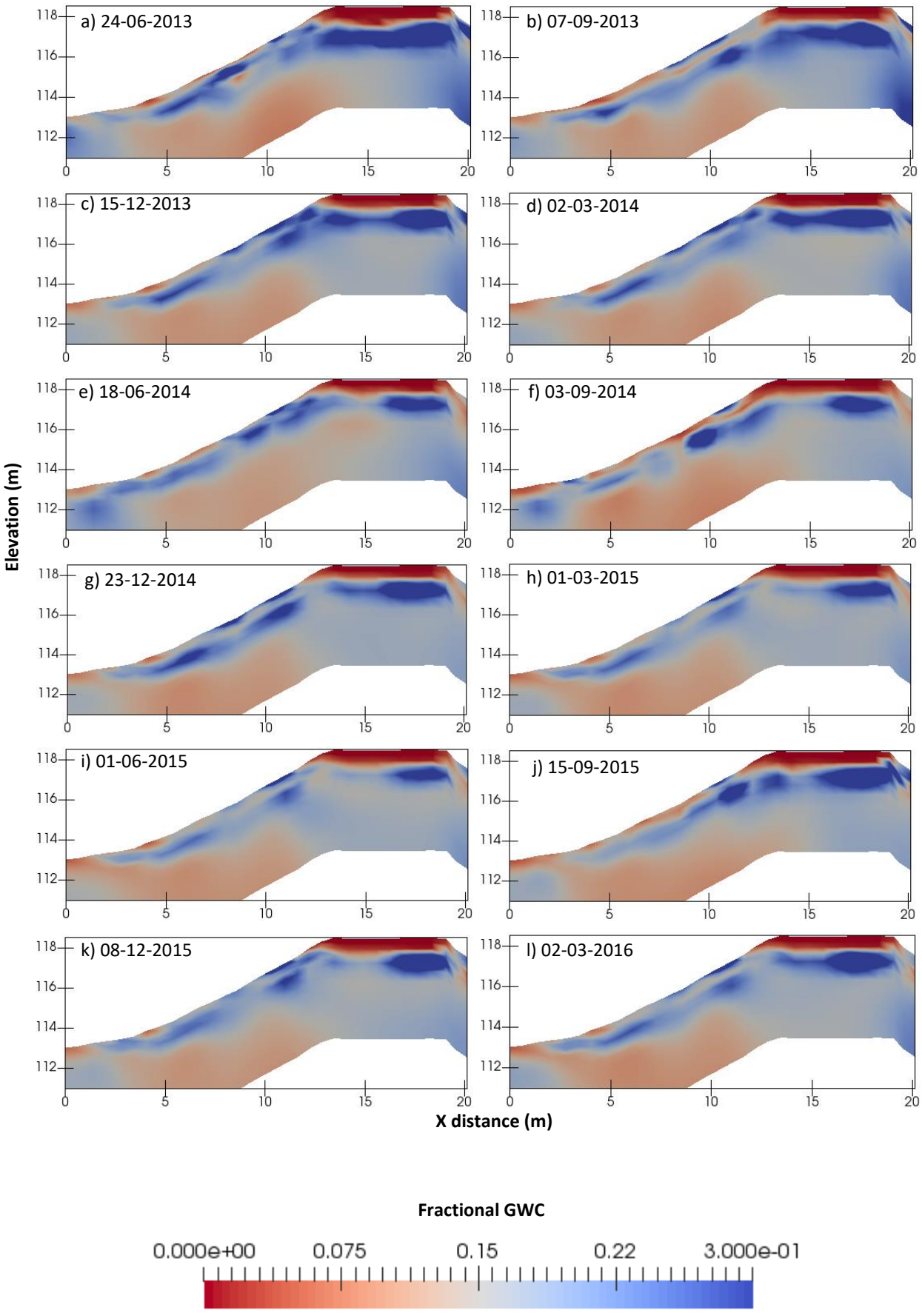

Figure 5.35 Gravimetric water content distribution at three monthly intervals extracted along line 5, derived from 3D ERT. Units shown are fractional gravimetric water content

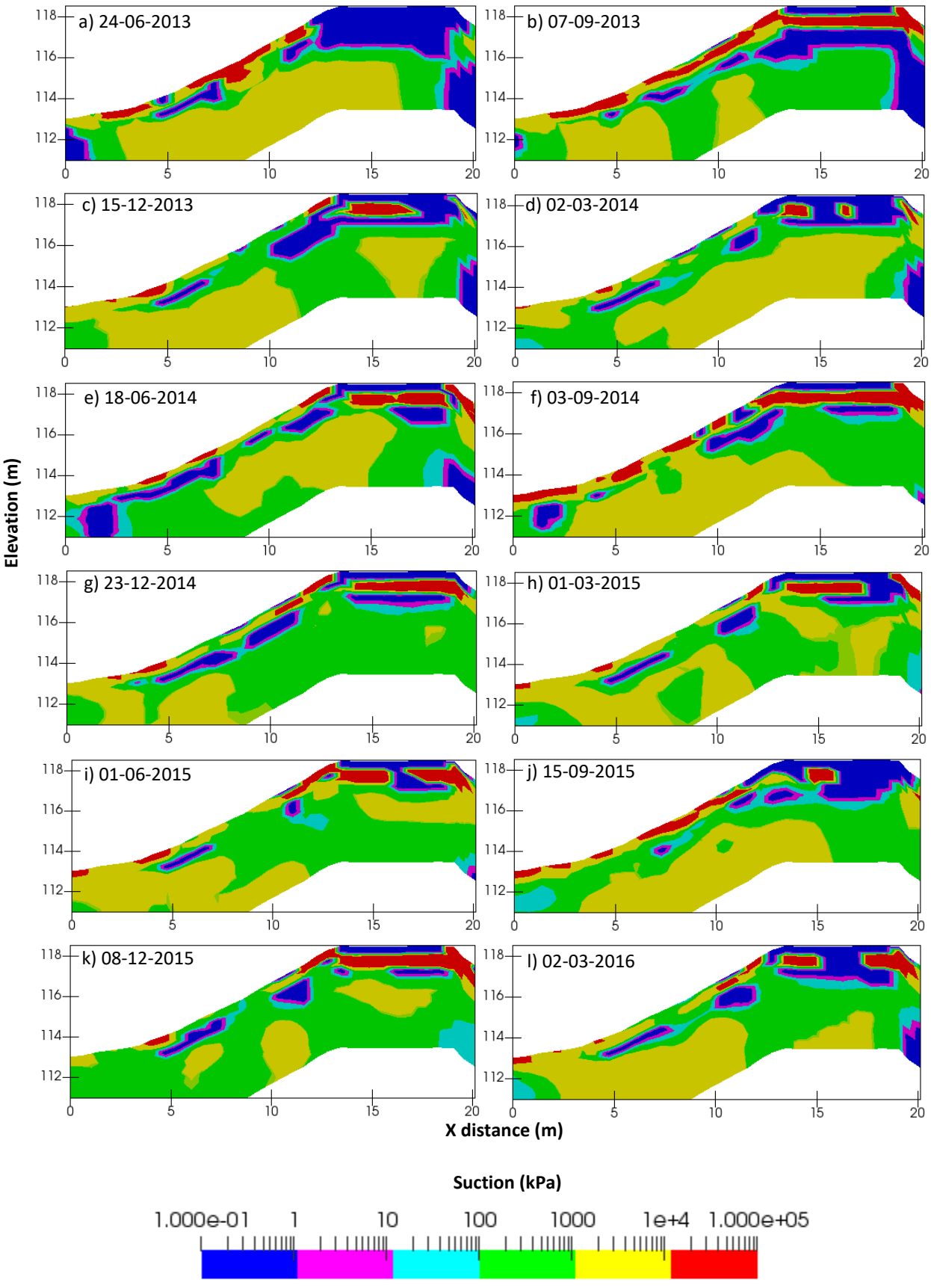

Figure 5.36 Suction distribution at three monthly intervals extracted along line 5, derived from 3D ERT

5.3.5 *Drying behaviour*

From the images presented in Figure 5.35, the BIONICS embankment was observed to dry out over the course of the summer months, identified by lower near-surface water contents nearer the end of the season. This is more clearly illustrated by Figure 5.37, which presents the same cross-section of the embankment, extracted from 3D volumetric ERT imaging, in terms of relative change in water content. Figure 5.35e (baseline) and f have been used to construct this image, thereby showing the change in water content between 18th June and 3rd September 2014. It can be observed that the topsoil has dried out to approximately half its previous value. At depth, the embankment core and the flanks have also dried, by up to 10 %. The zone beneath the topsoil, however, has become considerably wetter, as has the area beneath ballast. It is suggested that this increase is the result of heavy rainfall in the previous month.

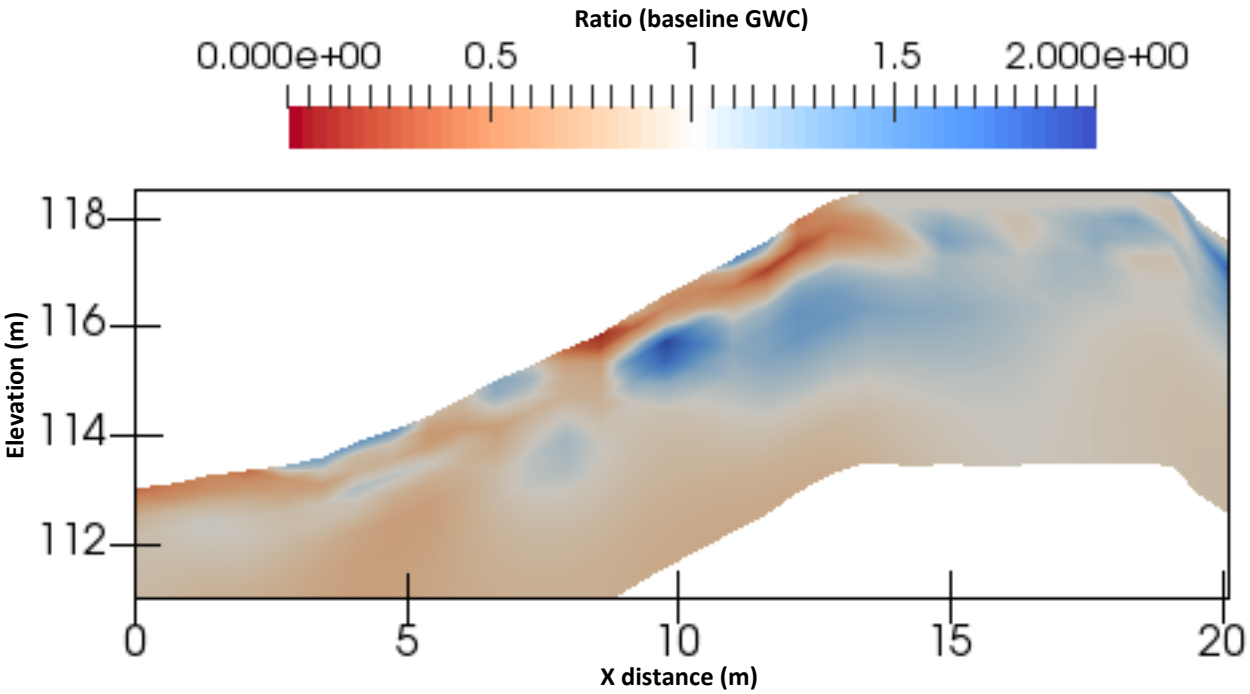

Figure 5.37 Relative change in gravimetric water content between start and end of Summer 2014 (18th June and 3rd September)

In order to investigate the general trend of drying during the summer months, 3D ERT cross-sectional slices were constructed (extracted from 3D volumetric images along the line Y = 2.8 m), for approximately weekly intervals. From Figure 5.21, it is estimated that the drying period in 2013 began in mid-June, lasting until September; this period is used for the investigation of drying behaviour.

Figure 5.38a shows the initial gravimetric water content distribution for the cross-section, which is relatively saturated due to particularly heavy rainfall in the preceding month (same scale as Figure 5.35). Subsequent images show the relative change in water content with respect to the previous week (rather than the water content itself, from which it is difficult to identify temporal changes in moisture distribution on a weekly scale).

With the exception of Figure 5.38h and i, all of the images highlight drying of the topsoil, with the most significant drying occurring between the 20th and 27th of July (Figure 5.38g), despite 8.4 mm of precipitation on the 24th. Ground temperatures at 0.1 m depth over the course of this week averaged 20.8 °C (average at point sensor location a1 – see Figure 5.21d, taken at quarterly daily intervals), compared to a mean ground temperature of 18.4 °C over the full twelve week investigation period. This observation suggests that the increased relative drying between these two dates compared to others is a result of elevated ground temperatures.

Between 27th July and 10th August (Figure 5.38h and i), it is plain that the embankment near-surface has become wetter, which is a result of heavy summer rainfall, and is discussed in the following subchapter.

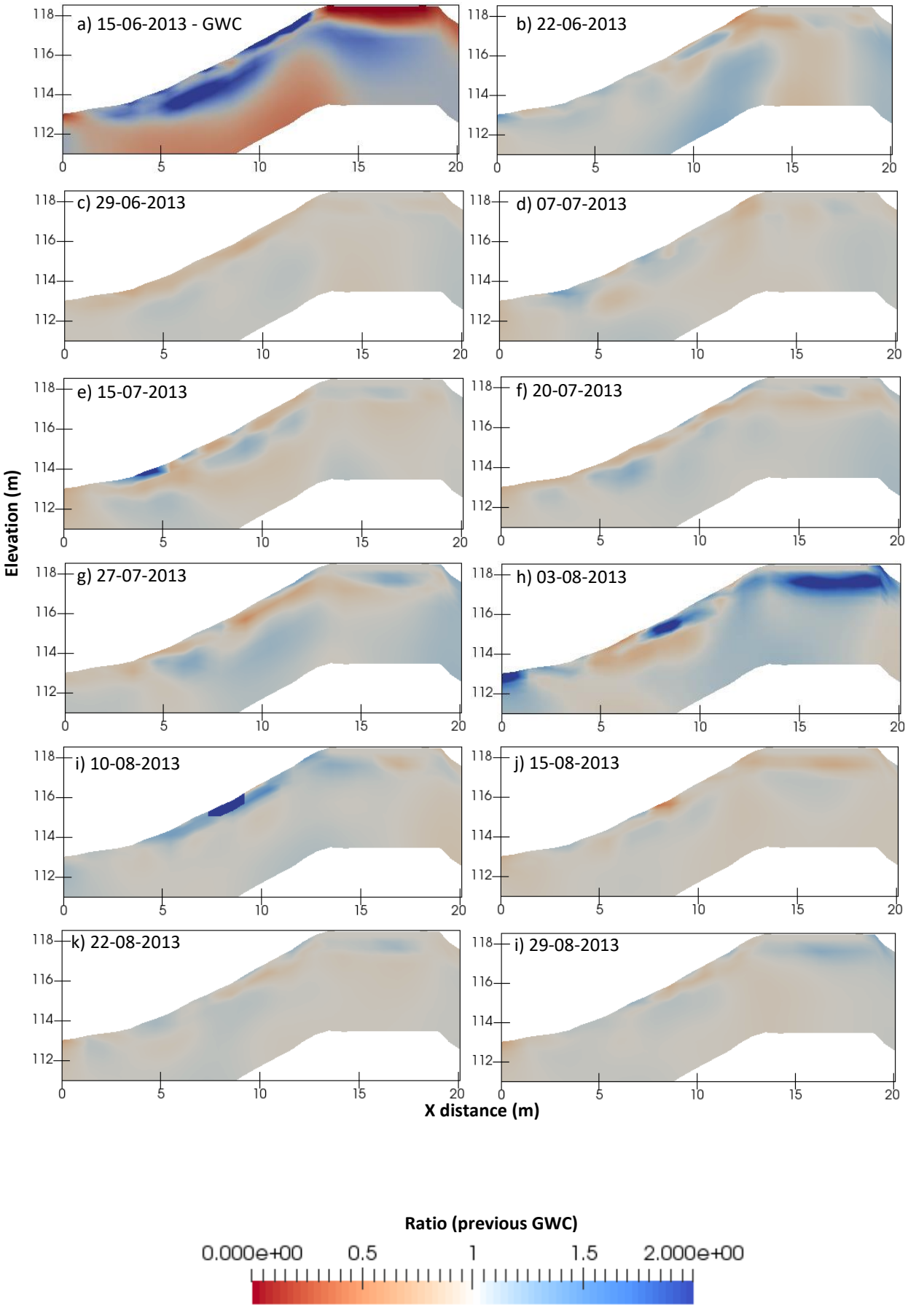

Figure 5.38 Relative change in gravimetric water content at weekly intervals – Summer 2013

In Figure 5.39, the same period (as in Figure 5.38) is investigated, in terms of relative change in resistivity, rather than water content. The ratio change in resistivity with respect to the first date, June 15th 2013, is shown. The associated colour scale has been chosen to highlight features characterised by a resistivity increase greater than 30 % (orange to red). The first image (Figure 5.39a is of the resistivity distribution on June 15th 2013, same scale as Figure 5.32). From this figure, the development of crack features on the Southern flank of the BIONICS embankment may be imaged, which tally with observations made during field surveys (see subchapter 4.2.2). Considering the trends observed from Figure 5.38, the development of these crack features may be described as follows:

In Figure 5.39b (22nd June 2013), following average ground temperatures of 16.8 °C over the course of the preceding week (0.1 m depth, sensor position a1 from Figure 4.39), the South-facing portion of the ballast crest has dried out, resulting in a localised (> 30 %) resistivity increase. Similar behaviour is observed the following week, and by 7th July, the first indicator of near-surface cracking presents itself, in the form of a localised high resistivity anomaly at an approximate horizontal distance of X = 8 m (crack OS2). By the following week (Figure 5.39e, 15th July), another such anomaly has appeared at X = 5.5 m (intersection of cracks OS0 and OS1). By 20th July (Figure 5.39f), all of these anomalies have increased in volume, and by the following week (Figure 5.39g), the topsoil has dried to the extent that the anomalies occupy much of the topsoil layer. Following heavy rainfall over the subsequent two weeks, the embankment surface wets up rapidly, and on 10th August (Figure 5.39i), only the bottom anomaly is visible (OS0/OS1). Drying of the near-surface then resumes; on 15th August (Figure 5.39j), a high resistivity increase occurs beside the crest (X = 12.5 m, OS4), with two more (re)appearing by the following week at X = 8 and 11 m (OS2 and OS3, respectively) (Figure 5.39k). On the final date (29th August, Figure 5.39l), the anomalies have increased in volume, clearly illustrating four distinct locations where soil resistivity has increased by more than 30 % with respect to the baseline date at the start of the summer drying period.

Comparing these images with observations made during cracking surveys made over the same period (Figure 4.35), these high resistivity anomalies are assumed to delineate crack features in the Southern flank of the test embankment.

Figure 5.40 presents a 3D volumetric image of the test embankment, showing relative resistivity change from 15th June to 29th August. Dashed lines have been added at X = 5.5, 8, 11 and 12.5 m, corresponding to the cracks observed from Figure 5.39. For the top three

cracks (OS2-4), the high resistivity anomalies extend the approximate width of the embankment, whereas for OS1, they extend only a third of its width. The fifth crack (OS0), running diagonally, was not initially observed during field surveys, but later confirmed. Following the identification of the four crack features in Figure 5.39 and Figure 5.40 during crack surveys, they were manually extended in May 2014, following the methodology described in subchapter 4.2.2.

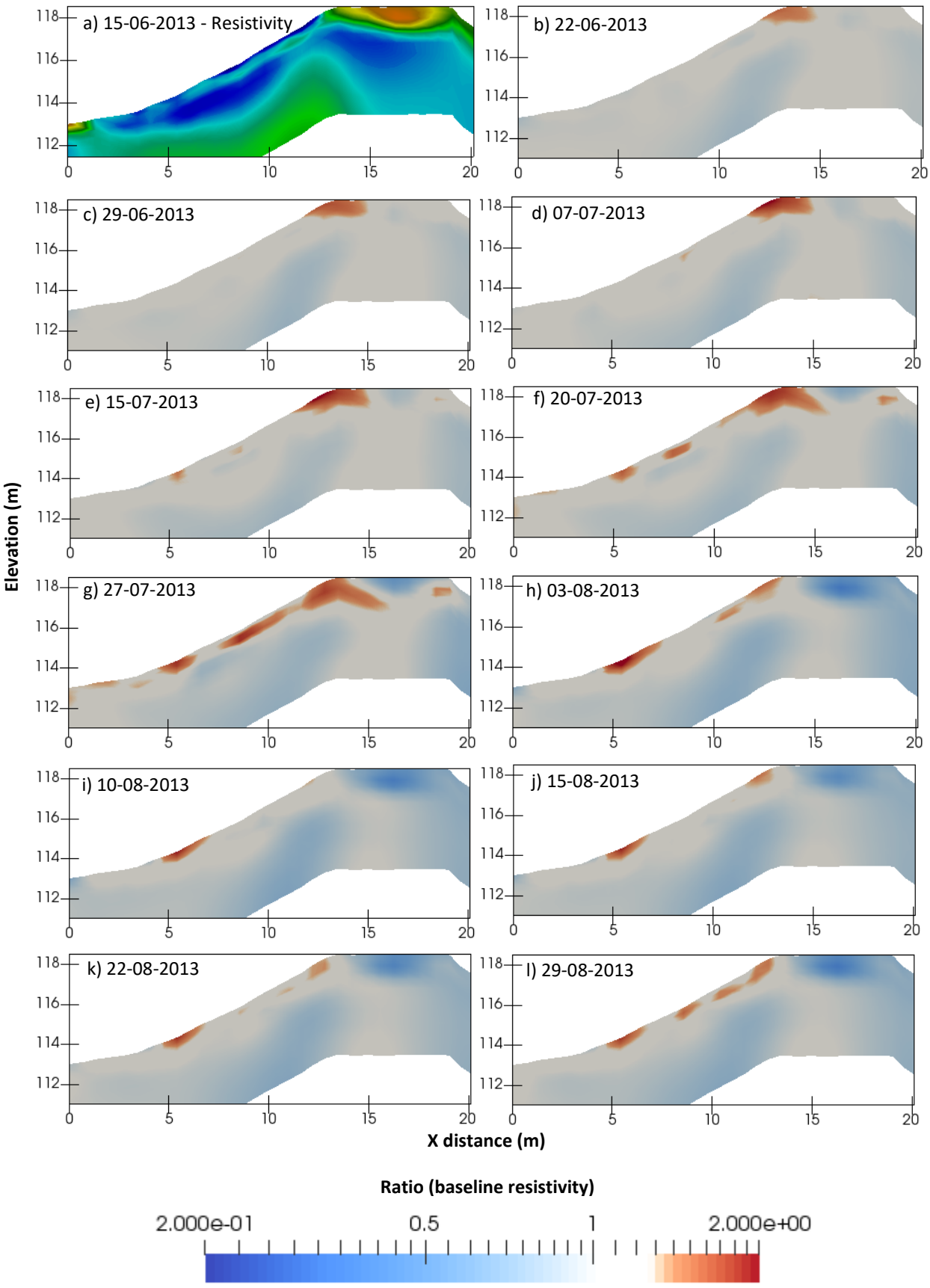

Figure 5.39 Imaging crack development - relative change in resistivity at weekly intervals – Summer 2013, relative to baseline date (15th June 2013)

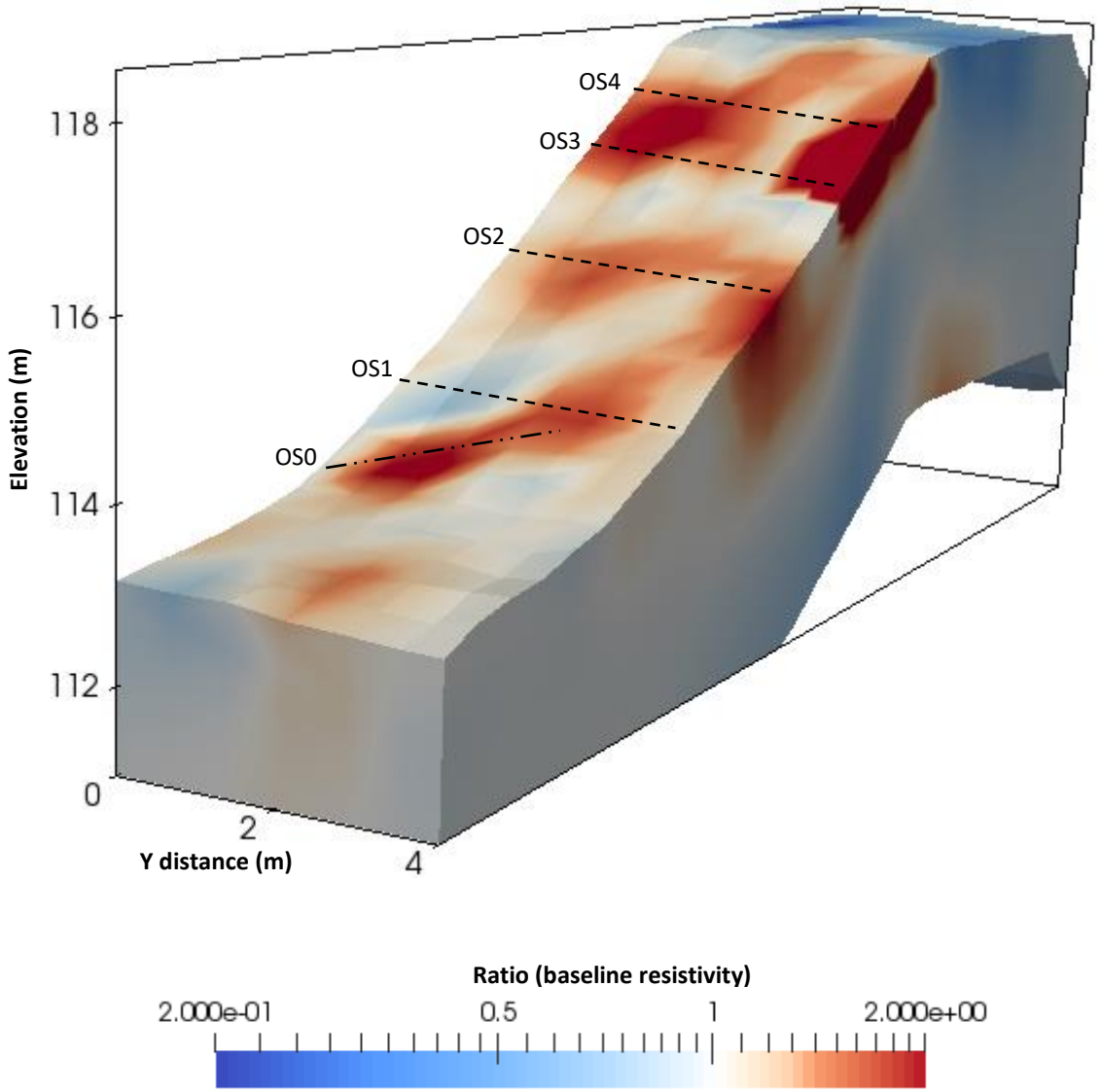

Figure 5.40 3D volumetric image of relative change in resistivity, between start and end of Summer 2013 (25th June and 29th August 2013)

Figure 5.41 presents 3D volumetric images showing the relative change in resistivity from the start (Figure 5.41a, 1st July) to the end of Summer 2014 (Figure 5.41b, 3rd September). The four extended are cracks (OS1-4) are identified by high resistivity anomalies which extend the full width of the embankment, showing that ERT imaging has successfully captured the extension of the cracks. As before, there is evidence of a smaller, diagonal crack near the toe of the slope (OS0). Figure 5.41c shows the increased depth of the cracks (considering the previous year), with additional drying occurring in their vicinity.

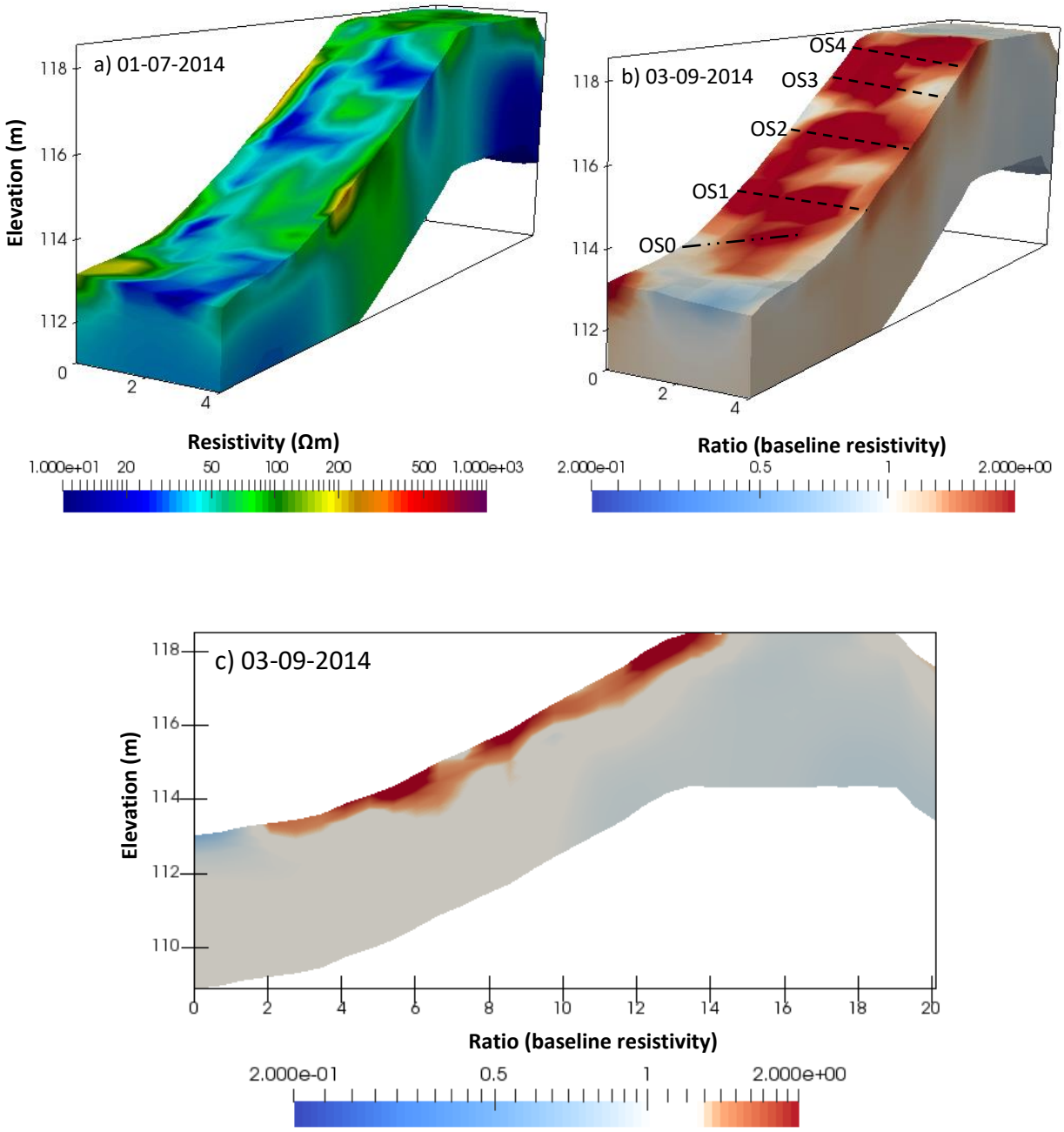

Figure 5.41 Relative change in resistivity between start and end of Summer 2014 (a) volumetric resistivity distribution on 1st July, (b) relative change on 3rd September, and (c) slice showing 3rd September extracted along line 5

5.3.6 *Wetting behaviour*

From the images presented in Figure 5.35, the BIONICS embankment was observed to wet up over of the course of the autumn/winter months, identified by increased water contents in the near-surface and at depth. This is more clearly illustrated by Figure 5.42, which presents the same cross-section of the embankment, extracted from 3D volumetric ERT imaging, in terms of relative change in water content. Figure 5.35f (baseline) and g have been used to construct this image, thereby showing the change in water content between 3rd September and 23rd December 2014 (Autumn 2014). It can be observed that the topsoil has experienced a more than two fold increase in water content compared to its previous value. At depth, the embankment flank has also wet up, by up to 50 %, although two localised zones demonstrate drying. The embankment core shows little change in water content.

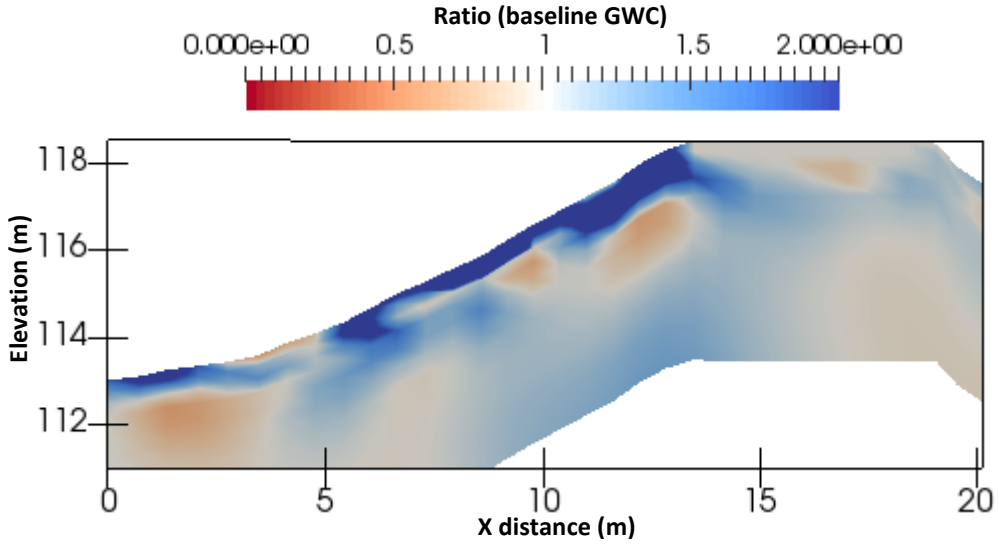

Figure 5.42 Relative change in gravimetric water content between the start and end of Autumn 2014 (3rd September and 23rd December)

Because of the difference in time taken for drying and wetting events, different timescales must be considered in order to investigate them: whereas drying occurs very slowly, over the course of the summer, considerable increases in slope water content may result from rapid rainfall events. Such changes may, in part, result from promoted rainwater infiltration via cracks developed in the soil during summer drying, or be affected by suctions developed in the soil during drying. Therefore, ERT-derived images for several different types of wetting event are presented: the onset of the wetting season in October 2013; a rapid heavy rainfall event in the summer of 2013 (mentioned in the previous subchapter); and the sprinkling experiments beginning in January 2015.

Figure 5.43 shows daily precipitation levels at Nafferton Farm during October 2013 (weather station approximately 50 m from BIONICS test embankment). A significant amount of rainfall is seen to fall on 14th October (17.6 mm), followed by several incidents of lesser amounts of rainfall throughout the rest of month.

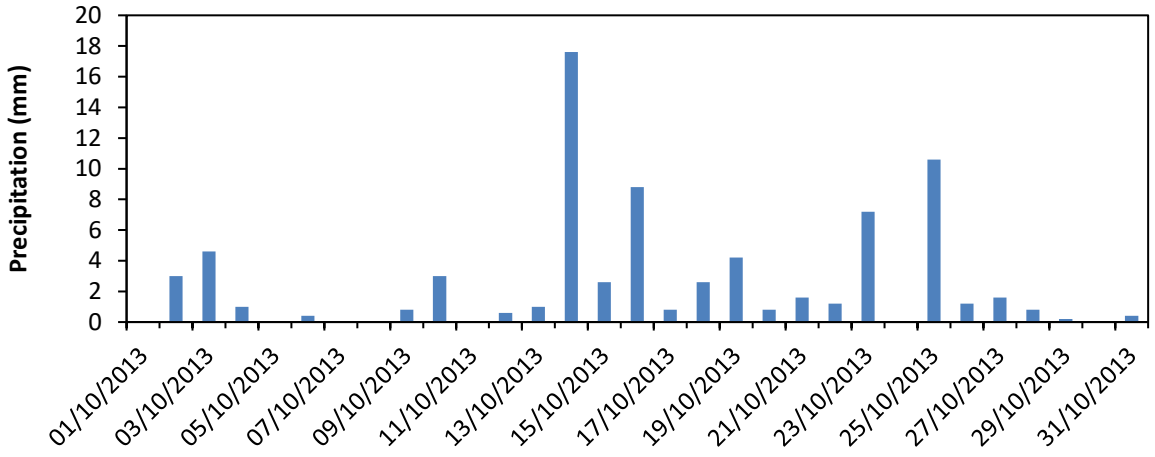

Figure 5.43 Precipitation during October 2013 – start of wetting season

Figure 5.44a shows the ERT-derived water content distribution on 1st October (same colour scale as Figure 5.35). The following images (Figure 5.44b to d) show the relative change in water content with respect to the previous date. As before, changes in the water content of the crest are not representative due to it having different Waxman-Smits properties than those of the embankment fill. Following minor rainfall in the earlier portion of the month, Figure 5.44b (13th October) shows a more than twofold increase in water content at the slope surface, at approximately X = 8 m, corresponding to crack OS2 Figure 5.44c, one day after heavy rainfall, shows considerable increases in water content in the zone beneath the crest ballast, and at the slope toe, as well as a 10 % increase at the core. Again, at X = 8 m, there is a considerable increase in the observed water content, permeating deeper into the embankment fill, suggesting water infiltration via crack OS2. Two distinct bands are observed where water content has in fact decreased, either side of the crack. By 17th October (Figure 5.44d), the entire flank near-surface has become wetter, as has the Southern side of the embankment core. Following consistent moderate rainfall over the following days, the flank near-surface demonstrates further wetting, evident from Figure 5.44e (22nd October).

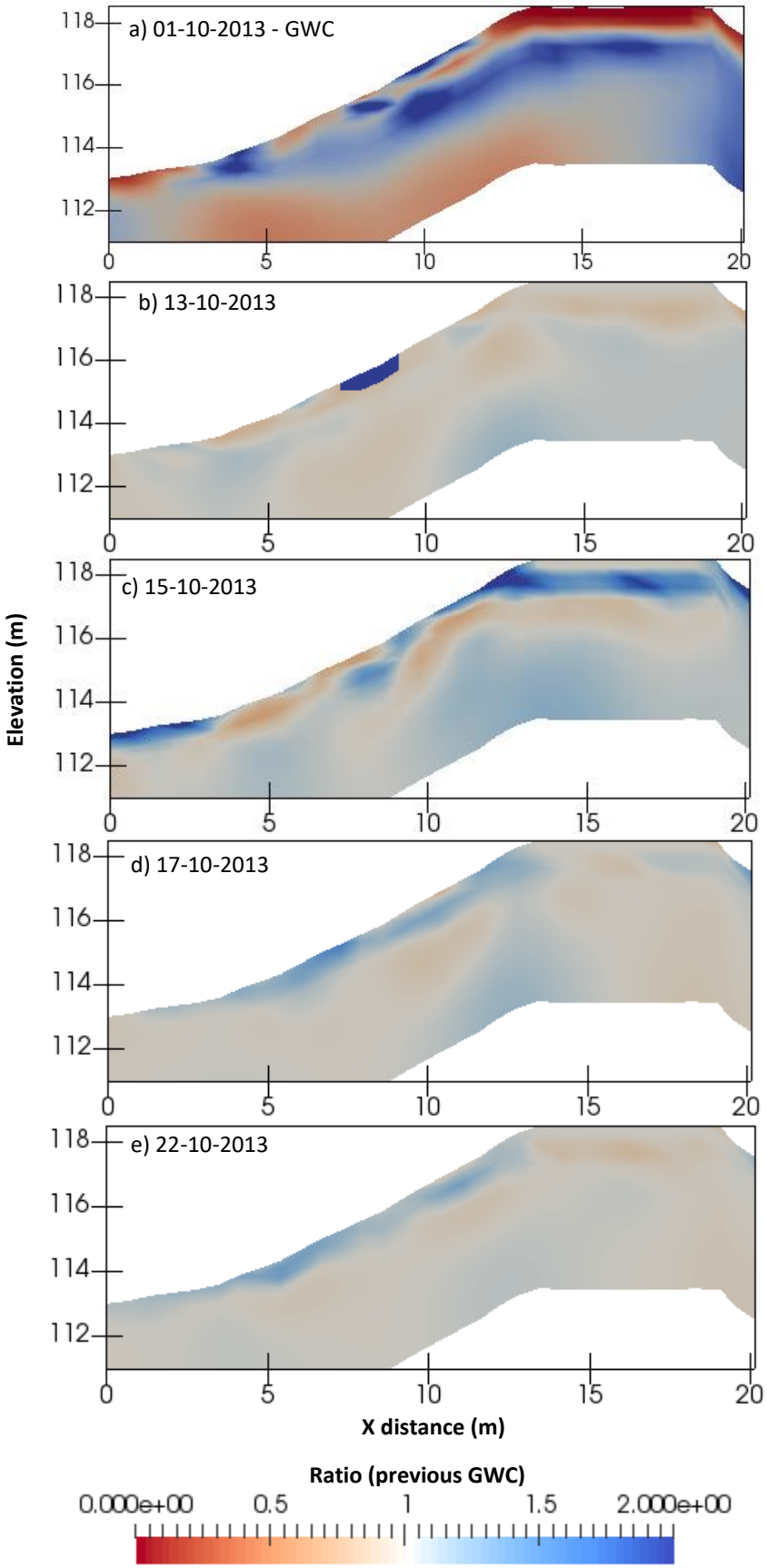

Figure 5.44 Relative change in water content – October 2013 (change relative to preceding date)

In Figure 5.45, the relative change in the volumetric resistivity across the embankment is shown for the same period, with respect to a baseline date prior to heavy rainfall (Figure 5.45a, 1st October 2013). The Contour and Opacity functions with ParaView scientific imaging platform have been employed to highlight areas where resistivity has decreased by 20 % or more (blue), to illustrate water infiltration. Figure 5.45a shows the resistivity distribution on 1st October (same colour scale as in Figure 5.41a). Following minor rainfall, the crest ballast experiences a > 20 % drop in resistivity values. Following the heavy rainfall in the latter half of October 2013: equivalent resistivity reductions are observed from Figure 5.45c to e, which appear to grow in volume towards the end of the month. Three principal inferences may be made: there appears to be preferential wetting along a central line running along the embankment; there is significant infiltration at the embankment core; and the crack locations identified from Figure 5.40 are full of water.

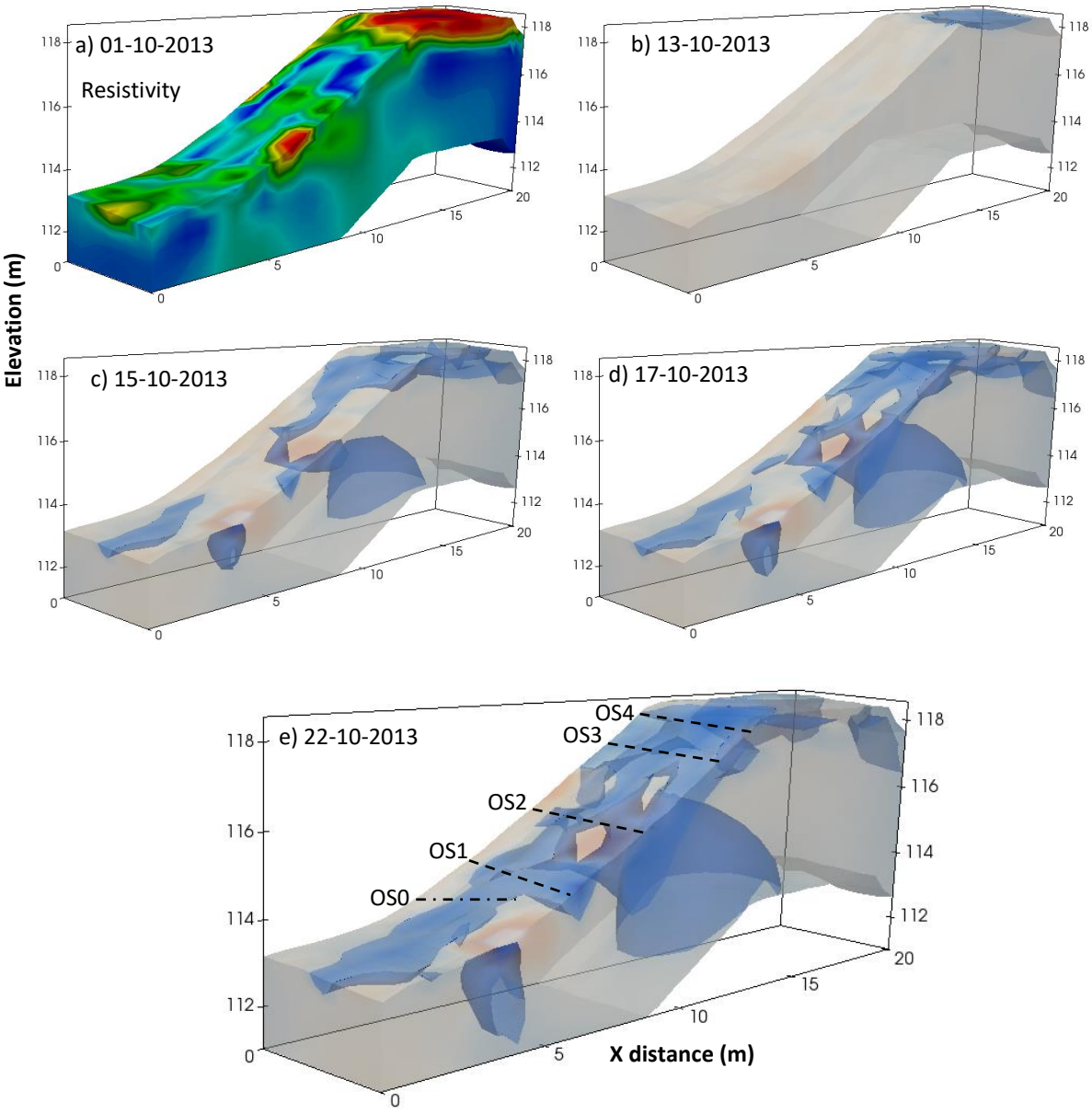

Figure 5.45 Relative change in volumetric resistivity distribution at onset of wetting season (October 2013), with respect to baseline date (1st October 2013)

The above constitutes a wetting event over the course of one month. In subchapter 5.3.5, ERT data from Summer 2013 demonstrated that the drying of the embankment was interrupted by unseasonably heavy rain in late July. As can be seen from Figure 5.46, 36 mm of rainfall was recorded on 28th July 2013, followed by two more occurrences of significant rainfall on 31st July and 5th August.

Figure 5.47a shows the water content distribution on 27th July (same colour scale as Figure 5.35); the following images display the relative change in water content with respect to the preceding date. Following extremely heavy rainfall on the 28th, much of the embankment fill

has become wetter (Figure 5.47b), even at depth within the flank, suggesting direct rapid infiltration from the surface. Over the course of the following days (Figure 5.47c to f) a trend may be observed, whereby additional rainfall events (31st July, 5th August) are accompanied by increases in the water content of the near-surface the following day.

Figure 5.48 shows volumetric images showing the change in resistivity distribution relative to 27th July (Figure 5.48a, baseline, same colour scale as Figure 5.41a) over the same period. As before, reductions in resistivity values greater than 20 % are highlighted in blue. From Figure 5.48b, such reductions are seen in several locations at the near-surface, and also beneath the ballast. There is a conduit extending from the slope surface near the ballast crest, to the depths of the slope flanks. Over the following days, the volume occupied by these zones of decreasing resistivity (relative to the baseline) increases steadily (Figure 5.48c to e). By 6th August (Figure 5.48f), most of the slope surface is characterised by resistivity reductions, permeating to the full depth of the embankment flanks. The locations of the crack features identified by field surveys and from subchapter 5.3.5 have been mapped onto the final volumetric image (dashed lines, Figure 5.48g). This shows that by and large, the crack locations correspond to near-surface resistivity reduction zones, suggesting that near-surface infiltration is dominated by such crack features. Contrary to the Autumn/Winter 2013 wetting event presented above, there is no evidence of preferential water flow running along the central line of the embankment. This observation implies that for summer rainfall, when the embankment surface is dry and cracked, infiltration is largely influenced by crack location, which allows infiltration at depth. During winter rainfall, however, when cracks are likely to have healed somewhat, there is less infiltration at depth, and therefore more surface runoff.

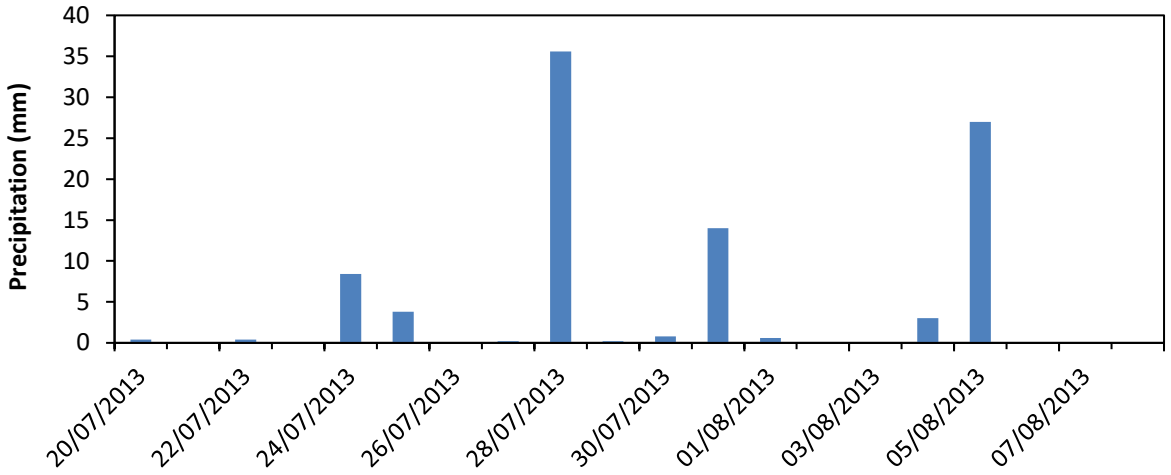

Figure 5.46 Summer 2013 precipitation (showing mid-July to early August)

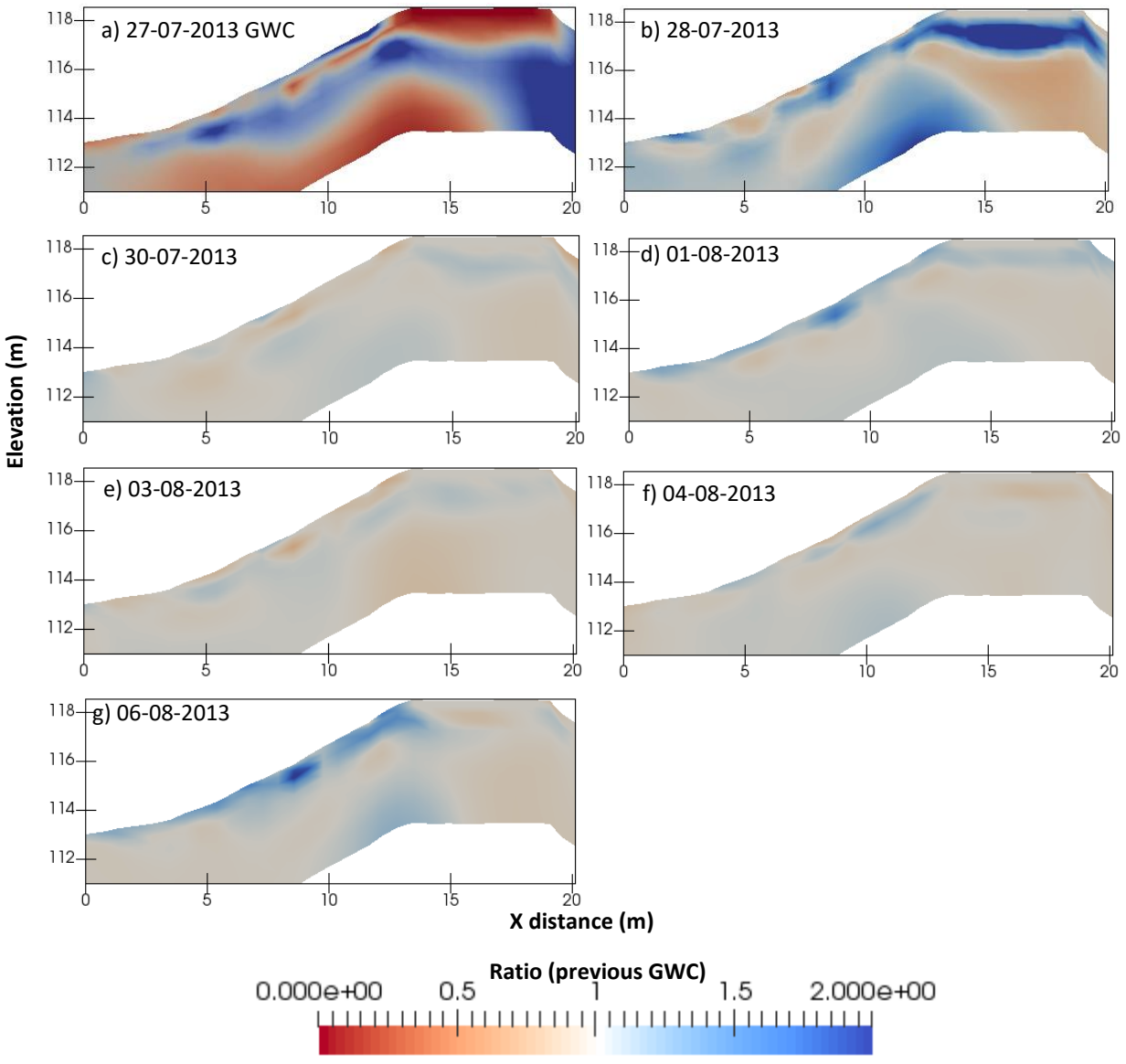

Figure 5.47 Relative change in gravimetric water content during Summer 2013 rapid rainfall event (change relative to preceding date)

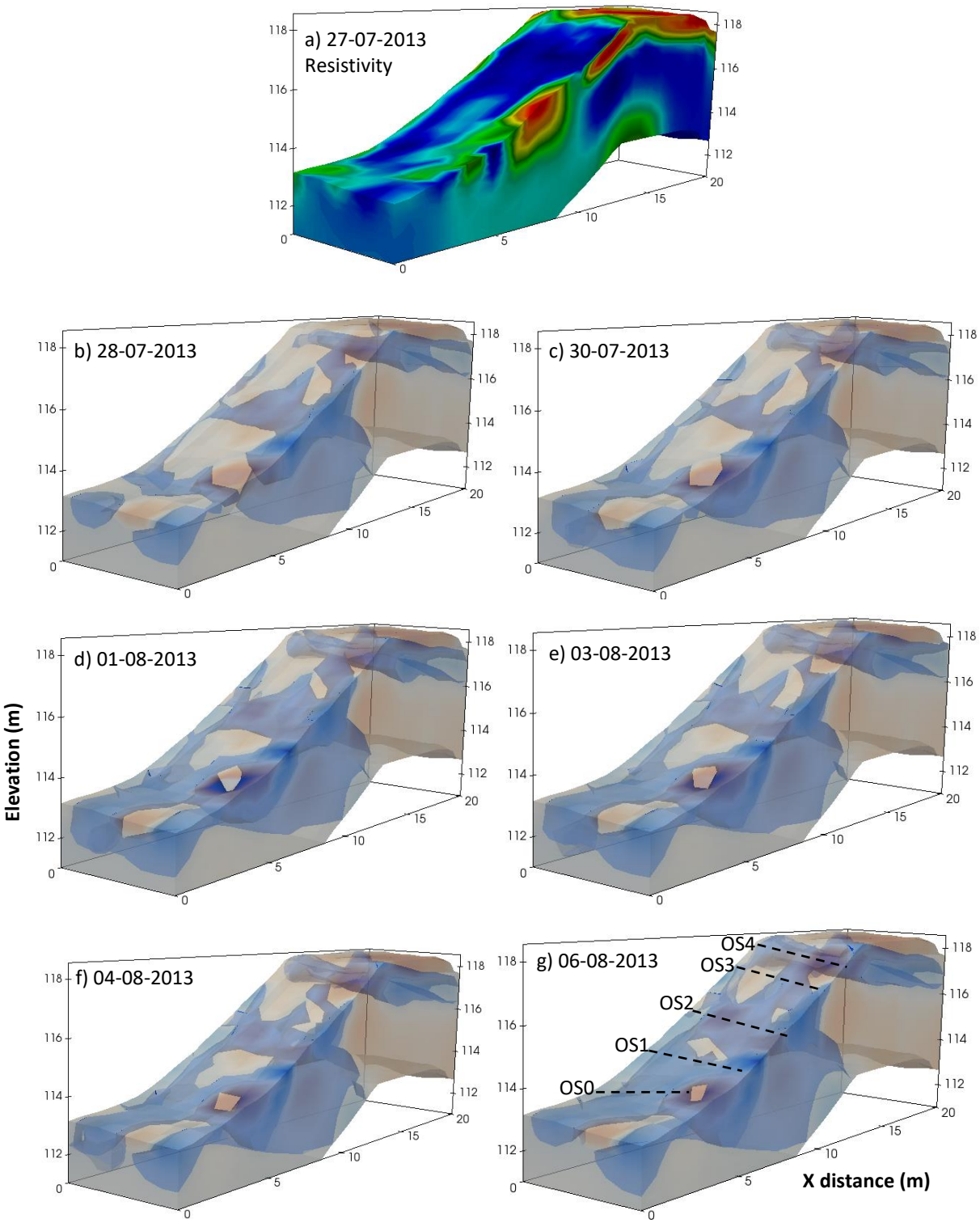

Figure 5.48 Relative change in volumetric resistivity distribution during Summer 2013 rapid rainfall event, with respect to baseline date (27th July 2013)

On 12th January 2015, the sprinkler system (described in subchapter 4.2.2) was activated. Figure 5.49a shows the inferred gravimetric water content distribution of the embankment along the line Y = 2.8 m (same colour scale as in Figure 5.35). The subsequent images demonstrate the relative change in water content with respect to the baseline date, 2nd January (note, the ratio scale employs a narrower range to previous GWC ratio images). On 10th January, a moderate amount of rainfall fell, reflected in Figure 5.49c by wetting of the near-surface flank and beneath the ballast crest. The sprinkler system was activated two days later, and, unexpectedly does not provide much evidence for ongoing wetting of the near-surface. Over the following days and weeks (Figure 5.49e to k), the near-surface in fact appears to getting drier. Moderate rainfall on 19th and 21st January is, however, accompanied by localised increases in water contents at the flank surface over the following days (Figure 5.49h to k).

The volumetric change in resistivity from the baseline date of 1st January 2015 is shown in Figure 5.50, where Figure 5.50a shows the initial resistivity distribution (same colour scale as Figure 4.41a). As before, the Contour and Opacity functions within ParaView have been employed to highlight zones of increased resistivity values (> 10 %). Subsequent images demonstrate the change in resistivity relative to this date. As with Figure 5.49, images made on dates following the activation of the sprinkler (Figure 5.50b to d) system exhibit unexpected behaviour, demonstrating near-surface resistivity increases. This observation may be a result of the following factors, discussed in detail in subchapter 6.3.2: relatively low resistivity water used in the sprinkling systems, and/or low temperatures of the water itself. As before, the locations of the cracks as determined previously have been mapped onto the final image, corresponding to regions of greatest resistivity change. Because the entirety of the slope surface demonstrates such considerable increases in resistivity values, it is difficult to resolve if there is any preferential flow along the centre of the slope, as for the October 2013 wetting event.

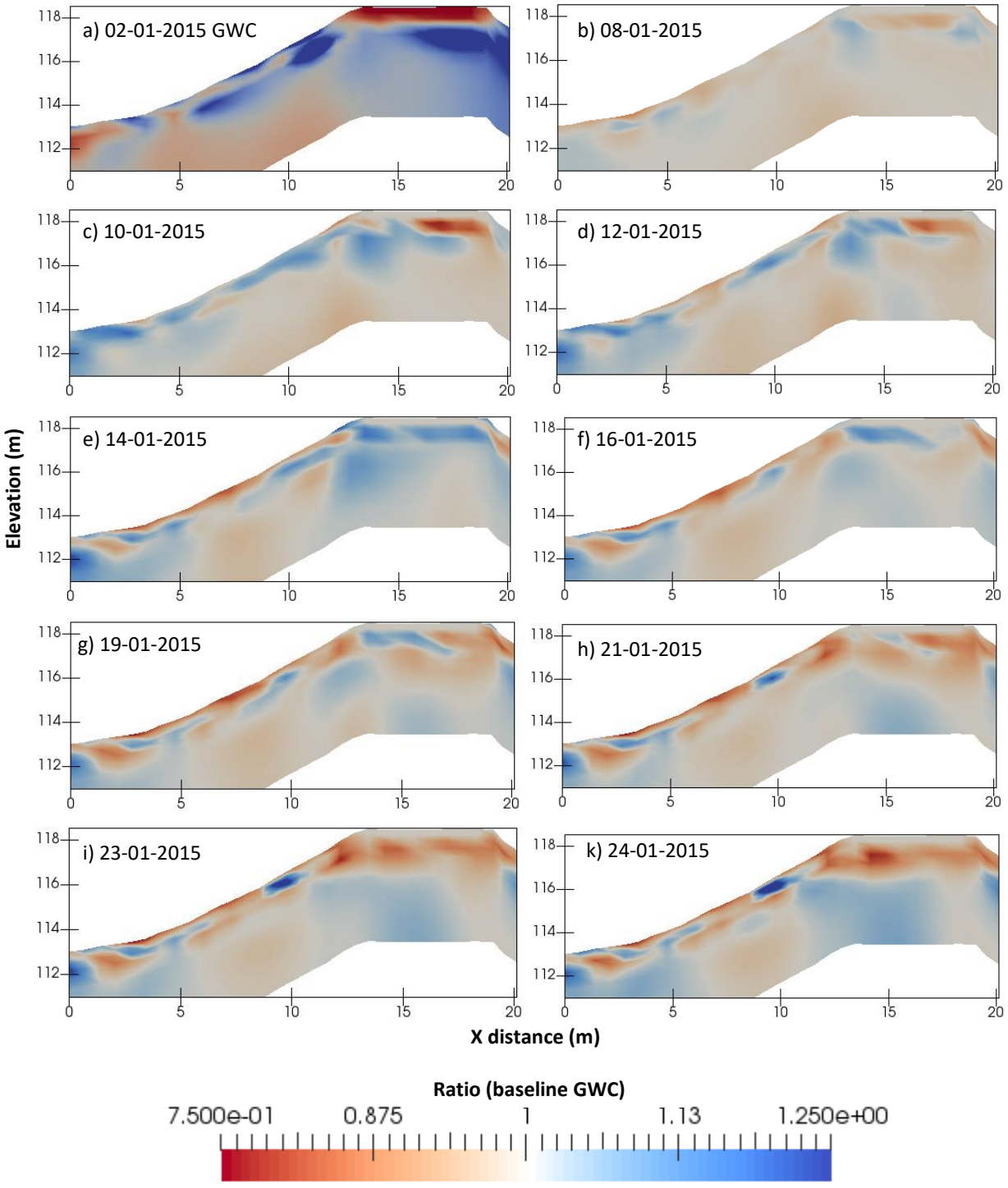

Figure 5.49 Relative change in gravimetric water content following January 2015 sprinkler activation, with respect to baseline date (2nd January 2015)

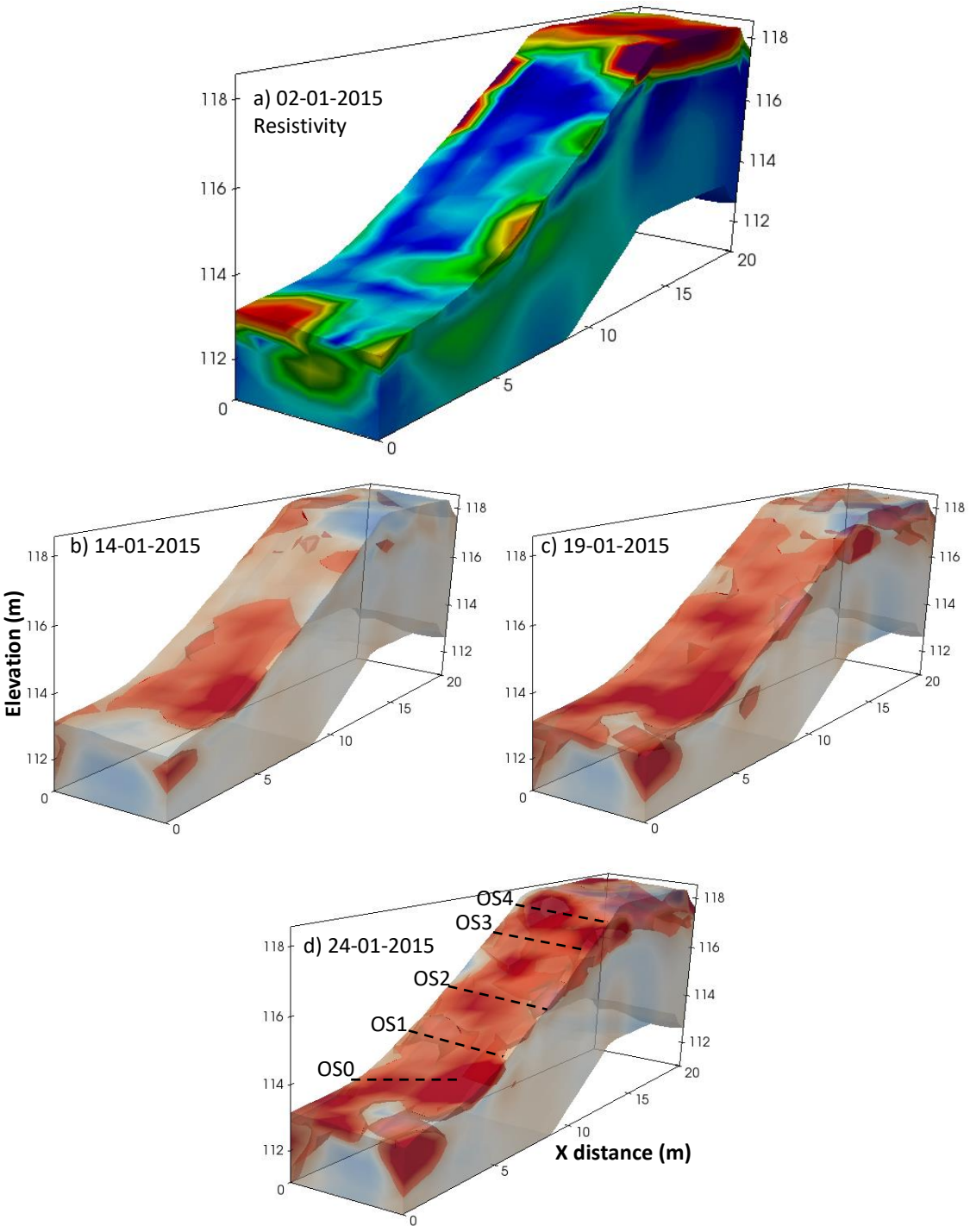

Figure 5.50 Relative change in resistivity following January 2015 sprinkler activation, with respect to baseline date (2nd January 2015)

5.3.7 *Aspect comparison*

In subchapter 5.3.3, the decision was made, where possible, to present 3D rather than 2D ERT data, in order to avoid including the effects of artefacts outside of the investigation plane. For this reason, no ERT images have, as yet, been presented of the Northern flank of the test embankment, as only line 5 extends into the Northern flank, capable of providing 2D data only. In the following subchapter, ERT images of line 5 are shown, allowing the Southern and Northern flanks to be compared, despite the limitations of 2D ERT imaging (because of the tendency of 2D ERT to underestimate inferred water contents, only resistivity data are presented). Only images which were captured prior to the manual crack extension experiment (May 2014) are shown, as any subsequent comparison of slope aspect moisture dynamics would certainly be affected by such intervention.

Figure 5.51 presents 2D ERT images for three monthly intervals, starting in June 2013. Whereas the Southern flank demonstrates considerable seasonal change in the near-surface as described previously, the Northern flank demonstrates very little: over the course of the year, a consistent band of low resistivity values is evident across the top 1.5 m thick layer. From Figure 5.51b, there appears to be infiltration from the Southern flank surface to a depth of 3 m, but no such deep conduits are observed in the Northern flank. This observation suggests that the South-facing slope contains deep crack features, but that the North-facing one does not. There is evidence of shallower cracking in the North (four cracks in total, ON1-4 from Figure 4.35), identified by relatively low localised resistivity values (approximately 20 Ωm) with respect to the rest of the near-surface band (50 Ωm). During crack surveys in Summer 2013, observations were made that the Southern crack features (OS1-4) were much more pronounced than those in the Northern slope, extending further in all directions. In general, near-surface resistivity values are higher in the Northern flank, but at depths beyond 1.5 m, the opposite is true. In the Northern flank, a patch of relatively low resistivity values may be seen at the bottom of the embankment (elevation 112.5 m), centred at X = 21 m. Additionally, Figure 5.51a to d all demonstrate a tendency for water infiltrated through the crest ballast to concentrate in the Northern portion of the zone beneath the crest.

In Figure 5.52, the resistivity standard deviation distribution for 2013/2014 is presented, constructed from Figure 5.51a to d. It can clearly be seen that the Southern slope demonstrates the highest near-surface deviations, concentrated within the upper half of the

slope. Much of the Northern slope exhibits very low standard deviations, implying that the Northern flank hydrodynamic response to environmental forcings is damped with respect to the Southern flank. This observation is in agreement with Figure 5.23 and Figure 5.24, which show muted water content, pore water pressure and temperature fluctuations of the Northern flank with respect to the Southern, at both the Lower and Upper positions.

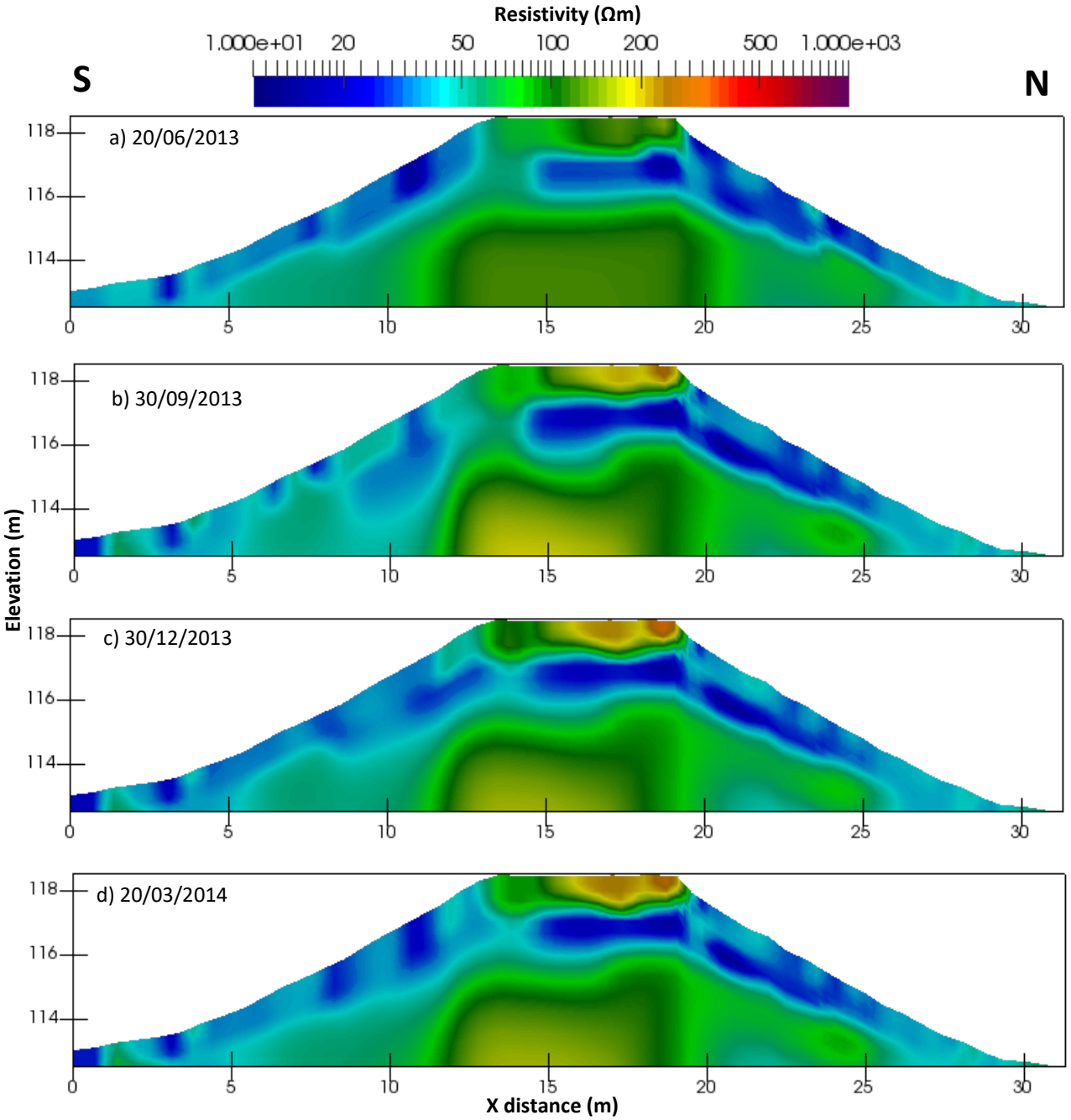

Figure 5.51 Aspect comparison – 2D ERT images along line 5

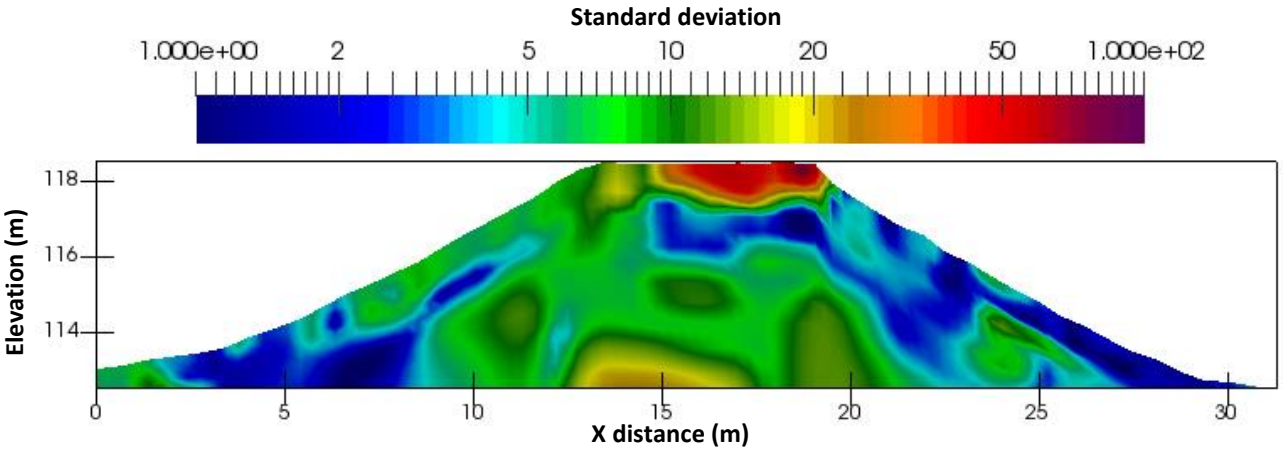

Figure 5.52 Aspect comparison – 2D ERT Resistivity standard deviation for 2013/2014

5.4 Comparison of ERT and point sensor measurements

The following subchapter presents the data which will serve as the principal basis for assessing the effectiveness of the ERT method, as a means of estimating in situ geotechnical parameters. These results are discussed in subchapter 6.3.3.

5.4.1 *Monthly time series*

The following images present a comparison of the data derived from the point sensor network and from ERT monitoring. In order to make a comparison between the two methods, data points corresponding to the locations of point sensors situated on the Southern flank were extracted from volumetric ERT images. The point sensors made direct measurements of (two point) resistivity, water content and matric suction; the ERT array made measurements of (four point) resistivity, which were then converted to both volumetric water content and suction via the use of proxy relationships, following the methods described in subchapters 4.3.8 and 4.3.9. As described in subchapter 5.3.6, the sprinkling experiments which started in mid-January 2015 caused high resistivity water to infiltrate into the embankment, causing the ERT method to underestimate field water contents; these data are dealt with separately from the rest of the data.

Figure 5.53 presents the ERT/point sensor comparison (“ERT”/”5TE”datasets in legend) for the South slope lower position, showing resistivity, water content and suction values, in Figures a, b and c, respectively, at approximately monthly time intervals. In subchapter 5.3, presented 3D resistivity images were corrected to the average field air temperature (9.35

˚C), however, in order to allow for comparison with the 5TE point sensors, the extracted data are corrected to 25 ˚C, assuming the temperature model described in subchapter 4.3.6. From all three parameters, it is evident that both methods have resolved the same qualitative trends, showing a highly variable near-surface (0.1 m), seasonally variable at 0.5 m, and relatively static at greater depth (1.0 m).

In terms of the resistivity response to environmental conditions (Figure 5.53a), generally good quantitative agreement is observed at depths of 0.5 m and 1.0 m, with the greatest deviations observed during Summer 2014. In subchapter 2.3.1, the incorporation of greater contact resistances within the two point resistivity method was explained, therefore, the fact that there is close agreement the two methods at these greater depths implies that these resistances are minimised by the point sensors being embedded at depth. At the near-surface (0.1 m), however, there exists very poor quantitative agreement, with the point sensor network recording considerably higher resistivity values than obtained from the ERT array, suggested to be due to poor coupling.

Measured and inferred water content values are shown in Figure 5.53b, and reflect the trends observed from the resistivity response, showing good general agreement at 0.5 m and 1.0 m, but poor agreement at 0.1 m. Both the point sensor and ERT results demonstrate the difference between the water content values at 0.5 m and 1.0 m to grow during the winter months, and to shrink during the summer months, as drying occurs to a greater extent at 0.5 m than at 1.0 m. Generally, the poorest agreement between the two methods is observed during the summer months: it can be seen that the deviation in resistivity values recorded during Summer 2014 (as noted previously) is accompanied by very poor agreement between the two methods in terms of measured water content values. During this period, the ERT results show unrealistically rapid drying (VWC drops of 16 % and 6 % at 0.5 m and 1.0 m depths, respectively, between June and July), suggesting the ERT results to be unreliable. In the near-surface, estimated water content values using the ERT method are generally shown to be 5 % lower than those recorded using the point sensors. In Figure 5.53a, the ERT-derived resistivity values were consistently lower than the point sensor values, implying higher water contents, however, the opposite is true from Figure 5.53b, which is explained by the fact of the two point method (point sensors) incorporating greater contact resistances than the four point method (ERT array), as explained in subchapter 2.3.1.

In Figure 5.53c, measured and inferred suctions for the lower position on the South slope of the ERT test plot are presented. The inferred suctions were obtained following the method described in subchapter 4.3.9, allowing for separate drying and wetting SWRCs to be applied to distinct parts of the embankment. Reasonable qualitative and quantitative agreement is observed between the two methods at 0.5 m, however, at 1.0 m the ERT-derived results provide a poor approximation of those recorded using the point sensor network.

Further upslope, Figure 5.54 demonstrates similar trends to those shown in Figure 5.53, describing a highly variable near-surface response which becomes progressively damped with depth. From Figure 5.54a, it can be seen that at all depths, the measured point sensor resistivity values are elevated with respect to the ERT-derived values, which may be a result of the inclusion of greater sources of contact resistance. As before, the greatest deviations between the methods occur during the summer months (at 0.5 m and 1.0 m depths). From Figure 5.54b, good agreement is observed between the water content values of the two methods at 1.0 m depth, during the wetter months only. Over the same interval, ERT-derived water content values at 0.5 m are consistently 5 % higher than the point sensor results. At 0.5 m, both methods do demonstrate similar qualitative behaviour, showing seasonally drier summer water contents. At 1.0 m, ERT-derived estimates appear to show the opposite, contradicting the results of the point sensors. Unfortunately, no 0.1 m data was available due to sensor malfunction. It can be seen from Figure 5.54c that there is very little correlation between the measured and derived suction values.

At the top of the South-facing slope of the ERT test plot, one point sensor was installed at a depth of 0.5 m, measuring both resistivity and water content, but not soil suction. It can be seen from Figure 5.55a that both the ERT array and the point sensors have resolved highly fluctuating resistivity values, which are reflected in the water content values shown in Figure 5.55b. In terms of both resistivity and water content, the two methods show consistently good qualitative and quantitative agreement during the winter months. As for two lower and upper positions, the greatest deviation between the two methods occurs during the summer months, corresponding to dry soil conditions.

In Figure 5.56, a reduced number of data points provide a comparison of the ERT array and point sensor network beneath the crest of the ERT test plot, owing to the fact the point sensors were installed much later in this portion of the embankment. At this location, the poorest agreement between the two methods is observed: at 1.0 m depth, ERT-derived

resistivity values show little variability, with values of approximately 20 Ωm (Figure 5.56a). The point sensors also demonstrate little variability, but with values of the order of 100 Ωm. Given the discrepancy between these two datasets, and the fact that similar values were not recorded anywhere else on the embankment, it is considered likely that the anomalously high point sensor resistivity values are the result of a sensor malfunction (or poor coupling). At 0.5 m, there is close agreement between the ERT and the point sensor resistivity values, following an initial period where the newly-installed point sensor was still homogenising. Figure 5.56b shows the measured and ERT-derived water content values, with all datasets demonstrating similarly static behaviour, however, the ERT-derived water content values are significantly higher than the point sensor values, which may imply a poor fit of the porosity model, discussed further in subchapter 5.4.3. From Figure 5.56c, suction values between the two methods both show little variability, but extremely poor quantitative agreement.

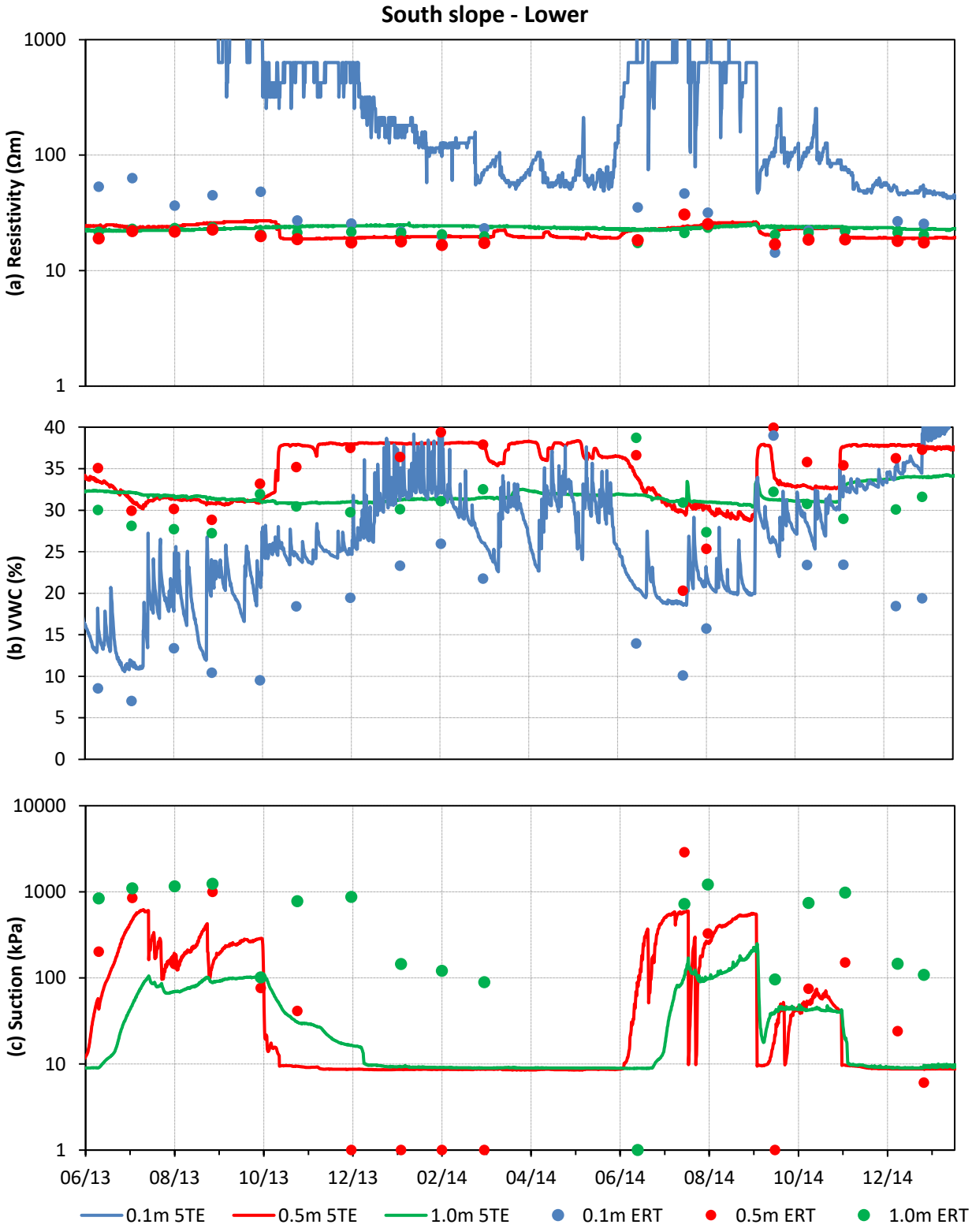

Figure 5.53 Comparison of geotechnical measurements obtained from ERT and the point sensor network - South slope lower position of the ERT test plot, showing (a) resistivity, (b) volumetric water content and (c) suction values. This position refers to location a1 on the sensor distribution map in Figure 4.39

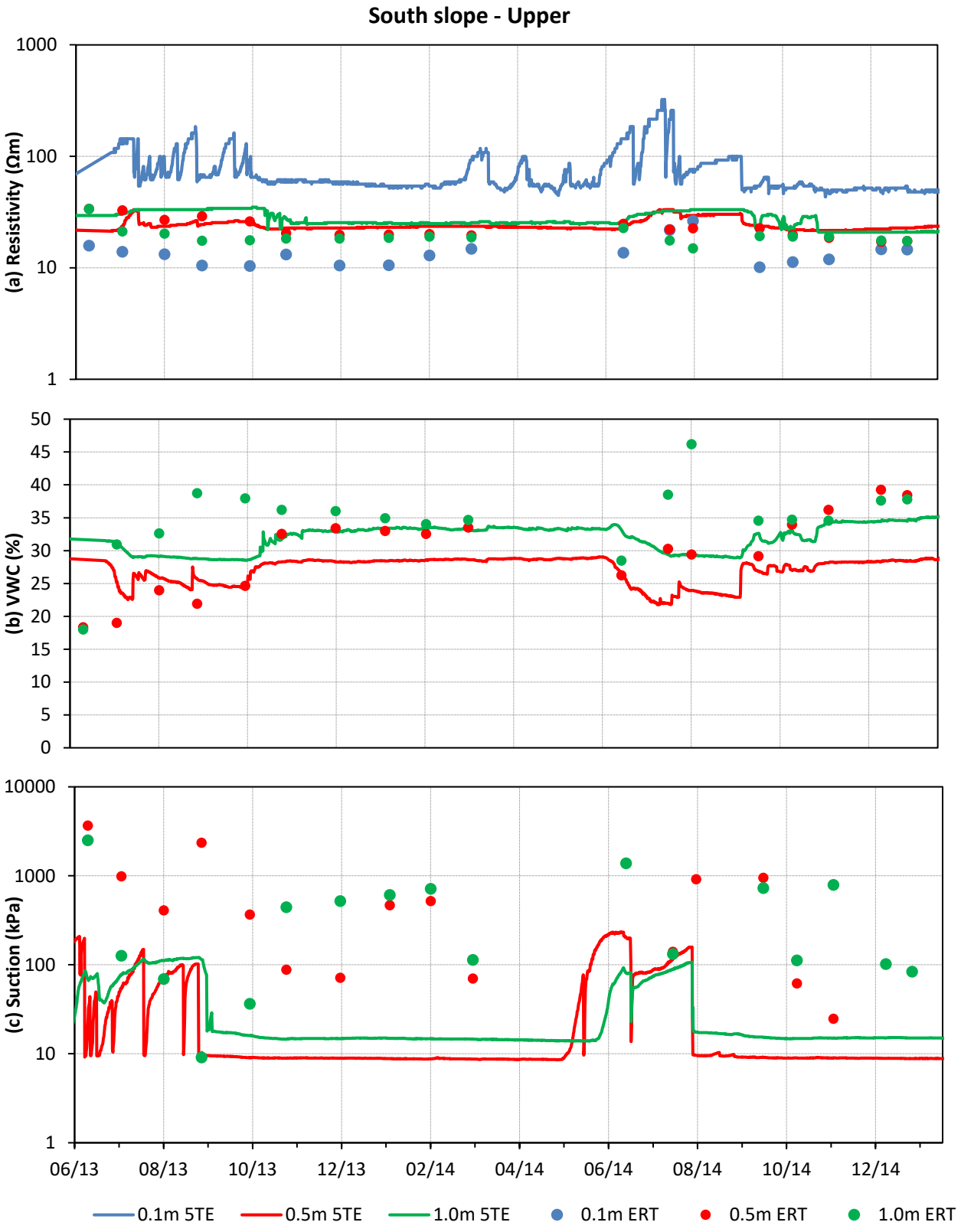

Figure 5.54 Comparison of geotechnical measurements obtained from ERT and the point sensor network - South slope upper position of the ERT test plot, showing (a) resistivity, (b) volumetric water content and (c) suction values. This position refers to location a2 on the sensor distribution map in Figure 4.39

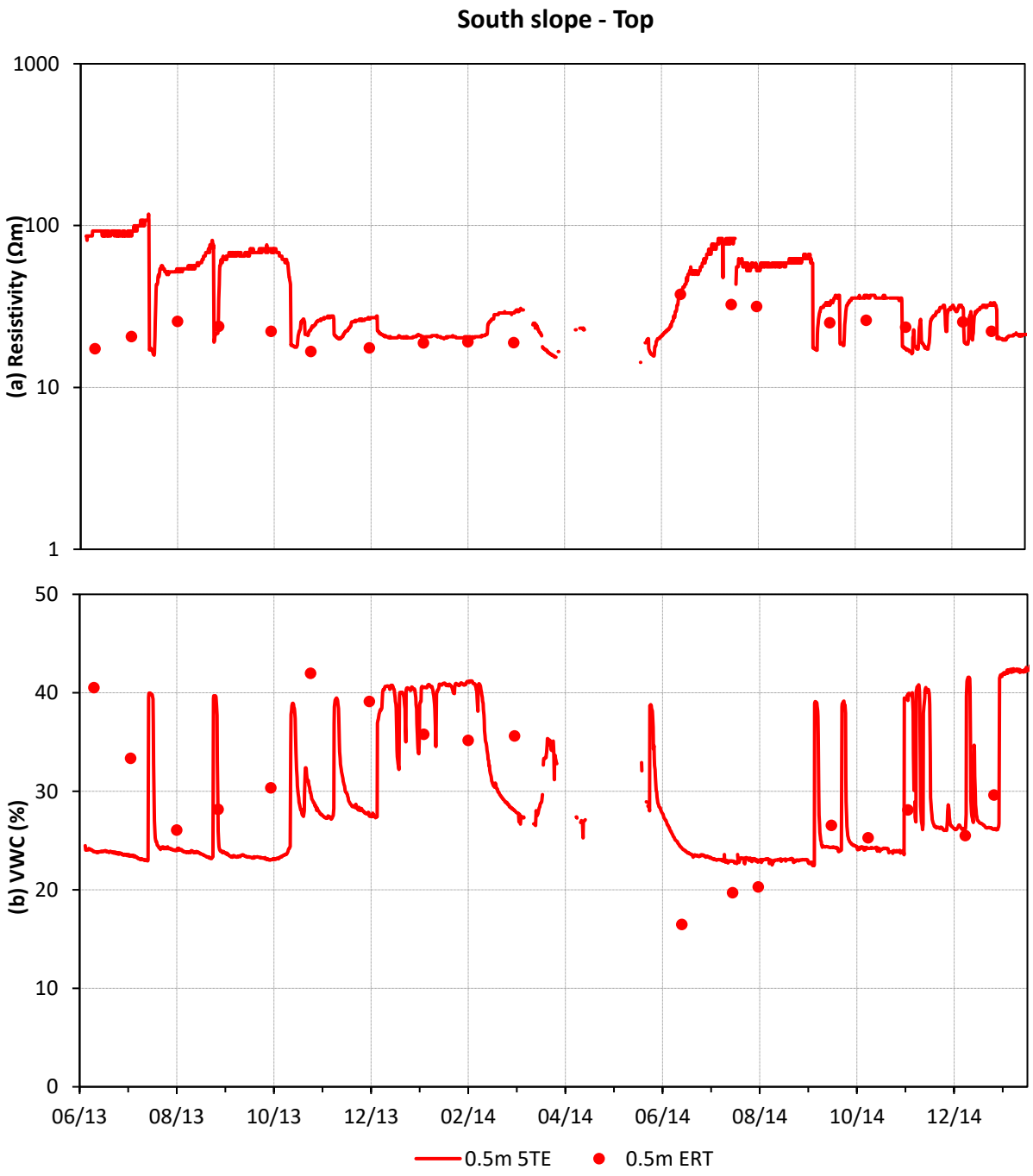

Figure 5.55 Comparison of geotechnical measurements obtained from ERT and the point sensor network - South slope top position of the ERT test plot, showing (a) resistivity and (b) volumetric water values. This position refers to location a3 on the sensor distribution map in Figure 4.39

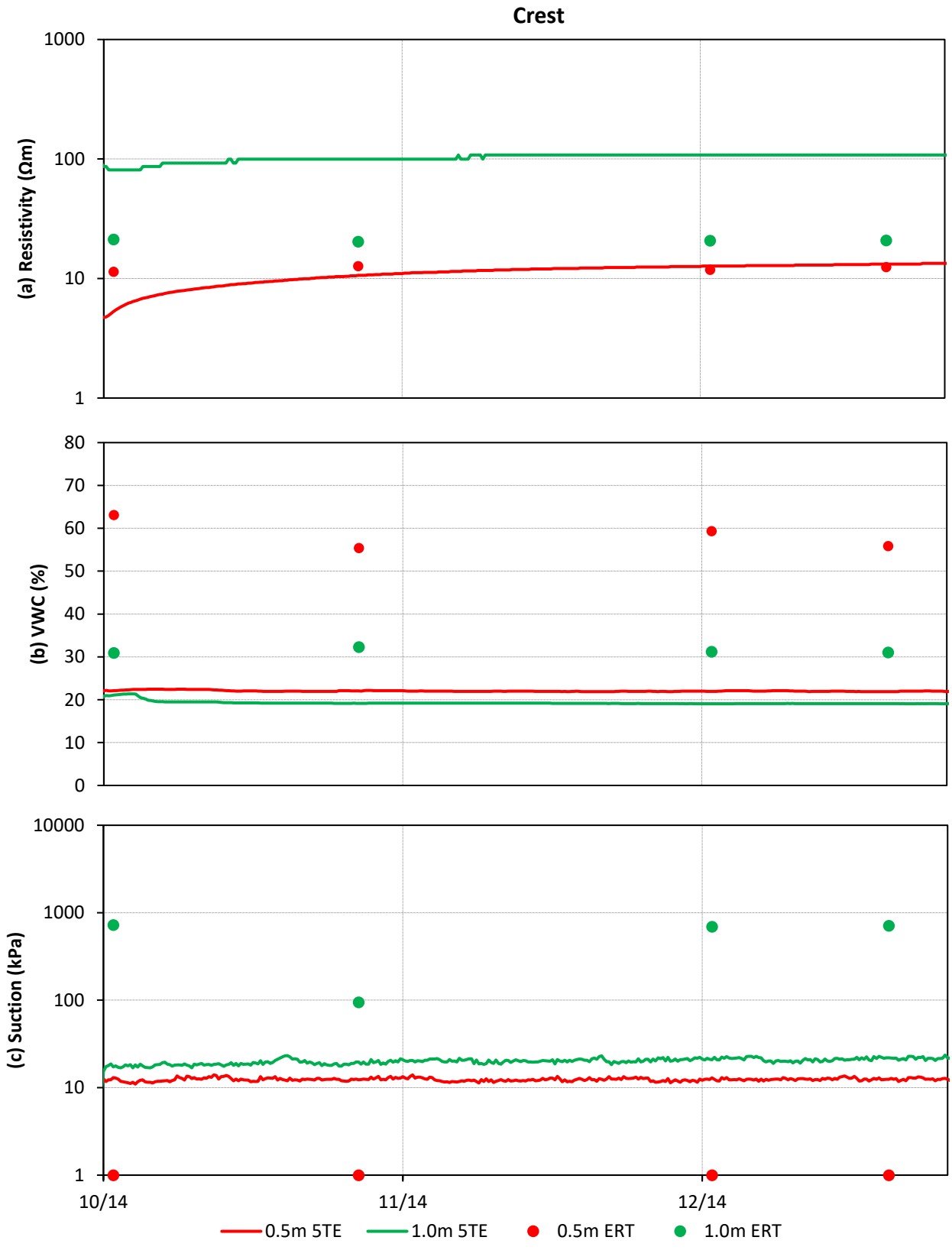

Figure 5.56 Comparison of geotechnical measurements obtained from ERT and the point sensor network – Crest position of the ERT test plot, showing (a) resistivity, (b) volumetric water and (c) suction values. This position refers to location a6 on the sensor distribution map in Figure 4.39

5.4.2 *Sprinkling experiments (January 2015)*

The following images present a comparison of the point sensor and ERT-derived geotechnical parameters at two locations on the South slope of the ERT test plot, during January 2015, when the on-site sprinkler system was activated (see subchapter 4.2.2). The sprinkler system was properly activated on the 12th, however, on the 10th and 11th, the functionality of the system was tested, thus there was some additional water infiltration on these days too. Figure 5.57 shows the environmental response to the sprinkler activation, at the lower position. It can be seen that in the near-surface (0.1 m), the system activation correlates directly with an immediate decline in point sensor resistivity values (which are automatically corrected for temperature by the sensor), and an increase in point sensor water content values. At the same depth, however, the ERT-derived resistivity values exhibit converse behaviour, consistent with rapid drying of the near-surface. To a lesser extent, the same phenomenon is observed from the 0.5 m ERT-derived dataset, consistent with more gradual drying behaviour, the point sensors, however, do not register any change at depths of 0.5 m and 1.0 m.

At the upper position, Figure 5.58 shows a less pronounced but still present decline in near-surface point sensor resistivity values. As before, the ERT-derived results show converse behaviour (unfortunately there is no water content data at 0.1 m depth due to sensor malfunction, therefore the VWC comparison cannot be presented). At 0.5 m and 1.0 m depths, gradually increasing resistivity values are observed from the 19th of January onwards, accompanied by a decline in reported water content values, suggestive of drying at depth. At the same depths, the point sensors demonstrate a small increase in measured water content values.

Given that the ERT test plot was subjected to an additional 134 mm of water (approximately) per day, it is evident that the apparent drying behaviour suggested by the ERT-derived results must be explicable by some other mechanism, as discussed in subchapter 6.3.2.

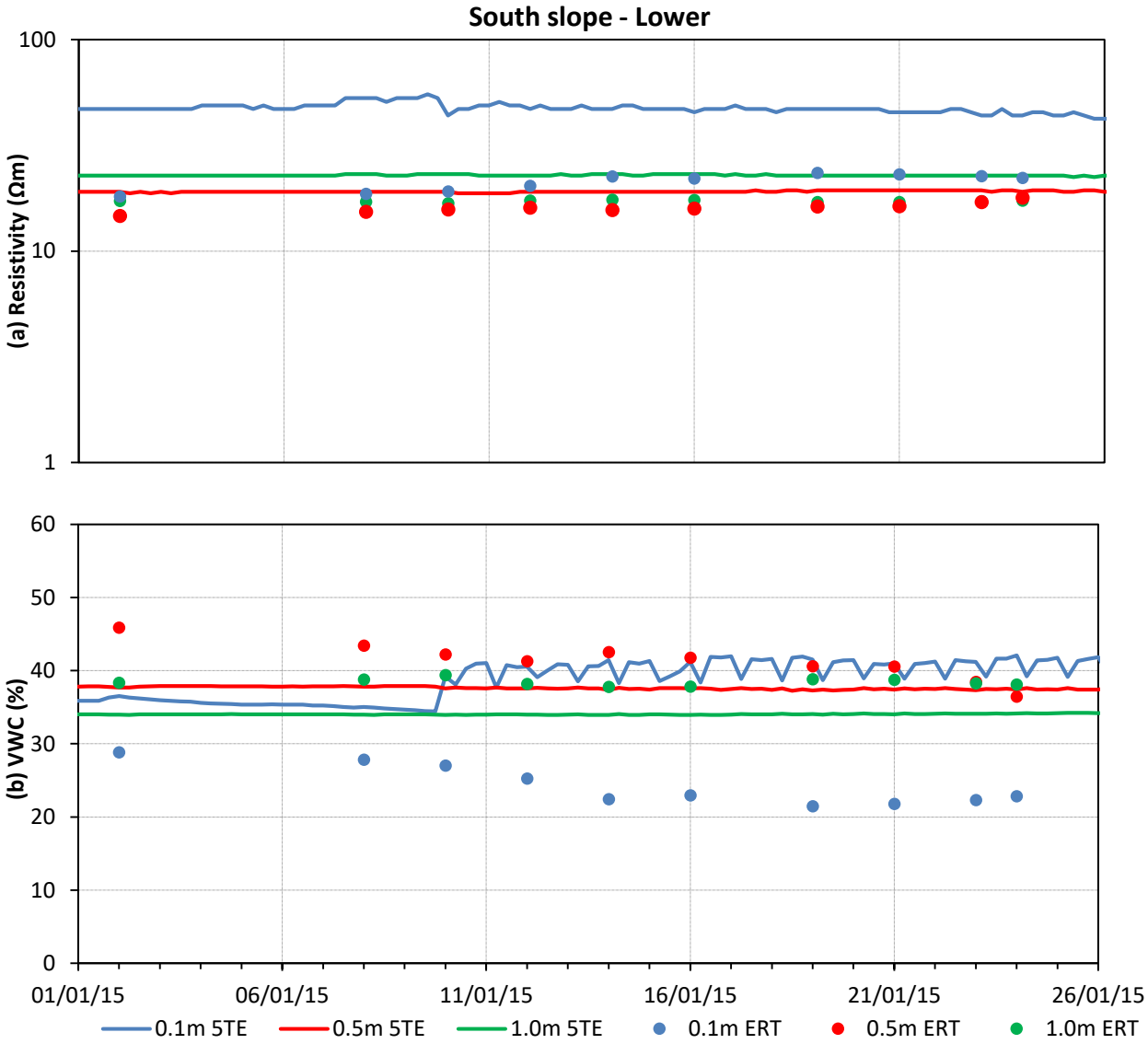

Figure 5.57 Comparison of geotechnical measurements obtained from ERT and the point sensor network (January 2015) - South slope lower position of the ERT test plot, showing (a) resistivity and (b) volumetric water content values. This position refers to location a1 on the sensor distribution map in Figure 4.39

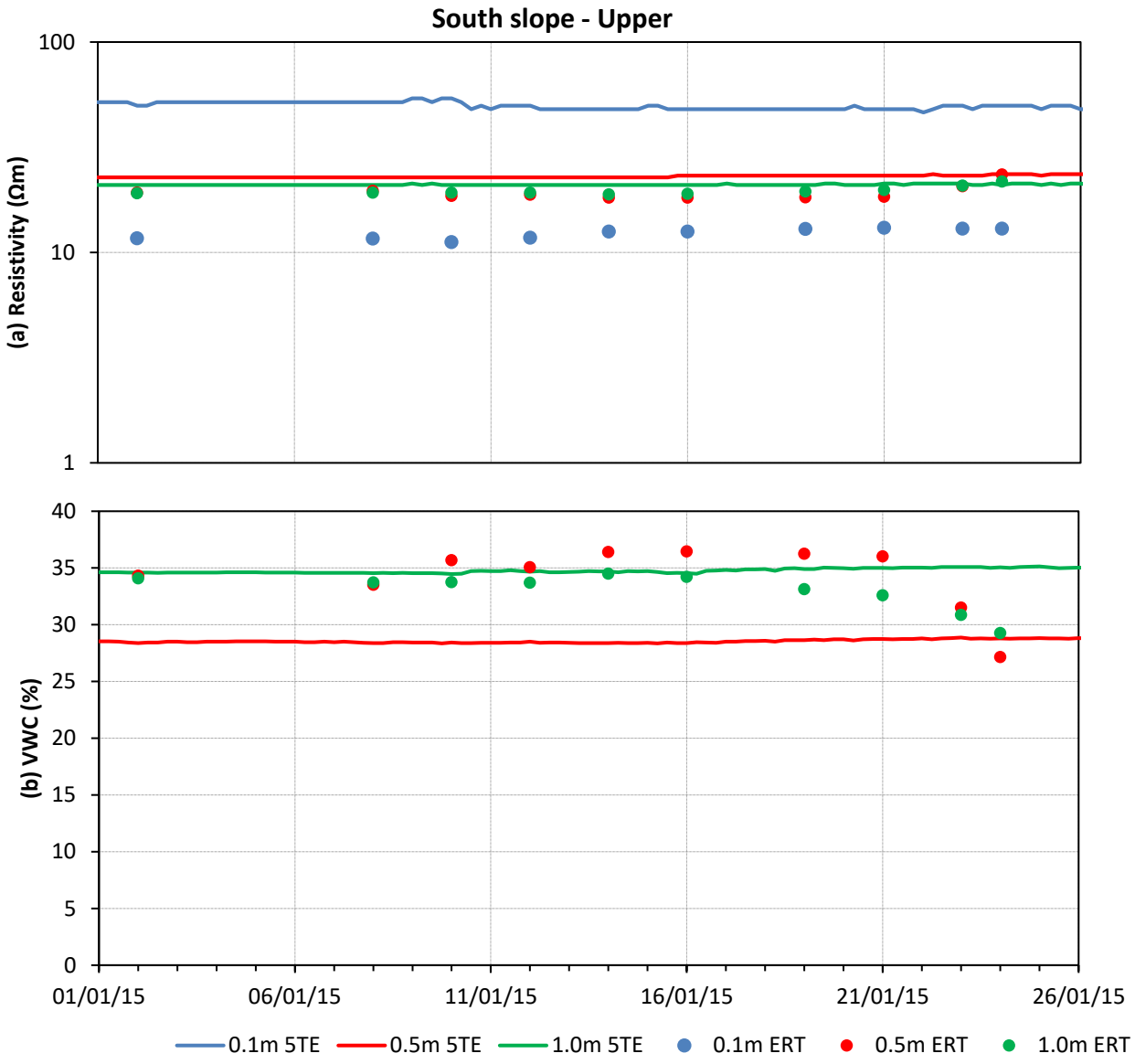

Figure 5.58 Comparison of geotechnical measurements obtained from ERT and the point sensor network (January 2015) - South slope upper position of the ERT test plot, showing (a) resistivity and (b) volumetric water content values. This position refers to location a2 on the sensor distribution map in Figure 4.39

5.4.3 *Assessment of temperature and porosity models*

In subchapters 4.3.6 and 4.3.7, the temperature and porosity models for the BIONICS test embankment were described. These, respectively, were then used as the basis for the correction of ERT data to a reference temperature, and as input for the Waxman-Smits equation translating recorded ERT data into estimated water content data, and ultimately, estimates of soil suction.

In the following images, the representability of the temperature model is assessed by plotting the deviation between the temperature values recorded from the point sensor network and those dictated by the temperature model. The deviation was calculated as follows:

$$Temperature\ deviation\ (\%) = 100 * \frac{T_{5TE} - T_{Model}}{T_{Model}}$$

where T_{5TE} and T_{Model} describe the temperatures recorded by the (5TE) point sensors and dictated by the temperature model, respectively. Following the above, positive temperature deviations describe measured temperatures which are higher than those described by the temperature model, for a given location, at a given time.

Figure 5.59 shows the temperature deviations corresponding to the comparison images presented in Figure 5.53 to Figure 5.56, describing the South slope and crest of the ERT test plot. For the most part, the temperature model is observed to underestimate actual soil temperature, an effect which is most pronounced in the near-surface, and least at 1.0 m depth. In general, the poorest agreement at the lower and upper positions on the South slope is observed during the winter months (Figure 5.59a and b), and at the top position during the spring and summer months (Figure 5.59c). The dataset describing the crest position only covers the winter period, therefore no assumptions may be made on the seasonal goodness of fit of the temperature model at this location.

The ERT/point sensor comparison images shown in Figure 5.53 to Figure 5.56 demonstrated poor agreement between the datasets to occur during Summer 2014, however, Figure 5.59 does not show notably high temperature deviations during this period. In general, however, the temporal variability of the goodness of fit of the temperature model demonstrates one mechanism for the variable agreement between the results of the ERT array and the point sensor network.

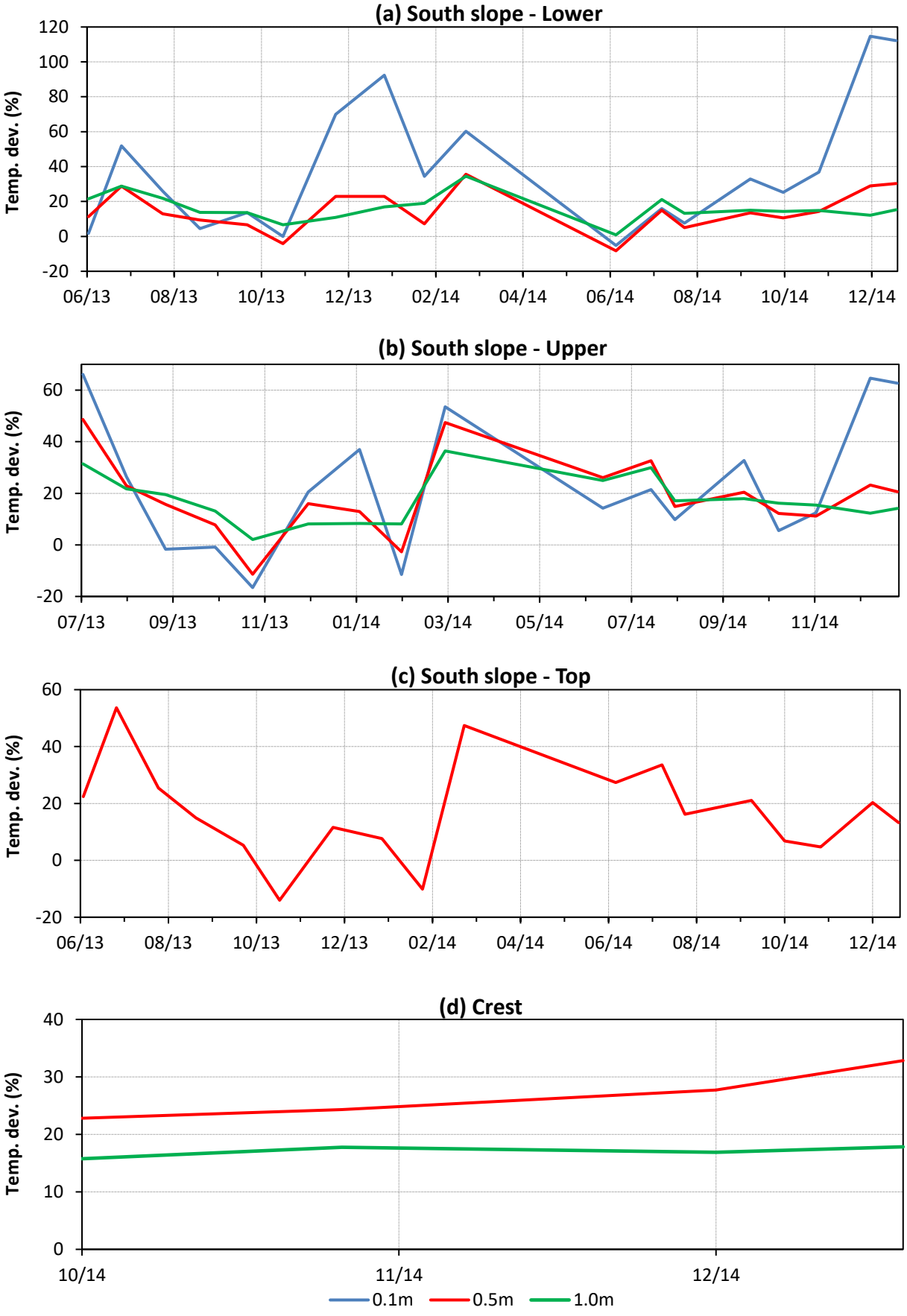

Figure 5.59 Deviation between recorded and model temperature values – monthly time series, showing (a) South slope lower, (b) South slope upper, (c) South slope top and (d) Crest positions on the ERT test plot, referring to locations a1, a2, a3 and a6 respectively on the sensor distribution map in Figure 4.39

In Figure 5.60, the temperature deviation is shown for the South slope lower and upper positions of the ERT test plot, during January 2015, when the sprinkler system was activated. It can be seen that following activation on the 12th, there is an immediate decline in the temperature deviation, at all depths, resulting in a reversal from positive to negative deviations, such that the measured temperatures fall to the extent that they become less than those predicted by the temperature model. In subchapter 2.3.1, the effect of temperature on resistivity was explained, whereby a decrease in temperature causes an increase in resistivity. Such an increase is observed in Figure 5.57 and Figure 5.58. Field observations during January and February 2016 noted the accumulation of ice on vegetation covering the surface surrounding the sprinklers (Figure 5.61), demonstrating the presence of freezing temperatures.

In subchapter 4.3.7, a method of estimating soil porosity values using the point sensor network was presented. These estimates are presented in Table 5.3, which also presents the porosity values at the point sensor locations as extracted from the porosity model. From Figure 5.53b, very good qualitative and quantitative agreement was observed between directly measured and ERT-derived water content values, at the South slope lower position (at 0.5 m and 1.0 m depths), where the two porosity datasets compare very well. Similarly, at the upper position, the two methods were in close agreement at 1.0 m depth (Figure 5.54b), also corresponding to closely matching porosity datasets. At the same position but at a shallower depth (0.5 m) the point sensor and ERT methods identified the same trends but significantly different quantitative values, which correlates with a considerable difference between the two reported porosity values. This correlation is also observed at the South slope top (0.5 m) and crest positions (0.5 m and 1.0 m depths). This correlation is discussed further in subchapter 6.3.3.

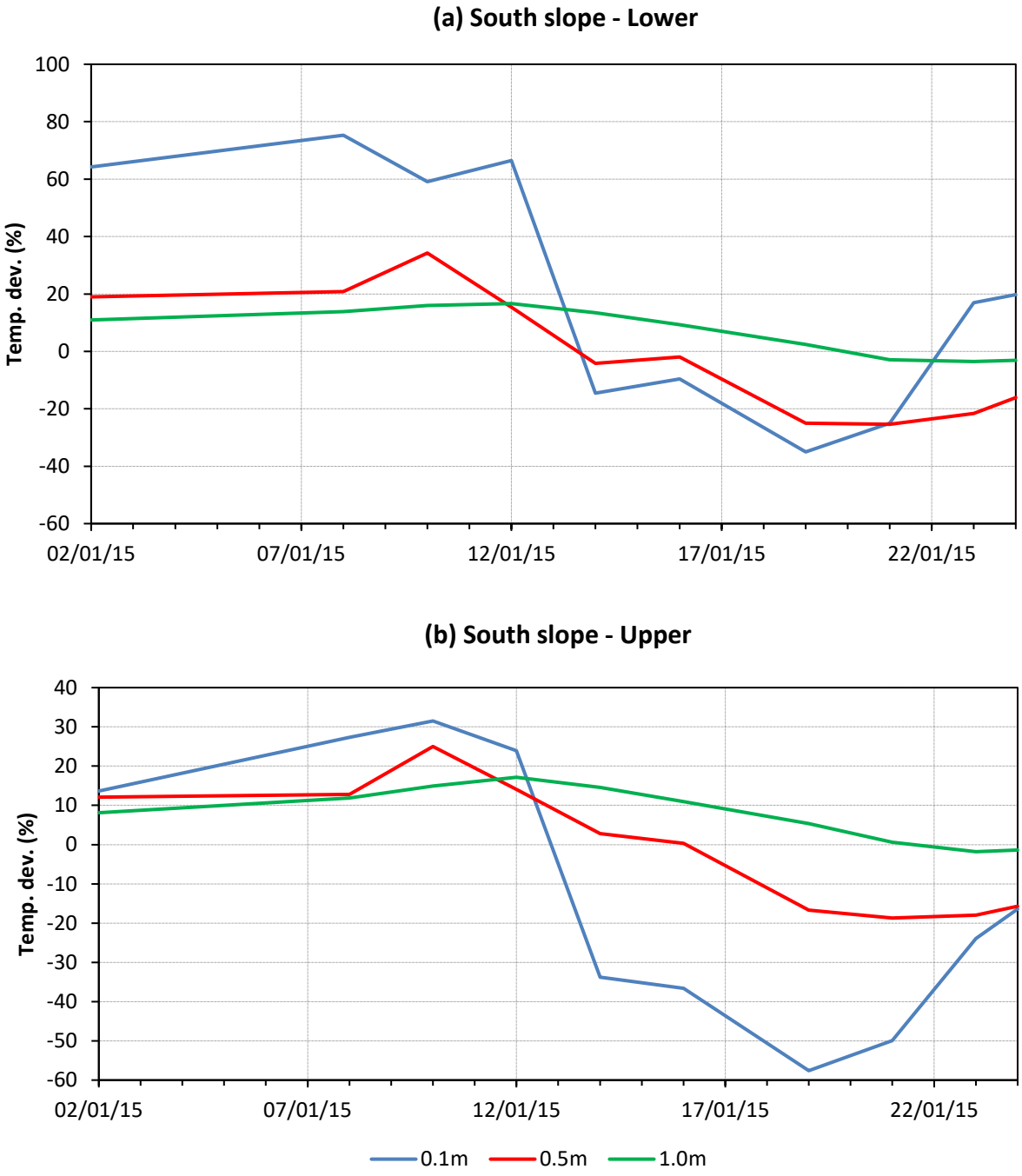

Figure 5.60 Deviation between recorded and model temperature values (January 2015) , showing (a) South slope lower, and (b) South slope upper positions on the ERT test plot, referring to locations a1, and a2 respectively on the sensor distribution map in Figure 4.39

Figure 5.61 Frozen sprinkler water at on the embankment surface

Table 5.3 Deviation between estimated and model porosity values

Sensor	**Porosity model**	**Estimated porosity from 5TE VWC**
a1 (South slope lower) 0.1m	0.4880	0.4962
a1 (South slope lower) 0.5m	0.3652	0.3776
a1 (South slope lower) 1.0m	0.3652	0.3437
a2 (South slope upper) 0.1m	0.4880	0.4962*
a2 (South slope upper) 0.5m	0.3535	0.2922
a2 (South slope upper) 1.0m	0.3652	0.3546
a3 (South slope top) 0.5m	0.3396	0.4269
a6 (Crest) 0.5m	0.3554	0.2407
a6 (Crest) 1.0m	0.3652	0.1976

Estimated porosity values obtained by assuming maximum recorded VWC to describe porosity surrounding point sensor. *a2 0.1m porosity assumed to be same as a1 0.1m, due to corrupted time series data

5.4.4 *Application of proxy relationships to point sensor resistivity data*

The previous subchapter compared direct measurements of geotechnical parameters to those derived from the application of proxy relationships to ERT data. In the following images, these proxy relationships (Waxman-Smits relating resistivity to water content; Van Genuchten for relating water content to soil suction) are applied to 5TE point sensor resistivity data, in order to investigate their applicability.

Waxman-Smits relationship

In Figure 5.62, the time series volumetric water content data are shown for three locations on the South slope of the ERT test plot. For each depth of investigation, two types of water content data are presented: directly measured water content data ("meas" dataset in legend), and that obtained by applying the Waxman-Smits relationship to directly measured resistivity data ("WS" dataset), where both original datasets were recorded using the 5TE point sensors. The resistivity data to which the Waxman-Smits relationship is applied have been corrected to a reference temperature of 20 ˚C (laboratory temperature), in order to allow for the laboratory-derived proxy relationships to be applied. These data have been corrected on the basis of soil temperatures which are also recorded by the 5TE sensors, rather than the temperature model, thereby obviating any issue relating to limitations of the temperature model.

As explained in subchapters 4.3.8 and 4.3.9, the translation of resistivity into water content and of water content into soil suction requires, as input, the soil porosity. Estimates of soil porosity were made from the measured point sensor data, following the method outlined in subchapter 4.3.7. The 5TE-derived porosity values shown in Table 5.3 were therefore used as input in the proxy relationships, as a means of mitigating the issue of inaccurate porosity estimates arising from the porosity model.

It can be seen from Figure 5.62a that at the South slope lower position, there exists good qualitative but poor quantitative correlation between the measured and WS-derived near-surface water content values, resulting from elevated near-surface resistivity values as seen in Figure 5.53. At 0.5 m depth, both datasets demonstrate the same temporal trends, with the WS-derived values consistently plotting lower than those which are directly measured, by between 2 % and 5 %, with closer agreement associated with higher water content

values. At 1.0 m, the offset between the two datasets is less pronounced, with WS-derived values consistently plotting between 1 % and 3 % below the measured dataset, again demonstrating the closest agreement during the wetter months, except after the activation of the sprinkler system.

At the upper position (Figure 5.62b), at depths of 0.1 m and at 1.0 m, and at 0.5 m at the top position (Figure 5.62c), similar behaviour is observed, where the WS-derived water contents follow the path of the directly measured values, but with a significant negative offset, such that water content values are drastically underestimated. At a depth of 0.5 m at the upper position, however, the offset between the two datasets is such that the WS-derived set overestimates water content values. After the activation of the sprinkler system, however, the WS-derived values appear to show rapid drying, which is a direct result of the resistivity increases observed from Figure 5.58.

The data described above pertain to the ERT test plot portion of the test embankment, which was built to “well-compacted“ specifications. In order to provide a comprehensive investigation of the representability of the proxy relationships, they were also applied to resistivity data gathered at Panel B, built to the same degree of compaction.

In Figure 5.63, the data for the South slope and crest of Panel B are shown. At all four locations (Figure 5.63a, b, c, d), the WS-inferred water content values closely follow the paths of the measured water content values, but with a negative offset of up to 20 %. At a depth of 1.0 m at the lower and crest positions (Figure 5.63a and d and c), similar offsets are observed. At the middle and upper positions (Figure 5.63b and c), however, the measured and WS-derived water content values compare very well, especially at higher water contents. At the upper, middle and lower positions on the North slope of Panel B (Figure 5.64a, b and c), it can again be observed that the greatest agreement between the measured and WS-derived datasets occurs at 1.0 m. The suggestion for this improved agreement at depth is that the 5TE sensors have better coupling with the surrounding soil than do the sensors at 0.5 m depth, resulting in the underestimation of inferred water content values.

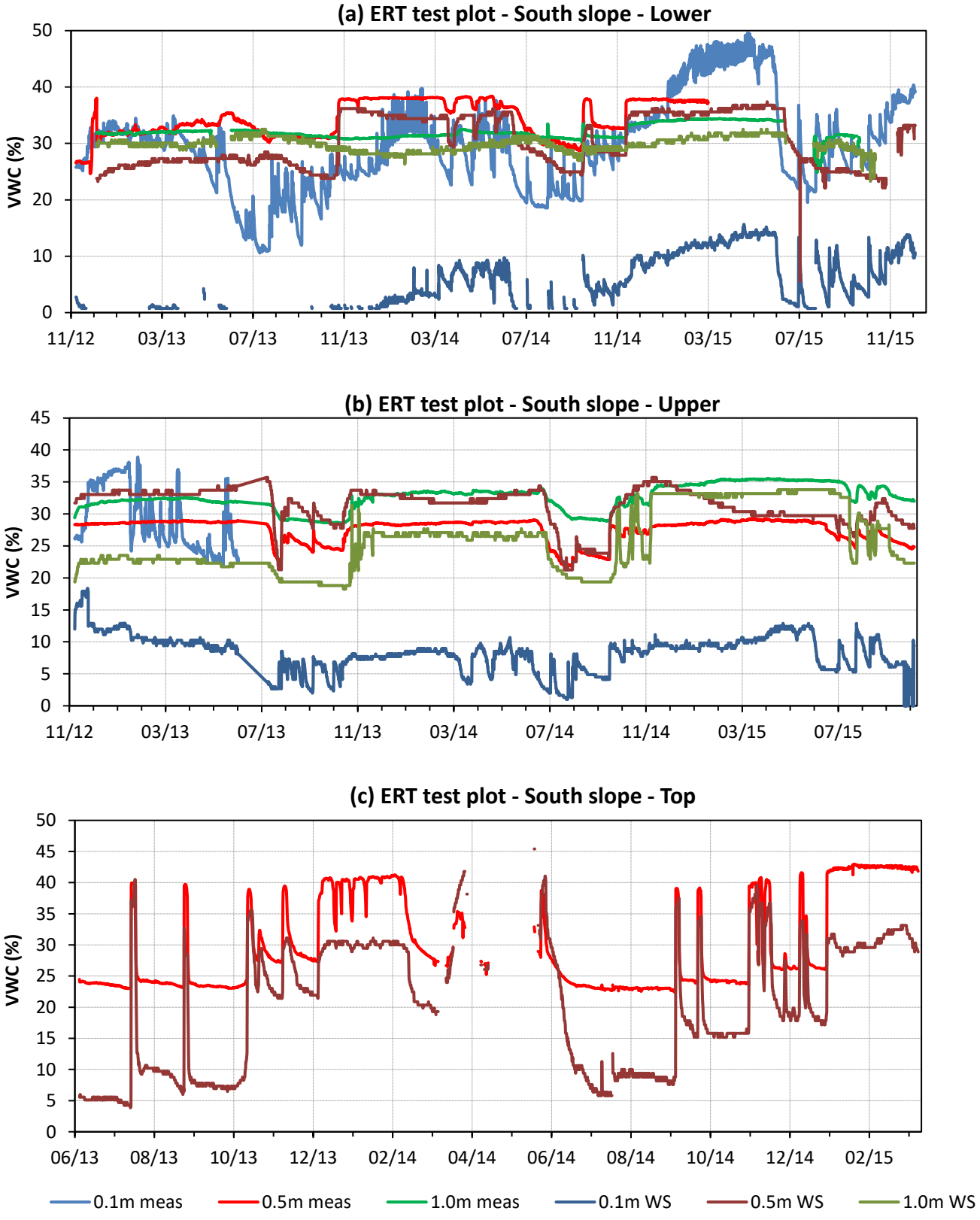

Figure 5.62 Comparison of measured and inferred volumetric water content values – ERT test plot . Measured water content values obtained directly from 5TE VWC sensors; inferred water content values obtained by applying Waxman-Smits relationship to 5TE resistivity values. Graphs shown pertain to the South slope of the ERT test plot, showing (a) lower, (b) upper and (c) top positions. These positions refer to locations a1, a2 and a3 on the sensor distribution map in Figure 4.39

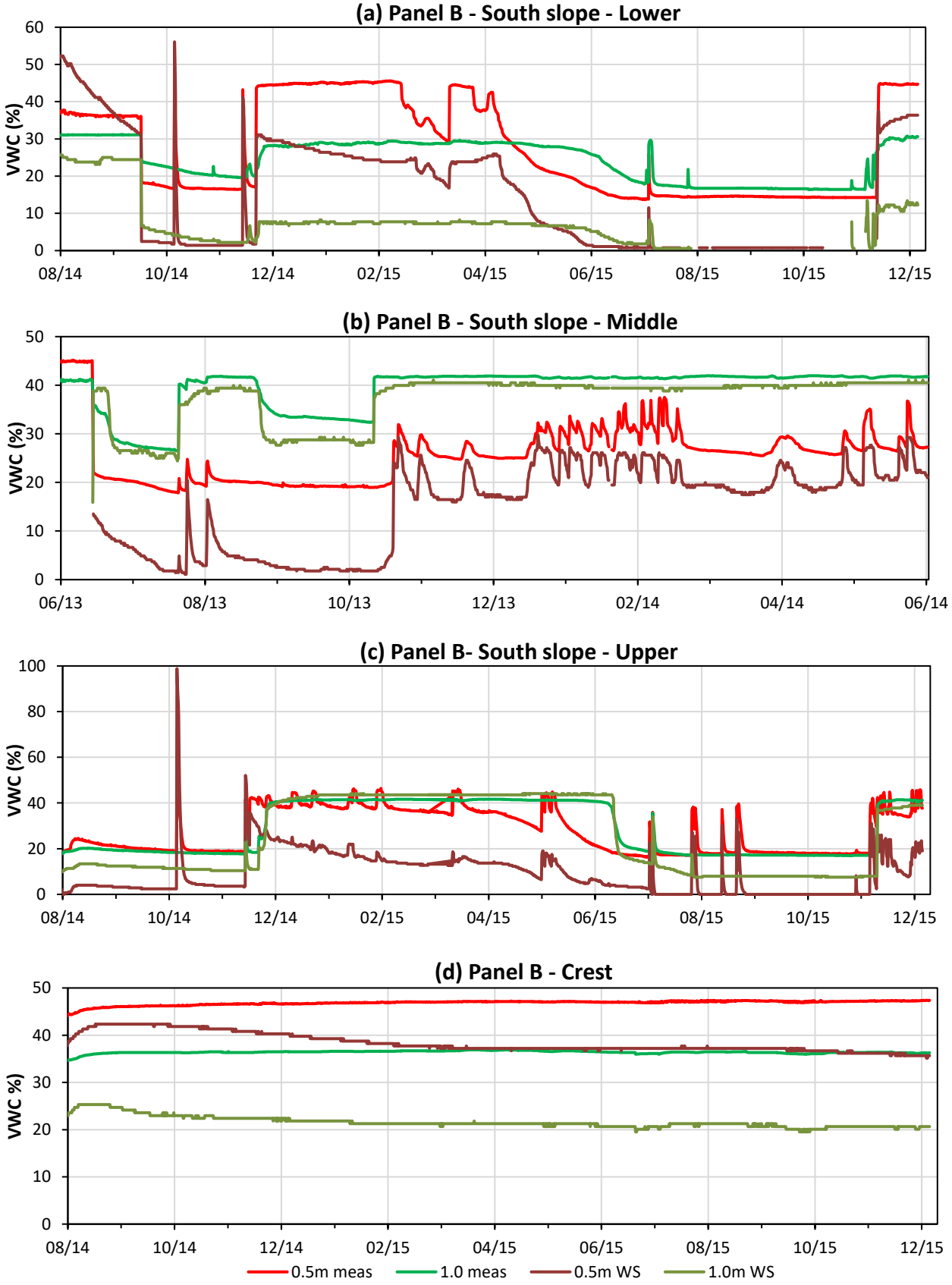

Figure 5.63 Comparison of measured and inferred volumetric water content values – Panel B South slope and crest . Measured water content values obtained directly from 5TE VWC sensors; inferred water content values obtained by applying Waxman-Smits relationship to 5TE resistivity values. Graphs shown pertain to Panel B, showing (a) lower, (b) middle, (c) upper and (d) crest positions. These positions refer to locations B1, BS1, B3 and B4.5 on the sensor distribution map in Figure 4.39

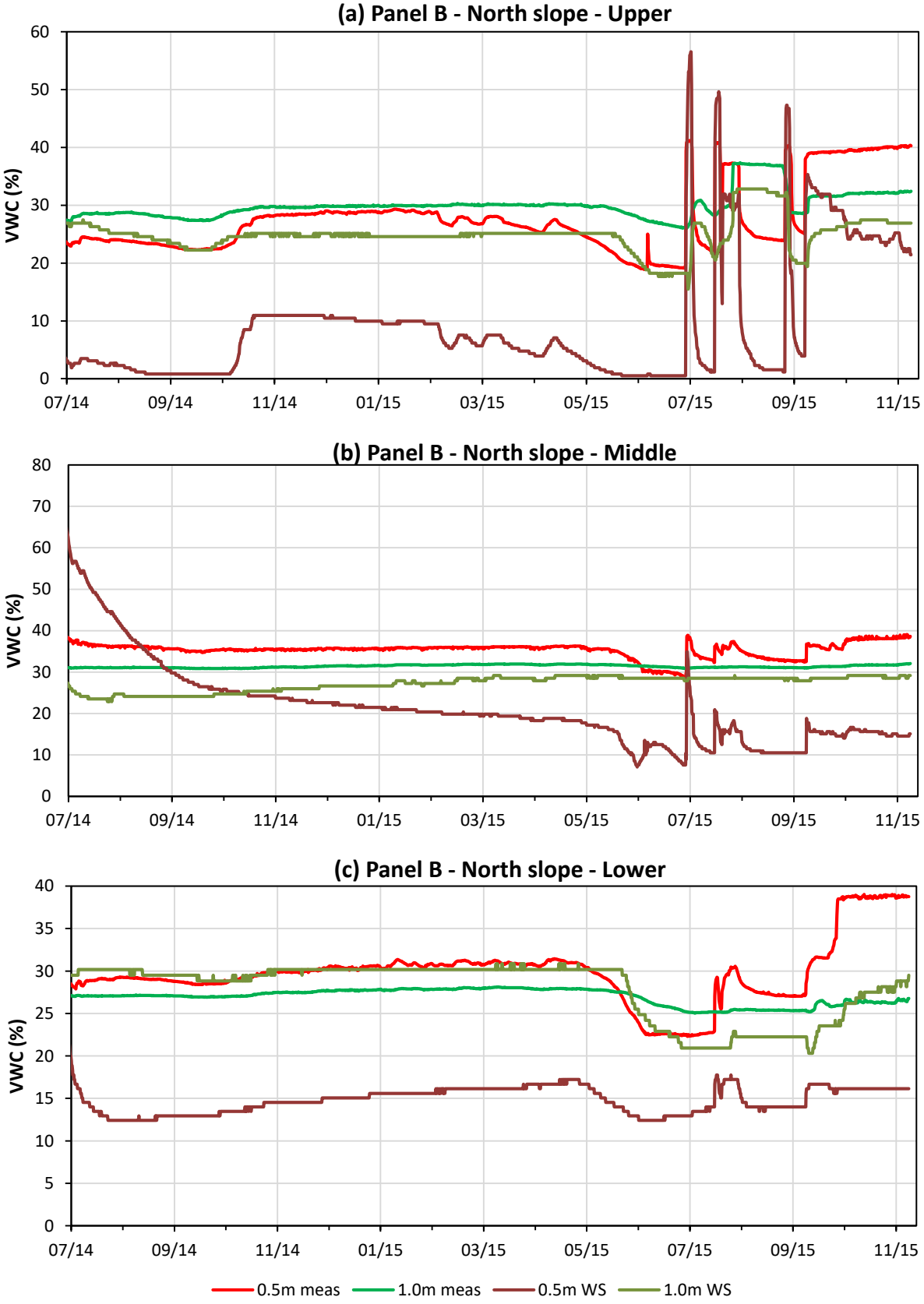

Figure 5.64 Comparison of measured and inferred volumetric water content values – Panel B North slope . Measured water content values obtained directly from 5TE VWC sensors; inferred water content values obtained by applying Waxman-Smits relationship to 5TE resistivity values. Graphs shown pertain to the North slope of Panel B, showing (a) upper, (b) middle and (c) lower positions. These positions refer to locations B5, B6 and B7 on the sensor distribution map in Figure 4.39

Van Genuchten relationship

In the previous subchapter, the Waxman-Smits relationship was applied to resistivity data gathered using the point sensor network. In order to assess the suitability of the Van Genuchten relationship, it was applied to the WS-derived water content data, yielding suction estimates ("VG" dataset on legend), which are compared to directly measured suction values obtained from MPS sensors within the point sensor network ("meas" dataset). In the following images, the Van Genuchten relationship is only applied to WS-derived water content values which compared reasonably with the measured values, in Figure 5.62 to Figure 5.64. The reason for this is that any agreement between VG-derived and measured suction values would be false if the original water content values which are used as input do not broadly agree. Due to the fact that the VG-derived suction values are based on point sensor resistivity data, the comparison between the datasets can only be made at locations where both a 5TE resistivity sensor and an MPS suction were installed.

In Figure 5.65, the measured suction values are presented for the South slope lower position, alongside the VG-derived data. In order to produce the VG-derived data, the method described in subchapter 4.3.9 was applied, allowing separate drying and wetting Van Genuchten parameters to be applied at discrete parts of the embankment. At both depths, the VG-derived datasets demonstrate unrealistically rapid variations of estimated suction values, of almost an order of magnitude, which is a result of distinct drying and wetting Van Genuchten parameters being applied, depending on the sign of the water content change with respect to the previous data point. From Figure 5.27 and Figure 5.28, it can be seen that the wetting portion of the Van Genuchten SWRC provides a better approximation of the residual field SWRC recorded using the point sensor network. For this reason, the decision was made to apply only wetting VG parameters to the WS-derived water content data.

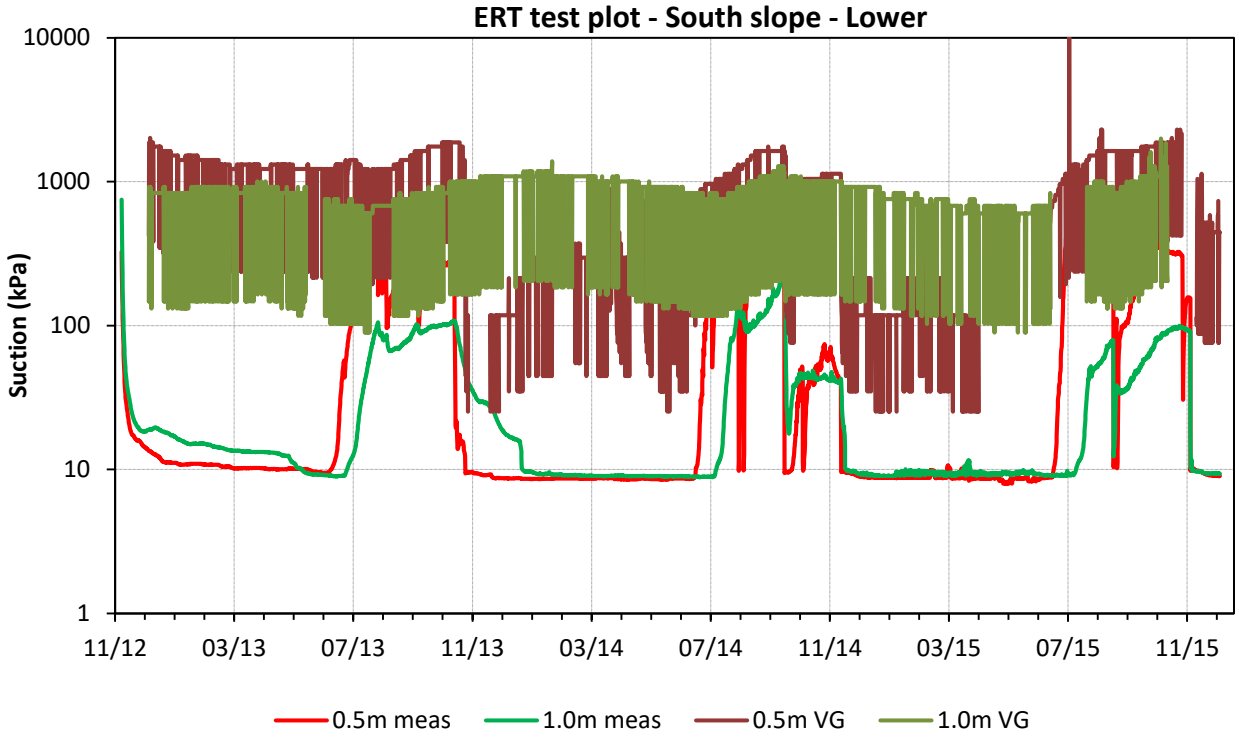

Figure 5.65 Comparison of measured and inferred suction values – method test . Measured suction values obtained directly from MPS matric suction sensors; inferred suction values obtained by applying Van Genuchten relationship to volumetric water content values, which were derived from 5TE resistivity values via the Waxman-Smits relationship. Suction values obtained using the method described in subchapter 4.3.9, employing both drying and wetting curves. Graph shown pertains to the South slope lower position at the ERT test plot. This position refers to location a1 on the sensor distribution map in Figure 4.39

In Figure 5.66, the measured and VG-derived soil suctions are presented for the South slope lower and positions of the ERT test plot. At the lower position (Figure 5.66a), both the VG-derived and measured suction datasets demonstrate higher values at 0.5 m than at 1.0 during the summer/autumn drying periods, yielding comparable suction estimates. At other (wetter) times of the year, however, the correlation between the datasets is poorer: at 0.5 m, the VG-derived data do demonstrate a suction loss, but not as severe as measured by the point sensors; at 1.0 m, the VG-derived data demonstrate increased suction values, not in keeping with wetting behaviour. At the upper position (Figure 5.66b). the two suction datasets demonstrate the same qualitative behaviour, showing elevated summer/autumn suction values, however, the quantitative agreement is much poorer.

In Figure 5.67, the measured and VG-derived soil suction values for Panel B are presented. Unfortunately, malfunction of the loggers has led to the loss of some of the recorded data. At the South slope upper position of Panel B (Figure 5.67a), both the measured and VG-

derived datasets demonstrate elevated summer/autumn values, however, these differ by up to three orders of magnitude, such that the VG-derived dataset significantly overestimates soil suction. During the wetter periods, the difference is one order of magnitude, with the VG-derived method underestimating soil suction with respect to the point sensors. On the North slope of Panel B (Figure 5.67b, c and d), there is much less variability in the recorded soil suctions, with the point sensors yielding values of the order of 10 kPa, and the VG-derived method overestimating suctions by an order of magnitude.mFrom these images, it is evident that the Van Genuchten proxy relationship has limited quantitative use, but may be useful as a qualitative interpretation tool.

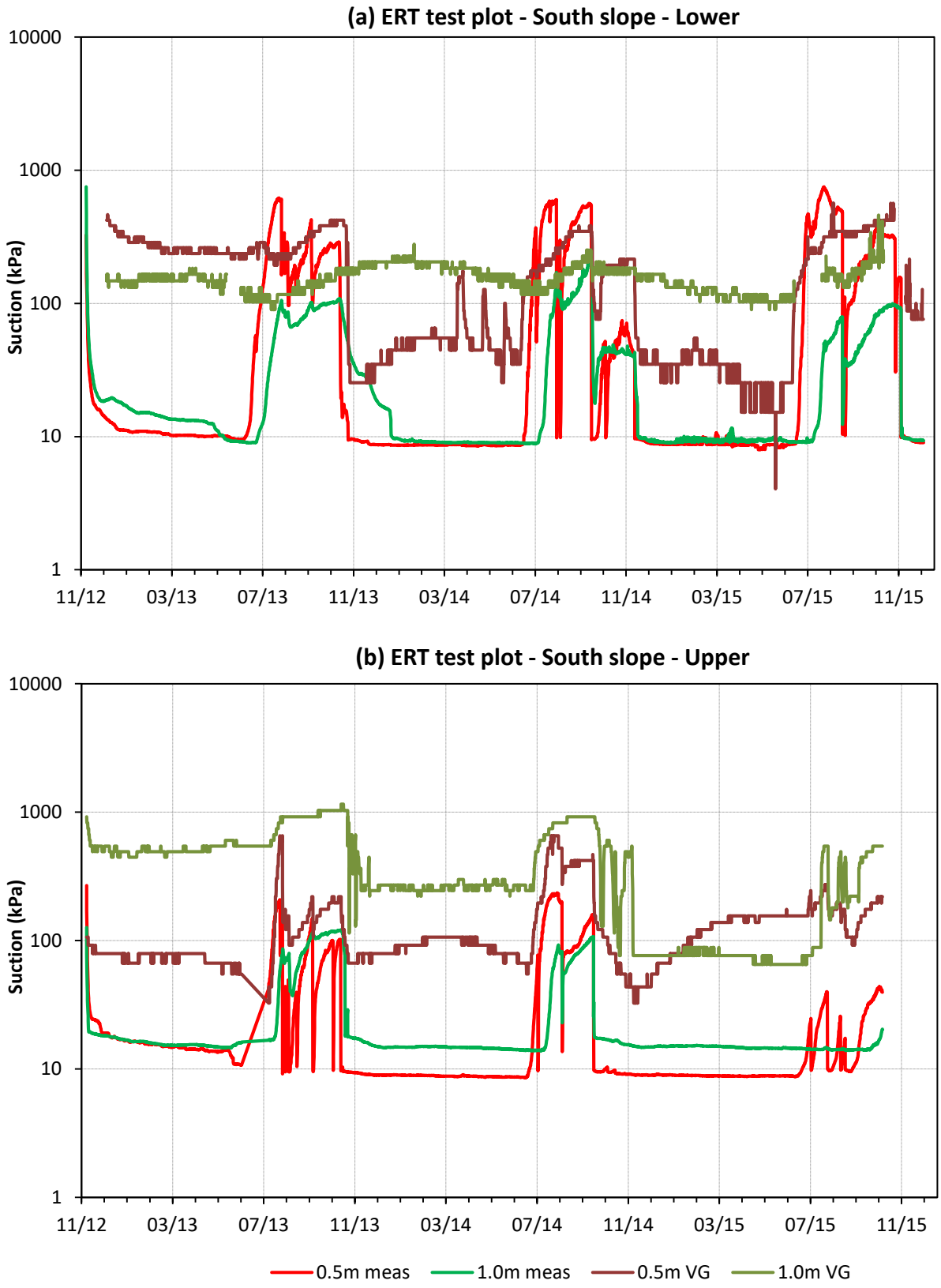

Figure 5.66 Comparison of measured and inferred suction values – ERT test plot . Measured suction values obtained directly from MPS matric suction sensors; inferred suction values obtained by applying Van Genuchten relationship to volumetric water content values, which were derived from 5TE resistivity values via the Waxman-Smits relationship. Suction values obtained using the wetting curve presented in Figure 5.1. Graphs shown pertain to the South slope (a) lower and (b) upper positions. These positions refer to locations a1 and a2 on the sensor distribution map in Figure 4.39

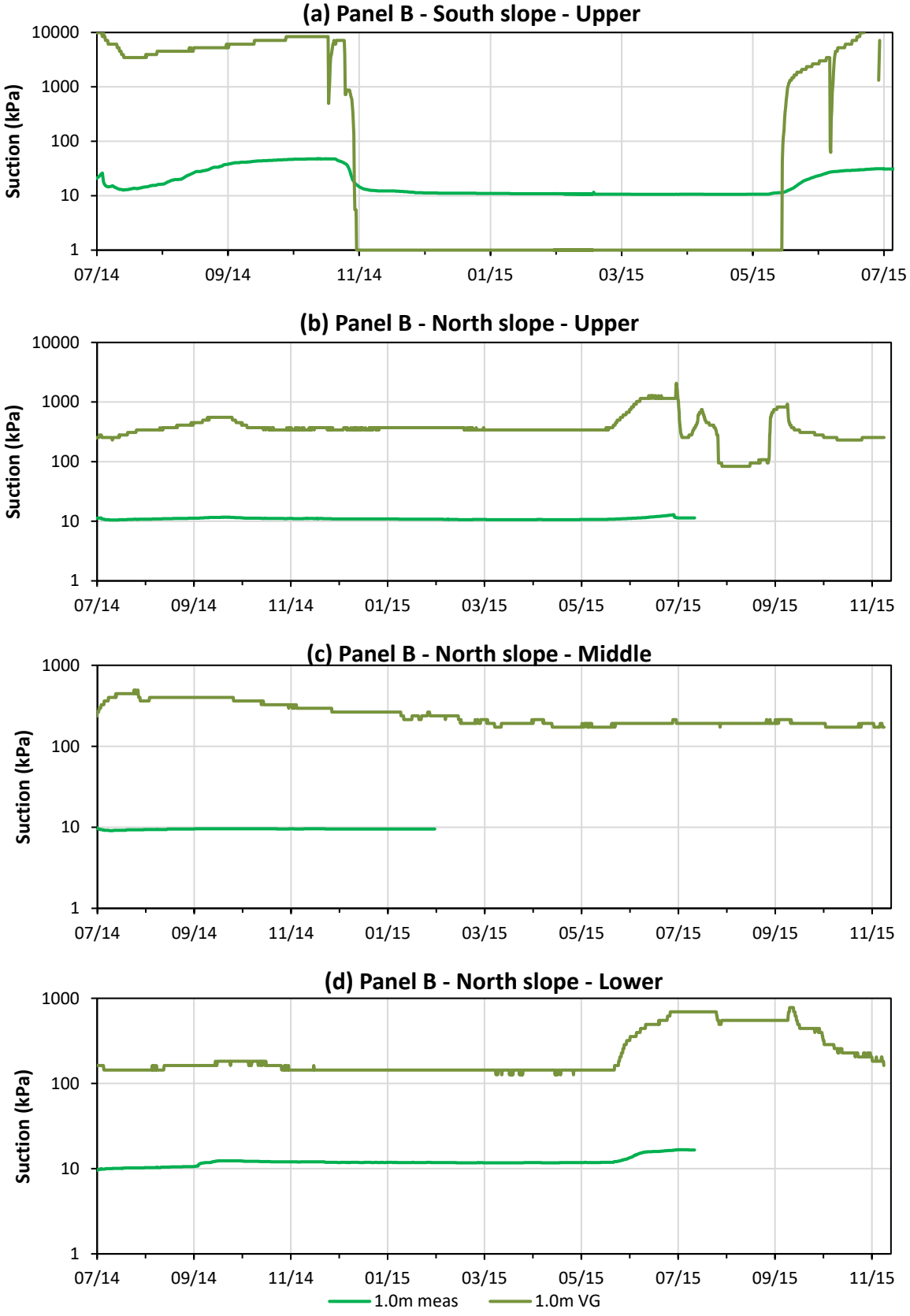

Figure 5.67 Comparison of measured and inferred suction values – Panel B . Measured suction values obtained directly from MPS matric suction sensors; inferred suction values obtained by applying Van Genuchten relationship to volumetric water content values, which were derived from 5TE resistivity values via the Waxman-Smits relationship. Suction values obtained using the wetting curve presented in Figure 5.1. Graphs shown pertain to (a) South slope lower, (b) North slope upper, (c) North slope middle and (d) North slope lower positions. These positions refer to locations B3, B5, B6 and B7 on the sensor distribution map in Figure 4.39

5.5 Summary of results

Laboratory

- A laboratory SWRC for the BIONICS clay material resolved distinct drying and wetting portions, in close agreement with previous, published work on the same material
- A comparison of two and four point resistivity methods resolved an inverse power relationship with water content, showing the more conventional two point method to over-estimate soil resistivity, due to higher contact resistances within electrical circuit
- Macro-fractures were observed to cause anomalously high bulk resistivity values
- Using both two and four point methods, the resistivity – water content curve was observed to follow the same path, irrespective of whether a drying or a wetting path was being followed, showing resistivity to be independent of pore water pressure
- Hysteresis of the resistivity – water content curve was observed between primary and secondary moisture cycles (each comprising both drying and wetting portions), such that resistivity increased at the dry end and decreased at the wet end, for successive cycles
- The method of compaction of soil specimens was found to have a considerable effect on measured resistivity values
- The resistivity of BIONICS clay was observed to decrease by 1 % per 2 °C temperature increase, in close agreement with literature values
- Both shear strength and unconfined compressive strength reduced drastically between drying and wetting cycles due to a loss of suction; shear strength was also significantly reduced by the development of micro-cracks resulting from shrink-swell behaviour
- Changes in soil shear strength were reflected in the recorded resistivity values
- Trends observed in the laboratory regarding the effects of seasonal moisture cycles at the micro-scale were supported by E-SEM imaging
- Considerable changes in the geophysical and geotechnical relationships investigated during the laboratory testing programme occurred at a critical GWC of 12 %, inferred to pertain to the continuity of the pore water phase within the compacted BIONICS clay material

Point sensor network

- The geotechnical response to environmental forcings (temperature, precipitation) was subject to damping relating to depth, aspect and degree of compaction, with the greatest diurnal and seasonal fluctuations observed in the near-surface, near the top of the Southern slope of the test embankment
- In situ SWRCs demonstrated a gradient change over time, describing a suction loss between progressive seasonal moisture cycles
- In situ field resistivity – water content relationships compared best with the four point laboratory-derived curve, despite constituting a two point measurement. Near-surface resistivity values were higher than those at depth, for a given water content
- Daily precipitation levels over the test period showed slightly elevated summer rainfall compared to winter; measured in situ water contents described the embankment fill to fluctuate contrastingly
- Individual rainfall events could not be resolved from the point sensor network, but could be clearly identified by resistivity fluctuations recorded during ERT monitoring

ERT monitoring

- 2D ERT imaging was observed to be sensitive to 3D resistivity anomalies outside of the measurement plane and to have low sensitivity at depth, therefore, emphasis was put on images derived from 3D ERT data
- ERT images were converted to water content and pore water pressure distribution images, describing a highly dynamic topsoil layer. Beneath the topsoil, high water contents were estimated in a moderately dynamic layer, observed to fluctuate seasonally. The embankment core was characterised by relatively low water contents, which varied little over time. A zone beneath the crest ballast demonstrated water contents consistently near saturation
- The greatest fluctuations in resistivity at the BIONICS test embankment corresponded to observed crack locations, which healed in the winter, reopening in the summer
- 3D resistivity and moisture images were able to resolve dynamic changes at a range of timescales, from general seasonal fluctuations (monthly) to capturing crack

development during warm, dry conditions (weekly), and the rapid infiltration of rainwater from heavy precipitation (daily)

- Rainwater infiltration during rapid wetting events was explored by volumetric imaging, which reflected differing seasonal ground conditions, showing more direct infiltration via existing cracks favoured during the summer, with greater runoff during the winter
- The sprinkling experiments resulted in an observed increase in embankment fill resistivity, which the ERT-derived moisture images falsely interpreted as a rapid drying event

Comparison of ERT and point sensor results

- Both methods demonstrated similar qualitative trends, describing a highly dynamic near surface (0.1 m) layer, with seasonable variability in the intermediate zone (0.5 m), exhibiting relatively static behaviour at depth (1.0 m)
- Similar qualitative trends were observed from both methods, in terms of resistivity and volumetric water content. The best quantitative agreement between the two methods was observed at locations where the porosity model most closely matched porosity estimates obtained from the point sensor network. Poor quantitative agreement was observed between the two data types, in terms of suction values
- Generally, two point resistivity measurements made using the point sensor network were higher than four point measurements obtained by ERT; similarities between the methods at certain locations were ascribed to point sensors being embedded at depth, improving coupling with the surrounding soil
- The closest agreement between the two methods was observed during wetter conditions; during the drier summer months, ERT-derived results demonstrated unrealistically rapid variations in soil conditions, and was suggested to be less reliable during this period, due to poor contact between the electrodes and the soil
- The temperature model of the embankment generally underestimated measured temperature values, and demonstrates one mechanism for temporally varying agreement between the ERT and point sensor results. Despite this, however, the periods of greatest temperature deviation do not correspond to the periods of least agreement between the ERT and point sensor datasets

- Following the activation of the sprinkler system, the ERT method yielded data indicative of rapid drying, whereas the point sensor network captured the rapid infiltration of additional water. This change in subsurface conditions was accompanied by a rapid decline in recorded subsurface temperatures
- Water content estimates which were inferred by the application of the Waxman-Smits relationship to point sensor resistivity data closely followed trends observed from actual recorded values, but consistently underestimated them. Estimates compared best to directly measured values at locations where the resistivity point sensors were thought to have good coupling with the surrounding soil, at greater depths
- Soil suction estimates arrived at by the application of both Waxman-Smits and Van Genuchten parameters to point sensor resistivity data showed some qualitative agreement with actual recorded values, but limited quantitative correlation

Chapter 6. Discussion

In the following chapter, discussions of the results of the three experimental components of this thesis are presented separately (laboratory, point sensors and ERT). There is considerable correlation between the three components, therefore, comparison is made between them, where relevant. At the end of this chapter, a general discussion of the common themes is presented.

6.1 Laboratory data

6.1.1 *Soil water retention*

Traditionally, soil water retention curves are produced using the filter paper method, which has two principal limitations: firstly, because the method involves equilibrium being reached between the soil and the filter paper, it can be time-consuming; secondly, it relies on the use of a suitable calibration curve, and therefore ultimately constitutes an indirect measurement (Bicalho et al., 2011). In this study, however, the WP4C dewpoint potentiameter was used, due to its rapidity of measurement (less than ten minutes), and because it provides a direct measurement of soil suction.

In Figure 5.1, the laboratory-derived soil water retention curve is presented, showing a clear loss of suction between drying and wetting paths. The fitted Van Genuchten parameters reflect this deviation, which is a function of the fundamental difference between the mechanics of desorption versus adsorption, as explained by Ward and Trimble (2004) and in subchapter 2.2.4. Saturation values between drying and wetting curves often differ as a result of entrapped air replacing volume previously occupied by water (Fredlund and Xing, 1994). However, a different concept has been considered in this study. During testing, it was observed that specimens undergoing wetting demonstrated more cracking than those on the drying path. Although there are no data points at water contents approaching saturation, the fitted Van Genuchten parameters have been modified to reflect an inferred elevated porosity resulting from such cracking.

In Figure 5.2 and Figure 5.3, the drying and wetting data points, respectively, are compared against published SWRCs for BIONICS material (Mendes and Toll, 2013), produced using the filter paper method. From Figure 5.2, very close agreement is observed between the drying data obtained in this study and the published primary drying curve (Noguchi et al., 2011, as

presented in Mendes and Toll, 2013), suggesting that the data are representative. An approximate AEV of 500 kPa was measured, in good relative agreement with the value obtained by Glendinning et al., 2014 of 600 kPa, which used a combination of the filter paper method and high capacity suction probes. Fewer data points were obtained on the wetting path (with no data at water contents greater than 14 % GWC), but also compare well with the published values (Figure 5.3).

The fitted Van Genuchten parameters (summarised in Table 5.1) were then used as the basis for estimating field soil suctions at the BIONICS test embankment from ERT-derived field water contents.

6.1.2 *Resistivity testing procedures*

The most widely used method of measuring soil resistivity is the two point method, as described in both the British Standard (BSI, 1990a) and ASTM (2012). The method relies on a relatively large area of contact between the plate electrodes and the soil specimen. At low water contents, contact resistances may be considerable, due to reduced coupling between the specimen and the electrodes, and to a decreased contact area resulting from shrinkage, potentially resulting in significant over-estimation of soil resistivity, not representative of the soil mass as a whole, as described in subchapter 2.3.3. Therefore, efforts were made in this study to mitigate these contact resistances by the addition of a conductive gel to the electrodes. Although not standard practice in geotechnical testing, similar methods are used in medical electrotherapy to improve electrode-skin contact (Bolfe and Guirro, 2009). The effectiveness of this gel is shown in Figure 5.4, where the addition of the gel has resulted in less scatter of the resistivity data points, and in lower reported resistivity values, suggesting improved contact at the soil-electrode interface. This amendment to the two point method was then employed for all subsequent two point resistivity tests performed on the cylindrical soil specimens.

In order to facilitate four point resistivity testing, bespoke testing chambers were developed by the British Geological Survey. From Figure 5.10, it can be observed that specimens compacted in four layers (parallel to current flow) demonstrate low values of resistivity compared to those extracted from proctor moulds, deviating further with decreasing water content. This is suggested to be due to the orientation of the layers, such that they create a

preferential pathway for current flow. In Merritt et al., 2016, four point resistivity measurements were made on clay specimens, using potential electrodes positioned both parallel and perpendicular to the bedding. Lower resistivity values were obtained using the parallel orientation, supporting this suggestion. In order to provide as accurate as possible a measure of the resistivity of BIONICS clay material, subsequent four point tests were performed using proctor-extracted specimens, which were considered to be more representative of in situ conditions at the test embankment.

6.1.3 *Resistivity – water content relationships*

Two point resistivity

In Figure 5.5, the BIONICS two point resistivity – water content relationship is compared against published data from similar clay soils, also obtained using two point methods (same literature data as shown in Figure 2.27). There is close agreement between all the datasets presented, demonstrating an inverse power relationship, with sharp increases in reported resistivity values observed below approximately 20 % VWC (corresponding to a GWC of 12 %). In Fukue et al., 1999, the authors suggest that this critical water content corresponds to a break in the continuity of the water phase within the soil pores, thereby interrupting the flow of current, resulting in increased reported resistivity values. The Waxman-Smits model of the clay resistivity – water content path describes electrical current flow through both the pore water and the soil matrix (Waxman and Smits, 1968 - as described in subchapter 2.3.2): as water content decreases, the contribution to conduction from the pore water decreases, causing the curve to behave asymptotically at very low water contents. This reduced conduction may be exacerbated by the development of desiccation fractures resulting from shrink-swell behaviour associated with clay soils. In Figure 5.6, the water content – resistivity relationship for deliberately-fractured specimens is presented alongside that for intact specimens. Elevated values of resistivity are seen to arise from macro-cracking due to the insulating nature of air acting to impede current flow, supporting the suggestion that desiccation fractures further interrupt current flow through dry soils, as in Hassan and Toll, 2014.

Four point resistivity

The four point resistivity - water content relationship shown in Figure 5.13 (using proctor-compacted specimens) also illustrates an inverse power relationship. The curve compares very well with that obtained by Merritt et al. (2016), for a similar silty sandy clay, and with that by Amidu and Dunbar (2007) for a Vertisol clay, as shown in Figure 2.29 and Figure 2.30, respectively. This agreement further reinforces the validity of the four point resistivity method, for which there are not currently a great deal of literature studies available for comparison.

Comparison of two and four point resistivity curves

A direct comparison of two and four point resistivity testing methods is provided in Figure 5.9, where both methods have been applied to the same specimens. It is evident that the two point method over-estimates resistivity values with respect to the four point, deviating further with decreasing water content. The reasons for this are explained in subchapter 2.3.1, and relate to the fact that the two point method makes a potential difference measurement across the electrical terminals, including all contact resistances within the circuit; the four point method measures the potential difference across the soil specimen, and therefore includes fewer sources of contact resistance (Heaney, 2003), yielding far lower soil resistivity values, as can be seen from Figure 5.9. Due to the fact that both two and four point tests were performed on the same specimens (using the resistivity test chambers), it can be concluded that the observed difference between them is indeed a direct result of the inclusion of contact resistances using the former method. Nearing saturation, the difference between the two methods is less pronounced as the presence of water acts as a coupling agent at the specimen-electrode interface.

Ultimately, it is plain that the two point method over-estimates resistivity values, and therefore constitutes a bulk measurement not representative of true soil resistivity, especially at low water contents. Despite this over-estimation, however, the method can still be used to provide qualitative information, regarding trends in the evolution of soil resistivity. This inverse power relationship between resistivity and water content apparent from both two and four point methods is suggested to be a function of the combination of several effects:

1. An increase in contact resistance resulting from reduced coupling at the soil-electrode interface at low water contents;
2. Reduced bulk mobility at low water contents of ions present in the soil dissolved in the pore water;
3. The development of fractures in the soil due to the volume-sensitive nature of the test material, which act to impede current flow.

The last two effects, which have already been touched upon, are affected by seasonal moisture cycles, and are discussed in greater detail in the following section.

Effect of seasonal moisture cycles

In addition to the effect of macro-scale cracking on soil resistivity (as shown in Figure 5.6), it is pertinent to consider desiccation cracking at the micro-scale, resulting from seasonal moisture cycles. In Tang et al., 2011, clay specimens were subjected to dry-wet cycles, resulting in the formation of both macro and micro-cracks, with the former observed principally during drying, and the latter principally during wetting. This trend suggests the potential for hysteresis of the resistivity – water content relationship between drying and wetting cycles, resulting from different cracking densities. In Figure 5.7, the two point resistivity – water content relationship has been divided into four distinct paths (1a, 1b, 2a, 2b from Table 4.2): the drying and wetting portions of the primary and secondary moisture cycles. In keeping with Muñoz-Castelblanco et al., 2012, no hysteresis could be observed between the individual drying and wetting paths, implying no discernible difference in crack density, and inferring resistivity to be independent of soil suction. The same observation was made for Hollin Hill clay, as shown in Figure 5.8. However, if the resistivity - water content relationship of the BIONICS material is separated more broadly into primary and secondary moisture cycles (each cycle including both drying and wetting portions), a hysteretic shift of the curve is observed: below approximately 12 % GWC, specimens subjected to more than one dry-wet cycle have increased values of resistivity with respect to those subjected to fewer than one. Interestingly, at water contents beyond 12 % GWC, the reverse is true. The effects of repeated seasonal moisture cycles on four point soil resistivity are shown in Figure 5.11, potentially also demonstrating a hysteretic shift of the path, centred at a water content of 12 %. This suggested hysteresis is much less pronounced using the four point method than it is using the two point (which is more affected by high contact resistances).

The increase observed from both resistivity methods at low water contents is suggested to be attributable to the development of fissures at the scale of the soil fabric itself, resulting from seasonal moisture cycles, supported by E-SEM imaging of micro-cracks in Figure 5.20. These fissures then act to impede current flow, raising the bulk soil resistivity. The observed decrease in resistivity at the wet end may also relate to an increased crack density: whilst these fissures act to impede the flow of current in dry soil, it is suggested that at the wet end, some persistent fissures may act a conduit for conductive pore water.

These micro-fractures may then promote further micro-scale structural changes, causing irrecoverable destruction of the clay soil structure, as described in Stirling et al., 2014. In Al-Hamoud et al., 1995, SEM imaging of clay specimens subjected to repeated moisture cycles illustrated a significant reorientation of the clay microstructure. This effect was most pronounced following the first moisture cycle, and showed the integration of clay structures along existing discontinuities (bedding). This particle aggregation then led to a decrease in clay content and hence plasticity, resulting in a reduced specific surface area available for water absorption (SSA, defined as the particle surface area per unit mass or volume). Similar observations were made by Subba Rao and Satyda, 1987. The same concept can be applied to the micro-fractures, whereby the presence of these discontinuities acts to re-orientate the surrounding clay structure during drying, as shrinkage occurs. This phenomenon is attributed to surface tension forces arising from the capillary menisci formed between individual particles (Al-Hamoud et al., 1995; Sorgi et al., 2008). These micro-scale structural changes provide an additional explanation for the increased resistivity between primary and secondary moisture cycles, at lower water contents.

In Kibria and Hossain, 2012, the authors observed soil resistivity to be highly sensitive to the SSA. They suggest that, at lower water contents, soils with large SSAs (e.g. clays) may struggle to develop a film of water around the soil particles, preventing ionic conductors from entering the pore water solution, suggesting that as soil moisture increases, so too may ionic mobility. Therefore, an additional suggestion for the reversal between the two phases as observed at 12 % GWC is the dissolution of clay particles in the pore water, such that they become further mobilised with ongoing dry-wet cycling, with existing cracks acting as a high conductivity conduit upon filling with water.

The hysteresis observed from Figure 5.7 and Figure 5.11 is supported by Figure 5.20, which illustrates the microscopic evolution of soil fabric changes during a seasonal cycle: Figure

5.20b shows a desiccation fissure with a distinct coating of clay particles along its walls, whilst the fissure shown in Figure 5.20d (after the addition of water) shows no coating (suggesting that it has been dissolved) and appears in be partially infilled, which may act as a conduit for additional current flow. Effectively, a clay film is developed during drying, which is mobilised into the pore water during imbibition, increasing its conductivity.

The micro-scale structural changes described above may be considered in terms of the Waxman-Smits relationship describing current flow through clay soil, as a function of water content, as presented in Eqn. 4.17. This allows a very simple algebraic justification for the observed hysteresis to be considered: at the dry end, the development of micro-scale fissures would ultimately act to increase the soil porosity, thereby raising the soil resistivity at a given water content; at the wet end, the dissolution of clay particles into the pore water would act to reduce the resistivity of the pore water, lowering the overall soil resistivity. A more convoluted explanation may be rooted in the evolution of other Waxman-Smits parameters subjected to seasonal moisture cycles, for example, affecting the cementation factor (*m*) due to evolving crack morphology, or elevated cation exchange capacity (*C*) resulting from increased ionic concentration (as in Liu et al., 2015).

Resistivity – water content proxy

In order to resolve the established resistivity – water content curves into a proxy relationship for use in translating field ERT data into estimates of water content, Waxman-Smits parameters were fitted to the laboratory data. To this end, the four point resistivity data shown in Figure 5.11 were used, rather than the more complete two point dataset, for two reasons: firstly, due to the inclusion of higher contact resistances within the two point measurement; and secondly, because the dipole-dipole ERT data acquisition method employed in this study is a four point method, as illustrated in Figure 2.19. Despite the fact that the nature of the relationship was suggested to be hysteretic, all data from both full seasonal moisture cycles were used to fit Waxman-Smits parameters, as shown in Figure 5.13. The fitted parameters (summarised in Table 5.2), include the saturation exponent ($p = 1.83$), which compares well with literature values for clay of between 1.6 and 2.3 (Lee, 2011).

6.1.4 *Thermal properties*

To account for varying ground temperatures in the field, the Waxman-Smits relationship was calibrated, by use of a temperature correction factor. An investigation into the effect of increasing temperature on soil resistivity, as shown in Figure 5.15, resolved a linear relationship, such that a 2 °C increase in temperature resulted in a 1 % decrease in soil resistivity. This figure agrees closely with the findings of Hayley et al., 2007, as described in subchapter 2.3.1, citing a value of between 1.8 °C and 2.2 °C.

From Figure 5.14, the thermal conductivity of BIONICS clay material was observed to decline sharply, due to the lower specific heat capacity of clay with respect to water (Chesworth, 2008). In subchapter 6.1.3, the concept was suggested of a critical water content delineating the continuity of the pore water phase, causing resistivity values to increase rapidly during drying. Therefore, an analogy can be made between resistivity and thermal conductivity at water contents below a critical value, whereby discontinuities within the pore water impede both the flow of current and the transfer of heat. At water contents in excess of this value, the thermal conductivity remains constant, unlike soil resistivity which demonstrates an inverse power relationship. Despite thermal conductivity being impaired at low water contents, the linear relationship between soil resistivity and temperature shown in Figure 5.15 is well represented at all three test water contents by the same relationship. This then simplified the temperature correction procedure for ERT data; had this linear relationship varied considerably between the test water contents, then different temperature correction factors may have had to have been applied for different water content ranges.

Ultimately, the above findings were compiled into a series of equations which were then used to directly translate field ERT data into water content, allowing resistivity to be used as a proxy for water content. The derived water contents were then converted to estimated soil suctions using the laboratory-derived soil water retention curve (Figure 5.1).

6.1.5 *Evolution of laboratory geophysical – geotechnical relationships*

Given the ultimate aim of ERT monitoring to inform on slope stability, understanding the effects of seasonal moisture cycles on strength relationships is paramount. In Figure 5.16, the unconfined compressive strength is presented as a function of water content,

demonstrating a linear relationship, with a higher gradient for the (primary and secondary) drying paths than for the (primary) wetting path. From subchapter 6.1.3, the development of micro-fractures between primary and secondary moisture cycles has already been established, therefore, the fact that no hysteresis is observed between the two drying paths implies that the unconfined compressive strength is unaffected by the presence of these micro-fractures. It can be observed, however, that specimens which fractured at the macro-scale during testing exhibit anomalously low UCS values.

The effects of micro-scale desiccation cracking may be better observed by considering the undrained shear strength response of BIONICS clay to seasonal dry-wet moisture cycles, given in Figure 5.17, showing hysteresis of the linear shear strength - water content relationship for successive cycles. It can be observed that the primary and secondary drying curves (Paths 1a and 2a respectively, from Table 4.2) follow the same initial path, but then deviate at water contents less than approximately 12 % GWC, when the Path 2a gradient decreases. The same is observed between primary and secondary wetting paths (Paths 1b and 2b respectively). 12 % GWC has already been identified as the transition between continuity and discontinuity of the pore water phase within the soil, but due to the decrease in the shear strength gradient, it can also be considered as the point at which fractures develop (and heal) in the soil, as the water meniscus is broken: cracks form along the initial drying path (1a), heal along the subsequent wetting path (1b), and reopen along the secondary drying path (2a, at 12 %), with new cracks also forming. This soil fabric deterioration is supported by Figure 5.20, which indicates a fundamental change in the micro-scale structure of high clay content material, when subjected to dry-wet moisture cycles. By imaging the grain scale structure of this material subjected to drying, the formation of permanent discontinuities is confirmed. Similar observations were made in Sorgi et al., 2008, which investigated the strength of chalk under different saturation conditions, in conjunction with E-SEM imaging, capturing the development and healing of observed fractures.

In addition to soil fabric deterioration promoting a reduction in shear strength, the role of soil water retention must be considered. Hysteresis of the soil water retention curve between drying and wetting is well-understood (Fredlund and Xing, 1994; Šimůnek et al., 1999, Fredlund et al., 2011), and is apparent from the laboratory SWRC shown in Figure 5.1, as suctions developed in the soil during drying cannot be recovered during wetting, due to

entrapped air. This loss is reflected in a decline in the unconfined compressive strength of BIONICS clay at the transition from the primary drying path (1a) to the primary wetting path (1b) (Figure 5.16). Near this boundary, specimens of equivalent water content on both drying and wetting paths will have undergone little seasonal cycling; therefore, soil fabric deterioration does not explain the strength loss. The same observation is made regarding the undrained shear strengths of BIONICS and Hollin Hill clay materials (Figure 5.17 and Figure 5.18, respectively). Figure 5.17b illustrates the sudden drop in shear strength at the transition boundary from a drying (1a) to a wetting path (1b), whereafter specimens resume a linear wetting path (1b). The concept of reduced suctions along the wetting path is supported by the secondary drying path (2a) exhibiting elevated shear strengths with respect to the primary wetting path: specimens are wetted up to saturation, effectively "resetting" their saturation history, and then dried out again, yielding strengths above those of the preceding wetting path.

Although soil fabric deterioration and hysteretic soil water retention have been considered separately, there is a possibility that the former factor could have an effect on the latter. The mechanics of soil fabric deterioration are discussed in detail in subchapter 6.1.3, and describe a reduction in the specific surface area resulting from seasonal moisture cycles, reducing the particle area available for water absorption. This was observed in Al-Hamoud et al., 1995, where clay specimens subjected to seasonal moisture cycles demonstrated considerable reductions in the swelling potential, relating to the soil water retention ability. Therefore, it is likely that seasonally-induced soil fabric deterioration acts to erode the soil water retention potential of clay over time, reducing the effective strength of the soil mass.

Both the unconfined compressive strength and undrained shear strength of BIONICS clay material have both been considered in this study. From a comparison of Figure 5.16 and Figure 5.17, it is evident that the maximum residual UCS (2750 kPa) is considerably higher than the maximum residual undrained shear strength (1650 kPa). This is due to the lack of drainage during the shear test, allowing the development of positive pore pressures, exacerbated by the confining pressure. From Terzhagi's principle of effective stress (Eqn. 2.2), these positive pore pressures act to lower the effective stress of the soil mass. As described in subchapter 2.2.5, the undrained shear strength does not allow for measurement of pore pressures during testing. It is recognised, however, as representative of short-term behaviour, which is relevant to slope stability assessments, particularly when

considering rapid changes in subsurface conditions, such as those associated with rapid rainfall infiltration.

In summary, two potential mechanisms exist for the reduction in soil shear strength: suction loss due to hysteretic soil water retention behaviour, and soil fabric deterioration via the development of micro-scale cracks. If ERT systems are to be used to inform on slope stability, then the ability to detect these factors would be advantageous. The mechanisms by which water affects soil resistivity and strength are well-understood (as discussed above and in subchapters 2.2.4 and 2.3.6), but no relationship exists between soil strength and resistivity directly. Even though these two parameters do not impact on each other explicitly, however, it is possible to resolve an implicit relationship between them as is presented in Figure 5.19). From this relationship, both the following may be observed: the drop in shear strength at the transition from drying to wetting events attributed to hysteretic soil water retention behaviour; and elevated resistivity values with corresponding decreased shear strengths resulting from soil fabric deterioration, between primary and secondary seasonal cycles. At the transition from the primary drying curve (Path 1a from Table 4.2) to the primary wetting curve (Path 1b), there is a considerable loss in shear strength from approximately 1650 kPa to 1100 kPa, and although there is also a fall in the corresponding resistivity values, this is attributed to the increase from 3 % to 4 % GWC, rather than being a function of suction loss. Soil resistivity was established to be independent of soil suction in subchapter 6.1.3, thus fluctuations in pore pressure will only be reflected in resistivity values if there is also a significant variation in water content, but as shown above, even a relatively small moisture increase can drastically reduce soil strength.

6.1.6 *Representability of laboratory tests*

The applicability of laboratory results to field conditions is limited by several factors, inherent to the nature of laboratory testing. The most basic consideration is the scale of laboratory tests, including both the size of specimens and of the forces acting on them. Many authors have sought to mitigate this issue by the use of large-scale test apparatus (e.g. large-scale triaxial testing of railway ballast material by William and Peter, 2008 and Trinh et al., 2012). This approach is not practical for the multi-phase nature of this research study, investigating a suite of geotechnical parameters, at a large range of water contents. Additional constraints relate to the specimen size prescribed by the laboratory testing

apparatus itself, including the WP4C Dewpoint potentiameter and the E-SEM microscope, which can only accommodate very small specimens. Another consideration is that the forces which may act on a soil mass in the field are not necessarily replicated in the laboratory. For example, the SWRC shown in Figure 5.1 was derived from specimens free from any confining pressure, differing from the in situ conditions.

In addition to the issue of scale, the representability of the test material itself is relevant. All of the laboratory tests performed during this research study involved using soil which had been processed according to the specifications described in subchapter 4.1.2, which included removing all particles of diameter greater than 2 mm. It can be seen from Figure 3.3 that the effect of this on the particle size distribution of BIONICS clay would be relatively small, with only 5 % of the material passing the 2 mm sieve. The justification of this stage in the processing is as follows: firstly, the inclusion of larger particles would have a considerable weakening effect within the relatively small-scale lab tests, not representative of their role in the field-scale scenario; and secondly, for the consistency of all laboratory specimens. Additionally, given the importance of matric current flow for clay soils, as described in subchapter 2.3.1, it is reasonable to focus the laboratory investigation on these smaller particles. Another important justification relates to the nature of the development of novel scientific methodologies for any application, whereby, in the first instance, the simplest condition is investigated before the addition of further complexities. Within the context of this study, the simplest condition, with the least unknowns, involves the use of a processed, homogeneous test soil.

For all of the reasons cited above, a justification is required as to why laboratory-derived, rather than field-derived proxies were established, in order to translate field ERT data into estimates of both water content and pore pressure. Due to the ability to sample a full range of water contents in the laboratory, controlled conditions were considered preferable, rather than relying on a considerably narrower range of field water contents, highly dependent on environmental conditions. Additionally, important geotechnical parameters, such as porosity, could not be directly quantified in the field, thereby introducing further unknowns. Both of the laboratory-derived proxies established in this research study were also investigated in the field using the network of point sensors, thereby providing a means of assessing the validity of the laboratory-derived proxies.

6.2 Field point sensor network

From Figure 5.21a, showing the recorded daily precipitation over a three year period from November 2012, there is little evidence to suggest seasonally drier summer weather compared to winter, with the opposite appearing to be true. This observation compares well with historic (1981 - 2010) climate data recorded at the Met Office weather station at Albermarle, approximately 8 miles from the test embankment, citing June as the wettest month, on average (Met Office, 2014). Comparison with the point sensor data gathered at the ERT test plot revealed little correlation between measured moisture properties (water content, pore water pressure at depths of 0.5 and 1.0 m) and recorded daily precipitation data. All of the geotechnical sensors on the Southern flank demonstrate seasonal fluctuations, characterised by higher winter water content values compared to the summer months. This seasonal variability follows the same period of oscillation as the corresponding temperature values shown in Figure 5.21d, enforcing the importance of net evapo-transpiration as a driver for seasonal dry-wet cycles, rather than simply precipitation.

6.2.1 *Preliminary hydrological model*

Damping

Using the time series data, a preliminary hydrological model for the BIONICS test embankment can be derived, providing a context within which the ERT data may be analysed. The geotechnical response to environmental forcings was investigated at a range of depths, in Figure 5.21 and Figure 5.22. These figures describe a highly dynamic near-surface layer, characterised by considerable diurnal and seasonal variations in water content and temperature. Rainfall events during the summer months demonstrate this diurnal variability to be a function of daily precipitation as well as of environmental temperature, reflected in perturbations to general trends of summer drying. At a depth of 0.5 m, the influence of diurnally fluctuating surface parameters is relatively insignificant, with the geotechnical response principally characterised by seasonal fluctuations in water content, pore water pressure and temperature. However, rapid reductions in soil suction (negative pore pressure) which are observed from individual summer rainfall events (e.g. 6th September 2013), demonstrate the influence of diurnal extremes at this depth. At the greater depth of 1.0 m, no diurnal fluctuation of geotechnical parameters is evident, only demonstrating a seasonally varying response, which is more pronounced upslope. These

observations describe the embankment to be highly dynamic in the near-surface, becoming increasingly damped with depth.

Similar damping effects were observed with differing aspect, whereby the Southern slope exhibited greater seasonal and diurnal variability than the Northern slope, as illustrated by Figure 5.23 and Figure 5.24. This is due to the Southern slope being orientated such that it receives more direct sunlight, causing it to warm to greater temperatures than the Northern slope. Additionally, the prevailing wind direction across the UK is South-westerly (Lapworth and McGregor, 2008), therefore, the Southern flank would likely have been subjected to preferential rainfall, and greater wind, accelerating near-surface wetting and drying. In comparison to the slope flanks, point sensors within the crest demonstrated little seasonal fluctuation of water contents thought to be near saturation due to the presence of near-zero suctions. This static behaviour is suggested to be due to the overlying ballast material allowing direct infiltration of rainwater, saturating the crest fill, the ballast then preventing the fill from drying.

The effects of the degree of compaction on the geotechnical response to environmental forcings was investigated by comparing the moisture properties of different parts of the BIONICS embankment (within the Southern slope), constructed to different compaction specifications. In general, uncompacted zones (Panel A) exhibited more variable behaviour, conducive to an increased pore volume, as shown in Figure 5.25. Greater suctions were also developed in the uncompacted fill, resulting from elevated matric tension due to a greater particle separation. Despite being constructed to the “compacted” specifications, water contents recorded at Panel B were more similar to those of the uncompacted Panel A, suggesting Panel B to be more porous than previously thought, however, this was not supported by recorded pore water pressure values.

As a result of the damping effects explained above, the moisture properties of the ERT test plot portion of the embankment can be qualified as follows: a highly dynamic, porous near-surface layer (0.1 m), within which water contents vary diurnally and seasonally; a seasonally varying mid-depth (0.5 m) layer, wetter nearer the crest; a deep (1.0 m), relatively static layer, more seasonally variable near the crest. Porosities estimated from saturated water contents during the sprinkling experiments showed the greatest suctions to be observed at 0.5 m depth at the upper slope position corresponding to the highest porosity, and the lowest suctions beneath the crest and in Northern flank.

Sprinkling experiments

Following the activation of the sprinkler system on the ERT test plot, between mid-January and June 2015, a dramatic increase in near-surface water contents was recorded. However, relatively little change was observed on the Northern slope or at 0.5 m depths on the Southern slope, suggesting them to be near-saturation. At 1.0 m on the Southern slope, water content values increased by up to 3 % with respect to normal winter values. The relatively limited effect of the sprinkling experiments can be explained by the fact that they were begun during the winter months, when much of the embankment would already have been near saturation. The effects of additional precipitation are, in fact, more readily identifiable in the months following the end of the sprinkling period, showing that the embankment has not dried out to normal summer minima (Figure 5.21), curbing the development of soil suctions. It can be seen that the additional water infiltration has acted to lower the temperature of the embankment fill with respect to maxima recorded during the summer months of the preceding two years. In Gance et al., 2016, the authors noted similar cooling of clay soil resulting from the infiltration of rainwater. Due to the fact that the water used in the sprinkler systems was stored in a tank at the ground surface, it is likely that the sprinkled water was colder than would be expected from rainfall. Field observations during January and February 2016 noted the accumulation of ice on vegetation covering the surface surrounding the sprinklers (Figure 5.61).

6.2.2 *Evolution of field geophysical – geotechnical relationships*

The effects of repeated seasonal dry-wet behaviour, as illustrated in Figure 5.26, are investigated in the field by comparing SWRCs for BIONICS embankment fill subjected to increasing numbers of moisture cycles. Only the drying portions of the SWRC are presented, owing to the difficulty in obtaining field wetting curves due to the rapid nature of in situ wetting. Figure 5.27 and Figure 5.28, describing the curves at two depths within two positions on the Southern slope of the embankment compare the in situ curves with those obtained in the laboratory (as shown in Figure 5.1). This comparison demonstrates very similar qualitative behaviour, further validating the use of the laboratory curve as a means of estimating pore water pressure trends in the field. In general, the in situ curves have a tendency to plot below the laboratory curves, such that for a given water content, the

resultant suction is lower. This is explained by the presence of confining pressures in the field, as described in Glendinning et al., 2014.

At all four individual positions, the highest ground suction values are recorded on the primary drying path (Cycle 1), showing varying degrees of similarity to the laboratory drying curve. The closest agreement is observed at 1.0 m depth in the upper slope position, suggesting the laboratory specimens to be most representative of this portion of the embankment. A relative loss of suction is observed from all subsequent drying curves (Cycles 2 to 9), occurring more gradually in the upper position compared to the lower, but resulting in a greater overall loss. In subchapter 6.1.3, the development of micro-fractures during soil drying was suggested as a mechanism for a decline in soil strength. The effect of such cracking would be an overall increase in soil porosity, which would act to raise matric tension, therefore, this suggestion does not account for the progressive loss of in situ suctions. In subchapters 6.1.3 and 6.1.5, these micro-fractures were suggested to promote the deterioration of the soil fabric itself, which is considered to play a significant role in the strength of compacted clays (Stirling et al., 2014). Therefore, the progressive loss of suction observed in situ is likely a function of fabric deterioration promoted by moisture extremes. The potential for such deterioration to erode the SWRC over time was discussed in subchapter 6.1.5. Reference was made to the study by Al-Hamoud et al., 1995, who observed a loss in the ability of clay specimens to retain water following seasonal moisture cycling, reaching a residual state after five cycles. In subchapter 6.2.1, greater seasonal variability was observed in the upper slope position, supporting the concept of fabric deterioration as a cause of reduced matric potential, as the more exposed upper slope fill deteriorates to a greater extent than that in the lower slope (Figure 5.27 and Figure 5.28). From both figures, a residual curve is reached after several cycles.

Given the observed evolution of in situ soil water retention curves as a result of soil fabric deterioration, it is reasonable to consider the simultaneous evolution of in situ resistivity – water content curves, as discussed in subchapter 6.1.3. However, there was little evidence of such hysteresis, which may be explained by the soil water retention datasets dating from 2009, whereas the resistivity datasets span only from November 2012 (many sensors having been installed even more recently), by which time the SWRCs follow a residual path.

In Figure 5.29, the in situ resistivity – water content curves are presented, demonstrating an inverse power relationship, in keeping with the laboratory findings. Near the surface (0.1 m)

the occurrence of relatively high resistivity values can be explained by very porous topsoil, and the development of cracks due to its highly dynamic behaviour (as discussed in subchapter 6.2.1), which are understood from Figure 5.6 to impede current flow. At greater depths (0.5 and 1.0 m), where such cracking is less important, the curves are generally in close agreement with each other at volumetric water contents beyond 22 % to 25 %. At lower water contents, however, the curves demonstrate steep increases in the recorded resistivity values, similar to the behaviour observed in Figure 5.5 and thought to relate to the break in continuity of the pore water phase. At higher water contents, the in situ curves demonstrate close agreement with the four point laboratory dataset, despite constituting a two point measurement. This is suggested to be due to increased contact resulting from the point sensors being embedded at depth. This close agreement further validates the use of the laboratory four point resistivity – water content proxy relationship, as shown in Figure 5.13.

6.3 Electrical resistivity tomography array

6.3.1 *Imaging technique*

In order to construct resistivity cross-sectional images of the Southern slope of the BIONICS ERT test plot, two approaches are employed, as shown in Figure 5.30 and Figure 5.32. The former is derived from measurements made using one profile of electrodes; the latter follows a similar method to that employed by Gance et al., 2016 and extracts the cross-section from a 3D resistivity model constructed using all available electrode data spanning the width of the ERT test plot. From these figures, showing the resistivity distribution at three month intervals, similar observations can be made, including a high resistivity ballast capping layer, a dynamic near-surface layer and a low resistivity zone beneath the crest (discussed further in the following subsection), as well as seasonally variable trends. This hydrodynamic model is supported by the results of the point sensor network, as detailed in subchapter 6.2.1. It is evident, however, that the 2D cross-sectional images demonstrate considerably more spatial and temporal variability than do the 3D-derived images of the same slice. This is more clearly illustrated by a comparison of the standard deviations across the 2D and 3D cross-sectional areas, as shown in Figure 5.31 and Figure 5.33 respectively. Because of the highly engineered nature of the BIONICS embankment, the degree of spatial variability associated with the 2D inversion technique is unlikely to be quantitatively

representative of the subsurface resistivity trends. Furthermore, it is anticipated that observed temporal resistivity changes would be relatively weak due to the high clay fraction of the fill material (Gance et al., 2016).

Inversion artefacts

One of the principal discrepancies observed between the 2D and 3D inversions is the extent of the low resistivity zone beneath the crest ballast: in 2D, this zone is approximately 2 m thick, with resistivity values of 10 to 20 Ωm, demonstrating severe contrasts with the surrounding fill (approximate values of the order of 100 Ωm). In 3D, the low resistivity zone exhibits comparable values, across a depth of only 1 m, and with far less contrast with the surrounding fill (values of only 30 Ωm). Effectively, the 2D inversion results illustrate the low resistivity zone as a discrete, conductive nodule within a resistive embankment core, whereas the 3D array results indicate the presence of a more gently varying conductive zone. Given the inverse relationship between water content and resistivity, both datasets indicate the presence of high water contents beneath the crest ballast. Results from the point sensor network, however, show relatively low VWC values (sensor location a6, see Figure 5.22a) of 22 and 19 % (0.5 and 1.0 m beneath the ballast), in contradiction to the low resistivity zone observed from ERT imaging. Despite these low water contents, near-saturation is implied by very low recorded suction values at the same location (see Figure 5.22b), and by the fact that water content values did not increase significantly during the sprinkling experiments. Point measurements of water content collected at Panel B (same compaction specifications) demonstrate consistent values of approximately 47 % and 37 % at depths of 0.5 and 1.0 m, respectively, (see Figure 5.63d, “meas” dataset). Broadly, these data are in agreement with the presence of a low resistivity, near-saturated zone beneath the ballast crest of the embankment. However, the discrepancies between the 2D and 3D ERT images in interpreting this zone are indicative of some type of ERT artefact relating to the different methodologies, i.e., producing resistivity anomalies not present in the field.

The difference between the two methods can be explained by considering the impact of 3D resistivity effects within 2D ERT surveys. Inversion of 2D apparent resistivity data makes the inherent assumption that all resistivity variations occur within the vertical plane beneath the profile itself, considering the medium to be invariant in the direction perpendicular to the profile. The presence of conductive anomalies outside of this plane, however, can deflect

current flow, which is three-dimensional, manifesting itself in the form of (non-existent) conductive anomalies which appear within the vertical plane (Gance et al., 2016). Other studies, including Dahlin, 1996, and Pannisod et al., 2001, discuss the significance of 3D effects, noting high data misfits of the inverted tomography. Owing to the highly engineered nature of the purpose-built BIONICS test embankment, it could be considered that such 3D effects may be relatively unimportant, particularly when compared to highly heterogeneous slope scenarios such as natural landslides. Due to the location of the ERT array within the BIONICS embankment, these 3D effects are indeed significant: the ERT plot is situated in between the reinforced earth ends of the embankment, and the uncompacted panel A, as shown in Figure 3.7 and Figure 3.9, both of which constitute considerable changes to the fill in terms of compaction, and interference from the reinforcement material. Furthermore, this zone is bound by hydrologically isolating geomembrane, as can be seen in Figure 3.11. Another additional consideration is the cracking features which are illustrated by high 3D standard deviations, as shown in Figure 5.33b, which may very laterally in terms of depth, width and orientation. All of these factors may contribute to the inclusion of 3D effects within the 2D ERT inversion, explaining the relative difference between 2D and 3D inversions of the same cross-sectional area. The result of the inclusion of these 3D effects is the presence of artefacts within 2D ERT inversions, as noted by several authors, including Fargier et al., 2012 and Portal et al., 2016. Therefore, the mapping of the low resistivity zone beneath the crest as a distinct, conductive nodule by the 2D ERT is suggested to be an artefact resulting from the 2D inversion technique. In the previous 2D ERT surveys of the BIONICS embankment (Glendinning et al., 2014, Gunn et al., 2015), these 3D effects are considered to have been less significant due to the location of the two profiles (further from the boundaries described above, as shown in Figure 3.7), resulting in a subsurface resistivity distribution more similar to the 3D ERT images shown in Figure 5.32.

In addition to these 3D effects, it is necessary to consider the sensitivity of the two methods. This is illustrated by Figure 5.34, which compares the sensitivity of the 2D and 3D inversion models for the cross-section, within the inversion software, showing the 3D model to demonstrate greater sensitivity, deviating further with depth. In Figure 5.31, the 2D resistivity cross-sections demonstrate unexpectedly high standard deviations at the embankment core, which can be explained by the very poor sensitivity of the model at depth. The improved sensitivity obtained from 3D ERT inversion can be explained by greater

volume of data used to construct the 3D model, thereby providing a more robust measurement with a greater sensitivity.

For all of the reasons described above, efforts were focussed on 3D inversion of raw data obtained from the 3D ERT array, which was deemed more accurate and therefore preferable to 2D inversion methods. These inversions are presented, mainly, in terms of cross-sectional "3D-derived slices", rather than volumetric images, as these allow slope moisture dynamics to be more clearly illustrated. There is a considerable trade-off with regards to processing power between 2D and 3D inversion methods, both in the pre- and post-processing stages. Although the aim of this study is to provide a quantitative method for imaging slope moisture dynamics, the application of the proxy relationships to the ERT data requires a considerable amount of processing power and hence, time. Therefore, the proxy relationships were only applied to the extracted 3D slices, rather than to volumetric images.

The suggestion is made that for geotechnically simple sites, considered to be laterally homogenous, 2D ERT may suffice, but that for more complex sites, the use of 3D ERT is recommended.

6.3.2 *Hydrodynamic behaviour*

General trends

From Figure 5.32, showing the (3D) cross-sectional resistivity distribution, some broad features can be identified, including the high resistivity ballast capping layer, a highly variable flank near-surface, and a low resistivity zone beneath the crest. These same features were observed in Glendinning et al., 2014, and Gunn et al., 2015, from 2D cross-sectional images made over the course of one year. Using the laboratory-derived proxy relationships, the ERT data were translated into water contents and suctions, for the same three month intervals, shown in Figure 5.35 and Figure 5.36, respectively. These clearly illustrate the following features, which are interpreted in hydrological terms, supported by the preliminary hydrological model described in subchapter 6.2.1, by the point sensor network:

1. A quasi-saturated zone beneath the crest, resulting from water infiltration through the high permeability ballast capping layer, impeded by the ballast from drying out, although some drying occurs towards the Southern portion resulting from greater exposure. The

presence of positive pore water pressures is inferred from Figure 5.36, which would cause water to flow away from this zone;

2. An embankment core, characterised by intermediate water contents and little dynamic change, as a result of relatively low porosities at depth;
3. The highly dynamic nature of the Southern flank near-surface, including the topsoil which was replaced following regrading of the slope, as described in subchapter 4.2.2. This can be explained by its relatively high porosity (estimated to be 0.488 from the point sensor network), and from its exposure to environmental conditions. This zone corresponds to the high standard deviations observed from Figure 5.33a;
4. A high water content zone beneath the Southern flank near-surface, resulting from water infiltration through the relatively porous and cracked overlying layer, and from water flow away from the zone beneath the crest ballast.;
5. Relatively dry Southern flank slope at depth, resulting from low porosities, and preferential flow away from the flank via the near-surface.

Near-surface processes

During the summer months (June to September), the lowest water contents occur in the near-surface, accompanied by very high suctions, of the order of 10^4 kPa (red contours in Figure 5.36). During the winter months, however, a reversal occurs, whereby the topsoil becomes wetter than the fill beneath, with estimated suction values reversing accordingly such that the highest suctions then appear below the topsoil (shown most clearly in Figure 5.36g and l). This reversal describes a cyclic process, whereby at certain times of the year, the stress field across the topsoil differs radically (by an order of magnitude) to that of the fill beneath, which could be highly significant to the development of tension cracks in the near-surface, and to the near-surface stability. Tension cracks generally develop from the ground surface as matric suction increases. These may occur at relatively low suctions due to low near-surface confining pressures; at depth, the cracks close due to increased confining pressures (Fredlund et al., 2010). The significance of the reversal of suction is as follows: cracks developed in the topsoil during the summer months were observed to heal in the winter months (from walkover surveys and ERT imaging) as suctions decrease; however, the presence of high suctions below the topsoil during the winter months would have two

effects: firstly, to promote the propagation of the cracks with depth (as in Hamid, 2008, and Bièvre et al., 2012); and secondly, to draw in moisture from the wet overlying topsoil, providing a "wicking" suction. This mechanism is supported by the presence of the underlying high water content zone beneath the near-surface layer. In general terms, this postulation has implications for slope stability because it describes a mechanism for drawing in additional water, which is understood to reduce the effective stress of clay soils (as in subchapter 2.2.5). More specifically, however, the mechanism described above could be a key ageing process, accelerating soil fabric deterioration of the near-surface by the application of drying and wetting fronts, which have been shown to erode the soil water retention potential of clay soils over time, as discussed in subchapter 6.1.5. In particular, the deterioration of soil structure in proximity to discontinuities such as cracks was discussed in subchapter 6.1.3, therefore, the influence of the tension cracks may be especially important in the ageing of the shallow subsurface. The locations of the breaks in the suction contours (most clear from Figure 5.36f) coincide with observed crack locations, as shown in Figure 5.33b. Ultimately, it is the breakdown of suctions which will lead to instability, therefore, the fact that these breaks occur repeatedly at the crack locations suggest that the tension cracks provide the seed for slip planes, which could lead to shallow translational failures.

Drying

Over the course of the three year test period, the embankment was observed to dry out over the summer months, as illustrated by Figure 5.37 (Summer 2013), showing the greatest relative change in water content to occur in the near-surface layer. Closer inspection of this period, as shown in Figure 5.38 on a weekly basis, revealed the greatest degree of drying to occur between the 20th and 27th of July, despite significant rainfall in the middle of this interval. Observations of elevated ground temperatures from the point sensor network during this period demonstrate the significance of evapo-transpiration in near-surface moisture dynamics.

Over the course of Summer 2013, crack surveys recorded the presence of four historic tension cracks in the South-facing slope of the ERT test plot (Figure 4.35), having been a regular feature of crack surveys undertaken since 2008 (Michelaki, 2013). Two of these locations corresponded to cracks observed in November 2005, shortly after the

embankment construction, as shown in Figure 3.14. This correlation demonstrates the formation of permanent discontinuities, which reopen during the summer drying months.

The reopening of these cracks is investigated in Figure 5.39, by imaging the relative change in resistivity with respect to a reference date at the start of the summer drying period (15th June 2013), and provides valuable insight into the mechanics of crack development. Rapid increases in resistivity occur in the Southern-facing crest ballast, corresponding to rapid drying due to its high porosity and Southern aspect (i.e. more exposed to the elements). This then promotes the development of the first crack (OS4), at the top of the Southern flank, potentially driven by wicking suctions from the crest ballast. The development of three additional crack features (OS3, OS2, OS1/OS0) is then associated with high summer temperatures and suctions in the near-surface. Following heavy rainfall in the first half of August, all but the bottommost crack heal, as the material surrounding the cracks swells. Subsequently, the cracks reform (first near the more exposed upper flank), and two weeks following the heavy rainfall, four distinct cracking features are evident (Figure 5.39l). Figure 5.40 shows the extension of cracks (OS1-4) in three dimensions, demonstrating the presence of a fifth crack (OS0), which was not observed during surveys prior to 2013. The fact of the four cracks being clearest following heavy rainfall demonstrates that they have been exacerbated by shrink-swell behaviour caused by rapid dry-wet moisture cycling.

Several other studies have had success in using ERT to identify slope fissures, including Bièvre et al., 2012, as described in subchapter 2.3.5, and Suryo et al., 2012. These studies, however, have focussed on deep, pre-existing cracks. Therefore, the success of the ERT images to capture the development and evolution of these cracks at the surface constitutes a novel approach to investigating near-surface moisture dynamics. The high spatial resolution of the ERT method is reinforced by comparing the volumetric resistivity change during Summer 2013 (Figure 5.40) with that during Summer 2014, after the manual extension of the cracks in May 2014 (Figure 5.41b). This comparison highlights the extension of the cracks in terms of both width (Y distance) and aperture (X distance), and shows that this intervention has resulted in deepened cracks, with increased drying of the near-surface in their vicinity (Figure 5.41c).

Wetting

Drying of the embankment as described in the previous subchapter is a slow process, occurring over several months. Wetting, however, as observed from Figure 5.42 showing the ratio change in water content between 3rd September and 23rd December 2014, can occur very rapidly, and is often associated with slope failures. Two different types of wetting events were investigated, reflecting summer ground conditions governed by the presence of tension cracks, and near-saturated winter conditions, when the cracks had largely healed.

The winter wetting event, characterised by daily precipitation of up to 18 mm in October 2013 (Figure 5.43), resulted in rapid wetting of the near-surface, with some infiltration at depth (Figure 5.44). Figure 5.45, showing the volumetric evolution of resistivity, demonstrates initial infiltration through the permeable crest ballast, and runoff along a central line down the slope, due to the near-saturated conditions of the slope and hence the near-zero suctions. Two weeks after the initial rainfall, Figure 5.45e shows some limited infiltration via the known crack features, which may be a function of the suction reversal described previously, drawing in moisture from the saturated near-surface layer. Deeper infiltration may then be driven by higher suctions at depth, inferred from Figure 5.36f and g.

Individual heavy rainfall events in late July/early August 2013 (Figure 5.46), result in very rapid wetting of the embankment, as shown in Figure 5.47b, d and g. Images of the volumetric resistivity change (Figure 5.48) show immediate direct infiltration via the crack features, with no evidence of surface runoff. The crack features provide a conduit for water infiltration at depth, as described by Stewart et al., 2015.

Ultimately, ERT imaging has allowed the near-surface hydrodynamic behaviour of the slope to be investigated for differing ground conditions, highlighting the water infiltration through tension cracks in the summer, and surface runoff due to low surface suctions in the winter. Observations of low resistivity values aligning along known crack locations show that despite swelling behaviour, these cracks do not heal fully over the winter months.

The sprinkling experiments, which started on the 12th of January 2015, also constituted a winter wetting event. Figure 5.49, which shows the change in water content with respect to a baseline date prior to the sprinkler activation, unexpectedly illustrates drying at the near-surface, and at greater depth. Extracted ERT data points (Figure 5.57 and Figure 5.58) show subsurface resistivity to increase directly following the sprinkler activation, an effect more

pronounced in the near-surface; correspondingly, there is a decrease in ERT-derived estimates of water content. Given the implausibility of such a result, the perceived drying was deemed instead to be a function of the failure of the Waxman-Smits proxy relationship to represent the wetting front caused by the simulated precipitation provided by the sprinkler system. This is evident from the increasing deviation between ERT-derived water content estimates and measured values, as shown in Figure 5.57b and Figure 5.58b. This could result from one or a combination of the following factors, linked to high resistivity values:

1. The relatively low temperature of the sprinkled water with respect to the embankment;
2. Freezing of the water on the embankment surface;
3. Low ionic content of the sprinkled water with respect to typical rainwater.

From Figure 5.57 and Figure 5.58, it can be seen that the directly measured point sensor resistivity and water content values demonstrate change consistent with additional water infiltration from the sprinkler system. Due to the fact that the point sensors also record soil temperature, measured resistivity values are accurately corrected to a reference temperature, rather than relying on a temperature model, as with ERT. Figure 5.60 presents the deviation between the temperature model and measured temperature values, at the upper and lower positions on the South slope of the ERT test plot. Prior to sprinkler activation, it is observed that the temperature model underestimates actual temperature, thereafter, however, a rapid decline in measured temperatures results in the model significantly overestimating soil temperature, especially the near-surface. In Gance et al., 2016, the authors noted the cooling of the near-surface resulting from rainfall. This effect may also be observed from Figure 5.21d, for example on the 18th May 2013. Because the sprinkling water was stored in tanks at the ground surface at Nafferton farm, sheltered from sunlight, it is assumed that it was at a very low temperature, lower than that typical of rainwater. Following activation of the sprinkler system in mid-January 2015, a considerable reduction in temperature is observed, at all investigation depths (Figure 5.60).

It is understood that decreasing temperature acts to raise apparent resistivity (as shown in Figure 5.15). Similarly high resistivity values corresponded to low water contents within the Waxman-Smits proxy relationship, which explain the apparent drying as shown in Figure 5.49 and Figure 5.50. Although the raw ERT data was corrected for temperature (as described in subchapter 4.3.6), this reflected seasonal fluctuations, derived from historic BIONICS point

sensor data. If the fill temperature differs significantly from this historic behaviour (as it evidently does during the sprinkling experiments, from Figure 5.60), then this temperature correction is no longer suitable. Therefore, when such models are not representative, it is necessary to combine ERT measurements with distributed soil temperature measurements, in agreement with Gance et al., 2016. Additionally, field observations in January and February 2015 noted freezing of the sprinkled water at the ground surface (Figure 5.61). As well as further lowering the surface temperature, this frozen layer could act to prohibit sprinkled water from permeating into the embankment.

In addition to issues pertaining to the temperature of the sprinkled water, its ionic content may be lower than that of typical rainwater. This may result from settling of ionic conductors within the water as it rests in the tank, or just be an inherent property of the water itself.

All of these factors link to the variation of groundwater temperature and conductivity as described by Chambers et al., 2014, and are considered in the explanation of false apparent drying of the embankment during the sprinkling experiments, resulting from increased resistivity values. Although trends of decreasing resistivity values were used in the previous sections to identify rainwater infiltration, the same approach can be applied with regards to the sprinkled water, using increases in resistivity. Figure 5.50 highlights zones where resistivity has increased by more than 10 %, and demonstrates that after two weeks of sprinkling (Figure 5.50d), the entire topsoil has become wetter, particularly concentrated in the zones corresponding to known crack locations (which were extended in the previous May). It is difficult to assess whether or not there has been any infiltration at depth, as it is likely that the high resistivity sprinkled water would become more conductive over time as it warms, and as conductive clay particles dissolve in it, resulting in little change in fill resistivity despite potentially considerable increases in water content.

Aspect comparison

The above discussions concern the hydrodynamic behaviour of the crest and Southern flank exclusively, resulting from the fact that 3D data were not available for the Northern slope, as explained in subchapter 5.3.7. A 2D comparison of the Northern and Southern flanks as shown in Figure 5.51 and Figure 5.52 demonstrates higher variability of the more exposed Southern flank. This aspect-related damping is in keeping with the results of the point sensor

network, as discussed in subchapter 6.2.1, and is supported by the Glendinning et al., 2014 previous study at the BIONICS embankment.

6.3.3 *Critical assessment of the ERT proxy-based method*

One of the principal attractions of the tomographic imaging method is the fact that it allows volumetric subsurface imaging of a soil mass, whereas conventional point sensors only permit discrete measurements. In subchapter 5.4, discrete data points were extracted from ERT-derived volumetric images of resistivity, water content and soil suction, corresponding to the locations of point sensors. These two data types were then used as the basis for assessing the effectiveness of the ERT proxy-based method.

The point sensor network and ERT array provide two point and four point measurements of soil resistivity, respectively. Therefore, discrepancies between the ERT-derived and point sensor resistivity values do not necessarily suggest contradiction of the two methods. From Figure 5.53 to Figure 5.58, it can be seen that the resistivity responses of both methods highlight the same qualitative trends: principally, elevated values during the drier summer months than during the wetter portion of the year, supporting observed laboratory trends. Generally, the point sensor results demonstrate slightly elevated resistivity values with respect to the ERT method (Figure 5.53 to Figure 5.58), which is in keeping with expectations, given that the two point resistivity values suffer more from the effects of contact resistances, as discussed in subchapter 2.3.1. In the near-surface, the deviation between the two datasets is more pronounced, as greater contact resistances arise as a result of both low water content values, and poorer sensor coupling, impeding the point sensor measurement.

Following on from this qualitative agreement between the resistivity datasets, both ERT-derived and measured point sensor water content values broadly exhibit the same behavioural trends. The degree of quantitative agreement between the methods is observed to vary both spatially and temporally. At the South slope lower position (at 0.5 m and 1.0 m depths, Figure 5.53b), ERT-derived water content estimates compare very well with directly measured values. The same is true at the upper position, at a depth of 1.0 m (Figure 5.54b). At the top position (Figure 5.55b), rapidly fluctuating water content was captured by both methods, showing reasonable quantitative agreement but with point sensor values

sometimes lagging slightly behind ERT-derived values. For all of the above, the largest deviations between the ERT-derived and point sensor data types occurred during the summer months, which was also observed from the resistivity datasets. As explained in subchapter 2.3.8, the ERT method requires good coupling between the electrodes and the surrounding soil. In Figure 4.49, an example of the recorded pre-filtering statistics from an ERT profile made at the BIONICS test embankment is presented (from Summer 2014), and highlights the presence of high reciprocal errors under dry conditions, which may yield unreliable data. Although data pertaining to reciprocal errors beyond a threshold value were filtered out (see subchapter 4.3.4), this still allows for some ERT data measurements to have higher associated errors than others. Therefore, increased deviation between ERT-derived estimates and measured water content values can be attributed to elevated reciprocal errors in the raw resistivity data, resulting from poor coupling under dry conditions. This issue provides one mechanism for variable agreement between ERT-derived and directly measured geotechnical parameters.

Measurements of resistivity using the 5TE point sensors are automatically corrected to a reference temperature, which is possible because the sensors also record soil temperature. Due to the fact that it would be impractical to use point measurements to continuously correct ERT data, subchapter 4.3.6 derived a temperature model for the BIONICS embankment, from point sensor results. This model was then used as the basis for correcting ERT data to a reference temperature, and therefore, discrepancies between model and actual values have the potential to cause significant misinterpretation of ERT data, affecting both resistivity and other proxy-derived parameters. From Figure 5.59, showing the deviation between model and recorded temperature values, it is shown that, in general, the model underestimated actual temperature values, on the South slope and crest of the ERT test plot. Previously, it was noted that the poorest agreement between the two methods was observed during the summer months, however, the temperature deviation during these periods is not significantly higher than at other times of the year. Despite the observed temperature discrepancies, good correlation between the ERT-derived and point sensor resistivity data provides support for the representability of the temperature model. Nevertheless, the temporal variability of the deviation provides another mechanism for the temporal variability of the correlation between ERT-derived and directly measured geotechnical parameters.

In addition to the temporally varying fit between the ERT array and the point sensor network, there is a spatial variability, as described above. In Table 5.3, porosity values at the point sensor locations are presented, from two sources: extracted values from the porosity model, and values estimated from the point sensors during saturated or near-saturated conditions. It can be seen that where there is the closest agreement between the two porosity datasets, the ERT-derived water content values provide the best approximation of the directly measured values, showcasing the importance of accurate porosity models in using resistivity as a proxy for water content. Locations where porosity estimates are not representative would then result in a consistent offset between ERT-derived and measured water content values: from Eqn. 4.17, overestimation of porosity acts to underestimate soil resistivity (and hence to overestimate water content), and vice versa; furthermore, the conversion of ERT-derived water content values from gravimetric to volumetric (for comparison with point sensor data) provides another mechanism for error propagation, as knowledge of soil porosity is required. This is demonstrated by Figure 5.54b, which shows excellent correlation between the two data types during Winter 2013/2014, at a depth of 1.0 m, where the porosity data sets agree well. At a depth of 0.5 m, however, where the model overestimates the porosity by 21 %, ERT-derived water contents consistently overestimate measured water content by 4.5 %, over the same period.

Following the translation of ERT data into water content values, the Van Genuchten relationship was applied, yielding estimates of soil suction. In general, these ERT-derived suction values show relatively little correlation with measured point sensor (MPS) values. The best agreement can be seen from Figure 5.53c (South slope lower location, 0.5 m depth), which also demonstrates close correlation in terms of both resistivity and water content, between the ERT-derived and point sensor data sets. Given that the SWRC which defines the proxy relationship (Figure 5.1) spans several orders of magnitude, and that relatively insignificant variations in water content can result in considerable change in soil suction, deviation between the ERT-derived suction estimates and measured values may be very large. For this reason, the effectiveness of resistivity as a proxy for soil suction is called into question.

In the preceding paragraphs, the spatial and temporal variability of agreement between the ERT and point sensor network results has been discussed, attributing the variability to misfits of both the porosity and temperature models. Additionally, the nature of the resistivity

measurement was considered, in terms of high contact resistances associated with the two point method. Another issue which must be considered in explaining why point sensor and ERT results may not agree is the resolution of the two methods: the point sensors provide only discrete measurements which may or may not be representative of the surrounding soil, whereas ERT data points extracted from the point sensor locations describe a voxel with a resolution of 0.35 m (see subchapter 4.3.5). As such, conflicting results do not necessarily contradict each other, as the volumes they represent may differ significantly.

An investigation into the applicability of the proxy relationships was undertaken, by applying them to resistivity data obtained from the point sensor network, in order to remove issues pertaining to the temperature and porosity models and the resolution of the two methods. In addition to the point sensors at the ERT test plot, those at Panel B were used, due to it having similar compaction characteristics. In the first instance, point sensor resistivity data (corrected using measured temperature values) were converted to inferred water content values using the Waxman-Smits relationship, inputting the porosity estimates shown in Table 5.3, thereby obviating possible errors arising from the temperature and porosity models. From Figure 5.62 to Figure 5.64, it can be seen that Waxman-Smits-inferred water content values generally underestimate those measured, which is a result of their being inferred from two point resistivity measurements, which include higher contact resistances than do four point measurements. Generally, inferred values best approximate the measured values at depths of 1.0 m, where, as previously discussed, the point sensors would be better embedded and therefore demonstrate better contact with the surrounding soil. From all of the figures, describing both the ERT test plot and Panel B, strong correlation between the measured and Waxman-Smits-inferred water content values is observed, supporting the resistivity-water content proxy relationship, where the offset is simply attributed to the use of two point resistivity measurements.

At the locations where the Waxman-Smits-inferred water content estimates best represented those measured directly, the Van Genuchten relationship was applied, yielding estimates of soil suction (Figure 5.66 and Figure 5.67). On the South slope of the ERT test plot (Figure 5.66) and of Panel B (Figure 5.67a), which is subject to more pronounced seasonal dry/wet cycles, Van Genuchten-inferred suction estimates highlight similar qualitative trends to the directly measured suction values, showing the development of high soil suctions during the summer months. The best quantitative agreement is observed at

these high suctions, particularly at the lower position of the ERT test plot (Figure 5.66a). On the North slope of Panel B (Figure 5.67b, c, d), both datasets demonstrate moisture conditions which are relatively static, however, there is an offset of up to two orders of magnitude. As discussed previously, due to the fact that the SWRC spans several orders of magnitude, and that relatively insignificant variations in water content can yield considerable changes in soil suction, the deviations between estimated and measured soil suction values may be very large. Given this potential for estimated soil suctions to be so far removed from actual values, the use of resistivity as a proxy for soil suction is undermined, although there may be some merit as a qualitative, rather than quantitative tool.

6.3.4 *Limitations*

The previous subchapters have demonstrated the ability of electrical resistivity monitoring to image subsurface moisture dynamics. There are, however, a number of limitations to the method which have been noted over the course of this research study.

Practical issues

Several practical issues were encountered over the three year test period. The most basic of these related to the ability to actually gather electrical resistivity data, which was impeded by various factors. One issue concerned the telemetry of the BIONICS site, whereby a poor GPRS signal caused interruptions of the connection when remotely downloading raw ERT data and when scheduling measurements. This was the principal reason between the lag in the ERT system installation in November 2012 and the commencement of recording in June 2013. In March 2014, the continuity of ERT imaging was interrupted by battery failures, as the batteries depleted rapidly and then did not recharge. This was overcome by replacement of the batteries. During the darker winter months, the reduction of available solar power caused another problem, which was overcome by combining the solar panels with a fuel cell for battery charging.

Although the four point resistivity measurement has lower associated contact resistance than does the two point method, it still requires good coupling in order to be able to make a resistivity measurement. During Summer 2014, low in situ water contents resulted in poor coupling and hence high reciprocal errors, causing considerable amounts of data to be filtered out, as described by Loke et al., 2013. Similar observations of poor contact were

made by Hesse et al., 1986, who proposed the injection of a conductive liquid into the subsurface by high-pressure jet in order to improve coupling. Within the UK climate, however, such dry conditions are unlikely to persist for long, and, in the case that they do, may be easily remedied by sprinkling with (suitably conductive) water.

An unexpected problem which was encountered relatively early on in the project was the presence of rodents within the cable housing for the ERT array, and within the battery and router storage units. Although this was easily remedied by proofing of the cable network using insulating foam, this issue highlights the need for maintenance of ERT systems which are used in long-term in situ slope assessments.

In order to translate resistivity data into water content and suction data, a porosity model was developed, as described in subchapter 4.3.8. In previous ERT studies made at the BIONICS embankment (Glendinning et al., 2014; Gunn et al., 2015), core cutter sample results were used directly to construct the porosity model. However, such data were not available for the ERT test plot, and therefore porosity values used in the model were estimated from the maximum volumetric water contents obtained using the point sensor network (depths of up to 1 m). At greater depths, however, an average value was estimated from the results of core cutter samples taken from Panel B (Table 3.3), which was built to the same compaction specifications as the ERT test plot. There is, however, evidence to support differing porosities between Panel B and the ERT test plot (as discussed in subchapter 6.2.1); it can be seen from Table 3.3 that although Panels B and D were constructed in the same way, their porosity values differ. Additionally, it must be considered that the compaction characteristics of the embankment may have changed over time since construction. For these reasons, the porosity model used in this study represents a “best estimate”, which may not be fully representative of the actual subsurface porosity distribution, as discussed further in subchapter 6.4.6. As such, the model would benefit from improvement by porosity testing of extracted core samples from the actual ERT test plot.

Interpretation issues

Many authors have described ambiguity as a principal issue associated with ERT as a means of subsurface imaging (e.g. Garambois et al., 2002; Samouelian et al., 2005; Perrone et al., 2008), as described in subchapter 2.3.8. These authors suggest combining ERT surveys with

geotechnical data, which has been accomplished in this study with by point sensor network. Hydrological trends highlighted by the point sensor network and the ERT results have demonstrated good qualitative agreement, and as can be seen from subchapter 5.4.1, good quantitative agreement as well. The most tangible example of ambiguity of ERT data was observed in the apparent drying of the embankment following activation of the sprinkler system. Whilst considering resistivity changes over time in reference to hydrodynamic processes, there is some ambiguity with regards to possible interpretation of the results, which is inherent from the non-intrusive nature of ERT. As such, these results were also interpreted in conjunction with field observations and other literature studies. Another known source of ambiguity of ERT data is the inclusion of 3D effects within 2D monitoring surveys (as in Gance et al., 2016), however, this issue has been mitigated by the predominance of 3D ERT within this study.

The issue of resolution of ERT imaging has also been discussed (e.g. Friedel, 2003). Within this study, however, the close grid spacing of the electrodes (0.7 m), combined with 3D ERT has resulted in a high spatial (and temporal) resolution, capable of capturing the development of cracks during the summer months.

6.4 General discussion

In the preceding subchapters, the three experimental components of this study were discussed individually. In the following, they are considered together as a whole, including their implications in terms of the use of ERT as a means for investigating slope moisture dynamics, and ultimately, assessing slope stability.

6.4.1 *Proxy relationships*

The main objective of this study was to develop a methodology for translating field ERT data into information more directly relevant to slope stability. This was accomplished using Waxman-Smits and Van Genuchten relationships, as described in subchapters 4.3.8 and 4.3.9. The limitations of (and justification for) using laboratory–derived proxy relationships are discussed in subchapter 6.1.6. In subchapter 6.2.2, it was shown that, in general, these relationships show very good qualitative agreement with those recorded in situ using the point sensor network (Figure 5.27 to Figure 5.29).

Despite constituting a two point resistivity measurement, in situ resistivity - water content curves showed close quantitative agreement with the four point Waxman-Smits proxy relationship. This is a function of good coupling resulting from the sensors being embedded at depth, reinforcing the validity of a (four point) laboratory resistivity proxy for accurately measuring subsurface water content. A comparison of time series water content data at discrete locations recorded using point sensors and derived from ERT measurements (Figure 5.53), showed broad qualitative and quantitative agreement. Disagreement between the two datasets is explained by misfit of the temperature or porosity models (as in subchapter 5.4.3) and by the fact that the ERT-derived data points describe average water content values across an entire voxel from the 3D resistivity model described in subchapter 4.3.5, whereas the point sensor data points are discrete. Therefore, some apparent disparity between the two datasets does not necessarily imply disagreement between the two methods, or failure of the ERT proxy-based method.

Primary in situ soil water retention (drying) curves demonstrated lower suction values for a given water content than the laboratory–derived Van Genuchten drying curve, thought to be due to the presence of in situ confining pressures. Over time, a progressive loss in suction was observed from the in situ curves, resulting from deterioration of the soil fabric, leading to a residual drying path. The laboratory-derived Van Genuchten proxy relationship described one full moisture cycle only, therefore, investigation of a greater number of cycles would allow a residual relationship to be derived, which may improve the accuracy of ERT-derived soil suction estimates. Currently, however, error margins associated with the soil suction proxy relationship render its quantitative use prohibitive.

6.4.2 *Cracking*

All of the experimental components of this research study demonstrated evidence of crack features induced by rapid drying, at both the macro and micro-scales. Laboratory-based resistivity experiments demonstrated the insulating nature of air-filled macro-cracks as an impediment to current flow, increasing bulk soil resistivity: the development of micro-scale fractures during drying was imaged using environmental scanning electron microscopy. From the point sensor network, relatively high resistivity values were associated with the near-surface, due to a higher porosity of the topsoil and the presence of desiccation cracks. Similarly, increases in near-surface resistivity values confirmed the presence of tension

cracks, observed from field walkover surveys. Using time-lapse ERT imaging, the development and evolution of these cracks during the summer months was captured, at high spatial and temporal resolutions.

6.4.3 *Soil fabric deterioration*

The concept of soil fabric deterioration evident from the in situ water retention behaviour was supported by the results of laboratory experiments, as discussed in subchapters 6.1.3 and 6.1.5. These described a progressive, irrecoverable reorientation of clay particle structure linked to the development of micro-fractures during seasonal moisture cycling. This combined effect then acted to compromise the water retention properties of the soil, resulting in a progressive loss of soil strength. Due to the development of micro-fractures, and the resulting soil fabric deterioration, the laboratory resistivity – water content relationship was seen to be hysteretic for continued seasonal moisture cycling. Due to the fact that the in situ soil water retention curves were observed to evolve over time, it is reasonable to consider that the in situ resistivity – water content relationship would also. However, these properties have only been recorded in the field since November 2012 (the start of this research project), after which time the in situ SWRCs follow a residual path. This suggests that soil fabric deterioration has already occurred, and therefore that the in situ resistivity – water content relationships shown in Figure 5.29 describe a residual state, representative of the entire three year ERT test period.

Throughout the laboratory tests, a critical water content (12 % GWC) was associated with significant changes in the geotechnical properties of compacted BIONICS clay. This was considered to describe the continuity of the pore water phase, and thereby, the point at which micro-fractures develop (and heal) in the compacted BIONICS fill. Given the link which has been established between micro-fractures and irrecoverable clay structure change, this critical water content may be key to the concept of soil fabric deterioration: if clay fill dries out beyond the continuity of the pore water phase, then high tensions are developed which promote micro-fracturing, resulting in soil fabric deterioration. Although this critical water content was observed to be 12 % in the laboratory, this would vary spatially in the field depending on localised compaction characteristics.

The implications of soil fabric deterioration for slope stability can be considered in general terms, whereby a progressive loss of suction over time reduces the effective stress of earthworks materials, lowering their factor of safety. More specifically, given the observation of exacerbated clay structure degradation near discontinuities, soil fabric deterioration is likely to be more severe in proximity to features such as tension cracks. Combined with a cyclic reversal of near-surface pore pressures as described in subchapter 6.3.2, this may result in an acceleration of the ageing process for clay fills which is particularly pronounced at the near-surface.

6.4.4 *Hysteretic soil water retention behaviour*

A key observation of the laboratory results was the hysteretic nature of the soil water retention curve, where measured suctions on the drying path were lower for a given water content than on the drying path. The effects of this hysteresis on soil strength were shown directly, affecting both the unconfined compressive strength and shear strength of BIONICS clay (subchapter 6.1.5). Although only the drying portions of the in situ SWRCs were produced, time series data also confirmed field suctions to be lower during wetting events than during drying events. This hysteresis was incorporated into time-lapse ERT-derived estimates of soil suction by inclusion of the saturation history, such that decreases in water content prescribed the use of the Van Genuchten proxy drying expression (Eqn. 4.19) and vice versa. In this way, individual voxels within ERT-derived suction models were described in terms of their saturation history, rather than applying either drying or wetting parameters to the entire embankment model.

6.4.5 *Implications for ERT monitoring of slope stability*

The main reason for investigating how the various parameters considered in this study interact with each other is to fully analyse electrical resistivity data gathered from ERT systems, with respect to slope moisture dynamics. Ultimately, the goal of ERT in this context is to make inferences about the stability of the subsurface itself.

It has been established that in situ geophysical and geotechnical relationships may change over time due to the cumulative effect of soil fabric changes induced by seasonal cycles of drying and wetting, particularly in the near-surface. If proxy relationships are to be used to

convert ERT data to information more directly relevant to slope stability, then this ageing effect (as in Delage et al., 2006) may be significant, particularly with respect to more recently constructed embankments which have yet to reach a residual state, or in natural slopes exposed to a changing climate. This effect is likely to be less important for resistivity – water content proxy relationships than it is for suction, due to the observation of considerable progressive loss of in situ suctions (Figure 5.27 and Figure 5.28), whereas the resistivity hysteresis was muss less significant. If used in conjunction with geotechnical instrumentation (to mitigate interpretative ambiguity), electrical resistivity tomography may offer the possibility to investigate this deterioration effect in situ, by the evolution of resistivity values. For older slopes, as in most cases, fill material will have undergone a large number of dry-wet cycles, therefore residual proxy relationships will be most applicable. These may be derived in the laboratory by the continuous moisture cycling of specimens until they demonstrate residual state behaviour, or by testing specimens which have already been subjected to moisture cycles in the field.

6.4.6 *Viability of ERT monitoring of slope stability*

Ultimately, this research project constitutes an investigation into the viability of electrical resistivity tomography as a means of monitoring slope stability. There is, however, a distinction to be made, between "qualitative" interpretation, which allows subsurface moisture dynamics to be observed, and "quantitative" interpretation, which enables specific geotechnical parameters to be measured using proxy relationships. Prior to discussing the viability of ERT with respect to these two applications specifically, the logistics of the ERT method itself are discussed.

Conventional methods of slope stability assessment rely on point sensor measurements, which are generally installed by inserting sensors in hand-augered boreholes. This installation raises the issue of disturbance to the soil, resulting, for example, in a release of confining pressure, or by the borehole acting as a preferential moisture flow path. Due to the non-invasive nature of tomographic imaging, the ERT method has the advantage of obviating the above. Over the course of this research project, many additions were made to the existing point sensor network at the BIONICS embankment (Figure 4.39a), culminating in the well-populated map shown in Figure 4.39b. The map demonstrates that, despite the number of sensors installed, much of the embankment is not sampled by the point sensor

network, due to its discrete sampling nature. As such, the point sensor network provides only sparse data coverage, with significant uncertainties in interpretation associated with deriving a subsurface conceptual model. The ERT electrodes, however, are installed at 0.7 m grid spacings, and allow comprehensive volumetric imaging of the ERT test plot, enabling large-scale imaging. Subchapter 5.3 demonstrated the high spatial resolution of ERT imaging, which can be improved by reducing the grid spacing during inversion. In theory, a 2D, cross-sectional ERT profile may be adequate for many monitoring applications, however, comparison of 2D and 3D ERT imaging methods demonstrated that two-dimensional inversion may be sensitive to resistivity anomalies out of the imaging plane, distorting the resultant image. As such, it is prudent to obtain ERT profiles for heterogenous test sites by extracting from volumetric images.

Installation of the ERT array took fewer than two days with a team of five people, and is therefore greater in terms of labour-intensity to the installation of the point network system. During this study, many difficulties were encountered with the point sensor network, including rodent damage, faulty sensors, faulty loggers, depleted batteries, and the requirement for frequent manual download visits. As a result of the aforementioned issues, ongoing manual maintenance of the point sensor network provided for a labour-intensive investigation method, with ongoing expense. The fact of recorded ERT data being remotely transmitted from the test site is highly attractive, removing the necessity of data download visits. Additionally, the functionality of the system can be assessed remotely, on an instantaneous basis. Although some similar issues were encountered with the ERT array (e.g. battery failure, see subchapter 6.3.4), these were largely mitigated. These issues were, for the most part, a function of new technology rather than an inherent flaw of the method. One problem that was encountered was that of high contact resistances, inhibiting the collection of ERT data during dry summer spells. Within the context of slope stability monitoring within the UK, however, this is not considered problematic, given that slope failures are generally associated with heavy rainfall, which is favourable for soil-electrode coupling. Ultimately, volumetric ERT data has been gathered with relative ease, given minimal maintenance, providing a viable method of data collection which then serves as the basis for both qualitative and quantitative slope monitoring.

Pure resistivity imaging – qualitative applications

Subchapter 5.3 demonstrated the merit of ERT in volumetric resistivity imaging of the subsurface, providing invaluable insight into moisture dynamics, on a range of timescales. To a certain extent, this imaging can be achieved with just a rudimentary understanding of the relationship between soil resistivity and water content (effectively, that low resistivity corresponds to high water content, and vice versa). Using this basic concept, it was possible to capture the development and evolution of cracks in the embankment slope, surface runoff, and infiltration mechanisms, which are all highly relevant to slope stability. In order to produce such resistivity images, a relatively minimal amount of processing and interpretation is required – following the installation and activation of the ERT array, recorded voltages and resistances are processed in order to remove poor-quality data, and are then ready for inversion within the resistivity inversion software (see subchapters 4.3.4 and 4.3.5), yielding a preliminary resistivity model. Temperature correction is then performed: in this project, a simple temperature correction expression was created by fitting model parameters to historic temperature data from the BIONICS test embankment using basic modelling software (see subchapter 4.3.6). It is well understood that for any physical model, the quality of the output is highly dependent upon that of the input; close agreement between directly measured resistivity values (using the point sensors) and those obtained from ERT validated the temperature model as a method of estimating in situ temperature values, under normal atmospheric conditions (i.e. before the sprinkling experiments). Therefore, it has been shown that relatively little computation is required for the use of ERT as a tool for imaging subsurface moisture dynamics. With the development and application of proxy relationships, however, quantitative measurement of other geotechnical parameters may be possible.

Proxy relationships – qualitative and quantitative applications

In this study, the basic concept of soil resistivity being inversely proportional to soil water content has been extensively investigated. A robust relationship between the two parameters has been derived in the laboratory. The development of this proxy relationship was a relatively convoluted process, involving several stages, including a review of resistivity testing methods, soil preparation and compaction methods, temperature effects and an investigation into seasonal effects of moisture cycling. This experimental programme was

crucial in order to fully interpret the results of what is essentially a pilot study into quantitative ERT slope monitoring, and it is simply not realistic to consider that it could be recreated for every site of interest in the UK, in terms of either practicality or cost. In order to quantitively investigate other sites, however, a far reduced laboratory experimental programme could be deployed, following the methodology for Experiment 4, resolving a Waxman-Smits relationship between resistivity and water content. Although primary and secondary moisture cycles were investigated in this study (each comprising both drying and wetting paths), hysteretic effects between the two were considered negligible, therefore, one drying curve would likely suffice, expediting the laboratory component. Figure 2.27 shows that, for some clay soils, the resistivity – water content relationship is very similar. Therefore, it is likely that a reduced number of Waxman-Smits curves could be produced, representing different clay compositions across UK sites of interest, increasing the feasibility of the use of laboratory proxies in the field.

The applicability of the developed Waxman-Smits relationship to the field is proven by Figure 5.29, which demonstrates generally good agreement between the field (point sensor network) and laboratory relationships at higher water content values (22 % - 47 % VWC); although the agreement is poorer at lower water content values, this is not considered prohibitive for slope stability monitoring as failure generally occurs in near-saturated soil, therefore, higher water contents are of greatest interest. The above reinforces the validity of the laboratory proxy method for translating a subsurface resistivity model into a water content model.

In practice, conversion of the resistivity model into the water content model involves two stages: the correction of raw resistivity values for temperature; and translation from resistivity into water content during which subsurface porosity must be accounted for. As such, the quality of the temperature and porosity models is key to the quality of the resultant water content model, the former having been deemed to well approximate field temperature values under normal atmospheric conditions. In this study, a porosity model was estimated from both point sensor water content values and core cutter density values. The construction of the model was relatively straightforward, in that it simply involved linear extrapolation of estimated porosity values. In subchapter 6.3.3, the correlation was made between poor agreement between estimated and measured porosity values, and between ERT-derived and directly measured water content values. As such, it can be seen that an

accurate porosity model is paramount, and that the current model is not suitably sophisticated to fully represent the spatial heterogeneity of field porosity across the ERT test plot. If the ERT proxy method is to be used to infer in situ water contents across a wide array of field sites, then accurate porosity models would be required for each of these sites. This could be accomplished by testing of extracted "undisturbed" samples: for embankments, it is suggested that these be extracted at various depths beneath the crest and slope flanks, allowing a more sophisticated porosity model to be constructed. Given that such testing may be undertaken relatively easily, at relatively low cost, the necessity of developing a representative porosity model should not be prohibitive in the deployment of the ERT proxy method.

In addition to a proxy relationship between resistivity and water content, a laboratory-derived Van Genuchten curve was applied, ultimately allowing resistivity to be translated into estimates of soil suction. Distinct drying and wetting curves show significant hysteresis (Figure 5.1), therefore, the appropriate curve was applied, depending on the sign of the inferred water content change. The result is drastic spatial and temporal variability of estimated soil suction values in the ERT test plot, as highlighted by Figure 5.36 and Figure 5.65, which are not considered a realistic representation of field conditions. Translation of resistivity values into soil suctions using only the laboratory wetting parameters (Figure 5.66 and Figure 5.67) showed some limited agreement with recorded values, though mainly qualitative in nature. Due to the fact that the recorded SWRCs span several orders of magnitude of suction, associated errors may be very large. For this reason, the qualitative use of resistivity as a proxy for soil suction cannot altogether be considered viable, under current circumstances.

From the previous sections, the viability of implementing quantitative ERT monitoring technology has been demonstrated, with respect to estimation of water content. In this study, a great deal of focus has been put on qualitative interpretation of ERT images, illustrating slope moisture dynamics. For quantitative ERT monitoring to be worth the effort, however, it should require minimal interpretation, such that resultant water content models may be used standalone, and are representative of in situ field conditions. To this end, a detailed understanding of the potential sources of error associated with ERT-derived estimates of water content, and their mitigation, is necessary. As previously discussed, low in situ water content values can result in poor contact at the electrode-soil interface, over-

estimating subsurface apparent resistivity values. In this study, reciprocal errors were calculated and resistivity values corresponding to those beyond a threshold value were discarded. Failure of the temperature model during extreme atmospheric conditions was shown to result in distortion of reported resistivity values; this may be mitigated by the use of in situ temperature sensors. As discussed above, inaccurate porosity estimates directly affect translation from resistivity to water content estimates, constituting an important source of error; it was suggested that spatially-distributed undisturbed field samples be used to derive a comprehensive porosity model. Ultimately, the most basic factor in determining the accuracy of the proxy-based method is the quality of the Waxman-Smits relationship itself, where efforts should be made to represent in situ conditions as closely as possible, and to minimise contact resistance. Ultimately, due to the fact that all of the above factors can contribute to errors in ERT-derived estimates of field water content, it may be difficult to gauge which, specifically, are responsible. In this study, the temperature and porosity models and the Waxman-Smits relationship were assessed by comparison against the results of in situ point sensors. Ultimately, it is necessary to assess the quality of the ERT-derived water content estimates, which was achieved by comparison with directly measured values. In general, the datasets showed close agreement, particularly at higher water contents, corresponding to lower contact resistance (a detailed critical assessment of the accuracy of the ERT proxy method is provided in subchapter 6.3.3). To a certain extent, however, it may be difficult to assess the quality of ERT-derived water content estimates in this way, due to the fact that the two methods (ERT and point sensors) measure different volumes of soil, which may respond differently to environmental forcings.

The main point to be conveyed from the previous paragraph is that, in order to mitigate interpretative ambiguity associated with the ERT-proxy method, additional geotechnical apparatus is required. This is particularly important at the start of an ERT-monitoring study, before the quality of the water content model has been established; in latter stages, comparison with other geotechnical data may not be as crucial. Given that part of the motivation for ERT monitoring is shortcomings associated with point sensors, it is not ideal that they are deemed necessary for successful quantitative ERT monitoring, however, a relatively small number of such sensors may be required to validate the method for a given test site.

In summary, the implementation of electrical resistivity tomography technology for slope stability monitoring purposes has been shown to be practically viable. Relatively little computation is required in order to provide for an invaluable tool in the high resolution imaging of slope moisture dynamics, from a qualitative point of view. Quantitative imaging of soil moisture may be achieved with a minimum of laboratory experimentation, to resolve a robust Waxman-Smits proxy relationship, however, the success of using resistivity as a proxy for soil suction is limited. In order to assess the validity of temperature and porosity models, minimise interpretative ambiguity and evaluate the quality of the resultant water content estimates, additional geotechnical apparatus must be installed at test sites. Given the requirement for further interpretation of proxy-derived tomographic images, the concept of a fully-automated slope stability monitoring system as described by Gunn et al., 2015 (see subchapter 2.3.7) is not currently viable. A more nuanced system, however, may be realistic, which, for example, alerts the user (e.g. Network Rail) when rapid moisture increases are recorded across a certain proportion of the site volume, prompting user attention.

Chapter 7. Conclusions

7.1 Conclusions

The aim of this research was to "use 3D time-lapse resistivity data to make quantitative assessments of the stability of engineered slopes", seeking, ultimately, to use resistivity as a proxy for the geotechnical properties associated with slope stability. This study has been successful in employing a comprehensive, multi-scalar approach to investigate the interaction between resistivity and these geotechnical properties. An understanding of these interactions has facilitated the development of a methodology for directly translating field resistivity data gathered using electrical resistivity tomography systems into water content. Using this approach, the hydrodynamic behaviour of the purpose-built BIONICS test embankment was investigated, providing invaluable insight into the subsurface processes which affect slope stability. In Chapter 1, the motivation for this study was explained, citing the need for improved infrastructure stability assessment methods within the context of a changing climate. In Chapter 2, further motivation was derived from an explanation of the ageing state of British transport infrastructure, largely constructed during Victorian-era expansion of the rail network. Within this study, ERT systems have been shown to provide a cost-effective solution capable of satisfying the monitoring requirements of infrastructure slopes. Several practical issues were encountered, however, these were mitigated, furthering the development of an automated slope stability monitoring system.

Over the course of this three year research study, the following conclusions have been drawn:

Resistivity can successfully be used as a proxy for water content, but has limited application to estimates of soil suction. In this study, a robust Waxman-Smits relationship relating resistivity and water content was derived in the laboratory, and compared well against that recorded in the field using point sensors; ERT-derived estimates of water content showed close agreement with values directly measured using point sensors, in both quantitative and qualitative terms. The translation of ERT-derived water content data into estimates of soil suction showed very limited quantitative agreement with directly measured suction values, despite laboratory and field soil water retention curves demonstrating some agreement. This is attributed to the fact that because SWRCs span several orders of magnitude, small differences in water content are associated with very large soil suction

changes, therefore, error margins associated with the use of resistivity as a proxy for soil suction are prohibitively large.

If laboratory-derived proxy relationships are used to translate ERT data into water content information, it is essential that appropriate procedures are employed to derive them. For the purposes of this research study, laboratory methods were considered optimal due to the degree of control over testing conditions. A comparison of two and four point resistivity methods showed the former (more widely used) method to significantly over-estimate resistivity values, prompting the suggestion of a review of current standard practice. The method of compaction of soil specimens was also found to affect measured apparent resistivity values, therefore, efforts should be made to ensure that these are as representative as possible of in situ conditions. The limitations of such relationships, however, must be considered, particularly with respect to the representability of laboratory test results. Proxy-derived data gathered at the BIONICS embankment using the ERT array compared well both qualitatively and quantitatively with point sensor results, reinforcing the validity of the laboratory-based proxy relationships.

The success of resistivity as a proxy for other geotechnical parameters relies on accurate description of environmental conditions. For the translation of a resistivity model into a water content model, both subsurface temperature and porosity must be accounted for; this was accomplished in this study by the use of physical models to represent them. Temporally varying agreement between the temperature model and measured temperatures was shown to provide a mechanism for temporally varying agreement between ERT-derived water content values and those measured directly; misfit of the porosity model with respect to actual porosity values at certain locations within the test site was also shown to result in poor agreement between ERT-derived and measured water content values. As such, the development of representative physical models for use within the inversion process is paramount.

Geotechnical relationships evolve over time, as a result of soil fabric deterioration induced by seasonal dry-wet cycles. Within the laboratory, E-SEM imaging supported the development of micro-scale fractures resulting from drying of soil, promoting the

reorientation of clay particles leading to irrecoverable changes to soil structure. These fractures were specifically linked to drying below the continuity of the pore water phase, describing a critical water content associated with fundamental changes in geotechnical property inter-relationships. The effect of this deterioration on the Waxman-Smits relationship relating resistivity and water content was limited. However, in situ soil water retention curves were observed to evolve considerably over time, resulting in a progressive loss of suction, eventually arriving at a residual path. In most cases, fill material will have undergone a large number of dry-wet cycles, therefore a residual SWRC may be appropriate, comprising both a drying and wetting path; in more recently constructed slopes, or in natural slopes exposed to a changing climate, a changing SWRC may be required.

Ambiguity of interpretation regarding inverted resistivity data can be minimised. The issue of ambiguity arising from inverse theory to resolve a subsurface resistivity model is well-documented, whereby an infinite number of models may fit recorded data. This ambiguity is exacerbated by the fact that several factors affect soil resistivity. In 2D ERT surveys, out-of-plane heterogeneities may distort the subsurface resistivity signal, however, in 3D, these may be spatially accounted for. Therefore, 3D ERT monitoring is advocated for laterally variable, complex investigation scenarios, even if simply to resolve a cross-sectional rather than volumetric model. Correlation of inverted resistivity images with both field observations and data obtained using point sensors may be valuable in the interpretation of inverted resistivity images. In particular, given the direct dependence of resistivity on temperature, temperature correction of inverted resistivity data is essential, and must be able to account for both seasonal and diurnal fluctuations.

3D ERT monitoring can inform on slope moisture dynamics across a range of timescales. Over the course of this study, seasonal trends in subsurface moisture processes were investigated, occurring over a period of months, demonstrating drying and wetting of the embankment surface in response to sustained environmental conditions. In this way, a structured hydrological model of the test embankment was resolved, characterised by distinct resistivity ranges, and differing geotechnical responses to environmental forcings. Localised damping of the geotechnical response was observed, with fluctuations more pronounced near the surface, and on the more exposed, South-facing slope, subjected to preferential wind, rain, sunlight and hence greater evapo-transpiration. On a weekly scale,

the development of near-surface cracks was captured during the summer months, identified by high resistivity anomalies, indicative of dry, air-filled crack features. Rainwater ingress following rapid rainfall events was investigated via daily time-lapse imaging of low resistivity anomalies, and highlighted seasonal differences in infiltration processes. During the summer months, these were characterised by direct crack infiltration, with additional surface runoff during the winter months, due to saturated conditions and partial healing of cracks. Long-term hydrodynamic behaviours were confirmed by point sensor results, however, these were not capable of providing the same temporal resolution as the ERT monitoring system and therefore could not resolve shorter term processes.

Near-surface ERT imaging can be used to provide invaluable information on the dynamic moisture processes which precede slope failure. From estimation of in situ soil suctions, a cyclic process was identified, whereby the stress field across the topsoil alternates between being periodically greater and lower than that of the fill beneath. This process was suggested to be highly significant to the propagation of tension cracks at depth, and to subsurface infiltration processes. From laboratory experimentation, suction losses due to seasonal dry-wet cycles were linked to both soil fabric deterioration and hysteretic water retention, driving the progressive strength reduction of clay soils. As such, the cyclic reversal mechanism described could be a key process, accelerating ageing of the near-surface by the application of cyclic drying and wetting fronts, promoting strain softening. In particular, the deterioration of soil structure in proximity to discontinuities such as cracks was discussed, therefore, their influence may be especially important in ageing of the shallow subsurface. Estimations of in situ soil suctions show the locations of breaks in the suction contours to coincide with observed crack locations. Ultimately, it is the breakdown of suctions which will lead to instability, therefore, the fact that these breaks occur repeatedly at the crack locations suggest that the tension cracks provide the seed for slip planes, which could lead to shallow translational failures.

7.2 Recommendations for further work

This study has been successful in employing a comprehensive, multi-scalar approach to resolving the geophysical - geotechnical relationships essential to using ERT for assessment of slope stability, however, further work is required. Within the context of this research

study, several such considerations exist. In order to convert field ERT data to water content, a porosity model was derived, however, this model could be improved upon by correlating with extracted core cutter specimens from the ERT test plot. Finally, inverted ERT data were corrected for seasonal temperature fluctuations, however, this correction could not account for temperature extremes, or potentially significant diurnal fluctuations. As such, further calibration of temperature models may be advantageous, which could be achieved by correlation with point sensor results.

It has been shown that soil fabric deterioration has a cumulative effect to reduce shear strength over time, with the simultaneous evolution of resistivity relationships. As such, a more detailed knowledge of near-surface soil deterioration is required if ERT is to be used over long time periods. Indeed, ERT itself could prove useful in the assessment of this deterioration in situ. In this study, one full soil water retention curve was produced, comprising distinct drying and wetting paths. As a result of the aforementioned ageing processes, residual proxy relationships should be used to translate field ERT data obtained from older slopes into geotechnical information. Therefore, it is suggested that further investigation into residual soil water retention relationships is undertaken, which may be achieved by subjecting soil specimens to repeated seasonal moisture cycles until residual behaviour is observed.

Although the material used in this study was deemed to be representative of UK glacial tills used in earthwork construction, if ERT is to be used in large-scale slope assessments across the UK then it will be necessary to establish the relevant geophysical - geotechnical relationships for a range of representative engineering soils. Once this is achieved, quantitative ERT-based slope assessment systems may also be devised for natural slopes, which will likely be characterised by more complex, heterogeneous field conditions. Finally, further work is necessary to promote the development of an automated ERT slope stability monitoring system, which was described conceptually by Gunn et al., 2014, in which critical geotechnical parameters trigger alerts prompting slope inspection.

Chapter 8. References

1. Aaltonen J, 2001. Seasonal resistivity variations in some different swedish soils. European Journal of Environmental and Engineering Geophysics, 6, pp. 33–45

2. Abrahamson LW, Lee, TS, Sharma S, and Boyce GM, 2001. Slope Stability and Stabilisation Methods. John Wiley and Sons, Inc. New York

3. Al-Hamoud AS, Basma AA, Husein Malkawi AI, and Al Bashabsheh MA, 1995. Cyclic swelling behaviour of clays. Journal of Geotechnical Engineering, 121(7), pp. 562-565

4. Amidu SA and Dunbar JA, 2007. Geoelectric studies of a seasonal wetting and drying of a Texas vertisol. Vadose Zone Journal, 6, pp. 511-523

5. Antonio-Carpio RG, Perez-Flores MA, Camargo-Guzman D, and Alanis-Alcantar A, 2004. Use of resistivity measurements to detect urban caves in Mexico City and to assess the related hazard. Natural Hazards and Earth System Sciences, 4, pp. 541-547

6. Archie GE, 1942. The electrical resistivity log as an aid in determining some reservoir characteristics. Petroleum Transactions of AIME, 146, pp. 54–62.

7. ASTM 2012. G187-12a: Standard test method for measurement of soil resistivity using the two-electrode soil box method. West Conshohocken: ASTM International

8. ASTM 2013. B539 – 02. Standard Test Methods for Measuring Resistance of Electrical Connections (Static Contacts). West Conshohocken: ASTM International

9. Atkinson JH, 2000. Non-linear soil stiffness in routine design. Géotechnique, 50, pp. 487-508

10. Bauer P, Supper R, Zimmerman S, and Kinzelbach W, 2006. Geoelectrical imaging of groundwater salinisation in the Okavango Delta, Botswana. Journal of Applied Geophysics, 60, pp. 126-141

11. BBC, 2014. Beaminster tunnel landslide warning ahead of deaths. BBC News Online, [online] 25 February 2014. Available at: <http://www.bbc.co.uk/news/uk-england-dorset-26338593> [Accessed 1 September 2016]

12. Bell FG, 1981. Foundation Engineering in Difficult Ground. Butterworths, London, pp. 33-34

13. Bell FG, 2002. The geotechnical properties of some till deposits occurring along the coastal areas of Eastern England. Engineering Geology, 63, pp. 49-68

14. BGS, 2010. Monitoring – Electrical Appliance. *Ground Engineering*, September 2010 [online] Available at: <https://www.bgs.ac.uk/downloads/directDownload.cfm?id=1872&noexcl=true&t=The%20first%20trials%20of%20the%20British%20Geological%20Survey%27> [Accessed 1 September 2016]

15. BGS, 2013. *Landslides (slope instability).* [online] Available at: <http://www.bgs.ac.uk/products/geosure/landslides.html> [Accessed 04/03/2013]

16. BGS, 2016a. UK Rainfall and Landslides [image online] Available at: http://www.bgs.ac.uk/research/engineeringGeology/shallowGeohazardsAndRisks/images/LandslidesandRainfalldataScotland.jpg [Accessed 1 September 2016]

17. BGS, 2016b. [image online] Available at: <http://www.bgs.ac.uk/products/geosure/landslides.html> [Accessed 1 September 2016]

18. Bicalho KV, Marinho FAM, Fleureau JM, and Correia AG, 2011. Evaluation of filter paper calibrations for indirect determination of soil suctions of unsaturated soils. In: Proceedings of the 5th International Conference on Unsaturated Soils in Barcelona, 1

19. Bichler A, Bobrowsky P, Best M, Douma M, Hunter J, Calvert T, and Burns R, 2004. Three dimensional mapping of a landslide using a multi-geophysical approach: the Quesnel Forks landslide. Landslides, 1, pp. 29-40

20. Bickerdike, 2013. Upheaval. [online] Available at: <http://www.railengineer.uk/2013/07/03/upheaval/> [Accessed 1 September 2016]

21. Bièvre G, Jongmans D, Winiarski T, and Zumbo V, 2012. Application of geophysical measurements for assessing the role of fissures in water infiltration within a clay landslide (Trièves area, French Alps). Hydrological Processes, 26, pp. 2128-2142

22. Binley AM, Shaw B, and Henry-Poulter S, 1996. Flow pathways in porous media: electrical resistance tomography and dye staining image verification. Measurement Science and Technology, 7 (3), pp. 384-390

23. Birch G and Anderson I, 2010. LiDAR monitoring for the Folkestone Warren landslide. *Ground Engineering*, May 2011 [online] Available at: <https://www.newcivilengineer.com/download?ac=1378994> [Accessed 1 September 2016]

24. Bolfe VJ and Guirro RJ, 2009. Electrical resistance of gels and liquids used in electrotherapy for electrode-skin coupling. Rev Bras Fisioter, 13(6), pp. 449-505

25. Boudreault J, Dube J, Chouteau M, Winiarski T, and Hardy E, 2010. Geophysical characterisation of contaminated urban fills. Engineering Geology, 116, pp. 196-206

26. Brinkgreve RBJ, Engin E and Swolfs W, 2012. Plaxis 2012. Plaxis BV, Netherlands

27. Brunet P, Clement R, and Bouvier C, 2010. Monitoring soil water content and deficit using Electrical Resistivity Tomography (ERT) – A case study in the Cevennes area, France. Journal of Hydrology, 380, pp. 146-153

28. Bruno F and Marillier F, 2000. Test of high-resolution seismic reflection and other geophysical techniques on the Boup landslide in the Swiss Alps. Surveys in Geophysics, 21, pp. 33–348

29. BSI, 1990a. BS 1377-1: 1990 Methods of test for soils for civil engineering purposes - General requirements and sample preparation, BSI, Milton Keynes

30. BSI, 1990b. BS 1377-2: 1990 Methods of test for soils for civil engineering purposes - Classification tests, BSI, Milton Keynes

31. BSI, 1990c. BS 1377-3: 1990 Methods of test for soils for civil engineering purposes - Chemical and electro-chemical tests, BSI, Milton Keynes

32. BSI, 1990d. BS 1377-7: 1990 Methods of tests for soils for civil engineering purposes - Shear strength tests (total stress), BSI, Milton Keynes

33. BSI, 1990e. BS 1377-8: 1990 Methods of test for soils for civil engineering purposes -: Shear strength tests (effective stress), BSI, Milton Keynes

34. Cassiani G, Godio A, Stocco S, Villa A, Deiana R, Frattini P, and Rossi M, 2009. Monitoring the hydrological behaviour of a mountain slope via time-lapse electrical resistivity tomography. Near-surface Geophysics, pp. 475-486

35. Caris JPT and Van Asch TWJ, 1991. Geophysical, geotechnical and hydrological investigations of a small landslide in the French Alps. Engineering Geology, 13 (3-4), pp. 249-276

36. CCRA, 2012a. *Summary of Key Findings from the UK Climate Change Risk Assessment 2012*. CCRA: London

37. CCRA, 2012b. *Transport Summary*. CCRA: London

38. Cenderelli DA, 2000. Floods from natural and artificial dam failures. In: Inland Flood Hazards; Human, Riparian and Aquatic Communities. Wohl EE (Ed.), Cambridge University Press, New York, pp. 73-103

39. Chambers JE, Gunn D, Wilkinson PB, Meldrum P, Haslam E, Holyoake S, Kirham M, Kuras O, Merritt A, and Wragg J, 2014. 4D electrical resistivity tomography monitoring in an operational railway embankment. Near Surface Geophysics, 12, pp. 61-72

40. Chandler RJ, 2000. Clay sediments in depositional basins: the geotechnical cycle. Third Glossop lecture. Quarterly Journal of Engineering Geology and Hydrogeology, 33, pp. 7-39

41. Chesworth W, 2008. Encyclopedia of Soil Science, Springer. Chesworth W (Ed), pp. 350

42. Collier L and Hobbs B, 2003. Resistivity imaging survey of Capo Long Barrow, Aberdeenshire. Wallace C (Ed.), Society of Antiquaries of Scotland

43. Collin A, 1846. Landslides in Clays. University of Toronto Press, 1956. Translated by Schriever WR

44. Coulomb CA, 1773. Memories de Mathematique et de Physique, Academie Roval des Sciences par divers savants, 7, pp. 343-382

45. Craig RF, 2006. Craig's Soil Mechanics. Spon Press, London

46. Cropico, 2017. A guide to low resistance measurement. [online] Available at http://www.duncaninstr.com/pdfs/Low%20resistance%20measurement%20guide.pdf [Accessed 1 September 2017]

47. Cripps JC and Taylor RK, 1986. Engineering characteristics of British over-consolidated clays and mudrocks in Tertiary deposits. Engineering Geology, 22, pp. 346-376

48. Cruden DM, 1991. A simple definition of a landslide. Bulletin International Association for Engineering Geology, 43, pp. 27–29

49. Cruden DM, and Varnes DJ, 1996, Landslide Types and Processes, Special Report, Transportation Research Board, National Academy of Sciences, 247, pp. 36-75

50. Cui YJ, Tang AM, Mantho A, and De Laure E, 2008. Monitoring field soil suction using miniature tensiometer. Geotechechnial Testing Journal, 31(1), pp. 95-100

51. Dahal RK, Hasegawa S, 2008. Representative rainfall thresholds for landslides in the Nepal Himalaya, Geomorphology, 100 (3-4), pp. 429-443. DOI:10.1016/j.geomorph.2008.01.014

52. Dahlin T, 1996. 2D resistivity surveying for environmental and engineering applications. *First Break*, 14

53. Dahlin T and Zhou B, 2004. A numerical comparison of 2D resistivity imaging with 10 electrode arrays. Geophysical Prospecting, 52, pp. 379–398. doi: 10.1111/j.1365-2478.2004.00423.x

54. Das BM and Sobhan K, 2014. Principles of Geotechnical Engineering. Cengage Learning, Stamford

55. Decagon Devices, Inc., 2014. WP4C Dewpoint Potentiometer, Operator's manual. Decagon Devices Inc. [online] Available at: <http://manuals.decagon.com/Manuals/13588_WP4C_Web.pdf> [Accessed 1 June 2015]

56. Decagon Devices, Inc., 2008. EC-TM Operator's manual. Decagon Devices, Inc.[online] Available at:

<http://manuals.decagon.com/Manuals/Discontinued/ECH2O-TEEC-TMv6-Operators-Manual-(discontinued).pdf> [Accessed 1 September 2016]

57. Decagon Devices, Inc., 2016. KD2 Pro Thermal Properties Analyzer Operator's manual. [online] Available at: http://manuals.decagon.com/Manuals/13351_KD2%20Pro_Web.pdf [Accessed 1 September 2017]

58. DeGroot-Hedlin C and Constable S, 1990. Occam's inversion to generate smooth, two-dimensional models form magnetotelluric data. Geophysics, 55, pp. 1613-1624

59. Delage P, Marcial D, Cui YJ, and Ruiz X, 2006. Ageing effects in a compacted bentonite: a microstructure approach. Géotechnique 56(5), pp. 291-304

60. Del Gaudio V, Wasowski X, Pierri R, Mascia U and Calcagnile G, 2000. Gravimetrie study of a retrogressive landslide in Southern Italy. Surveys in Geophysics, 21(4), pp. 391-406

61. Delta-T Devices, Ltd., 2014. User manual for the SM150 Soil Moisture Sensor. [online] Available at: <https://www.upgmbh.com/fileadmin/produkte/support/SM150%20Soil%20Moisture%20Sensor%20User%20Manual%20v1.0.pdf> [Accessed 1 September 2016]

62. Depountis N, Harris C, Davies MCR, Koukis G and Sabatakakis N, 2005. Application of electrical imaging to leachate plume evolution studies under in-situ and model conditions. Environmental Geology, 47, pp. 907–914

63. DGSI, 2016. *Standpipe Piezometer and Water Level Indicator.* DGSI. Available at: <http://www.slopeindicator.com/pdf/standpipe%20piezo%20datasheet.pdf> [Accessed 1 September 2016]

64. Dijkstra T and Dixon N, 2010. Climate change and slope stability in the UK: challenges and approaches. Quarterly Journal of Engineering Geology and Hydrogeology, 43 (4), pp. 371-385

65. Dixon N, Dijkstra TA, Forster A and Connell R, 2007. Climate change impact forecasting for slopes (CLIFFS) in the built environment. In: Proceedings of the IAEG conference 2006, paper number 528, The Geological Society of London, London

66. Dobecki TL and Upchurch SB, 2006. Geophysical applications to detect sinkholes and ground subsidence. *The Leading Edge*, March 2006 [online] Available at: <http://userpage.fu-berlin.de/geodyn/tutorials/Dynamik_der_Erde/pdf/WS2010_2011/Dobecki-etal2006_TheLeadingEdge.pdf> [Accessed 1 September 2016]

67. Dunnicliff J, 1988. Geotechnical Instrumentation for Measuring Field Performance. John Wiley and Sons, Inc. New York

68. Edgar TV, 1989. In-service corrosion of galvanised culvert pipe. In: Effects of Soil Characteristics on Corrosion. ASTM STP 1013. Chaker V and Palmer JD (Eds), American Society for Testing and Materials, Philadelphia, pp. 133-143

69. Edwards LS, 1977. A modified pseudosection for resistivity and induced polarization. Geophysics, 42, pp. 1020-1036

70. Fargier Y, Fauchard C, Meriaux P, Royet P,Palma-Lopes S, Francois D,Cote P and Bretar F, 2012. Methodology Applied to the Diagnosis of Dikes and Dams; Novel Approaches and Their Applications in Risk Assessment. Luo Y (Ed.), ISBN: 978-953-51-0519-. Available at: <https://cdn.intechopen.com/pdfs-wm/35512.pdf> [Accessed 15/06/2017]

71. Fell R, Stapledon D, and Macgregor P, 2012. Landslides and geological environments. In: Landslides: Types, Mechanisms and Modelling. Clague JC and Stead D (Eds.), Cambridge University Press, Cambridge

72. FHWA, 2001. Soil *Slope and Embankment Design Reference Manual - Report No. FHWA NHI-01-026.* Collin JG, Hung JC, Lee WS, and Munfakh G (Eds.), Federal Highway Administration, U.S. Department of Transportation, pp. 2

73. Fredlund DG, Houston SL, Nguyen Q, and Fredlund MD, 2010. Moisture movement through cracked clay soil profiles. Geotechnical and Geological Engineering, 28(6), pp. 865-888

74. Fredlund DG, Sheng D, and Zhao J, 2011. Estimation of soil suction from the soil water characteristic curve. Canadian Geotechnical Journal, 48, pp. 186-198

75. Fredlund DG and Rahardjo H, 1993. Soil Mechanics for Unsaturated Soils. John Wiley and Sons, Inc. New York

76. Fredlund DG and Xing A, 1994. Equations for the soil-water characteristic curve. Canadian Geotechnical Journal, 31(4), pp. 521–532

77. Friedel S, 2003. Resolution, stability and efficiency of resistivity tomography estimated from a generalised inverse approach. Geophysical Journal International, 153, pp. 305-316

78. Friedel S, Thielen A, and Springman SM, 2006. Investigation of a slope endangered by rain-fall-induced landslides using 3D resistivity tomography and geotechnical. Journal of Applied Geophysics, 60(2), pp. 100-114

79. Fukue M, Minatoa T, Horibe H, and Taya N, 1999. The microstructure of clay given by resistivity measurements. Engineering Geology, 54, pp. 43–53

80. Gance J, Malet JP, Supper R, Sailhac, Ottowitz, D, and Jochum B, 2016. Permanent electrical resistivity measurements for monitoring water circulation in clayey embankments. Journal of Applied Geophysics, 126, pp. 98-115

81. Garambois S, Senechal P, and Perroud H, 2002. On the use of combined geophysical methods to assess water content and water conductivity of near-surface formations. Journal of Hydrology, 259, pp. 32-48

82. Grandjean G, Gourry JC, Sanchez O, Bitri A and Garambois S, 2011. Structural study of the Ballandaz landslide (French Alps) using geophysical imagery. Journal of Applied Geophysics, 75, pp. 531-542

83. Glendinning S, Hall J, and Manning L, 2009. Asset-management strategies for infrastructure embankments. Proceedings of the Institution of Civil Engineers: Engineering Sustainability, 162(2), pp. 111-120

84. Glendinning S, Hughes PN, Helm P, Chambers J, Mendes J, Gunn D, Wilkinson P, and Uhlemann S, 2014. Construction, management and maintenance of embankments used for road and rail infrastructure: implications of weather induced pore water pressures. Acta Geotechnica, 9(5), pp. 799-816

85. Grim RE, 1962. Applied Clay Mineralogy. McGraw-Hill, New York

86. Gunn DA, Chambers JE, Hobbs PRN, Ford JR, Wilkinson PB, Jenkins GO, and Merritt A, 2013. Rapid observations to guide the design of systems for long-term monitoring of a complex landslide in the Upper Lias clays of North Yorkshire, UK. Quarterly Journal of Engineering Geology and Hydrogeology, 46, pp. 323-336

87. Gunn DA, Chambers JE, Uhlemann S, Wilkinson PB, Meldrum PI, Dijkstra TA, Haslam E, Kirkham M, Wragg J, Holyoake S, Hughes PN, Hen-Jones R, and Glendinning S, 2015. Moisture monitoring in clay embankments using electrical resistivity tomography. Construction and Building Materials, 92, pp. 82-94

88. Gupta SC and Hanks RJ, 1972. Influence of Water Content on Electrical Conductivity of the Soil. Soil Science Society of America Journal, 36, pp. 855-857

89. Hack R, 2000. Geophysics for slope stability. Surveys in Geophysics, 21, pp. 423-448

90. Hambrey 1994. Glacial Environment, University College Press, London

91. Hamid TB, 2008. Ultimate shear strength of unsaturated soils. In: Unsaturated Soils: Advances in Geo-Engineering. Toll DG, Augarde CE, Gallipoli SJ (Eds.), Taylor and Francis Group, London, pp. 429 - 434. ISBN 978-0-415-47692-8

92. Harvard University, 2007. A Summary of Error Propagation. HU. [online] Available at: <http://ipl.physics.harvard.edu/wp-uploads/2013/03/PS3_Error_Propagation_sp13.pdf> [Accessed 19 January 2017]

93. Hassan A, 2014. *Electrical resistivity method for water content characterisation of unsaturated clay soil.* PhD Thesis, Durham University

94. Hassan AA and Toll DG, 2014. Investigation of the directional dependence of soil resistivity in cracking clays. In: Unsaturated Soils: Research and Applications. Khalili, Russell and Khoshghalb (Eds.), Taylor and Francis Group, London

95. Hauck C, Vonder Muhll D, and Maurer H, 2003. Using DC resistivity tomography to detect and characterise mountain permafrost. Geophysical Prospecting, 51, pp. 273-284

96. Hayley K, Bentley LR, Gharibi M, Nightingale M, 2007. Low temperature dependence of electrical resistivity: Implications for near-surface geophysical monitoring, 2007. Geophysical Research Letters, 34

97. Heaney BM, 2003. Electrical Conductivity and resistivity. In: Electrical Measurement, Signal Processing, and Displays. Webster JG (Ed), CRC Press, Boca Raton, Florida, pp. 1-14

98. Helm P, 2012. *Simple modelling of the stability of the BIONICS embankment at Nafferton Farm*. Newcastle University internal report

99. Hen-Jones RM, Hughes PN, Stirling RA, Glendinning S, Chambers JE, Gunn DA and Cui YJ, 2016. Seasonal effects on geophysical-geotechnical relationships and their implications for Electrical Resistivity Tomography monitoring of slopes. Acta Geotechnica (article under review)

100. Heincke B, Maurer H, Green A G, Willenberg H, Spillmann T, and Burlini L, 2006. Case History. Characterising an unstable mountain slope using shallow 2D and 3D seismic tomography. Geophysics, 71, pp. 241-256

101. Hesse A, Jolivet A, and Tabbagh A, 1986. New prospects in shallow depth electrical surveying for archaeological and pedological applications. Geophysics, 51, pp. 581-594

102. Highland LM and Bobrowsky P, 2008. The Landslide Handbook – A Guide to Understanding Landslides. USGS, Denver

103. Highways Agency, 1998. Specification for Highway Works. The Stationary Office, London

104. Highways Agency, 2016. Design Manual for Roads and Bridges. The stationery Office, London

105. Hilbert C, Grandjean G, Bitri A, Travelleti J, and Malet J, 2012. Characterising landslides through geophysical data fusion: Example of the La Valette landslide (France). Engineering Geology, 128, pp. 23-29

106. Hilbich C, Fuss C, and Hauck C, 2011. Automated time-lapse ERT for improved process analysis and monitoring of frozen ground. Permafrost and Periglacial Processes, 22, pp. 306-319

107. Hirsch M, Bentley LR, and Dietrich P, 2008. A comparison of electrical resistivity, ground penetrating radar and seismic refraction results at a river terrace site. Journal of Environmental and Engineering Geophysics, 13 (4), pp. 325-333

108. Hsu H, Yanites BJ, Chen C, and Chen Y, 2010. Bedrock detection using 2D electrical resistivity imaging along the Peikang River, central Taiwan. Geomorphology, 114, pp. 406-414

109. Huggel C, Khabarov N, Korup O and Obersteiner M, 2012. Physical impacts of climate change on landslide occurrence and related adaptation. In: Landslides: Types, Mechanisms and Modeling. Cambridge University Press, Cambridge. ISBN 9781107002067

110. Hughes PN, Glendinning S, and Toll D, 2006. *Report on the design and construction of the BIONICS embankment*. Newcastle University internal report

111. Hughes N, Glendinning S, Mendes J, Parkin G, Toll DG, Gallipoli D, and Miller PE, 2009. Full-scale testing to assess climate effects on embankments. Proceedings of the Institution of Civil Engineers, Engineering Sustainability, 162, pp. 67-79

112. Hungr O, Leroueil S and Picarelli L, 2014. The Varnes classification of landslide types, an update, Landslides, 11(2), pp. 167-194

113. Hutchinson JN, 1988. General Report: Morphological and geotechnical parameters of landslides in relation to geology and hydrogeology. In: Proceedings of the Fifth International Symposium on Landslides. Bonnard C (Ed.), Balkema, Rotterdam, pp. 3-35

114. IPCC, 2014. *Climate Change 2014: Synthesis Report. Contribution of Working Groups I, II and III to the Fifth Assessment Report of the Intergovernmental Panel on Climate Change*. Pachauri RK and Meyer LA (Eds.), IPCC, Geneva, pp. 151

115. Itasca, 2011. FLAC – Fast Lagrangian Analysis of Continue v7.00 with Two Phase Flow – Manual. Itasca Consulting Group Inc. Minneapolis, USA

116. Janesch J, 2013. *Two-wire vs. Four-wire resistance measurements: which configuration makes sense for your application?* Report for Keithley Instruments, Inc. [online] Available at

<http://www.tek.com/sites/tek.com/files/media/document/resources/2Wire_4Wire%20Resistance%20Article.pdf > [Accessed 1 September 2016]

117. Jardine RJ, Potts D M, Higgins KG, Nyambayo VP, and Addenbrooke TI, 2004. The influence of permeability on the stability of embankments experiencing seasonal cyclic pore water pressure changes. In: Proceedings of the Skempton Conference - Advances in Geotechnical Engineering. Institution of Civil Engineers, London

118. Jomard H, Lebourg T, Guglielmi Y, and Tric E, 2010. Electrical imaging of sliding geometry and fluids associated with a deep seated landslide (La Clapiere, France). Earth Surface Processes and Landforms, 35, pp. 588-599

119. Jongmans D and Garambois S, 2007. Geophysical investigation of landslides: a review. Bulletin of the Geological Society of France, 178, pp. 101–112

120. Kavian M, Slob EC, and Mulder WA, 2011. Hysteresis in the nonmonotonic electric response of homogeneous and layered unconsolidated sands under continuous flow conditions with water of various salinities, 100 kHz to 2MHz. Journal of Geophysical Research, 116, B08214

121. Kemp SJ and Wagner D, 2016. *Mineralogical and clay mineralogical analysis of railway embankment samples.* Durham University internal report

122. Kibria G and Hossain M, 2012. Investigation of geotechnical parameters affecting electrical resistivity of compacted clays. Journal of Geotechnical and Geoenvironmental Engineering, 138(12), pp. 1520-1529

123. Kiessling D, Schmidt-hattenberger C, Schuett H, Schilling F, Krueger K, Schoebel E, Danckwardt E, and Kummerow J, 2010. Geoelectrical methods for monitoring geological CO_2 storage: first results from cross-hole and surface-downhole measurements from the CO_2SINK test site at Ketzin (Germany). International Journal of Greenhouse Gas Control, 4, pp. 816-826

124. Knight R, 1991. Hysteresis in the electrical resistivity of partially saturated sandstones. Geophysics 56, pp. 2139-2147

125. Korup O, 2012. Landslides in the earth system. In: Landslides: Types, Mechanisms and Modelling. Clague JC and Stead D (Eds.), Cambridge University Press, Cambridge

126. LaBrecque DJ, Heath G, Sharpe R, and Versteeg R, 2004. Autonomous monitoring of fluid movement using 3D electrical resistivity tomography. Journal of Environmental and Engineering Geophysics, 9(3), pp. 53-62

127. Lapenna V, Lorenzo P, Perrone A, Piscitell S, Rizzo E, and Sdao F, 2005. 2D electrical resistivity imaging of some complex landslides in the Lucanian Apennine chain, Southern Italy. Geophysics, 70 (3), pp. 11-18

128. Lapworth A and McGregor J, 2008. Seasonal variation of the prevailing wind direction in Britain. Weather, Volume 63 (12), pp. 365-368

129. Lebourg T, Hernandez M, Zerathe S, El Bedoui S, Jomard H, and Fresia B, 2010. Landslide triggered factors analysed by time lapse electrical survey and multidimensional statistical approach. Engineering Geology, 114, (3-4), pp. 238-250

130. Lee C, Yang C, Liu H, Wen K, Wang Z, and Chen Y, 2008. A study of the hydrogeological environment of the lishan landslide area using resistivity image profiling and borehole data. Engineering Geology, 98, pp. 115-125

131. Lee MW, 2011. *Connectivity Equation and Shaly-Sand Correction for Electrical Resistivity - Scientific Investigation Report 2011-5005*. USGS Geological Survey: Reston, Virginia

132. Lim TT, Rahardjo H, Change MF, and Fredlund DG, 1996. Effect of rainfall on matric suctions in a residual soil slope. Canadian Geotechnical Journal, 33, pp. 618-628

133. Liu X, Hicher P, Muresan B, and Hicher P, 2015. Heavy metal retention properties of kaolin and bentonite in a wide range of concentration and different pH conditions. Applied Clay Science, 119, pp. 365-374

134. Loke MH, 1999. Electrical imaging surveys for environmental and engineering studies – a practical guide to 2D and 3D survey. [online] Available at: </http://www.geo.mtu.edu/~ctyoung/LOKENOTE.PDF> [Accessed 1 September 2016]

135. Loke MH, 2015a. Res2DINVx64 ver. 4.05 Manual. Geotomosoft, October 2015

136. Loke MH, 2015b. Tutorial: 2-D and 3-D electrical imaging surveys. Geotomosoft, May 2015

137. Loke MH, 2016. Res3DINVx64 ver. 3.10 Manual. Geotomosoft, January 2016

138. Loke MH, Chambers JE and Kuras O, 2011. Instrumentation, electrical resistivity. In: Solid Earth Geophysics Encyclopedia (2nd Edition), Electrical & Electromagnetic. Gupta H (Ed), Springer, Berlin, pp. 599-604

139. Loke MH, Chambers JE, Rucker DF, Kuras O, and Wilkinson PB, 2013. Recent developments in the direct current geoelectrical imaging method. Journal of Applied Geophysics, 95, pp. 135-156

140. Loveridge FA, Spink TW, O'Brien AS, Briggs KM, and Butcher D, 2010. The impact of climate and climate change on infrastructure slopes, with particular reference to Southern England. Quarterly Journal of Engineering Geology and Hydrogeology, 43(4), pp. 461-472

141. Machan G and Bennet VG, 2008. Use of Inclinometers for Geotechnical Instrumentation on Transportation Projects – State of the Practice. Transportation Research Board, Washington

142. McCarter WJ, 1984. Electrical resistivity compacted clays. Géotechnique 34(2), pp. 263-267

143. McGillivray, P.R. and Oldenburg, D.W., 1990. Methods for calculating Frechet derivatives and sensitivities for the non-linear inverse problem: A comparative study. Geophysical Prospecting, 38, pp. 499-524

144. McKee CR and Bumb AC, 1984. The importance of unsaturated flow parameters in designing a monitoring system for hazardous wastes and environmental emergencies. In: Proceedings, Hazardous Materials Control Research Institute National Conference, Houston, TX. pp. 50-58

145. Meehl G, Stocker T, and Collins W, 2007. Global climate projections. In: Climate Change 2007: The Physical Science Basis. Contribution of Working Group I to the Fourth Assessment Report on the Intergovernmental Panel on Climate Change, Solomon S, Qin

D, and Manning M (Eds.), Cambridge and New York: Cambridge University Press. pp. 747-845

146. Mendes J and Toll DG, 2013. Influence of initial water content on the water retention behaviour of a sandy clay soil. In: Proceedings of the 18th International Conference on Soil Mechanics and Geotechnical Engineering, Paris, 2013

147. Merritt, Andrew, 2014. *4D geophysical monitoring of hydrogeological precursors to landslide activation.* PhD thesis, University of Leeds

148. Merritt AJ, Chambers JE, Wilkinson PB, West LJ, Murphy W, Gunn D, and Uhlemann S, 2016. Measurement and modelling of moisture – electrical resistivity relationship of fine-grained unsaturated soils and electrical anisotrophy Journal of Applied Geophysics, 124, pp. 155-165

149. Meskini-Vishkaee F, Mohammadi MH and Vanclooster M, 2014. Predicting the soil moisture retention curve from soil particle size distribution and bulk density data using a packing scaling density factor. Hydrological Earth Systems Sciences, 19, pp. 4053-4063

150. Met Office, 2012. [image online] Available at: <https://www.geolsoc.org.uk/~/media/shared/images/geoscientist/Geoscientist%2023_05/F%201%20PENNINGTON%203smallered.png?la=en> [Accessed 1 September 2016]

151. Met Office, 2014. [online] Available at: <http://www.metoffice.gov.uk/public/weather/climate/gcy9j0p48> [Accessed 1 September 2016]

152. Miccoli I, Edler F, Pfnur H, and Tegenkamp C, 2015. The 100th anniversary of the four-point probe technique: the role of probe geometries in isotropic and anisotropic systems. Journal of Physics: Condensed Matter, 27

153. Michelaki S, 2013. *Use of soil resistivity to monitor water content in infratrsucture embankments – field study*. MSc Thesis, Newcastle University

154. Michot D, Benderitter Y, Dorigny A, Nicoullaud B, King D, and Tabbagh A, 2003. Spatial and temporal monitoring of soil water content with an irrigated corn crop cover using electrical resistivity tomography. Water Resources Research, 39

155. Monego M, Cassiani G, Deiana R, Putti M, Passadore G, and Altissimo L, 2010. A tracer test in a shallow heterogeneous aquifer monitored via time-lapse surface electrical resistivity tomography. Geophysics 75(4) pp. 61-73

156. MottMacdonald, 2011. *The effects of railway traffic on embankment stability - RSSB 1386 (Revised).* MottMacdonald: Croydon

157. Munoz-Castelblanco J, Pereira J, Delage P, and Cui YJ, 2012. The influence of changes in water content on the electrical resistivity of a natural unsaturated loess. ASTM Geotechnical Testing Journal 35(1), pp. 11-17

158. Murthy VNS, 2003. Geotechnical Engineering: Principle and Practices of Soil Mechanics and Foundation Engineering (Civil and Environmental Engineering). Marcel Dekker, New York, pp. 311

159. Mohr O, 1900. Welche umstände bedingen die Elastizitätsgrenze und den bruch eines materials? Zeitschrift des Verenes Deutscher Ingenieure, 44, pp. 1524–1530

160. Nassir AA, Loke MH, Lee CY, and Nawawi MNM, 2000. Salt-water intrusion mapping by geoelectrical imaging surveys. Geophysics Prospecting, 48, pp. 647-661

161. Negri S, Leucci G, and Mazzone F, 2008. High resolution 3D ERT to help GPR interpretation for researching archaeological items in a geologically complex subsurface. Journal of Applied Geophysics, 65, pp. 111-120

162. Newgate Online, 2016. Nyogel 756G, 100 gram tube. [online] Available at: <http://newgateonline.com/nyogel-756g-100gram-tube.html> [Accessed 20 April 2016]

163. Noguchi T, Mendes J, and Toll D, 2011. Comparison of soil water retention curves following dry paths obtained by filter paper, high capacity suction probe and pressure plate. In: Unsaturated Soils: Theory and Practice. Jotisankasa, Sawangsuriya, Soralump and Mairaing (Eds.), pp. 409-414

164. O'Brien A, 2007. Rehabilitation of urban railway embankments – investigation, analysis and stabilisation. In: Proceedings of the 14th International Conference Soil Mechanics and Geotechnical Engineering, 1. Cuellar V, Dapena E (Eds.), Madrid, Millpress Science Publishers, Rotterdam, p. 125-143

165. Palacky GJ, 1988. Resistivity characteristics of geologic targets. In: Investigations in Geophysics: Electromagnetic methods in applied geophysics-theory, 1. Nabighian MN (Ed.), Society of Exploration Geophysicists, pp. 53–129

166. Perrone A, Vassallo R, Lapenna V, and Di Maio C, 2008. Pore water pressures and slope stability: a joint geophysical and geotechnical analysis. Journal of Geophysics and Engineering, 5, pp. 323-337

167. Perry J, Pedley M, and Reid M, 2001. *Infrastructure embankments: condition appraisal and remedial treatment – Report C550*. CIRIA: London

168. Pico Technology, 2014. PicoScope 3000 Series, User's Guide. Pico Technology. [online] Available online at <> [Accessed 19 January 2017]

169. Portal A, Fargier Y, Lenat JF, and Labazuy P, 2016. Contribution of 3D inversion of Electrical Resistivity Tomography data applied to volcanic structures. [Poster], European Geosciences Union General Assembly, Vienna, Austria, 17th – 22nd April 2016

170. Potts DM, Kovacevic N, and Vaughan PR, 1997. Delayed collapse of cut slopes in stiff clay. Géotechnique 47(5), pp. 953-982

171. Rail Technology Magazine, 2012.Protecting infrastructure against shallow landslides. April/May 2012 edition, pp. 139. [online] Available at: <http://content.yudu.com/A1wkts/RTMAprMay2012/resources/index.htm?referrerUrl=http%3A%2F%2Fwww.railtechnologymagazine.com%2F2012> [Accessed 1 September 2016]

172. Reeves GM, Sims I, and Cripps J, 2006. Clay Materials Used in Construction. Geological Society Engineering Geology Special Publication No. 21

173. Roberts JJ, and Lin W, 1997. Electrical properties of partially saturated Topopah Spring Tuff: Water distribution as a function of saturation. Water Resources Research 33(4), pp. 577-587. doi: 10.1029/96WR03905

174. Samouelian A, Cousin I, Tabbagh A, Bruand A, and Richard G, 2005. Electrical resistivity survey in soil science: a review. Soil and Tillage Research, 83, pp. 173-193

175. Samyn K, Travelletti J, Bitri A, Grandjean G, and Malet JP, 2012. Characterization of a landslide geometry using 3D seismic refraction traveltime tomography: The La Valette landslide case history. Journal of Applied Geophysics, 86, pp. 120-132

176. Santos FAM and Afonso ARA, 2005. Detection and 2D modelling of cavities using pole-dipole array. Environmental Geology, 48, pp. 108-116

177. Sass O, 2006. Bedrock detection and talus thickness assessment in the European Alps using geophysical methods. Journal of Applied Geophysics, 62, pp. 254-269

178. Schmutz M, Albouy Y, Guerin R, Maquaire O, Vassal J, Schott JJ, and Descloitres M, 2000, Joint inversion applied to the Super Sauze earthflow (France): Surveys in Geophysics, 21, pp. 371-390

179. Schmutz M, Guerin R, Andrieux P, and Maquaire O, 2009. Determination of the 3D structure of an earthflow by geophysical methods – the Case of Super Sauze, in the French Southern Alps. Journal of Applied Geophysics, 68, pp. 500-507

180. Šimůnek J, Kodešová R, Gribb M, and Van Genuchten MT, 1999. Estimating hysteresis in the soil water retention function from cone permeameter experiments. Water Resources Research 35(5), pp. 1329-1345

181. Skempton AW, 1996. Embankments and Cuttings in the Early Railways. Construction History, 11

182. Slater LD, Binley A, and Brown D, 1997. Electrical imaging of fractures using ground-water salinity change. Ground Water, 35, pp. 436-442

183. Smethurst JA, Clarke D, and Powrie W, 2006. Seasonal changes in pore water pressure in a grass-covered cut slope in London Clay. Géotechnique, 56 (8), pp. 523-537

184. Smith GN, 2014. Elements of Soil Mechanics. BSP Professional Books, Oxford

185. Sorgi C, De Gennaro V, Nguyen HD, and Delalain P, 2008. Recent advances in ESEM analysis of partially saturated geomaterials. In: Unsaturated Soils: Advances in Geo-Engineering. Toll DG, Augarde CE, Gallipoli SJ (Eds.), Taylor and Francis Group, London, pp. 151-157. ISBN 978-0-415-47692-8

186. Statnice, 2016. [image online] Available at:http://statnice.dqd.cz/_media/mgr-szz:in-gra:orezpolygonureseni.png [Accessed 1 September 2016]

187. Stirling R and Hen-Jones R, 2015. *Investigating geotechnical/geophysical relationships in unsaturated glacial till, Short term scientific mission report*. EU COST Action TU1202

188. Stirling RA, Hughes PN, Davie CT, and Glendinning S, 2014. Cyclic relationship between saturation and tensile strength in the near-surface zone of infrastructure embankments. In: Unsaturated Soils: Research and Applications. Khalili N, Russell A, Khoshghalb A (Eds.), Taylor and Francis Group, London

189. Stewart RD, Abou Najim MR, Rupp DE, Lane JW, Uribe HC, Arumi JL and Selker J, 2015. Hillslope run-off thresholds with shrink-swell clay soils. Hydrological Processes, 29, pp. 557-571

190. Subba Rao KS and Satydas GG, 1987. Swelling potential with cycles of swelling and partial shrinkage. In: Proceedings of the 6th International Conference on Expansive Soils, 1, New Delhi, pp. 137-142

191. Sub Surface Surveys, 2016. [online] Available at <http://www.subsurfacesurveys.com/em.htm> [Accessed 1 September 2016]

192. Suryo EA, Gakkage C, Trigunarsyah B, and Soemitro R, 2012. Application of electrical resistivity method to detect deep crack in unsaturated residual soil slope. In: Proceedings of the 5th Asia-Pacific Conference on Unsaturated Soils, Pattaya, Thailand

193. Tang C, Cui YJ, Shi B, Tang A M, and Liu C, 2011. Desiccation and cracking of clay layer from slurry state under wetting-drying cycles. Geoderma, Elsevier, pp. 111-118

194. Tanji, 1990. US Salinity Laboratory – Handbook No. 60. [online] Available at: <http://www.ars.usda.gov/News/docs.htm?docid=10158> [Accessed 1 September 2016]

195. Tenma Test Equipment, 2012. Tenma Model 72-7750: Operating Manual. [online] Available online at http://www.farnell.com/datasheets/70028.pdf [Accessed 19 January 2017]

196. Terzaghi K, 1925. Erdbaumechanik auf Bodenphysikalischer Grundlage. Franz Deuticke, Liepzig-Vienna

197. Terzaghi K, Peck RB and Mesri G, 1996. Soil Mechanics in Engineering Practice, 3rd Edition, John Wiley and Sons, Inc. New York

198. Thurlby Thandar Instruments, 2007. TS series, Precision Power Supplies, Instruction Manual. TTI [online] Available online at <http://www.av.it.pt/medidas/data/Manuais%20&%20Tutoriais/07%20-%20TTi%20Power%20Supply%20TSP3222/TS%20Series%20Instruction%20Manual%20-%20Iss%208.pdf> [Accessed 19 January 2017]

199. Tomlinson MJ, 2001. *Foundation Design and Construction: 7th Edition.* Pearson: Harlow, UK

200. Trenter NA, 1999. *Engineering in Glacial Tills. Publication 504*. Construction Industry Research and Information Association: London

201. TRL, 2016. About Us. [online] Available at: <http://www.trl.co.uk/about-us/our-history> [Accessed 1 September 2016]

202. Toll DG, Lourenço SDN, Mendes J, Gallipoli D, Evans FD, Augarde CE, Cui YJ, Tang AM, Rojas JC, Pagano L, Mancuso C, Zingariello C, and Tarantino A, 201. Soil suction monitoring for landslides and slopes. Quarterly Journal of Engineering Geology and Hydrogeology 44(1), pp. 23-33

203. Trinh VN, Tang AM, Cui YJ, Dupla JC, Canou J, Calon N, Lambert L, Robinet A, and Schoen O, 2012. Mechanical characterisation of the fouled ballast in ancient railway track substructure by large-scale triaxial tests. Soils and Foundations, 52(3), pp. 511-523

204. Tuller M and Or D, 2005. Water films and scaling of soil characteristic curves at low water contents. Water Resources Research, 41: doi: 10.1029/2005WR004142. issn: 0043-1397

205. UKCP, 2009. *The climate of the UK and recent trends*. Met Office Hadley Centre, Exeter

206. Van Genuchten MT, 1980. A closed-form equation for predicting the hydraulic conductivity of unsaturated soils. Soil Science Society of America Journal, 44(5), pp. 892-898

207. Vaughan PR, Kovacevic N, and Potts DM, 2003. Then and now: some comments on the design and analysis of slopes and embankments. In: Proceedings of the Skempton Conference - Advances in Geotechnical Engineering. Institution of Civil Engineers, London

208. Velde B and Meunier A, 2008. The Origin of Clay Minerals in Soils and Weathered Rocks. Springer-Verlag, Berlin, Heidelberg, New York, pp. 406 pp. ISBN 9783 540 75633 0

209. Veder, 1981. Landslides and Their Stabilisation. Springer-Verlag, New York

210. Ward AD and Trimble SW, 2004. Environmental Hydrology. Lewis Publishers, Boca Raton

211. Waxman MH and Smits LJM, 1968. Electrical conductivities in oil-bearing shaly sands. Society of Petroleum Engineers Journal, 8, pp. 107-122

212. Wilkinson PB, Chambers JE, Kuras O, Meldrum PI, Gunn DA, 2011. Long-term time-lapse geoelectrical monitoring. *The First Break*, p. 77-84

213. William FA and Peter F, 2008. Behaviour of railroad ballast under monotonic and cyclic loading. Journal of Geotechnical and Geoenvironmental Engineering, 134(3), pp. 316-327

214. Wood DM, 1990. Soil Behaviour and Critical State Soil Mechanics. University Press, Cambridge

215. Williams J, Prebble RE, Williams WT, and Hignett CT, 1983. The influence of texture, structure and clay mineralogy on the soil moisture characteristic. Australian Journal of Soil Research, 21, pp. 15-32

216. Zaytsev A, Pickles JE, Harnor SJ, Henderson AP, Alyasari M, Waddell PG, Cano C, Griffin RJ, and Golding BT, 2016. Concise synthesis of bridged morpholines. RSC Advances, 59

217. Zonge International, Inc., 2013. Electrical Resistivity Methods. [online] Available at: <http://www.1800geophysics.com/detailed_discussions/dm3.html> [Accessed 4 March 2013]

218. Zulfadhli HA, Mohd HM, and Khairul MN, 2010. Electrical resistivity of a subsurface: field and laboratory assessment. International Journal of Environmental, Chemical, Ecological, Geological and Geophysical Engineering, 4(9)

Appendix A – List of publications

- Stirling RA, Hughes PN, **Hen-Jones RM**, Davie CT, Glendinning S. The behaviour and influence of desiccation cracking on a full-scale, vegetated infrastructure embankment. *In: 7th International Conference on Unsaturated Soils*. 2018, Hong Kong

- **Hen-Jones RM,** Hughes PN, Stirling RA, Glendinning S, Chambers JE, Gunn DA and Cui YJ, 2017. Seasonal effects on geophysical-geotechnical relationships and their implications for Electrical Resistivity Tomography monitoring of slopes. Acta Geotechnica, 12(5), pp. 1159-1173. DOI: 10.1007/s11440-017-0523-7

- Davie CT, Stirling RA, **Hen-Jones RM**, Eminue OO, Glendinning S. Multi-scale Studies of Desiccation Cracking in Engineered Clay Fills – Numerical, Laboratory and Field Approaches. *XIV International Conference on Computational Plasticity (COMPLAS)* 2017. Barcelona, Spain

- **Hen-Jones RM,** Hughes P, Chambers J, Gunn D, Glendinning S and Stirling RA, 2015. Development of a landslide monitoring system using electrical resistivity tomography. [Poster], American Geophysical Union Fall meeting, San Francisco, 14th - 18th December 2015

- Stirling RA and **Hen-Jones R**, 2015. Investigating geotechnical/geophysical relationships in unsaturated glacial till, Short term scientific mission report. EU COST Action TU1202

- Uhlemann S, Chambers J, Wilkinson P, Gunn D, Stirling R and **Hen-Jones RM**, 2015. Geoelectrical imaging of moisture dynamics in engineered slopes. GELMON 2015, 3rd International conference on geoelectric monitoring, 24th - 26th November 2015, Vienna, Austria

- **Hen-Jones RM,** Hughes PN, Glendinning S, Gunn DA, Chambers JC, Wilkinson PB, and Uhlemann S, 2014. Determination of moisture content and soil suction in engineered fills using electrical resistivity. In Unsaturated Soils: Research and Applications. CRC Press, pp. 1695-1699

- Gunn DA, Chambers JC, Uhlemann S, Wilkinson PB, Meldrum P, Dijkstra T, Haslam E, Kirkham M, Wragg J, Holyoake S, Hughes PN, **Hen-Jones RM** and Glendinning S, 2015. Moisture monitoring in clay embankments using electrical resistivity tomography. Constructions and Building Materials, 92, pp. 82-94

- Gunn DA, Chambers JC, Uhlemann S, Meldrum P, Dijkstra T, Wragg J, Hughes PN, **Hen-Jones RM.** and Glendinning S, 2013. Moisture monitoring in clay embankments using electrical resistivity tomography. Railway Engineering 2013, London, United Kingdom, 10th – 11th July 2013

Appendix B – Circuit diagram for function generator

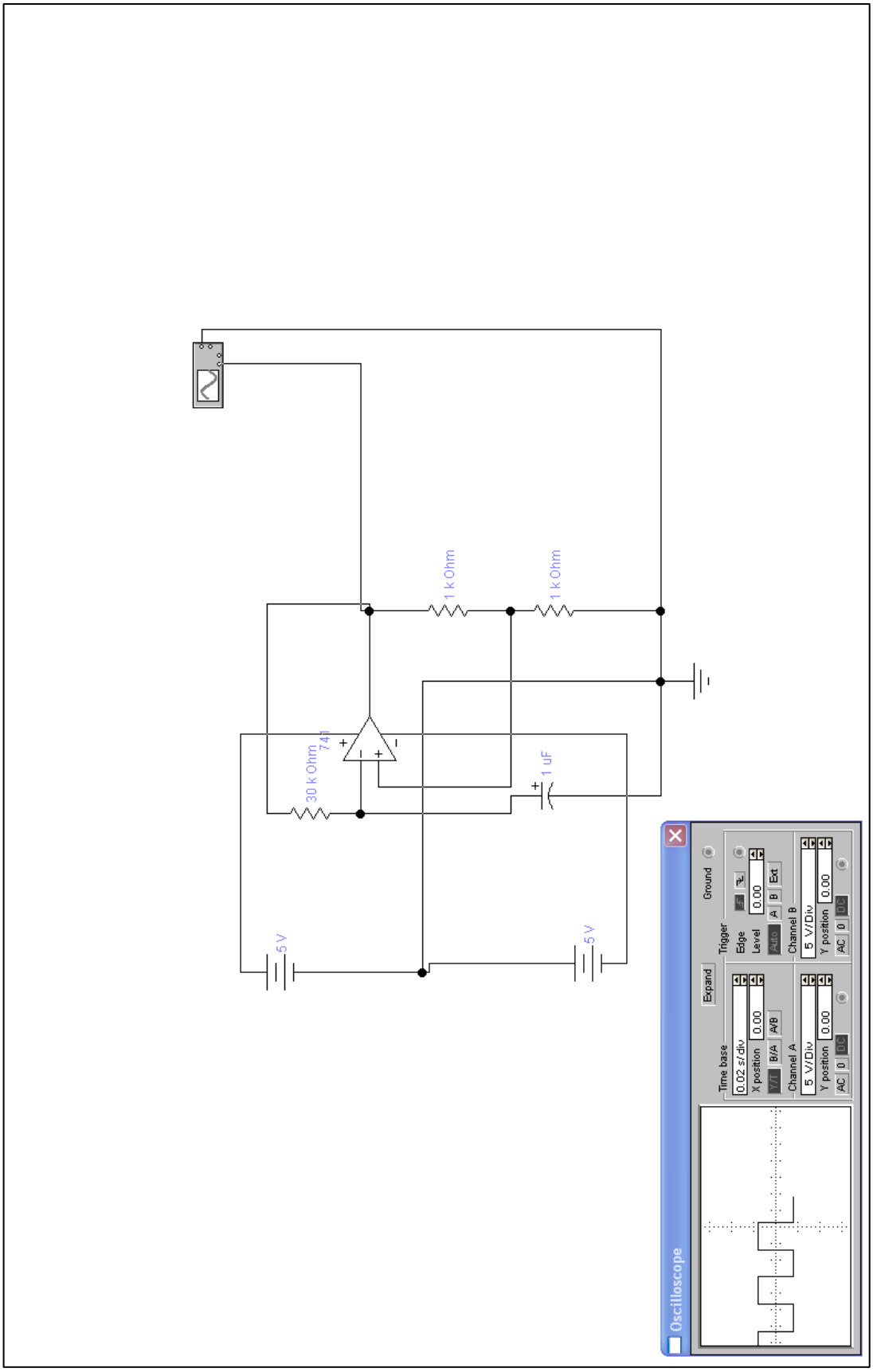

(Software: Electronic Workbench Personal Edition)

Appendix C – Resistivity error calculations

The equation for resistivity, ρ, is given by Eqn. 2.7:

$$\rho = RK$$

where K is geometric factor, and R is resistance. The resistivity error, ρ_{err}, can be expressed as follows, derived using the Harvard University Summary of Error Propagation (Harvard University, 2007).

$$\boldsymbol{\rho_{err}} = \frac{\delta\rho}{|\rho|} = \sqrt{\left(\frac{\delta R}{R}\right)^2 + \left(\frac{\delta K}{K}\right)^2} \approx \left(\frac{\delta R}{R}\right) + \left(\frac{\delta K}{K}\right) = \boldsymbol{R_{err}} + \boldsymbol{K_{err}}$$

From Ohm's law (Eqn. 2.5), the resistance is given by:

$$R = \frac{V}{I}$$

Following the same method of error propagation, the resistance error, R_{err}, is given by:

$$\underline{R_{err} \approx V_{err} + I_{err}}$$

where $V_{err} = \frac{\delta V}{|V|}$ describes the accuracy of the voltmeter.

In order to derive the error in measured current, I_{err}, using Ohm's law, it is necessary to consider both the accuracy of the voltmeter, and that of the resistor, $R_{err(res)}$:

$$I_{err} = V_{err} + R_{err(res)}$$

By summing the underlined components, the resistance error, R_{err}, is calculated.

***

The geometric factor, K, is given by Eqn. 2.6:

$$K = \frac{A}{L}$$

where A is the cross-sectional area, and L is the distance between potential electrodes. Following the same method of error propagation K_{err} yields:

$$\underline{K_{err} \approx L_{err} + A_{err}}$$

where $L_{err} = \frac{\delta L}{|L|}$, with δL, the resolution of the measurement of L, and $A_{err} = \frac{\delta A}{|A|}$.

Specific calculations for the individual resistivity experiments:

Experiment 2: Two point resistivity measurements made on cylindrical specimens of maximum dimensions: length, *L = 76 mm*, diameter, *D = 38 mm,* measured using Vernier callipers (*δL = 0.5 mm*, which is the maximum difference recorded between *L* measurements made at two locations on the specimen, 180° apart); voltage and current measurements made using the Thandar TS3022S digital multimeter, with $V_{err} = 0.2\ \%$ and resistor error, $R_{err(res)} = 10\ \%$ (Thurlby Thandar Instruments, 2007).

$$I_{err} = V_{err} + R_{err(res)} = 0.2\ \% + 10\ \%$$

$$\underline{R_{err} \approx\ V_{err} +\ I_{err} = 0.2\ \% + 10.2\ \% = 10.4\ \%}$$

***

$$L_{err} = \frac{\delta L}{|L|} = \frac{0.5}{|76|} = 0.658\ \%$$

$$A = \pi r^2 =\ \pi\left(\frac{D}{2}\right)^2$$

$$A_{err} = \frac{\delta A}{|A|} \approx r_{err} +\ r_{err} = D_{err} = \frac{\delta D}{|D|} =\ \frac{0.5}{38} = 1.316\ \%$$

$$\underline{K_{err} \approx\ L_{err} +\ A_{err}\ =\ 0.658\ \% +\ 1.316\ \% =\ 1.974\ \%}$$

$$\boldsymbol{\rho_{err(2pt\_cyl)} = R_{err} +\ K_{err} = 10.4\ \% + 1.974\ \% = 12.374\ \% \approx 12.5\ \%}$$

Experiment 3: Two point resistivity measurements made on specimens tested within the bespoke resistivity test chambers, of maximum dimensions: length, *L,* depth, d, *width, w = 25 mm,* measured using Vernier callipers (*δL = δd = δw = 0.5 mm*); voltage and current measurements as above, therefore, R_{err} is the same as above.

***

$$L_{err} = d_{err} = w_{err} = \frac{\delta L}{|L|} = \frac{0.5}{|75|} = 0.667\ \%$$

$$A = dw$$

$$A_{err} \approx d_{err} + w_{err} = 0.667\ \% + 0.667\ \% = 1.334\ \%$$

$$\underline{K_{err} \approx L_{err} + A_{err} = 0.667\ \% + 1.334\ \% = 2\ \%}$$

$$\boldsymbol{\rho_{err(2pt\_cham)} = R_{err} + K_{err} = 10.4\ \% + 2\ \% = 12.4\ \% \approx 12.5\ \%}$$

Four point resistivity measurements were also made within the bespoke resistivity test chambers, but the distance between potential electrodes differs: *L = 25 mm*; *d* and *w* are as above.

$$L_{err} = \frac{\delta L}{|L|} = \frac{0.5}{|25|} = 2\ \%$$

$$\underline{K_{err} \approx L_{err} + A_{err} = 2\ \% + 1.334\ \% = 2.334\ \%}$$

For calculation of R_{err}, additional error must be considered, owing from the use of the Picoscope 3206B (used to measure voltage across the soil specimen) (Pico Technology, 2014), and the Tenma 72-7750 digital multimeter (used to measure voltage and infer current) (Tenma Test Equipment, 2012).

$$V_{err} = V_{err(Thandar)} + V_{err(Pico)} = 0.2\ \% + 3\ \% = 3.2\ \%$$

$$I_{err} = V_{err(Tenma)} + R_{err(resistor)} = 0.5 + 10\ \% = 10.5\ \%$$

$$\underline{R_{err} \approx V_{err} + I_{err} = 3.2\ \% + 10.5\ \% = 13.7\ \%}$$

$$\boldsymbol{\rho_{err(4pt\_cham)} = R_{err} + K_{err} = 13.7\ \% + 2.334\ \% = 16.034\ \% \approx 16\ \%}$$

Experiment 5a: Four point resistivity measurements made on cylindrical specimens of maximum dimensions: length, *L = 76 mm*, diameter, *D = 38 mm,* measured using Vernier callipers (*δL = 0.5 mm*, which is the maximum difference recorded between *L* measurements made at two locations on the specimen, 180° apart); voltage and current measurements as above, therefore, R_{err} is the same as above. For this experiment, the use of point rather than plate electrodes meant that the electrical current could not be approximated as planar along the circular area of the specimen (as with the plate electrodes), but as spherical, therefore Eqn 4.6 could not be used to approximate the geometric factor, K. For this reason, the specimen geometry including the electrode positions were entered into Comsol modelling software (Figure 4.22), yielding a discrete geometric factor for the cylindrical specimens. Although there is an error associated with this geometric factor (K_{err}), because the geometry does not change over time (i.e. no shrinkage from drying as the specimens remain at constant water content), this is considered a systematic error, consistent across the entire temperature testing range. Given that this experiment aims to resolve the effect of changing temperature on resistivity, K_{err} does not affect the resolved relationship, and is not considered in the error calculation.

$$\boldsymbol{\rho_{err(4pt\_cyl)} = R_{err} = 10.4\ \%}$$

Appendix D – Inversion software: supplementary information

D.1 Iterative inversion procedure

The iterative procedure implemented within the Res2DInv and Res3DInv programs is based on the smoothness-constrained method (DeGroot and Constable, 1990). The following equation describes the iterative procedure mathematically:

$$(\boldsymbol{J^T J} + u\boldsymbol{F})\boldsymbol{d} = \boldsymbol{J^T g} - u\boldsymbol{F r} \qquad \text{Eqn. D.1}$$

where F is a smoothing matrix, such that $F = f_x f_x^T + f_z f_z^T$, where $f_{x,z}$ are the horizontal and vertical flatness filters, respectively. J is the Jacobian matrix of partial derivatives, r is a vector containing the logarithm of the model resistivity values, u is a damping factor, d is the model perturbation factor and g is the discrepancy vector (Loke, 2015a). Essentially, Eqn. D.1 describes an iterative procedure which uses a reference resistivity model as the basis for further refinement, attempting to reduce the RMS error between a measured and a calculated apparent resistivity pseudosection. This error is described by the discrepancy factor, g. In addition to attempting to minimise g, the equation attempts to limit the "roughness" of the model (i.e. the reciprocal of the smoothness). The damping factor, u, controls the weight given to smoothing the model during the inversion process, such that greater values of u result in a smoother model, however, a trade-off exists, whereby a smoother model results in greater data misfit (i.e. higher values of g). Therefore, Eqn. D.1 attempts to minimise a combination of these two factors, and solve for the model perturbation vector, d, which describes the change in model resistivity values, in order to produce a refined model which generally has lower data misfit.

D.2 Inversion parameters

Table D.1 provides supplementary information on the inversion parameters implemented within the Res2DInv and Res3DInv resistivity inversion software used in this study, as described in subchapter 4.3.5. The following is derived from Loke, 2015a.

Table D.1: Inversion software damping parameters

Parameter	**Value**	**Justification/Explanation**
Number of iterations used	7	Trial and error showed of a reference time-lapse set comprising six dates showed that after 5 iterations, there was negligible conversion in model resistivity. This number was increased by 2 in order to account for the possibility that some larger sets may take longer to converge.
Initial damping factor	0.25	Initial value of *u* as detailed in previous section. Loke, 2015a, suggest value between 0.1 and 0.3, depending on the data noise level (higher value of noisier data). Obtained by trial and error, such that this value yielded the lowest data misfit.
Minimum damping factor	0.1	Within the software, the damping factor is reduced after each iteration, but a minimum limit stabilises the inversion process. Obtained by trial and error such that values lower than this had no noticeable effect the true resistivity model.
Increase of damping factor with depth	1.1	Normally, value of 1.05 is used, however, because the resistivity cell width was set to half the electrode spacing (see subchapter 4.3.5), this value was doubled.
Convergence limit	5.0 (%)	Lower limit for the relative change in RMS error between two iterations. Value selected as relative change less than this was considered negligible.
Minimum change in RMS error	0.5 (%)	Inversion program ceases to perform iterations after the calculated error (between the reference model and the current iteration) is less than this value. Value selected as this was the lowest considered reasonable (although in practice values of less than 2 % were not achieved for any inversions produced in this study).
Vertical to horizontal flatness filter ratio	1.0	Unity selected in order to attribute equal importance to both horizontal and vertical anomalies.
Number of nodes between adjacent electrodes	2	Two nodes selected as four nodes resulted in prohibitively long computation time, where observed RMS errors of approximately 2 % were deemed acceptable.
Upper resistivity cut-off limit	50	Limit range of resistivity values within the model: here the limit is 50 times the average reference model resistivity of the previous iteration. Value selected after inspection of field point resistivity data showed a ratio of 50 (see Figure 5.29: minimum field resistivity = 10 Ωm, maximum = 500 Ωm).
Lower resistivity cut-off limit	0.02	See above; value selected as reciprocal.

D.3 Sample input file

The following is a sample .dat time-lapse input file, comprising five dates within the time-lapse sequence. This sample has been curtailed for the sake of brevity; a full input file has the same format but is considerably longer, including all data points (492 points for this example). Explanations as to the values shown have been added in bold font, where necessary.

```
2014-12-23.dat_TL name of input file
0.700 electrode separation (m)
11 array type (11 for dipole-dipole)
0 flag for IP data (0 for resistivity only)
Type of measurement (0=app. resistivity,1=resistance)
1
492 number of data points
Time sequence data
Number of time sections
5
Time unit
Days
2 Time Interval
2
3 Time Interval
2
4 Time Interval
2
5 Time Interval
2
Error estimate for data present
Type of error estimate (0=same unit as data)
0
Number of electrodes used for measurement, dipole separation, z
location C1, x-location C1, z-location P1, x-location P1, z-location
P2, x-location P2, measured resistance date 1, resistance error date
1, measured resistance date 2, resistance error date 2 etc.
4     1.4   113.272    0     113.027    9.8   116.245    11.2  116.922
      0.0212877  0.000122885      0.0210753  0.000029125
      0.0211875  1.28347E-05      0.0212084  4.48751E-05
      0.0213914  3.79601E-05
4     1.4   113.272    0     113.027    12.6  117.577    14    118.319
      0.00941668 0.000121381      0.00933311 0.000193586
      0.00939308 0.00021224 0.0093204  0.000211314      0.00948453
      0.000288907
4     1.4   113.272    0     113.027    15.4  118.473    16.8  118.48
      0.00656388 0.000036258      0.00645864 0.000179932
      0.00617447 0.000222808      0.00610075 0.000218798
      0.00627137 0.000293012
4     2.1   113.362    0.7   113.116    10.5  116.596    11.9  117.254
      0.0197301  7.23398E-05      0.0199669  5.75051E-05
      0.0202351  4.98949E-05      0.0202665  5.38501E-05
      0.0204164  6.56749E-05
```

```
4     2.1   113.362    0.7   113.116    13.3  117.981    14.7  118.529
      0.00688352 0.00005055 0.00662737 0.000100167      0.006722378
      1     0.006878901      1     0.00694127 6.22469E-05
4     2.1   113.362    0     113.027    10.5  116.596    12.6  117.577
      0.0333243  0.00000319 0.0333499  0.000022105      0.0336273
      5.26899E-05      0.0335749  0.000032365      0.0338431
      0.00002021
4     2.1   113.362    0     113.027    12.6  117.577    14.7  118.529
      0.0203848  0.00025653 0.0198897  0.000164395      0.0211474
      0.000569747      0.0210637  0.000638675      0.0200088
      7.31498E-05
4     2.1   113.362    0     113.027    14.7  118.529    16.8  118.48
      0.0180762  0.00028389 0.0182187  0.000396005      0.0170976
      3.94755E-06      0.0170465  3.42339E-05      0.017854
      2.81651E-05
4     2.1   113.362    0     113.027    16.8  118.48     18.9  118.499
      0.015094   0.00015066 0.0149366  6.24251E-05      0.0145027
      0.000198686      0.0144296  0.0001267  0.014817   0.000123305
4     2.8   113.455    1.4   113.272    9.8   116.245    11.2  116.922
      0.0344083  8.82002E-06      0.0348821  0.000021815      0.035254
      8.95501E-06      0.0355583  0.00002582 0.0356005  0.00003116
4     2.8   113.455    1.4   113.272    11.2  116.922    12.6  117.577
      0.0179752  0.000036545      0.0180964  0.000027905      0.018256
      8.09002E-06      0.0183851  0.000013415      0.0183947
      2.27899E-05
4     2.8   113.455    1.4   113.272    14    118.319    15.4  118.473
      0.0109413  0.000242706      0.0108038  0.000171825
      0.01077022 1     0.0105814  1.09921E-05      0.0112201
      0.000538281
4     2.8   113.455    1.4   113.272    15.4  118.473    16.8  118.48
      0.00908621 0.000019994      0.00913    0.00007977 0.00919503
      7.96756E-05      0.00925783 0.000054024      0.00914751
      0.000106807
4     2.8   113.455    1.4   113.272    16.8  118.48     18.2  118.503
      0.00847001 9.16896E-05      0.00853748 0.000133384
      0.00855909 0.000120454      0.00857175 0.000109233
      0.00863294 0.000135988
4     2.8   113.455    0.7   113.116    9.1   115.873    11.2  116.922
      0.0878044  0.00005635 0.0886532  0.00007554 0.0896531
      0.00006884 0.0902767  9.91852E-05      0.0906221  9.87998E-05
4     2.8   113.455    0.7   113.116    11.2  116.922    13.3  117.981
      0.0389997  5.05549E-05      0.0390965  5.05049E-05
      0.0394274  0.000013395      0.0395731  0.000013495
      0.0396644  3.65751E-05
4     2.8   113.455    0.7   113.116    13.3  117.981    15.4  118.473
      0.0209607  0.000342045      0.0206837  0.0002456  0.021123
      0.000473491      0.0211267  0.000419065      0.0211758
      0.000476559
4     2.8   113.455    0.7   113.116    15.4  118.473    17.5  118.483
      0.0192262  9.98753E-05      0.0191622  0.000245784
      0.0187819  0.000497179      0.0192453  2.30178E-06
      0.0189923  0.000517935
4     2.8   113.455    0.7   113.116    17.5  118.483    19.6  118.51
      0.0146658  8.63904E-05      0.014897   0.00011821 0.0147628
      0.000161044      0.0148706  0.000253255      0.0148508
      0.00013715
```

(File has been curtailed here)

Appendix E – Matlab code

All of the following Matlab code was originally written by Sebastian Uhlemann and Paul Wilkinson from the British Geological Survey, and then modified by Rosalind Hen-Jones. Both have given their permission for the following code to be included in this thesis. The code has been split into two parts, with part *a* corresponding to the pre-processing of raw resistance data prior to inversion, and part *b* corresponding to the processing of ERT data following inversion within resistivity inversion software.

Index of Matlab scripts:

E.1:

- readdir.m, which calls:
  i) Collate_tab_files.m
  ii) AlertQA.m
- createDAT.m, which calls:
  readBIONICS2D.m
- createTimeLapse2D.m

E.2:

- xyz2D_GMC.m, which calls:
  getDaysOfYear.m

For each set of code, a description is given in the commentary at the start of the code.

E.1 Pre-processing code (processing prior to inversion)

```
function [] = readdir(dirname)
%readdir reads the content of the chosen directory and converts tab files
%sent by ALERT to simplified xls spreadsheets. Additionally, returns plots
% of contact resistances and stats.
% -- call: readdir('Data/')
% -- data saved in the 'mergedData/' subfolder

listing = dir(dirname);
[status,message,messageid] = mkdir('Pics');
[status,message,messageid] = mkdir('mergedData');
cd Pics/
[status,message,messageid] = mkdir('CR');
[status,message,messageid] = mkdir('RecError');
[status,message,messageid] = mkdir('Ratio');
cd ..

clear status, clear message, clear messageid
% extract all .tab files

counter = 0;
for i = 1:length(listing)
    counter = counter + 1;
    if listing(i).isdir ~= 1
        if strcmp(listing(i).name(end-3:end), '.tab')
            filelist(counter,1).name = listing(i).name;
            filelist(counter,1).date = listing(i).date;
            filelist(counter,1).datenum = listing(i).datenum;
            dates(counter,:) = listing(i).name(8:17);
        end
    end
end

% find unique days
dates = datenum(dates, 'yyyy-mm-dd');
dates_uni = unique(dates);

% extract datasets of same date, run ALERT_QA on merged .tab files and save
% results in .tex file

texFile_stats = 'GeneralStats.txt';

fid  = fopen(texFile_stats, 'w');

% prepare texFile for General Stats
fprintf(fid, 'Date          0 - 0.5     0.5 - 1     1 - 2      2 - 5     5
- more   Reciprocal Pairs\n');

w = waitbar(0, '0%');

cmd_files = {'(5001)', '(5002)', '(5003)', '(5004)', '(5005)',
'(5006)', ...
    '(5007)', '(5008)', '(5015)', '(5009)', '(5010)', '(5011)', '(5096)'};

for i = 1:length(dates_uni)
    files = {};
   for j = 1:length(dates)
      if dates(j) == dates_uni(i)
          files{end+1} = [dirname filelist(j).name];
```

```
      end
      waitbar((((i-
1)*length(dates))+j)/((length(dates)*length(dates_uni))), w, ...
          sprintf('%3.2f %% done', (((i-
1)*length(dates))+j)*100/((length(dates)*length(dates_uni)))));
   end

   % rewrite .tab files into .xls files and calculate error stats

   xlsfile = ['mergedData/' datestr(dates_uni(i), 'yyyy-mm-dd') '.xls'];
   [Change, bin, banned, bad] = Collate_tab_files(files, xlsfile);
   fprintf(fid, '%s %10.3f %10.3f %10.3f %10.3f %10.3f %10.0f \n', ...
       datestr(dates_uni(i), 'yyyy-mm-dd'), bin(1), bin(2), bin(3), bin(4),
bin(5), length(Change.Change));
   for k = 1:length(Change.Change)
      if abs(Change.Change(k)) > 100
          Change.Change(k) = Inf;
      end
   end
   changes = Change.Change(~isinf(Change.Change));
   changes = sortrows(changes);

   % plot Reciprocal Error Distribution

   figure('visible', 'off')
   plot(linspace(0,100, length(changes)), changes, 'b.')
   hold on
   plot([0 100], [5 5], '-k');
   axis([0 100 0 10]);
   titlestr = ['Reciprocal Error Distribution --' datestr(dates_uni(i),
'yyyy-mm-dd')];
   title(titlestr, 'FontWeight', 'bold');
   ylabel('Data Fraction [%]');
   xlabel('Reciprocal Error [%]');
   grid on
   set(gca, ...
      'Box'         , 'off'     , ...
      'TickDir'     , 'out'     , ...
      'TickLength'  , [.02 .02] , ...
      'XMinorTick'  , 'on'      , ...
      'YMinorTick'  , 'on'      , ...
      'YGrid'       , 'on'      , ...
      'XColor'      , [.3 .3 .3], ...
      'YColor'      , [.3 .3 .3], ...
      'LineWidth'   , 1         );
  print('-dpng', '-r300', ['Pics/RecError/' datestr(dates_uni(i), 'yyyy-mm-
dd') '.png']);
  print('-depsc2', '-r300', ['Pics/RecError/' datestr(dates_uni(i), 'yyyy-
mm-dd') '.eps']);
  close

  % Plot logarithm of the contact resistances

  figure('visible', 'off')
  subplot(2,1,1)
  scatter(Change.C1, Change.C2, 10, log10(Change.CR), 'filled')
  colorbar
  titlestr = ['log10(Contact Resistances) --' datestr(dates_uni(i), 'yyyy-
mm-dd')];
  title(titlestr, 'FontWeight', 'bold');
  ylabel('C1');
  xlabel('C2');
```

```
  grid on
  set(gca, ...
      'Box'         , 'off'     , ...
      'TickDir'     , 'out'     , ...
      'TickLength'  , [.02 .02] , ...
      'XMinorTick'  , 'on'      , ...
      'YMinorTick'  , 'on'      , ...
      'YGrid'       , 'on'      , ...
      'XColor'      , [.3 .3 .3], ...
      'YColor'      , [.3 .3 .3], ...
      'LineWidth'   , 1         );
  subplot(2,1,2)
  hist(log10(abs(Change.CR(Change.CR>0))), 100)
  print('-dpng', '-r300', ['Pics/CR/' datestr(dates_uni(i), 'yyyy-mm-dd')
'.png']);
  print('-depsc2', '-r300', ['Pics/CR/' datestr(dates_uni(i), 'yyyy-mm-dd')
'.eps']);
  close


end

close(w);
fclose(fid);

end
%%%%%%%%%%%%%%%%%%%%%%%%%%%%%%%%%%%%%%%%%%%%%%%%%%%%%%%%%%%%%%%%%%%%%%%%%%%%%%%%

function [Change, bin, banned, bad] = Collate_tab_files(files, xlsfile)
%Collate_tab_files produced simplified xls spreadsheets from tab files sent
%by ALERT.
%--called by readdir.m.


for i=1:length(files)
    fid = fopen(files{1,i}, 'r');
    data = textscan(fid,
'%d %d %f %d %d %d %d %f %f %f %f %f %f %f %d %f %f %f %d %d %d %*f %*f %*f
%*f %*f %*f %*f %*f %*f %*f %*f %*f %*f %*f %*f %*f %*f %*f %*f %*f %*f %*f
%*f %*s %*s %*s', ...
    'Headerlines', 51, 'Delimiter', '\t');
    fclose(fid);

    if i == 1
        C1 = data{1,4};
        C2 = data{1,5};
        P1 = data{1,6};
        P2 = data{1,7};
        R  = data{1,3};
        CR = data{1,14};
        RA = data{1,17};
    else
        C1 = [C1; data{1,4}];
        C2 = [C2; data{1,5}];
        P1 = [P1; data{1,6}];
        P2 = [P2; data{1,7}];
        R  = [R ; data{1,3}];
        CR = [CR; data{1,14}];
        RA = [RA; data{1,17}];
    end
end
```

```
figure('visible', 'off')
RA_s = sort(RA);
plot(linspace(0,100,length(RA_s)), RA_s, '.');
axis([0 100 -4 5]);
titlestr = ['Voltage Ratio --' files{1,1}(14:23)];
title(titlestr, 'FontWeight', 'bold');
ylabel('Ratio]');
xlabel('Data Fraction [%]');
grid on
set(gca, ...
    'Box'         , 'off'     , ...
    'TickDir'     , 'out'     , ...
    'TickLength'  , [.02 .02] , ...
    'XMinorTick'  , 'on'      , ...
    'YMinorTick'  , 'on'      , ...
    'YGrid'       , 'on'      , ...
    'XColor'      , [.3 .3 .3], ...
    'YColor'      , [.3 .3 .3], ...
    'LineWidth'   , 1         );
print('-dpng', '-r300', ['Pics/Ratio/' files{1,1}(14:23) '.png']);
print('-depsc2', '-r300', ['Pics/Ratio/' files{1,1}(14:23) '.eps']);
close


xlswrite(xlsfile, C1(R~=0), 'Sheet1', 'A1');
xlswrite(xlsfile, C2(R~=0), 'Sheet1', 'B1');
xlswrite(xlsfile, P1(R~=0), 'Sheet1', 'C1');
xlswrite(xlsfile, P2(R~=0), 'Sheet1', 'D1');
xlswrite(xlsfile, R(R~=0) , 'Sheet1', 'E1');
xlswrite(xlsfile, CR(R~=0), 'Sheet1', 'F1');
xlswrite(xlsfile, RA(R~=0), 'Sheet1', 'G1');

fprintf('\n %d data points written into %s \n', length(C1), xlsfile);

[Change, bin, banned, bad] = AlertQA(xlsfile);

end
%%%%%%%%%%%%%%%%%%%%%%%%%%%%%%%%%%%%%%%%%%%%%%%%%%%%%%%%%%%%%%%%%%%%%%%%%%%%

function [MChange, bin, banned_list, bad_list] = AlertQA(filename)
%AlertQA locates banned electrodes and calculates reciprocal error
%distributions which are plotted by readdir.m
%--called by Collate_tab_files.m

%% read data file

data = xlsread(filename);
%% split into entries

C1 = data(:,1);
C2 = data(:,2);
P1 = data(:,3);
P2 = data(:,4);
R  = data(:,5);
CR = data(:,6);


%% find banned electrodes (R = 0), find electrodes with large
%  Contact Resistance (CR), calculate Reciprocal Error Distribution
countR     = 0;
```

```
countCR    = 0;
countRecip = 0;
bin = zeros(5,1);
bad_list = zeros(1,3);
banned_list = zeros(1,2);

for i = 1:length(C1)
   if R(i) == 0
       countR = countR + 1;
       banned_list(countR,:) = [C1(i) C2(i)];
   end
   if CR(i) > 2000
       countCR = countCR + 1;
       bad_list(countCR, :) = [C1(i) C2(i) CR(i)];
   end
   for k = 1:length(C1)
        if C1(i) == P1(k) && C2(i) == P2(k) && ...
                P1(i) == C1(k) && P2(i) == C2(k) && ...
                sign(C1(i) - C2(i)) == 1
            change = abs(R(k) - R(i))/(R(k)+mean([R(i),R(k)]))*100;
            countRecip = countRecip + 1;
            MChange.C1(countRecip,1)    = C1(i);
            MChange.C2(countRecip,1)    = C2(i);
            MChange.P1(countRecip,1)    = P1(i);
            MChange.P2(countRecip,1)    = P2(i);
            MChange.Base(countRecip,1)  = R(i);
            MChange.Value(countRecip,1) = R(k);
            MChange.Change(countRecip,1)= change;
            MChange.CR(countRecip,1)    = (CR(i) + CR(k))/2;
            if change >= 0 && change <= 0.5 || isnan(change)
                bin(1) = bin(1) + 1;
            elseif change > 0.5 && change <= 1
                bin(2) = bin(2) + 1;
            elseif change > 1 && change <= 2
                bin(3) = bin(3) + 1;
            elseif change > 2 && change <= 5
                bin(4) = bin(4) + 1;
            elseif change > 5
                bin(5) = bin(5) + 1;
            end
        end
    end
end

bin = 100*bin./length(MChange.Change);
bin = bin';

%%%%%%%%%%%%%%%%%%%%%%%%%%%%%%%%%%%%%%%%%%%%%%%%%%%%%%%%%%%%%%%%%%%%%%%%%%%
%%%%%%%%%%%%%%%%%%%%%%%%%%%%%%%%%%%%%%%%%%%%%%%%%%%%%%%%%%%%%%%%%%%%%%%%%%%
```

```
%createDAT.m creates .dat files for all .xls files in current folder
clc, clear all, close all

listing = dir();

counter = 0;
for i = 1:length(listing)
    if listing(i).isdir ~= 1
        if strcmp(listing(i).name(end-3:end), '.xls')
            counter = counter + 1;
            filelist(counter,1).name = listing(i).name;
            filelist(counter,1).date = listing(i).date;
        end
    end
end

for i = 1:length(filelist)
    readBIONICS2D(filelist(i).name, 'Geom.xlsx');
end

fid = fopen('filelist.txt', 'w');
for i = 1:length(filelist)
    fprintf(fid, '%s\n', filelist(i).name);
end
%%%%%%%%%%%%%%%%%%%%%%%%%%%%%%%%%%%%%%%%%%%%%%%%%%%%%%%%%%%%%%%%%%%%%%%%%%%

function [] = readBIONICS2D(filename, topo_file)
%READSTG reads in geom.xls file (file containing the geometry points of the
%Bionics embankment) and creates a Res2DInv input file
%--called by createDAT.m

data = xlsread(filename);
topo = xlsread(topo_file);

C1 = data(:,1);
C2 = data(:,2);
P1 = data(:,3);
P2 = data(:,4);
R  = data(:,5);
CR = data(:,6);
RA = data(:,7);

%% define filter values

f_rec_error = 5.0;      % 5% reciprocal error
f_low_ratio = 0.85;     % lower ratio filter
f_hig_ratio = 1.15;     % upper ratio filter
f_contact_R = 3000;     % contact resistance filter
f_resistanc = 100;      % low pass resistance filter


%% find reciprocal pairs

filterElectrodes = [33, -81, -88, -89];

counter = 0;
for i = 1:length(C1)
   for k = 1:length(P1)
       if C1(i) == P1(k) && C2(i) == P2(k) && ...
```

```
                P1(i) == C1(k) && P2(i) == C2(k) && sign(C1(i)-C2(i)) == 1
&& ...
                ~ismember(C1(i), filterElectrodes) && ~ismember(C2(i),
filterElectrodes) && ...
                ~ismember(P1(i), filterElectrodes) && ~ismember(P2(i),
filterElectrodes)
            counter = counter + 1;
            recip.C1(counter) = C1(i);
            recip.C2(counter) = C2(i);
            recip.P1(counter) = P1(i);
            recip.P2(counter) = P2(i);
            recip.R(counter)  = mean([R(i) R(k)]);
            recip.err(counter)= abs(R(k) - R(i))/abs(R(k)+recip.R(counter));
            recip.RA(counter) = mean([RA(i) RA(k)]);
            recip.CR(counter) = mean([CR(i) CR(k)]);
            break
        end
    end
end
 percent_err = recip.err.*100;

%% calculate error stats for each electrode location
ele = unique([C1;C2;P1;P2]);
Electrodes = [recip.C1; recip.C2; recip.P1; recip.P2]';
ele_1pc  = Electrodes(percent_err>1, :);
ele_2pc  = Electrodes(percent_err>2, :);
ele_5pc  = Electrodes(percent_err>5, :);
ele_10pc = Electrodes(percent_err>10, :);

for k=1:length(ele)
    count_fin(k,1) = sum(ele_1pc(:,1)== ele(k))+sum(ele_1pc(:,2)==
ele(k))+sum(ele_1pc(:,3)== ele(k))+sum(ele_1pc(:,4)== ele(k));
    count_fin(k,2) = sum(ele_2pc(:,1)== ele(k))+sum(ele_2pc(:,2)==
ele(k))+sum(ele_2pc(:,3)== ele(k))+sum(ele_2pc(:,4)== ele(k));
    count_fin(k,3) = sum(ele_5pc(:,1)== ele(k))+sum(ele_5pc(:,2)==
ele(k))+sum(ele_5pc(:,3)== ele(k))+sum(ele_5pc(:,4)== ele(k));
    count_fin(k,4) = sum(ele_10pc(:,1)== ele(k))+sum(ele_10pc(:,2)==
ele(k))+sum(ele_10pc(:,3)== ele(k))+sum(ele_10pc(:,4)== ele(k));
end

%% calculate Ratio stats for each electrode location

ele_ra01  = Electrodes(recip.RA>1.01, :);
ele_ra02  = Electrodes(recip.RA>1.02, :);
ele_ra05  = Electrodes(recip.RA>1.05, :);
ele_ra10  = Electrodes(recip.RA>1.10, :);

ele_ra99  = Electrodes(recip.RA<0.99, :);
ele_ra98  = Electrodes(recip.RA<0.98, :);
ele_ra95  = Electrodes(recip.RA<0.95, :);
ele_ra90  = Electrodes(recip.RA<0.90, :);

for k=1:length(ele)
    count_ra1(k,1) = sum(ele_ra01(:,1)== ele(k))+sum(ele_ra01(:,2)==
ele(k))+sum(ele_ra01(:,3)== ele(k))+sum(ele_ra01(:,4)== ele(k));
    count_ra1(k,2) = sum(ele_ra02(:,1)== ele(k))+sum(ele_ra02(:,2)==
ele(k))+sum(ele_ra02(:,3)== ele(k))+sum(ele_ra02(:,4)== ele(k));
    count_ra1(k,3) = sum(ele_ra05(:,1)== ele(k))+sum(ele_ra05(:,2)==
ele(k))+sum(ele_ra05(:,3)== ele(k))+sum(ele_ra05(:,4)== ele(k));
    count_ra1(k,4) = sum(ele_ra10(:,1)== ele(k))+sum(ele_ra10(:,2)==
ele(k))+sum(ele_ra10(:,3)== ele(k))+sum(ele_ra10(:,4)== ele(k));
```

```
    count_ra2(k,1) = sum(ele_ra99(:,1)== ele(k))+sum(ele_ra99(:,2)==
ele(k))+sum(ele_ra99(:,3)== ele(k))+sum(ele_ra99(:,4)== ele(k));
    count_ra2(k,2) = sum(ele_ra98(:,1)== ele(k))+sum(ele_ra98(:,2)==
ele(k))+sum(ele_ra98(:,3)== ele(k))+sum(ele_ra98(:,4)== ele(k));
    count_ra2(k,3) = sum(ele_ra95(:,1)== ele(k))+sum(ele_ra95(:,2)==
ele(k))+sum(ele_ra95(:,3)== ele(k))+sum(ele_ra95(:,4)== ele(k));
    count_ra2(k,4) = sum(ele_ra90(:,1)== ele(k))+sum(ele_ra90(:,2)==
ele(k))+sum(ele_ra90(:,3)== ele(k))+sum(ele_ra90(:,4)== ele(k));
end

h=figure('visible', 'off');
screen_size = get(0, 'ScreenSize');
set(findall(h,'type','text'),'fontSize',8)
set(h, 'Position', [0 0 screen_size(3)
screen_size(4) ],'PaperOrientation','portrait' );
set(h, 'Color', 'w');
set(gca, 'FontSize', 8)
subplot(3,2,1)
plot((0:100/(length(percent_err)-1):100), sortrows(percent_err'), 'bx', ...
    'MarkerSize', 2);
xlabel('Data Fraction', 'FontSize', 8);
ylabel('Reciprocal Error', 'FontSize', 8);
axis([0 100 0 10])
set(gca, 'FontSize', 8);
subplot(3,2,2)
plot(recip.C1, recip.CR, 'xr', 'MarkerSize', 2)
xlabel('C1', 'FontSize', 8);
ylabel('Contact Resistance', 'FontSize', 8);
set(gca, 'FontSize', 8)
subplot(3,2,[3,4])
bar(ele, count_fin(:,1),'FaceColor', [0 0 1]);
hold on
bar(ele, count_fin(:,2),'FaceColor', [0 0.8 0.2]);
hold on
bar(ele, count_fin(:,3),'FaceColor', [1 1 0]);
hold on
bar(ele, count_fin(:,4),'FaceColor', [1 0 0]);
xlabel('Electrode position', 'FontSize', 8)
set(gca, 'XTick', min(ele):10:max(ele), 'FontSize', 8)
ylabel('Counts', 'FontSize', 8)
hl1 = legend('>1pc','>2pc','>5pc','>10pc');
set(hl1, 'FontSize', 8);
text(0, max(max(count_fin))-5, 'Reciprocal Error Levels')

subplot(3,2,[5,6])
bar(ele, count_ra1(:,1)+count_ra2(:,1),'FaceColor', [0 0 1]);
hold on
bar(ele, count_ra1(:,2)+count_ra2(:,2),'FaceColor', [0 0.8 0.2]);
hold on
bar(ele, count_ra1(:,3)+count_ra2(:,3),'FaceColor', [1 1 0]);
hold on
bar(ele, count_ra1(:,4)+count_ra2(:,4),'FaceColor', [1 0 0]);
xlabel('Electrode position', 'FontSize', 8)
set(gca, 'XTick', min(ele):10:max(ele), 'FontSize', 8)
ylabel('Counts', 'FontSize', 8)
hl2 = legend('>0.01','>0.02','>0.05','>0.1');
set(hl2, 'FontSize', 8);
text(0, max(max(count_ra1+count_ra2))-5, 'Deviation from Ratio=1')

ax=axes('Units','Normal','Position',[.075 .075 .85 .85],'Visible','off');
set(get(ax,'Title'),'Visible','on')
title(filename(1:end-4), 'FontSize', 12);
```

```
print('-dpng', '-r900', [filename(1:end-3) 'png'])

%% assign electrode positions
[Lia, Lib] = ismember(recip.C1, topo(:,1));
recip.C1   = topo(Lib, 3);
recip.C1z  = topo(Lib, 4);

[Lia, Lib] = ismember(recip.C2, topo(:,1));
recip.C2   = topo(Lib, 3);
recip.C2z  = topo(Lib, 4);

[Lia, Lib] = ismember(recip.P1, topo(:,1));
recip.P1   = topo(Lib, 3);
recip.P1z  = topo(Lib, 4);

[Lia, Lib] = ismember(recip.P2, topo(:,1));
recip.P2   = topo(Lib, 3);
recip.P2z  = topo(Lib, 4);

counter = 0;

for i = 1:length(recip.C1)
    if percent_err(i) < f_rec_error && ...
            (recip.RA(i) > f_low_ratio && recip.RA(i) < f_hig_ratio) && ...
            recip.CR(i) < f_contact_R && abs(recip.R(i)) < f_resistanc
        counter = counter +1;
    end
end

TopoElec = unique([recip.C1 recip.C1z; recip.C2 recip.C2z; ...
    recip.P1 recip.P1z; recip.P2 recip.P2z], 'rows');

%% Save in ResInv Format
fid = fopen([filename(1:end-4) '.dat'], 'w');
fprintf(fid, '%s\n', filename(1:end-4));
fprintf(fid, '%3.3f\n', 0.7);
fprintf(fid, '11\n0\nType of measurement (0=app.
resistivity,1=resistance)\n');
fprintf(fid, '1\n%d\n2\n0\n', counter);
fprintf(fid, 'Error estimate for data present\n');
fprintf(fid, 'Type of error estimate (0=same unit as data)\n0\n');
for i =1:length(recip.R)
    if percent_err(i) < f_rec_error && ...
            (recip.RA(i) > f_low_ratio && recip.RA(i) < f_hig_ratio) && ...
            recip.CR(i) < f_contact_R && abs(recip.R(i)) < f_resistanc
        fprintf(fid,
'4\t%3.3f\t0\t%3.3f\t0\t%3.3f\t0\t%3.3f\t0\t%5.6f\t%2.6f\n', ...
            recip.C1(i), recip.C2(i), recip.P1(i), recip.P2(i), ...
            recip.R(i), recip.err(i)*recip.R(i));
    end
end
fprintf(fid, 'Topography in separate list\n2\n');
fprintf(fid, '%d\n', length(TopoElec));
for i = 1:length(TopoElec)
    fprintf(fid, '%f %f\n', TopoElec(i,1), TopoElec(i,2));
end
fprintf(fid, '1\n');
fprintf(fid, '0\n0\n0\n0\n0\n');
fclose(fid);
%%%%%%%%%%%%%%%%%%%%%%%%%%%%%%%%%%%%%%%%%%%%%%%%%%%%%%%%%%%%%%%%%%%%%%%%%%%%%%%
%%%%%%%%%%%%%%%%%%%%%%%%%%%%%%%%%%%%%%%%%%%%%%%%%%%%%%%%%%%%%%%%%%%%%%%%%%%%%%%
```

```
%%createTimeLapse2D.m reads in individual .dat files and merges them into
%%one timelapse.dat file for input into Res2Dinv

clear all

listing = dir();

counter = 0;
for i = 1:length(listing)
    if listing(i).isdir ~= 1
        if strcmp(listing(i).name(end-3:end), '.dat') &&
~strcmp(listing(i).name(1:end-4), 'timelapse')
            counter = counter + 1;
            filelist(counter,1).name = listing(i).name;
            filelist(counter,1).date = listing(i).date;
        end
    end
end

%% load data

for i = 1:length(filelist)
    fid = fopen(filelist(i).name);
    dump = textscan(fid, '%*d %f %f %f %f %f %f %f %f %f %f', ...
    'Headerlines', 12, 'Delimiter', '\t');
    data(i).R   = dump{1,9};
    data(i).C1  = dump{1,1};
    data(i).C1y = dump{1,2};
    data(i).C2  = dump{1,3};
    data(i).C2y = dump{1,4};
    data(i).P1  = dump{1,5};
    data(i).P1y = dump{1,6};
    data(i).P2  = dump{1,7};
    data(i).P2y = dump{1,8};
    data(i).err = dump{1,10};
    clear dump
    fclose(fid);
end

clear dump

%% data in data(1) is assumed to be the reference/baseline dataset

R_gather = zeros(length(data(1).R), length(filelist));
e_gather = ones(length(data(1).R), length(filelist));
R_gather(:,1) = data(1).R;
e_gather(:,1) = data(1).err;

for i=2:length(filelist)
   [Lia, Locb] = ismember([data(1).C1, data(1).C1y, data(1).C2,
data(1).C2y, ...
       data(1).P1, data(1).P1y, data(1).P2, data(1).P2y],...
        [data(i).C1, data(i).C1y, data(i).C2, data(i).C2y, ...
       data(i).P1, data(i).P1y, data(i).P2, data(i).P2y], 'rows');
    for k = 1:length(Locb)
        if Locb(k) ~= 0
            if sign(R_gather(k,1)) ~= sign(data(i).R(Locb(k)))
                R_gather(k,i) = (-1)*data(i).R(Locb(k));
                e_gather(k,i) = data(i).err(Locb(k));
            else
                R_gather(k,i) = data(i).R(Locb(k));
```

```
                e_gather(k,i) = data(i).err(Locb(k));
            end
        end
    end
     clear Lia, clear Locb
end


%% interpolate missing data points
h = waitbar(0,'Please wait...');

Gather_Interp = [];
for i = 1:size(R_gather,1)-5
    for j = 1:size(R_gather,2)
        if R_gather(i,j) == 0 || abs(R_gather(i,j)) > 10
            R_gather(i,j) = NaN;
        end
    end

    XQ = (1:size(R_gather, 2));
    Y  = R_gather(i, ~isnan(R_gather(i,:)));
    X  = XQ(~isnan(R_gather(i,:)));

    %% interpolation: Nearest Neighbour
    try
        R_gather_NN(i,:) = interp1(X,Y,XQ, 'nearest', 'extrap');
    catch exception
    end

    %% interpolation: inverse distance

    ND = length(X);
    NI = length(XQ(isnan(R_gather(i,:))));

    if ND >= NI
        XI = XQ(isnan(R_gather(i,:)));
        YI = shepard_interp_1d(ND, X', Y', 2, NI, XI');
        all_data = [X', Y'; XI', YI];
        all_data = sortrows(all_data, 1);
        R_gather_ID(i,:) = (all_data(:,2))';
        Gather_Interp = [XI, Gather_Interp];
    end

end

for i = 1:size(R_gather,1)-5
    for j = 1:length(R_gather_NN(i,:))
        if R_gather_NN(i,j) == 0
            R_gather_NN(i,j) = NaN;
        end
    end
end
for i = 1:size(R_gather,1)-5
    for j = 1:length(R_gather_ID(i,:))
        if R_gather_ID(i,j) == 0
            R_gather_ID(i,j) = NaN;
        end
    end
end

close(h)
```

```
figure(1)
hist(Gather_Interp, size(R_gather, 2)-1);

RR_NN  = R_gather_NN(~any(isnan(R_gather_NN),2),:);
C1_NN  = data(1).C1(~any(isnan(R_gather_NN),2),:);
C1y_NN = data(1).C1y(~any(isnan(R_gather_NN),2),:);
C2_NN  = data(1).C2(~any(isnan(R_gather_NN),2),:);
C2y_NN = data(1).C2y(~any(isnan(R_gather_NN),2),:);
P1_NN  = data(1).P1(~any(isnan(R_gather_NN),2),:);
P1y_NN = data(1).P1y(~any(isnan(R_gather_NN),2),:);
P2_NN  = data(1).P2(~any(isnan(R_gather_NN),2),:);
P2y_NN = data(1).P2y(~any(isnan(R_gather_NN),2),:);
e_NN   = e_gather(~any(isnan(R_gather_NN),2),:);
figure(2)
imagesc(log10(abs(RR_NN))); colorbar


RR_ID  = R_gather_ID(~any(isnan(R_gather_ID),2),:);
C1_ID  = data(1).C1(~any(isnan(R_gather_ID),2),:);
C1y_ID = data(1).C1y(~any(isnan(R_gather_ID),2),:);
C2_ID  = data(1).C2(~any(isnan(R_gather_ID),2),:);
C2y_ID = data(1).C2y(~any(isnan(R_gather_ID),2),:);
P1_ID  = data(1).P1(~any(isnan(R_gather_ID),2),:);
P1y_ID = data(1).P1y(~any(isnan(R_gather_ID),2),:);
P2_ID  = data(1).P2(~any(isnan(R_gather_ID),2),:);
P2y_ID = data(1).P2y(~any(isnan(R_gather_ID),2),:);
e_ID   = e_gather(~any(isnan(R_gather_ID),2),:);
figure(3)
imagesc(log10(abs(RR_ID))); colorbar

A = [RR_ID(:,1) e_ID(:,1)];
for i = 2:size(R_gather, 2)
   A = [A RR_ID(:,i) e_ID(:,i)];
end

%% save data in Res2DInv format
file_out = 'timelapse.dat';
fid = fopen(file_out, 'w');
fprintf(fid, '%s\n', [filelist(1).name '_TL']);
fprintf(fid, '%3.3f\n', min(data(1).C2)-min(data(1).C1));
fprintf(fid, '11\n0\nType of measurement (0=app.
resistivity,1=resistance)\n');
fprintf(fid, '1\n%d\n2\n0\n', length(RR_ID));
fprintf(fid, 'Time sequence data\n');
fprintf(fid, 'Number of time sections\n%d\n', size(R_gather, 2));
fprintf(fid, 'Time unit\nDays\n');
for i = 1:size(R_gather, 2)-1
   fprintf(fid, '%d Time Interval\n', i+1);
   fprintf(fid, '%d\n', datenum(filelist(i+1).name(1:10))-
datenum(filelist(i).name(1:10)));
end
fprintf(fid, 'Error estimate for data present\n');
fprintf(fid, 'Type of error estimate (0=same unit as data)\n0\n');
fclose(fid);

output_Mat = [ones(length(RR_ID), 1)*4, C1_ID, C1y_ID, ...
    C2_ID, C2y_ID, P1_ID, P1y_ID, ...
    P2_ID, P2y_ID, A];
xlswrite('timelapse.xls', output_Mat);
```

E.2 Post-processing code – following inversion

```
function [] = xyz2D_GMC()
%2DXYZ2PV_TL takes a Res2DInv timelapse inversion result (.xyz file,
%employing an extended grid) and produces nt number of .vtk-output files.
%1. Exports Res2DInv timelapse inversion result (.xyz file) and corrects
%for temperature.
%2. Translates into GMC and Suction.
%3. Extracts data corresponding to the locations of the point sensors
%(these %positions are read in in 'xz.xlsx')
%4. Outputs vtk files which can then be read into ParaView.
%function reads in 'porosityModel_UnCompactedPanel.csv', = porosity cells,
%and 'porosity_U.dat' containing the assigned porosity values.
%Directory must contain original .dat files in order to run successfully

[filename,PathName] = uigetfile('*.xyz', 'Select Inversion Output File');
dump = inputdlg('Number of timesteps:', 'Input');
folder_name = uigetdir(pwd,'Select Folder containing timelapse files');
porMod_file = 'porosityModel_UnCompactedPanel.csv';
porVal_file = 'porosity_U.dat';

nt = str2double(dump{1,1});
clear dump;
%% read data
f = fullfile(PathName, filename);
fid = fopen(f, 'r');
number = textscan(fid, '%*s %*s %*s %*s %d', 1, 'HeaderLines', 1);
dump = fgetl(fid);
while isempty(strfind(dump, '/Block')) && feof(fid) ~= 1
    dump = fgetl(fid);
end
ff = '%*d %*f %f %*f %f %*f %*f %*f %*f';
for i = 1:nt
   ff = [ff ' %f'];
end
data = textscan(fid, ff, number{1,1}, 'HeaderLines', 1, ...
    'delimiter', 't');
block_depths = data{1,1} + ((data{1,2}-data{1,1})/2);

for i = 3:length(data)
    data2{1,i-2} = data{1,i};
end
clear data

data = data2;
clear data2

dump = fgetl(fid);
while isempty(strfind(dump, '/Coordinates of model blocks (with
topography).')) && feof(fid) ~= 1
    dump = fgetl(fid);
end
corners = textscan(fid, '%*d %f %f %f %f %f %f %f %f %f', number{1,1}, ...
    'HeaderLines', 4, 'delimiter', '\t');

%%%% read in xz points of Decagon point sensors in Bionics, and locate
%%%% corresponding cells (there should be nine (5005) or eleven (5015))
Pt_sensor_locs = xlsread('xz.xlsx');
merged_corners = [corners{1,1} corners{1,2} corners{1,3} corners{1,4}
corners{1,5} corners{1,6} corners{1,7} corners{1,8}];
```

```
for k = 1:length(Pt_sensor_locs)
[cell_ID, Found] = find (merged_corners(:,1) <= Pt_sensor_locs(k)...
    & merged_corners(:,5)>= Pt_sensor_locs(k)...
    & merged_corners(:,2)>= Pt_sensor_locs(k,2)...
    & merged_corners(:,4)<= Pt_sensor_locs(k,2));
Pt_sensor_cell_ID(k) = cell_ID(1);
end
%%%%

dump = fgetl(fid);
while isempty(strfind(dump, '/the model blocks after incorporating the
surface topography.')) && feof(fid) ~= 1
    dump = fgetl(fid);
end
centres = textscan(fid, '%f %f %*f %*f', number{1,1}, ...
    'HeaderLines', 4, 'delimiter', '\t');

fclose(fid);
clear dump
%% find unique points

nx = [centres{1,1} centres{1,2}];
nx = unique(nx(:,1), 'rows');
nx = length(nx);

PP = [corners{1,1} corners{1,2}; corners{1,3} corners{1,4}; ...
    corners{1,5} corners{1,6}; corners{1,7} corners{1,8}];

PP = unique(PP, 'rows');

[IDC1 IDP1] = ismember([corners{1,1} corners{1,2}], PP, 'rows');
[IDC2 IDP2] = ismember([corners{1,3} corners{1,4}], PP, 'rows');
[IDC3 IDP3] = ismember([corners{1,5} corners{1,6}], PP, 'rows');
[IDC4 IDP4] = ismember([corners{1,7} corners{1,8}], PP, 'rows');

%% calculate Resistivity ratios

for i = 1:nt
    if i == 1
        ratio(i).res    = ones(length(data{1,1}),1);
        ratio(i).logres = ones(length(data{1,1}),1);
    else
        ratio(i).res    = data{1,i}./data{1,1};
        ratio(i).logres = log10(data{1,i})./log10(data{1,1});
    end
end

h = waitbar(0, 'Writing output files');

%% load fractions
if ~exist('fractions.mat','file')
    frac = createPorCells(f, porMod_file);
    save('fractions', 'frac');
else
    load('fractions.mat')
end

fid = fopen(porVal_file, 'r');
dump = textscan(fid, '%f %f', 'Delimiter', '\t');
por(:,1) = dump{1,1};
por(:,2) = dump{1,2};
```

```
fclose(fid);

%% correct resistivity values
c = -2.0;
Tmean = 9.35059;
Tcor = 20;
dT = 12.8467;
d = 2.78354;
phiT = -1.88466;

por_C = frac*por(:,2);
[t, files, dates] = getDaysOfYear(folder_name);
A_por = csvread(porMod_file);
A_por_size = length(A_por) - 1;
surface   = [corners{1,1}(1:A_por_size) corners{1,2}(1:A_por_size)];

depth = centres{1,2} - interp1(surface(:,1), surface(:,2), centres{1,1},
'pchip');
block_depths = floor(block_depths*1000)/1000;

%% load Waxman-Smiths parameters

m  = [1.5 3.48];
n  = [2.0 1.83];
a  = [1.5 0.82];
Rw = 15;
omega_w = 1/Rw;
Pw = 1.0;
Pg = [2.4, 2.65];%phi= por_C;
cWS  = [0.1, 15.2];
Bws= [0.1, 1.97797];
options = optimset('Display', 'off', 'FunValCheck', 'off');

%%
for i = 1:length(t)
    %% correct for seasonal temperature effects (field air temp)
    R_tcor_field1 = data{1,1}.*(1+(c/100).*(Tmean - (Tmean + (dT./2).*exp(-
abs(depth)./d).*...
    sin((2.*pi.*t(1)/365) + phiT - (abs(depth)./d)))));

    R_tcor_field = data{1,i}.*(1+(c/100).*(Tmean - (Tmean + (dT./2).*exp(-
abs(depth)./d).*...
    sin((2.*pi.*t(i)/365) + phiT - (abs(depth)./d)))));
%%%% calculate standard deviation for resy cells, over time
for k = 1: length(R_tcor_field1)
     R_tcor_field_tl(k,i) = R_tcor_field(k);
     st_dev(k) = std(R_tcor_field_tl(k,:));
end
%%%%
%% correct for seasonal temperature effects (lab temp for GMC)
    R_tcor1 = data{1,1}.*(1+(c/100).*(Tcor - (Tmean + (dT./2).*exp(-
abs(depth)./d).*...
    sin((2.*pi.*t(1)/365) + phiT - (abs(depth)./d)))));

    R_tcor = data{1,i}.*(1+(c/100).*(Tcor - (Tmean + (dT./2).*exp(-
abs(depth)./d).*...
    sin((2.*pi.*t(i)/365) + phiT - (abs(depth)./d)))));

%% calculate GMC
    h2 = waitbar(0,'Please wait -- Calculating GMC');
    for j = 1:length(R_tcor)
```

```
        message = sprintf('File %d of %d. %3.3f %% done.', i, length(t),
100*(j)/(length(R_tcor)));
        waitbar(j/(length(R_tcor)), h2, message);
        GMC_tl(j,i) = 0.0;
        %%%%
        VMC_tl(j,i) = 0.0;
        %%%%
        R_tcor_field_tl(j,i) = R_tcor_field(j);
        %%%%
        if por_C(j) > 0 && por_C(j) < 1
            porf = sum(por(:,2)'.*frac(1,:));
            mf = sum(m(por(:,1)).*frac(1,:));
            nf = sum(n(por(:,1)).*frac(1,:));
            af = sum(a(por(:,1)).*frac(1,:));
            Pgf= sum(Pg(por(:,1)).*frac(1,:));
            cf = sum(cWS(por(:,1)).*frac(1,:));
            Bwsf = sum(Bws(por(:,1)).*frac(1,:));
    %             GMC_func = @(g)
log10((((a(por(k,1))/phi(j)^m(por(k,1))))*(((1-
phi(j))*Pg(por(k,1))*g)/((phi(j)*Pw)))^((-1)*n(por(k,1))))*...
    %                 (omega_w +
(Bws(por(k,1))*((cWS(por(k,1))*Pw)/(100*g))))^(-1)) - R_tcor(j);
            GMC_func = @(g) (((af/(porf^mf))) * ...
                ((((1-porf)*Pgf*g)/(porf*Pw))^(-nf)) * ...
                (omega_w+Bwsf*(((1-porf)*Pgf*cf)/(100*porf))*...
                ((porf*Pw)/((1-porf)*Pgf*g)))^(-1))-R_tcor(j);

            exitflag = 0;
            x0 = 0.001;
            while exitflag ~= 1 && x0 <=0.5
               [GMC_it, fval, exitflag, output] = fzero(GMC_func, x0,
options);
               x0 = x0+0.005;
            end
            if GMC_it < 1.0
                GMC_tl(j,i) = GMC_it;

            else
                GMC_tl(j,i) = 0.0001;

            end
        else
            GMC_tl(j,i) = 0.0001;

        end
    %%%% Convert GMC to VMC and Sr
    Gs = 2.64;
    e(j) = (por_C(j)./(1-por_C(j)));
    VMC_tl(j,i) = (1-por_C(j)).*Gs*GMC_tl(j,i);
    Sr_tl(j,i) = (Gs*GMC_tl(j,i))./e(j);

    %%%% convert VMC to Suction (basic, no accouting for drying/wetting,
and using overlapping VG params)

    %VG parameters
    alpha_D = 0.0097;
    alpha_W = 0.1001;
    n_D = 1.5448;
    n_W = 1.2900;
    m_D = 1-(1/n_D);
    m_W = 1-(1/n_W);
    Theta_s_D = 0.3600;
```

```
    Theta_s_W = 0.3750;
    Theta_r_D = 0.0250;
    Theta_r_W = 0.0010;

    g = 9.81; %gravity (for conversion from suction units m to kPa)
    % drying
    Psi_D_tl(j,i) =(g)*(1/alpha_D)*(((((Theta_s_D -
Theta_r_D)/(VMC_tl(j,i)-Theta_r_D))^(1/m_D))-1)^(1/n_D));
    % wetting
    Psi_W_tl(j,i) =(g)*(1/alpha_W)*(((((Theta_s_W -
Theta_r_W)/(VMC_tl(j,i)-Theta_r_W))^(1/m_W))-1)^(1/n_W));
    %%%%
    end

    close(h2)

    if i == 1
        ratio(i).TCres    = ones(length(data{1,1}),1);
        ratio(i).TClogres = ones(length(data{1,1}),1);
        ratio(i).TCrespd  = ones(length(data{1,1}),1);
        ratio(i).GMC       = ones(length(data{1,1}),1);
        ratio(i).GMCrespd  = ones(length(data{1,1}),1);
        %%%%
         Psi_tl = Psi_D_tl;
        %%%%
    else
        ratio(i).TCres    = R_tcor_field./R_tcor_field1;
        ratio(i).TClogres = log10(R_tcor_field1)./log10(R_tcor_field1);
        R_tcor_field1 = data{1,i-1}.*(1+(c/100).*(Tmean - (Tmean +
(dT./2).*exp(-abs(depth)./d).*...
    sin((2.*pi.*t(i-1)/365) + phiT - (abs(depth)./d)))));
        ratio(i).TCrespd  = R_tcor_field./R_tcor_field1;
        ratio(i).GMC       = GMC_tl(:,i)./GMC_tl(:,1);
        ratio(i).GMCrespd  = GMC_tl(:,i)./GMC_tl(:,i-1);
        %%%%
        for j = 1:length(R_tcor)
            if ratio(i).GMCrespd(j) <= 1
            Psi_tl(j,i) = Psi_D_tl(j,i);
           else
            Psi_tl(j,i) = Psi_W_tl(j,i);
            end
        end
        %%%%
    end

    %%%% export data corresponding to locations of Decagon point sensors
    %%%% installed at Bionics
    R_tcor_tl_field_pt_sens = R_tcor_field_tl(Pt_sensor_cell_ID,:);
    VMC_tl_pt_sens = VMC_tl(Pt_sensor_cell_ID,:);
    Psi_tl_pt_sens = Psi_tl(Pt_sensor_cell_ID,:);
    GMC_tl_pt_sens = GMC_tl(Pt_sensor_cell_ID,:);
    Sr_tl_pt_sens = Sr_tl(Pt_sensor_cell_ID,:);

    % write to excel file
    filename1 = 'ERT_Pt_sensor_locs.xlsx';
    xlswrite(filename1, R_tcor_tl_field_pt_sens,1)
    xlswrite(filename1, VMC_tl_pt_sens,2)
    xlswrite(filename1, Psi_tl_pt_sens,3)
    xlswrite(filename1, GMC_tl_pt_sens,4)
    xlswrite(filename1, Sr_tl_pt_sens,5)
    xlswrite(filename1, dates,6)
    %%%%
```

```
   fid = fopen(sprintf('%s_ts%d.vtk', filename(1:end-4), i), 'w');
   fprintf(fid, '# vtk DataFile Version 3.0\n');
   fprintf(fid, sprintf('%s\n', filename));
   fprintf(fid, 'ASCII\nDATASET UNSTRUCTURED_GRID\n');
   fprintf(fid, sprintf('\nPOINTS %d double\n', length(PP)));
   for j = 1:length(PP)
    fprintf(fid, '2.8\t%f\t%f\n', PP(j,1), PP(j,2));
   end
   fprintf(fid, sprintf('\nCELLS %d %d\n', length(corners{1,1}),
length(corners{1,1})*5));
   for j = 1:length(corners{1,1})
      fprintf(fid, '4\t%d\t%d\t%d\t%d\n', IDP1(j)-1, IDP2(j)-1, IDP3(j)-1,
...
          IDP4(j)-1);
   end
   fprintf(fid, '\nCELL_TYPES %d\n', length(corners{1,1}));
   fprintf(fid, '%d ', ones(length(corners{1,1}),1)*9);
   fprintf(fid, '\n\nCELL_DATA %d\n', length(corners{1,1}));
   fprintf(fid, 'SCALARS Resistivity double 1\nLOOKUP_TABLE default\n');
   fprintf(fid, '%f ', R_tcor_field);
   fprintf(fid, '\nSCALARS Res(log10) double 1\nLOOKUP_TABLE default\n');
   fprintf(fid, '%f ', log10(R_tcor_field));
   fprintf(fid, '\nSCALARS Ratio(res) double 1\nLOOKUP_TABLE default\n');
   fprintf(fid, '%f ', ratio(i).TCres);
   fprintf(fid, '\nSCALARS Ratio(log10(res)) double 1\nLOOKUP_TABLE
default\n');
   fprintf(fid, '%f ', ratio(i).TClogres);
   fprintf(fid, '\nSCALARS Ratio(res_prev) double 1\nLOOKUP_TABLE
default\n');
   fprintf(fid, '%f ', ratio(i).TCrespd);
   fprintf(fid, '\nSCALARS GMC double 1\nLOOKUP_TABLE default\n');
   fprintf(fid, '%f ', GMC_tl(:,i));
   fprintf(fid, '\nSCALARS Ratio(GMC) double 1\nLOOKUP_TABLE default\n');
   fprintf(fid, '%f ', ratio(i).GMC);
   fprintf(fid, '\nSCALARS Ratio(GMC_prev) double 1\nLOOKUP_TABLE
default\n');
   fprintf(fid, '%f ', ratio(i).GMCrespd);
   fprintf(fid, '\nSCALARS Porosity double 1\nLOOKUP_TABLE default\n');
   fprintf(fid, '%f ', por_C);
   fprintf(fid, '\nSCALARS VMC double 1\nLOOKUP_TABLE default\n');
   fprintf(fid, '%f ', VMC_tl(:,i));
   fprintf(fid, '\nSCALARS Sr double 1\nLOOKUP_TABLE default\n');
   fprintf(fid, '%f ', Sr_tl(:,i));
   fprintf(fid, '\nSCALARS Suction double 1\nLOOKUP_TABLE default\n');
   fprintf(fid, '%f ', Psi_tl(:,i));
   fprintf(fid, '\nSCALARS SuctionD double 1\nLOOKUP_TABLE default\n');
   fprintf(fid, '%f ', Psi_D_tl(:,i));
   fprintf(fid, '\nSCALARS SuctionW double 1\nLOOKUP_TABLE default\n');
   fprintf(fid, '%f ', Psi_W_tl(:,i));
   fprintf(fid, '\nSCALARS St_Dev double 1\nLOOKUP_TABLE default\n');
   fprintf(fid, '%f ', st_dev);
   fprintf(fid, '\n\nPOINT_DATA %d\n', length(PP));
   fclose(fid);
   waitbar(i/length(t), h)
end
close(h)

end
%%%%%%%%%%%%%%%%%%%%%%%%%%%%%%%%%%%%%%%%%%%%%%%%%%%%%%%%%%%%%%%%%%%%%%%%%%%%

function[daysofyear, filelist] = getDaysOfYear(directory)
```

```
%getDaysOfYear.m reads in .dat files in given directory and returns vector
%containing days of year defined by filenames in directory
%--called by xyz2D_GMC.m

listing = dir(directory);

counter = 0;
for i = 1:length(listing)
    if listing(i).isdir ~= 1
        if strcmp(listing(i).name(end-3:end), '.dat') && ...
                strcmp(listing(i).name(1:2), '20')
            counter = counter + 1;
            filelist(counter,1).name = listing(i).name;
            daysofyear(counter) = datenum(listing(i).name(1:end-4), 'yyyy-
mm-dd') - ...
                datenum(str2num(listing(i).name(1:4)), 1, 1)+1;
        end
    end
end


end
```